# Piezoelectric printing and pre-corrosion: Electrical Resistance Corrosion Monitors for the conservation of heritage iron

A Thesis submitted to the University of Manchester for the degree of

Doctor of Philosophy (PhD)

in the Faculty of Engineering and Physical Sciences

**2014**

**James P. Dracott**

**School of Materials, Corrosion and Protection centre**

# Contents

**Thesis Word Count: 73,990**

# List of Figures

## Chapter 4: Treatment and storage of archaeological iron



## Chapter 5: Electrical Resistance Corrosion Monitors

## Chapter 6: Experimental Materials and Methodology

## Chapter 7: Experimental Results

## Chapter 8: Discussion

## Chapter 9: Conclusions

-

# List of Tables

## Chapter 6: Experimental Materials and Methodology



## Chapter 7: Experimental Results

## Chapter 8: Discussion

## Chapter 9: Conclusions

-

# List of Abbreviations

| | |
|---|---|
| ANOVA | Analysis of Variance analysis |
| CD | Compact disc |
| Dpi | Dots per inch |
| EN | Electrochemical noise |
| ERCM | Electrical resistance corrosion monitors |
| PC | Personal Computer |
| PCB | Print circuit board |
| ppm | Parts per million |
| QCM | Quartz crystal microbalance |
| $R^2$ | The square of the Pearson product moment correlation coefficient |
| RH | Relative humidity |
| SEM | Scanning electron microscope/microscopy |
| TOST | Two one sided tests |
| XRD | X-ray Diffraction analysis |

# Abstract

The University of Manchester

James P. Dracott

Doctor of Philosophy

'Piezoelectric printing and pre-corrosion; Electrical Resistance Corrosion Monitors for the conservation of heritage iron'

December 2014

Heritage iron objects are ubiquitous in the archaeological assemblage, frequently covered in thick, chloride-containing corrosion layers. Accurate monitoring of their corrosion rates is crucial for continued preventative conservation. Measurement of storage environment corrosivity is commonplace for a variety of metals, but use un-corroded metal as a proxy. Corrosion rates measured will be different with respect to chloride infused and corroded artefacts and data recovered difficult to reconcile with actual artefact degradation. Electrical resistance corrosion monitors have been applied to create proxy corrosion rates for various metals in industry, academia and heritage contexts. Pre-corrosion of such has previously been shown to be effective in providing altered corrosion rates in atmospheric environments. This research sets out to develop and refine the manufacture of such probes, to create sensors which will corrode similarly to chloride infested heritage iron and can be used in heritage environments to inform conservation strategy.

Photochemical milling was used to create ERCM. Salt loading on the surface was achieved through a piezoelectric inkjet printer, shown to be adept at printing a variety of salt concentrations (down to 4μg/cm) and patterns, with consistency, regularity and reliability. The results of the methodology show the potential of the technique for future salt loading and corrosion testing applications. Corrosion products were grown on the treated ERCM by controlled atmospheric corrosion, shown to create a constant corrosion layer, no significant localised corrosion and good reproducibility. The products formed were shown to be compositionally similar to those found on archaeological iron. The sensors have been tested in both stable and dynamic relative humidity environments, within a test chamber and in ersatz heritage type, desiccated boxes. The corrosion rates and reactions were compared to those of heritage iron.

Pre-corroded ERCM are shown to give similar corrosion rates to heritage iron; though direct calibration was not possible, further research is likely to remedy this. The final outcomes of the project are discussed with respect to the closeness of fit between proxy and archaeological iron corrosion rate data, benefits and shortcomings of the system and how the corrosion data affects current conservation understanding. It is concluded that the technique can detect corrosion rates down to storage relative humidity levels, provides more accurate representation of corrosion rate for chloride infested iron objects than bare metal ERCM, can be calibrated to suite specific objects and could represent excellent cost-effectiveness for environmental monitoring in heritage institutions.

# Declaration

No portion of the work referred to in the thesis has been submitted in support of an application for another degree or qualification of this or any other university or other institute of learning.

# Copyright Statement

i. The author of this thesis (including any appendices and/or schedules to this thesis) owns certain copyright or related rights in it (the "Copyright") and s/he has given The University of Manchester certain rights to use such Copyright, including for administrative purposes.

ii. Copies of this thesis, either in full or in extracts and whether in hard or electronic copy, may be made **only** in accordance with the Copyright, Designs and Patents Act 1988 (as amended) and regulations issued under it or, where appropriate, in accordance with licensing agreements which the University has from time to time. This page must form part of any such copies made.

iii. The ownership of certain Copyright, patents, designs, trade marks and other intellectual property (the "Intellectual Property") and any reproductions of copyright works in the thesis, for example graphs and tables ("Reproductions"), which may be described in this thesis, may not be owned by the author and may be owned by third parties. Such Intellectual Property and Reproductions cannot and must not be made available for use without the prior written permission of the owner(s) of the relevant Intellectual Property and/or Reproductions.

iv. Further information on the conditions under which disclosure, publication and commercialisation of this thesis, the Copyright and any Intellectual Property and/or Reproductions described in it may take place is available in the University IP Policy (see http://documents.manchester.ac.uk/DocuInfo.aspx?DocID=487), in any relevant Thesis restriction declarations deposited in the University Library, The University Library's regulations (see http://www.manchester.ac.uk/library/aboutus/regulations) and in The University's policy on Presentation of Theses

# Acknowledgements

Before we begin, I must take a moment to thank those people without whom this research may well have devolved into an exercise in banging one's head against the wall. Apologies for anyone who might have been left out; my eternal thanks must go to everyone who helped, assisted or otherwise buoyed me through the last four years.

I must express my deepest gratitude to my supervisor, Professor Stuart Lyon for his guidance, teaching and, above all, patience throughout the process. The atmosphere in which to do research, the freedom to play with ideas and the tolerance and support when said ideas failed utterly were hugely valuable. Also to Professor David Watkinson and Dr. Melanie Rimmer from Cardiff University, whose exceptional hard work and vision on their end of the project, contribution of ideas and provision of apparatus and guidance made much of the research possible.

I am hugely grateful to the Engineering and Physical Sciences Research Council (EPSRC) and the Arts and Humanities Research Council (AHRC), both for funding the research through the Science and heritage program, and the former for giving me a job afterwards.

Massive plaudits must go to the technical staff of the Centre for Corrosion and Protection at Manchester University, particularly Simon, Steve, Malcolm, Harry and Paul, whose forbearance in the face of streams of niggling questions and requests for (possibly fictional) tools was admirable. Special thanks to Derrick Bradshaw from the school of Electrical and Electronic engineering, who guided me through photochemical milling, and whose advice profoundly affected the finished methodology. Thanks to Andrij Zadoroshnyj and Garry Harrison, for training and guiding me through Raman spectroscopy and X-ray diffraction, respectively.

To my lab mates and colleagues, James, Giancarlo, Philip, Fred, Ash, Zoi and Alice, huge thanks and appreciation: It would have been a lonely lab without you all and at times the lively debate may even have devolved into useful science.

Love and thanks to my family; Paul, for putting me through most of the education and supporting me for all of it; and Sally, William and Edward, for accepting the fact they lost a brother for four years. And thanks to my mother, Jane, who didn't quite get to see me start the PhD, but was with me through all of it.

Finally, thanks to my wife-to-be, Elly Buttery, for her never-ending support, putting up with the mania, saying yes, and learning far more about heritage iron corrosion products than she ever really wanted to.

For Paul, who won't read it,

For Jane, who never got to see it,

and for Elly, who wishes she hadn't.

# Chapter 1

# Introduction

The material study of humanity's shared past is of huge importance and to the benefit of mankind. From archaeological studies and shared appreciation of heritage national and international identities are formed, reformed and renewed. Studies of the past inform our present and future paths, tell us more about ourselves and even explain or uncover technologies which have never been replicated or bettered. This academic importance is, perhaps unusually, translated into public enthusiasm and, though not mirrored by government spending or large institutional budgets, equates to significant economic importance. In the Anholt nations Brand Index 2009 57% of the 10,000 polled respondents agreed that history and culture were strong influences on their choice of destination [1], placing it as a major factor in holiday location. Oxford Economics puts estimated value of heritage based tourism in the UK at £26.4 billion, supporting 393,000 jobs [2].

For economic and cultural benefit, it is incumbent upon us to preserve our material heritage. The archaeological resource is finite, restricted and non-renewable; when it is gone, it will truly be gone. It can also be highly vulnerable to destruction from natural and man-made alterations in environment and the simple march of time. It is of intellectual, social and economic importance, and the ethical duty of every generation, to preserve our heritage for future generations and maximise the retrieved data.

Within this context, iron is perhaps the most significantly imperilled material. Its past ubiquity and importance is such that it not only represents a large physical portion of the archaeological assemblage and within structural building material, but also a vast informational source. It is also under threat; the susceptibility of iron to corrosion is such that

it will continue to corrode in all but the most controlled of low humidity environments. Furthermore, the existing corrosion layers in which the majority of iron artefacts are clad are often unstable and suffused with chloride, decreasing the humidity at which corrosion can occur, increasing the rate of corrosion and creating products which cause stresses and physical damage to the object [3-4]. Removal of these layers can severely damage artefact integrity and cause loss of archaeological information about the original artefact, including pseudomorphic remnants of additional attached materials, metallographic processes, artefact morphology and the post-depositional processes of a particular site [5]. The State of English Heritage Collections report 2010 [6] identified iron as their most damaged material, mostly attributed to environmental failures and poor monitoring. The loss of these objects represents a clear threat to our understanding of the past and the permanent loss of part of the world's heritage.

Steps are being taken to prevent and control this gradual erosion of the archaeological iron collection. Active removal of corrosive species within corrosion layers [7], the encouraged growth of passivating corrosion products [8] and the control and management of storage to reduce humidity and increase stability in an artefact's atmospheric environment [9-10] are all employed within the heritage sector. These methodologies will not be completely effective, especially where resources are insufficient to treat the problem fully. Chloride cannot be completely removed from an artefact and corrosion layers must be left intact to preserve integrity and intellectual value. Continued environmental control is the only way to continue preservation and control further corrosion and degradation.

Increasingly the conservation paradigm in these situations is shifting to controlling and decreasing corrosion rate. Complete prevention is difficult to achieve, due to the fundamentally different corrosion rate, processes and phenomena caused by extant corrosion layers and pollutants. Control and decrease of rate, by comparison, allows conservators, curators and archaeologists to deploy resources according to the importance of an artefact and the cost which this will incur. A vital part of any methodology, therefore, is an understanding of the processes involved and the quantification of rates of corrosion for artefacts in given environments and settings. Direct measurement is near impossible without altering the artefact or corrosion factors, while proxy methods struggle to create similar rates and reactions to environmental change. The complexity has made writing conservation strategy difficult, with applied methodology based around control of environmental corrosivity as opposed to physical damage. This methodology does not allow for easy detection of strategy failure and relies on anecdotal, not empirical evidence.

## 1.1 Evidence-based corrosion monitoring of archaeological iron

'Evidence-based corrosion monitoring of archaeological iron' is a research project, of which this project forms part, run jointly partnership between the *Department of Archaeology and Conservation* at Cardiff University and the University of Manchester *School of Materials*. Part of the AHRC/EPSRC funded Science and Heritage programme, it aims to define and measure the variables which influence the corrosion rate of chloride infested archaeological and historic iron artefacts and develop methods of measuring the corrosivity of standard and specific storage and display environments. The Cardiff arm of the project is performing the first large-scale real-time monitoring of actual corrosion rates of post-excavation heritage iron, linking this data to the chloride content and storage atmosphere. It will also consider the effects which the corrosion causes to the integrity of the objects and the useful lifespan which this will entail. This data will then be used to create a heritage iron corrosion control framework based around predicting corrosion rates in set environments, timescales of preservation, best practice guidelines and resource management.

The Manchester role in this project, reported in this thesis, was proposed to develop the use of pre-corroded Electrical Resistance Corrosion Monitors (hereafter ERCM) for detecting corrosion rates in low humidity environments, such as those found in museum and heritage storage. ERCM have fairly ubiquitous use in monitoring corrosion rates of metals in industrial settings for clean iron, but not for the different corrosion rates and reactions caused by extant corrosion layers and pollutants. Our sensors would be chloride contaminated, develop similar corrosion products to heritage iron, and therefore corrode similarly, in rate and reaction, to heritage iron in similar environments. Previous research by Kapatou and Lyon [11] had already demonstrated the capability of such sensors in returning corrosion rate data in atmospheric environments of stable relative humidity and testing the effect of desalination treatment on the same. Their reactions were used as a proxy for the rates of heritage iron, used to create assumptions as how chloride infested artefacts would react in similar environments.

This study was proposed to take this research further, advancing the technology from feasible to applicable. The monitors are tested in environments previously unexamined by the technology. Creation methodologies have been redesigned to give greater accuracy, repeatability and reliability. A new method of chloride contamination has been developed and tested in order to create corrosion products and corrosion rates more similar to heritage iron in identical conditions. We will also show how the sensors might be used in both an expanded and existing heritage conservation strategy, and how their generated results can be used to examine associated heritage iron.

## 1.2 Research aims and Objectives

In order to achieve improved ERCM for use as proxy corrosion monitors for chloride infested heritage iron, a number of key aims and associated objectives were identified:

1. To improve and standardise the production of iron foil electrical resistance corrosion monitors to allow their mass production with high accuracy.
   a) To investigate changes to the ERCM design to achieve optimal accuracy, lifetime and functionality
   b) To investigate alternative procedures for creation oof these patterns in metallic iron
   c) Refine such processing into a technique both repeatable and accurate, which would allow for mass production of the sensors within the budgetary constraints of the heritage sector.

2. To develop a technique for chloride contamination and controlled corrosion of a metallic iron surface, which could be applied to our ERCM surface
   a) Specifically, to alter and adapt a piezoelectric printer to allow for deposition of precise amounts of chloride, building on previous research by Schindelholz and Kelly[12]
   b) To create a methodology for chloride salt deposition of specific amounts over a specific pattern.
   c) To examine the limits and methods of the inkjet printing methodology to determine an optimal level of deposition.
   d) To combine the contamination with controlled atmospheric corrosion to create corrosion products similar to those found on heritage iron (notably akaganeite, goethite, lepidocrocite and magnetite), examined using compositional techniques and microscopy.
   e) To use the methodology to deposit known and repeatable levels of chloride on the probes' surface, create similar corrosion products of similar thickness for each sensor, which create similar reactions in similar environments, to each other and to heritage iron.

3. To test the corrosion sensors to investigate their accuracy, data reproducibility and limits of detection at controlled, low-relative humidity values comparable to those used in the heritage sector.
   a) To place the ERCM in a circuit which allows high accuracy readings of metal loss, evaluated for consistency, accuracy and flexibility.

b) To use the ERCM to monitor metal loss of the sensors in atmospheric chambers held at stable low relative humidity levels within the range used in conservation environments.
c) To use the ERCM to monitor metal loss of the sensors in atmospheric chambers programmed to have changing relative humidity environments, to examine the sensors' reaction in terms of reaction time, corrosion rate and consistency.
d) To use the ERCM to monitor metal loss of the sensors in heritage type desiccated storage boxes

4. Compare the results of our sensors to those of un-corroded ERCM and actual archaeological iron, and use this knowledge to suggest a methodology for their use in the heritage sector.
   a) Use the measurements of corrosion levels to suggest corrosion models and kinetics of the ERCM for stable and dynamic relative humidity results.
   b) Compare the corrosion rates with anecdotal kinetics and rates of heritage iron, and corrosion rates of actual artefacts monitored by the Cardiff University team, to evaluate similarities in rate and reaction and suggest calibration or alteration of their results to provide better proxy corrosion rates.
   c) Use the data gained to compare with alternative corrosion monitoring and passive conservation techniques, to build a methodology for the use of the sensors as part of a wider heritage iron conservation strategy.

During the course of the research, additional results allowed further examination of the inkjet printing methodology as a tool for future corrosion testing and salt deposition. While not specific aims of the project, the usefulness of these results and the applicability of such a discussion to the validity of our own manufacturing process make them appropriate for inclusion in this thesis and as part of further discussions for approaches to the study of corroded artefacts.

## 1.3 Thesis layout:

In this first chapter we have set out the aims and predications of our research and outlined how we initially approached the stated scientific and engineering challenges achieving our goals would present.

Chapters 2 to 4 set out a literature review of previous research in the area. The extent of this review has been designed to cover the corrosion products, processes and phenomena that will lead to the iron corrosion products evident in the archaeological record; the corrosion phenomena we might expect on such iron; the environments in which we should expect

heritage iron to be found, and therefore our sensors to operate; and the monitoring methods previously used or applicable to heritage iron, allowing comparison and evaluation of conflicting or complementary methodologies. Chapter 2 details the basics of iron corrosion and the corrosion products it will produce, providing evaluation of their presence in archaeological contexts. Chapter 3 examines the pathways of iron production, subsequent corrosion during its useful lifetime and the continuing corrosion experienced in its current environments; to reflect on the variety of corrosion processes, rates and reactions we might expect from any given heritage iron assemblage. Chapter 4 will examine the existing conservation methods applied to heritage iron, to evaluate to environments used for storage and which the ERCM must operate, changes in corrosion products and phenomena from active treatments which may alter corrosion rates, and alternative methods of monitoring, to provide benchmarks and alternatives for our own methodology.

Chapter 5 will examine and explain ERCM themselves, detailing their theory, methodology and past usage. Previous use for monitoring heritage metals is documented. In addition, a brief overview of the methods used for pre-corrosion are mentioned, to evaluate the methods available to achieve controlled corrosion.

Chapter 6 provides the methodology for our experiments, including discussions of alternatives and the way in which our approach developed and was refined. Importance is given to the inkjet printing methodology, as it is likely the development of the methodology itself and how it might be adapted and reused will be as important as its deposition results.

Chapter 7 presents the results of our methodologies, including: results of probe fabrication; chloride levels and form from inkjet printer deposition; observations of the pre-corrosion methodology and alterations of chloride levels, optically, using microscopy and compositional techniques; and corrosion loss and rate data from the various environments in which the probes were exposed and monitored.

Chapter 8 will discuss the results of the study in relation to previous work and its potential for the future. The inkjet printer methodology is evaluated and compared to alternatives. The results of the sensor thickness loss readings are discussed for all environments, including what they mean for the corrosion dynamics, differences between sensors and environments and validity of corrosion rates derived. These are further examined in relation to archaeological iron, both anecdotal and the Cardiff results, and potential uses within the heritage sector are suggested. Future directions for similar academic research are identified.

Finally, Chapter 9 will sum up the conclusions of this research. A bibliography is provided, with each chapter numbered separately.

# Chapter 2

# Iron Corrosion:

# Mechanisms and Products

This chapter will detail the basis of iron corrosion, including the thermodynamics, mechanisms and types, and the solid corrosion products which these form on iron.

## 2.1 Metallic Corrosion

Corrosion is an electrochemical process resulting in dissolution of metal and the deposition of more thermodynamically stable products [1]. It comprises oxidation of metal to positive ions at anodic sites, balanced by the production of electrons or negative ions at cathodic sites, connected by a conducting electrolyte. The anodic processes can be defined as the transfer of metallic atoms to hydrated ions and electrons into solution according to equation 1.

$$M \rightarrow M^{X+} + Xe \qquad \textbf{[Eq. 2.1]}$$

Where M is the elemental metal and x is the number of electrons evolved and positive charge obtained [2]. This is balanced by cathodic reactions, maintaining electro-neutrality. Specific cathodic reaction will depend on chemical and electrical properties of the ambient electrolyte. Dependant on pH, these reactions will comprise reduction of either oxygen or the metal itself, or the evolution of hydrogen (Table 2.1). The reactions are redox and result in

the transformation of a metallic substrate into (predominantly) oxides, hydroxides and aqueous salts.

| Reduction process | pH | |
|---|---|---|
| | Acidic | Neutral/Base |
| Oxygen reduction | $O_2 + 4H^+ + 4e^- \rightarrow 2H_2O$ [Eq. 2.2] | $½O_2 + H_2O + 2e^- \rightarrow 2OH^-$ [Eq. 2.3] |
| Hydrogen evolution | $2H^+ + 2e^- \rightarrow H_2$ [Eq. 2.4] | $2H_2O + 2e^- \rightarrow H_2 + 2OH^-$ [Eq. 2.5] |
| Metal reduction | $M^{x+} + Ye^- \rightarrow M^{(x-Y)+}$ [Eq. 2.6] | |

**Table 2.1:** Possible cathodic reactions in corrosion cells, dependant on pH [1]

### 2.1.1 Corrosion Thermodynamics

The likelihood of the above reactions relies on the thermodynamic value of the system, described by the Gibbs free energy (G). The net release of free energy, ΔG, associated with a chemical reaction can be expressed by equation;

$$\Delta G = -nFE \qquad \textbf{[Eq. 2.7]}$$

Where n is number of electrons, E is the overall electrical potential and F is Faraday's constant [3]. The electrical potential of the system comprises the combined potentials of the anodic and cathodic reactions; the reducing potential of the cathode added to the oxidising potential of the anode. When overall potential is positive, the value of free energy is negative. Therefore, an electrochemical couple can form without exterior applied voltage, hence metal ions will be released and corrosion occurs [3]. Where ΔG is negative, the reaction will release energy and may occur spontaneously, dependant on the activation energy required. If ΔG is equal to 0 (the system is in equilibrium) or positive (final energy state is higher), corrosion will not occur [4]. In corrosion, ΔG is negative; it is not necessary to apply a current to create these reactions.

Each electrode potential gives a measure of reaction likelihood; the more reactive and prone to corrosion a metal, the more negative its standard potential. Any surface subject to a conducting environment will spontaneously adopt a characteristic charge, depending on the overall chemistry. The charge causes nearby molecules to preferentially orientate, creating a space-charge capacitive layer known as the Helmholtz layer (Figure 2.1). In the absence of absolute values, electrode potentials are quoted against a standard electrode, usually a half cell in which the hydrogen reaction takes place (Standard Hydrogen Electrode, hereafter SHE). For iron, the standard potential is -0.440V vs. SHE (Table 2.2). This value can be used

to consider under what conditions iron will corrode and place iron within the electromotive series to determine what will happen when it is coupled with another metal; the metal with the lowest or most negative potential will corrode preferentially.

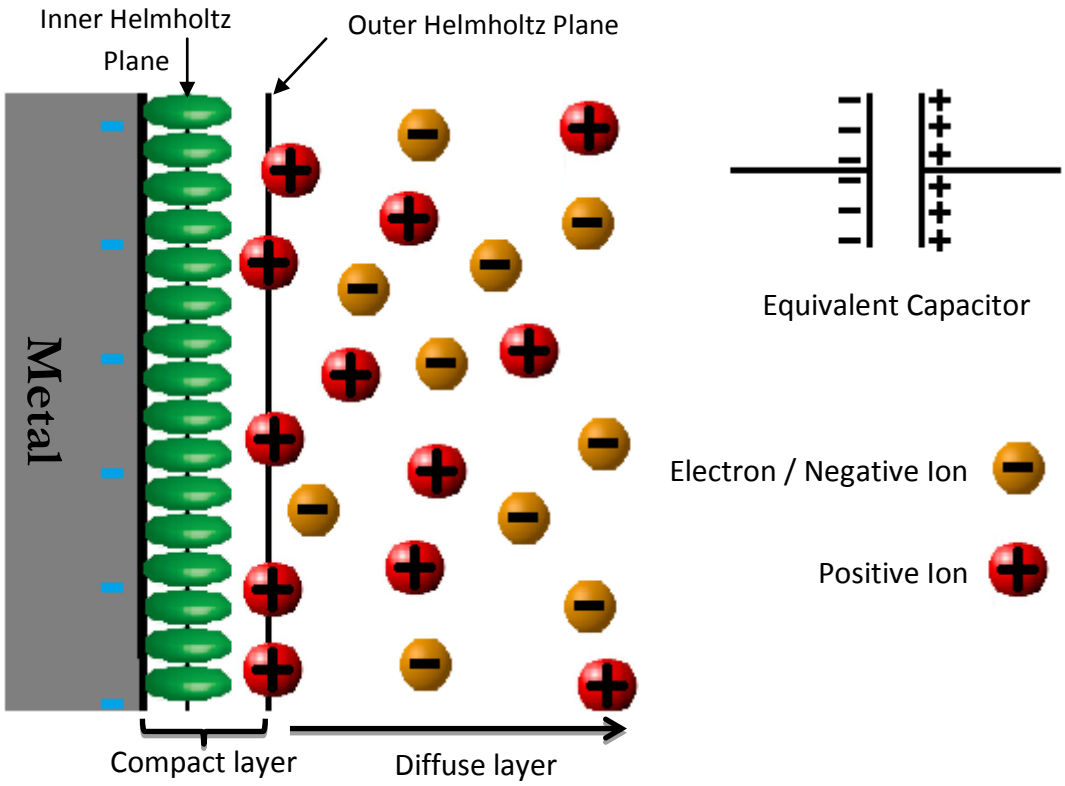


**Figure 2.1:** Surface structure of the metal as an electrode (after [1])

| Metal | Reaction | Standard Potential vs. SHE |
|---|---|---|
| **Gold** | $Au^{3+} + 3e^- = Au$ | 1.498 |
| **Silver** | $Ag^+ + e^- = Ag$ | 0.8 |
| **Copper** | $Cu^{2+} + 2e^- = Cu$ | 0.337 |
| **Lead** | $Pb^{2+} + 2e^- = Pb$ | -0.13 |
| **Tin** | $Sn^{2+} + 2e^- = Sn$ | -0.14 |
| **Nickel** | $Ni^{2+} + 2e^- = Ni$ | -0.26 |
| **Iron** | $Fe^{2+} + 2e^- = Fe$ | -0.44 |

**Table 2.2:** Electrode potentials of the typical heritage metals in order of galvanic potential [2]

Corrosion rates depend on the electrode kinetics of the partial reactions occurring within the corrosion cell. There is a linear relationship between the metal dissolution rate at a given potential and the current density of the partial anodic reaction.

$$V_m = \frac{i_{aM}}{nF} \qquad \textbf{[Eq. 2.8]}$$

Where $V_m$ is the dissolution rate, $i_{aM}$ is the current density at the anode, n is the number of electrons exchanged and F is the Faraday constant [3]. Reactions comprise a series of progressions from one polarity to another; the overall corrosion rate is controlled by the slowest reaction in the sequence.

### 2.1.2 Corrosion types

| Corrosion type | Description |
|---|---|
| **Crevice** | Stagnant electrolyte in crevices in metal act to create anodic sites within to cathodic sites on the exposed metal surface where anions are prevalent. [5] |
| **Erosion** | Occurs where the electrolyte is in motion, especially containing additional gas or solid phases, wearing away and removing corrosion products, creating pitting, crevices and roughness to increase overall corrosion. [6] |
| **Galvanic** | Two galvanically different metals are connected in corroding conditions, turning the more active into an anode and the other to a cathode. |
| **Intergranular** | A form of galvanic corrosion between grains of a metal caused by variance of chemical composition. Attacks grain boundaries. [5] |
| **Pitting** | Occurs as a hole in a passivating corrosion layer which burrows into the metal creating higher concentrations of electrolyte within. [7] |
| **Thermogalvanic** | Galvanic corrosion created by a temperature gradient into a metal system, the hotter element acting as anode. [5] |
| **Stress Corrosion cracking** | The brittle failure of a metal due to corrosion. Caused by loss of ductility. Cracks occur along the tensile component stress [8] |
| **Corrosion fatigue** | Stress Corrosion cracking caused by cyclic applied stress. [9] |

**Table 2.3:** Physical corrosion processes in non-uniform conditions

These corrosion models above describe a homogenous and chemically uniform surface on which both cathodic and anodic reactions occur at separate sites. Other physical circumstances will create additional corrosion mechanics, summarised in table 2.3. Build up of solid corrosion products will affect the corrosion system, created through metal

dissolution; the transfer of metal ions into solution; the combination of the ions into new chemicals in solution; and the precipitation of the insoluble solid corrosion products [10].

## 2.2 Iron Corrosion

Iron corrosion obeys the rules described by the steps for general corrosion outlined above**.** The initial process comprises the oxidation of metallic iron to Ferrous ions (Iron (II), $Fe^{2+}$) at anodic sites (Equation 2.9) [11, 12] in the presence of water. Ferrous ions are released into the electrolyte, forming a hexa co-ordinated complex (Equation 2.10)

$$Fe \leftrightarrow Fe^{2+} + 2e^{-} \qquad \text{[Eq. 2.9]}$$

$$Fe_{(s)} + 6H_2O_{(l)} \rightarrow [Fe(H_20)_6]^{2+}_{(aq)} + 2e^{-} \qquad \text{[Eq. 2.10]}$$

This reaction is balanced by reduction at cathodic sites, generally through either the reduction of oxygen (Equation 2.11) or hydrogen (Equation 2.12) [12].

$$O_2 + 2H_2O + 4e^{-} \leftrightarrow 4OH^{-} \qquad \text{[Eq. 2.11]}$$

$$2H^{+} + 2e^{-} \leftrightarrow H_2 \qquad \text{[Eq. 2.12]}$$

Reaction 2.5 occurs only when sufficient concentrations of $H^{+}$ions are present; in strongly acidic conditions below pH 4. The majority of corrosion processes will be provided with sufficient ambient oxygen and water to proceed primarily through reaction 2.4.

Where reactions 2.11 and 2.12 occur together, the products combine to form insoluble ferrous hydroxide, ($Fe(OH)_2$).

$$Fe + \frac{1}{2}O_2 + H_2O \rightarrow Fe(OH)_2 \qquad \text{[Eq. 2.13]}$$

This is normally further oxidised to form Ferric hydroxide ($Fe(OH)_3$) (Equation 2.14), by the presence of Ferric ions, ($Fe^{3+}$), created by the continued oxidation of ferrous ions (Equation 2.15).

$$Fe(OH)_2 + \frac{1}{2}O_2 + H_2O \rightarrow 2Fe(OH)_3 \qquad \text{[Eq. 2.14]}$$

$$Fe^{2+} \leftrightarrow Fe^{3+} + 2e^{-} \qquad \text{[Eq. 2.15]}$$

Ferrous and ferric ions continue to interact with the electrolyte chemistry, forming additional corrosion products, dependent on factors including pH, redox potential, oxygen concentration, and concentration of other ionic species within the electrolyte and the thickness, structure and chemistry of extant corrosion layers [13].

Figure 2.2 shows a Pourbaix, or potential-pH, diagram; the graphical representation of the thermodynamic equilibrium states of a system [3]. It illustrates the conditions within which specific species of iron have the lowest free energy state (thermodynamically stable) for given Electrode potential (generally given versus SHE) and pH of a system. The graph is divided by lines of equilibrium, derived by the Nernst equation to determine the equilibrium point between two species. On either side of the line one species will be predominant and reactions will tend towards creating that specific species over others [14]. Additional factors, such as temperature, concentration of different chemical species (especially ligands) and pressure will create separate diagrams based on set levels of these conditions.

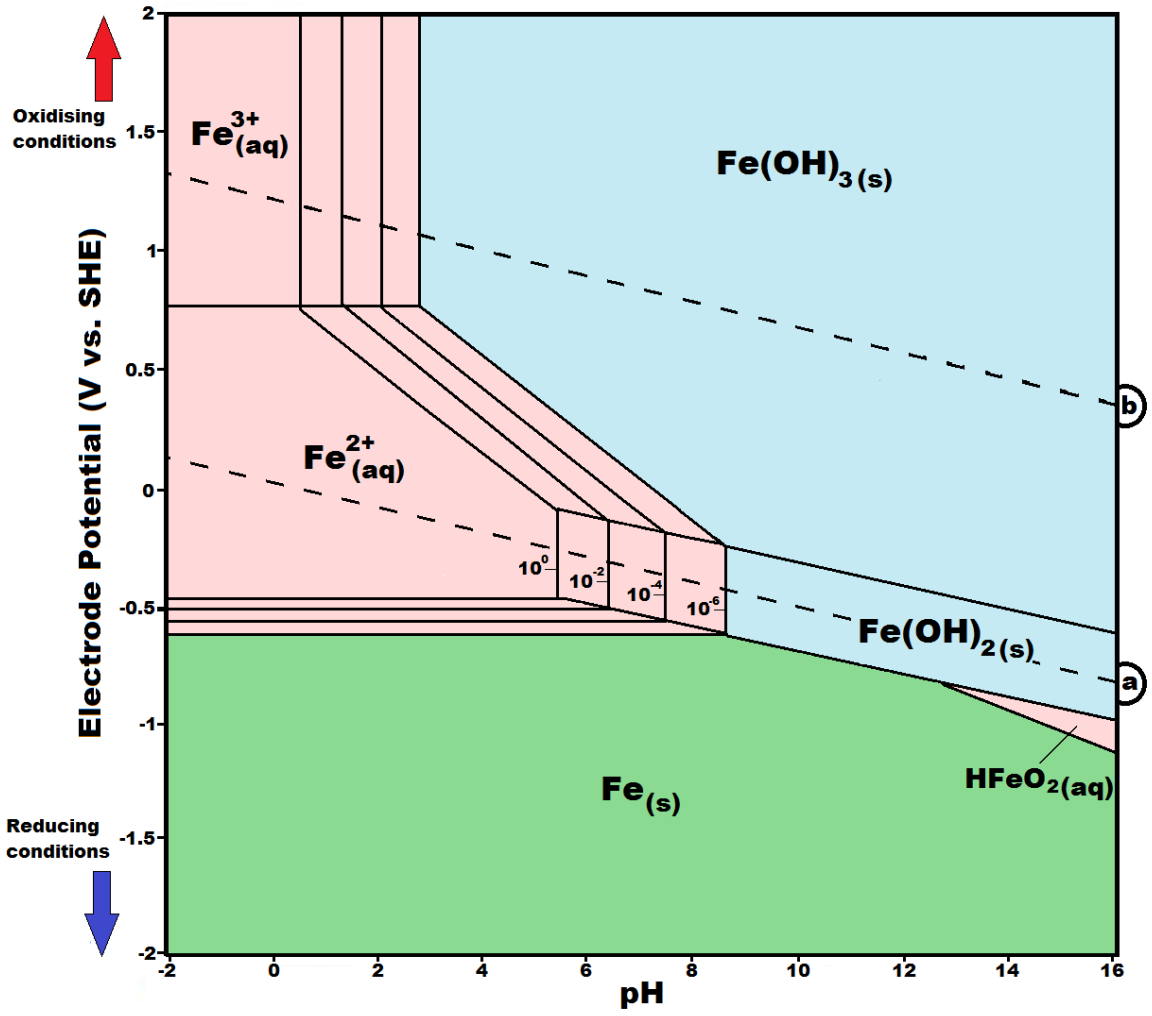


**Figure 2.2:** Potential-pH ('Pourbaix') diagram for iron at 25°C considering hydrated oxide forms [14]

Figure 2.2 shows the system for iron and water at 25°C. The diagram is split into regions of thermodynamic stability; corroding, passivating or immunity. In the green 'immunity' region iron is in an equilibrium state; no corrosion will occur as iron tends to reduction. Above this iron will corrode, producing predominantly the species labelled. The red 'corroding' region represents soluble ionic products, leading to a build-up of ferric and ferrous compounds in an

aqueous state. In the blue 'passivating' region, the created products are insoluble. These build up and deposit on the metal, preventing electrolyte-metal interactions and inhibiting further metal dissolution. 'a' and 'b' on the diagram delimit the stability region for water. Below line 'a' the conditions will be so reducing that water will be reduced and hydrogen reduction will occur until all water is used up. Similarly above line 'b' oxygen evolution will occur, precluding any further rise in oxidising conditions. [14].

Potential changes over time lead to build up of insoluble species, depositing as corrosion products. Type of precipitate can change on an instant to instant basis according to those factors listed above.

## 2.3 Corrosion Products of Iron

Many of the products of iron corrosion will be formed only under specific conditions and will not be common amongst iron artefacts from the archaeological record. Others will not be precipitated, existing only within the electrolyte surrounding the artefact or within moist pores in corrosion layers [10]. Corrosion products previously reported on archaeological artefacts are listed in Table 2.4. They can be divided into ferrous and ferric oxides, ferrous oxyhydroxides, and complexes containing chlorides, carbonates, phosphates and sulphates. Below we will consider the occurrence of each of these products on archaeological iron, their structure and their effect on corrosion rates.

### 2.3.1 Goethite ($\alpha - FeOOH$)

Goethite is one of the most common corrosion products found on archaeological iron [15], usually formed either as an end-product of the transformations of the less stable products, such as ferrihydrites and other amorphous phases [16], or through slow oxidation in highly aerated electrolytic environments. Generally found close to the metal-corrosion product interface [15], over time it often becomes the predominant corrosion product within a corrosion matrix.

| Product | | Formula | Crystal Structure | Colour | Electrical Resistivity |
|---|---|---|---|---|---|
| **Goethite** | | α-FeOOH | Orthorhombic | Yellow - Brown | Insulator |
| **Akagéneite** | | β-FeOOH | Monoclinic | Red - Brown | Insulator |
| **Lepidocrocite** | | γ-FeOOH | Orthorhombic | Orange | Insulator |
| **Magnetite** | | $Fe_3O_4$ | Cubic | Black | Conductor |
| **Hematite** | | α-$Fe_2O_3$ | Hexagonal (rhombohedral) | Red or Black | Insulator |
| **Maghemite** | | γ-$Fe_2O_3$ | Cubic | Brown | Semiconductor/ insulator |
| **Ferrous hydroxychloride** | | β-$Fe_2(OH)_3Cl$ | Orthorhombic | Colourless-pale green | No information |
| **Siderite** | | $FeCO_3$ | Hexagonal | Yellow - Brown | Insulator |
| **Sulphur containing phases:** | Greigite | $Fe_3S_4$ | Cubic | Blue - Black | Half metal conductor |
| | Mackinawite | $Fe_{1.01-1.08}S$ | Tetragonal | Yellow - Brown | Semiconductor |
| | Pyrite | $FeS_2$ | Cubic | Yellow | Diamagnetic semiconductor |
| | Pyrrhottite | $Fe_{0.8-1}S$ | Monoclinic | Yellow - Brown | Conductor |
| | Rozenite | $FeSO_4.4H_2O$ | Monoclinic | Green | No information |
| **Phosphate containing phases** | Vivianite | $Fe_3(PO_4)_2.8H_2O$ | Monoclinic | Dark blue or White | Insulator |
| | Strengite | $FePO_4.2H_2O$ | Orthorhombic | Pink | Insulator |

**Table 2.4:** Summary of corrosion products reported on archaeological iron and their properties

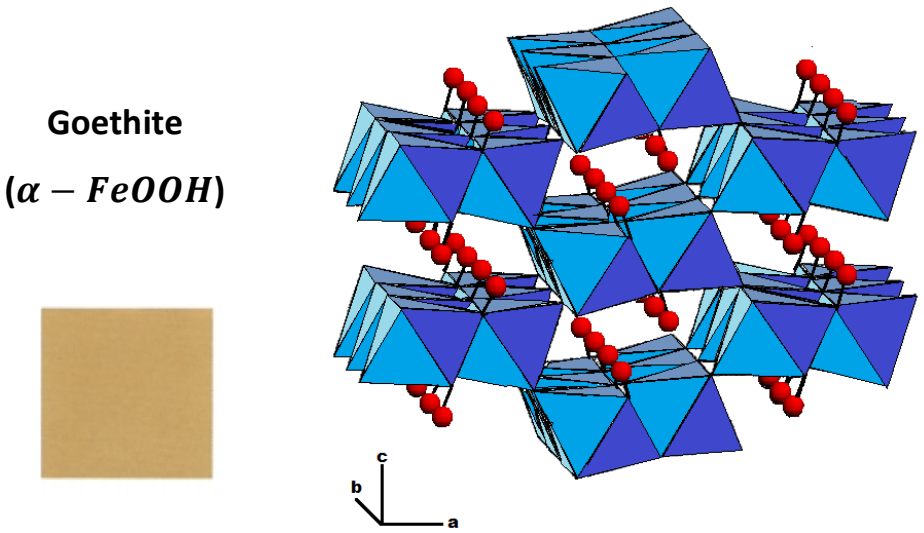


**Figure 2.3**: Standard colouration and crystal structure of Goethite, showing tunnel structure (adapted from [17;pp.xxii & 17])

It occurs as a brown crystalline concretion of varying shade. It is non-magnetic and relatively noble, being the most stable of the four polymorphs of ferric oxyhydroxide, (FeOOH) [18], two more of which are discussed below. Its crystal structure is orthorhombic (figure 2.3) with a tunnel structure. Crystal size is dependent on conditions: Larger crystals are formed by either the presence of anions within the formation environment [19] or through Ostwald-ripening (a dissolution/precipitation process which causes older corrosion layers to display larger crystals than younger) [20].

Goethite build up is considered to reduce corrosion rate, creating an insoluble barrier between the environment and the metal surface, preventing oxygen ingress. It is non-conductive, and will not allow the passage of ions for electrochemical corrosion. However, Goethite has been shown to be capable of adsorbing hydrogen ions onto its surface in small quantities (between 0.2 and 0.6 wt. % [21, 22]) which can have an effect on subsequent corrosion rates.

### 2.3.2 Lepidocrocite ( $\gamma - FeOOH$)

Lepidocrocite is extremely common on archaeological iron corroded in atmospheric [23, 23] or terrestrial environments [15, 25]. It is formed through the rapid aerated oxidation of ferrous ions and green rusts [26: p.359]. When atmospherically deposited, it is found close to the metal surface as the first formed stable corrosion product [17]. Conversely, studies by Wang et al. [27] have shown simulated soil corrosion to exhibit primary lepidocrocite concentrations in regions with poorer oxidation; more aerated regions producing goethite. These phenomena can be explained by its lower thermodynamic instability; under oxidising

conditions it will gradually convert to goethite. Therefore, areas with a lack of oxygen will, over time, present higher concentrations of lepidocrocite than the well aerated regions.

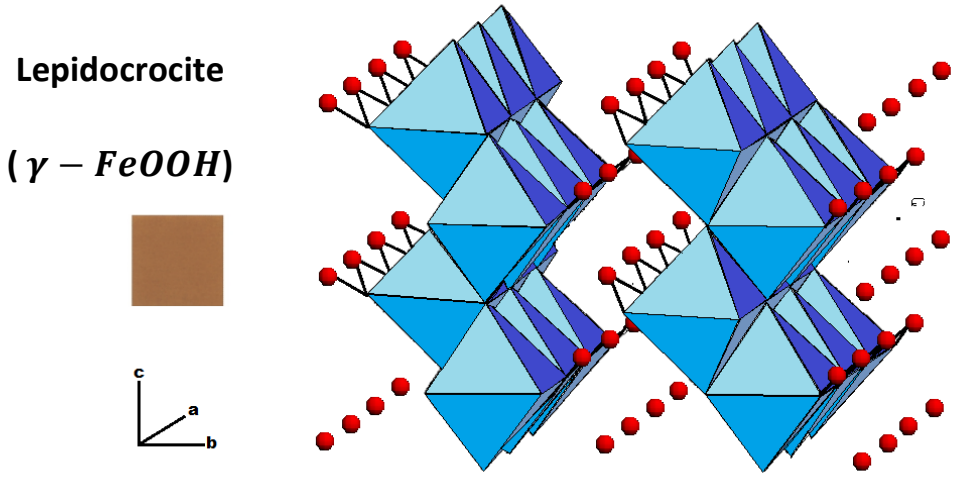


**Figure 2.4:** Colour and structure of Lepidocrocite (adapted from [17;pp. xxii & 19])

Lepidocrocite shares many of the properties of goethite, but is less stable. It is Orthorhombic but, unlike Goethite, has a layered cubic close-packed structure (figure 2.4). It ranges in colour from red through to a blackish brown.

Lepidocrocite is a considered to have non-protective properties. In an atmospheric environment, with sufficient ferrous ions, its reduction to magnetite or goethite [20] can have the effect of acting as a cathodic reaction, promoting metal dissolution [27]. The mineral is also semi-conductive, which may allow additional pathways between anode and cathode and therefore increase the rate of corrosion of an artefact [17].

### 2.3.3 Akaganeite ($\beta - FeOOH$)

Akagéneite is found on chloride polluted iron samples and as such is common on heritage and archaeological iron. It has been suggested that chloride ion concentrations greater than 2 Molar are a prerequisite for its formation [28]. However, experimental results would suggest it can be produced down to 1.6M of chloride, comprising the sole corrosion product above 3.2M [29]. Its creation will also be influenced by the concentration of ferrous ions; low concentrations will not allow the creation of the intermediate products required for akaganeite production. It has been suggested that it can also be created where there no obvious sources of chloride ions, through the vaporous phase of hydrochloric acid [30].

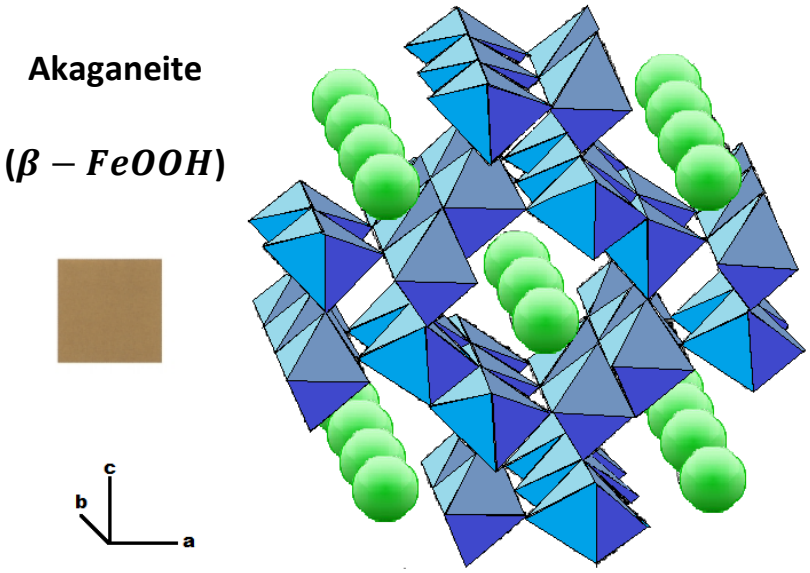


**Figure 2.5:** Colour and crystallography of Akaganeite, illustrating the tunnel structure and enclosed halogen ions (green spheres) (Adapted from [17;xxii & 20]

The exact structure of akaganeite is disputed. With the exceptions of observations by Bland et al. [31] and DeGrigny et al [32], akaganeite is always found with significant levels of chloride, both free and adsorbed on the surfaces of the crystal structure. The exact amount of chloride (or other ions) incorporated is disputed, though it is agreed that 0.25-0.5mmol/mol is a minimum to maintain its stability [33]. Typical accepted values range from 2-7mol% [17], though Watkinson and Lewis [30] have suggested that while synthetic akaganeite may reach 17% chloride ion content, natural values will range from 0.3-5%. Its overall chemical formula has thus been characterised: $FeO_{0.833}(OH)_{1.167}Cl_{0.167}$. [34]. It can have a number of different crystalline structures depending on the formation conditions [17, 35], based around a tunnel structure with a body-centred cubic arrangement (figure 2.5) and crystal sizes between 0.1 – 1 μm. At a pH of greater than 2, crystals will not be well formed and above pH 6 will not be formed at all. This has been attributed to additional protonation of akaganeite in these conditions, allowing the incorporation of chloride ions, crucial to its structure [34-5]. Its crystallography and structure make the mineral less dense than goethite and lepidocrocite [17].

Akaganeite is the least stable of the common oxyhydroxides and its properties are such that it can accelerate corrosion rate. The crystals are also highly hygroscopic; water will easily become adsorbed to its surface [36] (though not within the tunnel structure [34]). This is confirmed at low relative humidity, where water adsorption occurs faster than desorption [21, 30]. Akaganeite can also transform to non-chloride containing phases, through dissolution/re-precipitation to Goethite in acidic conditions [37] and hematite in neutral and alkali pH [18], both without intermediary products and limited only by the availability of

$OH^-$ ions [13]. In addition, solid state transformations to goethite [38], magnetite [39] and hematite [40] have been observed. This has a twofold effect on corrosion: The changed volume can cause cracking through internal stresses on other corrosion products and chloride may be released, accelerating corrosion rate (see chapter 3).

### 2.3.4 Magnetite ($Fe_3O_4$)

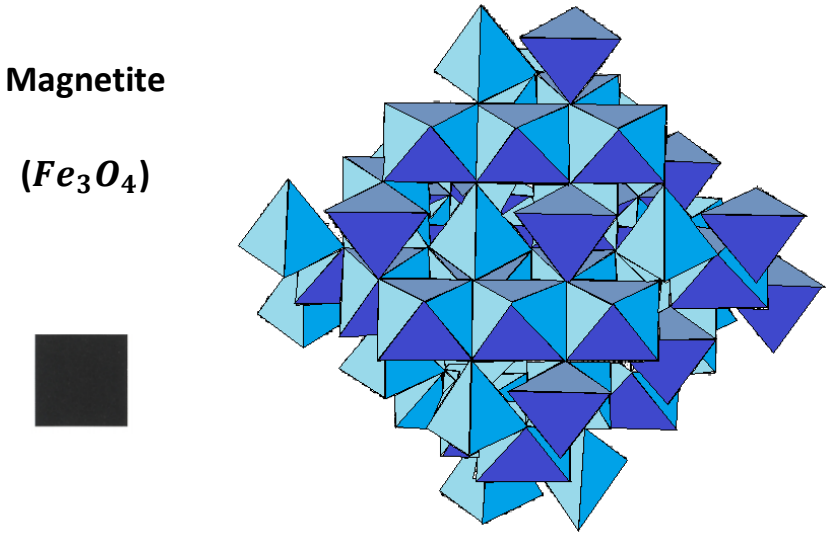


**Figure 2.6:** Colour and crystal structure of Magnetite (adapted from [17; xxii & 33])

Magnetite is the most stable corrosion product of those expected to be present on heritage iron. It forms under less aerated conditions than goethite, and from slower oxidation than that of lepidocrocite [17]. It can generally be found deep within corrosion layers, close to the metal-oxide interface, where oxygen is limited. Part of the Spinel family of minerals, with an inversed spinel structure, it crystallises into a cubic system around a tight packed lattice of ferrous and ferric ions (figure 2.6). It has some magnetic properties, is denser than ferric oxyhydroxides and occurs with a variety of crystal forms dependant on conditions [13]. It can be non-stoichiometric and incorporate other divalent cations from available metals (which will change its properties).

Magnetite is seen as passivating. It is very insoluble, especially in relatively neutral pH conditions. With sufficient oxygen it will slowly oxide to Maghemite (see below), but the process is slow and can be prevented by overlaying corrosion layers. Under these conditions it forms compact thermodynamically stable layers just above the metal surface, preventing further electrochemical reactions occurring [41-2].

### 2.3.5 Hematite ($\alpha - Fe_2O_3$)

For archaeological objects, hematite is mostly associated with cremation or burnt soil contexts [13]. As one of the most stable of all iron's corrosion products, requiring a positive ΔG for formation, it will generally be formed by de-hydroxylation of the oxyhydroxides in high temperature conditions. This reaction can occur both in solution, above 85°C [18], and as solid state thermal transformation [43] at above 270°C (Equation 2.9).

$$2\alpha - FeOOH \rightarrow \alpha - Fe_2O_3 + H_2O \qquad [2.9]$$

Garcia [44] suggests that it is also possible for goethite to form hematite at temperatures as low as 70°C when subjected to an acidic medium. It has also been suggested that, it may form from excess ferrihydrite, ($Fe_2O_3 \cdot 0.5H_2O$) in soils [45] or a dissolution/precipitation reaction of akaganeite [46].

Hydrated hematite has very similar properties to goethite. It has the same hexagonally close packed structure (figure 2.7), though is denser at 5.26g/cm$^3$, composed of alternating layers of cations and oxygen atoms, with only two thirds of the cation groups filled. It has a passivating effect. While it is an n-type semiconductor, it has a high resistivity and dense structure which prevents electrochemical transfer. It has been suggested that hematite is one of the prime components of the initial passivating layer formed on steel in oxidising conditions [47], though the structure is too small to characterise it.

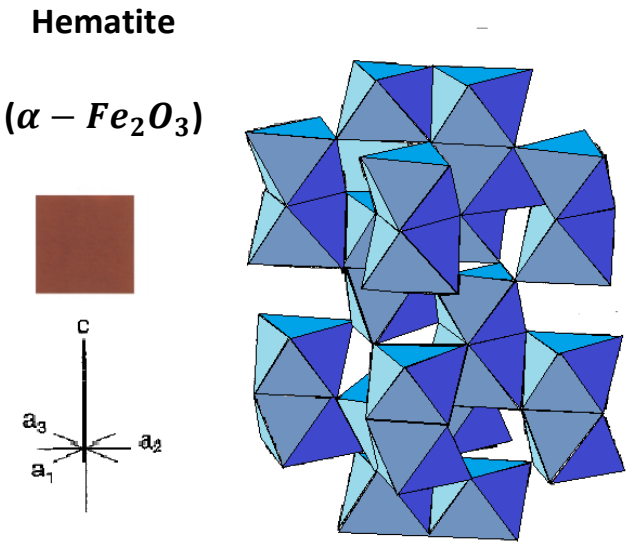


**Figure 2.7:** Colour and crystal structure of Hematite (adapted from [17; xxii & 30])

### 2.3.6 Maghemite ($\gamma - Fe_2O_3$)

Maghemite is mostly found in small quantities in the porous structure of artefacts from buried contexts and from weathered soils themselves. Its formation has been linked to a combination of pollutants in the ambient environment and the alloying of metallic iron leading to areas with increased potential within corrosion layers [15, 48]. It may also incorporate from weathered magnetite in the soil matrix itself [17]. In heated contexts, for example where a burning event has occurred, it can be created by goethite transformation in the presence of large amounts of organic material [49] and lepidocrocite dehydration in temperatures in excess of 260°C [17].

Maghemite has the same as cubic lattice structure as magnetite, but has vacancies in its structure, corresponding to a lower level of ferrous ions. It is less stable than magnetite, but shares its magnetic properties [17]. It is very passivating, especially in low pH environments in which it is slow to dissolve and more passivating than hematite or magnetite [37]. It has been associated with the high corrosion resistance of weathering steels, forming small compact crystals to block electrochemical pathways [48].

### 2.3.7 Ferrous hydroxychloride ($\beta - Fe_2(OH)_3Cl$)

There is debate around the existence of ferrous hydroxychloride on archaeological iron. It will only form in conditions with a chloride ion concentration greater than 1.5M, or 20% by weight, and a pH of 4-6 [50]. In oxidised environments, ferrous hydroxychloride will transform into either akaganeite or goethite. Therefore it is likely that its proportions will be higher in newly excavated, untreated iron. It has been argued by Turgoose [22] that it occurs only as intermediate products in iron corrosion and will not be deposited. This is supported by Foley [51], who believes that ferrous complexes occur as intermediate products in neutral solutions, only occurring within pits and crevices. However, more recent research lead by Réguer has used synchrotron X-ray absorption spectroscopy [52] and XRD and Raman spectroscopy [53] to demonstrate its presence on recovered subterranean iron, occurring as layers of less than 20 microns thick at the metal-oxide interface. It has also been found on an artefacts in a marine context [54] and, possibly, in conjunction with akaganeite in architectural iron in outdoor atmospheric environments [16].

β-Ferrous hydroxychloride is the pure iron form of the mineral Hibbingite, though there is discussion as to whether this or another crystallography should be defined as such [55]. It is clear that the hexa-rhombohedral structure, with a cubic close- packed array of anions, appears to be predominant in corrosion products. It is fairly soluble in a neutral to alkali pH.

Ferrous hydroxychloride is stable and passivating in anoxic environments. In normal atmospheric environments it will either transform into akaganeite, which accelerates corrosion [54], or goethite with disassociated or adsorbed chloride [52]. It may also oxidise into green rust, which may redeposit as lepidocrocite.

### 2.3.8 Other Products

In addition to those corrosion products above, others have been identified in previous studies of archaeological iron objects. However, they are deemed by this author to be too rare or unlikely to be considered here in depth.

North and Pearson [56] identified iron oxychloride (FeOCl) as a major component of marine iron corrosion, but later research has refuted this [57]. It is thermodynamically unstable at natural temperatures in water, so is highly unlikely to be present in solid form in naturally corroded artefacts. Its tendency to oxidise to ferric oxyhydroxide in all but the most anoxic of conditions make it even more unlikely to be found on a stored artefact.

Green rusts are suggested to be key transformative products in archaeological iron corrosion, but are so unstable it is doubtful they would be observed in stored assemblage. They are characterised by mixed iron valences and anion content and are generally regarded as intermediate corrosion products, swiftly converting to other minerals [58]. It is believed that akaganeite formation will only occur in the presence of chloride containing green rust. For sulphate containing green rust, high sulphur content is thought to oxidise to goethite, with lower concentrations favouring lepidocrocite [48].

Siderite is a carbonate iron corrosion product with much debated properties of passivation. It has been observed as a corrosion product on archaeological iron from anoxic soils, within completely mineralised artefacts from oxygenated soils and from marine contexts [59]. The exact method of its deposition is unknown, but has been linked to the activity of bacteria in anoxic environments. It has been shown to build up as a protective scale, though without significant adherence [50]. While it is a semiconductor, it has very high resistivity, so will not function as a cathode for corrosion. When oxygen is readily available, it is unstable and known to dissolve below pH 6 ± 1 [60]. Therefore, in normal atmospheric conditions, a constant, thick layer of thick siderite is considered to be passivating, while a non-continuous layer may actually promote corrosion. Its prevalence on archaeological iron may be greater than previous studies have shown, but it is unlikely that it will be significantly represented in the archaeological iron assemblage as a whole: Formation conditions limit it to certain sites and prolonged storage is likely to remove its passivating properties and allow it to oxidise to more stable forms of corrosion product.

Sulphides within the corrosion cell can cause sulphur containing corrosion products. On recovered iron artefacts this can be caused by sulphur reducing bacteria (*Vibrio Desulfuricans*) in anaerobic soils and marine contexts, and from atmospheric pollution. This has been classified as a process of mackinawite ($Fe_{1+x}S,\ x = 0.01 \rightarrow 0.08$) deposition, followed by transformation to pyrite, ($FeS_2$), greigite, ($Fe_3S_4$), and even pyrrhotite, dependant on the oxidising conditions [61]. All of these have been reported on archaeological finds [62-4]. Stability and passivating effects of mackinawite mean artefacts covered in sulphurous corrosion products are likely to be well preserved and exhibit low corrosion rates [65]. The scarcity of archaeological sites, at least in the UK, in which the conditions will be right for their formation means that they can be discounted for the purposes of this study.

Phosphate containing corrosion products are associated with archaeological finds from highly organic and waterlogged sites with low levels of sulphur. Decomposition of bone and animal tissues provide high levels of phosphate in soils. In reducing conditions, or in oxidising conditions in the presence of at least $10^{-3}$ mol/litre complex phosphate compounds, Vivianite ($Fe_3(PO_4)_2 \cdot 8H_2O$) can form [66]. This creates a very stable layer of corrosion products, reducing corrosion rate. When exposed to an oxidising atmospheric environment it will be unstable and oxidise to other forms, such as strengite ($FePO_4$). While it has been reported on archaeological finds, and has been noted to create excellent preservation conditions, the formation are too rare for the products to be plentiful in the archaeological record.

# Chapter 3

# Archaeological Iron:

# Metallurgy and Corrosion

The stability and frequency of the above discussed corrosion products within specific corrosion layers, and the presence of any additional transient products, will be dependent on the environment in which they are found, combined with their own structure and hydration [1]. The formation conditions are dependent on the potential of the electrolyte-metal system, the additional chemicals and pollutants provided by the ambient environment and the properties of the metal, existing corrosion layers and other bodies present. In order to predict the types and proportions of corrosion layers we may expect on archaeological iron, we must review the forms of iron which we will expect to see in the archaeological record, mechanisms of corrosion in different environments encountered during artefact lifetime and how these factors can interact.

## 3.1 Archaeological Iron

Iron comprises about 5% of the earth's crust, its various ores are plentiful on every continent and its advantages as a material have made it fundamental to the growth and form of human civilisation [2]. The difficulty of extracting the metal from its constituent ores and its relative impracticality in pure form has meant that its modern structure, metallurgies and chemistry have only developed over the last few thousand years. Until relatively recently, historical iron was extremely heterogeneous; up to the industrial revolution, iron from the same source, and

even from within the same smelt, could have radically different structural and chemical properties. These differences not only altered how iron was used, but impact on how fast it will corrode and the corrosion products and phenomena we are likely to encounter. While these differences will be slight compared to those of the environment of corrosion, they will change characteristics within the corrosion layers which will change how we might conserve an object, the corrosion mechanisms which may be present and the reactions we can expect once an artefact is recovered.

### 3.1.1 Naturally Occurring and Accidental Iron

While iron ores themselves have been in use as pigmentations since the middle Palaeolithic [3], the technological difficulty of iron extraction meant that it was not until relatively late that iron was produced by separation from its ore. Prior to this iron occurred rarely in metallic form, largely used in small quantities as a luxury and ceremonial material.

Meteoric iron, extracted from naturally occurring Nickel-Iron meteorites, is found across the near east, china and northern Europe. It is not known how early in humanity's progress this resource was used, but early examples include tube shaped beads from the Egyptian cemetery at Girzeh dating to 3300 BCE and Chon dynasty iron blades from China, dating to around 1000 BCE [4], with widespread examples across Eurasia by the fifth century BCE. Mostly represented as jewellery and ornamental weapons [5], the metal was typically worked by cold hammering and very low temperature annealing, preserving its original metallurgy and chemistry. It is characterised by its high nickel content, around 5-12%, and one of two structures; hexahedrites consisting primarily of kamacite (alpha-iron, ferrite, 5-7% nickel), known as Neumann lines, and octahedrites consisting of lamellae of kamacite and taenite (gamma-iron, austenite, 30-50% nickel), known as Widmanstatten structures [6-7]. Additional trace elements, including cobalt, copper, gallium, germanium, phosphorus and carbon, are recorded but rarely make up more than 2% of the metal [7].

The nature of this iron is such that it can have unpredictable corrosion rates. If largely unworked, the extant layering structures of low-nickel kamacite and high nickel taenite create a series of tiny galvanic cells [6]. This leads to preferential corrosion of the kamacite and destruction of artefact integrity. Similar galvanic cells can also be formed when the iron contains a high abundance of phosphates, with preferential corrosion of the nickel bearing phases over prismatic rhabdite $(Fe, Ni)_3P$ crystals. However, when substantially worked or heated, the iron may lose some of its original structure, becoming more homogenous. In this case, the high nickel content can provide some corrosion protection [8]. The nickel itself can either be found within corrosion layers built up around the artefact or leached away into surrounding environments [6]. The reported corrosion products for meteoric iron are the

same as those found on smelted cast iron, albeit with the original impurities present within the corrosion layers.

Naturally occurring terrestrial, or Telluric, iron bears great similarity to that of celestial origin, but has a typical Nickel content of only 0.5-4% [5]. It occurs in large quantities only in Western Greenland. While geologically much studied, it is limited to around eleven examples, of Inuit bone-handled knives, in European museums and a smattering more worldwide [6, 9]. It has been characterised to corrode similarly to modern cast iron, with similar rates in atmospheric conditions and identical corrosion products.

### 3.1.2 Early Iron extraction

Iron extracted from ore is known from the third millennium BCE. Oxidised copper ores, smelted for copper extraction from as early as 4000 BCE, maximise their yield when rich in ferric minerals, so such ores were used preferentially as technology developed. As furnaces developed to hotter temperatures, around 1200°C, iron oxides were reduced and deposited as small flakes in the upper reaches of the furnace, well away from the molten copper at the base. These flakes were constantly melted and precipitated, building up into solid lumps of iron which could be removed. The paucity of the material made it a high value fabric for the creation of status artefacts. Examples from Mesopotamia date from 2800-2500 BC, Anatolia from 2500 BC and the Levant, Africa and India by the end of the same century [10-11]. This fairly pure iron has similar properties to natural metallic iron, though with lower nickel content [11]. It was worked similarly and will corrode similarly.

The earliest industrially produced iron shares many of its properties with that produced within the earlier cottage industries. The Hittites are traditionally regarded as the first true iron smelters, using iron preferentially for tools and exports from the middle of the 14$^{th}$ century BC [11]. The high price of the metal at the time likely encouraged further experimentation and, whether the technology was exported to other civilisations or was developed independently, the process was adopted sufficiently for iron production to have spread to much of the eastern Mediterranean by the end of the 12$^{th}$ century BC [12].

Iron was produced, and would be in much of the world until the industrial revolution, by a bloomery [11]. Earliest bloomery furnaces comprised a pit insulated with ceramic bricks or stones, in which charcoal was burned. Openings in the base allowed air to enter the furnace, either naturally or, later, by bellows [11, 13]. Charcoal and small chunks of iron ore were introduced to the top of the furnace once sufficient heat had built up. The high temperature and concentration of carbon monoxide within the furnace removed water from the ore and reduced the iron oxides to particles of metallic iron. These particles agglomerated and built up below the air intake, protected from oxidation by a build-up of glassy slag, in a sponge

form known as a bloom [13]. This iron was poor quality, its high carbon content making it too brittle for tools and weaponry.

The current paradigm in archaeology speculates a shortage of bronze affected the eastern Mediterranean during the last two centuries of the second millennium BC. The need for a replacement metal, coupled with the spread of iron extraction technology following the break-up of the Hittite empire [13], saw iron take a new importance in the region, and subsequently across the world. This increased demand lead to major advancements in the refining process, still using the bloomery furnace. Iron was reheated after removal (typically to above 1,250°C) and worked on a forge. Repeated procedures of beating and folding removed much of the slag, which could then itself be re-smelted. This process creates a form of wrought iron [15]; very low carbon iron with about 3% slag inclusions and low levels of other impurities (dependant on the ore and other foreign objects present in the furnace). The quality, chemistry and metallurgy of this metal were highly variable, not only between regions and times, but from separate smelts in the same forge.

Advances in smithing and conscious preferential selection of iron types drove continued improvement [15]. The first of these processes was likely staged annealing, reheating the metal at temperatures below 720°C (in an open hearth for example), and then warm hammered. This altered the lamellar pearlite structure to spherical particles within the metal. Slow cooling will create a more malleable and softer metal, easier for working [11,16]. Quenching appeared soon after; a process of slowly heating the iron in an open hearth before quickly cooling, often by plunging it into water. This transformed the pearlite into the finer, granular martensite, leaving the iron harder, though also more brittle [11, 17-18]. Cold forging or additional reheating, a basic form of tempering, can reduce this brittleness and increase the strength and useful characteristics of the metal [18]. Quenching is mentioned in Homer's *Odyssey*, so was certainly well known by the 9$^{th}$ century BC and may date as far back as the 12$^{th}$ century BC [11].

Changes to the produced metal mean that the iron at this time starts to take on steel like characteristics. The precise chronology of these discoveries is not known, but the amount of carbon within the produced iron was being deliberately manipulated for specific items by the end of the 10$^{th}$ century in the eastern Mediterranean and Middle East [18]. Sponge iron can reabsorb carbon as it passes through the furnace, creating mild steels. Increased levels of carbon in shaft furnaces lead to accidental steels of up to 1% carbon content [15]. From the evidence, it is also possible that wrought iron was being treated in open furnaces after smelting; both these methods adsorb carbon into the outside of the iron, but only to a thickness of around 1mm [11]. This is of particular note to our studies as it creates a situation where parts of an artefact will corrode at different rates dependant on the part of the bar iron

that it was sourced from. The typical values for wrought iron from the early bloomery smelt and subsequent treatment are between 0.6 and 2% [11].

The corrosion characteristics of early steels, which may make up the majority of heritage iron collections, depend on the amount of carbon and other impurities which are found within the metal itself. Changing technology altered these levels, and therefore the corrosive characteristics of the metal, from one geographic and historic region to another.

### 3.1.3 Crucible steels: ironworking in India

The first true steels arose in around the 3rd century BC in India. Wootz steel, also known as Damascus steel, was a high carbon banded metal containing microcarbides layered around martensite and pearlite matrices [11, 19]. Wrought iron was hot forged to remove impurities and sealed in a crucible furnace with charcoal, various local vegetation and rocks and, later, glass. The high temperatures forced the iron to absorb carbon, reaching a typical content of about 1.5% [19]. This created a very fine steel with very low corrosion rates. The exact origin and methodology for creating this steel has, sadly been lost.

A useful aside for the corrosion scientist would be to consider the iron pillars which appear in India at around 500 AD. The earliest of these is found at Delhi, though the largest and most well-known is the 42 foot long Dhār iron pillar. These pillars are characteristic of ancient Indian iron; containing high levels of phosphorous and trapped fayalitic slag inclusions. The pillars present, despite constant exposure to alternating extremely damp and dry conditions in an exterior atmosphere for over a thousand years, very low levels of corrosion. This has been attributed to the high level of surface passivity which the non-metallic elements have created [20]. Indeed, the high levels of phosphorous impurities contained within Indian iron throughout their history of manufacture of crucible steels, indicate that artefacts which would benefit from corrosion protection were preferentially created from the most resistant alloys. As such, objects from India will often have a much lower corrosion rate than those from other regions of the world, as well as producing phosphorescent corrosion [20], This is indicative of the effect impurities can have on iron and the variation we can expect from differently sourced iron artefacts in historic assemblages.

### 3.1.4 Cast Iron

Cast iron is produced by complete melting of iron to liquid form, then cast in moulds. It is created using a blast furnace with sufficient oxygen intake, reaction bed height and excess carbon to carburize iron to a level of 4%. This allows the formation of liquid cast iron [11] which can be poured into moulds to cast the required shape. Cast iron itself is brittle and

unsuitable for working, though can be decarburised to steel or wrought iron if heated in the atmosphere over a period of days.

Originating in Southern China, the practice had been adopted across the region by the early fifth century BC [21]. By the 1st century BC cast iron was also being melted together with wrought iron to produce steel [11]. It was not introduced on any large scale into the western world until the 15th Century CE (through the demand for cast iron gunpowder weapons). Similarly to the replacement of bronze, it is not sufficient to see this as a simple shift from one technology to the other; wrought iron is still used for a large amount of ironwork today. Instead, from the 15th century onward, especially in the UK, the methodologies used to produce iron vary hugely. The technologies developed over this period include; the blast furnace for the manufacture of pig iron; the finery process for the decarburisation of pig iron; cementation of steel to produce blister steel; the development of a chafery for the manufacture of wrought iron and the invent of puddling furnaces [22-4]. The ultimate result of the increasing technological superiority came with the introduction of the Bessemer process which is still used in iron and steel production today.

### 3.1.5 Effects of Impurities and Technology on Corrosive Characteristics

The effects of the various technologies used to create iron gives the archaeological assemblage enormous heterogeneity, reflected in the corrosion products and rates which will be exhibited. The methods described above, and their associated impurities, are broadly summarised in Table 3.1.

Typically, the most abundant impurity in iron is carbon. It has been shown by Cleary and Greene that higher carbon content in iron will increase corrosion rate [25], though its structure will be of primary importance. In general, smaller iron carbide particles will create a faster corrosion rate. The forms of these particles are different dependant on the technologies employed in the extraction and processing of iron. Tempering quenched steels will produce a very fine dispersion of carbide particles, observed as causing very high corrosion rates [25]. Heat treated annealing has also been shown to increase corrosion rate [26]. Additionally, for marine corrosion, higher carbon levels have been linked to increase corrosion rates in anoxic environments where anaerobic bacteria are present [27]. In cast irons, the inherent carbon will, on corrosion, be deposited as graphite flakes. This has the effect of creating a 'pseudomorph' of the original artefact shape and may also create galvanic cells within the iron [28]. The latter can lead to increased localised corrosion. Similar cells can form between the iron and incorporated fayalitic slags in wrought iron, leading to increased iron oxidation around the inclusions [29]. Typically, older, less worked iron will contain more of these slag crystals; thought it will also depend on the quality of the smith [11].

| Type of iron | | Carbon content | Reported High concentration impurities | Reported Low concentration impurities |
|---|---|---|---|---|
| **Meteoric iron** | | Neg. | 5- 7 % Ni | Si, P, S, Cu, Co |
| **Telluric Iron** | | 0-4% | 1.5-4% Ni | Si, P, S, Cu, Co |
| **Early Bloomery wrought iron** | Untreated | 0.1-0.9%, (Typically less than 0.1%) | Dependent on source of ore. E.g. Ni up to 10% in Greece. | Mn, Si, S, P, Cu, As, Ni, Al, Cr, slag |
| | Treated | 0.4- 1.6% | | |
| | Forged | 1% | | |
| | Carburised | 0.6 – 2%, often as low as 0.2% at the centre | | |
| **Indian Iron** | | 0.1-1.2%, | P ≈ 1% | Mn, Si, S, P, Cu, As, Ni |
| **Crucible Steel** | | 2% | - | S, Mn, Si, P |
| **Cast iron** | | 2.1-4% | Si ≈1-3% | Cr, Mn, Cu, V, Co, As, Al, Ni, P |
| **Wootz steel** | | 1.3 - 1.8 % | 0.1% P | Mn, S, Si |
| **Medieval Wrought iron** | | 0.05-0.9% | - | Cr, Mn, Cu, V, Co, As, Al, Ni, P |
| **Pig Iron** | | 3.5-4.5% | - | Cr, Mn, Cu, V, Co, As, Al, Ni, P |
| **Early "cemented" Steel** | | 0.8-1.8% | - | Cr, Mn, Cu, V, Co, Al, Ni, P |
| **Bessemer steel** | | 0.2-2.1% | High oxygen content | Mn, Ni, Cr, V, W |

**Table 3.1** Summary of Archaeological Iron types by technology and typical chemistries, information taken from [6, 8, 11, 15, 19-20, 30]

Of greater effect on corrosion rates are other present impurities: Higher levels and differing distributions of impurities can make an object more passivating or prone to corrosion. For example, the high nickel Telluric and meteoric irons corrode preferentially in certain areas, causing overall artefact degradation, whereas iron smelted in the early Iron Age in Greece will also have high nickel content, but this will be spread more evenly through the metal, affording high corrosion resistance [8]. The phosphorous content of Indian steels has a similar effect, creating a passivating oxide layer when exposed to the atmosphere [14, 20, 31]. Copper can have a similar effect [32], while levels of Manganese and silicone tend to inhibit corrosion rate [3]

The differences in corrosion rate the above discussion reveals will make characterising metallic archaeological iron difficult. The homogeneity will ensure corrosion rates will depend on the source of the iron artefacts, the technology used in their extraction and production and the time period from which they come. Further research should be prioritised into this area to investigate the overall corrosion characteristics of each iron production technology, ancient iron source and mixture of impurities.

## 3.2 Describing the corrosive lifetime of an iron object.

Throughout the lifetime of an iron object, it can, at any stage, be characterised as inhabiting a certain type of environment; atmospheric, subterranean or marine. For the majority of the historical assemblage, artefacts will have spent their useful life in an atmospheric environment, before being lost in either a subterranean or marine environment. They will subsequently have been recovered and re-exposed to an atmospheric environment. This is not the exclusive path. Some artefacts will never have been removed from an atmospheric environment, either through non-abandonment, being part of an architectural installation or simply by never succumbing to complete burial. Still others will have been moved between two abandonment environments, through the exposure of archaeological sites to erosion or geomorphological activity. It is certain that all iron objects will have started in an atmospheric environment, but the length of time, and therefore the corrosion produced, of this exposure might be limited.

We must consider, therefore, the end corrosion products of each of the environment types and take into consideration that in any assemblage we shall see a cross section of each set of processes, or a combination of those therein.

## 3.3 Atmospheric Corrosion

The process of atmospheric corrosion is governed by the formation of a surface electrolyte, the thickness it attains, its chemistry and the length of time that it is present [33]. This is reliant on factors of both the external environment and the properties of the metal and present corrosion layers themselves. The most significant factors which will affect the rate of corrosion in the atmosphere are the availability of oxygen, water, carbon dioxide and pollutants [34].

### 3.3.1 Initial exposure to air

Prior to atmospheric corrosion, the surface of any ferrous material will undergo a process of dry oxidation. This occurs almost instantaneously and forms an irreversible oxyhydroxide layer [3, 35]. Typically the depth of this oxide layer will be approximately 30nm. It is non-protective and allows water to be adsorbed by the metal surface below the dew point RH (see section 3.4.2). Subsequent to this reaction, no corrosion will occur until an electrolyte is formed on the surface of the metal, allowing the start of redox reactions [36].

### 3.3.2 The formation of an electrolyte

The point at which a liquid layer will form through precipitation or adsorption on the surface of an object is dependent on the Relative humidity of an environment. Absolute humidity is the amount of water present in the air at any given time, measured in grams per cubic metre [37]. Relative humidity (hereafter RH) is the percentage amount of water in the air compared to that of water saturated air at the same temperature [36] (equation 3.1 [38])

$$RH = \frac{Absolute\ humidity\ at\ T°C}{Absolute\ humidity\ of\ saturated\ air\ at\ T°C} * 100\% \qquad \textbf{[Eq. 3.1]}$$

As RH levels increase, so too will the thickness of the electrolytic layer on a metal surface. Assuming a clean, pollutant free surface of the metal, the thickness of the water film will be around a single molecular layer thick at about 20% RH. This thickens as additional hydrogen bonds form between the water molecules [39]. At 100% RH, the atmosphere is, by definition, saturated [36]. The temperature at which this event occurs is known as the dew point and droplets of moisture will occur, often visibly, on the metal surface. At above 65% RH the layer will have thickened to over three monolayers [40-1]. At this point the electrolyte is thick enough to allow the dissolution of ions and electrochemical corrosion can occur. The

'*critical relative humidity'* is the RH at which this film is thick enough to produce measurable electrochemical corrosion reactions. It is determined by the presence of hygroscopic species within the metal, the tendency of the surface layers to form solutions, insoluble corrosion products and pollutants on the surface. Cai and Lyon [42] have shown that even at 95% RH, there will be insufficient water on a clean iron surface for detectable corrosion to occur. The presence of pollutants in the atmosphere (such as sodium chloride (NaCl) and sulphur dioxide ($SO_2$)) will lower the critical RH due to their hygroscopic properties. The RH at which the aerosol forms of atmospheric pollutants convert to an aqueous or mixed solid-aqueous phase, is known as their deliquescence point. For sodium chloride, for example, this RH will remain fairly constant with temperature at 72-75% [43].

Critical RH may also be lowered by extant corrosion products. Capillary condensation can occur at very low levels of RH, in cracks or flaws in the metal or within porous corrosion products. The increased number of van der Waals interactions in a confined space, increasing as the space becomes more confined as governed by the Young-Laplace equation, will cause condensation to occur at lower saturation vapour pressure and therefore at lower RH [41]. Additionally, electrolytic solution can form within insoluble iron compounds, due to the chemical condensation of soluble corrosion products.

For iron and most carbon steels, this means corrosion can be assumed to cease below an RH of 12% [44]. However, above around 75% RH, the rate of corrosion is increased, regardless of the presence of corrosion products or pollutants, as the amount of water is no longer a limiting factor [41].

Of note is the effect that temperature has on RH. A rise in atmospheric temperature can cause a drop in ambient relative humidity, which, as we shall see, will reduce the thickness of the electrolyte on the metal surface, and hence the corrosion rate [39]. However, temperature of the metal itself will increase the thermodynamics of the redox equations. This temperature will be an expression of the atmospheric temperature with temperature coefficient of any given alloy, the positioning of the metal to wind and sunlight, the reflectivity of the metal or corrosion products and the thermal capacity of overall object [36, 39]. As such, the relationship between ambient temperature and atmospheric corrosion rates will not necessarily be linear.

### 3.3.3 The Wet and Dry Corrosion model.

All but the most controlled environments will have constantly shifting relative humidity, causing constantly shifting presence, coverage and thickness of electrolyte layer. The phase during which an electrolyte is present on the surface of the metal, and therefore the phase in which electrochemical reactions can occur, is known as the 'time of wetness' [45]. The

alternation between this phase and no electrolyte presence is known as the 'wet-dry cycle', first modelled by Evans and Taylor [46]. The frequency of these cycles, the duration of each stage and the role of the atmosphere in maintaining the form of the electrolyte govern much of how corrosion will progress, the rate at which it occurs and the form it shall take. An illustration of a wet-dry phase cycles is shown in figure 3.1.

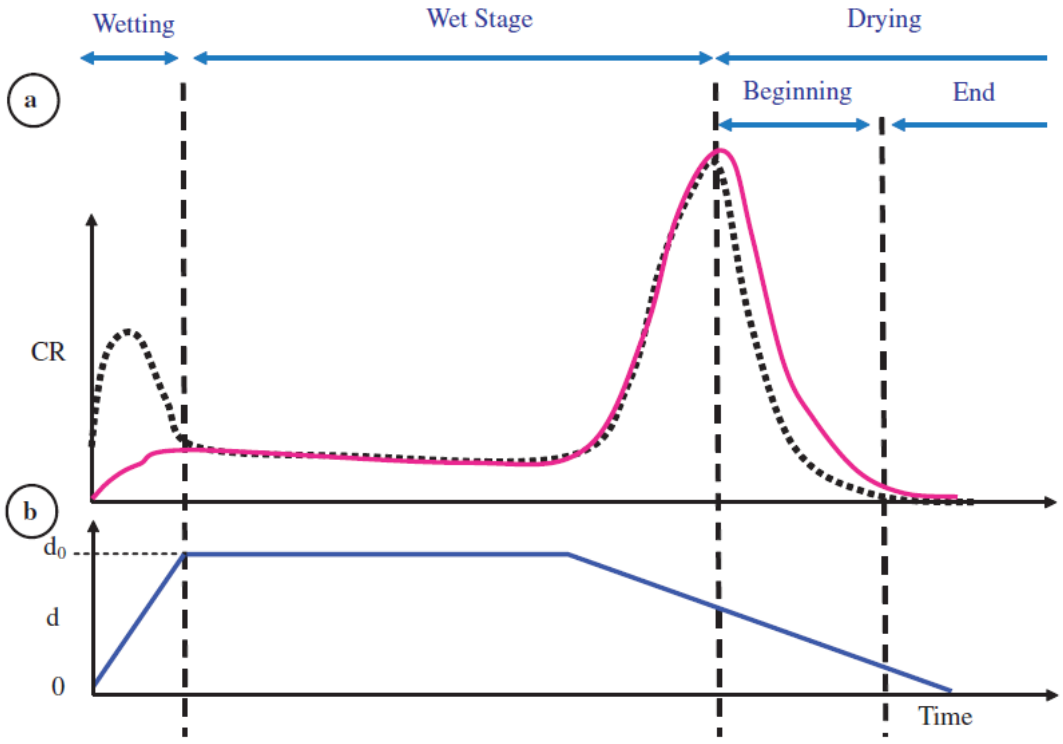


**Figure 3.1:** A Schematic representation of the Wet-dry cycle (from [45: p. 1439]), showing iron (dotted line) and oxygen (pink line) consumption rates. Schematic (b), indicates the variation of electrolyte thickness

3.3.3a Wetting phase

The low thickness of the electrolyte in this phase creates a redox reaction in which iron is dissolved at the anode, balanced in charge by the reduction of ferrous oxyhydroxides to magnetite. It produces a reduced, conductive form of lepidocrocite. An electrolyte of low thickness forms at the surface of the metal. This breaks down the passivity of the iron substrate and polarisation between the metal substrate and the iron oxyhydroxide layer allows redox reactions to begin. It has been shown by Stratmann [47] that oxygen is not consumed during this phase, so does not form the dominant cathodic reaction. The higher oxidation rate of iron over oxygen instead causes the reduction of the more reactive ferric oxyhydroxides present in the initial iron oxidation layer; γ-FeOOH to magnetite [46-9], ferrous hydroxide and ferrous ions and Iron (III) Oxide to Magnetite [50]. These reactions

are balanced by dissolution of iron and the release of anionic ferrous ions. The most prolific and most likely reaction under these conditions will be the reduction of lepidocrocite to a conductive species according to reaction 3.2 [51]

$$\gamma\text{-FeOOH} + e^- + H^+ \rightarrow \gamma\text{-Fe.OH.OH} \qquad \textbf{[Eq. 3.2]}$$

This reaction occurs at the metal interface, creating a reduced lepidocrocite layer which forms a galvanic couple with the iron surface, allowing electrons and hydrogen ions to diffuse through it [45]. Oxygen is prevented access to the metal, further restricting its reduction.

The limiting factor of corrosion rate will be the amount of lepidocrocite available for reduction. The reduction current ($i_\gamma$) can be expressed as equation 3.3.

$$i_\gamma = Fk_{FeOOH}[H^+]a_{FeOOH} \qquad \textbf{[Eq. 3.3]}$$

Where $k_{FeOOH}$ is the rate constant of the reaction, F is the faraday constant, $[H^+]$ the concentration of hydrogen ions and $a_{FeOOH}$ the activity of lepidocrocite on one monolayer in moles per cathodic surface unit [52]. In the case of iron with extant corrosion layers, we can therefore predict corrosion rate in terms of the ratio of lepidocrocite ($\gamma$) over the total amount of corrosion product (e.g. goethite ($\alpha$) and lepidocrocite). This ratio ($\beta$) (Equation 3.3) can be used to calculate the total damage (metal consumed by lepidocrocite reduction, $p_\gamma$) done to the metal in this phase (Equation. 3.4).

$$\beta = \frac{\gamma}{\alpha+\gamma} \qquad \textbf{[Eq. 3.3]}$$

$$p_\gamma = \frac{\beta nes}{2V_{mFeOOH}} V_{mFe} \qquad \textbf{[Eq. 3.4]}$$

Where n is the number of reduced monolayers, e is the thickness of a single monolayer, S is the area of pores per surface unit, $V_{mFeOOH}$ is the molar volume of lepidocrocite and $V_{mFe}$is the molar volume of iron [52].

3.3.3b Wet Phase

This phase is characterised by the presence of a thick, stable electrolytic layer on an object surface. Oxygen may now diffuse into the electrolyte and down to the metal surface and conductive lattice of γ-Fe.OH.OH at the surface of the rust pores [45]. Oxygen begins to reduce at cathodic sites on the lepidocrocite, according to Equation 3.4, facilitated by the excess of ferrous ions within it. The reduction rate is determined by the electron transfer rate

at potentials above -0.2 mV vs. SHE, and the diffusion of oxygen at less anodic potentials [45]. The ferrous ions will pair with counter ions within the electrolyte.

This phase may overlap with the wetting phase; oxygen reduction can occur as soon as lepidocrocite has been reduced, possibly prior to the establishment of a stable electrolyte. Similarly, lepidocrocite reduction can continue, albeit at a lower rate than that of oxygen, when an object is considered to have entered the 'wet' phase.

The damage done during this phase has been characterised to be dependent on the ability of oxygen to reach the cathodic areas [45]. This can be expressed using Fick's Law's to give an equation that will present us with the diffusion of oxygen first through the electrolyte and then through the pores of the rust. This will give us the average depth of oxygen penetration into the rust layer, $\lambda$ (equation 3.5).

$$\lambda = \sqrt{\frac{\varepsilon D_O}{\tau \beta s_a k_{O2}}} \qquad \textbf{[Eq. 3.5]}$$

Where $s_a$ is the surface area of the pores per volume unit, $k_{O2}$ is the rate constant of the oxygen reduction reaction, $\varepsilon$ is the porosity of the rust layer, $\tau$ is the tortuosity of the corrosion layer (the ratio of the diffusivity in the free space to the diffusivity in the solid corrosion product), $\beta$ is defined in equation 2.13 and $D_O$ is the diffusion coefficient of oxygen. We can calculate total damage done to the metal by oxygen reduction ($p_O$) by incorporating Fick's first two laws to give equation 3.6

$$p_O = \frac{\varepsilon}{\tau} \cdot \frac{D_O C_O}{\frac{\varepsilon}{t} d + l + \lambda} * 2V_{mFe} \left[1 - \exp\left(\frac{L-l}{\lambda}\right)\right] \Delta t \quad \textbf{[Eq. 3.6]}$$

Where $D_O$ is the diffusion coefficient of oxygen, $C_O$ is the oxygen concentration at the electrolyte/gas interface, $\varepsilon$ is the porosity of the rust layer, $\tau$ is the tortuosity of the corrosion layer, $V_{mFe}$is the molar volume of iron, $\Delta$t is the duration of the wet phase, d is the thickness of the electrolyte, L is the thickness of the rust layer and l is the average distance through the pores between electrolyte and cathode [45].

The end of the wet phase has an accelerated corrosion rate compared to the start [53]; water loss reduces electrolyte thickness, creating a higher concentration of pollutants and corrosion products. This promotes transport of water through corrosion layers and increases the conductivity of the solution.

3.3.3c Drying phase

As the time of wetness ceases and the electrolytic layer thins, two distinct phases occur. First the evaporation of the electrolyte shortens the diffusion paths of the oxygen ions. This increases oxygen reduction rate at the cathode, in turn increasing the rate of iron oxidation. The loss of water molecules serves to make the electrolyte more concentrated, with corrosion products, ions and pollutants, and more conductive, facilitating the rate of corrosion further [50]. At this point, the γ-Fe.OH.OH present may oxidise to $Fe_3O_4$ or $Fe_2O_3$. This shifts the dynamic of the reaction until the rate of anodic dissolution of metallic iron becomes the limiting factor.

The second stage creates layers of re-oxidised insoluble corrosion layers. The initial phase creates a high concentration of $Fe_3O_4$, $Fe_2O_3$, γ-Fe.OH.OH and $Fe^{2+}$ ions in the electrolyte, along with higher concentrations of feroxyhite ($\delta - FeOOH$), ferrihydrite ($Fe_2O_3 \cdot nH_2O$) and $Fe(OH)_3$ [54-6]. These corrosion products will re-oxidise to form insulating layers of FeOOH which block the anodic sites and decrease the area of conductive lattice, reducing the capacity for anodic activity. The reaction of the oxygen at the cathode also increases the pH of the electrolyte, decreasing the corrosivity of the liquid. The combination of these processes creates a passivating phenomenon. Finally, the remaining electrolyte evaporates from the metal surface, leaving the insoluble corrosion products. This will not always be the case; wet dry cycles can be seen to progress into the drying phase, before regressing back into the wetting or wet phase.

When complete dryness does occur, corrosion ceases and there are no longer electrochemical reactions. Structural change may still occur within the corrosion products, from dry oxidation and through chemical degradation. This will have an impact on their corrosion protection characteristics [45, 47, 53].

### 3.3.4 Corrosion products of the 'wet-dry' corrosion model

The process of wetting and drying leads to the deposition of solid state corrosion products, according to the overall equilibrium equation 3.7 (in the absence of pollutants).

$$4Fe + 3O_2 + 2H_2O \leftrightarrow 4FeOOH \qquad \textbf{[Eq. 3.7]}$$

Solid corrosion products are deposited first as a result of nucleation and then through coalescence of a corrosion layer [36]. The exact manner and proportions of their depositions depend on the species present within the electrolyte. The initial forms of corrosion, especially on carbon steel, create green rusts, which will evolve into the more stable phases. Subsequent

cycles of wetting will react differently depending on the corrosion layers which have previously deposited and the localised potential of the system.

The most common corrosion products found on atmospherically corroded iron are goethite, lepidocrocite and magnetite, along with an amount of amorphous, non-crystalline FeOOH. Magnetite will be deposited at potentials below -0.5V (SCE) from lepidocrocite and below -0.9V (SCE) from goethite [57]. Hematite has also been found in traces in steel rust films by Garcia [58] and attributed to solution transformation of amorphous FeOOH.

In an environment free of pollutants, it is likely that these will be the only stable corrosion products. As has been mentioned, goethite is the most stable of these phases, whereas lepidocrocite will form in the earliest stages of corrosion. The progression of wet-dry phases will facilitate the build-up of the least soluble and most electrochemically stable forms of corrosion product [59]. This is illustrated by analyses of rust layers of exposed iron from Japan [60-1], (Figure 3.2). The makeup of the layers was shown to shift from the most soluble of the products to the least soluble. It can be expected that artefacts present in a heritage collection subject solely to atmospheric corrosion will have significantly higher amounts of goethite.

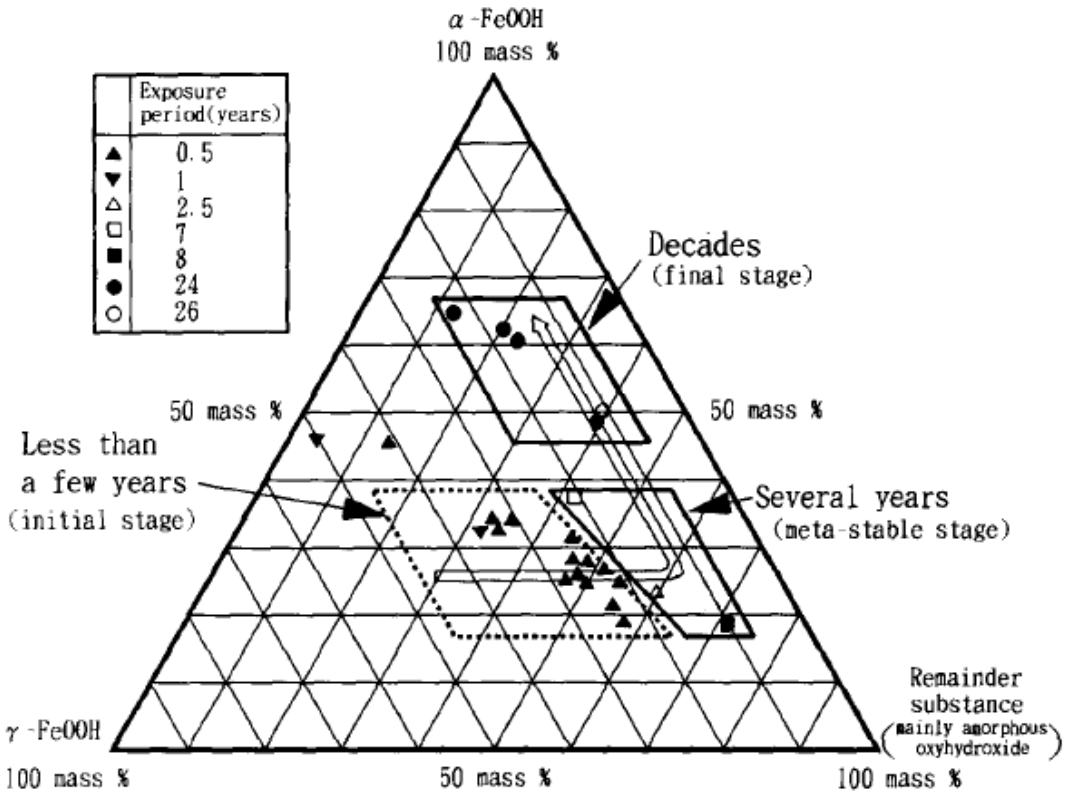


**Figure 3.2** Exposure vs. Time dependence on the fractions of rust constituents formed on exposed low alloy steels from an investigation of atmospheric corrosion in industrial and Rural Areas [60: p. 296]

The ratio of the passivating goethite compared to other corrosion products can be used to predict the protection this will afford the remaining metal, characterised as the Protective Ability Index [62]. In areas high in pollutants, the ratio may be altered to mass of goethite against the sum mass of lepidocrocite, akaganeite and magnetite [108]. For archaeological artefacts, the value, defined as the ratio of concentrations of goethite to lepidocrocite $\left(\frac{\alpha}{\gamma}\right)$ has been found to be between 1 and 5 [63].

### 3.3.5 Pollutants within the Wet/Dry model and their products

Pollutants comprise various chemicals which alter the electrochemical balance of corrosion or the state of the electrolyte. They include sulphurous and nitrogenous compounds and, perhaps most damaging and ubiquitous of all, chlorides. The introduction of pollutants will have a profound effect on both the rates and products of atmospheric corrosion: Long term exposure of mild steel in three different environments has shown corrosion rates are highest in industrial and marine environments, where pollutants are plentiful, compared to urban or rural areas, where they are more scarce [64].

#### 3.3.5a Chlorides

Chlorides are perhaps the most dangerous pollutants for ferrous metals. Most prevalent towards the coast, from marine vapour, they are also introduced from industrial pollution. They are generally found in salt forms (most often with sodium, magnesium and calcium) are almost universally corrosives and will form hygroscopic surfaces. These deliquescent properties are exacerbated by their tendency to form hydrochloric acid (HCl) and ferric chloride ($FeCl_3$) both of which can act to dissolve corrosion layers of the artefact, removing their protective and passivating properties. These processes of deposition and dissolution can be self-catalytic. Finally, chlorides will, as all salts, increase the conductivity of the electrolyte, increasing the corrosion currents and hence corrosion kinetics, of the system [65].

The chloride ions themselves can be incorporated into the lattice structure of corrosion products, fundamentally changing their nature and removing passivating abilities. Higher chloride conditions are crucial in the production of akaganeite and favour formation of lepidocrocite and magnetite, as opposed to the more passivating goethite.

These effects work together to hugely increase atmospheric corrosion rates. Tests of accelerated wet dry cycles by Dunn et al. [53] have found that the presence of chloride ions in the electrolyte increase the corrosion rate by a factor of 2.5 over a chloride concentration increase of 10. Exposed low carbon steels in atmospheric marine environments, closer to a

ready source of chlorides;, have been shown to exhibit a higher rate of corrosion compared to industrial settings, attributed to the high levels of akaganeite which this produced [66]. It has also been demonstrated that the closer samples are placed to the coast, the quicker corrosion layers are built up [66-7]. Even stored in relatively stable, apparently chloride poor, indoor atmospheres, heritage artefacts can build up high levels of chloride and akaganeite [68].

### 3.4.5b Other pollutants

The increasing presence in the atmosphere of sulphur dioxide, ($SO_2$) from industrial processes has an effect on corrosion products [64]. It was suggested by Dünnwald and Otto [57], that in atmospheres of this type, sulphuric acid ($H_2SO_4$) will be formed during the wet phase. This will react to form iron sulphate ($FeSO_4$), which is transformed through intermediate products to form $Fe(OH)_3$ during the drying phase. Cai and Lyon [42] proposed a modification to this, with the formation of sulphurous acid ($H_2SO_3$) (reaction 3.8) and the subsequent oxidation to sulphate or sulphite ions as a rate controlling action (reaction 3.9).

$$H_2O + SO_2 \leftrightarrow 2H^+ + {SO_3}^{2-} \leftrightarrow H_2SO_3 \qquad \textbf{[Eq. 3.8]}$$

$${SO_3}^{2-} + \frac{1}{2}O_2 \leftrightarrow {SO_4}^{2-} \qquad \textbf{[Eq. 3.9]}$$

This reaction will become easier as ferrous ions are produced. It has also been demonstrated that sulphate ions can induce the transformations of magnetite to goethite or lepidocrocite [69]. The effect of increased sulphates in the atmosphere compared to clean air is shown in figure 3.3

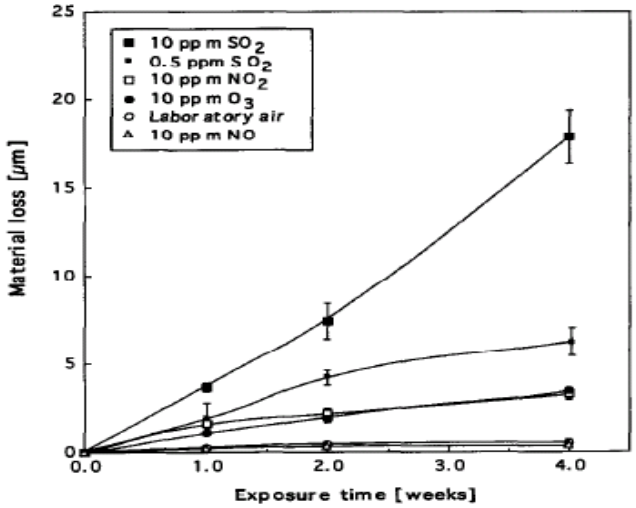


**Figure 3.3** The material loss of the unalloyed steel samples exposed to air containing different air pollutants ($SO_2$, $NO_2$, $O_3$, NO, laboratory air) at 25°C and 90% relative humidity (from [70; pp. 1361]

Other atmospheric pollutants catalyse corrosion. Hydrocarbon particulates in smoke have been shown to create corrosion filaments on metal surfaces [71]. The smoke itself enhances the action of $SO_2$, while also causing localised corrosion around particulates, acting as nuclei for water deposition, thereby increasing time of wetness. The same phenomena occur with other atmospheric dust [72]. Other pollutants recorded include ozone, hydrogen peroxide, and organic acids [73].

## 3.4 Corrosion of iron in the abandonment environment

For the majority of archaeological objects, there will be a period of abandonment prior to recovery and subsequent storage or display. The corrosion layers acquired during atmospheric corrosion, varying from a simple passivating oxide layer to multiple layers of mineral deposits, will have an impact on continuing corrosion once it has entered the abandonment environment. Most artefacts will have been abandoned and gained corrosion layers from abandonment on land, from which site formation processes will create subterranean contexts, or in a marine aqueous environment.

### 3.4.1 Subterranean corrosion.

Soil or subterranean corrosion occurs within an electrolytic film, created by the moisture constantly present within the inter-granular spaces and humified organic matter of soil or sediment. The variation of chemical and physical properties of soil and soil water alter the properties of the electrolyte in terms of pH, pollutants and oxidising properties. Over a single site, a matter of inches or even on a single artefact, objects can corrode radically differently.

When first interred, it is likely that the metal surface will be easily accessible to the surrounding electrolyte. Assuming sufficient oxygen and water are present, the reduction of oxygen is the predominant cathodic reaction. Both the anodic and cathodic reactions occur at the metal surface [74]. The primary anodic reaction is oxidation of iron to its divalent cation, $Fe^{2+}$, which can then be further oxidised to form the ferric ion, $Fe^{3+}$ (equation 2.15). Ferrous ions diffuse towards the cathodes. These can combine with the hydroxyl ions produced there to form ferrous hydroxide, decreasing corrosion rate [75].

The nature of continued reactions will depend on local chemistry, specifically the concentrations of $Fe^{2+}$, $O_2$ and $H^+$, and the presence of aggressive anions from the sediment profile or in existing corrosion products. In most soils, these will include chloride and sulphide species. Ferric hydroxide and hydroxyl chloride may form as transition states in low oxygen environments [75]. In conditions too reducing to form lepidocrocite and more

oxidising than the conditions required for goethite, these oxidise further to create green rusts [76]. As with atmospheric corrosion, these intermediate compounds will eventually oxidise further into ferric oxyhydroxides, the type of which will depend on the temperature, oxygen concentration and chloride levels. In addition to goethite and lepidocrocite, high levels of chloride can cause the formation of akaganeite, through the oxidation of ferrous hydroxychloride ($\beta Fe_2(OH)_3Cl$) [75]. Soils with high levels of oxygen and a localised pH<6 create a low rate of oxidation of ferrous to ferric ions, maintaining a high solution concentration of ferrous ions [77]. Conditions with both high oxygen levels and a localised pH>6 will hydrolyse the ferrous hydroxide to Ferric hydroxide, $Fe(OH)_3$, which is far less soluble and tends to be transformed to goethite and water.

Either through action prior to burial or after corrosion has progressed, a solid corrosion crust of insoluble corrosion products (magnetite and oxyhydroxides) forms, separating cathodic and anodic sites. Anodic dissolution of iron continues at the metallic surface, reduction occurs towards the exterior of the corrosion layers where oxygen is more plentiful [78]. Electrons are carried through the corrosion layer via semiconductors, such as magnetite or hydrated lepidocrocite, or pore solutions. This creates a high concentration of cations at the metal surface, which, combined with their mobility, will determine the anionic current produced. The build-up of charge draws naturally occurring anions towards the metal surface from the surrounding sediment. The mobility of chloride ions (compared to comparable naturally occurring ions [79]) and its abundance in most soils generally creates an influx of $Cl^-$ ions, unless blocked by particularly high levels of an alternative ion. This leads to a concentration of ferrous chloride solution ($FeCl_2$) close to the metal interface. These concentrations have been mapped and confirmed using spectrographic techniques [80].

Ferrous ions will eventually hydrolyse according to reaction 3.10. Hydrogen ions are liberated, decreasing local pH to an extent dependant on the equilibrium constant of the hydroxide produced and the activity of the metal ions [81].

$$Fe^{2+} + H_2O \leftrightarrow Fe(OH)^+ + H^+ \qquad \textbf{[Eq. 3.10]}$$

$$Fe(OH)^+ + H_2O \leftrightarrow Fe(OH)_2 + H^+ \qquad \textbf{[Eq. 3.11]}$$

$Fe(OH)^+$ is soluble, preventing neutralisation of the acid by an increase in hydroxyl ions. The hydrolysis of 1M of ferrous ions in this manner has been measured to create a surrounding solution pH of around 4.8 [81]. Acidity is further increased by the continued production of ferrous ions, leading to higher localised pH around the cathodic sites than the anodic sites, due to the production of hydroxide and hydrogen ions respectively. Overall electrolyte pH will remain the same as the bulk solution in which the artefact is corroding.

$Fe(OH)^+$ deposits are not protective; low pH at the anode serves to stimulate metal dissolution, drawing in more chloride ions from the surrounding environment to maintain charge balance. The rate of this autocatalytic cyclic process increases with time [82]. Low oxygen concentration around anodic sites prevents ferrous ions from readily oxidising to ferric [75, 77]. Oxygen levels will be depleted further by reaction with the ferrous ions and through cathodic action. The maintenance of a high concentration of $H^+$ ions at the anode demonstrates that the predominant cathodic reaction is one of oxygen reduction and not the evolution of hydrogen: At sufficiently low pH (< 4) hydrogen evolution can occur, balanced anodic oxidation of iron to ferrous anions. The released hydrogen could have the effect of creating internal stresses within the artefact, leading to the physical flaking of the corrosion layers and new pathways for corrosion.

On exposure to a less humid environment, for example on water table decrease or changes in sediment, the electrolyte decreases in thickness. This has the same effect as in atmospheric corrosion; oxygen reduction is increased [78]. The potential of the system rises and the reduction rate will become controlled by the charge transfer kinetics of the system.

The result of subterranean corrosion processes appear as a bulky orange/brown bloom. The metallic centre is surrounded by grey/black corrosion products, themselves covered with the bulbous reddish mass. The inner corrosion products were initially thought to be magnetite. This was used by Turgoose [78], to argue that there was low oxygen penetration, creating high acidity close to the metal and the range of stability for magnetite. More recent work by Neff et al. instead identifies the black layers as goethite, incorporating strips of magnetite and maghemite ($\gamma - Fe_2O_3$) [83]. Akaganeite is formed close to the anodes, within regions of high chloride concentration and acidic local pH. Lepidocrocite initially forms, but transforms to goethite in areas with sufficient oxygen; it will be present only in freshly corroded regions where oxygen levels were low, but pH was sufficiently high, or chloride content sufficiently low, to prevent akaganeite production.

Neff et al. [83] characterised the corrosion products of subterranean iron as constituting three phases, layered from the metal surface to the exterior (Figure 3.4) The inner dense product layer (DPL) has the structure mentioned above, contains no soil minerals and is likely a close approximation of the original shape of the object. It contains numerous cracks and pores, typically measuring between 6-300μm, representative of the channels through which the electrolyte can reach the metal surface [75, 84-7]. These may contain deposited minerals from the soil water solution, such as calcite. Neff et al. [83] suggest that these cracks are caused by the expansion of goethite during the first phases of corrosion. Ferrous ions at the anode diffuse into the pores away from the metal surface. The potential will be such that magnetite or maghemite is formed and deposited as strips in pore spaces (Figure 3.5).

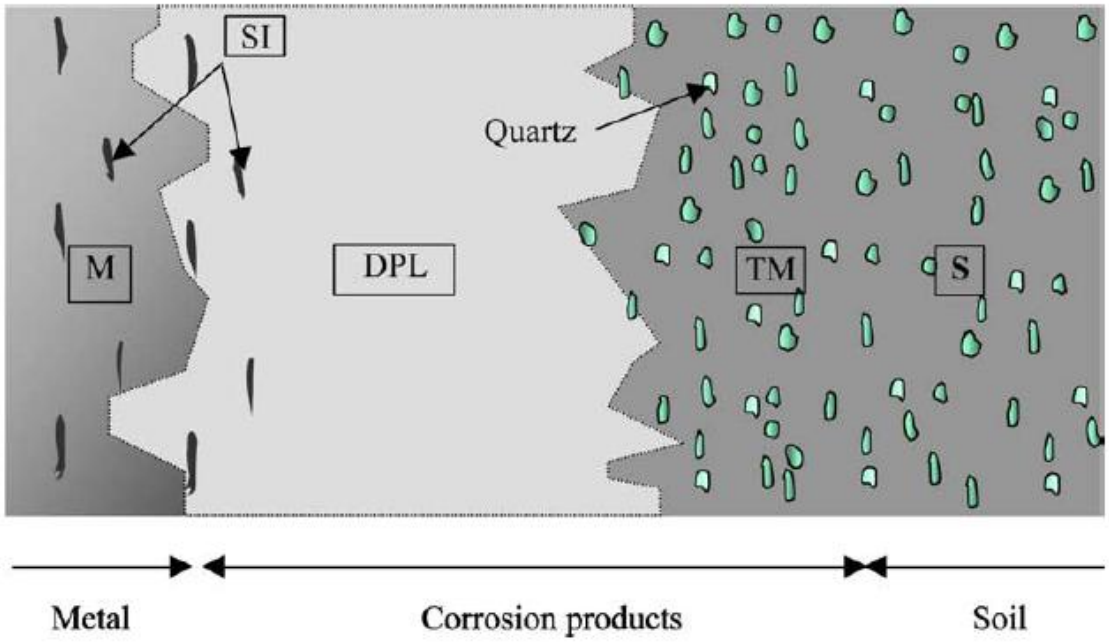


**Figure 3.4** Schematic Description of the corrosion system of archaeological iron buried in soil, where; M: Metal, Sl: Slag inclusions, DPL: Dense Product Layer, TM: Transformed Medium, S: Soil (from [83] Fig. 1)

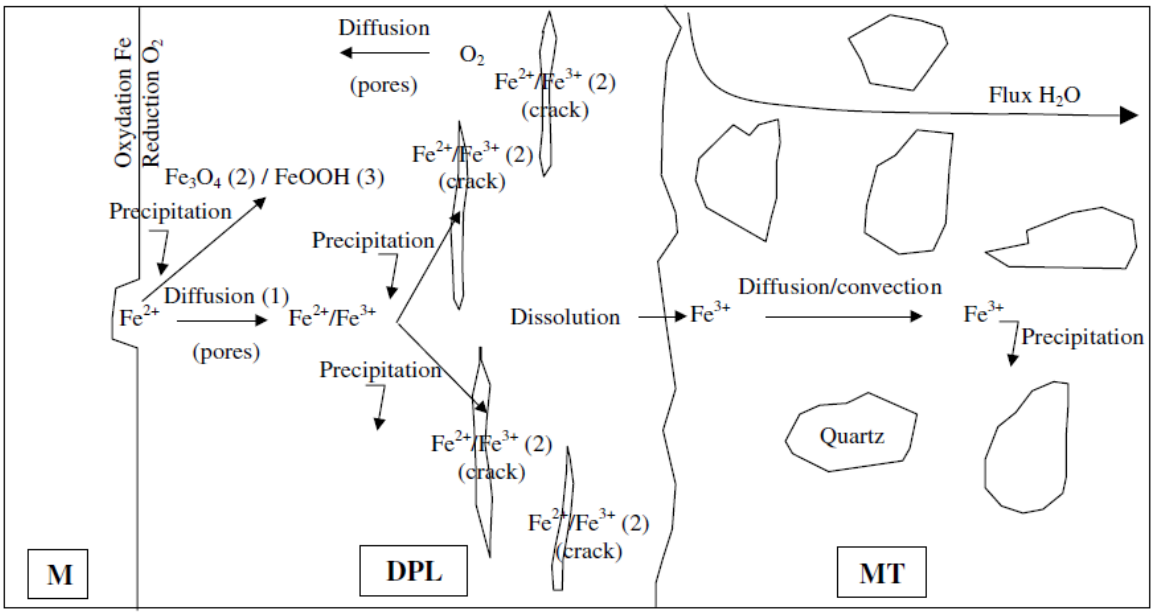


**Figure 3.5** Schematic of long term iron corrosion of soil, as proposed by Neff et al. (from [83], fig. 16, p. 532)

However, Chitty et al. [86] have observed that the magnetite veins are not always connected to the metal surface, implying that both anodic and cathodic reactions were occurring at the metal interface. This theory has been backed up by the use of oxygen tracers by Vega et al. [88], showing the apparent diffusion of oxygen through the pore solution as the rate controlling factor. This runs contrary to the apparent charge accumulation which is the

attributed cause for the influx of chloride ions; any incursion of negative hydroxyl ions from oxygen reductions would counter the charge. This in turn has been refuted by Réguer et al. [89] who suggest that some, though not all, of the veins will be connected to the metal surface, allowing charge transfer from the outer corrosion layers. This model indicates oxygen diffusion to be the rate control factor, diffusing part way into the object and to corrosion layers unconnected to the exterior. It allows the build-up of charge in certain areas, which explains the influx of chloride and the apparent localisation over which this occurs. It is also possible that lepidocrocite and goethite in the DPL can act as semiconductors. Similarly to the wet phase of atmospheric corrosion, the phase of the ferrous ions within the lepidocrocite lattice will increase the conducting regions of the oxide crystals in the oxide layer, providing pathways for further oxygen to diffuse in from the electrolyte (Figure 3.5). The reduction rate of the oxygen will be controlled by the diffusion of the electro-active species into the oxide layer and the electron-conducting regions [51, 55]. The TM (transformed medium) of the outer layer is comprised primarily of goethite and soil minerals. It is likely formed through the dissolution of the DPL and subsequent re-precipitation [83]. The exact makeup of this layer will depend on the surrounding soil, and soil water, chemistry.

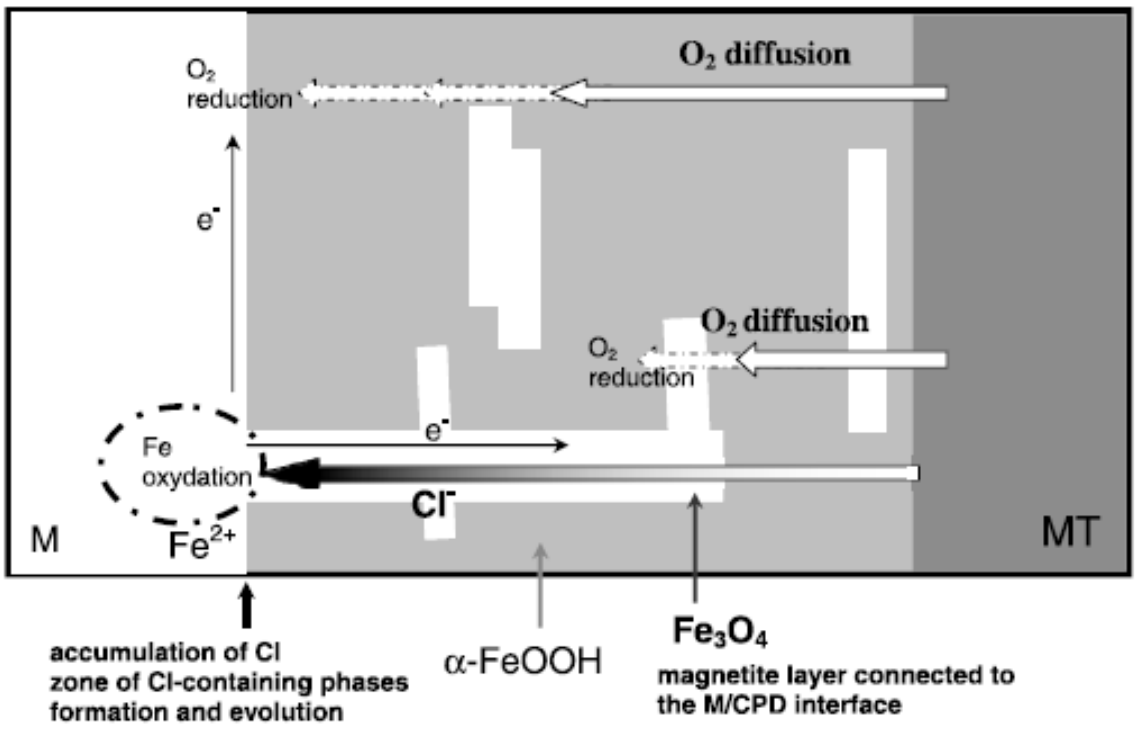


**Figure 3.6** Schematic of Chloride accumulation process at metal/corrosion layer interface during burial in soil (From [89], fig.11, p. 2741)

This gives us an overall process of soil corrosion as modelled by Neff et al. [15] (Figures 3.4 and 3.5), but with the modifications made by Réguer et al. [89] (Figure 3.6) as clarifying processes.

### 3.4.1a Corrosion products of subterranean corrosion

Archaeological artefacts removed from sediments are likely to have followed all or part of the model proposed above: Precise product makeup will be dependent on soil properties. The most common oxide layers on excavated iron artefacts are magnetite, goethite and lepidocrocite. Goethite is ubiquitous. Lepidocrocite is mainly found on artefacts which have had an increased exposure to air. Burial in the prevalent damp, aerated soils will produce predominantly iron oxides; magnetite, goethite and maghemite with an outer layer and pore structure which may also contain minerals deposited from the soil solution. Hematite has been found within the structure of the DPL, observed as a bright red product in corrosion layers [58]. Close to the metal surface, akaganeite will be concentrated, with lepidocrocite in poorly oxidised regions. There will be variations in corrosion product thickness and makeup according to the access of oxygen and water to the metal surface and corrosion layers.

In the majority of cases we will observe high levels of chloride uptake to the metal/product interface. This is not to say that they will be the only ion drawn into the metal. In alkali soils, potassium and sodium cations are common, calcareous soils will be higher in magnesium and calcium ions, while acidic soils will have very low levels of any free cations. In anoxic calcareous soils, with a high abundance of carbonate ions, siderite has been found in the TM outer layers of corrosion products [90]. Goethite and ferrihydrite are often associated, lying between it and the metal. As a rule, carbonates and phosphates in a soil will form relatively protective corrosion layers, whereas chloride and sulphide ions will lead to higher corrosion rates. Hydroxyl-carbonate ($Fe_2(OH)_2CO_3$) can also form close to the goethite, but always beneath the siderite layer. In wet and organic layers of soil with plentiful phosphorous, a layer of vivianite $Fe_2(OH)_2CO_3$ can form [28], with extremely protective characteristics.

In the case of anoxic soils with low acidity, the environment can be electrochemically non-corrosive. However, the presence in these soils of anaerobic bacteria will cause the creation of sulphates which can react to create sulphur containing corrosion products [91].

### 3.4.1b Corrosion rates in sediments

Experimental burial of iron has confirmed that differential access of water and oxygen are the controlling factors in soil corrosion; the reaction rate is under cathodic control [79]. The separation of the electrochemically active sites and the concentration equilibrium formed with the local soil environment is likely to reduce corrosion rates. Traditionally, the corrosion rate of carbon steels in soils is given as between 35-68μm/year. Long term interred, equilibrated iron will be expected to be much lower. There are at present no studies on instantaneous corrosion rate in situ for archaeological iron in soil. Neff et al. [54], in their study of 40 archaeological artefacts, used the assumed delimited areas of the DPL/metal

interface, combined with the age of the artefact and the solubility of the deposited minerals, to estimate a maximum previous corrosion rate of approximately 4μm/year. The study was limited and the assumptions used somewhat understated. However, it does indicate the significantly lower overall corrosion rates compared to freshly buried modern analogues. Further studies have given a range of observed corrosion rates in different subterranean environments; 0.025-1.2 μm/y in waterlogged soil, 15 μm/y in sandy soil and 1.3μm/y in soil containing organic matter and chlorinated water [54].

### 3.4.2 Marine Corrosion

Iron objects abandoned in the sea or in fresh water are subject to constant contact with an electrolyte, filled with additional dissolved gases, suspended silts, flora and fauna. Corrosion may occur either completely within the water itself or buried under various degrees of marine sediment. For those completely buried, it is possible that the mechanisms will be similar to that of a water saturated, or anoxic, soil environment.

In open water, in the absence of thick corrosion layers, dissolved oxygen in the sea water will reduce at the cathode, producing an increase in oxidation rate of the metal at the anode. For freshwater and stagnant areas it is possible that anoxic environments can form. In this case, other gases may form part or all of the cathodic reactions. Where the electrolyte has a pH>6, carbon dioxide ($CO_2$) and hydrogen sulphide ($H_2S$) may be dissolved, leading to the cathodic reactions 3.12 and 3.13 respectively. Both can lead to hydrogen evolution at the metal surface, and even hydrogen enbrittlement in steel [92].

$$H_2CO_3 \rightarrow H^+ + HCO_3^- \qquad \textbf{[Eq. 3.12]}$$

$$2H_2S + 2e^- \rightarrow 2H + 2HS^- \qquad \textbf{[Eq. 3.13]}$$

Corrosion products will form in accordance to the conditions of the system, similarly to subterranean corrosion. Additional precipitation of minerals will occur through action of marine organisms and deposition of marine salts. These form thick, amorphous encrustations of ferrous concretions, calcium carbonate and insoluble debris from the ocean (figure 3.7) [93]. The outer surface of these concretions is formed by deposition of corrosion products and seawater minerals. Precipitated material will largely be made up of calcium carbonate, magnesium carbonate and the hydroxides of both. When these built up layers are porous, corrosion may continue, where thick and compact, they can isolate the metal from exterior conditions and prevent further corrosion.

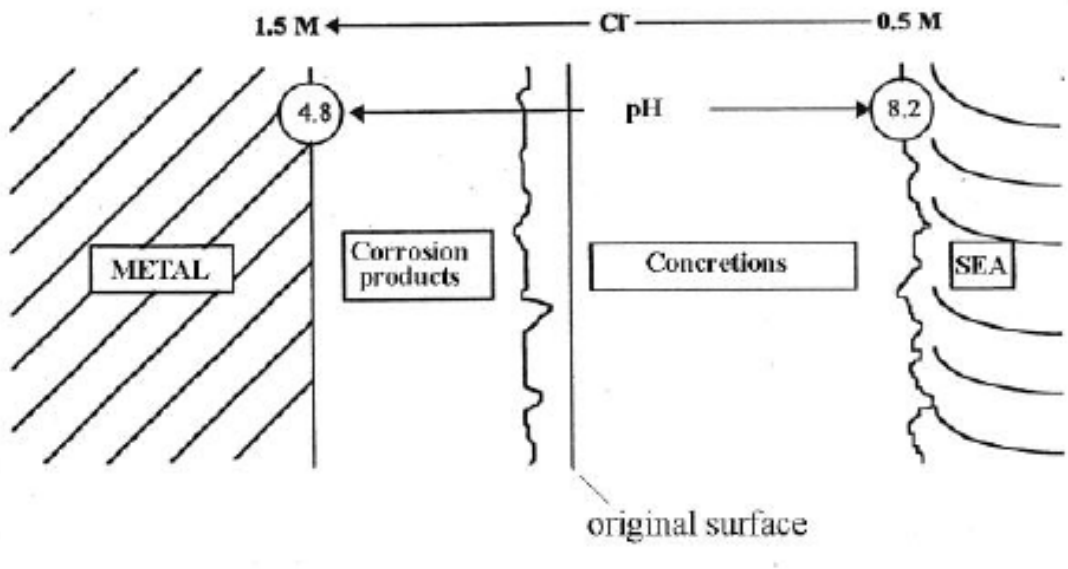


**Figure 3.7:** Cross section of wrought iron metal-concretion system, illustrating the movement of chloride ions (adapted from [100])

The levels of hydrogen may drive pH low enough for hydrogen evolution. North [94] suggested that this is the main cathodic reaction in seawater, citing the lack of effect of oxygen levels on corrosion rate and the levels of hydrogen within retrieved concretions. Such evolution would be expected to be coupled with a lowering of pH at the anodic sites [95]. However, this has not been the case observed in many marine concretions. Instead it has been observed experimentally that chloride ions are drawn in, similarly to the processes of soil corrosion, producing $Fe(OH)_2$ [85, 96] (Figure 3.7). Chloride concentration has been measured up to 1.5M with pH at 4.8 at the metal-concretion interface [81], a situation which would hugely increase corrosion rate compared to ambient conditions.

In general, reduction of oxygen is the main cathodic reaction within corrosion layers away from the metal surface [95]. This has been evidenced by correlation between corrosion rates of iron cannons in seawater and levels of dissolved oxygen in the local marine system [97]. Anoxic regions can form, often associated with bacterial action, producing sulphide ions which catalyse hydrogen evolution and additional reduction [98]. This may lead to the creation of black ferrous sulphide (FeS) corrosion product, typical of completely anaerobic conditions such as those found on burial in the seabed [99]. Similar bacteria have been cited as the creators of green rusts within concretions. These may also be found independently if the interior microclimate of the concretion has low oxygen, high pH and significant chloride concentration [101].

Cast iron reacts differently compared to wrought iron. In the system in figure 3.7, the original extent of the wrought metal is lost to the concretion layer. Continued corrosion often leaves a hollow shell of corrosion product: Metallic iron is removed but never precipitated due to the extremely acidic internal conditions. Where there are remains they form a typically fibrous, wood grain like structure, caused by galvanic corrosion between iron and slag inclusions [77, 93]. In less corroded areas of cast iron, a layer of graphite and cementite, $FeC_3$, can be formed. Graphite carbon structures inherent in the metal will be unaffected by corrosion, maintaining the original structure though the iron phases have been transformed to corrosion products [100]. This can form a galvanic corrosion cell between the graphite (cathode) and the ferrite and pearlite metallic iron crystals (anode) [81]. Such conditions transform the cementite to hydrocarbons according to equations 3.14 and 3.15.

$$Fe_3C + 4H^+ + 4e^- \rightarrow 3Fe + CH_4 \qquad \text{[Eq. 3.14]}$$

$$Fe_3C + 2H^+ + 2e^- \rightarrow 3Fe + (CH_2) \qquad \text{[Eq. 3.15]}$$

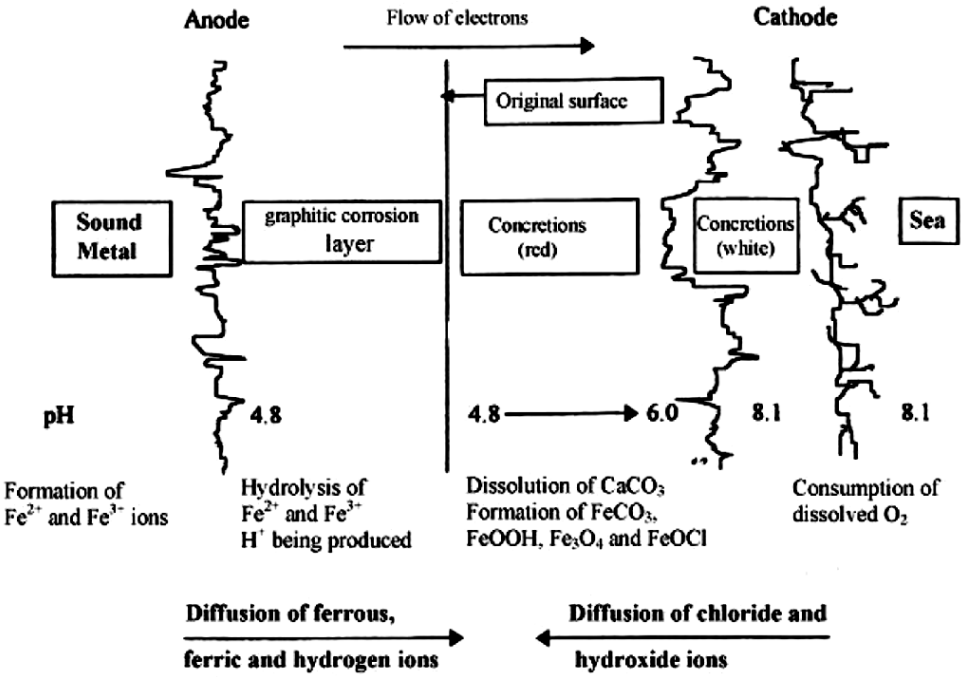


**Figure 3.8** Suggested cross section of cast iron undergoing marine corrosion in seawater (adapted from [100])

This creates a layer of 'graphitised corrosion products' (figure 3.8). The concretion itself acts as a semi-permeable membrane, creating conditions similar to those of wrought iron corrosion, with separated anodic and cathodic sites, low internal pH and high levels of internal chloride [103]. In both cases, this creates distinct zones in the corrosion layers. On the surface, the main part of the concretion will be formed of seawater-deposited calcium and magnesium carbonates and hydroxides. Siderite may be found due to the anaerobic microclimate; caused by marine life or the build-up of passivating protective scales of the material through high carbonate levels [102]. Within the concretion, magnetite and goethite

are formed in similar processes to other environments. Magnetite forms a dark adhesive layer at the metal surface, with other oxyhydroxides overlying it. Lepidocrocite is rarer in these concretions. The high level of chloride in seawater facilitates adsorption of chloride ions, forming ferric and ferrous salts. When exposed to air, these can quickly deposit as akaganeite [95]. With chloride concentrations above 1M, this can be the dominant corrosion product by mass. Amorphous ferric oxyhydroxide has been recorded in marine corrosion layers, consisting of microcrystalline goethite and amorphous FeOOH, likely created by quick oxidation upon removal into air.

### 3.4.2a Corrosion rate in a marine environment

In open water, corrosion rate of iron will be controlled by oxygen concentration, salinity of the bulk solution, temperature, pH, biological activity and the velocity and motion of the water [81]. Each of these factors will have an effect on all the others, exacerbating or nullifying additional corrosion pressures. For example, in normal conditions an increase in temperature will be expected to thermodynamically increase the rate of corrosion. However, in a marine environment, a higher temperature often means a greater amount of marine life and biological activity, increasing levels of calcareous precipitation in the area. This tend to form protective layers over artefacts, reducing corrosion rate [103]. Local currents and electrolyte velocity affect diffusion rates of ions; higher velocities remove more ions and increase corrosion kinetics. More powerful turbulent movements can rupture corrosion layers, removing passivating properties.

Dissolved gases in the environment will usually be the rate controlling step. Without these dissolved gases, corrosion can effectively cease (figure 3.9). Oxygen concentration is the most important: Dissolved levels in any part of the sea will vary according to local conditions and can reach up to 12ppm at 4°C (8ppm at 20°C) [103]. Other gases can form substitutes in anoxic environments, but will limit the overall corrosion rate.

Salinity will have an effect on corrosion rate and can vary hugely. Up to a point, higher salinity will increase corrosion rate. At very high salt concentrations, oxygen concentration decreases, lowering corrosion rate. This can be illustrated by lab based observations of the corrosion rate of steel, where maximum corrosion rate occurs at concentrations of 3 to 4 NaCl wt. % (figure 3.10). Conversely, lower levels of salinity increase precipitation rates of carbonates, which protect the metal from corrosion. Salinity typically varies from between 32 to 37.5 grams per kg of seawater.

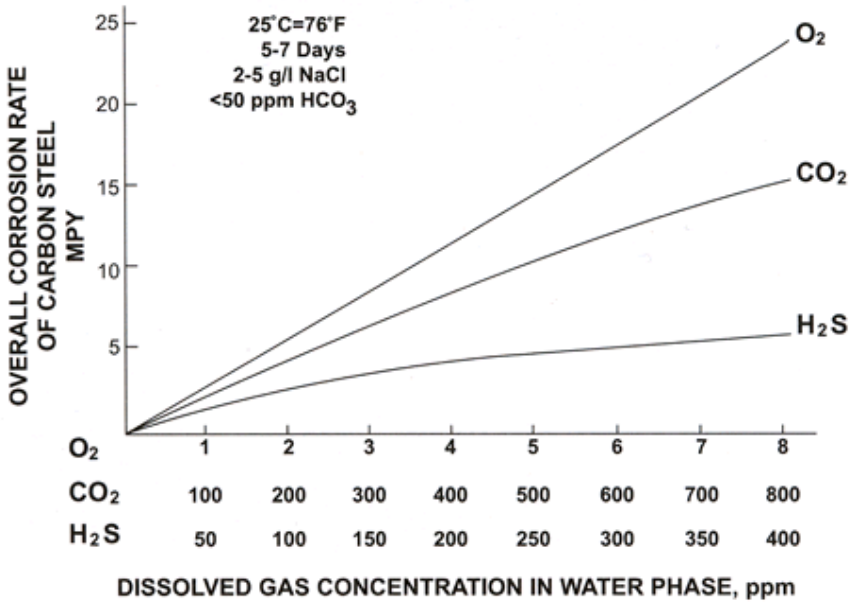


**Figure 3.9** Corrosion rates of steel versus oxygen, carbon dioxide, and hydrogen sulphide (from [104: p. 43]

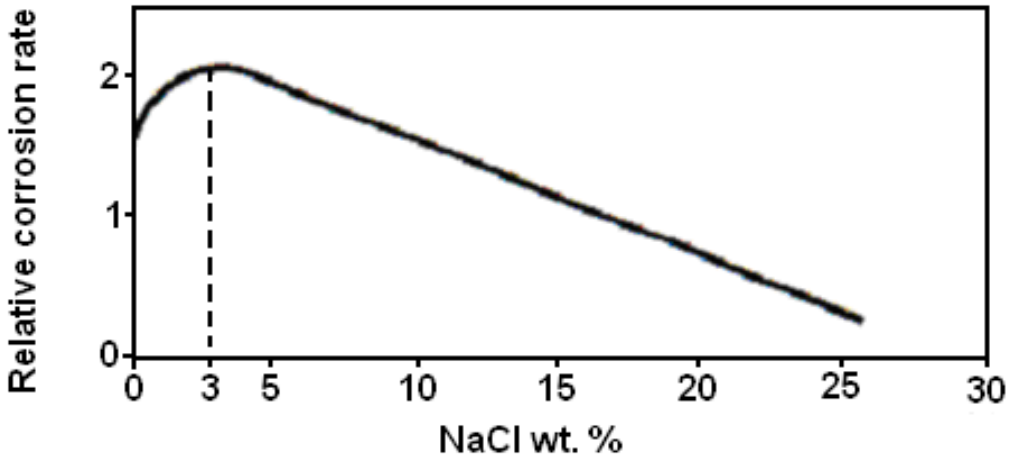


**Figure 3.10:** NaCl concentration effect on the corrosion behaviour of steel. (from [98])

The pH of Seawater is on the alkaline side, typically varying from only 8 to 8.2 [103]. Localised variations are often slight, due to biological influence or the local geology of the seabed.

The average corrosion rates for iron and iron alloys on immersed infrastructure have been estimated at 100μm/year. For archaeological iron, we can assume rate will be decreased, depending on time submerged and the equilibrium achieved within the concretions and ambient environment.

## 3.5 Post excavation corrosion

Upon reclamation from the abandonment environment, artefacts may or may not still have metallic iron at their core. Those without will have ceased corrosion entirely; continued physical degradation through the transformation of corrosion products may still occur, albeit at a reduced rate. For those with extant metallic iron, atmospheric corrosion will continue, similarly to the processes described in section 3.3 [105]. Pollutants introduced and corrosion products formed through abandonment cause additional processes, often to the detriment of the object. The variety of corrosion rates and mechanisms will be large, even from samples from the same site. For example, mineralised artefacts recovered from the same organic rich soil have been observed to range in post-excavation corrosion rate from 0.03μm/y to 5μm/y [106].

High levels of chloride within archaeological corrosion layers, coupled with the evaporation of the electrolyte, can cause very high corrosion rates and formation of detrimental corrosion products immediately upon object exposure. Measurements of chloride levels within recovered artefacts range from as low as 0.02%w/w and up to 13%w/w (in marine iron) [94]. Observations of marine corroded wrought iron plates have given a typical variation of between 3.2%w/w in heavily corroded plates, to 0.01%w/w for minor visible corrosion [107], with highest levels found in areas of pitting corrosion [109]. Removed from the abandonment context, moisture within the corrosion products begins to evaporate and extant chloride levels cause an increase in electrolyte chloride concentration. Ferrous chloride will form $FeCl_2.4H_2O$ and the concentration of Ferrous hydroxyl-chloride ($\beta - Fe_2(OH)_3Cl$) (common from archaeological iron from low oxygen and high chloride environmnets), will rise. These two compounds precipitate as solid ferric oxyhydroxides, the majority of which will be akaganeite. The bulky, elongated crystals create internal pressures and stresses on the internal corrosion layers [75], leading to cracking of the corrosion products. This is often observed as the flaking of rust and deterioration of physical hardiness, often with an orange akaganeite powder observed beneath the flakes [109]

Initial physical cracking creates new pathways for oxygen ingress into the artefact, facilitating increased corrosion. Oxygen may reach and diffuse within oxide layers, oxidising ferrous ions to ferric oxyhydroxides. As above, the conditions will continue to favour akaganeite precipitation (Equation. 3.16).

$$2Fe^{2+} + \frac{1}{2}O_2 + 3H_2O \xrightarrow[Cl^-]{} 2\beta - FeOOH + 4H^+ \quad \textbf{[Eq. 3.16]}$$

This has an accelerating effect on the corrosion rate. In standard conditions below 19% RH, iron in contact with ferrous chloride will convert its ferrous chloride tetrahydrate to a non-corrosive double hydrate. Therefore, below this level corrosion will cease. However, the hygroscopic nature of akaganeite means that corrosion may continue to occur down to 15%

RH [110]. It should be noted that this value was achieved using artificial products and direct contact in powder form; though the results give a good worst case scenario. The akaganeite will generally form between the metal and the hydrated ferrous chloride, creating a film of concentrated electrolyte with highly hygroscopic properties [84]. Watkinson and Lewis [44, 110] have shown that iron corrodes a lot faster when in contact with both compounds; above 25% RH they symbiotically increase corrosion rate.

A bi-product of akaganeite deposition from ferrous chloride is the formation of hydrochloric acid (equation 3.17) [84,111].

$$2FeCl_2(aq) + 3H_2O + \frac{1}{2}O_2(g) \rightarrow 2FeOOH(s) + 4HCl(s) \qquad \textbf{[Eq. 3.17]}$$

$$2Fe(s) + 4HCl(aq) + O_2 \rightarrow 2FeCl_2(aq) + 2H_2O \qquad \textbf{[Eq. 3.18]}$$

The hydrochloric acid dissolves metallic iron, creating more ferrous chloride (equation 3.18). The process then repeats. The result of this cycle is that the hydrochloric acid will react with extant solid corrosion products, particularly magnetite. This in turn will produce and deposit more akaganeite; combining to create substantial degradation of the artefact's physical integrity [84]. The presence of the chloride also increases the ionic conductivity of the solution, further increasing corrosion rate. This process is known as the 'acid regeneration cycle' [112]. The validity of this phenomenon has been questioned by Selwyn et al. [75], who argue that it has not been shown that ferric chloride will dissociate into constituent ions or will form an intermediate compound in solution. Without this step, the participation of chloride ions could be limited to increasing the electrolytic conductivity. However, both explanations will increase corrosion rate appreciably.

Archaeological iron has been observed to undergo a phenomenon known as 'weeping'. This is observed as the formation of highly acidic, yellow or brown droplets of electrolyte, containing mostly ferric and chloride ions, on the surface of the outer corrosion layers [47, 113-4]. It occurs on highly chlorinated corrosion products moved to dry atmospheric environments from unstable damp conditions [114] and is attributed to the hygroscopic nature of iron chloride salts, specifically the transformation of aqueous $FeCl_2$ to yellow dihydrate $FeCl_2.2H_2O$ and green tetrahydrate ferrous chloride $FeCl_2.4H_2O$ [112]. Low pH within the corrosion layers release ferric ions from akaganeite and hydrolyse them to hydroxyl species, including $Fe(OH)^{2+}$. Starting at the metallic iron, this subsequently extends to above the surface of the corrosion layer, producing the droplets at the surface. It is currently unclear whether direct physical contact between the metal surface and the ferric chloride is required.

The products of weeping are thin shells of corrosion products, formed by deposition across the droplet surface. Ferric and ferrous ions react with oxygen to form FeOOH according to the reaction 3.19:

$$2Fe^{2+} + \frac{1}{2}O_2 + 3H_2O \rightarrow 2FeOOH + 4H^+ \qquad \textbf{[Eq. 3.19]}$$

This only occurs where oxygen is plentiful; at the droplet/atmosphere interface. Surface tension holds the droplet in shape as these products coalesce into a solid shell. Electrolyte continues to evaporate, leaving characteristic hollow shells. Selwyn et al. [75] have identified goethite and lepidocrocite within these shells on archaeological artefacts, and speculated that akaganeite may have initially been present.

Sulphate ions within the iron corrosion layers will have a similar effect, though less extreme, to chloride. Ferrous sulphate will lower critical RH to 90% RH, but the deliquescent properties of $FeSO_4.7H_2O$ and $FeSO_4.4H_2O$ lower it to 60% [44]. A similar acid regeneration cycle can be observed for sulphates, specifically the oxidation of $Fe_2SO_4$ to $H_2SO_4$. This cycle will, as in the case of insoluble chloride salts, break down eventually due to a build-up and precipitation of hydroxyl sulphates, $Fe(OH)SO_4$ and $Fe_2(OH)_4SO_4$ [46].

Oxidation of the metallic iron will continue in the presence of pollutants until all the metal is used up. The corrosion rate may be sustained by the presence of a conducting link between the metal and exterior of the corrosion layers, such as magnetite and the electrolytic chloride solution present in the pores. The latter may be removed by the deposition of akaganeite, closing the pores and reducing the pathways for electrochemical redox reactions [46].

## 3.6 Summary of the corroded assemblage of archaeological iron

The processes above create the majority of the iron corrosion products present in a heritage assemblage. Depending on the previous environments in which artefacts were exposed, we are likely to be faced by a variety of different corrosion layer make-ups and depths.

By considering the history of any given artefact we have created a broad set of guidelines for the corrosion products expected. Goethite, lepidocrocite, akaganeite and magnetite can form on artefacts which have been stored in the atmosphere, or abandoned in a soil environment. The proportions of these minerals (and other, more transitory, products) will determine the passivation or catalysis of any consequent corrosion rate. We might find siderite, phosphates and sulphates deposited from the soil in the outer layers in specific environments and in polluted atmospheric environments. This is also true of marine corrosion, where we must expect concretion over the surface of the artefact, and perhaps the total dissolution of the

metallic iron within. The artefacts will contain various levels of pollutants which affect their corrosion rates, of which chloride is the most common.

For the collections themselves, we will observe interaction of the corrosion layers from the past with the ambient atmospheric environment. Continued corrosion processes may lead to increased levels of akaganeite and precipitate hollow bubbles of goethite and lepidocrocite. There may be autocatalytic processes maintaining high acidity, and high corrosion rates, even at low RH. They will still be governed by the wet dry cycles which we have looked at for atmospheric corrosion, but will have a greater susceptibility to corrosion at lower RH and at greater rates, due to the presence of pollutants within the corrosion layers.

For the purposes of sensor design the primary corrosion products of archaeological heritage iron will be magnetite, goethite, lepidocrocite and akaganeite. The creation of these on any proxy corrosion sensor, combined with a level of associated chloride, will give the closest approximation to the corrosion layers we are likely to find within an archaeological iron collection.

# Chapter 4

# Treatment and storage of archaeological iron

## 4.1 Iron conservation

The tendency of archaeological artefacts to begin rapidly corroding upon removal from their abandonment environments creates the need for methodologies to prevent or control continued corrosion. These methods can be broadly categorised as being either passive, by controlling the environment in which the artefacts are kept, or active, by changing the characteristics of the objects themselves. Active stabilisation treatments involve either the introduction of compounds (to preserve or increase the passivating properties of the corrosion layers), the removal of aggressive ions (typically chloride) or the coating of an artefact (to prevent further oxygen intake). A brief review of the various methods is given here, to highlight their effects on heritage artefacts, and which we might expect our sensors to encounter.

### 4.1.1 Temporary post excavation methods of archaeologists

It can take months, or even years, before treatment of iron objects is started, dependant on the rigour of the individual archaeologist, company or institution carrying out the recovery. However, the problems of immediate degradation are recognised within the profession and

some immediate methodologies are in place. Temporary stabilisation methods are implemented between excavation site and archaeological finds room. From the authors personal experience, these can include all, any number of, or none of the following methods used in archaeological companies. On initial excavation from the soil, artefacts are sealed within a closed environment, a plastic bag or container, before shipping for finds processing. On arrival, the artefacts will be thoroughly and carefully washed in aqueous solution. For the majority of archaeological iron, treatment then ceases; the iron will subsequently be transferred into a low RH environment and stored. In well funded situations, for finds of importance and for the purposes of iron which will be taken to a museum, this can be followed by the impregnation of the iron artefacts with an alkaline solution. Typically 0.5M sodium hydroxide is used, preventing access of oxygen, neutralising the pH and drawing chloride out of the corrosion layers to the corrosion layers [1].

### 4.1.2 Active Conservation: Past methods

Larger, better funded projects and museum collections use more advanced stabilisation techniques. The majority focus on desalination. This can be achieved through; the submersion of an artefact in a solution promoting the diffusion of chlorides out of the artefact, the electrolytic removal of chloride ions or heating the artefact to a level where the chlorides will be volatised.

Historical methods concentrated on removal of corrosion products and pollutants, considered here as their effects may still be felt in modern day collections. At the start of the 19$^{th}$ Century, extremely high temperatures were used to completely remove corrosion products [2], ruining many artefacts and physically destabilising many others [3]. In the 1970s chemical replacement methods were introduced. A mixture of lithium hydroxide (LiOH) and ethanol (or similar solvent) was applied to reduce corrosive effects [1,4]. Anhydrous ammonia, ethylene oxide, methanol, and various types of aqueous washing were also tested [4-5]: All were largely ineffective. Ethylenediamine was tried together with sodium hydroxide solutions [6], but is as likely to cause corrosion as it is to prevent it [7]. Similarly, hydroxylamine use has recently been stopped; it oxidises $Fe^{2+}$ ions and dissolves magnetite [8]. All these methods may have been used on objects, the majority of which will increase the corrosion rate we are likely to encounter and attempt to emulate.

### 4.1.3 Alkaline Sulphate treatment

The most common active archaeological iron conservation method in Britain is alkaline sulphate treatment. Developed in 1975 by North and Pearson for marine iron [1, 8-9], it has

subsequently been used for iron artefacts from any abandonment environment, with high levels of success [10, 11]. Over two collection surveys of treated objects at the Museum of London, Keene [12] has shown alkaline sulphite and sodium hydroxide were the most successful methods in extending the lifespan of iron objects. A similar study of French artefacts observed a re-corrosion rate of only 0.02% [13]. It has also been shown to preserve the graphitised region within marine cast iron, retaining details of an artefacts surface [14].

The methodology employs a strong alkali and a solution for the passivation of corrosion products. Alkaline sodium sulphite is used as solution of 0.5M $Na_2SO_3$mixed with 0.5M $NaOH$ in deionised water. Prior to introduction, archaeological iron is subjected to de-aerated conditions to remove oxygen from the corrosion layers. Objects are placed in solution, whereupon sulphite ions in the solution oxidise to sulphate ions (reaction 4.1), acting as a reducing agent to change ferric ions to ferrous.

$$SO_3{}^{2-} + 2OH^- \rightarrow SO_4{}^{2-} + H_2O + 2e^- \qquad \textbf{[Eq. 4.1]}$$

$$3FeOOH + H_2 + e^- \rightarrow Fe_3O_4 + 2H_2O + OH^- \qquad \textbf{[Eq. 4.2]}$$

$$3Fe(OH)_2 \rightarrow Fe_3O_4 + H_2 + 2H_2O \qquad \textbf{[Eq. 4.3]}$$

Gilberg and Seeley [15] show the reduction strength of sodium sulphite is such that akaganeite and lepidocrocite may be reduced to the passivating magnetite (reaction 4.2) and goethite. They also suggested that in the less oxygenated conditions, the reduction to magnetite will actually involve the evolution of hydrogen (reaction 4.3).

NaOH acts as base, neutralising acidity at the metal interface and within pores [16]. Production of ferrous ions at the anode ceases and oxygen levels fall rapidly. Chloride concentrations fall in the bulk electrolyte, drawing more into the solution [17]. Soluble ferrous compounds deposit as ferrous hydroxides and oxides at anodic sites, blocking and pacifying them [18]. The efficacy of sodium hydroxide as a standalone treatment has been demonstrated; short immersion in the solution can cause a drop of -1000mV (SCE) in corrosion potential, rising to around -200mV vs. SCE after a few days and eventual pacification [19-20].

The solution is replenished to maintain pH and concentration, with chloride levels monitored. Immersion continues until remnant chloride reaches a required level. Upon removal, objects are typically washed in $NaOH$ solution [21] and distilled water, often containing inhibitors such as $NaNO_2$ or $Na_2CrO_7$ [22], to remove solution and remnant ions. Barium hydroxide, $Ba(OH)_2$ has been used at this stage to remove sulphate ions, but can

deposit undesirable barium salts. Finally, the artefact may be dehydrated with acetone and sealed with a coating of Paraloid B44 [16].

The exact methodologies for treatment can be different depending on the conservator. For example, it has been suggested that a solution of only 0.05M $Na_2SO_3$mixed with 0.1M $NaOH$, will be sufficient, and reduce chemical hazards [16]. The duration of iron exposure can vary from between 8 weeks to a year [15, 23], depending on object size and the amount of trapped chloride. Solution temperature can be held at between 60 and 90°C. Biocides are often added to eradicate sulphate reducing bacteria inhabiting marine cast iron [24].

It should be noted that in the United Kingdom, alkaline sulphate treatment has lost favour. Lack of manpower and funds within the heritage sector have contributed, as have perceived weaknesses in the methodology. Continued corrosion after treatment will always occur, albeit at a reduced rate [25]. Too concentrated solutions or too long exposure have been reported to soften, break down and even destroy corrosion layers [7, 11]. Deposition of ferrous oxyhydroxides within corrosion pores may actually prevent chloride removal and promote electrochemical imbalance [26]. However, a survey of German conservators in 2009 showed that 40% were still using desalination treatments regularly, of which alkaline sulphate was the most common [27].

### 4.1.4 Plasma treatments

Application of plasma, generally formed from hydrogen, to iron objects, can be used to reduce corrosion products or remove them [28-30]. Originally, the methods were only operable under high temperatures, degrading the metal structure [31], but more recent advances allow plasma methods to be carried out as low as 80°C [28]. Alone, the method will only remove exterior corrosion layers and, at low temperatures, will not affect the chloride content not bound up within these layers [29]. It has been suggested that plasma treatments on artefacts can be beneficial for subsequent alkaline sulphate treatment, allowing better access of solution to the anodic sites [29-30], but this is yet to have been proven [32]. The method is often prohibitively expensive and requires sophisticated equipment and training.

### 4.1.5 Electrolytic reduction

Electrolytic reduction involves the removal of chloride ions by electrolysis, the iron object effectively becoming a cathode in an electrochemical cell. As such it is only applicable where extant metal is available. An applied potential can increase the porosity of the layers [21],

encourage the formation of a passive layer at the metal surface [33] and draw chloride from the corrosion layers. Marine crusts can also be removed, by evolution of hydrogen at the metal surface [34-5], though this may be detrimental to object integrity [34].

External anodes, generally mild steel rods or sheets, are placed around an object. Typical distances range from 20 to 80cm, maintaining equal distances to avoid preferential electrolysis. In some cases, such as a cannon or metal container, an additional anode may be placed within, but not touching the artefact. NaOH is generally used as an electrolyte for its previously mentioned properties (section 4.1.3), high conductivity and wetness. Concentration varies according to iron type: 0.5M for cast iron and 0.5-1M for wrought iron has been suggested [21]. Applied potential varies dependent on artefact type; to remove concretions from wrought iron, required potential is likely to exceed that of hydrogen evolution, at which cast iron would undesirably lose its graphitised regions [9]. The hydrogen evolution potential will be different for each artefact, so gradual voltage increase is used to find the limit, by observations of bubbling and sudden current increase. Current is monitored; lower current densities remove chloride more efficiently than higher current densities, but are less effective at removing concretions [36].

## 4.2 Passive conservation: Storage and display of iron artefacts.

To passively conserve iron antiquities, heritage organisations control the atmosphere of cases, storage and display environments. This may include control of relative humidity, availability of oxygen, temperature of the artefact (largely governed by ambient temperature and light intensity) and removal of air pollutants.

All historical artefacts will benefit from a constant climate in their ambient environment; artefacts not made of iron often have vastly different optimal stabilisation RH and temperature levels. Wood and organic materials, for example, tend to warp and crack in the dry environment in which iron is best conserved [37]. It is often convenient or even necessary for museums to display artefacts of various materials within a single case, dependant on chronological theme, the creation of a narrative and the needs of curatorial illustration. For smaller museums where space is at a premium, this may also be the case in store rooms, with iron objects placed cheek by jowl with the rest of the collection. Conditions can range from standard indoor conditions through to a carefully controlled environment optimised for conservation of iron. Between these two extremities will be a variety of atmospheres, artificially created as a balance of the needs, practicalities and funding of a particular heritage organisation.

### 4.2.1 Closed container storage

Heritage artefacts will, where possible, be kept in a closed environment. Those too large or impractical to enclose, or those better presented outside a case or immovable from their original position, will be kept within the ambient atmosphere of the buildings in which they are housed. In the majority of cases, and certainly for small finds, storage and display occur within a closed system, benefitting from relative ease of climate control and prevention of additional oxygen or pollutants entering the system. These can range from plastic zip-lock bags, through to Tupperware, through to display cases. The actual amount of protection these will provide from the ambient environment vary dependant on the quality of the container.

For iron, a decrease in ambient RH to below 12% should prevent corrosion, or at least decelerate it to an acceptable level [38]. For recently excavated artefacts, an RH this low can damage the physical integrity of an artefact and promote corrosion. Gradual decrease of RH is sometimes applied, preventing the degradations sudden RH change induce. In the majority of situations, microclimates of sealed containers of iron objects will have measures to reduce the levels of RH within them, generally using moisture buffers to hold RH at a required level. For iron, corrosion rate is assumed to have ceased at 12% RH, be minimal between this level and 30%, with a rapid increase at around 50% RH [39]. We cannot assume that a monitored and buffered environment will necessarily be designed to completely stop corrosion. Due to budgetary and manpower constraints, maintaining levels below 12% are not always realistic. Instead museums adopt strategies of risk management, mitigating, not preventing, corrosion and maintaining extant, but low, corrosion rates [40]. The SS Great Britain's hull is kept at a realistically obtainable 22% RH by the installed air curtain. While this won't completely prevent corrosion, it will theoretically increase lifespan by a factor of 4 while keeping costs at an acceptable level [41-2].

Inexpensive measures for controlling humidity lower RH within a small closed environment. Previous methods have included water absorption by paper, wood, cotton and saturated salts. Saturated salts, in particular, were very popular for much of the twentieth century [43]. Under humid conditions, these absorb moisture, which is released when the RH drops to below its critical level. They have a high absorption and desorption capacity, are efficient in the maintenance of an RH, and can alter RH dependant on salt type used. They have now fallen out of favour, thanks largely to the re-deposition of salt which could occur within the environment and their tendency to release gaseous pollutants [43]. Today silica gel is the dominant moisture buffer used. Moisture is adsorbed at high RH and released as RH decreases in the same manner as salt solutions. The gel benefits from being chemically inert, non-flammable, a high water capacity and a very fast response time to changes in RH [37]. Methodologically, oven dried silica gel is introduced at a quantity of about 1kg per cubic meter of enclosed space. The RH level of a container can be indicated by a simple

colorimetric card sensor, which will indicate when gel needs replenishing. The amount which must be introduced to maintain the RH in a non-sealed container is such that it will be essentially useless for these purposes.

For environments of greater importance; inside a display case perhaps or for a large container of many iron artefacts; mechanical RH control can be used. Dehumidifiers with humidistats to monitor the absolute humidity can be connected to environments, or monitor entire rooms. They regulate a flow of air of varying RHs to either increase or decrease the amount of moisture in the atmosphere and can be fitted with filters to remove pollutants [44]. While the initial cost of these units is great, it has been argued that in the longer term they will be cost effective, both monetarily and in manpower. The high financial cost of the initial set up of such a system make them rare except in the more financially secure heritage institutions.

Other methods of corrosion control have been attempted. The reduction in temperature of an environment has been previously mentioned as having a mixed impact on corrosion rate: Any decrease in temperature must be balanced with a removal of water from a system to maintain a low RH. For the majority of containers, temperature will be the same as the ambient environment. Deep freeze storage has been attempted in Germany for iron artefacts, but over a long period had damaging effects [45]. Removing oxygen entirely from a closed system to store iron has been attempted, with some limited success [46]. However, this creates problems of access to the artefacts, severely limits the options for display, and requires expensive sealed environments. It is unlikely that it would be encountered in many heritage contexts.

### 4.2.2 Mixed collections and pollutants

Where iron artefacts are displayed with other materials, a separate set of RH levels must be considered. RH is generally maintained between 45 and 65% RH, a level at which significant iron corrosion may occur [47]. In addition, the environments of sealed containers, particularly in older museums, may be themselves harmful to iron objects. A suggested interaction between a mixed object container and a metallic artefact can be seen in Figure 4.1, including introduced pollutants and atmospheric interactions. So called “closed” environments will still interact with the surrounding atmosphere, allowing ingress of pollutants. The British museum analysed the pollutants found in the atmosphere of a number of display cases and rooms using silver tokens and a subsequent analysis of their corrosion layers [48], showing pollutants to be present in all cases. Concentration of pollutants depended on the case contents; artefacts acted as pollutant sinks, trapping the spare pollutants that were present and decreasing those available in the air.

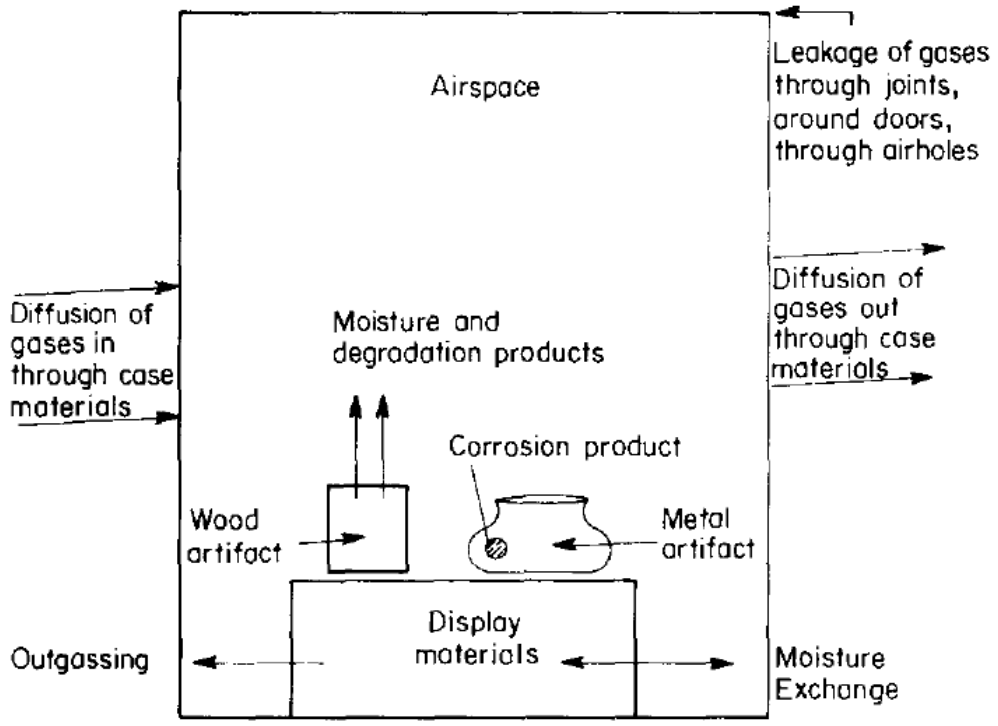


**Figure 4.1:** Model of the possible movement of gases and pollutants in an exhibition case (from [49], fig. 2, p.304)

Pollutants my also come from the containers themselves. Wood is known to release corrosive acetic and formic acids [48-50]. These compounds are readily adsorbed on glass and can be rereleased on a change in RH or temperature [49]. Sulphides can be released from glues and rubber used in the construction of a case of from textiles used for backing [48, 50].

### 4.2.3 The ambient museum environment

The removal of artefacts from their closed storage or display environments change corrosion condition to those of the ambient atmosphere. The new, assumedly higher, corrosion rates will alter the artefact and have an extended effect when the artefact is returned to its original atmosphere. There may also be artefacts constantly exposed in the ambient atmosphere, due to convenience or positioning.

New museum design incorporates architectural features and mechanical methods to closely control the uniformity and nature of the climate in each room and older buildings have been renovated to protect areas from external environmental factors [51]. Regulating an entire building through architecture has a high initial financial outlay, but may be more cost effective in the long term. Thicker and better insulted walls, smaller and higher windows, and the specific layout of rooms and floor plans have all been used to decrease the effect of seasonal and diurnal changes in temperature and humidity [52]. Moisture buffer materials

are used within the structure to reduce and control RH. Highly permeable paints are applied to walls and surfaces to increase their absorption of water. The floors are insulated for moisture but allow heat conductance, allowing ground heat to permeate during the colder periods. Active climate control is practiced; humidity buffers and climatic control machines can be installed to control rooms or suites.

We can characterise the environment of a museum as varying between typical indoor conditions, through to a controlled low RH environment with no pollutants and low oxygen access. The artefacts will inhabit one point in this spectrum for the majority of its storage or display, while being subjected to other conditions within the scale when it is moved or otherwise disturbed. The standard which is generally prescribed for museum ambient environments is an RH of 50%, a temperature of 20°C and 100 Lux of illumination [37]. However, for old building conditions could be considered, at the worst, to approach 100% RH, temperature fluctuations at close to the external climate and a variety of pollutants.

## 4.3 Corrosion Monitoring of Archaeological metals

The high cost of corrosion, both in terms of manpower and funds, has led to the development of a wide range of corrosion monitoring techniques. It has been estimated that the cost of corrosion in the United States in 1998 was approximately $276 Billion; equating to 3.1% of GDP [53]. In the UK, the Corrosion and Protection committee set the cost of corrosion in 1972 at 3.5% of GDP [54]. The same report estimated that up to a quarter of this amount could be saved through applications of corrosion monitoring and control; in order to test the effectiveness of corrosion prevention techniques it is essential to be able to monitor corrosion rates. These rates will not necessarily be calculable from our knowledge of the systems in which the metals are found and must be actively measured.

Corrosion monitoring of archaeological metal presents additional challenges and constraints, requiring the development of separate approaches. Tests on artefacts must, in the main, be non-destructive and non-altering. When a proxy is used, care must be taken to ensure the effects of corrosion products and past heritage lifetime are factored in to monitored rates. When monitoring *in situ*, sensors must be unobtrusive and avoid changing corrosion conditions, the artefact or the environment. Finally, there will be constraints in funding, expertise and time which may not be present for industrial plant monitoring. The choice of technique will depend on the above considerations, the type of environment in which they will be used, the type of measurement required and the available funds of the organisation. Each will give corrosion rate and phenomena in different terms, will be applicable in different

and distinct situations and have different strengths and weaknesses therein. Not all industrial techniques will be appropriate for use on archaeological metals.

An outline of those methods of corrosion monitoring which have been previously used on archaeological metals, and the alternatives we might consider, are presented here to cast this study in context. Electrical resistance corrosion monitors, the methodology chosen for this study, will be reviewed separately and in depth in Chapter 5.

### 4.3.1 Visual techniques

Visual techniques use two dimensional optical maps of the exterior or interior of corroding metal, giving corrosion rates in terms of corrosion product or feature growth, number of corrosion features or change in base metal dimensions. Comparison of images over time is a commonly used method for determining the state of heritage metals, employed by English Heritage [55] and the Museum of London [56] to assess their heritage iron collections. Both make simple optical comparisons of object change over time, with an assigned numeric score based on observed damage by a conservator. Collection corrosion rates are given in terms of number of artefacts lost or observed to be in a more degraded state over time, while qualitative and subjective corrosion observations can also be made.

#### 4.3.1a Digital Image comparison

Digital imaging of artefacts allows physical damage and corrosion phenomena to be mapped using imaging software. Successive digital images of a material surface are taken, by a CCD camera or digital scanning of film images, and quantitative methodologies used to process and highlight areas of change and displacement. A chemical indicator may be introduced to map changes in chemical concentration or acidity over a material. The most common methods are digital image correlation (DIC) or differential digital imaging technique (DDIT). In the former, each image is split into multiple parts and patterns of pixels within each sub-image are identified. The deformation of these patterns and the movement of the sub-image compared to the others allow the calculation and mapping of strain vectors within the metal or corrosion product [57]. In DDIT, the image is converted into an algorithm which maps the intensity of each region against its placement. Each successive image has the former images subtracted from it, leaving an image which shows only regions of changes in intensity; mapping areas where displacement has occurred [58]. Technique accuracy relies on image bit-depth, resolution and frequency, while the resolution of the final image will rely on either the size of the sub-images (in DIC) [59] or the accuracy of the algorithms (in DDIT) [60]. DIC is more sensitive to small surface displacements, allowing the imaging of very

small field strain across a material [59], corrosion phenomena in chloride induced atmospheric stress corrosion cracking [60], inter-granular crack growth [61] and a variant of the technique using a laser has been used to observe degradation of aircraft [62]. DDIT has been used to highlight streaking corrosion in abraded aluminium [63] and chloride contamination effects on pre-treated steel [58]. The methods need only a digital camera and the relevant software to operate, making them less expensive than comparable techniques, easy to use and with the potential for on-line monitoring. However, accurate analyses will require corrosion expertise, corrosion rates will not be in terms of metal loss and corrosion which doesn't cause surface deformations will be missed. It would be most effective when coupled with corrosion product analysis and on surfaces with significant speckling or other contrasting elements.

DIC has been applied to archaeological materials and it has been suggested that it would be of great use for non-contact monitoring of museums. Bronze artefacts have been observed and evaluated by combining DIC with Fourier transform analysis to create an algorithm based on reflective brightness to monitor film growth on archaeological bronze samples [64]. The method does not give quantitative corrosion rates, but is effective for highlighting changes in uniformity and estimating environment corrosivity, while combination with on line cameras could provide automatic flagging of fast corroding specimens in museum environments. Such automated systems have been suggested by Gros et al. [65] and Choi and Kim [66]; image analysis tools to identify, classify and quantify individual surface corrosion damage events using software analysis. More research is required, but the studies suggest the possibility of automated probabilistic computerised identification of corrosion from online images. DIC has also been used to detect the optimal stop point for electrochemical conservation methods by comparison between non-corroded and corroded specimens [67].

#### 4.3.1b X-Radiography imaging

Changes in X-ray intensity and modulation as they pass through an object are directly related to the density of the material they pass through. Mapping of the results can create thickness and density maps of a material, allowing identification of corrosion phenomena and observation of the spread of corrosion products, cracks, voids and other changes in density to be observed [68]. Image analysis of radiographs provide corrosion rates in terms of corrosion feature growth or metal loss over time over time and has been used to observe the ingress of intergranular corrosion in Aluminium [69] and stress corrosion cracking in steel [70]. Thickness loss can also be plotted over time from X-ray intensity measurements; a standard method of determining remaining pipe-wall thickness in the oil and gas industry [71]. Current methods can be portable and easily applied in situ. X-rays travel easily through air, and relatively easily through water, allowing monitoring without physical contact with the

specimen. However, the method can be expensive, and would be difficult to run as an online monitor within a museum environment.

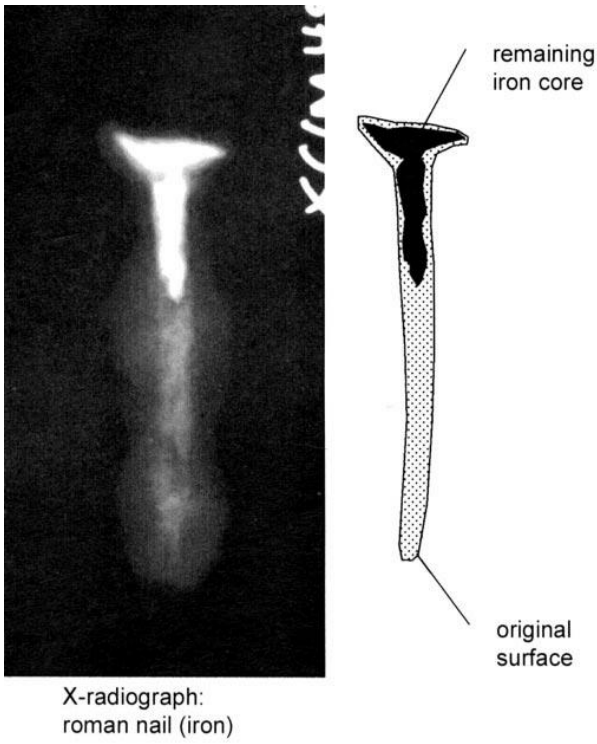


**Figure 4.2** X-radiograph of a nail with illustration of predicted corrosion extent and original surface projection (Taken from [73], p. 69)

X-ray images have been used in archaeology largely for observation of an original object without removing corrosion layers [68]. For iron objects, notably iron lances from the waterlogged site of Nydam [72] and iron nails from sites across Germany [73], corrosion rates have been calculated from radiographs showing the original metal surface (from graphitisation) against the amount of extant metal at time of excavation (figure 4.2). For Bronze plates, Yahagi et al [74] have combined radiographs with a form of DDIT to give thickness measurements of extant metal and measurements of corrosion depth from calculated original metal state. While these methods have been used only to evaluate previous corrosion rate, it would take little to adapt the technique for continuous monitoring in a museum or heritage setting. Advances in technology and decrease in price for hand held X-ray devices will increase the popularity of this technique in the future.

### 4.3.1c Thermal imaging

Heat escaping from a material will be a function of the heat input, the volumic temperature and the local thermal conductivities [75]. The emitted heat can be intensity mapped by

infrared camera. Areas with differing metal thicknesses, different thermal properties or voids will emit heat differently to the bulk metal, allowing these phenomena to be identified. In metals which maintain a different temperature to the ambient environment, mapping can highlight corrosion defects without additional apparatus; a technique commonly used in pipeline corrosion monitoring [76]. For non-plant metals, heating can be applied from an external source, with heat intensity, dissipation and speed of diffusion measured. The method is noncontact; changes can be monitored in metals covered in coatings, behind insulation or with extant corrosion layers. The technique has been applied to give thickness measurements from direct observation of heat travelling through a metal [77], mapping of surface corrosion by diffusion of heat into surrounding material [78] and illustration of corrosion phenomena on a surface through coatings [79]. Depending on the application, data can be retrieved almost instantly, is of high resolution and is relatively easy to interpret. However, corrosion rates are largely qualitative, unless a proxy of similar metal can be found to configure thermal conductivity [75]. While non destructive, heating of the material may alter adhesion of corrosion layers or create internal stresses in an artefact. It is, perhaps, more suited to highlighting and inspecting corrosion phenomena rather than assessing corrosion rate.

The technique has been used to investigate corrosion in archaeological material: Scudeieri et al [75] used short thermal perturbations, created by flash bulb and mapped by infrared video camera, to map temperature variation against time across the surface of archaeological samples, giving information on the subsurface structure. The method was used to study a bronze statue of Marcus Aurelius, successfully measuring the remaining thickness of the bronze without access to the interior and mapping cracks and voids from mechanistic failures. While corrosion rate was not directly inferred, it is easy to see the application for future studies. For iron and steel, thick corrosion layers may cause problems with low thermal conductivity.

### 4.3.2 Gravimetric techniques

Measuring the change in weight associated with corrosion processes can give comparative corrosion rates of mass gain (from creation of corrosion products) or direct quantitative rates of metal loss (by corrosion and removal of products) [80]. Technique accuracy relies on the apparatus used and the strength of assumptions about the corrosion processes.

### 4.3.2a Coupons

Monitoring of sacrificial coupons is perhaps the simplest, cheapest and most widely used way to study corrosion. Metal coupons, of similar or identical material to that to be monitored, are placed into the same environment as the metal to be monitored. By harvesting coupons at regular intervals and comparing their change in mass or thickness, one can estimate average corrosion rate over the time of exposure [81]. Additional information is provided by optical inspection and analysis of the corrosion layers. The use of coupons in low corrosivity environments is covered under an International Organisation of Standardisation standard (ISO 11844) [82-3]. The method benefits from being very simple, cheap and highly effective in any corrosive environment. However, recording the results generally requires coupons to be removed from the environment or otherwise tampered with, altering their continuing corrosion rate. Result resolution is dependent on the number of coupons and is typically very low.

Coupon exposure and harvesting is a standard measure of corrosivity of museum and storage environments. (Wrongly) known as dosimeters, copper coupons are often used as a standard to give an overall value of environment corrosivity [81]. Rhyl-Svednsen [84] has illustrated that lead coupons may also be used in this role, setting out guidelines for their long term use. Usually mass gain is used as a proxy for corrosion rate. It has been suggested that this method, while simpler, cheaper and requiring less expertise, will be prohibitively inaccurate. Rhyl-Svednsen [84], Johansson and Leygraf [85] and Mohamed et al. [86] have assessed mass gain against measured weight loss after removal of corrosion layers. All conclude the latter to be more accurate, but find very good correlation between the techniques for copper and lead. For silver, or in environments where additional mass, such as dust or air pollutants, can be added to the coupons, correlation is less convincing. The technique is adaptable to storage condition; Castian [86] used weight loss measurements to investigate the corrosion rate of clean iron coupons in wet storage solutions. This adaptability is indicative of the necessity to alter coupon methodology dependant on individual circumstance and to use complementary evaluative methods to create stronger assumptions and results.

### 4.3.2b Quartz crystal microbalances

Corrosion may cause very small changes in mass in the short to medium term, requiring specialist equipment to monitor. Quartz crystal microbalances are highly accurate devices for measuring small (down to picogram) changes in mass, utilising the reverse piezoelectric effect of quartz crystals. Applied strain alters the electrical resonant frequency of the crystal, measurable through application of an alternating current. Mass change is calculated using Sauerbrey's equation [80]. For corrosion sensing, the selected metal is coated on top of the

crystal. For aqueous corrosion, electrochemical QCM can be used to measure mass change of an electrode within a solution by taking into account solution pressure, density and viscosity [88]. The sensitivity of the technique means it may be used to monitor the formation of oxidised layers on the surface of a metal [88], deposition of corrosion products [89], moisture accumulation [90] and the effects of environment corrosivity and pollutants [91]. QCM have been field tested for copper, nickel, gold and silver in uncontrolled indoor environments [92-3] and for aluminium, gold and copper in outdoor environments [94]. The system allows automated online logging, generating high resolution corrosion rate data. Detailed knowledge of the processes is required to properly assess data, especially when using weight gain measurements. Similar complicating factors to those discussed for coupon measurements, such as dust and pollutants, may also skew results.

QCM are often deployed in museums to monitor corrosion and the decay of other materials. Odlyha et al. [95] have reported on the research and preventative conservation undertaken by English Heritage and the MIMIC project, both of which use QCM to monitor collections, answer corrosion questions and provide corrosion warning systems. Lead coatings were used to judge the effects of atmospheric acetic acid on antique organ pipes, and briefly cover the extent to which the method is used across the organisation. Other studies have focussed on low humidity environments. Sjogren and Bosec [96] used QCM to monitor film growth on copper and silver in museum display environments, reporting high accuracy and result definition. Zakipour and Leygraf [97] observed adsorption of thin films, growth of corrosion product and the effect of atmospheric pollutants on silver in museum storage rooms. Both studies reported accuracy in the region of $10^{-8}$ $gcm^{-1}$, but highlight the necessity of complementary analyses, of either corrosion products or electrochemistry, to calculate true corrosion rates. The method is popular in large organisations, but may be prohibitively expensive for smaller heritage organisations.

### 4.3.3 Electrochemical methods

Electrochemical measures of corrosion rate use charge flow in corrosion reactions to calculate metal loss. The balanced electrochemical reaction of free corrosion means corrosion rate, in terms of net metal dissolved, is proportional to the anodic (or cathodic) half-cell current. Faraday's law states the mass of a metal altered will be directly proportional to charge transfer and the equivalent weight of the metal in question [98]. Calculation of the corrosion current, $I_{corr}$, and the surface area across which the current flows, allows calculation of corrosion rate. Assuming an even distribution of current, corrosion rate in terms of metal loss, MR ($g/m^2$), can be calculated by;

$$MR = K.i_{corr}.EW \quad \textbf{[Eq. 4.4]}$$

Where $i_{corr}$ is the current density ($\mu A/cm^2$), EW is the equivalent weight (mass of substance oxidised by the passage of one faraday), and K is $8.954 \times 10^{-3}$ $gcm^2/\mu Am^2$ [99].

Electrochemical measurements can be made to calculate $i_{corr}$. Running a current through the material is generally impractical, so proxy electrodes of the same material are placed within the same or simulated identical environment. This usually comprises a three electrode system; a working (corroding) electrode which approximates the metal to be assessed, a counter electrode and a reference electrode (fig 4.3). In a lab experiment, the system will use a defined reference electrode (usually a saturated calomel electrode), though field tests may use three identical electrodes and forgo the luggin capillary [99].

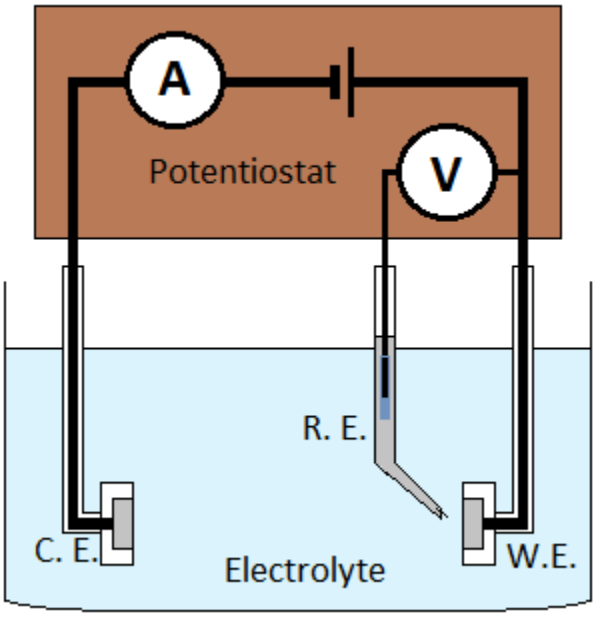


**Figure 4.3**: Schematic of a standard electrochemical cell for corrosion measurements

To find $I_{corr}$, exterior potential is applied between the working and counter electrodes, while monitoring resultant potential and current. The potential during corrosion, when no exterior potential is applied and there is no net current flow, is the open circuit potential (OCP) of the electrode/electrolyte system. The difference between this value and any applied voltage is known as the over overpotential, $\eta$. Once applied, this polarizes the working electrode and controls and separates the anodic and cathodic reactions on the working and counter electrodes. By monitoring the potential and resultant current of the system, the corrosion current, $I_{corr}$, and the OCP may be extrapolated. $E_{corr}$, the corrosion potential, is equivalent to the OCP. A steady $E_{corr}$ indicates that corrosion rate will approximate to constant.

While electrochemical techniques were previously limited to wet systems or bulk solutions created to mimic electrolyte films, methods for monitoring atmospheric corrosion have been developed. Within such systems, the aqueous aspect of the cell is formed by the

atmospherically deposited electrolytic layer, while electrodes are deployed flush to, and separated by, a non-conductive substrate. Stratmann [100] applied the system to study corrosion kinetics of aqueous film electrochemistry on iron, using an external Kelvin probe and a differential pressure meter. The method was limited by the apparatus, suited only for specialist research applications. Zhang and Lyon used both tri-electrode [101] and bi-electrode [102] systems to monitor polarisation curves in electrolytic layers; demonstrating the cathodic processes of zinc, copper and iron and the initial, passivating stages of atmospheric corrosion of iron. Similar studies by Nishikata et al. [103], minimised error through reduction of electrodes separation, while studying the initial corrosion mechanisms of copper, stainless steel and iron. Alternative layouts have also been proposed for tri- [104] and bi- [105] electrode systems. The most recent is an interweaving bi-electrode comb, which maximises the contact with the electrolyte, minimises distance between electrodes, and maintaining a constant electrolytic film (figure 4..4) . Designed by Fu et al. [106], it allows readings in lower RH atmospheres than previous, improves electrolyte continuity and correlated well with simultaneous mass measurements for corrosion rates and electrolyte thickness. Thee et al. [107] used the same design to study wet dry corrosion of weathering steel in simulated marine atmospheres, demonstrating that the sensors could be used as online corrosivity loggers, could monitor electrodes with existing corrosion layers and would work over a large number of cycles and long time period. Further improvements in the technology would allow these techniques to become more prevalent in industrial and heritage settings.

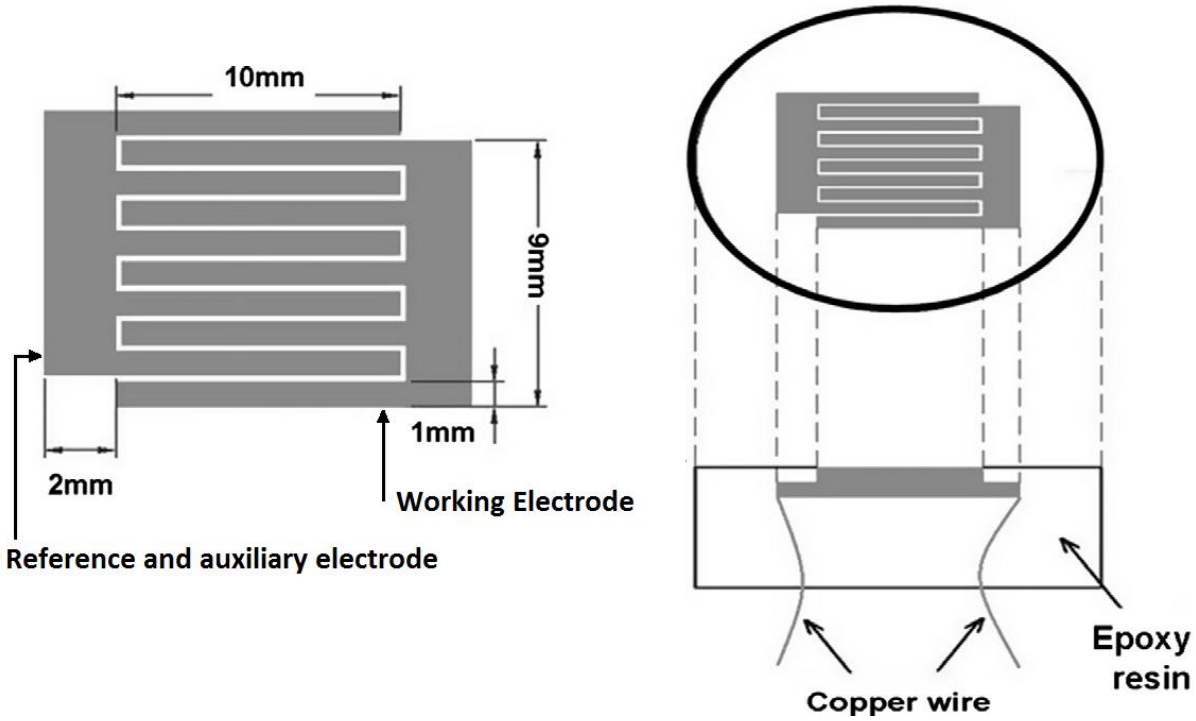


**Figure 4.4**: Interweaving comb electrode design for measurement of electrochemistry of electrolyte during atmospheric corrosion (adapted from [107], p.131)

Mechanical methodology for generating electrochemical readings will depend on circumstance, budget and desired results of the monitoring. Choice of application and interpretation will allow differing generation of corrosion kinetics, phenomena and rates. A series of these methods are used in research, industry and heritage.

4.3.3a Polarisation resistance techniques

The simplest method for extracting the $I_{corr}$ and $E_{corr}$ of a system is through application of a potentiodynamic DC current to the electrochemical cell. This will generate resistance to polarisation equal to the ratio of the overpotential against the resultant current. The slope of plotted overpotential against current can be extrapolated to a point where the overpotential is zero ($E_{corr}$), to give $I_{corr}$. At very low applied potentials (≈0-30mV, typically <10mV [99]), the relationship will approximate to linear; calculation is made through differentiation of the linear plot, multiple point measurement across positive and negative over-potentials or a single point measurement compared against the OCP. This form of extrapolation is known as linear polarisation resistance (LPR) [108]: Standard practice is documented in the ASTM standards ASTM G3 for reporting data [109], ASTM G5 for instruments used [110] and ASTM G59 for applied methodology [111]. At higher potentials, resistance to polarisation will not be linear. Tafel analysis may instead be carried out, using logarithmic plots and the Tafel equation [99];

$$\eta = \beta \log (i/i_0) \qquad \textbf{[Eq. 4.5]}$$

where $\eta$ is the overpotential, i is the measured current density at the applied potential and $i_0$ is the current density at $E_{corr}$. $\beta$ is the Tafel constant, which is experimentally measured by plotting log i against the applied potential and measuring the gradient current curve at high potentials (where the line becomes linear) [98]. Combining both the anodic and cathodic curves, gives the Butler-Volmer equation for deriving $I_{corr}$[99]:

$$I = I_{corr}(e^{(2.3\eta/\beta a)} - e^{(2.3\eta/\beta c)}) \qquad \textbf{[Eq. 4.6]}$$

where I is the measured current, $\eta$ is the overpotential) and the Tafel constants for anodic and cathodic curves are denoted as $\beta_a$ and $\beta_c$ respectively. Standard practice is documented in the ASTM standard ASTM G5 [109].

Linear polarisation resistance and Tafel analysis are both used to generate corrosion data in research and industr. LPR is very fast, non-destructive, highly repeatable and accurate (to around 2.5μm a year [99]), generally used as a constantly monitoring online apparatus. It has been applied in industrial corrosion monitoring in situations including; soils, concrete, pipelines, marine and terrestrial infrastructure and aeronautics [98, 99]. LPR is limited in the

amount of corrosion data it provides, is better suited for comparative, rather than absolute, corrosion rates and can give poor results if corrosion is overly localised, electrodes lose integrity or the electrolyte conductivity is low. Tafel analyses give more accurate results, with Tafel plots themselves providing additional data on corrosion phenomena. Such analysis is unsuitable for in situ analysis or sustained tests as high overpotential may permanently alter the working electrode surface and release corrosion products into the electrolyte. It is more likely to be used in simulated environments.

#### 4.3.3b Electrochemical Impedance Spectroscopy

Electrochemical impedance spectroscopy (EIS), calculates corrosion rate from AC current applied to an electrochemical cell, generating an impedance. Alternating between positive and negative potentials in a sinusoidal wave function, AC potential at low levels (1-10mV) will have a pseudo-linear relationship with current, governed by impedance (Z) [112]. Impedance may be calculated from application of a range of A.C. frequencies. The resultant generated current will be phase shifted and of magnitude governed by impedance, from which overall system impedance may be calculated. By modelling the data against an equivalent electrical circuit, electrochemical rates and reaction kinetics of each system component may be derived by their individual capacitances and resistances of hypothetical circuit components [113]. Higher applied A.C. voltages may be studied using more complex models, reflecting the non-linear relationship between current and A.C. voltage [114]. Investigation of individual system components, including high-resistance paints, coatings and the electrolyte, the capacitance of the Helmholtz layers, and resistance to charge transfer, are possible. From the last of these, it is possible to calculate the exchange current density and corrosion rate.

EIS is non-destructive and results give highly accurate, time-dependant quantitative results, of great use for modelling complex systems with high resistance components. Results will share whichever weaknesses lie with the assumptions and models used in analysis, but the extent of previous research minimises the risk of misinterpretation. The main disadvantages will therefore be based in the high economic and skills expense and accessibility to samples. When used *in situ*, specialist equipment may be required [115], and it is unlikely that the necessary personnel would be able to cover all monitored stations. Instead it is likely results will be sent offsite for analysis [116].

4.3.3c Zero resistance Ammetry and Electrochemical Noise analysis

Zero resistance ammetry and electrochemical noise analysis both operate without applied voltage and can give corrosion rate and phenomenon information. The electrode system uses a zero resistance ammeter: Using feedback potential to neutralise circuit potential within a known resistor, thereby measuring current with no applied resistance [117]. Corrosion within the system is separated into half cell reactions on the working and counter electrodes (defined by electrode nobility), creating a potential difference. Current is drawn through the ammeter proportional to the rate of the reductive anodic processes on the working electrode. This method may be used to give corrosion current, especially between galvanicaly different electrodes. Three electrode systems can be used to monitor electrochemical noise: The fluctuation of both the current and potential which occur on a working electrode, due to sudden corrosion events such as pitting, crack propagation, breaks in passivating corrosion layers and other phenomena [118]. The standard deviation of the potential and current measurements can be used with sample size to give corrosion resistance times unit area, $R_n$, equivalent to the LPR. Noise current power and potential noise can be calculated, directly related to corrosion rate and electrode [119]. Other statistical techniques can be applied to the data over time, including skewness and kurtosis of noise, shot noise parameters, spectral methods and coulomb counting [120], all of which may give additional data on corrosion.

Zero resistance ammetry is most often used to measure systems likely to encounter galvanic corrosion, and genrally require significant understanding of corrosion processes to interpret. Electrochemical noise has the great benefit that it may be able to indicate the type of corrosion occurring, most often used in situations where pitting, localised and cracking corrosion may occur [121]. The techniques are non-destructive and low impact, allow time variable measurements and identification of a variety of corrosion types. However, the equipment used for monitoring must be of the highest accuracy to deal with low current and potential values, the readings are vulnerable to exterior interference. Significant experience and expertise are required for assessing the results.

4.3.3d Electrochemical corrosion monitoring of Archaeological metal

When applied to conservation methods and corrosion of metal antiquities, electrochemical methods have been applied both *in situ* on actual artefacts and using proxy electrodes or environments. Methodologies and apparatus have been selected dependant on circumstance and measurements required, directly adapted from industrial standards. While aqueous storage is more suited to electrochemical measurements, *in situ* measurements have also been made on atmospherically stored and architectural heritage metal.

Proxy electrochemical cells, using either polished artefact samples or proxy electrodes can be used to investigate archaeological corrosion, but are limited to providing expected models or predicted corrosion rates. Actual artefacts may be dissected such that specific sections of corrosion product or metal can be studied. Pons et al. [122] used EIS and chronoamperometry to assess porosity and protectiveness of archaeological corrosion layers on archaeological nails thus prepared. Chaves and Melchers [123] used EIS and zero resistance ammetry on prepared samples of pilings from Newcastle harbour, inserted into electrochemical cells with collected local seawater as electrolyte. Both studies produced evidence for localised passivation, pitting and corrosion rates, creating credible models for the corrosion system as it would occur *in situ*. Where direct samples cannot be taken, proxy electrodes and bulk solutions have been designed to mimic, and therefore model, conditions. Adriaens and Dowcett [124], and latterly Adriaens et al. [125], emulated treatment conditions of archaeological copper, while measuring electrochemical activity and using X-ray diffraction to characterise and quantify corrosion products. The two methods can be combined for greater accuracy of results and model justification; Rocca and Mirambet [126] used electrochemical techniques to test the effectiveness of a range of inhibition treatments on proxy metals, tested against fragments of actual conserved archaeological metal in corrosive environments. These studies have value in answering specific corrosion questions, revealing complex product transformations, corrosion rates and corrosion process models on archaeological metal. Such readings will not give corrosion rates of archaeological artefacts in storage or display, only replications and predictions.

Electrochemical methods form a vital part of aqueous conservation treatment and storage and are excellent at evaluating and suggesting efficacy, but results must be carefully interpreted. Metallic antiquities will often be stored, permanently or during conservation treatment, in alkali or other stabilising solutions. Electrochemistry is often monitored as a matter of course for determining end points for conservation treatments: When corrosion current is minimal and stable or potentials indicate complete passivation. An excellent review is given by Degrigny [127], highlighting the value of electrochemical monitoring to stability, removal of pollutants and passivation of corrosion products. Hjelm-Hansen et al. [128] monitored heavily corroded archaeological iron in conservation treatment solution, using potential stability to show passivation. These results have been evaluated and enlarged upon by Degrigny and Spiteri [129], who monitored metal coupon analogues and actual heritage artefacts in stabilising treatments. The similarity of potential change over time between samples allowed suggestion of conservation best practice and corrosion rate estimation, dependant on corrosion product type. A similar study by Hernandez-Escampa et al. [130] analysed the effectiveness of aqueous conservation methods, using proxies and samples from a heavily corroded anchor to suggest optimal conservation strategies for marine heritage iron. More complex analyses were performed by Domonéch-Carbó et al. [131] using EIS

measurements, coupled with micro-voltammetry, to evaluate the progress of alkaline stabilisation washes on archaeological iron. Analysis allowed modelling of the porosity and passivity of individual products within corrosion layers. They highlighted the weaknesses of non-complex electrochemical monitoring, where results can provide demonstrably false corrosion rates from separated reactions within corrosion layers.

*In situ* analyses on underwater archaeological iron have largely centred on evaluating conservation work on marine ship wreck sites. Macleod and Steyne's research on the wreck of the HMVS Cerberus [132] and Macleod's work on the Duart point wreck [133] have set a standard for employed methodology. Small holes are drilled through marine concretions to the extant metal, at which electrochemical measurements are taken using wet electrodes. Results of $E_{corr}$ are used to monitor corrosion stability, generate subjective corrosion rates and detect locality of corrosion. The same method was used by Gregory [134] to investigate the passivity of the marine crust and inform conservation on the civil war submarine Resurgam, and Heldtberg et al. [135], to monitor the effectiveness of applied zinc sacrificial anodes on the wreck of the James Matthews. The studies illustrate the importance of electrochemical methods in determining comparative corrosion rates and artefact stability. They are less useful for measuring absolute rates.

Electrochemical *in situ* corrosion monitoring of metal artefacts stored in atmospheric environments is difficult, but can provide valuable corrosion data. In addition to the specialist equipment required, archaeological metal presents problems including corrosion layers, access and limiting detrimental effects to an object. Monitoring by sinuous foil electrodes are challenged by simulation of corrosion layers, formation of a continuous electrolyte and resistivity. Instead, specialist electrochemical cells have been designed. Carullo et al. [136] describe a system for taking EIS measurements on metallic antiquities: An o-ring and porous membrane seal an electrolytic cell adjacent to a section of the metal, exposing a known surface area to the electrolyte. Progressive modelling can account for corrosion layers and systematic effects. The device was used *in situ* by Angelini et al. [137], to examine and characterise the porosity of various paints (applied since the 19$^{th}$ century) on the historic Palazzo Reale railings in Turin. A similar setup was used by Mudali and Raj [138] for *in situ* studies on the Delhi iron pillar, to compare the pillar to modern analogues and shed light on its passivating properties. Ongoing monitoring of the archaeological metal within Amiens cathedral by Grassini et al. [139] have used electrochemical cells bounded by foam pads, exposing the archaeological iron to a minimal amount of fluid for a minimal amount of time. The short time span of the tests allow readings to be attributed to the wetting phase of atmospheric corrosion and specific models of the corrosion products were created for each monitored location. The study is an excellent example of how electrochemical measurements may allow three dimensional, time dependant corrosion rate measures and modelling, but also on problems for an on-line system; constant exposure to an electrolyte

will impact the corrosion it monitors and is unavoidable for wet electrode systems. An alternative method, suggested by Corbellini et al. [140], uses dry and gel based coated-foam electrodes which deform around a rough surface to monitor electrochemistry, providing sufficient liquid is present. The system benefits from closer modelling to atmospheric conditions and can deal with high resistance coatings and products, but the gel based system requires additional wetting of the objects to perform electrochemical measurements and information on localised corrosion will be limited. The studies illustrate the importance of validity testing of laboratory studies and the limits of wet electrochemistry for monitoring atmospheric corrosion, but also the potential for portable systems in answering specific corrosion questions.

For monitoring heritage iron within structures, standard ASTM C876-91 [141] applies when considering concrete embedded structural support and standard atmospheric test can be used otherwise [139]. Duffó et al. [142] studied steel rebars within an abandoned 70 year old hotel, directly applying industry techniques to historical and heavily corroded rebars. The measurements of potential did not tally with corrosion rate measured by metal loss against original size, which the authors attributed to seasonal differences in corrosion rate. Electrochemical measurements on steel rebars within the historical Notre-dame de royan church, performed by Marie-Victoire [143], observed similar anomalies, also attributed to seasonal phenomena. Both studies highlighted the problems with such tests on older structures, including uneven struts, corrosion products and pollutants. Adaptations to industrial techniques, on-line monitoring with high definition readings and better understanding of corrosion mechanisms may lead to better application of the technique in the future.

### 4.3.4 Sonic methods

Sonic methods of corrosion monitoring use feedback from, or generation of, sound waves within corroding metal to detect flaws, cracking, corrosion processes and metal loss. They can be used to monitor corrosion rate over time, either in terms of thickness (metal) loss or number of detected flaws.

#### 4.3.4a Ultrasonic Corrosion monitoring

Ultrasonic corrosion monitoring utilises the reflection or dampening of sound waves within a metal to determine thickness and flaws. High frequency (>20kHz) sound wave pulses travel through metal from an emitter to a receiver, either directly or reflecting from the obverse limit [144]. Flaws, voids and changes in material create fluctuations in signal, indicating

their depth, size and frequency. Wave form attenuation and pulse transmission time allow calculation of metal thickness. Corrosion rate can be monitored by comparing thickness loss, or through number of detected cracks, pits and corrosion phenomena, over time. Ultrasonic monitoring is widely used in industrial settings, particularly in monitoring pipe wall thickness. It benefits from being non-destructive, able to accurately detect corrosion on the far side of a material, relative cheapness, small size and online capabilities.

In archaeological contexts, ultrasonic corrosion monitoring is a standard technique for measuring thickness change in iron panels from shipwreck sites. Measurements of remaining metal thickness are taken and compared to initial specifications for determining long term corrosion rate [145], used by Brossia et al. [146] on the wreck of the *USS Monitor*, Macleod and Steyne on the HMVS Cerberus [132] and on the Submarine wreck HMAS AE2 [147]. However, research by Russell et al [148], on the *USS Arizona,* highlights the problems with the technique; proper contact requires removal of (likely protective) corrosion concretions, significant preparation of the metal surface and problems with uneven obverse surfaces for reliable thickness measurements. Tests are non repeatable; destruction of the concretion prevents repeat measurements at the same site. While the technique is effective, its use is limited to calculating past corrosion rates and monitoring subjective differences in corrosion over time and across a site.

#### 4.3.4b Acoustic emissions

Acoustic emission corrosion monitoring detects sonic waves generated by deformation or stress in corroding metal or a surrounding material. Corrosion events which create changes in volume or create stress cause stress events, generating transient elastic waves within the metal or surrounding matrix. These create small acoustic movements at the material surface, which can be externally detected by receivers and analysed in terms of size, location and frequency of event [144]. Events include pit growth and propagation, physical cracking, corrosion product growth, the breaking of passive films and bubble activities. The technique is used in industry to monitor large infrastructure and steel pipes [149], giving corrosion rate in terms of number and size of acoustic events over time [150]. While non-destructive, the technique requires direct contact with smooth metal surfaces, aided by applied grease. Results require careful analysis to remove ambient noise, increasing the expense of the technique.

Acoustic emission corrosion monitoring can be used on archaeological objects; research has focussed on weather related stresses in archaeological bronze statues. Accardo et al. [151] examined acoustic events in the bronze statue of Marcus Aurelius, with respect to thermal imaging events. Cracking events were also monitored in the bronze statue of Nike by Caneva

et al. [152], in order to aid conservation efforts. Both studies allowed exhaustive investigation of internal stresses, but do not link corrosion phenomena to acoustic events, instead focussing on atmospheric and environmental factors. However, they do make clear the potential for the technique, suggesting methods for preserving corrosion layers and illustrating the technique's accuracy for detecting corrosion location.

### 4.3.5 Respirometry

Corrosion may be monitored by measuring the uptake or release of gases involved in corrosion processes. This requires a sealed environment and accurate reading of changes in either the gaseous or dissolved form of the gas. Corrosion rates in terms of metal loss can be calculated with knowledge of the surface area of the metal and the corrosion processes occurring, or comparative estimates made.

Respirometry uses the amount of oxygen consumed as a proxy for corrosion rate; the dominant reducing reaction in normal conditions will be oxygen reduction, creating a close relationship between metal loss and oxygen consumption. The technique usually consists of a corroding object, or surface, sealed within a container with an optical oxygen electrode, which emit specific wavelengths of light when excited by other specific wavelengths. The presence of oxygen absorbs energy from the received wavelengths, directly linking oxygen concentration with emitted luminosity and luminescent decay of the electrode [153]. These can be read through the walls of the container using a two way optical filament and laser light. Oxygen concentration can be tracked over time, producing values of percentage saturation converted to consumption rate by;

$$\text{Oxygen Consumption rate } \left(\frac{g}{day}\right) = \frac{VC\left(\frac{\Delta O_2}{\Delta t}\right)}{100} \qquad \textbf{[Eq. 4.7]}$$

where V is volume of air in the container ($cm^3$), C is initial concentration of oxygen ($gcm^{-3}$), and $\left(\frac{\Delta O_2}{\Delta t}\right)$ is the slope of the percentage saturation against time (%sat/day) [153]. Decreasing monitored volume gives sharper decreases in oxygen percentage and a faster response time. The methodology benefits from simplicity, relative cheapness and adaptability for use on metal in any condition and for any environment in which oxygen is the dominant cathodic reaction. On line monitoring is achievable, though difficult. The technique is limited to situations where the corroding environment can be enclosed and conditions exclusively favour oxygen consumption. The act of sealing may also affect corrosion rate in the long term.

Respirometry is a relatively new technique when applied to archaeological artefacts, but highly suited to both object storage and avoiding artefact alteration. The corrosion monitors

designed by this project will be compared to and calibrated by corrosion rates of chloride infested archaeological iron objects monitored by respirometry at Cardiff University. The preliminary results by Rimmer et al., along with the methodology followed (covered in greater depth below), have been published previously [154], explore the effectiveness of chloride removal techniques on reducing corrosion rate. The change in oxygen consumption rates before and after treatment shows the technique as an effective subjective measure of corrosion rate. The generated results were well within predicted ranges, and future publications will provide more in depth results. The research builds on the methodology developed by Matthiessen and Wonsyld [153] to monitor iron and copper samples, of varying age, corrosion state and under various atmospheric conditions. The studies showed good correlation to weight loss measurements of the same samples, showed high reproducibility and were used to calculate corrosion rates as low as 0.1 μm/year. The methodology as described gives convincing results, but concurrent complementary measurements would help justify calculated corrosion rates. Thickett et al. [155] used respirometry to monitor archaeological iron and copper artefacts and evaluated the technique for use on heavily corroded iron. Good correlation was shown between corrosion product build up (by weight) against oxygen consumption, while examination of the artefacts at varying RH allowed conservation guidance for a large display of mixed metal artefacts.

It is clear that respirometry would benefit from further research and calibration, but can provide a simple, valuable and effective tool for monitoring archaeological metal corrosion.

### 4.3.6 Monitoring Methods not used for archaeological metal corrosion

There are a range of techniques used within research and industrial control of corrosion which have not been previously used on archaeological materials. These methods are generally either destructive or altering to the metal monitored, or may present methodological problems. They are mentioned here briefly for comparison and consideration of future use.

Radioactive tracer methods monitor the amount of metal loss into a solution by measurement of gain or loss of radioactivity to the electrolyte or metal respectively, caused by the transfer of previously irradiated material [156]. The technique is generally used within autoclave experiments or on site flow systems, limited to situations where samples may be irradiated or coated and there is a constant removal of the dissolved metal or corrosion products. While the technique has been used to study atmospheric corrosion of archaeological bronze analogues by Laguzzi et al. [157], the method required complete removal of corrosion layers after exposure. Chitty et al. [158] have used an adaptation of the technique, tracing the passage of the stable oxygen 18 isotope through corrosion layers

during corrosion processes; a non radioactive variation to determine corrosion product location and quantity. These isolated studies illustrate the possibility for the technique's application in methods using proxies or where artefact destruction is permissible.

Magnetic flux leakage measures escaping flux from a magnetically stimulated metal to create 3-dimensional models of extant metal distribution, identifying abscesses caused by corrosion [159]. It is most commonly used on pipelines, giving qualitative corrosion rates and identifying potential failures. However, it is limited to situations where magnets and sensors may make direct contact with the metal and results of non-regular or bulbous materials may create anomalous results. It would therefore be difficult to apply to archaeological materials, especially heavily corroded examples.

Eddy Current monitoring measures the feedback within a stimulating coil passed over a metal, identifying areas of differing conductivities, geometries or physical properties and giving measurements of metal thickness [144]. It is often used in conjunction with magnetic flux leakage on pipelines and is most suited to low, uniform thickness materials. While it does not require contact with the metal, it is disadvantaged for archaeological purposes in that it suffers when applied through low conductivity corrosion layers or where there are many flaws close to the metal surface.

Hydrogen analysis is similar to respirometry, measuring the evolution of hydrogen gas as the product of the cathodic corrosion reactions in situations where this is the dominant cathodic reaction. Evolved hydrogen volume will be directly related to corrosion rate, and can be monitored as quantity of evolved gaseous or dissolved hydrogen, or through hydrogen penetration analysis in steel [160]. It is very unlikely that stored archaeological metal would encounter hydrogen evolving conditions, so such analyses are unlikely to be relevant.

# Chapter 5

# Electrical Resistance Corrosion Monitors

The focus of this research is the development and application of electrical resistance corrosion monitors (ERCM) for operation in low humidity environments to mimic corrosion rates of heritage iron. The methodology has previously been used in industry and for proxy monitoring of heritage artefacts, standardised for use by ASTM G96 [1].

## 5.1 ERCM Theory

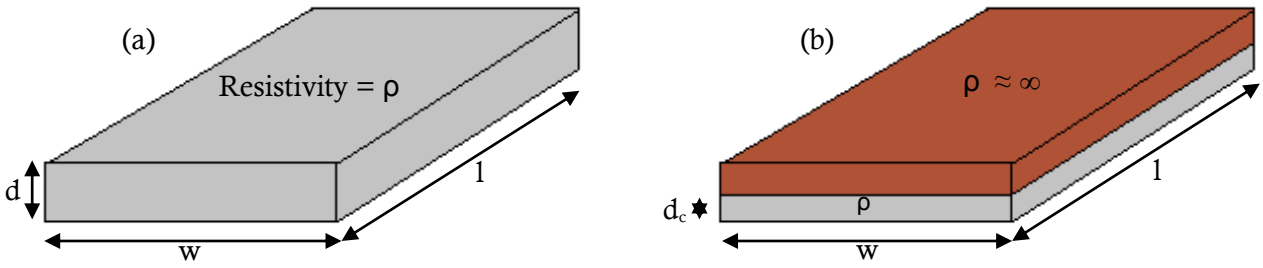


**Figure 5.1:** Diagram of uniform rectangular conductor before (a) and after (b) ideal uniform corrosion in one plane

ERCM monitor corrosion cumulatively, through the increase in electrical resistance caused by conductive metal loss. This is best described by considering a uniformly cross sectioned conductor (Figure 5.1a). The encountered resistance to electrical current can be described;

$$R = \frac{\rho l}{A} \qquad \textbf{[Eq. 5.1]}$$

Where R is electrical resistance, l length, A cross sectional area (calculated from width (w) times length thickness (d)) and ρ resistivity of the conductor [2]. During corrosion, the physical dimensions of the conductor decrease as metal is lost or converted to non- (or semi-) conductive corrosion products. The resistance will be raised by a factor of the change in dimensions and the resistivity. If we consider a conductor which corrodes on only a single face, with constant resistivity, we can link increase in resistance over time directly to thickness loss ($d_\Delta$) by considering initial resistance ($R_0$) and resistance after a period of corrosion or metal loss ($R_c$) (figure 5.1b; Eq. 5.2, 5.3).

$$R_0 = \frac{\rho l}{w d_0} \qquad R_c = \frac{\rho l}{w d_c} \qquad d_\Delta = d_0 - d_c \quad \textbf{[Eq. 5.2]}$$

$$d_\Delta = \frac{\rho l}{w R_0} - \frac{\rho l}{w R_c} = \frac{\rho l (R_0 - R_c)}{W (R_0 R_c)} \qquad \textbf{[Eq. 5.3]}$$

Loss of thickness over time can be calculated by a 2 point measurement of resistance. This can be converted to mass loss by using the constant dimensions, the thickness loss and the density (P) of the monitored metal.

$$Mass\ loss = P * w * l * d_\Delta \qquad \textbf{[Eq. 5.4]}$$

Therefore, by measuring resistance of this ideal conductor, either after set times or continuously, thickness or metal loss can be calculated and corrosion rate (in terms of either) derived by plotting results against time. The gradient of the plots give corrosion rate in terms of dimension or mass loss respectively. Where specific resistivity, length and width are not known, it can be shown that:

$$\frac{R_0}{R_c} = \frac{\frac{\rho l}{W d_0}}{\frac{\rho l}{W d_c}} = \frac{d_c}{d_0} \qquad \textbf{[Eq. 5.5]}$$

Plotting the ratio of before and after resistances gives a plot directly proportional to thickness loss. Where length, width and resistivity are unknown but constant, the gradient of this plot can be used as a proxy for corrosion rate. In practice, this allows us to create sensors which monitor corrosion, or measure it directly in an electrified artefact, by making specific assumptions and accounting for real world errors.

In reality, thickness loss will never be entirely uniform (figure 5.2). Measured resistance of our rectangular conductor will instead be dependent on the average value of $d_\Delta$. Extreme localised corrosion may give skewed results, and pitting corrosion can create non-linear increases in measured resistance against average thickness change. Where pits reach the reverse of the metal, they may also cause additional corrosion, reducing accuracy for non-identical proxy strips.

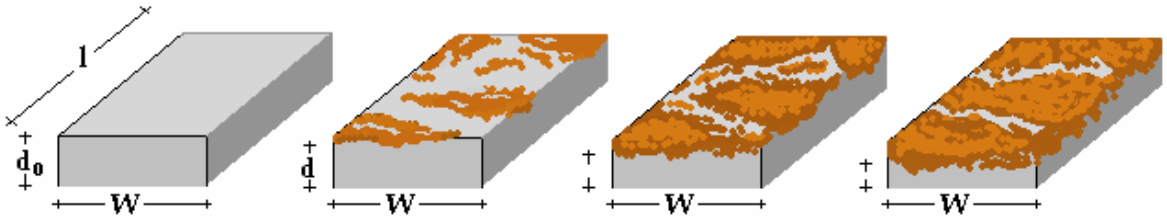


**Figure 5.2:** Illustration of corrosion in a single plane of a conductor; measured thickness loss by electrical resistance will be equal to the average thickness loss across the plane. Adapted from [10]

While it is practicable to maintain constant width and length, resistivity will not remain constant, varying with temperature, and must be compensated for mechanistically. The change in resistivity is compensated within the design of ERCM. A secondary, non-corroding, initially identical, arm of the circuit is monitored, identically to the corroding probe. The protected filament must be close enough to the corroding filament to mirror any changes in temperature that the corroding element may experience, such that both arms may be assumed to have the same instantaneous resistivity. E.g. $\rho_0 = \rho_{r0}$ and $\rho_c = \rho_r$, where r signifies the reference electrode [2]. Assuming constant width and length, we can express equation 5.3 in terms of start of instant resistivity and the initial thickness of the filament:

$$\frac{l}{W} = \frac{R_0 d_0}{\rho_0} \qquad \therefore d_\Delta = d_o\left(1 - \left[\frac{\rho_c}{\rho_0}\right]\left[\frac{R_0}{R_c}\right]\right) \qquad \textbf{[Eq. 5.6]}$$

Modelling resistivity as identical in both corroding and reference filaments (equation 5.7) allows an expression of thickness loss substituting the resistance of the reference filament for resistivity (equation 5.8):

$$\frac{\rho_c}{\rho_0} = \frac{\rho_r}{\rho_{r0}} = \frac{\left[\frac{R_r W_r d_r}{l_r}\right]}{\left[\frac{R_{r0} W_r d_r}{l_r}\right]} = R_r/R_{r0} \qquad \textbf{[Eq. 5.7]}$$

$$d_\Delta = d_o\left(1 - \left[\frac{R_r}{R_{r0}}\right]\left[\frac{R_0}{R_c}\right]\right) \quad \text{or} \quad d_\Delta = d_o\left(1 - \left[\frac{R_0}{R_{r0}}\right]\left[\frac{R_r}{R_c}\right]\right) \qquad \textbf{[Eq. 5.8]}$$

The initial resistance ratio will be constant, determined by the manufactured dimensions and materials of the ERCM; plotting change in the ratio of reference and corroding filaments over time will reveal a gradient directly correlating to thickness loss or corrosion rate. By maintaining a constant D.C. current, we may also use ohms law to give equation 5.9, allowing corrosion rate to be calculated directly from potential measurements.

$$\frac{R_r}{R_c} = \frac{\left[\frac{V_r}{I}\right]}{\left[\frac{V_c}{I}\right]} = \frac{V_r}{V_c} \qquad \textbf{[Eq. 5.9]}$$

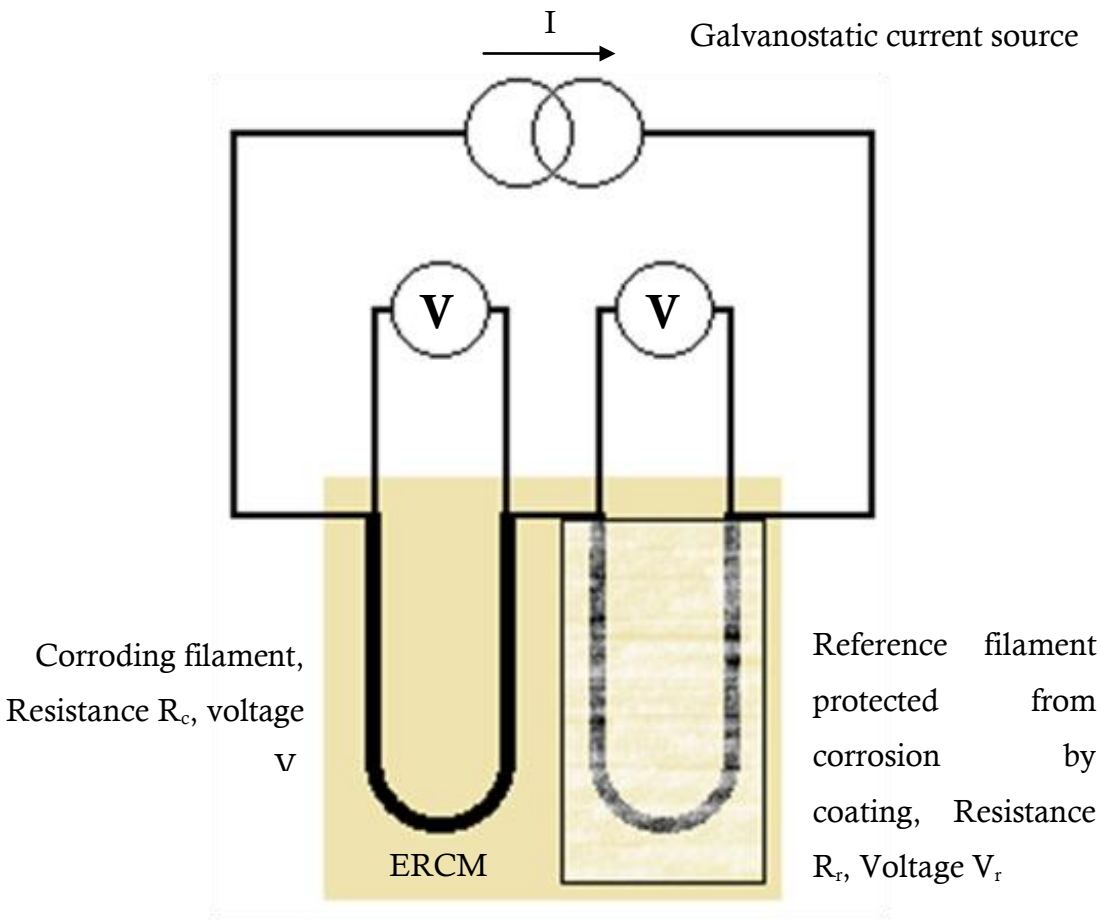


**Figure 5.3:** Circuit diagram of ERCM showing current application and voltage measurement of corroding and reference filaments

Standard ERCM design is represented in figure 5.3. Two filaments of known dimension are electrified with a galvanostatic current. Both identical filaments are subjected to the environment to be studied, with one protected from corrosion to act as a reference. The resistance of both filaments is monitored, usually by measurement of the potential drop with a constant known current; allowing measurement to ignore the resistance of connecting wires and sundries. Measurements may be taken continuously or discretely over time.

Comparisons may be taken between initial resistances or over set time periods. Corrosion rate may be calculated in terms of metal or thickness loss. Resolution and accuracy will depend on the frequency of readings and dimensions of the filaments: Response will be higher for greater percentage thickness loss, so thinner, lower width and longer filaments will give higher accuracy results.

ERCM are deployed as measures of corrosion by proxy; they themselves corrode within an environment, allowing their measured corrosion rates to be used as ersatz corrosion rates for identical or similar metal within the same environment. Calibration between corrosion so measured and actual corrosion rates (measured through other methods) allow greater accuracy of calculated results and higher credence to, and confidence in, the method.

ERCM benefit from being versatile and providing direct measurements of metal loss [2]. Their design allows for deployment in any form of environment. This makes them especially useful for atmospheric tests, where electrochemical measurements are difficult. They provide direct measure of metal loss in an easy to interpret form, and can be operated and interpreted remotely and through automated software.

The drawbacks of the system have been somewhat rectified by increased research into better designs, but can present problems with localised corrosion, response time and accuracy. Traditionally the method was seen to be slow to respond to corrosion; thickness loss will only be detected when enough has been caused to create an increase of one unit of the smallest discrete measureable unit resistance or voltage. However, lower initial filament width and thicknesses (created by higher technological methods such as physical vapour deposition or silk printing), longer serpentine patterns and higher accuracy volt- and ohmmeters have reduced reaction time and increased accuracy. Localised corrosion may also be a problem; pitting corrosion causes significant damage without equating to high levels of metal loss. Where pits reach the obverse of the metal foil, they are likely to spread rapidly and laterally. This, or any form of intense localised corrosion, may cause exponential rise in resistance, a broken circuit and probe failure. Unlike other methods, additional information about corrosion will not be directly revealed by the corrosion data given, though existing models and rate mechanisms may be inferred.

## 5.2 ERCM in Industry and research

The electrical resistance method for corrosion monitoring has been used in a wide variety of situations, using designs and analysis best suiting the demands of each circumstance. A review of its use up to the 1960s is given by Winegartner [3] and modern applications by Brossia [2]. Today, commercial sensors for a range of environments and metals are available,

including silver, copper, nickel, zinc, iron and carbon steel, and can be found integrated within multimethod corrosion monitoring devices [4]

ERCM have obvious applications in atmospheric corrosion monitoring, where electrochemical monitoring is difficult, and can provide constant, ongoing systems of corrosion monitoring. Placing of probes across a mapped area allows identification of key areas of corrosivity and environmental factors. Stropki et al. [5], documented the deployment of automated ERCM to log corrosivity within active aircraft for the U.S. military, using a fully automated, on-line system to present data tables of results and corrosion rates. The MUSECORR project has suggested and performed similar applications, discussed in section 5.3.1. ERCM may also be deployed quickly and easily into a corrosively problematic atmospheric environment. Whited [6] and Fitzgerald et al. [7] used ERCM to monitor corrosion beneath aboveground storage tanks, testing the efficacy of vapour phase corrosion inhibitors and cathodic protection. Both studies illustrate the ease of introduction of ERCM to an environment and the latter highlights the extreme conditions in which ERCM may operate and generate accurate results. Extreme conditions were also monitored within furnace walls by Farrell et al. [8]. The system used the corroding walls of the furnaces themselves as the corrosion filament, with temperature compensation and multiple receivers to create three dimensional models of thickness loss over entire structures, in extremely adverse conditions. The on-line, continuous monitoring of the system allowed alerts for panel replacement or emergency shutdown, is complemented by portable systems for periodical inspections. The study provides an excellent methodology for ERCM application within a corrosion mitigation framework.

High accuracy ERCM are most common in atmospheric research environments, created to answering specific questions in atmospheric corrosion. Cai & Lyon [9] achieved sensitivity of a few nanometres with ERCM monitoring the initial corrosion kinetics of atmospheric corrosion of iron and zinc, as did the later study by Kapatou and Lyon on iron [10]. MØller [11] used high sensitivity ERCM to examine the corrosion of coated steel surfaces in salt spray chambers. Staged corrosion kinetics in accelerated salt spray corrosion testing from the automobile industry was examined using thin film ERCM by Prosek et al. [12]. The fast response time and accuracy of the results allow corrosion kinetics and the corrosive timeline of the test itself to be investigated. High accuracy may come at a cost to lifespan, meaning such ERCM may be unsuitable for highly corrosive environments and very long term monitoring projects.

In subterranean environments ERCM are commonly used to monitor pipelines, infrastructure and soil corrosivity, using both standardised and tailored probes. Commercially available ERCM allow monitoring of a range of soil types and corrosivity, at the cost of precise mimicry between the probe and the monitored metal. A review of the

types of commercial soil ERCM and their use is given by Kahn [13]. Jankowski et al. [14] have demonstrated the use of a single probe type in investigating cathodically protected pipelines, mounded LPG tanks in sandy soil, under structure pipelines and high resistivity soils. The results provide excellent guidelines for dealing with corrosion threats and illustrate the high accuracy and lifespan of the probes, despite their lack of calibration. Standard probes were used by Doniguian and Robinson [15], to monitor lengths of cathodically protected pipeline, and Nielsen et al. [16] to monitor AC corrosion on buried power cables. Both studies illustrate how ERCM may be applied to share environmental pressures or manufactured protections with the monitored metals, allowing direct evaluation of effectiveness and higher confidence results, and form a fully on-line, fast response network. For more specific applications, tailored probes may be manufactured; Bell et al. [17] tested coatings of buried sewage pipelines with ERCM designed to sit flush to pipeline exteriors and mimic pipe metallurgy as closely as possible. The similarity between probe and pipe situation and material allowed greater confidence in proxy readings, though at the cost of expense and convenience. Blumer et al. [18] demonstrated an ERCM for downhole applications in oil and gas, coping with pressures exceeding 10,000 psi and 177°C. The adaptability of ERCM allowed the single design to take readings at multiple heights over long time periods, providing *in situ* readings in previously unreachable and unobservable conditions. Further developments in tailored ERCM will allow greater accuracy and application of ERCM in soils: Li et al. [19] have developed general use ERCM for soil environments, based around single and multiple line patterns deposited by PVD, later tested by Li et al. [20] in soil environments with and without AC corrosion interference. The increased fabrication accuracy and reduced thickness was shown to give fast response times, high accuracy (down to 0.01μm/year) and coped well with wet/dry conditions. Both studies use the corrosion rates to link soil properties to corrosion rates and kinetics, though improvements, including temperature consideration, are ongoing.

Within structures, ERCM may be deployed embedded adjacent to steel rebars and metal supports. Legat [21] has deployed ERCM in conjunction with microelectrode Electrical noise arrays to monitor the corrosion of concrete in steel. The methods complemented each other well; ERCM providing general corrosion rate and cumulative damage, while EN provided information on localised corrosion events. However, it does illustrate the weakness of ERCM when localised, intense corrosion is dominant, a conclusion also reached by Zheng and Song [22] in their review of concrete embedded corrosion monitoring. Taveira et al [23] used ERCM to monitor the corrosion formation in mock-up anchor assemblages from suspension bridges, both in atmospheric and within grout filled concrete void environments. The corrosion rates monitored were compared with mass loss measurements, exhibiting good correlation for both datasets despite a large difference in measured corrosion rate. Živica [24] used ERCM to monitor corrosion of steel rebars in concrete, measuring differences between

concrete compositions in differing environments. While the laboratory results showed good correlation between corrosion rates by ERCM, visual inspection and mass loss, field tests returned no measureable corrosion, so assessment of sensor effectiveness is difficult. The ability to create three-dimensional models of concrete corrosivity and react immediately to changes highlights the benefits of the system.

For aqueous applications, ERCM are underused, due to the accuracy and reliability of results from electrochemical methods. ERCM are therefore generally limited to situations in which electrochemical methods would be difficult to perform. Yang et al. [25] utilised ERCM to monitor flow assisted corrosion in simulated generator feeder tubes, the high temperatures and flow of which would make electrochemical readings difficult. The sensors showed no loss of accuracy in the high pressure, high-temperature and high flow velocity conditions. Top of the line corrosion subjected to wet gas environments and foam plugs have been investigated using in-pipe ERCM by Jevremović et al. [26]. The system was effective at monitoring corrosion rate changes in transient wet/dry conditions. Similar mixed phase environments were monitored by Bieri et al. [27], in their screening of inhibitors, both in the laboratory and in the field. The ERCM used allowed the methodology for testing of inhibitors to be cut to a matter of days by using high accuracy, continuous monitoring to quickly characterise corrosion rate and identify complete inhibition. Conversely, static environments in which minimal impact to the electrolyte is required are also suited to ERCM; corrosion rates of anaerobic bacteria-rich marine conditions have been examined by Weimer et al. [28] and Hardy and Bown [29].

## 5.3 Heritage applied and Pre-corroded ERCM

The non-destructive methodology of ERCM make them ideal for monitoring corrosion of heritage metals by proxy. However, the use of resistivity methods is mentioned in standards for plant monitoring [1], but not in standards applied to low corrosivity environments [30]. The low corrosion rates expected in heritage storage and the difficulty in calibrating modern proxies to ancient metallurgy and heavily corroded specimens have previously limited their use. Commercially available sensors have been applied to heritage storage environments, Johansson and Leygraf [31] evaluated the method in a variety of indoor test sites. The problems encountered in rate calibration help to explain the techniques' under use.

### 5.3.1 MUSECORR Project

The MUSECORR project has designed and applied ERCM to monitor corrosion rates of various heritage metals within heritage environments, establishing the efficacy of the

technique for such. The ERCM are designed with very thin, sinuous filaments (to maximise accuracy in low corrosivity environments), routed to an automated wireless logger (figure 5.4). Prosek et al. [32-33] described the methodology of manufacture and range of sensors, along with initial results from cyclic wet-dry, high relative humidity and varied pollutant atmospheric testing on copper sensors. Sjögren and Bozec [34] detail the development of the corrosion logging device itself and the first field exposures of the copper and silver ERCM. Further testing of bronze ERCM with organic acids and copper, zinc and steel ERCM in industrially polluted atmospheres and salt spray tests were reported by Prosek et al. [35] and Kouril et al. [36]. The laboratory tests showed high accuracy results (with sensitivity down to a few angstrom) short response time, good reproducibility and no observed localised corrosion errors. The sensor performed well in low corrosivity environments (modelled on expected heritage atmospheres) and provided high confidence corrosion rates.

(a)

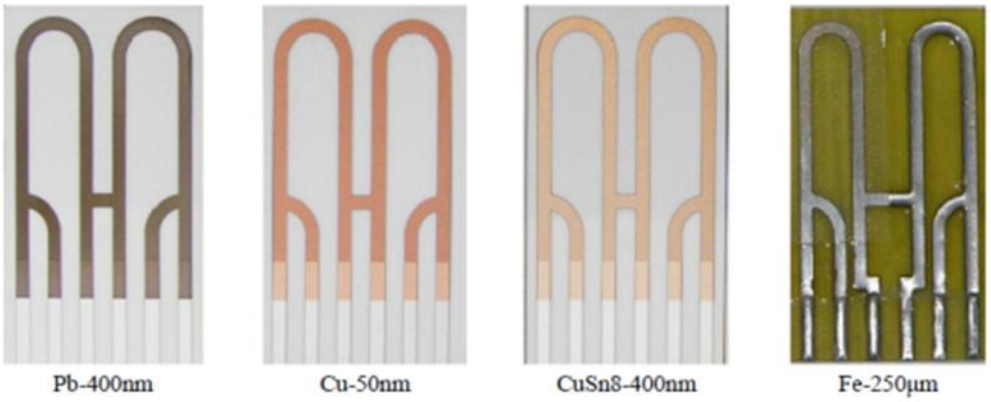


(b)

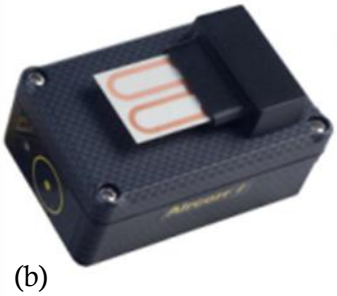

(c)

| Material | Indoor, high sensitivity | Indoor, long lifetime | Outdoor, high sensitivity | Outdoor, long lifetime |
|---|---|---|---|---|
| Copper | 50 nm | 500 nm | 5 µm | 12 µm |
| Silver | 50 nm | 500 nm | | – |
| Lead | 400 nm | 25 µm | | |
| Iron/steel | 800 nm | 25 µm | | 250 µm |
| Zinc | – | 25 µm | | 50 µm |
| Aluminium | – | 14 µm | | |
| Tin | – | 10 µm | | |
| Bronze | 400 nm | | 5 µm | |
| Brass | – | 10 µm | | |

**Figure 5.4**: MUSECORR designed ERCM tracks and loggers: a) Example sensor designs and metals; b) photograph of logger with filament pad; c) table of ERCM metals and thicknesses dependant on accuracy and lifespan. Adapted from [39]

Large scale end user tests of the MUSECORR project were presented by Dubus and Prosek [37], using both copper Musecorr ERCM and commercial loggers for monitoring indoor heritage environments over the course of a decade. The average calculated corrosion rates, obtained over repeated thirty day stretches, allowed easy classification of each participating

institution according to existing air corrosivity standards, highlighting buildings and locations most at risk (figure 5.5a). The rate data allowed identification of corrosive factors and direct intervention in highly corroding areas. The large scale of the study allowed information to be gained on the corrosive properties of various storage types (figure 5.5c/d).

(a)

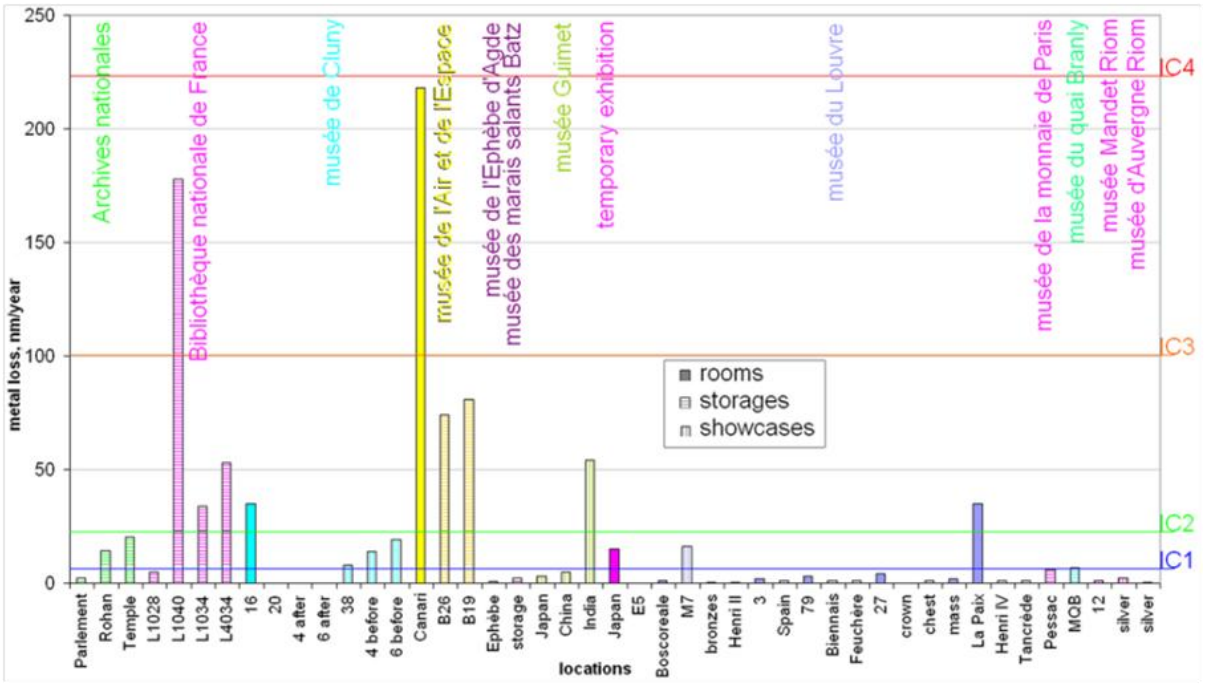


(b)

| Corrosivity class | C1 Extremely pure | C2 Pure | C3 Clean | C4 Slightly contaminated |
|---|---|---|---|---|
| Corrosion build-up (nm/30 days) | < 9 | < 15 | < 25 | < 35 |

(c)

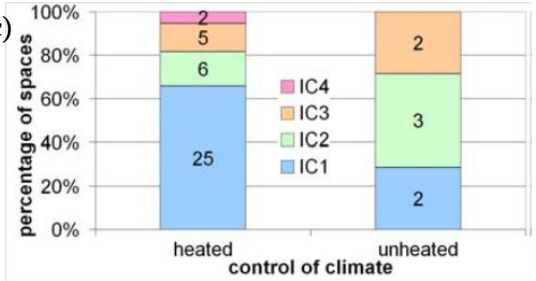


(d)

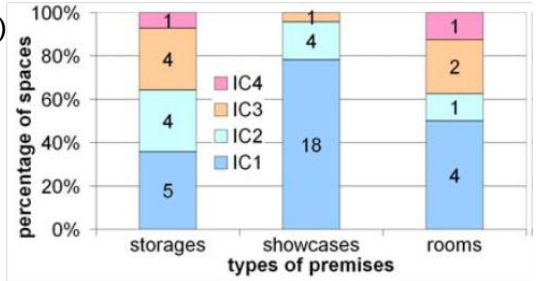


**Figure 5.5**: Findings of the MUSECORR end user tests in French Heritage institutions: a) Corrosion data in thickness loss, showing comparisons between institution corrosivity, with indicators of standard air corrosivity of ISO 11844-1; b) Standard Air corrosivity measures and ERCM measured equivalents over 30 days; c) Measured air corrosivity, converted to ISO format compared between heated and unheated storage; d) Measured air corrosivity, converted to ISO format compared in different storage and display environments. [Adapted from [37]]

Within end user tests, specific questions, atmospheres and corrosion phenomena have been investigated. Sjögren and Bozec [34] compared copper and silver ERCM to QCM techniques in three industrial locations, showing ERCM to be of higher reliability, maintained high accuracy and could be used to give corrosivity readings for the environment in varying climates and corrosivities. Kouril et al. [36] tested silver, copper and lead loggers in modern and archaic archive buildings against QCM. Both parts of the study gave unexpected results, affected by seasonality and pollutants, illustrating the importance of monitoring to identify factors in corrosion. ERCM were again shown to be significantly less prone to errors caused by dust, humidity or temperature fluctuations than QCM. A series of smaller studies were reported by Prosek et al. [39]: Monitoring corrosion of copper weave within loaned tapestry during transit; evaluation of abrasive wear and corrosion benefits of brass binding cleaning techniques; corrosivity mapping within the Danish Royal library to inform metal object placement; proposal of standardised corrosivity levels using copper and lead ERCM; and monitoring of a heavily polluted industrial environment. The breadth of environments, metals and corrosivities studied is testament to the adaptability of the sensors and the accuracy and repeatability of results produced was more than adequate to address questions posed. The research illustrates how ERCM may be incorporated into existing standards, used to create guidelines for conservators or inform corrosion investigations.

### 5.3.2 Precorroded sensors

The MUSECORR sensors give good results in monitoring corrosivity of heritage environments, but it is difficult to directly reconcile their corrosion rates with those of archaeological metal with extant corrosion layers. This will be especially true for iron, illustrated by the use of ERCM by Matthiesen et al. [40] to examine in situ corrosivity of sediments containing archaeological iron at Nydam Moss. ERCM were inserted into anoxic environments, with corrosion rates compared to EIS and mass loss of modern proxies and past corrosion rates of archaeological metal determined by corrosion depth. Much higher corrosion rates were recorded with all modern analogue methods; attributed to the passivating properties built up around the archaeological iron by continued corrosion. The opposite will likely be true for post-excavation iron and activation levels may be significantly lower (see section 3.6).

Introduction of pollutants or creation of corrosion layers on modern proxy electrodes, coupons or filaments prior to use as corrosion monitors allows closer resemblance to corroded metal and greater similarity in corrosion rate and phenomena. McKenzie and Vassie [41] pre-rusted both ERCM and mass loss coupons for exposed atmospheric corrosion testing, by resubjecting old samples along with new for comparison. The rusted ERCM exhibited lower corrosion rates than clean ERCM when unsheltered, but gave higher

corrosion rates when protected from the elements. This was attributed, convincingly, to chloride removal by precipitation and run off (leaving protective corrosion layers) when unsheltered, and chloride encouraged corrosion when sheltered. Cai and Lyon [9] used chloride contaminated ERCM to study the corrosion kinetics of initial atmospheric corrosion of zinc and iron. Chloride contamination on iron was shown to completely alter the rate limiting kinetics during atmospheric corrosion, suggesting an acid regeneration cycle as reported in section 3.6. Kapatou and Lyon [10] used sensors which were pre-corroded to mimic heritage archaeological iron; creating constant, stable, chloride-rich corrosion layers including akaganeite, goethite and lepidocrocite. The pre-corroded probes were shown to give reproducible, accurate and fast response corrosion rates to assesscorrosion rates of chloride contaminated iron, passivation effects of corrosion products and de-chlorination method effectiveness [42]. All the above studies reported differing corrosion rates on corroded or contaminated ERCM compared to clean metal, emphasising the importance of this methodological step in monitoring similar material. Accuracy of sensors was maintained, though errors were introduced from inaccuracies in the contamination or corrosion methodology.

5.3.2a Methods for pre-corrosion

The selected methodology for pre-corrosion or pollutant loading is important to reduce introduced error. Salt loading methodologies must be controlled, quantifiable and deposit salt particles in well dispersed and even patterns.

Droplets of salt solution have been directly applied to a metal surface for corrosion studies, generally using pipette or micropipette to deposit a known volume of a known salt concentration. The corrosive, geometrical and chemical properties of electrolyte so deposited have been investigated and methodology reported. Tsuru et al. [43] reported the formation of micro-droplets around a single deposited electrolyte droplet as an unavoidable and unpredictable alteration of droplet dimensions and hence salt and corrosion spread. Tsutsumi et al. [44] directly linked probability of pitting occurrence and droplet size with $MgCl_2$ electrolyte on Type 304 stainless steel, indicating smaller droplets would reduce the opportunity for localised attack. Dubuisson et al. [45-46] monitored the change in electrolyte droplet dimensions and induced corrosion rate in galvanised steel over time and showed that differing droplet volumes had a non-linear initial relationship with height and diameter. Alternatively, Zhang et al [47] placed finely-milled individual NaCl particles of approximately 50$\mu$m diameter onto a metal surface and raised relative humidity to 90%, forming deliquesced droplets around the crystals. The above research presents excellent methodologies for studying corrosion within droplets, but illustrate the difference of corrosion profiles formed under droplets than otherwise corroded metal. The required

evaporation of the droplet leads to unpredictably distributed salt spread and corrosion products.

An alternative method for loading salts is through droplets of dissolved salts in ethanol, deposited similarly to electrolyte. This method is discussed by Chen et al. [48], who deposited 20μl drops of saturated NaCl solution in 99.5% ethanol to examine corrosion in copper. The ethanol volatilised quickly, depositing NaCl crystals in clusters, primarily of >10μm feret diameter. This method was used by Cai and Lyon to chloride contaminate their ERCM [9].

Solid salt clusters may be deposited directly onto a metal surface through aerosol. Lobnig et al. [49] used an atomised salt spray and a cascade impactor to thermophoretically deposit submicrometer $(NH_4)_2SO_4$ particles onto a copper surface to study corrosion mechanisms of dust deposition. The technique allowed deposition of concentrations as low as $1\mu g/cm^2$ with homogenous particle distribution. Aerosol deposition was evaluated by Cole et al. [50] to investigate marine salt deposition; droplet sizes of 1-3μl of 5% NaCl solution, 5% NaCl in ethanol and saturated seawater solution were deposited on various metals and allowed to air dry in ambient conditions. The study highlighted the differences in crystal deposition and initial corrosion depending on salt concentration and metal type (table 5.1). At droplet sizes above 3μl, crystal distribution was shown to follow a pattern of increased crystal frequency at the droplet edge; smaller droplets gave more sporadic but homogenous distribution. Li and Hihara [51] deposited NaCl particles from a very fine aerosol mist created by an ultrasonic humidifier, with a 2 second exposure time followed by air drying at very low RH. This produced particles of diameter 1-10μm, used to study deliquescence and re-deposition at high humidity.

| Solution | Material | Salt patch diameter (μm) | Salt distribution | Corrosion product formation |
|---|---|---|---|---|
| **5% NaCl** | Al, Au, Gal | - | Isolated crystals | None |
| **5% NaCl in ethanol** | Al, Au, Gal, Zn | - | Isolated crystals | None |
| **Saturated Seawater** | Al, Au, Zn | - | Isolated crystals | None |
| **Saturated Seawater** | Zn | 10-30 | Crystal growth at edge of patch | Light- all |
| **5% NaCl** | Zn | 10-30 | Crystal growth at edge of patch | Medium - all |
| **5% NaCl** | Zn | 5-15 | None | Heavy - all |

**Table 5.1:** Observed salt crystal distribution and initial corrosion levels of aerosol applied, air dried solutions onto various metals by Cole et al. [50]

Salt deposition has also been achieved using piezoelectric inkjet printing; the methodology chosen for this research. A 'drop on demand' technology, inkjet printing uses nozzles connected to sumps to deposit binary patterns (drop or no drop), creating dotted patterns which appear solid to the naked eye. The recent development and use of piezoelectric filaments (as opposed to heating elements) for ink-propulsion allows the 'printing' of a greater variety of liquid viscosities and chemistries; previously applied to a variety of thin film materials, including Nano-particles [52-53], polymers [54] and latex based inks [55]. For deposition of salts for atmospheric corrosion testing, a feasibility study of this technique was carried out by Schindelholz and Kelly [56] using NaCl solution and an unmodified Epson printer. High precision of printed area, good salt crystal distribution homogeneity and low distribution of modal feret diameter were achieved for densities between 10 and 170$\mu g/cm^2$. The technique could be adjusted to vary loading density (through solution concentration or pattern opacity) to create varying levels of corrosion in atmospheric exposures (figure 5.6). Mi et al. [57] used a similar method with an unmodified Canon printer to deposit $MgCl_2$ on 304 stainless steel in densities of 7±1 to 350±50 $\mu g/cm^2$ for evaluation of pitting behaviour. Comparison of the technique to pipette deposited droplets revealed improved consistency of corrosion area, though initial deliquescence of deposited salt was required to ensure constant coverage of loaded area.

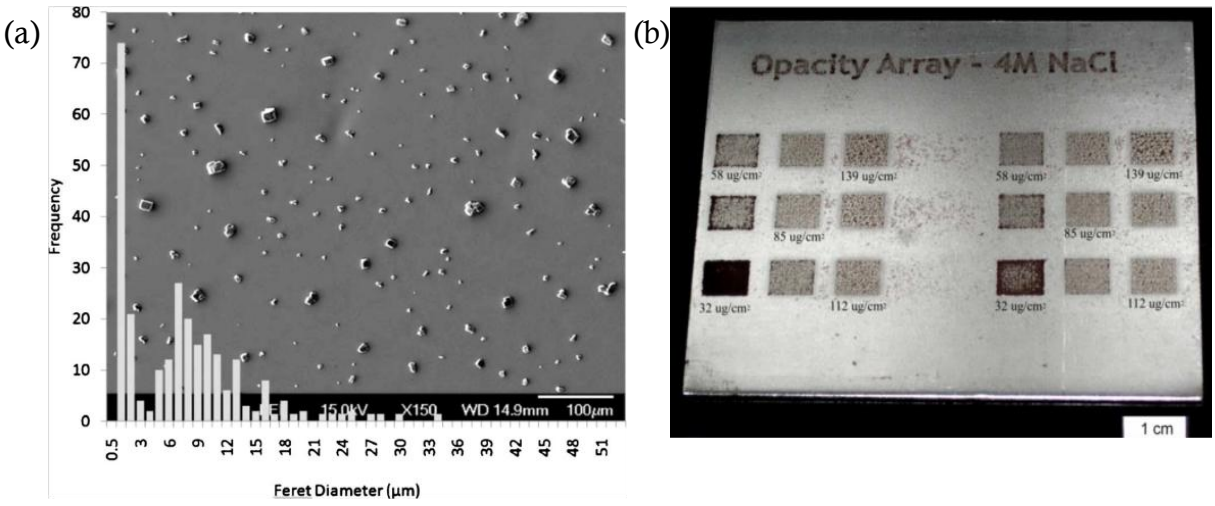


**Figure 5.6** Deposition of NaCl crystals by Schindelholz and Kelly showing: a) Particle size distributions for 1M, 40% opacity printed salt solution observed under SEM; b) Steel coupon with prints of varying opacity of 1M NaCl solution

Corrosion layers may be formed by exposure to corrosive environments; levels of corrosion are controlled by length of exposure and environment corrosivity. Schindelholz and Kelly [56] demonstrated differing levels of corrosion achieved through different levels of salt loading and equal exposure time (figure 5.6). Similar could be achieved using other salt

loading techniques, or altering the length of exposure to increase corrosion depth or coverage. Clean metal in corrosive environments may also be used; Kapatou and Lyon [10] pre-corroded ERCM filaments within a desiccator over 2.5%vv HCl solution. This produced chloride concentrations between 0.3 and 1.0 $mg/cm^2$ within fairly constant corrosion layers of high adhesion to the surface. Alternative corrosive environments include salt spray chambers [11] and corrosive bulk electrolytes.

# Chapter 6

# Experimental Materials and Methodology

This chapter will describe and discuss the methodologies used in creation and testing of the pre-corroded ERCM, and their deployment in controlled and *in situ* environments.

## 6.1 Creation of ERCM

The ERCM design requires constant thickness iron foil in serpentine patterns, secured to an insulating substrate, with one arm protected from corrosion. Filaments must be close enough for homogeneity of temperature, unobtrusive enough to operate in small storage display spaces and allow ease of connection to a measuring circuit. Proposed methodologies were considered with respect to accuracy, lifespan and reliability of manufacture of the ERCM

### 6.1.1 Discussion of alternative designs and methods

This section will review the progression and development of the ERCM creation methodology.

6.1.1a Alternative Sensor Design

Initial sensor design was taken from the methods used by Cai and Lyon [1] and Kapatou and Lyon [2]; thin iron foil was milled into a serpentine pattern of filaments and connecting fronds (figure 6.1). Depending on which are protected, filaments are used as corroding or reference electrode. Pad layout allows selective monitoring of filament resistance by the voltage drop method of resistance calculation. Kapatou and Lyon [2] deployed the sensors in series; four sensors corroding with one covered as reference. This method gave high accuracy, but is impractical for *in situ* measurements.


**Figure 6.1**: Initial design of ERCM, taken from [1,2]. Suggested sensor use illustrated; corroding filaments in red, reference in blue and the black areas non-monitored conducting pads.

Cylindrical wire filaments were considered; eliminating error from corrosion of the side planes and removing some perspective bias. However, wire thickness which provides adequate accuracy is too thin to allow for a pre-corrosion methodology and would be unwieldy and delicate *in situ*.

Changes in ERCM design were considered, respecting accuracy, practicality, cost and lifespan. Accuracy can be increased through increased sensor length or reduced sensor width and thickness, magnifying resistance magnitude. Layout was altered to facilitate connection to circuitry, while minimising unused track length, reduced noise and signal aberration. Material waste was minimised to reduce cost. Against these improvements, considerations of lifespan and usability were made: decreases in filament thickness decrease sensor lifetime; decreases in width may exacerbate pitting corrosion and lead to a broken circuit; increases in sensor length increase overall sensor size and obtrusiveness; distance between filaments must be sufficient to prevent short circuits (either directly or via connecting electrolyte) and avoid interference between lateral growths of corrosion products. Based on these factors, an original design was created, facilitated by changes in the methodology of manufacture, discussed below. The final design is discussed in section 6.1.2.

6.1.1b Initial Manufacture methodology and alternative methodologies

Initial ERCM manufacture followed the basic photochemical milling methodology used by Kapatou and Lyon [2]; iron foil pre-attached to inert PVC substrate was coated with photoresist, developed to the design negative and etched by dissolution in 50%ww ferric chloride solution. As reported by the previous research, the methodology had an inherent failure rate of approximately 50% per batch, with an inbuilt fabrication error of 11.6%, mostly attributable to error in width [3] (figure 6.2). These problems were attributed to poor adhesion of the photoresist, etchant gathering between foil and substrate or foil and photoresist and pitting corrosion by the ferric chloride.

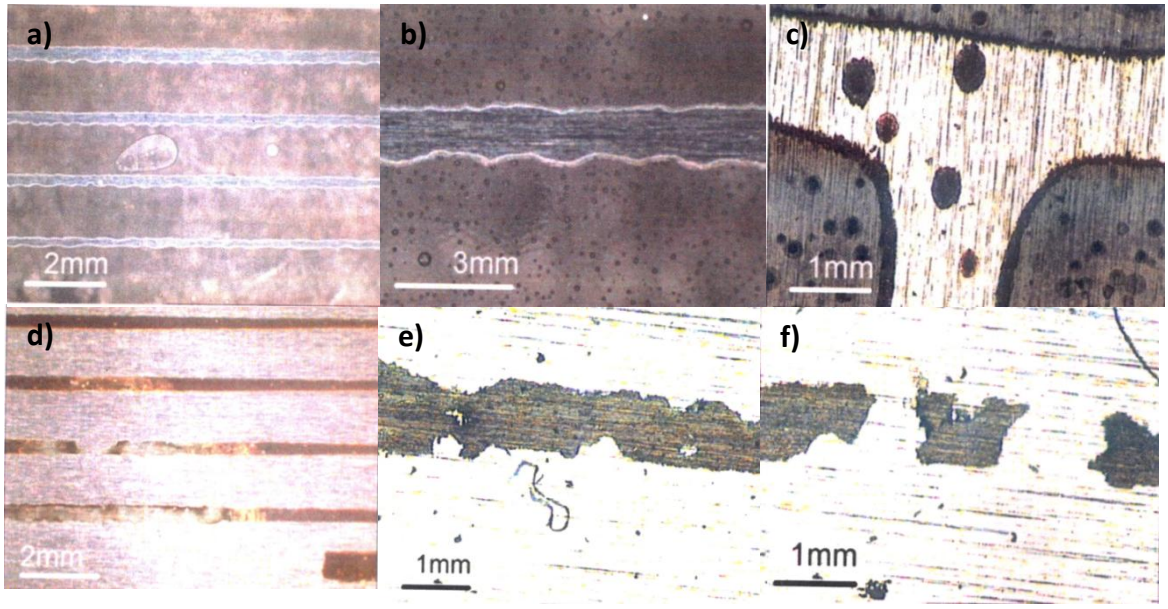


**Figure 6.2:** Etching failures from original methodology, attributed to: a) and b) over etching by prolonged etcchant exposure; c) pitting corrosion from prolonged etchant exposure; d) over etching from poor adhesion of etch resistant coating; e) bubbles beneath the transfer sheet; and f) smearing of the developed photoresist (from [3])

To create ERCM viable for use in the heritage sector, creation methodology required improvement in reliability and accuracy of manufacture while maintianing low production cost and time. Alternative ERCM manufacturing methodologies were considered; summarised in Table 6.1. Each presented weakness compared to photochemical milling. As used by the MUSECORR project [4,5], physical vapour deposition of metal onto a masked substrate was the most likely alternative technique. However, sputter deposition was evaluated as too slow for mass manufacture, electron beam PVD was unavailable and both techniques were evaluated as too costly for mass production for the heritage market. Laser based methodologies were too unpredictable in finished metallurgy and foil dimensions [6].

Mechanical milling was considered and attempted, but available drilled resolution was low and stress on low thickness foils caused warping and breaking.

| Methodology [References] | Theory | | Advantages | Disadvantages |
|---|---|---|---|---|
| **Sputter Deposition [7]** | Form of physcial vapor deposition of films. | 1. Sputter deposition onto negative mask to create design<br>2. 'Dry etching', PVD removal of foil by PVD particles | Very high resolution<br>Very even foil thickness and smoothness<br>Perfect bonding to substrate | Very slow production rate<br>High cost<br>Low availibility of PVD Machines |
| **Electron Beam Physical vapour deposition [8,9]** | Physical vapour deposition by excited particles from a target material bombarded by an electron beam. | | Very high resolution<br>Very even foil thickness and smoothness<br>Perfect bonding to substrate<br>Fast deposition<br>Succesfully used for iron deposition | Very high cost<br>Very low availibility of machines |
| **Selective Laser melting [6,10]** | Selective melting of metal powder by laser into molten metal, directed into desired design by negative mask. | | Fast fabrication time<br>Good bonding to substrate<br>High resolution | Non-uniform foil thickness<br>High cost |
| **Laser Cutting [6,10-11]** | Cutting of prefabricated foil into patterns by laser. | | Very fast<br>High resolution and accuracy | Heat likely to oxidise or warp foil |
| **Mechanical Milling** | Mechanical removal of material using spindle drill bits following a laser guidance over a drawn pattern. | | Reproducible and accurate | Low resolution<br>Possble warping of foil<br>Removal of inert substrate |

**Table 6.1**: Alternative methodologies considered for creation of serpentine iron foil pattern

Alteration to the photochemical milling methodology was accepted as optimal practice for probe creation. This methodoolgy was therefore developed for foil creation

6.1.1c Development of Photochemical milling methodology

Cause of failures and errors in photochemical milling were identified (table 6.2). Pattern failure rate could be reduced through better adhesion of design transfer, photoresist and metal foil; preventing bubbles, ferric chloride ingress or errors during photo-development. Accuracy of etch and the onset of pitting corrosion were controlled by etchant conditions, specifically the concentration of etchant, temperature and exposure time.

| Problem | Cause | Proposed Solution |
|---|---|---|
| **Etching of metal exterior to design** | Poor adhesion of photoresist | Very high contact and adhesion between design transfer and photoresist. |
| | Separation of photo-resist and design transfer | Immediate removal or neutralisation of ferric chloride at end of etching. |
| | Smearing of developed photoresist | |
| **Over etching of design, leading to dimensional errors and roughness of edge** | Undercutting of design due to known 'etch undercut phenomena' | Double sided etching of vaporous etchant |
| **Pitting Corrosion** | Over exposure in Ferric chloride etchant | Minimise exposure to etchant. |
| **Irregularity of etching between and within batches** | Changes in etchant concentration and temperature over time | Maintain constant etchant concentration, diffusion gradient and temperature. |

**Table 6.2**: Identified problems in initial photochemical milling methodology and proposed solution.

Different materials and methods were tested to increase adhesion and contact between photo-resist, transfer and foil. Initial coating of Electrolube® Positive Photoresist spray presented low adhesion to metallic iron, susceptibility to flaking and variable thickness of coating. The reuse of laser printed transfers for design imprinting caused smearing on removal, possible slippage during development and allowed air pockets to form. Attempts to adhere the transfers more closely created problems with removal of adhesives. Alternative methodology using a laminate photo-resistant sheet, applied under high temperature and pressure, coupled with a laser photo-plotted photographic negative design transfer, similarly

applied. Laminated above the separate photoresist, the transfer laminate prevents UV light penetration through the pre-developed design, allowing the lower photoresist to harden, creating an etch-resistant positive. The application method created high adhesion, eliminated the possibility of bubbles or gaps, and prevented smearing on transfer removal. Both film and transfer were extremely photosensitive, reducing development time. Transfers were not re-used, but removed as part of the etching process.

Alternative etchant solution mixtures were considered. Nageswara and Kunzru [12] suggest optimal resolution and accuracy for steel etching through aqueous $FeCl_3$, HCl and $HNO_3$. Repeat tests, in this case, gave optimal etch resolution and speed with 10%ww $FeCl_3$ solution with no additives: HCl was found to increase etching rate, but decrease accuracy and encourage pitting corrosion. Decrease in ferric chloride concentration during etching, and subsequent loss of quality, is reported in the literature [13]. While the regenerative effect of free iron is likely to reduce this effect [14], care was taken to renew the etchant prior to each batch etch.

Etch methodology was improved through a fine-line rotary etch solution developing unit. Solution is released fast spinning rotary tube, releasing solution as a fine mist which deposits as a thin, uniform layer on the coated film surface and develops both sides of the foil simultaneously. Two development units were used; the first filled with LCAF4 developing solution, used to remove the photo-developed non-hardened laminate, decreasing the required time of exposure to the etchant. Etching was achieved in the second chamber. Double sided etching decreased exposure time, increased etch accuracy and reduced undercutting of the design (figure 6.3). The apparatus maintains etchant temperature (46°C) and concentration, decreasing localised corrosion and etch variation.

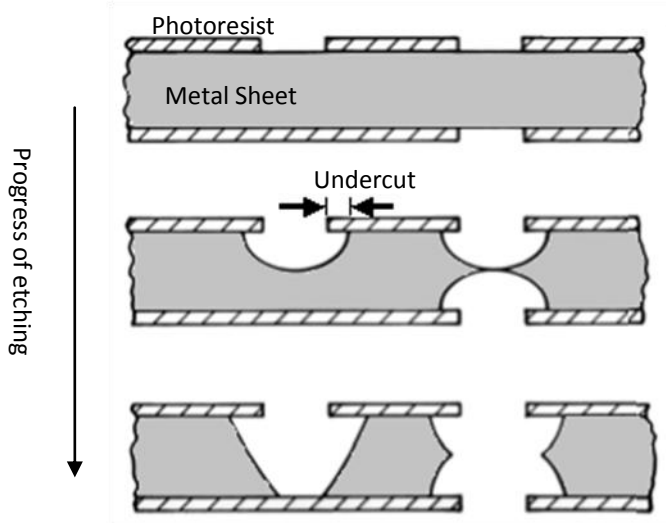


a) Gaps in photoresist allow contact of etchant and metal

b) Etchant removes material vertically and laterally, creating undercuts of changing shape

c) Double sided etching allows quicker milling, smaller undercuts and straighter

**Figure 6.3**: Profile of metal removed by chemical etching in single and double sided etching

Alkaline solution was applied subsequent to etching, to prevent continued metal dissolution by neutralising remaining $FeCl_3$, and remove the remaining laminate. A bubble etch stripper tank was initially tested. Removal of the transfer in this way proved overly energetic, occasionally damaging the serpentine pattern. Alternative methodology was devised using gentle movement in an alkaline bath. The full methodology is described in section 6.1.3

### 6.1.1d Development of mounting and protection of ERCM

The mounting substrate must be inert, insulating and unaffected by environmental change. Initial tests used 3mm PVC board. Flattened Evo-Stik® metal epoxy putty (Bisphenol A-epichlorohydrin epoxy resin) was tested; pressing the foil into the moulded sheets with no adhesive. While this benefitted in creating a flush profile, reducing error from corrosion of the foil sides, the methodology was prone to failure, bending or creasing of the iron foil and low adhesion. Final chosen substrate was 1.57mm FR-4 Epoxy Fibreglass board. This provided high strength, electrical and thermal insulation with minimal thermal volume change. Practically, it was lightweight, smooth (minimising the chance of voids beneath the foil) and easy to cut and form to the chosen design.

Implementation of double sided etching required the development of mounting methodology to attach the serpentine foil pattern. In early tests, Araldite® epoxy resin was applied by paintbrush and partially dried prior to application of foil. Partial drying prevented flow of araldite onto the exposed foil surface and increased the adhesiveness at time of initial contact. The method provided poor adhesion to the metal foil and was liable to warp and crack on exposure to alternating atmospheres (attributed to hydroxylation and thermal volume change). Electrolube® clear protective lacquer was used as an alternative. Designed for corrosion protection of print circuit boards, the lacquer has high insulation, clarity, elasticity, low oxygen permittivity and resistance to atmospheric change. The adhesion was extremely high with no observed hydrolysis or volume change in alternating environmental tests. The flexibility of the cured lacquer prevented warping through growth or shrinkage of the other components. Application was via aerosol, using butyl acetate with dimethyl ether as propellant and an isopropyl alcohol solven, providing an even coating.

Clear Protective lacquer was also chosen to coat the reference electrode and non-corroding elements of the ERCM, due to the properties listed above. Application was by paintbrush; aerosol application was prone to cause contamination of the corroding filament despite attempted use of masks.

Additional metallic connections were mounted at the terminals of the ERCM to allow easier connection to the operating circuit, provide corrosion protection and reduce mechanical stress on the foil terminals. Initial ERCM tests used copper wires directly soldered to the

terminal segments. The flexibility of the wires caused stresses and breakages of the foil and terminals on movement of the ERCM. Additional protection was introduced by covering the terminals with Evo-Stik® metal epoxy putty. Unclad thick copper wire was used to allow direct and easy connection of ERCM to terminal blocks. Exposed regions were covered in clear protective lacquer, leaving 1cm clear for insertion of the wire into terminal blocks.

### 6.1.2 Design of ERCM

The ERCM was designed with corroding and reference filaments of 150 mm length and 1mm track width, a total monitored surface area of 150mm² (figure 6.4). The design itself was created for use with 25μm thick foil, chosen for to its high accuracy in previous experiments and ease of photochemical milling.

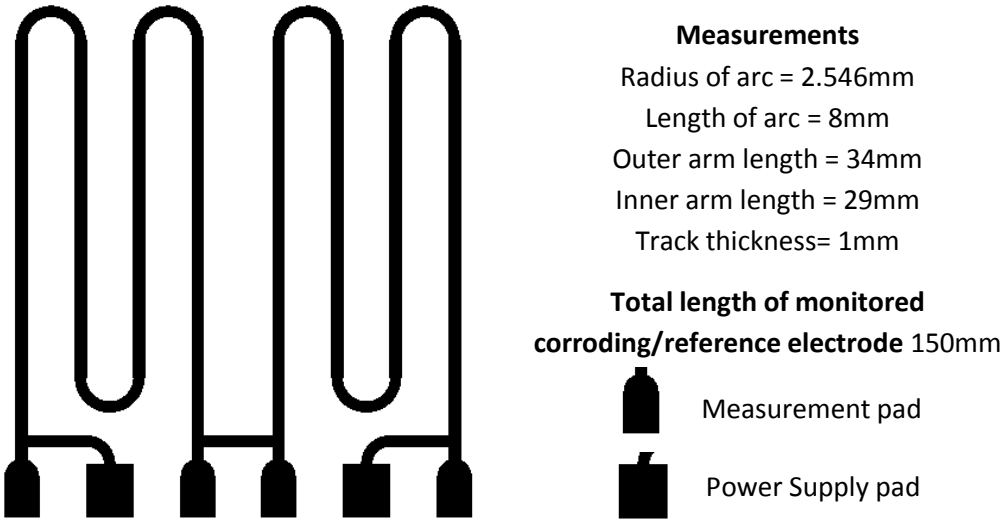


**Figure 6.4:** ERCM design, with dimensions

Curved design allowed greater track length with a more compact, less intrusive sensor. Connector pads are located at one end for convenience and use with single track connecting apparatus. The shape is varied to indicate connection type, and size maximised for easier connection. Spaces between filaments and pads are large enough to prevent interference of corrosion products or short circuit via electrolyte build up. Respecting this, the distance from filament to connecting pad has been minimised to prevent heat alterations and signal aberration from these elements. The design requires a minimum backing substrate size around 45mm square, minimising the obtrusiveness of the final sensor.

The design operates as an ERCM as described in chapter 5; galvanostatic current is applied through both filaments, with the measured drop of potential between two points on either

side of each filament allowing calculation of instantaneous resistance. The necessary circuit connections and monitored cross sectional area are illustrated in figure 6.5.

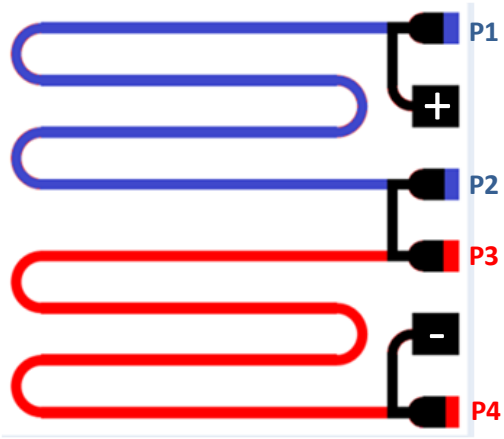


**Figure 6.5**: ERCM design with operational parameters of exposed and corroding filaments, and circuit connections.

The design was created digitally in Altium PCB Designer software; providing resolution down to 5 μm, full compatibility with the etching process and easy plotting of design. The digital design was converted to a 2-dimensional binary vector image 'Gerber X' file (the industry standard for PCB image format). For etching, the design was rotated and repeated around a 9cm square (figure 6.6), allowing the minimum (for adhesion) 1cm margin when applied to 10*10cm, to create four sensors per etch run (see section 6.1.3). Additional lines were added between the filaments to minimise metal removed; reducing etch time and enhancing accuracy.

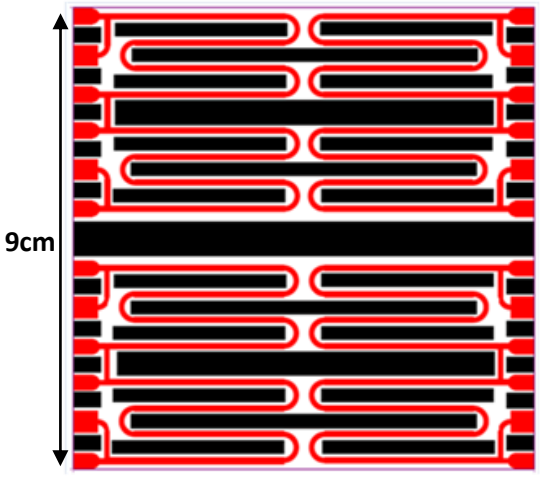


**Figure 6.6:** Design as etched on 10*10cm iron foil

Prism NT driver software was used to load the Gerber file to a photo-plotter, which laser exposed the design onto photo-resist laminate. Subsequent handling of the laminate was

performed under green dark room conditions to prevent overdevelopment. The film is developed, bleached and affixed using an ICP 42 photo-processor, before washing and drying in an IWD 40 washer dryer unit. The produced laminate positive may be trimmed to size for use in photochemical milling.

### 6.1.3 Photochemical machining of Iron foil

The iron foil for creation of ERCM was received as 10cm*10cm square sheets of 25μm thick 99.5% iron foil of hard temper. This was cleaned by the careful use of a low-hardness abrasive wire wool and a silicone block, rinsed with deionised water and dried with a hair drier on cold settings. Prior to use the foil was stored in a silica gel desiccated enclosed environment.

Foils were coated on both sides by Riston PM 200: 215 dry film photo-resist laminate under yellow light dark room conditions. The laminator used was a GX 12 inch dry laminator, coating the iron sheets at high pressure and 110℃ (figure 6.7a). Excess laminate was trimmed by guillotine. Laminate positive (created according to section 6.1.2), was applied under green light conditions, preventing photo-damage to either laminate. Identical designs were applied to both sides; alignment was assured by connection of the two laminates with an adhesive strip hinge joint.

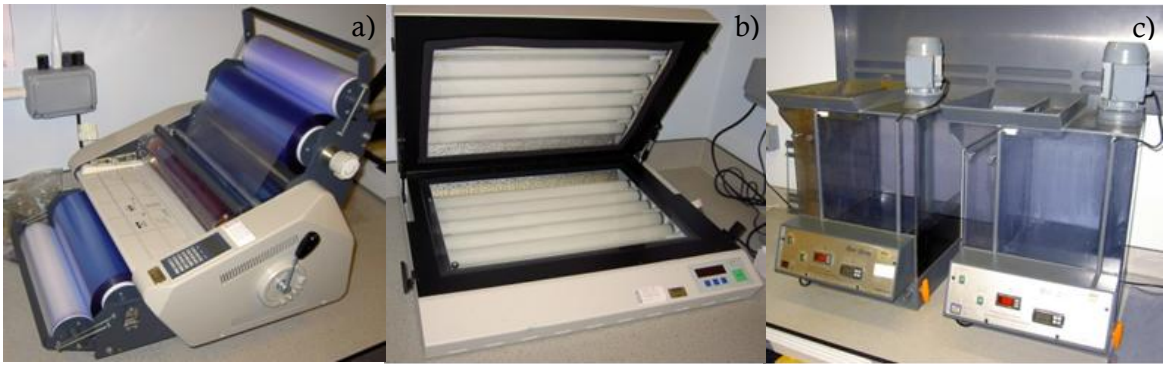


**Figure 6.7**: Apparatus used for photochemical milling of iron foil: a) GX 12 inch dry laminator; b) Mega-electronics y80 Ultraviolet light box; and c) 2 fine-line rotary etch solution developing units

The film was imaged using a mega-electronics y80 Ultraviolet light box, exposing both sides of the foil and laminate (figure 6.7b): The laminate was exposed for 18 seconds, hardening and making insoluble the photo-resist laminate unprotected by the stencil. Maintaining dark room conditions, the design transfer laminate was removed and the developed foil-laminate negative placed within a fine-line rotary etch solution developing unit, containing LCAF4 developing solution (figure 6.7c). Vaporous developing solution is applied for two minutes,

dissolving the soft elements of the laminate photoresist. The foil-laminate was removed and placed in a separate, identical developing unit, containing 10%ww $FeCl_3$ solution. This was applied vaporously for 70 seconds, an experimentally derived time of etching for complete and optimal exposed foil removal. Once complete, the remnants were immediately rinsed with deionised water and placed in a tray containing alkaline solution warmed to 70°C. The solution, foil and laminate were gently excited, removing the photo-resist laminate from the foil.

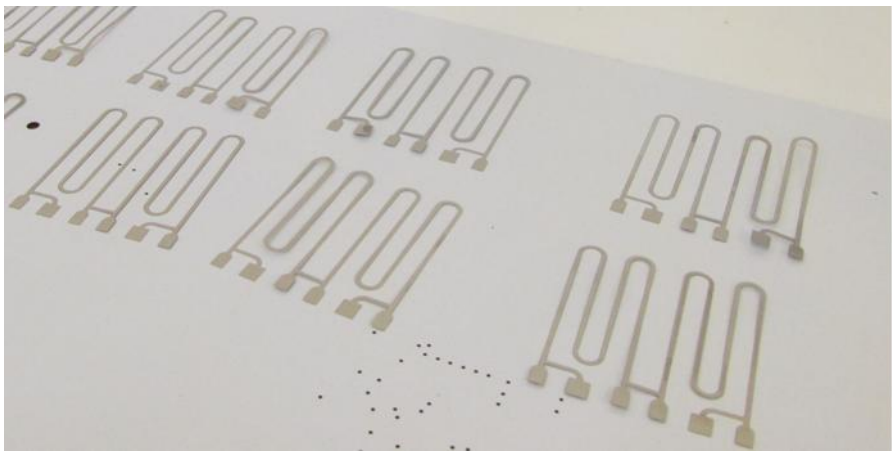

**Figure 6.8**: Photochemically milled iron foil in ERCM design after creation methodology

The created foil designs were rinsed in deionised water, degreased with ethanol and air dried (figure 6.8). The foils were stored in a silica gel desiccated environment until needed and handled only with clean latex gloves.

### 6.1.4 Mounting of foil pattern and protection of reference electrode

Inert substrate mounts for the serpentine iron foil were prepared: 1.57mm FR-4 Epoxy Fibreglass board was cut into 50mm*50mm squares by guillotine. The edges of the mounts were smoothed with 120 and 800 grit silicon carbide abrasive paper, washed in deionised water and air dried in an oven at 50°C.

To mount the foil pattern, Electrolube® Clear Protective Lacquer was applied by aerosol across one face of the fibreglass (figure 6.9a). Care was taken to leave an even and equal layer on each mount and prevent application to the reverse. The lacquer was left to dry for five minutes to increase its tackiness and viscosity. Each serpentine iron foil pattern was removed from storage and positioned vertically, connecting pads down, at one end of the coated fibreglass (figure 6.9b). This was allowed to fall into position and lightly pressed into the lacquer using a plastic rod, taking care not to dent or warp the metal nor allow adhesive to

encroach the upper foil surface. The ensemble was subsequently left to dry in position for two hours.

The reference electrode and other un-corroding, but non-connecting, parts of the ERCM were coated with Electrolube Clear Protective Lacquer to protect them from corrosion (figure 6.9c). The lacquer was applied with a fine haired paintbrush, creating a thin film over the protected areas. This was air dried at room temperature for two hours. A further two coats were applied using this method, to ensure an even, unbroken coating. Once completely dry the coated iron circuits were returned to desiccated storage environments.

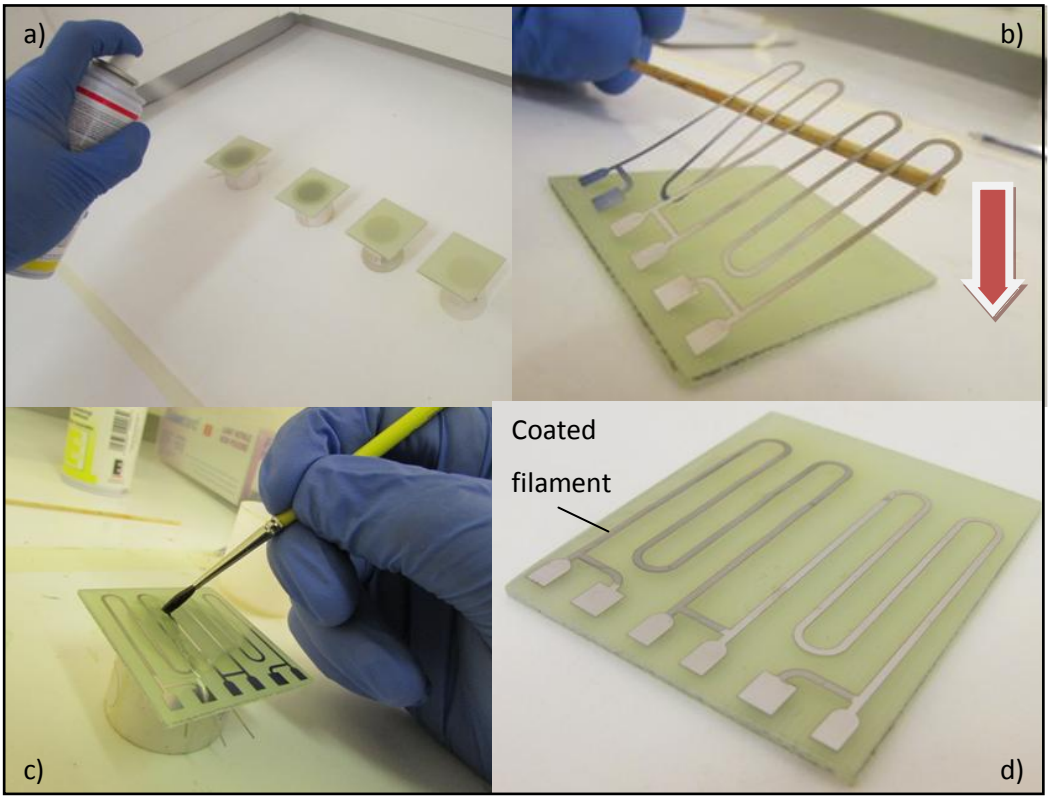


**Figure 6.9**: Methodology of ERCM assembly: a) coating of substrate with lacquer; b) placement of foil on adhesive; c) application of lacquer to reference electrode; and d) final ERCM prior to pre-corrosion and attachment of connection and strengthening paraphernalia

ERCM were finalised by the application of circuit connectors and protective putty to prevent breakages. For pre-corroded sensors, this was applied after contamination with chloride salts as described in section 6.2.6, but before the pre-corrosion methodology of section 6.3.2. Unclad 1mm diameter copper wire was soldered to the connecting pads, affixing 30mm of wire to each. Once cooled, the soldered elements were coated with protective lacquer in a similar manner as for the reference electrode. Additional strength was added to the connection by Bisphenol A-epichlorohydrin epoxy resin, applied as a premixed putty to cover the terminals, soldering and wires up to the edge of the substrate. Once applied, putty

was cured at room temperature for an hour, before the completed ERCM were returned to desiccated environments.

### 6.1.5 Resistance of produced ERCM

Prior to contamination or corrosion, the resistance ratio for each ERCM was noted; for comparison over the probe lifetime and measure fabrication error. Connections were made by custom made crocodile clips, incorporating copper fronds to increase connectivity, connected to clad copper wires. The power pads of the ERCM were connected to an ACM Instruments Potentiostat, configured to supply a galvanostatic current of 10mA. The measurement pads were wired to the front panel Keithley 2000 6 ½ digit multimeter such that each filament was monitored on a separate channel. The voltage generated by the application of the current through each filament was recorded and used to calculate resistance.

Calculated resistances were compared. Results of the analysis are presented in section 7.1.1.

## 6.2 Deposition of chloride by Inkjet Printer

In order to pre-corrode ERCM to create corrosion products similar to archaeological iron, various pre-corrosion and salt contamination methodologies from the literature were considered; detailed in section 5.3.2 and summarised in table 6.3.

Deposition by droplets or deliquescence of salt crystals has been shown previously to be effective, but shape of deposited pattern and uniformity of salt concentration is difficult to control [15-19]. Corrosion by HCl vapour had been previously successful in corrosion of ERCM [2], but created chloride levels difficult to control and of relatively low accuracy and resolution. Similar problems were expected from corrosion by salt spray and other corrosive environments.

Evaluation of the above methods, coupled with academic curiosity, lead to inkjet deposition of chloride salt coupled with atmospheric corrosion in controlled environments to be chosen for the pre-corrosion methodology. This was considered superior to alternative methodologies. Previous research on piezoelectric printing [24-5] had indicated the potential of the technique; through reported uniformity of deposition, homogeneity of deposited crystal size, accuracy of deposited salt volume, and ease of alteration of the pattern, concentration and corrosion depth (see section 5.3.2).

| Methodology [References] | | Advantages | Disadvantages |
|---|---|---|---|
| **Droplet deposition** | Aqueous solution [15-18] | Precise control of deposited chloride | Unpredictable salt spread<br>Chance of localised corrosion |
| | Ethanol solution [1,19] | Precise control of deposited chloride<br><br>Good crystal distribution | Lack of control of salt pattern |
| **Deliquesced solid salt cluster [20]** | | Precise control of deposited chloride | Unpredictable salt spread<br><br>Chance of localised corrosion |
| **Aerosol deposition [21-23]** | | Small crystal sizes<br><br>Uniform deposition at low concentration, down to 1µg/cm$^2$ | Unpredictable crystal deposition at higher concentrations<br><br>Differing deposition dependant on metal |
| **Inkjet Printer [24-25]** | | Very precise levels of chloride<br><br>Precise control of salt pattern | Underused in literature<br><br>Difficulty of sample loading |
| **Exposure to HCl Vapour [2-3]** | | Corrosion and contamination<br><br>Highly adhesive corrosion layers | Unpredictable chloride concentrations |
| **Salt spray chamber [26]** | | Automated methodology<br>Corrosion and contamination | Unpredictable salt concentrations |

**Table 6.3**: Considered chloride contamination and pre-corrosion methodologies

Methodology was based around that described by Schindelholz and Kelly [24]: Replacement of ink with NaCl solution allowed this solution to be printed onto a surface. Volume and concentration of chloride deposited is dependent on, and may be controlled through, solution concentration of the sump electrolyte and/or the intensity and quality of the printed pattern. The methodology as initially attempted was altered after repeat deposition cycles, with changes made to reduce error and increase ease of use, accuracy and reliability.

### 6.2.1 Choice of Materials

Sodium chloride was chosen as the salt to infest the surface of the ERCM: NaCl has a deliquescence point which stays at a fairly constant 75-76% RH within normal atmospheric temperature ranges, is commonly found on archaeological iron, and was successfully printed

by Schindelholz and Kelly [24]. It was deemed that an electrolyte of a single salt would be beneficial for controlled atmospheric corrosion, especially in the creation of wet and dry cycles and preventing additional chemical reactions and products. Other salts considered were those other chlorides commonly found in conjunction with archaeological iron; Magnesium chloride, Potassium chloride and Calcium chloride. The low deliquescence points of $MgCl_2$ (≈33% at ambient temperature), and $CaCl_2$ (≈31% at ambient temperature) were adjudged to be difficult to corrode controllably. KCl has a very high, but very temperature dependant, DRH (88%-84% in ambient temperatures), making controlled corrosion difficult, and is less commonly found within archaeological iron.

Printers considered contained piezoelectric print heads, were inexpensive, commercially available for home use, and contained the ability to print onto inflexible samples. This latter requirement was expressed through CD printing capability with an exposed tray, allowing the substitution of different size of sample. The printer chosen for use was the Epson Stylus Photo P50 (marketed as the Stylus Photo T50 outside of the UK) (figure 6.10). This printer has high resolution (down to reported 1.5pl individual deposited droplet size), a front loading stationary CD printing function, individually loaded print cartridges and was of relatively low cost.


**Figure 6.10**: Epson Stylus P50 printer used for deposition of sodium chloride

Refillable third party clean ink cartridges were chosen as electrolyte reservoirs. Initial trials using a continuous ink system with a large external sump offered advantages in the ease of electrolyte change and reduced number of refills, but suffered from difficult cleaning procedures, frequent blockages of connecting tubes and experimental failure through over or under electrolyte supply. Cleaning and re-use of Epson brand cartridges risked contamination

of the electrolyte. For the final method, third party cartridges were purchased empty, thoroughly cleaned prior to use, and filled by clean syringe.

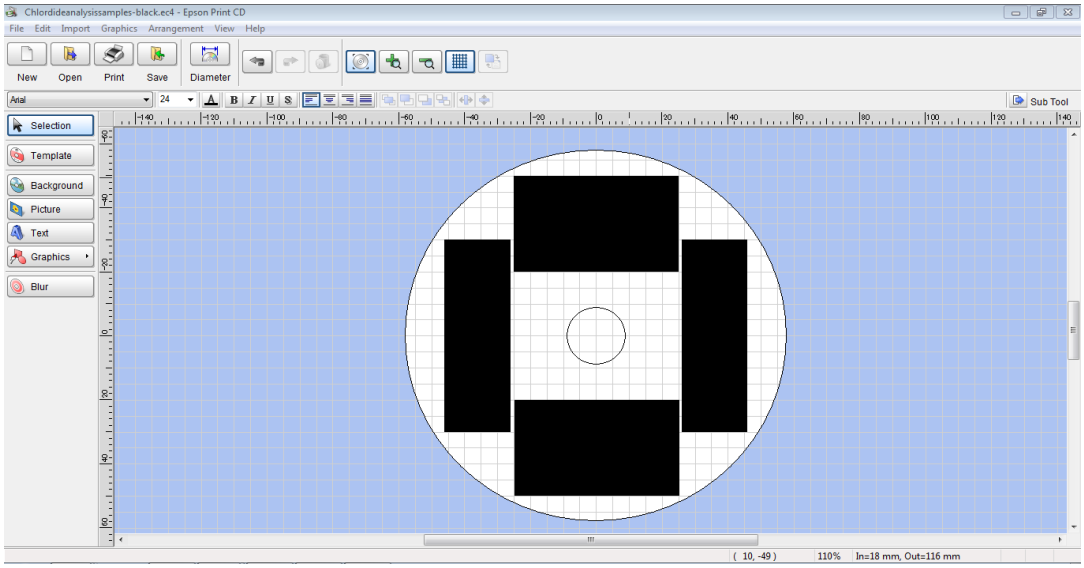


**Figure 6.11**: Screen grab of the CD design software. This allows designs to be placed within a guide grid for accurate printing. Pictured is the 50cm² design used for chloride analysis.

The designs for printing were created using vector software from the manufacturer, Epson Print CD v2.00.00E. Designs were created on a virtual CD image covered in a grid mesh down to 0.1mm resolution, which could be calibrated to allow accurate deposition onto samples (figure 6.11). The software allowed ultrafine changes to greyscale intensity, with 240 steps of luminosity from white to black. Print quality was set to 'best photo' level, equating to 2,880 dpi.

### 6.2.2 Development of Printer methodology

The methodology was developed from flawed initial test printing, through to a reliable and accurate methodology. 4 molar NaCl Electrolyte was created from NaCl crystals and deionised water by gravimetric monitoring on a five figure balance. The electrolyte was inserted into the black ink cartridge sump by syringe. All other cartridges were filled with deionised water. Default, highest quality CD printing settings were used and the printer configured to print only in shades of grey, (only the black print cartridge would deposit). Initial printings of simple block designs onto the reflective surface of CDs created visible patterns of salt identical in dimension and position to those created virtually, of high quality and with high uniformity.

Visual examination after repeated printings indicated variations in print quality and salt deposition. Defects included fading towards the end of individual prints, pattern smearing, patchiness within the pattern and visibly lessening of deposition after repeated printings.

Build up of salt crystals within bubbles in the electrolyte was suspected, causing blockages at bottlenecks within the flow system. The third party printer cartridges were made of a clear plastic, allowing inspection of the interior before and after use. Areas liable for the formation and build up of salt crystal were identified, including the connecting nozzle, the metal flow valve, and air lock chambers (Fig. 6.13a). These areas were associated with alternating wet and dry conditions as the sump is emptied and printing proceeds. Salt deposition was also observed within the print cartridge carousel around the black cartridge connecting frond (Figure 6.13b). Solid salt crystals were noted falling from the base of the carousel and causing streaking of the print pattern, possibly indicating a build up of crystals in and beneath the print head.

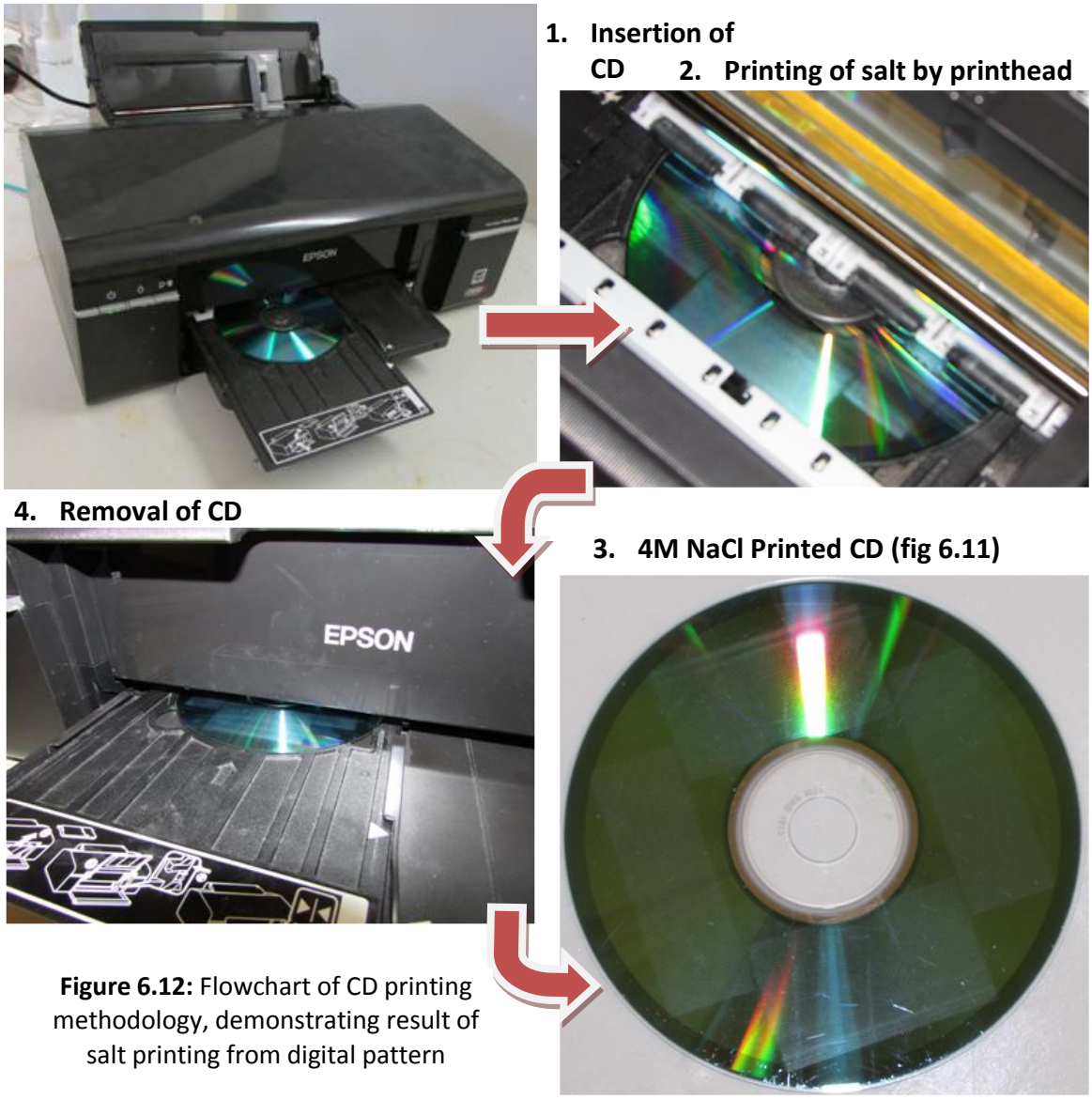


**Figure 6.12:** Flowchart of CD printing methodology, demonstrating result of salt printing from digital pattern

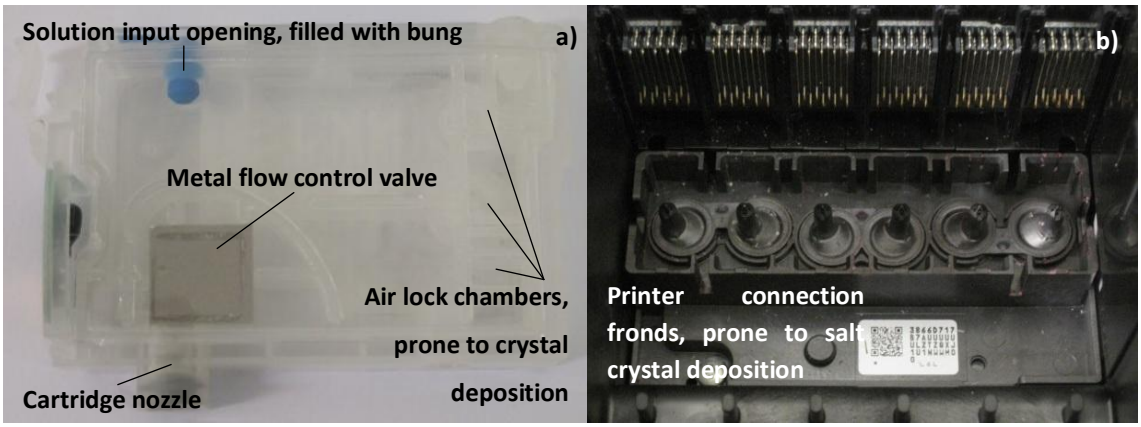


**Figure 6.13:** Salt crystal deposition problem areas: a) within the print cartridge; and b) within the print carousel.

To address these issues, methodology was created to reduce salt build up and remove extant salt crystals. Molarity of the electrolyte was reduced to 1 molar: Subsequent tests used this concentration or lower. Additional cartridges were purchased to allow increased changing and refresh of clean cartridges. Each cartridge was stored dry and repeatedly rinsed with deionised water and air dried prior to and after use. Between prints, software cleaning of the print head was carried out, allowing deionised water from the unused cartridges to remove excess salt. At the start and end of daily printer use, a black cartridge filled with deionised water was inserted and third party software used to flush and replenish the ink head. When not in use, the print head was kept charged with deionised water. Cleaning of the carousel and printer fronds was carried out as needed, using wetted cotton wool buds and air jets. Streaking of the pattern was prevented by positioning of printed patterns to minimise contact with the printer and movement rollers.

The altered methodology gave visually consistent printed patterns. Further assessment by chloride analysis was carried out on CD printed designs.

### 6.2.3 Calibration of salt concentration by chloride analysis

A 50cm$^2$ pattern or four equal size rectangles was created within the driver software as a standard repeat pattern (figure 6.11). Initial analysis of pure black patterns assessed the printed concentration of chloride per cm$^2$. Other shades of greyscale, repeat printings and application of alternative printer methodologies were deposited in an identical pattern, to observe the effect on salt concentration.

CDs were prepared by dishwasher washing, rinsing with deionised water and air drying in ambient conditions (figure 6.14c). Immediately on printing, the CD was removed, using clean latex gloves to prevent contamination, and deionised water used to rinse the patterned side of the CD, collected via funnel in a 50ml beaker. Rinsing was continued until around

19g of solution had been collected, measured by Fisher-Brand DP-1500 4 figure balance. This was then made up to 20g with deionised water. This solution was immediately analysed by argentometric coulometric titration.

Argentometric coulometric titration analyses chloride by titration; stable current across two silver electrodes within an acid buffer electrolyses dissolved salts and deposits suspended insoluble silver chloride (figure 6.14b). The point at which all chloride has been removed from solution is detected by a sudden change in solution conductivity, measured by detector electrodes, caused by the availability of free silver ions. The time it takes to electrolyse and bind a single unit of chloride at a set current is known; the time taken from commencement to change in conductivity is used to measure the volume of chloride in solution. The method was chosen as convenient, accurate and fast, with capability of measurement down to a few parts per million. Conductivity measurements of solution had been trialled as an alternative measure of salt concentration, but measured salt concentrations were too low for reliable detection with the equipment available.


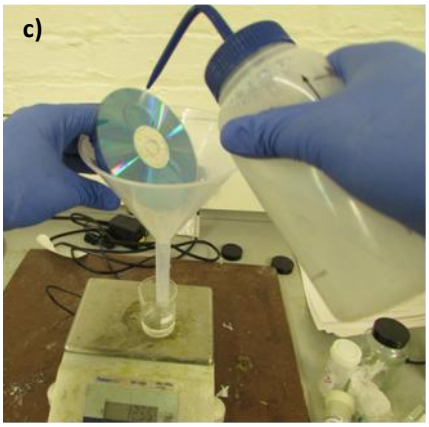


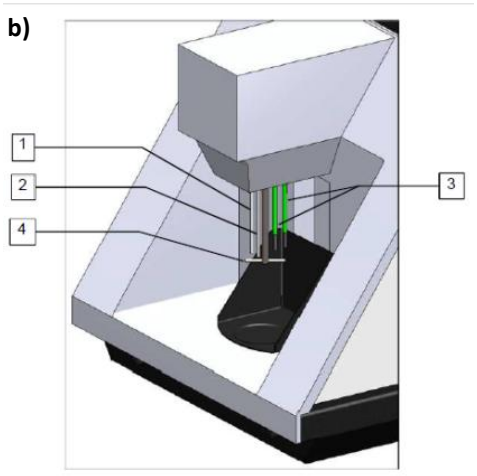


1. **Silver Anode**
2. **Silver Cathode**
3. **Detector electrodes**
4. **Stirrer**

**Figure 6.14:** Chloride analysis methodology: a) Sherwood 926 chloride analyser with standard and buffer solutions and micropipette; b) Operational diagram of chloride analyser (from [27]; and c) methodology for removal of salt from CD to electrolyte with deionised water

Titration was performed by a Sherwood 926 Chloride analyser. Calibration was performed by titration of 0.5ml of 200mgCl/l standard solution, inserted by micropipette into the Combined Acid Buffer containing detection and silver electrodes. 5 0.5ml samples of each

rinsed salt solution were similarly titrated, using fresh micropipette heads for each solution. Buffer solution was replaced and calibration was repeated after every set of five titrations. Results were displayed and recorded as milligrams/litre (ppm) of chloride. The average concentrations for each solution were used to calculate printed chloride concentration for each print methodology and design. The amount of chloride present within the 20mg was calculated and divided between the 50cm$^2$ to give printed concentration in terms of μg/cm².

The results of the chloride analyses are reported in section 7.1.2. Reference solutions were titrated to create values of expected error and evaluate the testing methodology. Reliability of individual printing methodologies were investigated, leading to the introduction of additional methodological steps (section 6.2.6). Use of repeat printings and printing at less than 100% greyscale were examined to test the bounds of the methodology and provide a range of possible chloride contamination levels for pre-corrosion. The final methodology was decided based upon these findings, their error and their standard deviation.

### 6.2.4 Printing to alternative substrates

CDs were altered to hold samples of other dimensions and materials. Positioning between the virtual and real CD was achieved by printing of a 2cm mesh design, subsequently over-scored into a blank CD. This allowed direct comparison of the on-screen design outlines and deposited design on the modified CD. Sections were machine or hand cut from CD samples in correlation to this grid, with adhesive backing added to the CD reverse. Different areas were removed to accommodate a range of samples, including glass slides, various sizes of iron foil and the ERCM themselves (figure 6.15). Each design was mapped within the software for ease and accuracy of printing.

Separate CD print trays were modified for each sample type. Marks on the tray were created to tally to marks on the CD mounts, allowing accurate placement for prints and reprints. Part of the raised design was filed away to accommodate additional substrate depth and overlap. Trial prints of a blank fibreglass board revealed problems with print head collisions and refusal to print. To accommodate the additional depth in ERCM printing, an input tray had part of the rear surface removed and backed with adhesive tape. CD mounts were still required, to force the printer to recognise the presence of a sample.

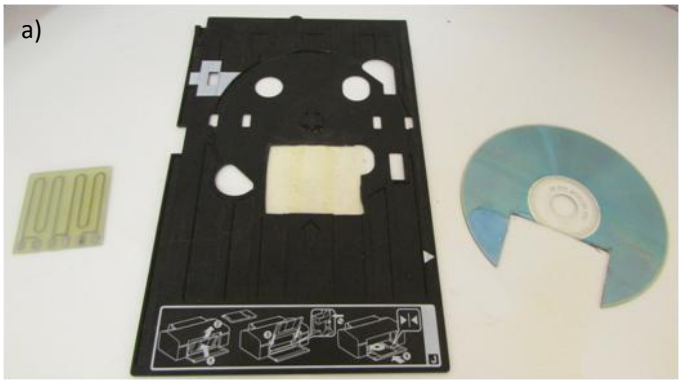


b) Software outlines for creation of patterns for printing onto foil (1) and ERCM (2) samples

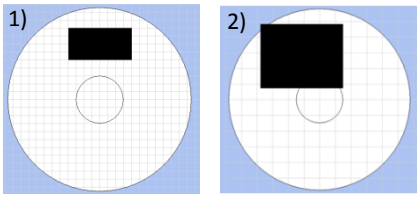


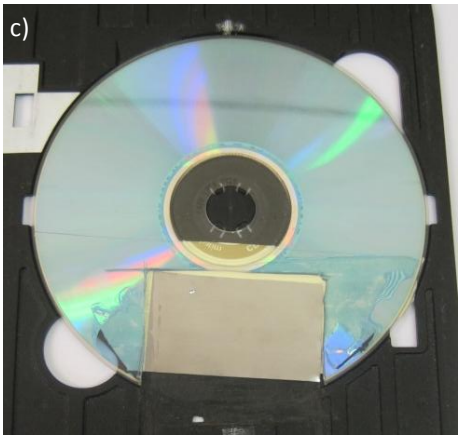


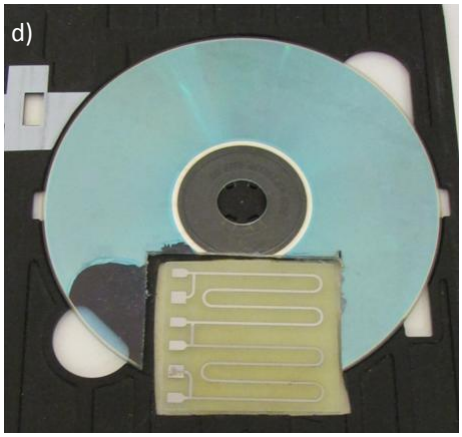



**Figure 6.15**: Altered CD and input tray method for printing on alternative samples: a) illustration of modified input tray with associated sample and CD mount; b) Digital outline of areas to be printed, allowing creation of patterns within outline; c) and d) mounted samples for printing of iron foil sample and ERCM respectively; and e) illustration of input tray in print position.

### 6.2.5 Optical microscopy of printed salt crystals

Designs were created within the Epson CD printer driver software. 1M sodium chloride electrolyte was printed onto glass microscopes slides using the methodology described above. Variations in methodological steps, pattern type and size, were examined, creating multiple prints for microscope analysis. On printing, the samples were air dried and stored within a desiccated environment prior to analysis.

Image analysis was conducted by qualitative microscopy using a Zeiss AxioLab.A1 binocular microscope with a moveable stage and white light source. Analysis was carried out using transmitted light, under magnification between x10 and x100. Images were captured using a 5 megapixel Zeiss AxioCam ERc5s microscope camera and saved as .tiff files within Zeiss driver software. Quantitative digital image analysis of images were conducted using NIH public domain Image-J software. Particle size, distribution frequency and granulometry were examined and quantified. The results are reported in section 7.1.2d.

### 6.2.6 Final printer deposition methodology

Feedback from chloride analysis and microscopic observations were used to finalise a methodology for the printing of sodium chloride. Differences in printed concentrations over the course of print cartridge life were addressed by preliminary printings prior to sample contamination and increased refilling of the cartridge. Optical microscopy analysis prompted the use of 100% greyscale and single prints to provide even crystal size and distribution. A full printer maintenance methodology was used to prevent blockages, increase deposition accuracy, extend cartridge life and minimise internal corrosion of the printer. Printing itself followed strict and identical procedures to ensure repeatability and maintain salt concentration.

Prior to printing, the printer was held with no cartridges inserted. The printer was turned on, connected to a PC loaded with the vector driver software and the print carousel moved to the central position. Deionised water was syringed into empty, washed printer cartridges until all air was displaced. These were inserted into the print carousel and the printhead charged. SSC Service Utility software was used to perform three deep clean cycles and the print carousel returned to central position.

1M NaCl solution was created by addition of a set mass of NaCl crystals to a set mass of deionised water. This was syringed into a clean ink cartridge, which replaces the cartridge in the black position of the print carousel. The service utility software was used to charge the printhead. A CD was loaded into the print drawer and Epson Print CD software used to print 10 repetitions of a 50cm$^2$ design (figure 6.11), washing the CD to remove salt between each printing. A single printhead cleaning cycle was then performed.

Samples were placed in the modified print tray/CD combination and inserted for printing. The loading pattern was applied within the printer software and the salt printed onto the ERCM surface. The loading design, coupled with precise positioning of the ERCM, allowed selective block printing onto the ERCM corroding filament.

The contaminated sample was removed from the printer and placed in a desiccated environment. A single printhead cleaning cycle was performed and the next sample inserted for printing. This was repeated up to ten times, before the ink cartridges were removed and refilled, and the methodology repeated from cleaning with deionised water. During this stage, any visual build up of salt crystals were removed by wet cotton wool buds and pressurised air jets. Printing would then continue as above. Once complete, the NaCl ink cartridge was removed and three printhead cleaning cycles run with deionised water filled cartridges. All cartridges were extracted, visual salt removed and the printer disconnected and powered down.

This methodology created uniform and accurate deposition of sodium chloride contaminated patterns. The specific designs and procedures used for covering the corroding filament of the ERCM designs are outlined in section 6.4.1. The amount and distribution of chloride deposited by the final methodology are reported in section 7.1 and 7.2

## 6.3 Atmospheric corrosion of contaminated iron

To design and examine pre-corrosion methodology, iron foils of identical thickness and material to that used in ERCM creation were printed with sodium chloride and subject to atmospheric corrosion in controlled temperature and humidity environments. Foils were recorded visually and samples taken for analysis after varying time spans. Cross sections of the foils were observed using scanning electron microscopy (hereafter SEM) to assess degree of corrosion, localised corrosion phenomena and corrosion product layout and adhesion. The corrosion products were compositionally analysed using X-ray diffraction and Raman Spectroscopy to assess similarity to archaeological iron. This lead to a final methodology for the atmospheric corrosion of the chloride contaminated ERCM.

### 6.3.1 Creation of iron foil samples

The foil tested was identical to that used in ERCM creation; 10cm$^2$ square sheets of 25 μm iron foil of 99.5% purity. Foil was washed, degreased in ethanol and one surface coated with aerosol deposited Electrolube Clear Protective Lacquer to prevent corrosion. The lacquer was cured in ambient conditions for 24 hours. Foil was handled with protective gloves to prevent contamination. A scalpel was used to separate the foil into 5cm by 2.5cm strips. A jet of compressed air was used to remove dust, foil and lacquer fragments after the cutting process. Foil was stored in desiccated environments until needed.

A separate CD mount was devised for insertion of foil into the printer (figure 6.15c). Chloride was deposited onto the non-protected surface of the iron foil using the methodology described above, in 40mm by 20mm rectangles. Various greyscale percentages were applied to create different concentrations of salt deposition per unit area. Printing was carried out directly before insertion into an atmospheric corrosion chamber.

### 6.3.2 Atmospheric corrosion test chambers

Controlled atmospheres were created within sealed airtight PVC boxes; chosen for low permeability, ease of access and small size. Relative humidity was controlled by saturated

salt solution. Two salts were used in testing: MgCl, to give a low humidity environment, and KCl, to give a high humidity environment (table 6.4).

| Salt | Saturated form | Relative humidity equilibrium (%) | | | |
|---|---|---|---|---|---|
| | | 20 | 25 | 30 | 35 |
| **Magnesium Chloride** | $MgCl_2.6H_2O$ | 33.07±0.18 | 32.78±0.16 | 32.44±0.14 | 32.05±0.13 |
| **Potassium chloride** | KCl (aq) | 85.11±0.29 | 84.34±0.26 | 83.62±0.25 | 82.95±0.25 |

**Table 6.4**: Relative humidities created by saturated salt solutions of KCl and MgCl (from [28])

Solid salt of the appropriate type was introduced to the base of the container up to 2cm depth, and slowly impregnated with deionised water (following the methodology of the ASTM Standard ASTM E104-2 [29]). Impregnation stopped once deionised water was no longer absorbed by the salt. The containers were modified by the creation of a suspended inert plastic wire net, separating the samples from the salt solution by approximately 3 cm (figure 6.16). This distance was deemed close enough to maintain a fairly constant relative humidity, while decreasing the possibility of splashing or other contamination of the foil surface.

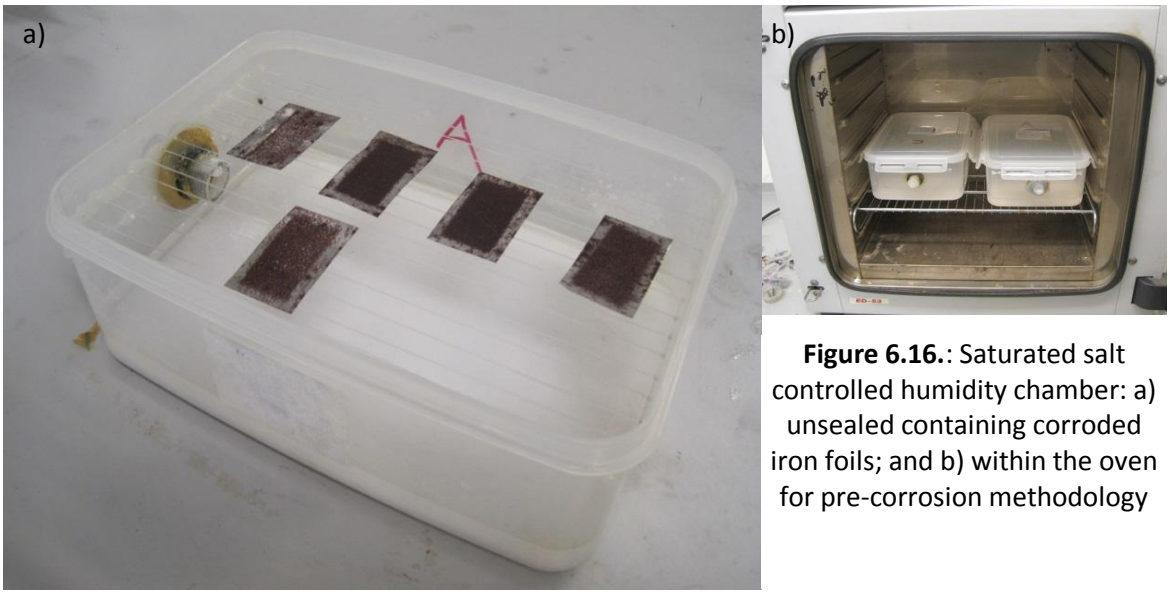


**Figure 6.16.**: Saturated salt controlled humidity chamber: a) unsealed containing corroded iron foils; and b) within the oven for pre-corrosion methodology

Temperature was controlled by a WTB Binder ED53. Temperature was set at 30°C to encourage corrosion without fundamentally changing the reactions. The chambers were

prepared and placed within the oven 1 hour prior to their use as corrosion chambers, to stabilise at required temperature and humidity.

For corrosion tests, the chambers were removed, opened and iron foil samples placed within, maintaining a gap of at least 1cm between each sample and the container walls. The chambers were sealed and returned to the oven. Both chambers and oven were subsequently kept sealed where possible to maintain internal conditions.

### 6.3.3 Visual observation of Corrosion

Chloride contaminated foils of various greyscale and repeat prints were corroded within the chambers to assess the effect of salt loading on the progress of corrosion in varying environments, with a view to creating a final methodology for pre-corrosion of the ERCM. Daily optical records were kept of corrosion progress, to examine corrosion processes over time, identify pitting corrosion (which may cause probe failure) and map the spread of corrosion from and within the original printed pattern. Removed foils were processed and their cross sections examined by SEM to assess the thickness, continuity and profile of corrosion layers

#### 6.3.3a Visual recording

Photographs were taken at 24 hour intervals using a static 10.1 MP Canon Digital IXUS 95 IS camera. A custom made rig was devised to hold the camera over a lined backing board. Camera height was kept constant and a spirit level used to ensure no distortion of image. Camera settings were set to highest quality and the shutter speed set to low. A five second timer was used to prevent instability or shaking on capture.

Foils were removed in batches for analysis. Each container was removed individually from the oven. Foils were removed, photographed straight on to the corroding face and returned individually, minimising the time the foil was exposed or the chambers were open. Care was taken to ensure foils were positioned identically for each picture. Where corrosion was observed on the reverse, this was also photographed. The visual records of the corrosion process are reported in section 7.2.2.

#### 6.3.3b Scanning electron microscopy

For observation of the thickness and structure of corrosion layers, SEM was performed on prepared cross sections of corroded foils. Samples were removed from the corroding

environments during photography, setting the intervals of removal at 24 hours. Preparation occurred immediately on removal from the environments.

To prevent warping of the foil during cutting and polishing, thin layers of epoxy resin were painted onto each face, allowed to dry and re-applied for a further four repetitions. Encased foil was guillotine cut at right angles to its length to expose a representative obverse cross section of the chloride contaminated section. Plastic holding clips positioned the foil, cut side down, within plastic moulds. These were filled with araldite epoxy resin and cured in an oven at 40°C overnight. The resulting samples were ground and polished with silicone carbide abrasive paper, ranging from 240 – 1200 grit, on a Mecapol p260 grinder and polisher, building up a mirror finish of the cross section. A Polaron E5100 sputterer was used to sputter coat the samples with gold; previously shown to produce good clarity of image for back scattered and secondary-electron scanning electron micrographs. Sputtering was carried out at 10mA applied current, 0.1 Torr Argon atmosphere, at a distance of 50mm, for approximately 1 minute; creating a sputtered coating of approximately 75 Å (according to manufacturers thickness calculations).

SEM images were taken using a Carl Zeiss AG - EVO® 50 Series electron microscope, delivering a 3nm resolution at 30kV. Back scattered electron images were taken to better distinguish corrosion products from metallic iron, and possibly separate corrosion product concentrations. 15-20 images were taken along the cross section of each analysed foil at a constant magnification of x1500. The images were subsequently knitted together using Corel Paint Shop Pro Photo X-2, to create a single image for each foil. The maximum, minimum and average thickness of remaining iron foil and corrosion product thickness were examined and corrosion phenomena identified.

Additional secondary electron images were taken of cross sections to examine the grinding methodology for introduced errors from material smearing or deformation. Results influenced the standardised corrosion methodology for the ERCM, reported in section 7.2.3.

### 6.3.4 Compositional analysis of corrosion products

Compositional analysis of corrosion products from pre-corrosion was performed to assess similarity with corrosion products anecdotally present on archaeological iron.

#### 6.3.4a X-ray Diffraction

X-ray powder diffraction methodology was employed to examine the crystalline corrosion products and phases of corroded iron foil. The technique was chosen for the well established

catalogue of iron corrosion spectra and previous success of the technique on iron corrosion products [2-3, 30].

Iron foils were treated with the final methodology for pre-corrosion of the ERCM. Chloride contamination by inkjet printer covered a $2cm^2$ area of the foil, corroded as described in section 6.4.1. Foil was stored in a desiccated environment prior to analysis, which was performed not more than 48 hours after corrosion.

Data collection was by powder diffraction method, using a Phillips X-Ray diffractometer PW3710 with a cobalt anode and X'pert SW data collector software. Continuous scans from 5° 2θ to 90° 2θ, with a step size of 0.05 sec and a scan rate of 7 seconds/step, were performed at 25°C over a 1cm2 area of the corroded face of the foil. Elements highlighted for attention were Iron (Fe), Oxygen (O), Chlorine (Cl), Hydrogen (H) and Sodium (Na). Analyses of spectra were by comparison to the International Centre for Diffraction Data (ICDD) Powder Diffraction File Database.

### 6.3.4b Raman Spectroscopy

Raman spectroscopy was performed on the pre-corroded ERCM to provide complementary and improved compositional analysis. Raman spectroscopy was chosen for high spatial resolution, the well established library of spectra for iron corrosion products, the high speed of data generation and the non-destructive nature of the tests.

Analyses of ERCM were conducted on the exposed corroded surface; no additional sample processing was performed. Scans were monitored for quality to prevent errors in analysis caused by rough surfaces. Points of interest were selected by visual inspection using an optical microscope based on perceived differences in corrosion product. Multiple spectra were acquired for each sample.

Spectra were generated using a Renishaw RM system 1000 Mk1 Raman spectroscopy system, with a Renishaw RL633 Helium Neon laser and 1800l/mm VIS diffraction grating. Samples were positioned and examined using an Olympus BH2 microscope, fitted with a PULNIX CCD TMC 312 camera and wide angle lenses (to prevent contact with the specimen). The software used for data capture and analysis was Renishaw Wire 1.3. Data collection was performed by continuous grating scan over five iterations of thirty seconds, examining shifts between 0 and 1700 $cm^{-1}$. Spectra processing and peak identification was carried out within the driving software and composition determined from comparison to existing libraries of iron corrosion products [30, 31].

## 6. 4 ERCM Pre-corrosion, Testing and Calibration

Through the development outlined above, a final methodology was created for the creation, contamination and pre-corrosion of iron ERCM. Sensors so created were used to monitor corrosion rates within controlled environments. Changes to the environment were simulated to mimic changes to stored archaeological iron and test sensor operation in these conditions.

### 6.4.1 Final ERCM creation methodology.

ERCM were created for exposure tests using a strict repeat methodology, ensuring maximum uniformity. The method of manufacture is detailed in section 6.1. Chloride contamination was carried out using the printing methodology outlined in section 6.2. The design used pure black, 100% intensity greyscale, applied in one printing (figure 6.17).

Corrosion of contaminated ERCM was carried out using the methodology described in section 6.3.2. The ERCM were corroded within the high RH environment for 6 hours, then the low RH environment for 18 hours. This was repeated three times, for a total of 4 x 6 hours in the KCl saturated salt chamber and 4 x 18 hours in the MgCl saturated salt chamber. This methodology gave a fairly uniform corrosion layer with no obvious pitting or localised corrosion phenomena (figure 6.18). On completion ERCM were stored in desiccated environments until needed.

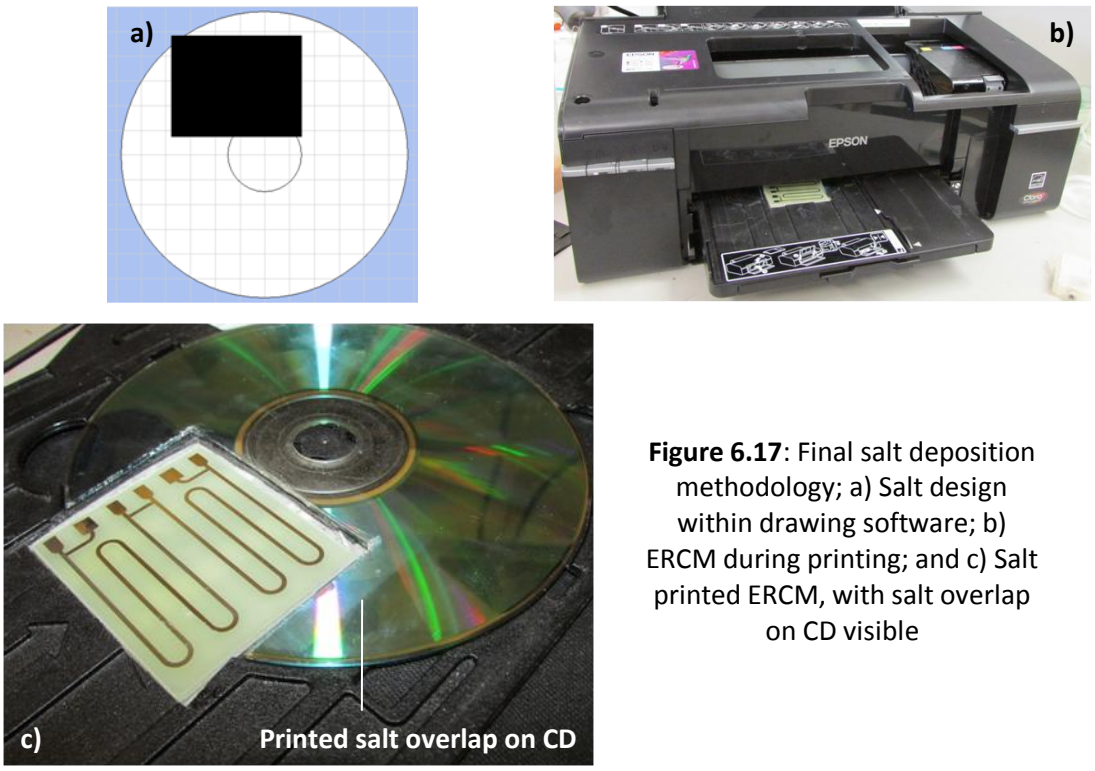


**Figure 6.17**: Final salt deposition methodology; a) Salt design within drawing software; b) ERCM during printing; and c) Salt printed ERCM, with salt overlap on CD visible

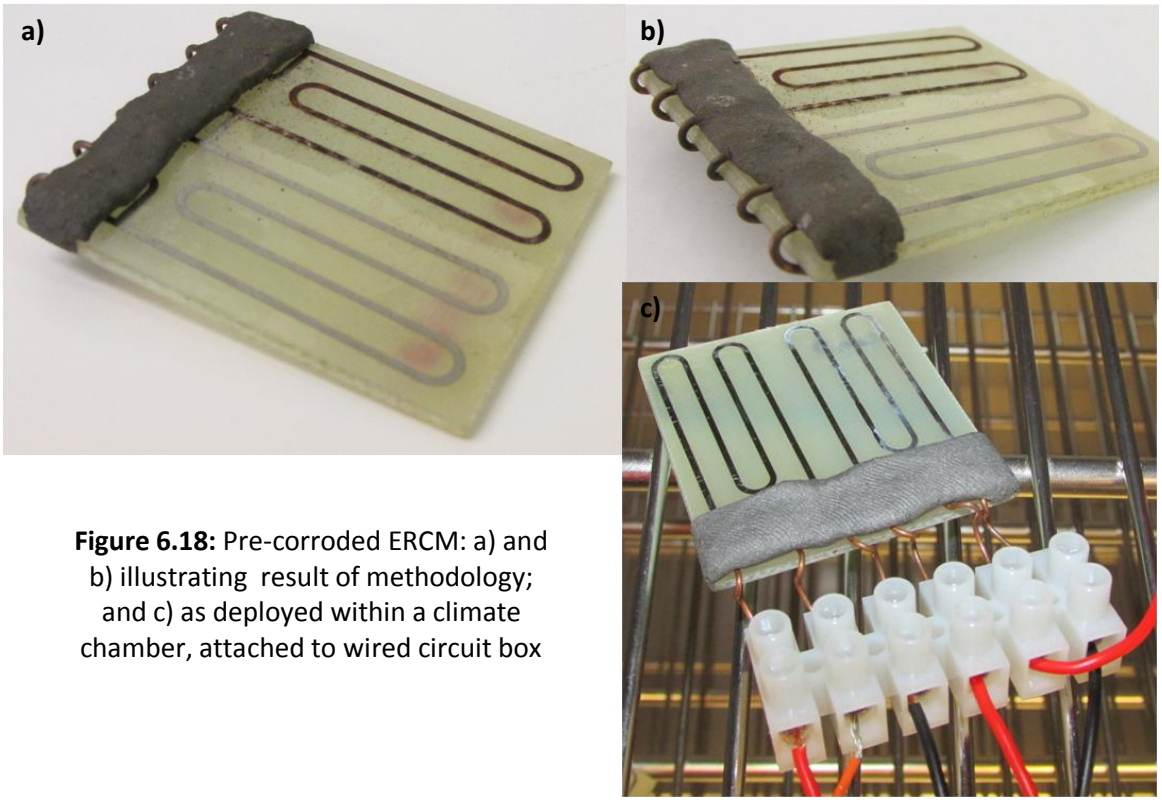


**Figure 6.18:** Pre-corroded ERCM: a) and b) illustrating result of methodology; and c) as deployed within a climate chamber, attached to wired circuit box

### 6.4.2 ERCM testing in a climate chamber

To test accuracy, reliability and operational limits, calibrate the sensors and generate corrosion data for stable and simulated environments, ERCM were corroded within a Binder APT.line™ KBF 240 (E5.2) constant climate chamber (fig. 6.18c). The chamber provided an electronically controlled temperature range of 10°C to 70°C (±0.3°C) at RH between 10% to 80% (±1.5%). It allowed controlled corrosion of the ERCM in known environments, to assess corrosion rates within controlled stable and programmed alternating environments.

#### 6.4.2a Operational setup

ERCM were inserted into terminal blocks trimmed to size, allowing easy attachment to circuit components via flexible, clad copper wire.

Power was supplied from a galvanostatic circuit assembled on an electronic circuit box, designed to provide a constant 10 mA current (figure 6.19c). The current was tested, and shown to be stable up to 200 Ω. Parallel wiring was considered to prevent complete system failure on a single probe losing conductivity, but the additional wiring complicated the layout of the sensors within the climate chamber. Power was instead connected in series; care was taken to identify and replace failing ERCM quickly.

Voltage measurements were made for each filament by Keithley 2000 6 ½ digit multimeter (figure 6.19b), providing 100nV resolution and an accuracy of ±0.0085%, fitted with a 10

channel Model 2000-SCAN internal scanner card. Each filament was connected to an individual channel. The wired ERCM were deployed within the climate chamber, placed with reasonable distance between each to prevent interference between connecting wires and filaments. Connecting wires were passed through the flexible door seal to the exterior, attached by masking tape to maintain their position (fig. 6.19a). Care was taken to minimise the chance of leaks in the seal.

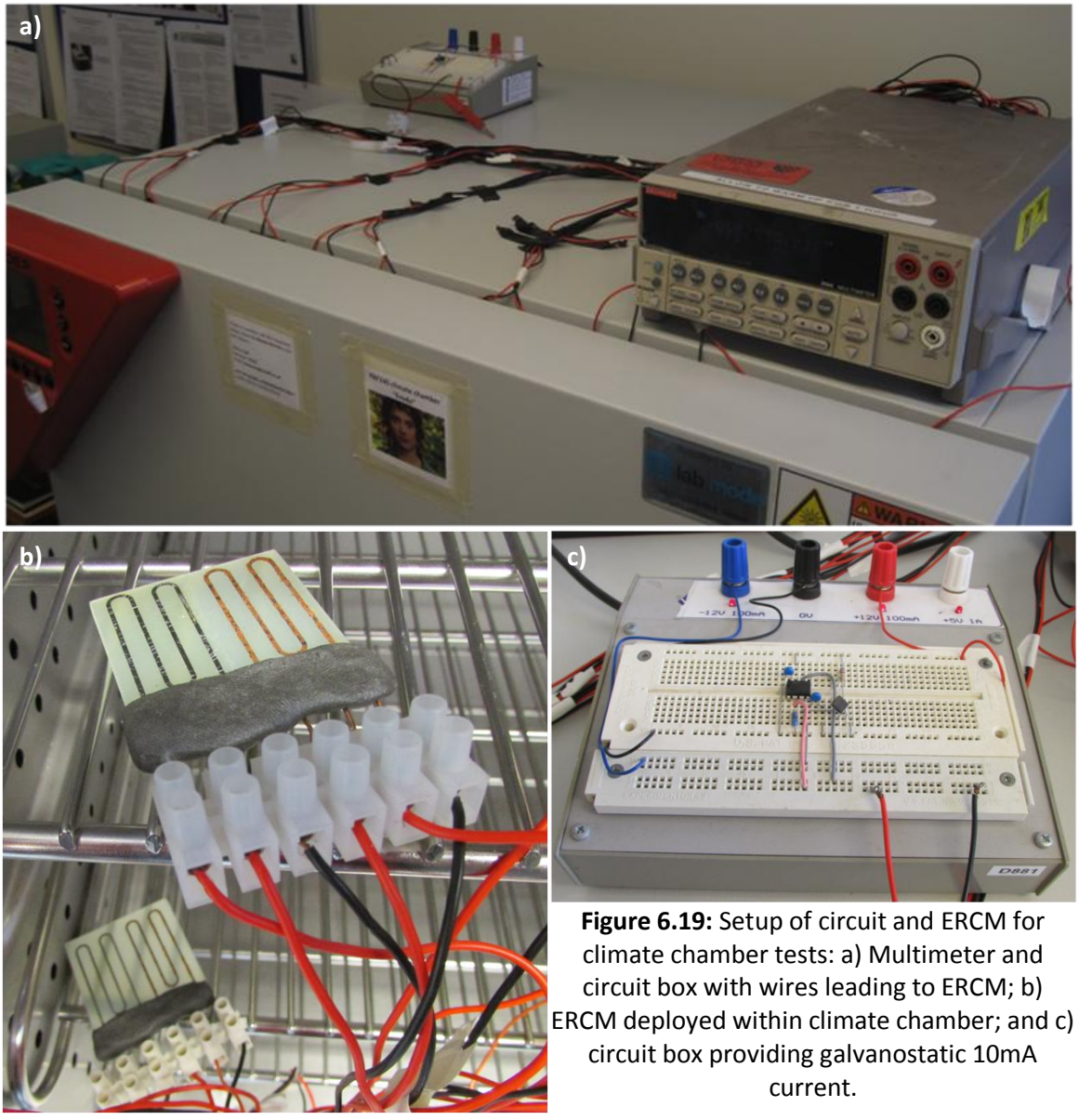


**Figure 6.19:** Setup of circuit and ERCM for climate chamber tests: a) Multimeter and circuit box with wires leading to ERCM; b) ERCM deployed within climate chamber; and c) circuit box providing galvanostatic 10mA current.

The multimeter was interfaced to PC by IEEE-488 GPIB connector. National Instruments LabVIEW Software was used to develop a program to control and take readings from the digital multimeter. Measurements were automatically logged with time at five minute intervals; each measurement cycle consisting of a two point measurement of voltage for each

channel. The measurements were both displayed on screen and automatically stored to a TDMS file. The filename was automatically adjusted after each hour, creating individual packets of readings for each 60 minute interval. These results could be read within Microsoft Excel and a macro was created to sort the data into hourly, weekly and daily tables of results for each sensor.

Power was applied and monitoring was commenced once the ERCM were sealed within the climate chamber.

### 6.4.2b Climate chamber test environments

Changes to the climate chamber settings were made without alteration to the ERCM apparatus; the chamber was kept closed apart from sensor replacement. Where problems were detected or sensors failed, individual sensors were replaced by removal from their terminal block and the insertion of a fresh sensor. Operation of the chamber was by the front panel during constant atmosphere tests and by the supplied driving software for programmed cycles.

Initial environments examined were held at constant temperature (20°C) and relative humidities of 15%, 20%, 30%, 40%, 50% and 60%, chosen to mimic those expected in heritage storage or display environments and to mirror those tests undertaken at Cardiff on actual heritage iron. Tests typically ran for two weeks for each condition: 60% RH tests ran for ten days, to prevent sensor failure, and 15% RH tests for 42 days, to allow detection of the low corrosion rate. Internal climate of the chamber was monitored by internal logger.

ERCM were examined under alternating environments. Binder APT-C2OM™ DataControlSystem GLP Edition software was used to create the programs, controlling both temperature and humidity. 3 programs were developed to test specific aspects of the sensors or simulate specific events in the storage of heritage iron. Programs altered RH while maintaining constant temperature of 20°C. Program 1 (figure 6.20) was designed to simulate the movement of iron artefacts from desiccated storage environments to an ambient environment; constant humidity was switched from very low to standard room levels. The higher relative humidities were varied to assess effect on corrosion rates and reaction time. Program 2 stepped up through relative humidities, from 15% to 20% then 10% steps up to 60% and back down in 3 hour steps, to investigate difference in reaction times at different RH levels and the effect of wet to dry and dry to wet phasing. Program 3 increased then decreased RH steadily over time, to investigate and identify the RH levels at which major changes in corrosion rate occur. ERCM reaction times, corrosion rates, consistency and uniformity were assessed.

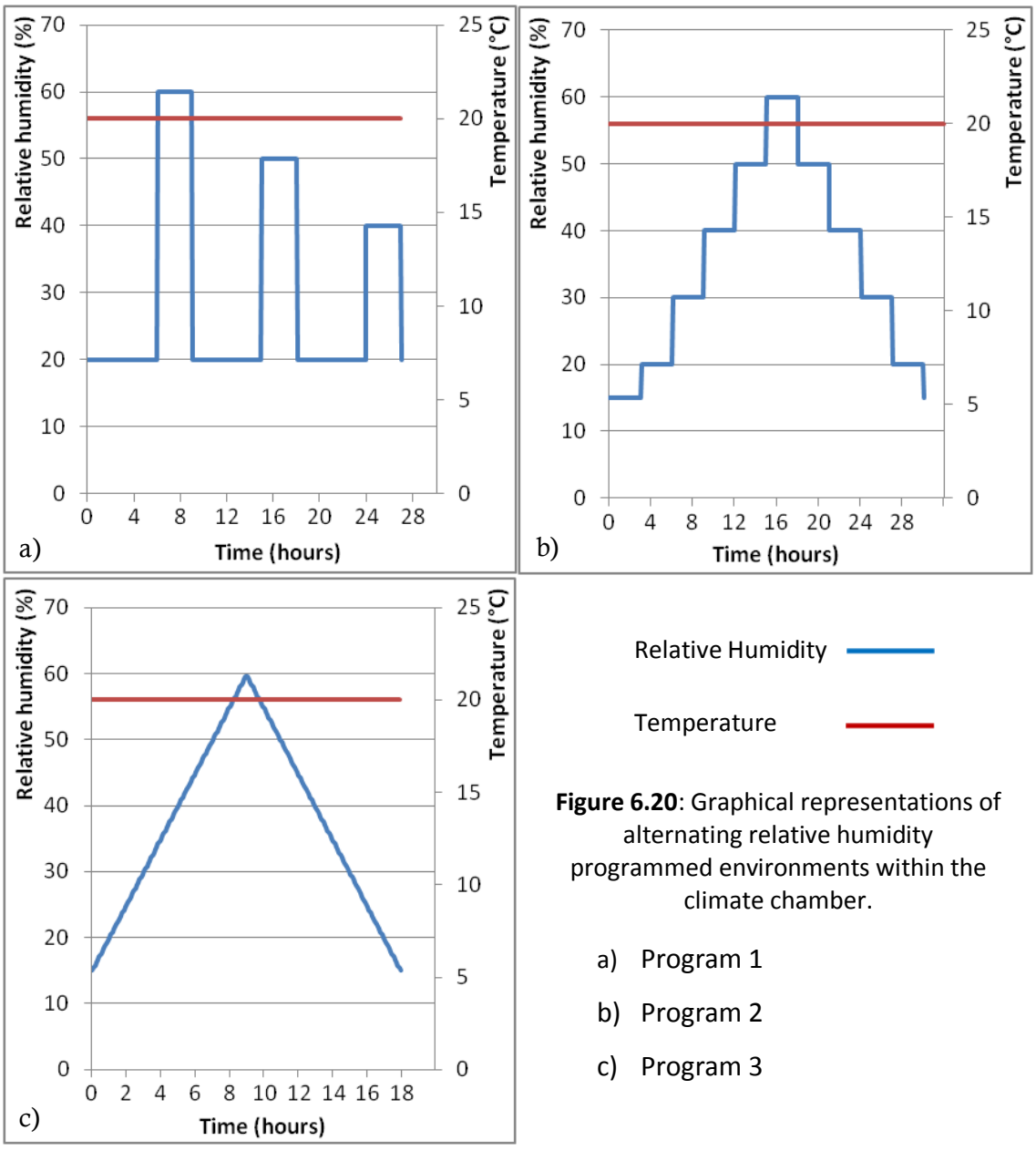


**Figure 6.20**: Graphical representations of alternating relative humidity programmed environments within the climate chamber.

a) Program 1

b) Program 2

c) Program 3

Programs were monitored over repeated cycles for 1 week per program, achieving a number of revolutions based on program time. Results from the climate chamber experiments are reported in section 7.3.

### 6.4.3 Calibration with archaeological iron

Attempted calibration of the ERCM against corrosion rates of actual archaeological iron was carried out using the corrosion rates generated in static environment tests and corrosion rates of archaeological iron in identical conditions. This calibration is discussed in section 8.5.The methodology detailed below was not carried out by the author, but is included for comparison, discussion and evaluation.

Chloride-infested archaeological iron corrosion rates were received by the author as generated by Dr. Melanie Rimmer and Prof. David Watkinson of Cardiff University. Heritage iron was represented by Roman iron nails excavated from two British terrestrial archaeology sites: From excavations at the Roman Cemetry at Billingsgate (London) and the Roman legionary fortress at Caerleon (Newport) donated by the Museum of London and The Caerleon project respectively. The nails were covered in corrosion layers from their time in the ground, had extant iron cores and had been stored in desiccated environments since disinterment. Oxygen consumption was used as a proxy for corrosion rate, the theory of which is documented in section 4.3.5.

Oxygen consumption rates were measured through exposure of individual nails to an enclosed controlled atmosphere monitored by oxygen sensor. To create the environments, optical oxygen sensor pads were affixed to the interior of cleaned and degreased 250 ml Kilner Jars with two-part brass lids, such that the pads could be read externally by fibre-optic cables attached to a WPI OxyMini Oxygen meter. Internal relative humidity was controlled by silica gel, conditioned and weighed to provide set levels of RH between 20% and 80%, in 10% intervals. Temperature was kept at a constant 20°C by insertion of the jars into a Binder APT.line™ KBF 720 (E5.2) constant climate chamber. Both variables were monitored by Madgetech RHTemp101A humidity and temperature dataloggers, positioned on top of the silica gel. Environments were stabilised before use.

Nails were weighed and placed in weighing boats prior to introduction to the environments. The boats were placed on top of the silica gel quickly, to minimise alteration to the internal atmosphere and containers restored to the climate chamber. The containers were stabilised for 60 minutes prior to initial oxygen measurements. With the climate chamber closed, the oxygen meter stimulated and recorded optic response of the oxygen sensor pads via fibre optic cable at 10 second intervals for four minutes. External atmospheric pressure, temperature and optic signal amplitude were monitored to prevent anomalous readings due to seal failure, pad variability or poor contact between fibre-optic cable and glass, respectively. After monitoring, samples were reweighed and digested in 5M nitric acid, subsequently analysed with a Radiometer Analytical PHM250 to determine chloride concentration.

Average readings for each four minute monitor were plotted against time to give oxygen consumption rate, used as a proxy for corrosion rate for calibration of the ERCM. The Cardiff team also made comparisons of proxy corrosion rate, chloride content, artefact mass (as a proxy for surface area) and actual visible damage to examine artefact lifespan. Visible damage was assessed through photographic visual records of iron nails exposed in the corrosive environments.

## 6.5 ERCM in heritage type environments

To evaluate performance of the sensors in a heritage environment, ERCM were sealed and monitored within a desiccated plastic container, similar to those used in museums. The effects of box opening and placing of the box in different conditions were examined.

Containers used within the heritage profession for the storage of iron and silica gel crystals were procured after consultation with Pre-construct Archaeology, the SS. Great Britain, Bolton Museum and Library Service and Maidstone museum (fig 6.21). The chambers were modified similarly to the atmospheric chambers used for corrosion, with a nylon wire net to support the sensors above the desiccant. A 1cm diameter hole was machine cut in the box wall to allow passage of the connecting wires, sealed with Evostick metal epoxy putty and moulded paraffin wax. Internal wires were attached to terminal blocks to allow insertion of ERCM. Silica gel was oven dried and conditioned to provide the lowest possible RH. The chamber was filled to 2cm depth with the desiccant and left for 24 hours to allow atmospheric stabilisation.

External operational setup, monitoring and results logging was identical to that used for climate chamber monitoring, described in section 6.4.2a. Three pre-corroded and one blank, un-corroded ERCM were inserted into the terminal blocks and positioned on the nylon wire. The time for which the chamber was opened was kept to a minimum and the chamber allowed to stabilise for 1 hour prior to initiation of testing.

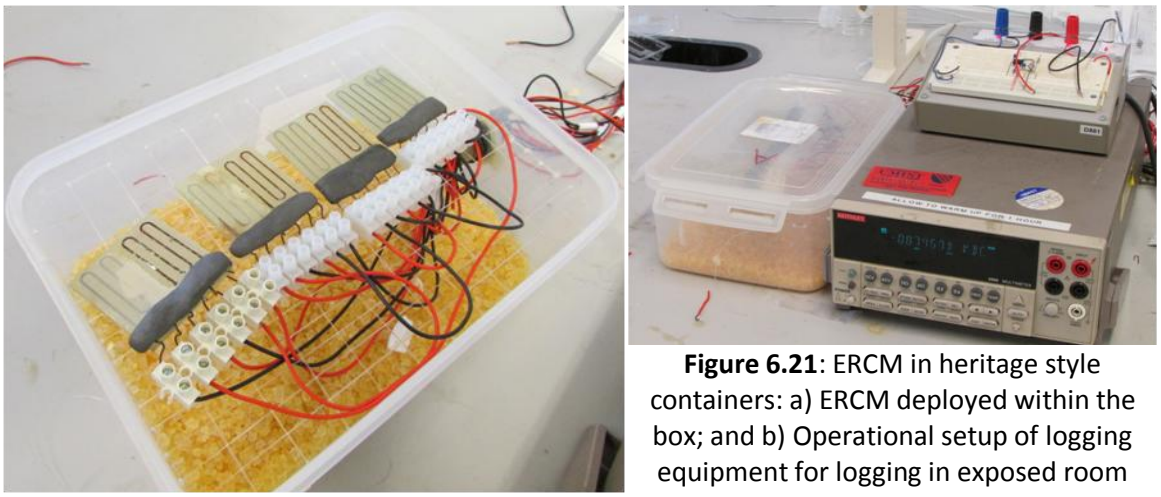

**Figure 6.21**: ERCM in heritage style containers: a) ERCM deployed within the box; and b) Operational setup of logging equipment for logging in exposed room

The chamber was observed while closed in the centre of an active laboratory, sealed within a cupboard and during periods with the lid removed, to assess any changes in corrosion rate. Each iteration was monitored for a period of two weeks.

The results of the storage box corrosion tests are reported in section 7.3.5.

# Chapter 7

# Experimental Results

This chapter presents the results gained from the application of the methodologies described and discussed in Chapter 6. This will include the results of the ERCM creation, salt contamination and pre-corrosion methodologies, compositional analyses of the corrosion products and testing of the ERCM in static and programmed climate chamber environments and simulated heritage environments.

## 7.1 ERCM creation and Inkjet deposition of NaCl crystals

The final methodologies, as described in the preceding chapter, were developed to minimise ERCM fabrication error, failure rate and cost while producing an unobtrusive sensor with high accuracy, sensitivity and reliability and to allow ease of monitoring. The results of the fabrication methods are presented in terms of optically observed and resistance calculated errors, and the printer salt deposition in terms of chloride concentrations and salt particle distributions.

### 7.1.1 Fabrication parameters and error

3 batches of iron foil were photochemically milled to the ERCM design, attached to an inert substrate and analysed immediately upon curing of the protective lacquer. All were initially

inspected, subjected to resistance measurements and one sample from each batch observed under an optical microscope.

Initial optical inspection revealed no errors from the fabrication methodology. Occasional failures occurred in transport of the foil patterns; 2 breakages and five patterns displaying bent or creased filaments, which were discarded. Optical microscopy was used to observe the edges (figure 7.1), using the methodology and apparatus described in section 6.2.5. Under increased magnification, edges appear less smooth and the results of the chemical etching become clear. At very high magnification the characteristic roughness of the etched surface can be observed, typical of steel etching [1].

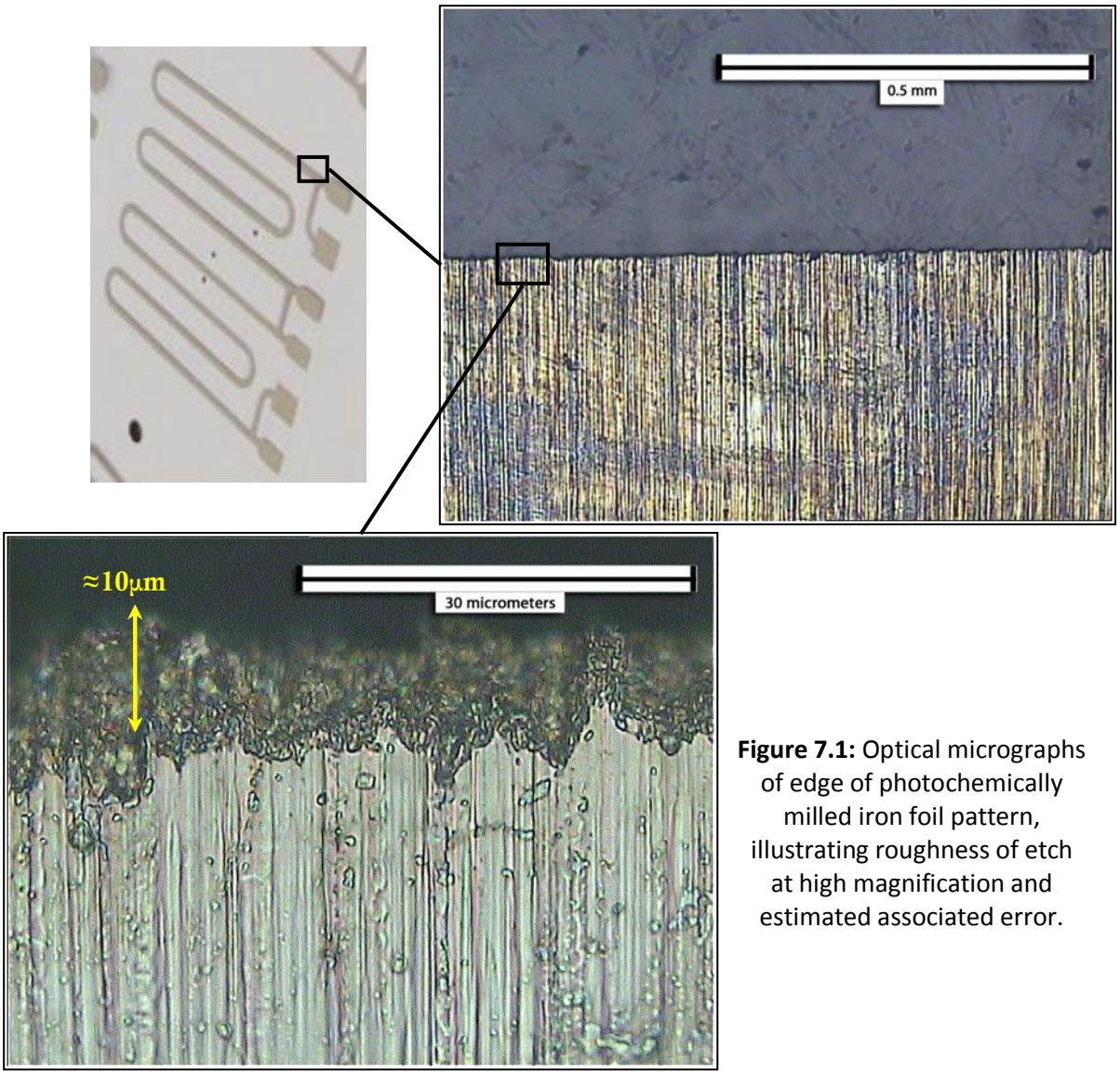


**Figure 7.1:** Optical micrographs of edge of photochemically milled iron foil pattern, illustrating roughness of etch at high magnification and estimated associated error.

The observed undercut and roughness were measured by graticule. The maximum estimated thickness disparity was around 10μm. This provides an optically estimated fabrication error of 2% across the width of the sensor. This error would not affect length or thickness.

| Sensor Batch (Creation date) | | A (24/06/2013) | | B (09/07/2013) | | C (01/09/2013) | | All sensors | |
|---|---|---|---|---|---|---|---|---|---|
| Ambient temperature (°C) | | 21 | | 23 | | 24 | | - | |
| No. of sensors (filaments) | | 22 (44) | | 12 (24) | | 8 (16) | | 42 (84) | |
| Individual filament resistance | Average filament resistance (Ω) | 0.844 | | 0.870 | | 0.885 | | 0.859 | |
| | Minimum/Maximum filament resistance (Ω) | 0.817 | 0.861 | 0.852 | 0.887 | 0.87 | 0.912 | 0.817 | 0.912 |
| | Batch Standard Deviation (Ω) | 0.010 | | 0.009 | | 0.013 | | 0.020 | |
| | Sample Variance | 1.05E-04 | | 7.32E-05 | | 1.82E-04 | | 4.00E-04 | |
| | Average/maximum error $(x- \bar{x})/ \bar{x}$ | 0.93% | 3.14% | 0.78% | 2.02% | 1.33% | 3.05% | 1.92% | 6.17% |
| ERCM Resistance Ratios | Average resistance ratio ($R_r/R_c$) | 1.00002 | | 0.99970 | | 0.99921 | | 0.99978 | |
| | Minimum/Maximum ratio | 0.989 | 1.009 | 0.991 | 1.014 | 0.989 | 1.007 | 0.989 | 1.014 |
| | Batch Standard Deviation | 0.006 | | 0.007 | | 0.006 | | 0.006 | |
| | Batch Sample Variance | 4.11E-05 | | 4.61E-05 | | 3.16E-05 | | 3.89E-05 | |
| | Average/maximum error $(x- \bar{x})/ \bar{x}$ | 0.58% | 1.06% | 0.52% | 1.35% | 0.42% | 1.10% | 0.53% | 1.35% |

**Table 7.1:** Summary statistics for initial measured filament resistance and resistance ratios, calculated error and variance of ERCM

| ANOVA Analyses | | | | | |
|---|---|---|---|---|---|
| **Compared datasets** | | **F-value** | **$F_{crit}$ (95%)** | **P-value** | **Sig. Dif?** |
| **Reference and corroding filaments within ERCM batch** | A | 0 | 4.073 | 100.00% | **No** |
| | B | 0.0063 | 4.301 | 93.75% | **No** |
| | C | 0.0116 | 4.600 | 91.59% | **No** |
| **Filament resistance variation across all batches** | | 110.0982 | 3.109 | 0.00% | **Yes** |
| **Resistance ratio ($R_r/R_c$) between all batches** | | 0.0480 | 3.238 | 95.32% | **No** |

**Table 7.2:** Analysis of Variance (ANOVA) statistics of the initial resistance measurements of ERCM, calculated with respect to a 95% degree of accuracy (α=0.05). If F-value>F-crit, there is significant difference (non-equivalence) of data and rejection of the null hypothesis (that there is no difference between datasets)

More accurate data were obtained from resistance measurements for each ERCM filament, generated as described in section 6.1.5. The temperature at the point of measurement was recorded. Table 7.1 contains the average resistance data for each of the ERCM batches, and the whole dataset together. The error of each filament was calculated by subtracting measured filament resistance from the average resistance of each batch, or the whole dataset, expressed as an absolute percentage of the mean. The ratio error was calculated from the

difference in the ratio of the reference against the corroding filament to the ideal starting ratio (1), expressed as a percentage. Each batch is considered separately; the final column assesses the entire dataset. Table 7.2 summarises the analysis of variance statistics for comparison between the reference and corroding electrode within each batch, the filament resistance variance between all batches and the variance in the resistance ratio between all batches.

The data reveal large differences between average measured resistance, spread, variance and error of filaments within each batch, illustrated by the very large F-value (confirming significant difference in ANOVA analysis) in table 7.2. When filaments within the same dataset are compared, the error, range and variance are much smaller. Assuming fabrication error is approximately equal across each batch, this error can be attributed to difference in resistivity from the effects of temperature. Moment to moment differences in temperature also account for error between filaments within the same dataset. When this variation is removed (by normalising each ERCM through the ratio of the resistances of both filaments), the error is reduced still further.

### 7.1.1a Temperature error and calculated metal properties

The 6.17% maximum error of filament resistance readings illustrates the impossibility of comparing resistances for sensors in different temperatures and the importance of the reference electrode. This adverse effect can be investigated by using the calculated dimensions (see section 6.1.2) (ignoring fabrication error) with the measured resistance. While not vital for the operation of the ERCM, these results illustrate the effect of temperature, give comparative readings for material resistivity and temperature coefficients and provide comparative data for similar studies.

The calculated resistivities for each batch are displayed in table 7.3. Variance, standard deviation and other statistics are directly related to the resistance data and are not shown here. To calculate the temperature coefficient, the percentage increase between one batch average and another was calculated. This was the divided by the temperature difference in °C, to give the resistance coefficient of temperature ($\alpha$). The average of the calculated values was then used to calculate resistivity for each probe as it would be at 20°C. Reference resistivities from the manufacturer and quoted sources are given as a comparison within the table.

The regressed standard resistivity 13.84 $\mu\Omega$cm is fairly constant over the dataset, with a low range and variance. While the low number of readings make the data insufficient for a true material test, the consistency of the reached value would indicate the metal is acting as expected, increasing linearly with temperature with a constant temperature coefficient.

| Resistivity assumptions and calculations | | | | | | |
|---|---|---|---|---|---|---|
| **Filament dimensions and resistivity calculation** | | | **Coefficient of temperature (α)** | **Reference characteristics [2]** | | |
| | | | | Metal | ρ (μΩcm) | α (K-1) |
| **Length (mm)** | 150 | R=ρl/wd | R=R0 [1+ α(T-T0)] | Iron | 10.1 | 0.0065 |
| **Width (mm)** | 1 | ρ= R/600000 | α=((R/R0)-1)/ ΔT | Mild Steel 1010 | 14.3 | 0.0066 |
| **Thick (μm)** | 2.5 | | | Stainless steel 201 | 69.0 | 0.001 |

| Calculated Iron resistivities | | | | | | | | |
|---|---|---|---|---|---|---|---|---|
| | A | | B | | C | | Average | |
| **Average measured resistance, R (Ω)** | 0.844 | | 0.870 | | 0.885 | | 0.859 | |
| **Average calculated resistivity, ρ (μΩcm)** | 14.07 | | 14.50 | | 14.75 | | 14.32 | |
| **Min/max resistivity, $\rho_{min}/\rho_{max}$ (μΩcm)** | 13.62 | 14.35 | 14.21 | 14.79 | 14.50 | 15.20 | 13.62 | 15.20 |
| **Measured ambient temperature, T(°C)** | 21°C | | 23°C | | 24°C | | - | |
| **Percentage increase ($R_1/R_2$ or $\rho_1/\rho_2$)** | (a»b) +3.08% | | (b»c) +1.72% | | (a»c) +4.86% | | - | |
| **Calculated coefficient of temperature, α ($K^{-1}$)** | 0.0154 | | 0.0172 | | 0.0162 | | 0.0163 | |
| **Modelled resistivity at 20°C (μΩcm)** | 13.84 | | 13.82 | | 13.85 | | 13.84 | |

**Table 7.3:** Calculations of resistivity and temperature coefficient from measured resistance and temperature of ERCM within and across batches

The calculated average coefficient of temperature and the modelled resistivities are not the quoted values supplied by the manufacturer. The average resistivity before regression is calculated at 14.32 μΩcm, with a coefficient of temperature of 0.0163 leading to a standard resistivity of 13.84 μΩcm at 20°C, compared to the supplied characteristics of 10.1 μΩcm and α=0.0065. Within steels, resistivity typically increases with percentage carbon, and other impurities, and decreases with temperature during tempering [3]. The manufacturers quoted carbon level is <600ppm, with 3000ppm Manganese, 1000ppm Silicone, <400ppm Phosphorous and <500ppm Sulphur. It is possible that the quoted resistivity covers the most pure form of iron and our measurements represent the differences created by metal heterogeneity and compositional error. Our measured resistivity lies between that of pure iron and very low carbon mild steel, which is to be expected from the quoted composition. However, it is unlikely that the levels are significant enough to be the only cause of the resistivity inaccuracy.

Error in calculated resistivity may be influenced by fabrication error, due to the undercutting process (see section 6.1.1c). The strict methodology may have led to a constant degree of undercut, as opposed to a constant straight edge, leading to a fairly constant value of width

below 1mm. Etch factor can never exceed a 1:1 ratio if etching is ceased immediately on removal of the whole thickness. From our implemented methodology of double sided etching, it is unlikely that the under-etch would consistently exceed 12.5μm, or at most 25μm (2.5%). Expected resistivity (10.1) and average measured resistance (0.86) would require an average filament width of 0.7mm, 30% undercut. This is an extremely unlikely level of removal which would have been easily identified under optical microscopy. While undercut and fabrication error may contribute to the difference in resistivity, it is not a major factor.

The over-large coefficient of temperature, difficult to explain in terms of increased impurities, may be indicative that the measured ambient temperature was not equal, or directly related, to the metal temperature. The ERCM were stored in sealed, desiccated and darkened environments, and only removed briefly for testing. The temperature of the storage was not monitored, and it is not known whether the foil would have altered to room temperature prior to monitoring. Intense ambient lighting within the laboratory may have caused an increase in heat in the metal filaments compared to surroundings.

It is likely that the difference in measured and expected values is caused by a combination of the above factors. Whatever the cause, it will not have a significant effect on the operation of the sensors, which substantially remove temperature, and therefore resistivity, error as a factor by the two electrode system. The spread and variance of the data, in addition to the similarity of the regressed standard resistivity, indicate that all batches behaved similarly and the electrical properties of the metal are consistent. This is illustrated in the consistency of the calculated fabrication errors and ERCM resistance ratios.

#### 7.1.1b ERCM fabrication error and reliability of method

Where resistivity is removed as a variable, through the resistance ratio or within batch datasets, the spread, error and variance of the readings are acceptably low. Table 7.2 illustrates that there was no significance difference, when analysis of variance was performed at 95% certainty rate, between data for corroding and reference electrodes within the same batch or between the resistance ratio of all batches. This can be further evaluated through equivalence, using the probe fabrication error to work out acceptable bounds of confidence.

The fabrication error can be taken directly from measurements of the resistance ratio in table 7.1: Average error = 0.5% and maximum error = 1.4%, of which the latter will be regarded as the true fabrication error by this author. This inaccuracy will be made up of errors in the components of the resistance; resistivity, width, length and thickness between the two filaments of a single ERCM. For both filaments, length and resistivity may be assumed constant and equal due to the materials and design of the sensor; error is derived directly from the transverse cross sectional area of the filament. Foil thickness error was quoted by

the manufacturer as ±15%. It is likely that this will be distributed across the entire thickness of a foil section, allowing it to be regarded as a constant for each sensor. This is backed up by the much lower calculated fabrication error and from examination of the foil using SEM (see section 7.2.3). Therefore, the fabrication error can be attributed almost exclusively to width. This translates to a width variation of 13.5μm along the length of the filament, or 6.75μm for each etched edge. This correlates well with our optical observations (figure7.1).

No significant difference was detected within batches or for the resistance ratio across all sensors, but this is not enough to conclude that there are no difference: P-values from ANOVA provide a measure of evidence against the null hypothesis, not in support of it. To assess this, equivalence analysis was performed between the datasets, using Two one-sided tests (TOST) (table 7.4). The method tests joint null hypotheses to create a range of F values. If this range falls entirely within a user defined range of variance, equivalence is proved. The generated p-value shows the probability of non-equivalence; if p<5% equivalence is proved within a 95% significance level.

| Comparison of equivalence between Resistance ratios of ERCM batches | | | | | | |
|---|---|---|---|---|---|---|
| **Chosen equivalence range and tested dataset** | | **Range** | **Lower Bound** | **Upper bound** | **P-value** | **Equivalent** |
| Error range of 0.675% (fabrication error) | A-B | ± 0.00675 | -0.00366 | 0.00429 | 0.50% | **Yes** |
| | B-C | ± 0.00675 | -0.00454 | 0.00552 | 2.24% | **Yes** |
| | A-C | ± 0.00675 | -0.00356 | 0.00518 | 1.41% | **Yes** |
| **Comparison of corroding and reference electrode resistances within a single batch** | | | | | | |
| Error range of 1.35% (fabrication error for two filaments) | A | ± 0.01139 | -0.00526 | 0.00526 | 0.04% | **Yes** |
| | B | ± 0.01174 | -0.00585 | 0.00641 | 0.20% | **Yes** |
| | C | ± 0.01198 | -0.01154 | 0.01304 | 6.54% | **No** |
| | All sensors | ± 0.01160 | -0.00708 | 0.00753 | 0.57% | **Yes** |

**Table 7.4:** Results of Two one-sided tests (TOST), to ascertain equivalence between ERCM batches and between corroding and reference filaments in batch and across whole dataset.

The chosen range for equivalence was ±0.675%. At half the maximum recorded error, this was judged a fair assessment of equivalence; the majority of sensors should fall within this range, and future batches could be tested based on this level of error. While higher than the average error, it is significantly lower than the maximum error for any of the batches. The results show that, within this constraint, resistance ratios for all batches may be considered equivalent to each other: Each batch can be said to have created similar ERCM. This illustrates the reliability and repeatability of our photochemical milling methodology, within our chosen error limits.

Equivalence tests were also performed between corroding and reference electrodes of each batch, to ascertain the whether ERCM within the same batch acted equivalently. The chosen range of error was extended to 1.35%; doubled to reflect the error in both filaments. Batch A and B showed equivalence, with a strong P-value. This would indicate no difference between the two filaments for ERCM from these batches. Batch C was not judged equivalent within these boundaries. While the exact cause of this disparity is unclear, it may be down to the small sample size and high temperature at time of measurement; magnifying any small error due to temperature fluctuation. Batch C also exhibited the greatest standard deviation and variance between filaments and had the highest individual resistance measurements for an ERCM, indicating additional errors in temperature or thickness may have been to blame. Taken as a whole dataset, the corroding and resistance filaments were shown to be equivalent, within the set error range. This highlights both the consistency of fabrication and the lack of any formed disparity, through corrosion or damage, during the manufacturing and storage process.

The results show the creation methodology for the manufacture and mounting of the ERCM results in consistent and equivalent readings for resistance ratio, with a maximum fabrication error of 1.4%. The role of temperature and the importance of the reference electrode have been highlighted and taken into consideration for assessment of later results. The filament ratios above were used in calculation of corrosion depth and rate when results from the ERCM deployment are considered.

### 7.1.2 Chloride analysis of inkjet printer deposition of NaCl

Chloride contamination of the ERCM by inkjet printer was evaluated by measurement of deposited surface chloride, described in section 6.2.3. Chloride analysis was conducted at each stage of printer methodology development, evaluating magnitude and consistency of chloride deposition. The results are included here to illustrate the progression of the methodology, the errors inherent in deposition, the range of chloride with which our sensors were covered, validate our choice of chloride contamination level, and provide comparison against other deposition methodologies.

#### 7.1.2a Chloride analysis inherent error

Initial analysis was performed on reference liquids to ascertain the accuracy of the apparatus and provide comparative controls. Deionised water and KCl reference solution of 200 ppm were used to ascertain error and variation inherent in the chloride analysis methodology itself. To examine possible contamination within the methodology, a blank CD was prepared

without printer contamination and rinsed as described. The results are presented in table 7.5. Standard deviations were taken across the 5 titrations to illustrate the spread of results for each sample. Error was calculated by subtracting the measured chloride level from the expected reading, expressed as an absolute.

| | No. of samples | Average Chloride (ppm) | Average Standard deviation | Average error (ppm) (x-expected) | Maximum error (ppm) (x-expected) |
|---|---|---|---|---|---|
| **KCl reference solution (200ppm)** | 10 | 200 | 2.4 | 2 | 9 |
| **Deionised water** | 5 | 6 | 6.8 | 7 | 21 |
| **Rinsed Plain CD** | 5 | 7 | 6.0 | 6 | 16 |

**Table 7.5:** Control tests for chloride analysis methodology; testing deionised water, rinsings from a blank CD and Potassium chloride reference solution of 200ppm

Results using the manufacturer provided KCl standard solution give a very low average error of ±2ppm, well within the manufacturer's guideline ±3ppm. While the maximum observed error was 9 ppm, the error is distributed such that it largely disappears over the five reading cycle, as suggested by the very low standard deviation.

The titration of deionised water and CD rinsings prepared gave very similar results but illustrate the difficulties of detection of low chloride levels within this analysis. Of the 25 readings each for the deionised water (5 samples over 5 repetitions) and the test rinsings, 8 of the former and 11 of the latter registered 0 ppm. Readings immediately subsequent to these results were frequently over twice the average reading, as exhibited by the maximum errors of both datasets. This is indicative of a failure to remove present chloride, subsequently recorded in the next titration. Readings obtained outside these failures and subsequent results, gave readings much closer to the average, presenting a maximum error of 4 and 3 ppm respectively. If the hypothesis above is accepted, then all chloride is taken into account over the course of the 5 readings (assuming a non-zero final result): We may use the average chloride levels with some degree of confidence.

Deionised water, which should have 0 ppm chloride, measures at 7±4 ppm chloride. This may be methodological error or indicate chloride introduction to the solution at an unknown stage. CD rinsings give almost identical readings, indicating no additional error is introduced during the titration methodology.

Error was continually analysed throughout subsequent analysis of CD rinsings: The value of every titration was subtracted the calculated average for that set of five to give deviation from the mean. Only one result was sufficiently low to present results of zero, with 95 other sets of 5 recorded. Discounting this result, the highest error for an individual measurement was 10ppm, average error was 4ppm and highest average error for a set of 5 titrations was 7ppm.

The highest of these (10 ppm) has been selected as the characteristic error, equating to ±0.3 μg/cm$^2$ over a 50cm$^2$ print rinsed into a 20ml sample

7.1.2b Analysis of methodology by argentometric titration

Chloride analysis was used to evaluate and improve the printer methodology; each methodological redesign was evaluated by repeated printings of 1M NaCl solution over 50cm$^2$, using a pure black 100% intensity greyscale and the highest print settings. Results were evaluated for level of chloride deposited and consistency, error and deviation of results (table 7.6). Results were first taken from print runs with no set methodology. The two sets of alterations represent bulk changes in methodology, discussed in section 6.2.2. Set of alterations 1 were based around implementing a set methodology of printing. Set 2 were alterations in cleaning of the print head between printings. The 'final methodology' represents the methodology described in section 6.2.6, as used for contamination of sensors. The results are presented to illustrate progression of the methodology and give comparative levels of average chloride concentration and statistical distribution, variance and error.

| | Methodology | No standard methodology | | Set of alterations 1 | | Set of alterations 2 | | Final methodology | |
|---|---|---|---|---|---|---|---|---|---|
| | Number of samples | 16 | | 10 | | 10 | | 10 | |
| Chloride deposition level (μg/cm$^2$) | Average chloride level | 24.1 | | 67.9 | | 86.4 | | 107.8 | |
| | Min/Max chloride level | 8.9 | 43.7 | 61.1 | 74.0 | 77.8 | 94.6 | 98.8 | 113.1 |
| | Range | 35.70 | | 12.91 | | 16.85 | | 14.27 | |
| Accuracy of printed samples | Standard Deviation | 11.47 | | 4.14 | | 5.56 | | 3.99 | |
| | Standard Error | 2.85 | | 1.31 | | 1.76 | | 1.26 | |
| | Variance | 130.37 | | 17.13 | | 30.91 | | 15.91 | |
| | Kurtosis | -0.80 | | -0.61 | | -1.19 | | 2.32 | |

**Table 7.6:** Results of chloride analysis for inkjet printer deposition of 100% black patterns of 1M NaCl, from initial depositions through to the final applied methodology

Without applied methodology, the amount of chloride deposited was low, with very high range and variance of results. Kurtosis is a measure of the shape of the distribution curve of the data, compared to the normal distribution. Negative kurtosis here denotes a flat curve with a high peak, positive kurtosis denotes a squat curve with lower results range. The former

can be seen as an indicator of consistency and reliability of method, assuming a comparable range to the latter.

Each methodological set of alterations showed progressively higher levels of chloride deposition (indicative of fewer blockages and greater consistency of deposition) and decrease in variation. Interestingly, cleaning of the print head between prints increased the variance and resulted in a highly negative kurtosis; denoting a greater variation of concentration over a smaller range. It was visually evident that more solution was deposited once this method was implemented; the greater volume may have naturally increased the variation of deposition or it may be the result of remnant deionised water in the print head. The final methodology added further modifications, increasing average deposited chloride to 108$\mu g/cm^2$, decreasing variation to its lowest observed level of 15.91 and minimising the percentage range of values. The kurtosis has reversed to a high positive; describing an increased consistency of concentration. The range indicates a maximum error around the mean of $\pm 9\mu g/cm^2$.

Further tests of the 100% prints were made in the evaluation of lower greyscale and repeat printings, reported below. These results maintain the values reported here, with an overall (inclusive) average of $108\pm 9\mu g/cm^2$, the same maximum and minimum and a variance of 12.97. The Kurtosis of the data lowers to 1.03, but this is as expected for a larger dataset and is not viewed as a reflection of any loss of accuracy.

### 7.1.2c Changing chloride levels: Repeat printing and alternate levels of greyscale

To ascertain the possibility of altering chloride deposition levels, chloride analysis was performed prints of 1M NaCl deposited on CDs using shades of greyscale, and over repeat 100% prints onto the same substrate area. The results are included here to provide an analysis of inkjet printing as a technique for use in future corrosion testing or pre-corrosion methodologies, and explain our decision to use 100% greyscale.

Printing of greyscale was performed identically to previous prints. Levels of greyscale were ranked by percentage intensity (0% being no colour and 100% being pure black). Greyscale down to 50% in steps of 10% were attempted, to evaluate any link between the percentage greyscale and the resultant deposition of chloride. Lower intensity greyscale shades were not evaluated, due to the higher levels of error associated with measurement of low chloride levels. 5 sets of prints were evaluated for each dataset and averages taken (table 7.7, figure 7.2). Error around the mean was calculated from individual results subtracted from the average value for that percentage greyscale, expressed as an absolute and as a percentage of the mean.

The results show a strong linear correlation between greyscale intensity and detected chloride intensity. A direct relationship between software plotted intensity and deposited solution was hoped for, to facilitate future methodologies. Taking our 100% start point of 108±9μg/cm², we would therefore hope for a relationship of around 1.1 (±0.1) :1 between observed chloride content and printed greyscale. The regression line in figure 7.2 gives a relationship of approximately 1.2:1, within the suggested model. The regression leads to a value for 0 mg Cl deposited at 11% greyscale; in reality it is likely deposited chloride will only reach 0 when no printing occurs. While correcting this flaw requires greater error than the stated 9μg/cm², the high $R^2$ value illustrates good correlation and confidence in the predicted relationship. Modelling using a line which passed through 0 gave a very similar regression line (y=1.0086x, $R^2$= 0.92). While results generated do not allow a precise analysis, we may infer that the relationship is somewhere in the region of 1.1:1, as expected.

| Percentage greyscale | Average Contamination level (μg/cm²) | Min/ max chloride level (μg/cm²) | Range of chloride concentration (μg/cm²) | Variance of sample | Error around the mean (x-x̄) (absolute/%) |
|---|---|---|---|---|---|
| **100** | 108 | 104/114 | 10 | 14.0 | 3/2.5% |
| **90** | 90 | 82/97 | 15 | 44.8 | 5/5.8% |
| **80** | 78 | 70/83 | 13 | 32.7 | 5/6.0% |
| **70** | 70 | 63/76 | 14 | 20.6 | 4/5.0% |
| **60** | 57 | 52/61 | 9 | 18.4 | 4/6.3% |
| **50** | 48 | 41/52 | 4 | 19.1 | 3/7.0% |

**Table 7.7:** Table of chloride concentration of inkjet deposition of varying levels of greyscale, including calculated variance and error of result

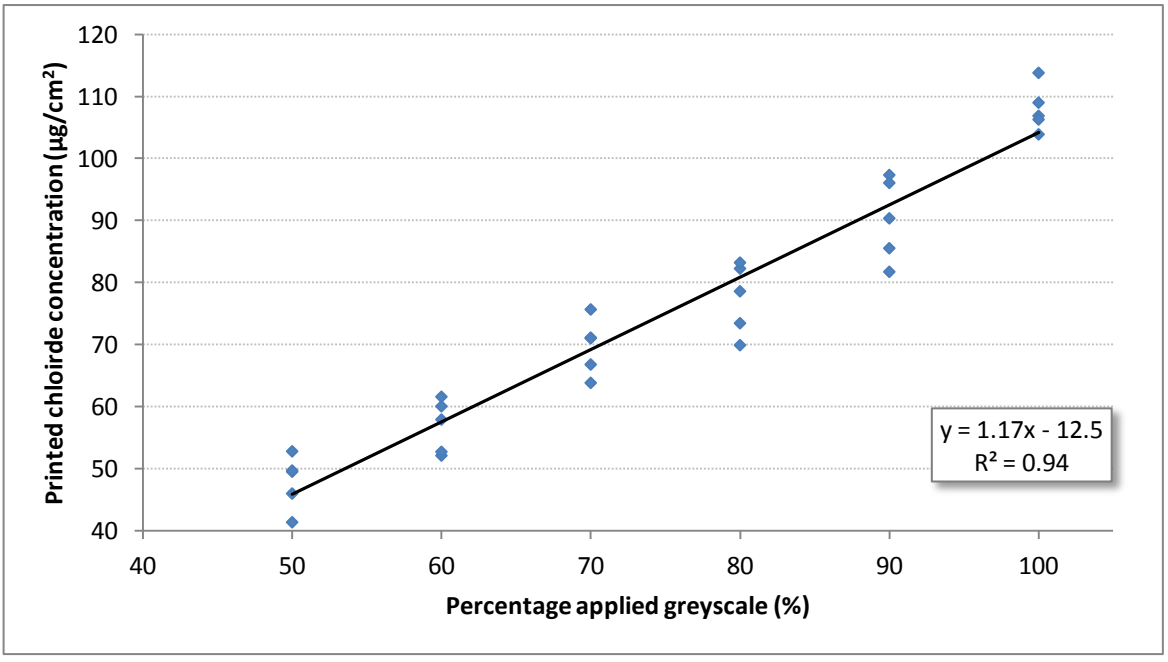


**Figure 7.2:** Graph of percentage greyscale printed patterns against measured chloride contamination of CD surface, including trend line, suggested line equation and $R^2$ value of correlation.

The variance and error of the samples both rise when printing at less than 100% greyscale. In absolute terms, error around the mean decreases with chloride level and greyscale; in percentage terms it stays about the same, between 6 and 7% of the average concentration. This is significantly higher than printing of pure black. The additional variation may be due to errors of constant value associated with printing (deposition of chloride from past prints, removal of chloride through movement of the CD, etc.) becoming greater factors at low chloride levels.

Repeat printings were used to increase chloride levels on a sample. Printing methodology was identical to that used for 100% greyscale, with reinsertion of the specimen in the same position to achieve additional overlying prints. Only 100% black greyscale was used, with 1-4 repetitions carried out (table 7.8; fig. 7.3): Above this point chloride levels became too high for analysis equipment without alterations to the methodology and possible increased error.

| Number of Prints | Average Contamination level (µg/cm$^2$) | Min/max chloride level (µg/cm$^2$) | Range of chloride concentration (µg/cm$^2$) | Variance of sample | Error around the mean (x-x̄) (absolute/%) |
|---|---|---|---|---|---|
| 1 | 108 | 102/110 | 8 | 11.4 | 2.3/2.2% |
| 2 | 206 | 197/214 | 17 | 41.5 | 4.7/2.3% |
| 3 | 294 | 256/313 | 57 | 529.3 | 17.4/5.9% |
| 4 | 356 | 314/390 | 76 | 857.3 | 22.6/6.4% |

**Table 7.8:** Chloride analysis data from repeat inkjet deposition of 1M NaCl, 100% black greyscale, including variance and perceived error.

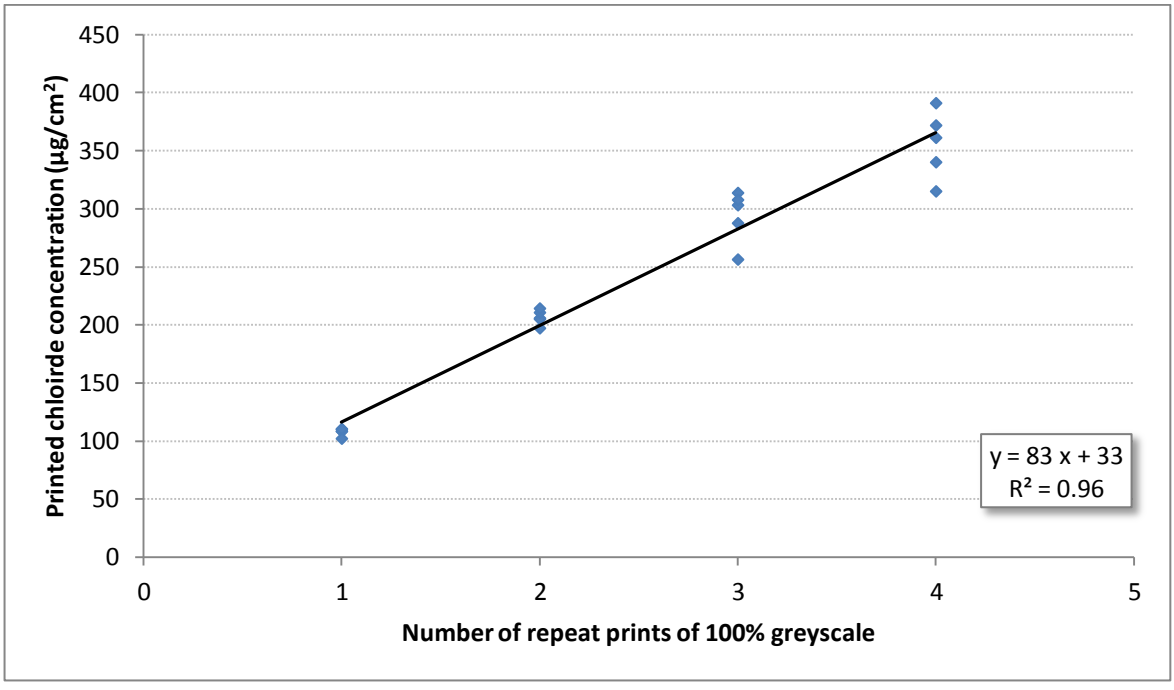


**Figure 7.3:** Graph of repeat printings of 100% greyscale onto a single CD against measured chloride contamination of CD surface, including trend line, suggested line equation and $R^2$ value of correlation.

Repeat printing of salt onto a surface gives strong linear correlation to recorded chloride content, but deviates from predicted values. Instead of increasing by the same factor as print number, the increase over each print is around 85μg/cm$^2$, with variance and error much increased. Error of individual chloride analyses stayed largely constant for repeat prints, indicating the error lies within the print method itself.

Optical observation indicate NaCl crystals are being detached and lost from the CD surface during the repeat prints and it is possible the act of printing onto a ready contaminated surface reduces the amount of solution deposited. This may be due the jerky movement of the printing process, contact between the CD surface and printer parts (the movement rollers, holding bar and printhead) or from existing salt crystals preventing deposition of additional solute. The high percentage and absolute error introduced will make it difficult to control chloride content through the use of repeat prints with the same accuracy as for a single print run. This effectively removed this method as an option for our methodology.

### 7.1.2d Image analysis of deposited chloride salts

Chloride deposition by inkjet printer was analysed by optical microscopy, the methodology for which is described in section 6.2.5. Deposited crystals were observed printed onto both metal foil and microscope slides. Samples were examined with respect to the distribution, size and consistency of deposited salt crystals, and the accuracy and limits of software designs against actual printed salt.

Initial printings were conducted using a print pattern of 2cm by 2cm squares. Observations illustrated uneven printings of salt crystals across the surface of both substrates (figure 7.4). Crystal size was inconsistent, with clear horizontal bands of closely-set elongated crystals between more dispersed evenly sized regions. These strips have been interpreted as cross over areas between lines of deposition (forming a region which is coated twice), caused by the different height of the inserted sample compared to that of a CD, creating a slight print head misalignment. The disparity in crystal size and the unevenness in deposition was unlikely to produce the even corrosion layer it has been hoped would coat the ERCM.

Improvements to the print methodology (detailed in section 6.2.2) created a deposition pattern of higher regularity and more even spread (figure 7.5). Crystal size was more regular, with smaller gaps between particles and without any noticeable regionalism. Slight bands of overlap can still be observed. It is hoped that the increased density of crystals between the bands will prevent preferential corrosion and decrease the effect of localised increases in chloride concentration.

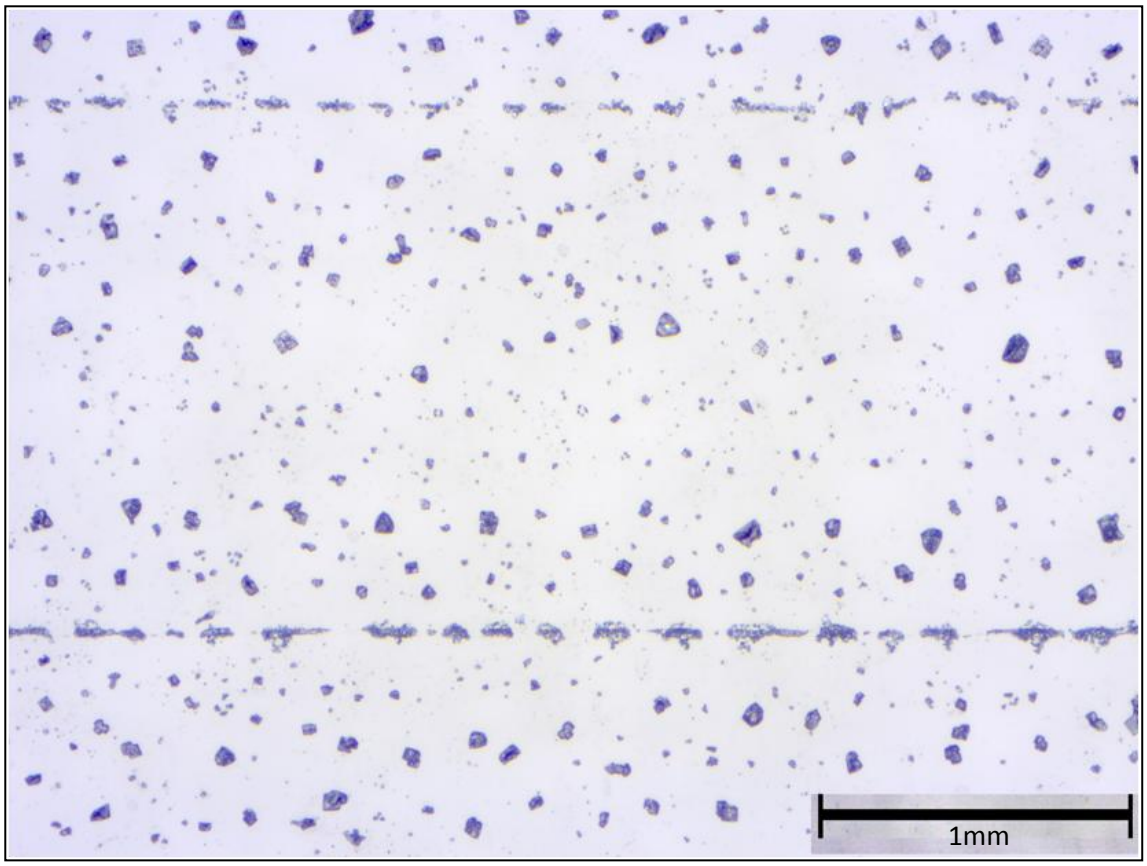


**Figure 7.4:** Optical microscope photograph of inkjet printer deposited NaCl crystals, deposited with 1M NaCl solution and without strict methodological steps

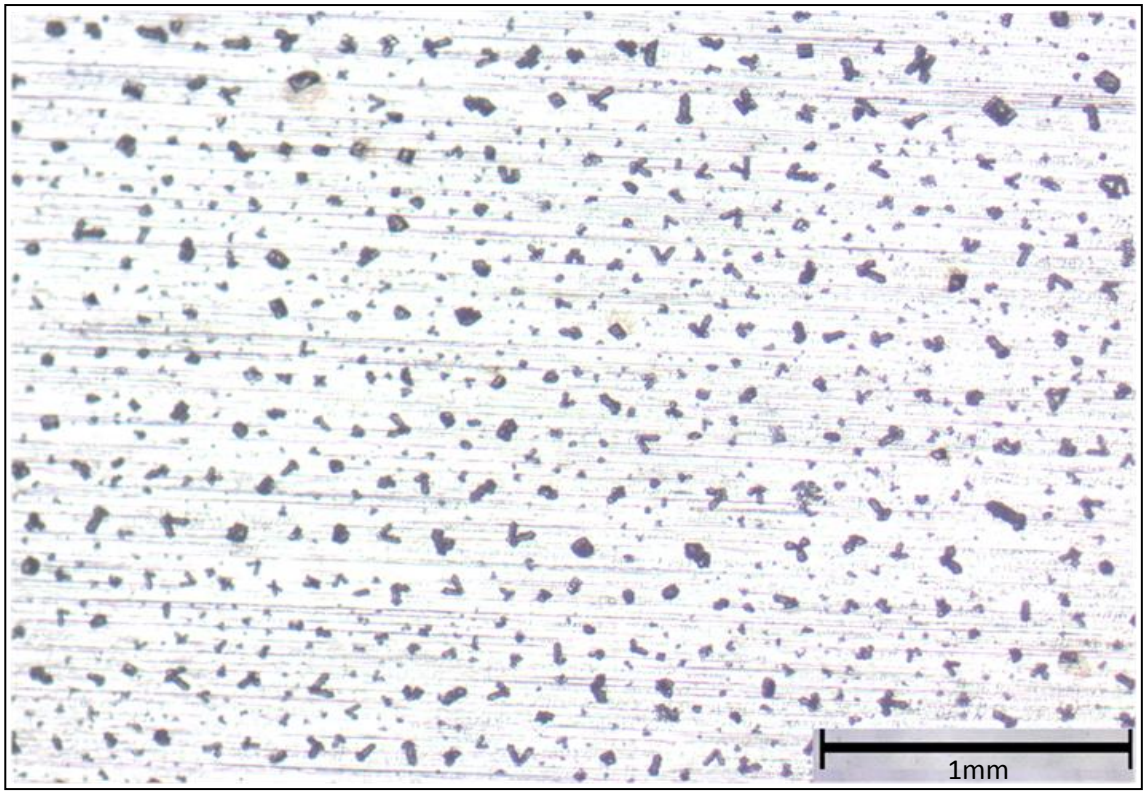


**Figure 7.5:** Optical microscope photograph of inkjet printer deposited NaCl crystals, deposited using the final printer methodology

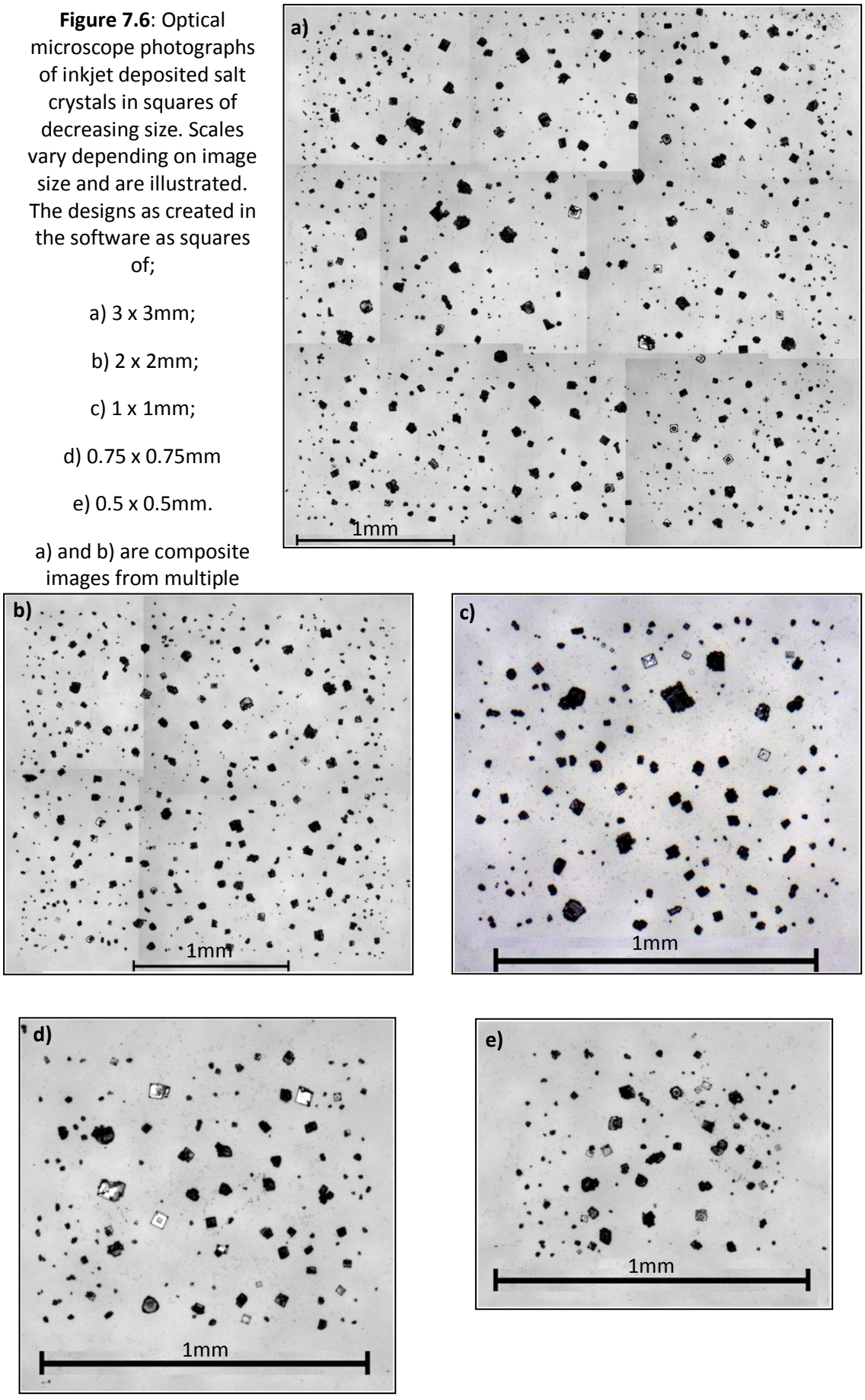


**Figure 7.6**: Optical microscope photographs of inkjet deposited salt crystals in squares of decreasing size. Scales vary depending on image size and are illustrated. The designs as created in the software as squares of;

a) 3 x 3mm;

b) 2 x 2mm;

c) 1 x 1mm;

d) 0.75 x 0.75mm

e) 0.5 x 0.5mm.

a) and b) are composite images from multiple

The finalised methodology was used to print out small square designs to assess the limits of the accuracy of the printed methodology. These were viewed to ascertain how small the

printing methodology could be made to deposit, prior to a loss of resolution. The results are presented here for comparative purposes, to allow understanding of the changes which occur at the boundaries of salt deposition and to allow validation of inkjet printing as a salt deposition method. Multiple samples were examined for each design. Example optical microscope images of squares of 3, 2, 1, 0.75 and 0.5 mm are displayed in figure 7.6.

The prints show good accuracy and adherence to the design specified within the software. The 3mm and 2mm squares (fig7.6a & b) showed clear and defined edges, made up of small crystals. The smaller squares have, as expected, lower resolution, caused by relative size of the crystals to pattern dimensions. Samples of 1mm square and below exhibited a rectangle shape, with an increased width compared to the input pattern. The error stays approximately constant at 0.2mm horizontal spread, more noticeable in the smaller squares, but detectable up to the largest. It is likely that this is caused by the print process, possibly due to the slight misalignment of print head from using non-standard samples. The error is small enough that it may be discounted for larger patterns, but must be taken into account when making precision, or very small, prints.

The distribution of the crystals in the smaller print designs differs from the larger prints (figure 7.6). The larger interiors contain more spread out, larger crystals, with more areas of high or low concentration, compared to the edges of the design, where crystal size is smaller and the pattern less diffuse. This may be due to the difference in drying times; faster evaporation of the solute creates smaller crystals. The central areas take longer to dry, leaving a solute of higher concentration, facilitating the growth of larger and more complex crystals. Clumping of droplets during the drying phase may also explain the disparity of deposition, creating crystals at the nexus of several droplets. This hypothesis is reinforced by the smaller discrepancy in the smaller squares (fig. 7.6c-e), for which drying of the whole design will be quicker, creating less disparity.

Optical micrographs were evaluated by Image-J software: Each picture was converted to a binary image and smoothed to prevent crystals registering as multiple particles. These were analysed to count, quantify and sort the individual crystals (table 7.9). Histograms of salt crystal feret diameter frequency from each design type are illustrated in figures 7.7-7.12.

| Sample and example figure | | Average Crystal count | Av. Crystal density ($mm^{-2}$) | Av. size of crystal ($\mu m^2$) | Salt surface coverage | Av. feret diameter (µm) | Feret Std. Dev. (µm) |
|---|---|---|---|---|---|---|---|
| **20 x 20 mm** | 7.5 | 1545 | 172 | 686 | 10.9% | 30 | 27.8 |
| **3 x 3 mm** | 7.6a | 1189 | 132 | 557.1 | 7.4% | 24.7 | 21.7 |
| **2 x 2 mm** | 7.6b | 597 | 149 | 572.9 | 8.6% | 26.6 | 20.8 |
| **1 x 1 mm** | 7.6c | 214 | 214 | 416.6 | 8.9% | 22.4 | 17.5 |
| **0.75x0.75mm** | 7.6d | 155 | 276 | 369.7 | 10.2% | 22.4 | 15.7 |
| **0.5 x 0.5 mm** | 7.6e | 120 | 480 | 349.9 | 16.8% | 20.9 | 15.4 |

**Table 7.9:** Image-j analysis of crystal count, size and coverage for multiple printed designs

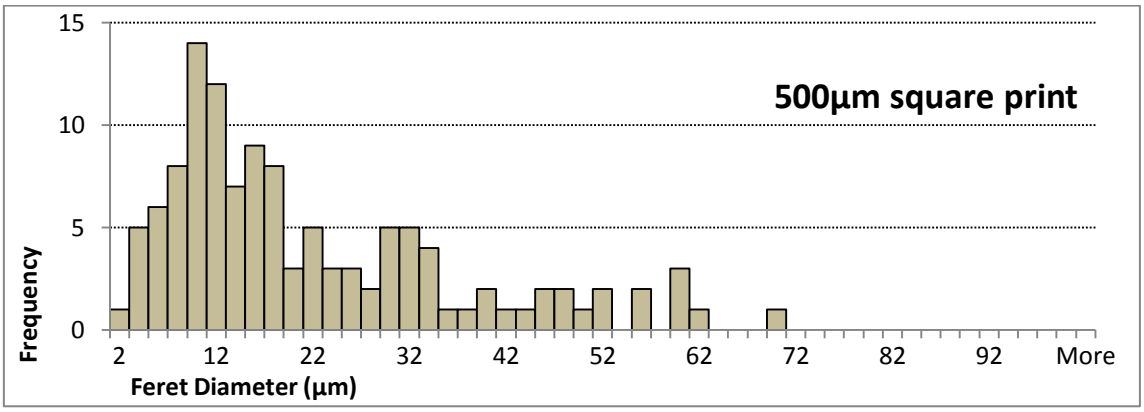


**Figure 7.7**: Histogram of average NaCl crystal feret diameter, in groupings of 2 µm, for print of 1M solution in 100% greyscale over a square of 500 µm by 500 µm (fig. 7.6e)

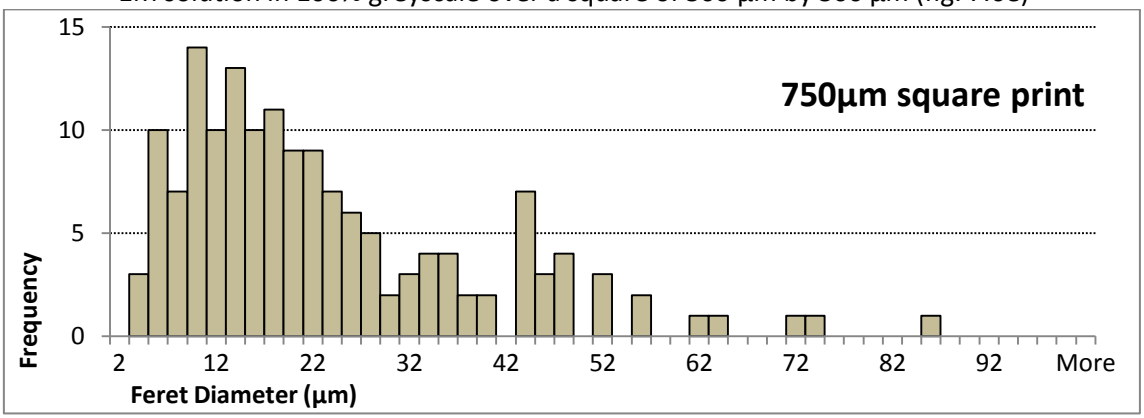


**Figure7.8:** Histogram of average NaCl crystal feret diameter, in groupings of 2 µm, for print of 1M solution in 100% greyscale over a square of 750 µm by 750 µm (fig. 7.6d)

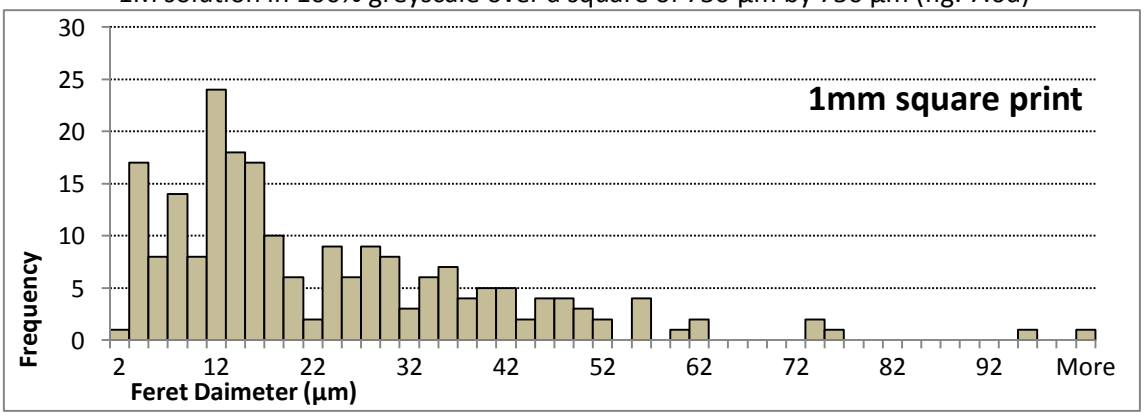


**Figure 7.9:** Histogram of average NaCl crystal feret diameter, in groupings of 2 µm, for print of 1M solution in 100% greyscale over a square of 1mm by 1mm (fig. 7.6c)

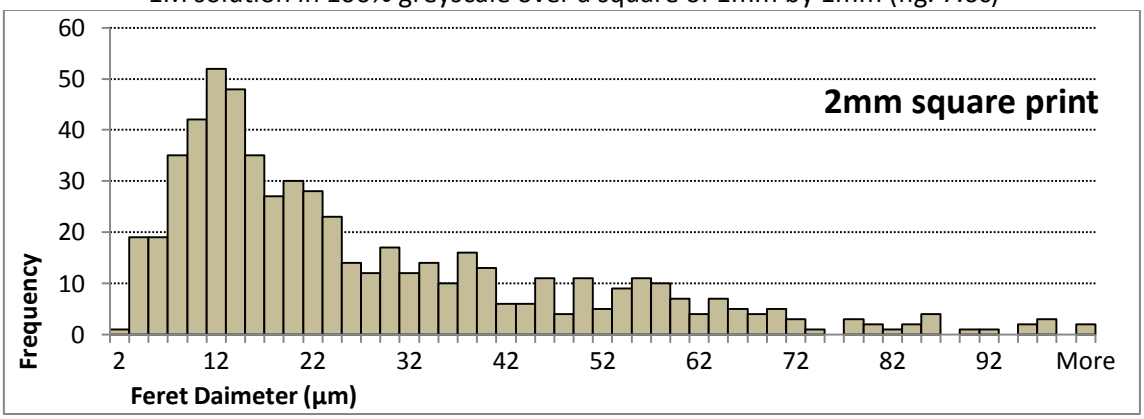


**Figure 7.10:** Histogram of average NaCl crystal feret diameter, in groupings of 2 µm, for print of 1M solution in 100% greyscale over a square of 2mm by 2mm (fig. 7.6b)

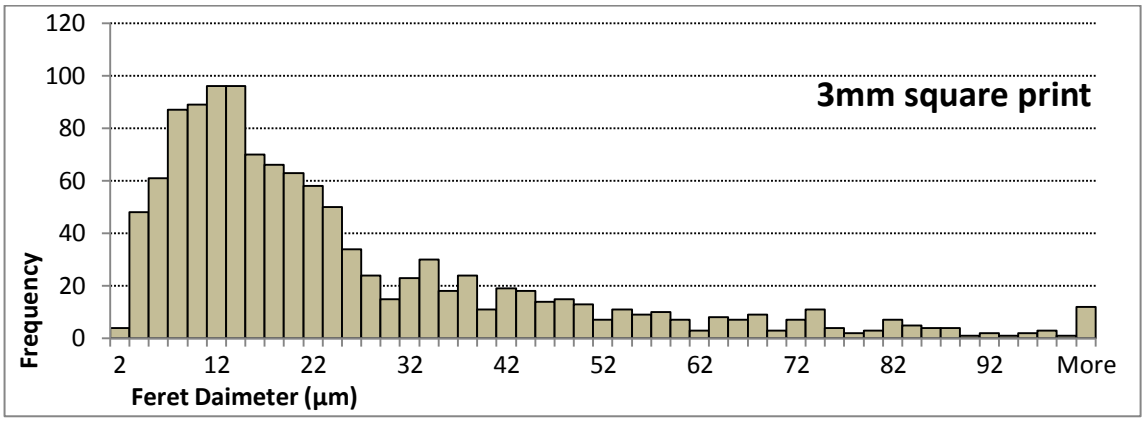


**Figure 7.11:** Histogram of average NaCl crystal feret diameter, in groupings of 2 µm, for print of 1M solution in 100% greyscale over a square of 3mm by 3mm (fig. 7.6a)

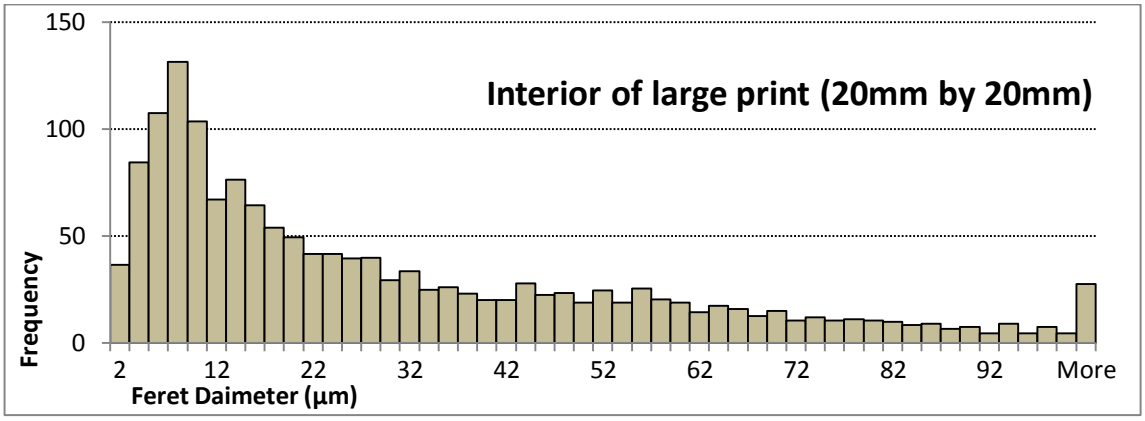


**Figure 7.12:** Histogram of average NaCl crystal feret diameter, in groupings of 2 µm, for selected interior pictures of a print of 1M solution in 100% greyscale over a pattern of 2cm by 2cm (fig 7.5)

The crystal count, size and density measurements confirm the observations from the optical micrographs: Larger prints have greater average crystal size and lower density in terms of crystals per square mm. Sum crystal area was used to calculate the total represented covered surface area, using the software specified dimensions to calculate percentage cover of salt crystals (expected to be fairly constant across sample sizes). These results show far greater covered surface areas for the smaller printed designs. This may partially attributed to the additional lateral deposition of around 0.2mm, noted in the optical microscope images and indicated by the higher crystal density. While analysis of the two-dimensional images may not be truly indicative of the total mass of deposited chloride, the results indicate that the printed design will have an effect on both density of chloride deposited and crystallography.

The samples representing the interior of a larger print (fig 7.5) exhibit higher density and surface coverage than may be expected from the trend of other results. This likely due to the change in crystal size and distribution observed at pattern edges, ignored within these samples.

All samples exhibited very large standard deviations around the mean, increasing (as expected) with sample size. Histograms 7.7-12 illustrate the spread of crystal sizes more effectively. All samples exhibit a single modal peak, centred between 8 and 16µm. For the

print designs up to 1mm$^2$, there are negligible crystals with a feret diameter above 60μm. Larger prints have an increased maximum crystal size and average feret diameter; the higher average feret diameters of these samples, shown to be caused by an increase in crystals above 50μm. These are distributed with even frequency up to 100μm, with no demonstrable shift in the modal peak. The smallest detected feret diameter was 1.6μm, constant across multiple samples and likely to be indicating the limits of detection of the optical microscopy/image-j methodology.

Comparison between the generated results and previous published research of inkjet deposition of chloride salts, by Schindelholz and Kelly [3] and Mi et al. [4], reveals both similarities and disparities, discussed in section 8.1.

## 7.2 Results of Pre-corrosion Methodology

Corrosion of pre-contaminated iron foils were conducted in set environments to ascertain optimum chloride contamination level, create a pre-corrosion methodology and examine the results of that methodology, as described in section 6.3. Corrosion products were observed optically and by scanning electron microscope and analysed by X-ray diffraction.

### 7.2.1 Microscope photographs of salt deliquescence and initial corrosion

Initial deliquescence of salts was observed. Results are reported to illustrate the mechanism of initial salt spread and corrosion, as an examination of how our deposition method might influence final corrosion product structure. Iron foil was contaminated using standard methodology at 100% greyscale, over a 2cm by 2cm square. The print was placed in the high RH environment for 5 minutes. Foil was removed and immediately observed by optical microscope (fig. 7.13) to identify droplet deliquescence and corrosion around salt crystals

Crystals were largely dried out in the process of transport to, and setup of, the microscope. Initial low magnification observations showed increased rounding of the crystal edges from adsorbed water, though no obvious droplets. Observed brown staining has been interpreted as corrosion product, arranged exclusively around salt crystals. Stained areas and salt crystal spread show evidence for dried droplets (fig 7.13a). Not all crystals show evidence of either.

Crystals and their surrounding stains were observed at x1000 magnification (fig 7.13b-e). Stains ranged from slight (fig. 7.13b), though to pronounced brown discolouration (fig 7.13c) up to around 40μm diameter (fig 7.13d-e). All form a rounded shape, often with darker colouration along the periphery, centred on crystals. This is strong evidence for deliquesced droplets, creating a typical ‘coffee stain’ penumbra of increased corrosion product deposition

at the air/solute interface [5]. Within these droplet bounds, re-deposited crystals are observed. Crystal structure is unclear at this magnification.

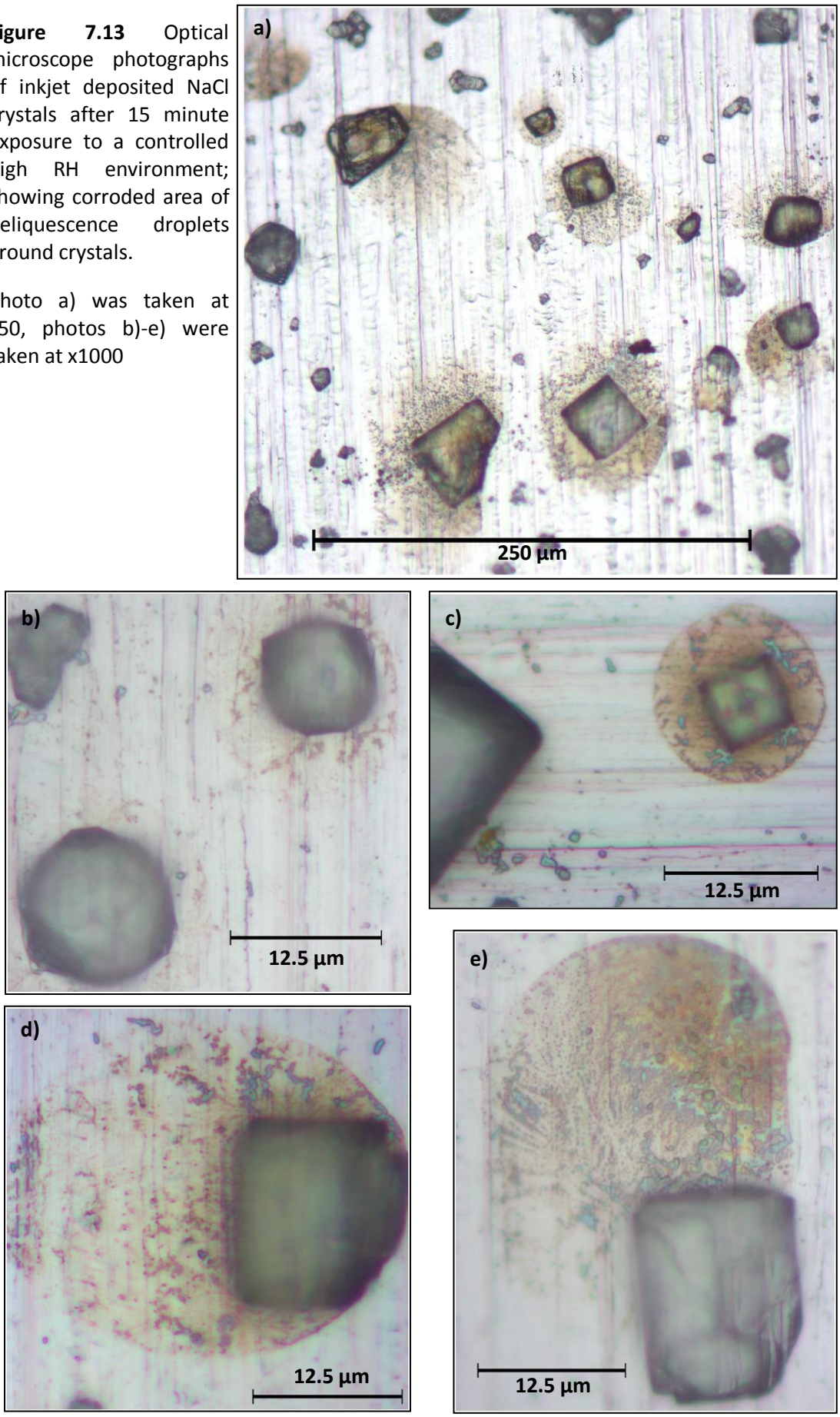


**Figure 7.13** Optical microscope photographs of inkjet deposited NaCl crystals after 15 minute exposure to a controlled high RH environment; showing corroded area of deliquescence droplets around crystals.

Photo a) was taken at x50, photos b)-e) were taken at x1000

The results indicate wetting and drying of the salt. Relative humidity above the deliquescence point causes adsorption of water to the salt surface, leading to droplet formation. Corrosion is localised to the droplets. Upon removal to a lower relative humidity environment, droplets evaporated, depositing corrosion products and re-depositing NaCl crystals within the droplet footprint. Droplet volume and speed of formation and evaporation depends on the morphology and characteristics of individual crystals, varying time of wetness and solute concentration (and therefore levels of corrosion observed). Salt re-deposition appears to be more concentrated at the droplet penumbra, creating an effective 'spread' of the salt laterally across the metal surface. The corrosion resembles several forms of salt deposition; through wet aerosol in a marine environment [6], by deliquescence of manually placed salt crystals [7] and mechanical wet aerosol deposition [8].

Similarity to other methods suggests similar continued corrosion and re-deposition of NaCl during additional wet-dry atmospheric cycling. Reintroduction to the high relative humidity environment will cause formation of droplets around the crystals. Continued salt spread will lead to a more continuous electrolyte layer. Series of wet-dry cycles should therefore be sufficient to create an even spread of smaller crystals and fairly homogenous corrosion across the surface area.

The process suggests inkjet deposition of NaCl crystals to create corrosion layers of even thickness will be best achieved with immediate exposure to a high relative humidity environment, to prevent localised salt concentrations and corrosion. This methodology was also suggested by Mi et al. [4] for consistent corrosion over small areas. The crystal spread will have the effect of altering the deposited area from original software dimension specifications. From initial observations, the spread will not exceed 100μm. Optical micrographs of more corroded foils were not revealing of the form and state of NaCl.

### 7.2.2 Optical records of corrosion

Foils were contaminated by Inkjet printer and placed within the corroding environments, as described in section 6.3.2. Optical records were kept of corrosion progress using the methodology outlined in section 6.3.3a. Variables examined included varying the time and combination of exposure to the two environments, altering levels of greyscale and using repeat printings. All tests were carried out at 30°C.

#### 7.2.2a Set Relative humidity environments

Initial tests placed 100% greyscale prints into either the potassium chloride controlled high (84%) humidity environment or the magnesium chloride controlled low (33%) humidity

environment. Within the low RH environment, corrosion products were clearly noted after 24 hours exposure; yellow-brown and limited to the salt contaminated area (figure 7.14). Darker brown corrosion products developed after 3 days to cover the remainder of the contaminated region, plus additional spread. The colours suggest initial deposition of goethite and lepidocrocite, with akaganeite and lepidocrocite in the darker patches. Within the high humidity environment, corrosion completely covers the contaminated area in thick, dark brown to black product after 24 hours (figure 7.15). After 2 days, the corrosion is apparent exterior to the printed pattern and corrosion patches could be observed on the protected, lacquer-covered reverse. The colour suggests magnetite deposition, possibly obscuring other corrosion products. Corrosion reaching the reverse is taken as evidence for pitting and localised corrosion extending through the entire foil thickness.

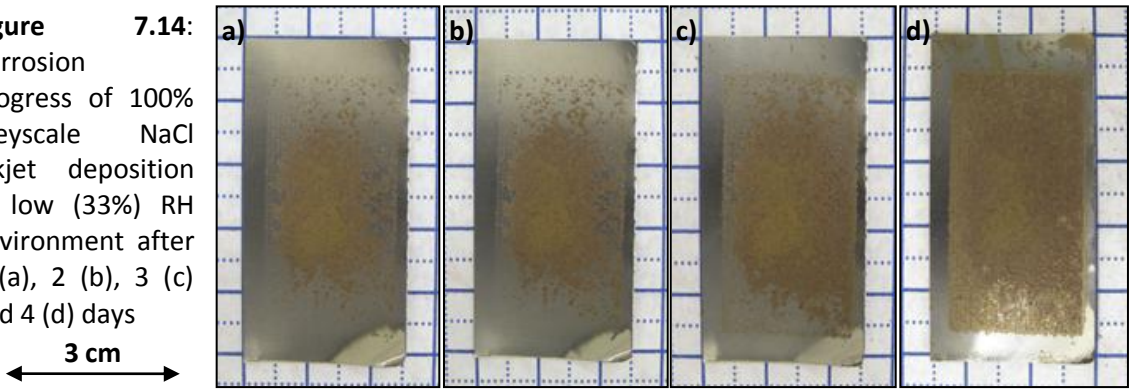


**Figure 7.14**: Corrosion progress of 100% greyscale NaCl inkjet deposition in low (33%) RH environment after 1 (a), 2 (b), 3 (c) and 4 (d) days

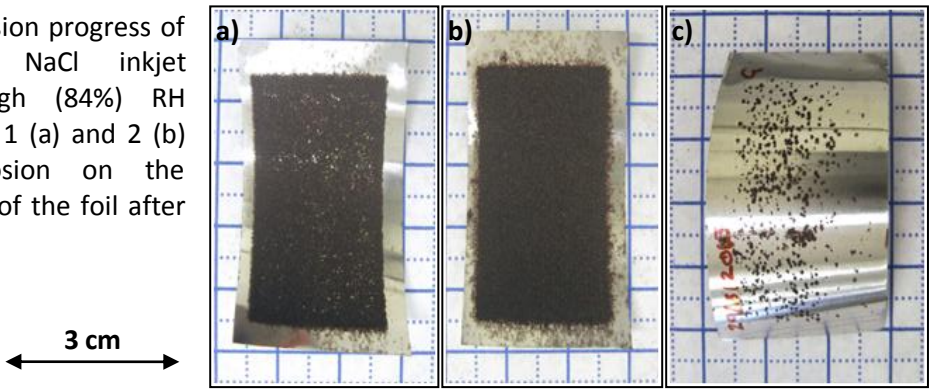


**Figure 7.15**: Corrosion progress of 100% greyscale NaCl inkjet deposition in high (84%) RH environment after 1 (a) and 2 (b) days, and corrosion on the lacquered reverse of the foil after 2 days

The results illustrate the effect of varied contamination, causing selective initial corrosion on the iron surface. Measurements at the macro scale showed no appreciable spread or distortion of corrosion area against the specified dimensions. Over time, additional corrosion outside the pattern occurs, either through salt and corrosion product spread or through external pollutants or dust. Inkjet deposition of chloride creates (initially) apparently homogenous corrosion layers, especially when corroded in low humidity environment.

Alternating cycles of high and low humidity were applied to maintain the homogeneity of the low humidity environment while accommodating the larger variety of corrosion products

provided by the higher humidity environment. These were designed to simulate the traditional wet/dry model of atmospheric corrosion and avoid localised corrosion.

7.2.2b Alternating environments

A single print of 100% greyscale NaCl solution was deposited on iron foil and subjected to alternating wet and dry conditions as described in section 6.4.1: 6 hours in the high RH environment followed by 18 hours in the low RH environment for each repetition.

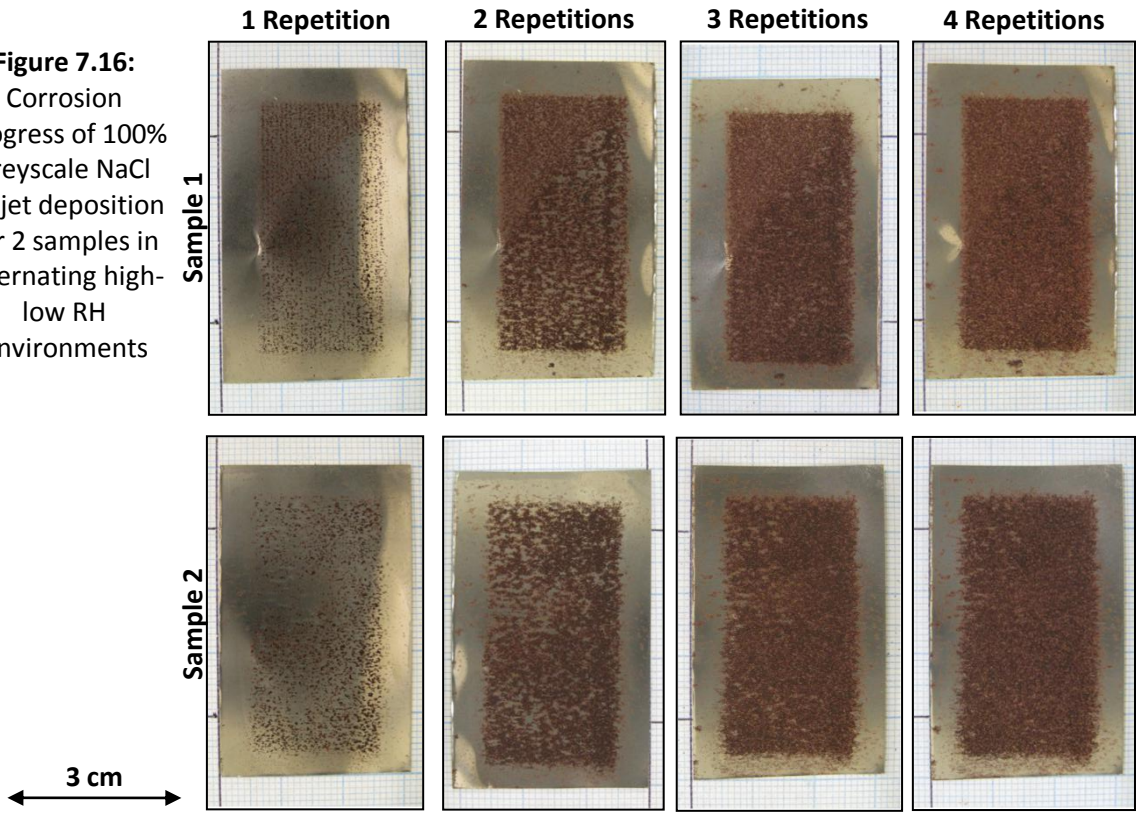


**Figure 7.16:** Corrosion progress of 100% greyscale NaCl inkjet deposition for 2 samples in alternating high-low RH environments

Corrosion stays within the bounds for the contaminated area, in common with the single environment procedures (figure 7.16). Initial corrosion appears more localised, without the continuous patches observed in figure 7.14. Further repetitions cause the smaller areas to spread and join, forming a continuous layer of corrosion product after four repetitions. Initial depositions resemble brown nuclei surrounded by yellow coloured scale, possibly indicating akaganeite or lepidocrocite deposits surrounded by goethite scale. The dark reddish brown colouration of the longer corroded samples indicates akaganeite as a primary corrosion product. Additional small patches of black can be observed, indicating possible areas of haematite or magnetite. Further analysis of the products was performed by compositional analysis, reported in section 7.2.4.

The corrosion product continuity and spread were deemed adequate for use on ERCM. No corrosion was observed on the reverse. Further analysis by SEM was used to check the corrosion depth, reported in section 7.2.3.

### 7.2.2c Corrosion of greyscale and repeat printing inkjet deposition

Corrosion of foils contaminated with greyscale levels below 100% and using repeat printings were carried out and corroded, to establish the effect changes in chloride level had on corrosive action. The results are reported here to illustrate alternative levels of deposition for further ERCM creation and corrosion testing.

It is clear that lower chloride levels, represented by lower greyscale percentages, create less visible corrosion (figure 7.17). 50% greyscale prints created widely spaced corrosion scale after a single repetition, increasing in spread over subsequent repetitions but without ever forming a coherent layer across the foil surface. From 60% to 80% greyscale prints, visible corrosion after a single repetition covered greater surface area than 100% greyscale prints. For subsequent repetitions, rate of spread is reduced; corrosion products remained discontinuous, with visible un-corroded regions within the salt pattern. At 90% greyscale, there is little difference to 100% greyscale, with somewhat less corrosion after a single repetition but a full coverage of corrosion products after four. Total corrosion coverage after four repetitions increased with printed greyscale intensity. Pattern fidelity remains high, with little corrosion outside the contaminated area. Certain samples exhibit patches of additional corrosion, possibly due to additional introduced pollutants during the printing or corrosion methodologies. Corrosion product colour indicates similar constituents to 100% greyscale prints; akaganeite and lepidocrocite with flecks of yellow goethite in the initial stages. Black haematite or magnetite is only noted in small flecks in the 90% samples, and around localised corrosion from additional pollutants.

In repeat prints of 100% greyscale corroded under identical repeat conditions (figure 7.18) samples showed less predictable levels of corrosion, particularly for those contaminated with 5 depositions. Corrosion coverage after one repetition for 2 to 4 repeat prints are noticeably higher than for any of the single print patterns; increasing with repeat prints. Samples covered with 4 repeat prints gave almost complete coverage of the pattern after a single repetition. The corrosion products are of similar form and colour to corrosion of 100% greyscale, with the addition of dark brown or black coloured flecks, interpreted as magnetite or haematite, at the centre of the product patches. Additional repetitions caused corrosion spread across the foil surface. The corrosion products are noticeably darker and thicker than lower concentration salt prints, with higher levels of black flecking. The concentration of yellowish product, assumed to be goethite, is noticeably lower or non-existent for all samples.

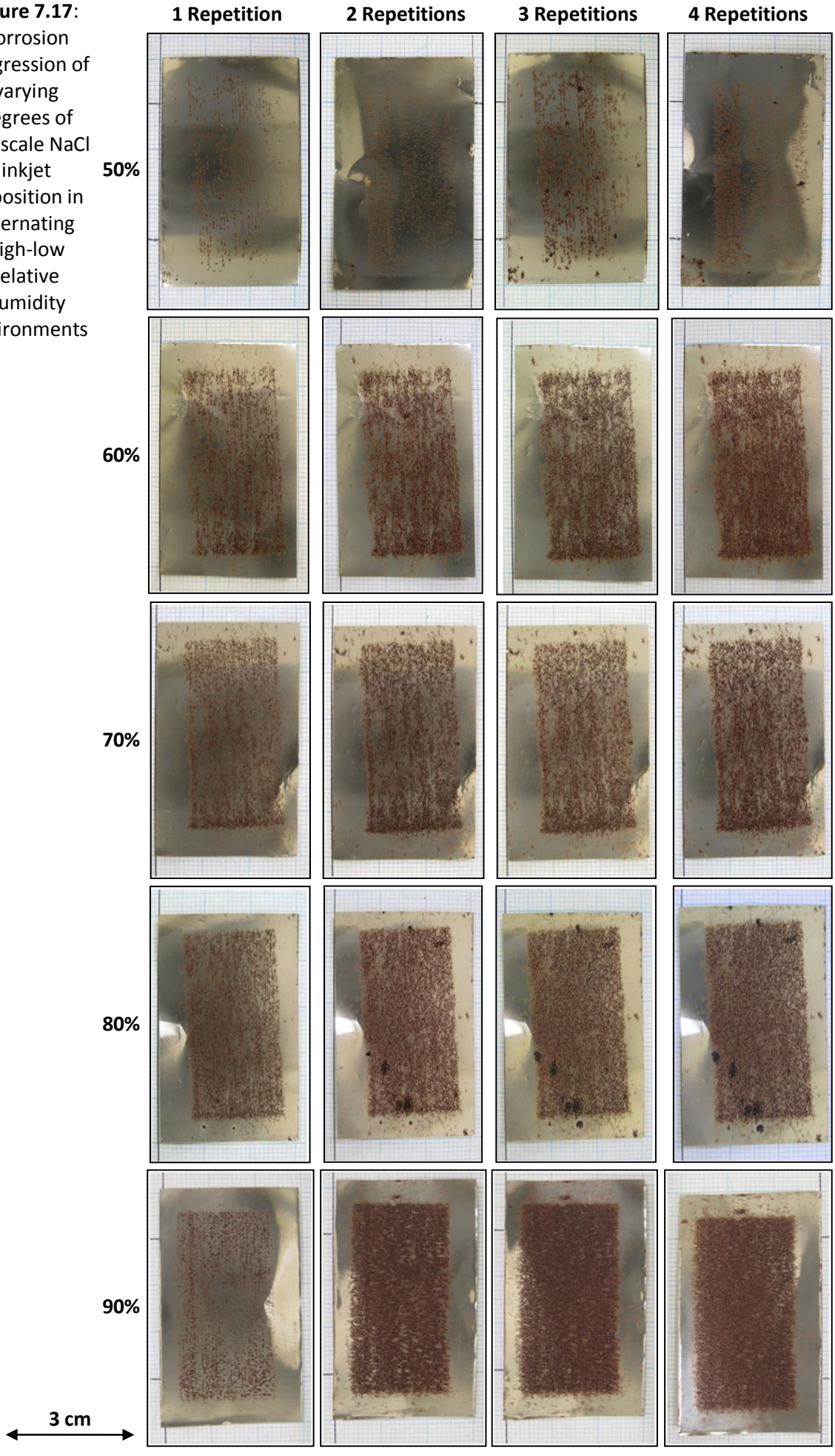


**Figure 7.17**: Corrosion progression of varying degrees of greyscale NaCl inkjet deposition in alternating high-low relative humidity environments

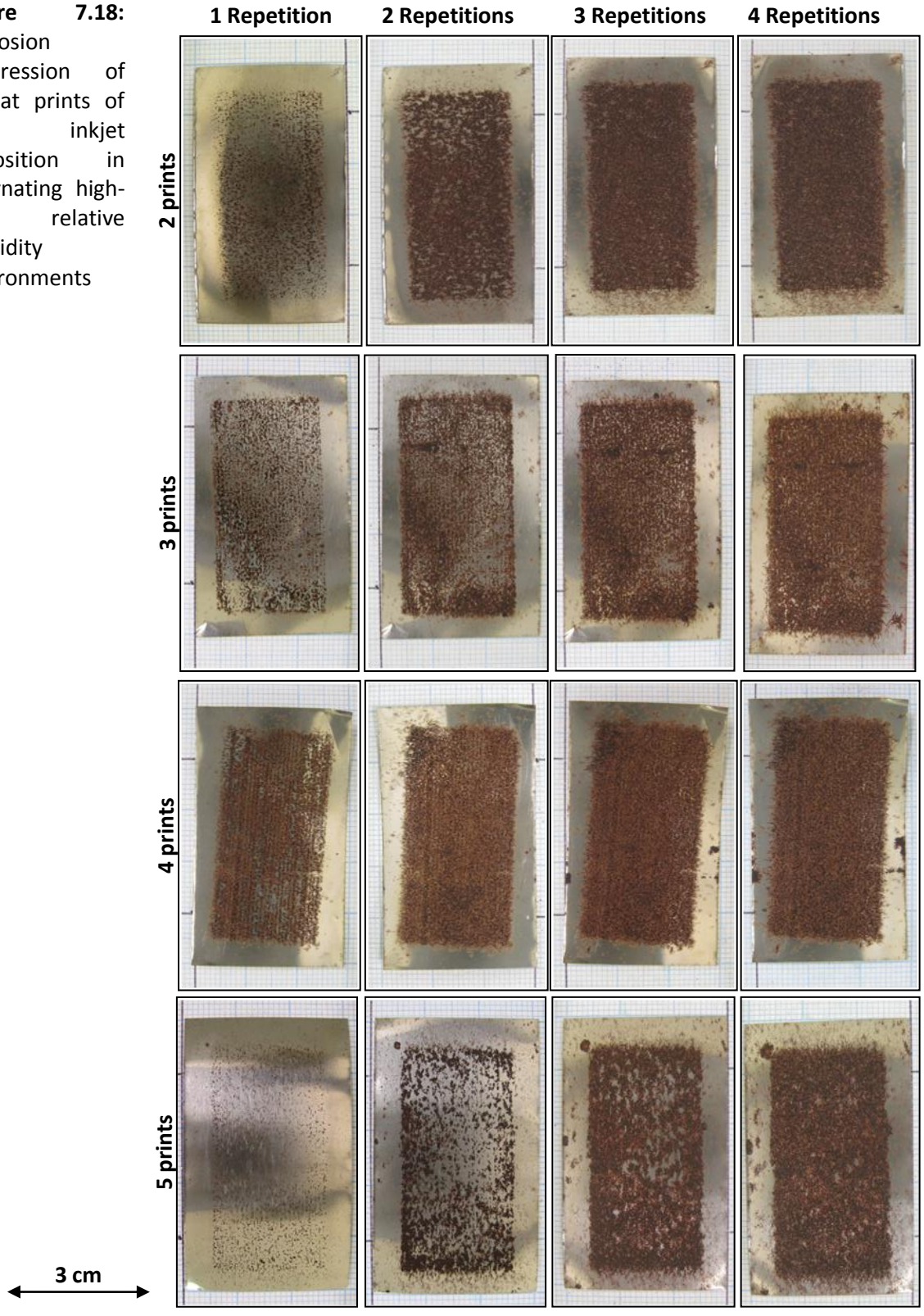


**Figure 7.18:** Corrosion progression of repeat prints of NaCl inkjet deposition in alternating high-low relative humidity environments

Corrosion is largely concentrated within the contaminated pattern, though pattern fidelity is decreased and there are more patches of additional corrosion. Lower pattern definition may be due to slight discrepancies in alignment for each print run, combined with additional spread caused by the inkjet stream encountering extant salt crystals at the metal surface. The additionally pronounced corrosion exterior to the pattern is increased evidence for extraneous salt (or other pollutant) deposition during the printing process. Small patches of corrosion are found scattered around obvious nuclei, similarly to single print runs.

Additional light corrosion is also observed in many samples, localised between the pattern and the foil edge at one end of the foil. This is interpreted as streaking: Salt dragged outside the design by the action of the print head. Closer inspection of single prints indicated that the effect may also be present with this methodology, though the effect is too small to be conclusive. ERCM contamination methodology was therefore altered to orient the sensor to prevent this effect; any streaking would drag salt away from the rest of the sensor. It is possible that this effect explains some of the loss of expected chloride concentration discussed in section 7.2.1e. It is not thought that the effect will noticeably affect chloride concentration calculations on single print runs.

The samples contaminated with 5 repeat inkjet depositions exhibited different features than other repeat samples. After one repetition, very little visible corrosion could be identified. After another repetition, sporadic and very dark corrosion product could be observed in patches across the contaminated regions, but with no consistent scale formation. It takes until 4 repetitions for a consistent corrosion layer to completely cover the contaminated area. The effect is similar to that observed by Schindelholz and Kelly; higher contaminations of chloride caused lower levels of visible corrosion [3]. However, the levels of chloride for our repeat prints were previously measured to be at least four times higher than the highest levels for that study, making comparison difficult. It is possible that the decrease in relative level of visible corrosion products is not indicative of less corrosion damage. In common with the single prints exposed exclusively to the high relative humidity environment, multiple printed samples showed evidence of corrosion reaching to the reverse of the foil (figure 7.19). Two repeat print designs did not show this effect, but from 3 repeat prints and above, all samples showed some corrosion reaching the protected reverse. This effect was most pronounced for the higher repetition prints, with clear corrosion forming and spreading across the reverse of x4 and x5 prints. This ruled out the repeat prints for use in contamination our ERCM and indicates higher vertical corrosion, despite surface coverage appearing reduced at x5. This may explain the results; higher corrosion levels cause significant localised corrosion, forming deep pitting corrosion at the expense of visible lateral corrosion


**Figure 7.19**: Reverse, lacquered side of iron foils, corroded in alternating conditions for 4 repetitions, contaminated by repeat inkjet contamination with NaCl: a) 2 printings; b) 4 printings; and c) 5 printings

Further research is required to elucidate change in corrosion behaviour at very high chloride deposition levels. It may be that high chloride levels create a solid/liquid system at the foil

surface from the saturated surface electrolyte, preventing corrosion product formation and retarding corrosion rate. The unpredictability of repeat prints and obvious pitting corrosion ruled the technique out for use within the ERCM pre-corrosion methodology.

The results have illustrated the potential of inkjet printing in salt loading for corrosion testing, reinforcing the benefits discussed in section 7.1.2e. Changes in printed intensity and the use of repeat prints have been clearly demonstrated to affect levels and behaviours of subsequent corrosion. As discussed in section 7.1.2e, contamination of ERCM was by a single print from 1M NaCl solution by inkjet printer. The results of the visual observations informed our decision to use 100% greyscale prints for the final methodology. The consistency of coverage after only a couple of wet/dry repetitions was high, mimicking the condition of heritage iron. Optical observation indicates a large number of different corrosion products, while depositing the maximum level of chloride under our methodology. The measured level of chloride also corresponds to the 0.1mg/cm$^2$ level, previously utilised by Kapatou and Lyon [9] and shown to be effective for creating pre-corroded ERCM. Alternating environments were shown as effective for creating corrosion products with low chance of pitting attack. Further examination under SEM, XRD and Raman spectroscopy was conducted to confirm the suitability of the methodology.

### 7.2.3 Examination of corroded foil cross sections by scanning electron microscope

To ascertain thickness consumption of metallic iron and the consistency and physicality of solid corrosion products by our chosen pre-corrosion methodology, iron foil samples were prepared with a single 100% greyscale print and corroded using the alternating conditions set out above. Uncontaminated foil was also subjected to the conditions to provide a comparison. Scanning electron microscopy was used to examine cross sections of the corroded samples, using the methodology laid out in section 6.3.3b. Back scattered electron detection was utilised, to identify, delimit and compare materials of different atomic makeup.

#### 7.2.3a Control: Uncontaminated iron foil after 4 repetitions

The lack of visible corrosion products or phenomena exterior to the contaminated area of the foil observed in section 7.2.2, inferred that little corrosion occurred on clean foil under the chosen conditions and within the chosen timeframe. This is reinforced by examination of the cross section of the uncontaminated samples (figure 7.20) at magnifications up to x4000. No distinct solid corrosion product was observed on the corroding (upper) or reverse surface. Figure 7.20a illustrates the homogeneity of the sample, with greater detail provided by 7.20b and c.

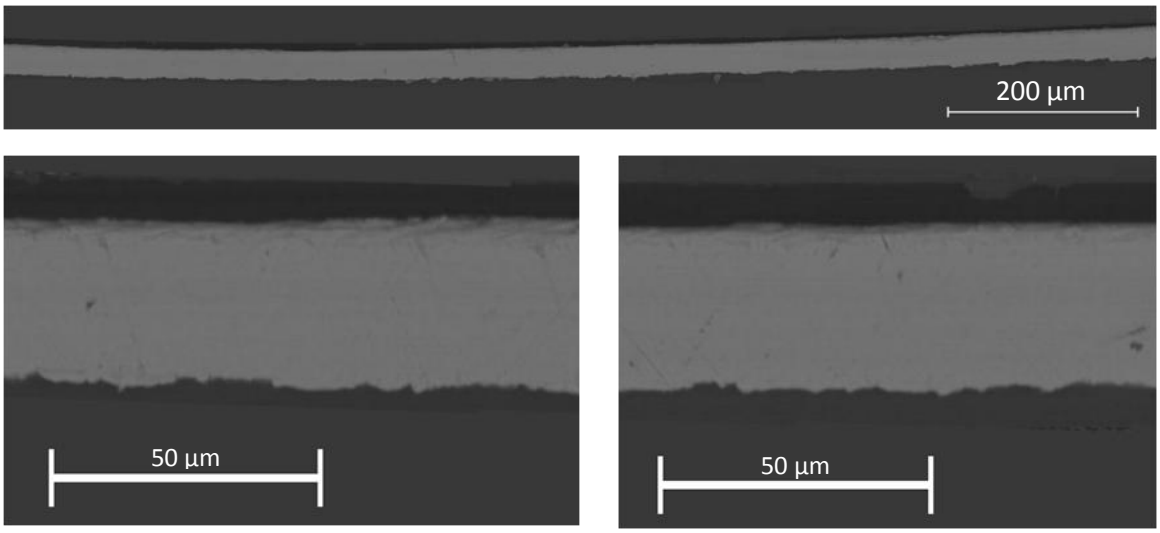


**Figure 7.20**: Scanning electron micrographs of uncontaminated iron foil, subjected to 4 repetitions of high and low relative humidity conditions

It is unlikely that the profile above is representative of the state of the unprocessed foil. It had been hoped that warping of the foil during grinding and polishing would be minimised through the described methodological steps, but the roughness of the foil surface, observed on the lower edge of figure 7.20, is characteristic of this. This reduces confidence in measuring the overall thickness of the uncontaminated metal foil and explains why the typical thickness measurement is around 26µm, 1 µm greater than expected. Introduced error appears to be constant along the length of the foil. This warping would not be expected to affect any corrosion products, with their lower malleability.

Likewise, the darker grey region of the metallic iron along the top edge of the foil in fig 7.20 is not a change in atomic make-up, but an aberration, caused by the rough surface and the aforementioned warping of the exposed foil. This was confirmed by examination of the region using secondary electron scans, showing the detailed topography of the surface and removing the image of any metal beneath the epoxy.

The darker regions within the epoxy resin and surrounding the foil are the layers of resin applied prior to the main batch, as detailed in section 6.3.3b.

### 7.2.3b Multiple repetition corrosion of contaminated foil

Pre-corroded iron foil was examined after 1, 2, 3 and 4 repetitions of the wet/dry cycle, similar to those reported in 7.2.2b. The repeated micrographs were formatted into a single, composite high resolution image along a length of cross section. In all cases, corrosion products were observed optically on the surface prior to preparation of the samples.

All examined foil cross sections showed extant corrosion products on the pre-corroded surface, without significant pitting corrosion and maintained integrity of the metallic iron foil

along the entire examined length (fig. 7.21). Metal thickness loss was observed to a greater or lesser extent, with areas of thicker corrosion product largely correlating to areas of greater thickness metal loss.

In places, the corrosion layer was detached (7.21b, c & d), forming empty voids between the metal surface and the corrosion product. It is clear that this is generally a result of the preparation methodology, either during application of the epoxy resin to the corroded surface, or during grinding of the sample: It is not indicative of voids in the original corrosion layers. It is not clear whether any of the smaller voids are inherent, possibly as evidence of droplet formation or the disappearance of a soluble species within the corrosion layers.

Features associated with warping of the foil during the preparation methodology, similar to those observed on un-corroded foil (detailed above), are seen along the uncontaminated surface. It is unknown whether the presence of corrosion layers altered the amount or form of the warping effect, on either surface. The error is judged fairly uniform and relatively small. Measurements and observation of the foil were therefore made ignoring this effect, except in those situations in which it was a clear factor.

After 1 repetition of the wet dry cycle the cross section showed clear, but sporadic, corrosion products across the contaminated surface (fig7.21a), though the majority of the surface remained largely unchanged. Where observed, corrosion products are typically found above areas of localised corrosion, manifested as small hollows in the extant foil (fig 7.22) of approximately 5 to 6 μm in depth, with a similar volume of corrosion product filling and overlying them. The longest continuous extent of stretched 210 μm. A single highly localised area of corrosion was identified where foil thickness was reduced to 8 μm, and associated corrosion product reached 40 μm. However, the majority of the surface showed little or no corrosion product at magnifications of up to x10, 000.

Corrosion product form appears uniform. Crystals were identified in a single feature (7.22a) forming what has been interpreted as a 'dome' of product [10]. The increased size of this feature compared to the amount of metal loss may indicate that these are akaganeite crystals (the most voluminous of our expected corrosion products) [11]. In the majority, only amorphous structures can be identified, with small pores and cracks running laterally from the metal surface.

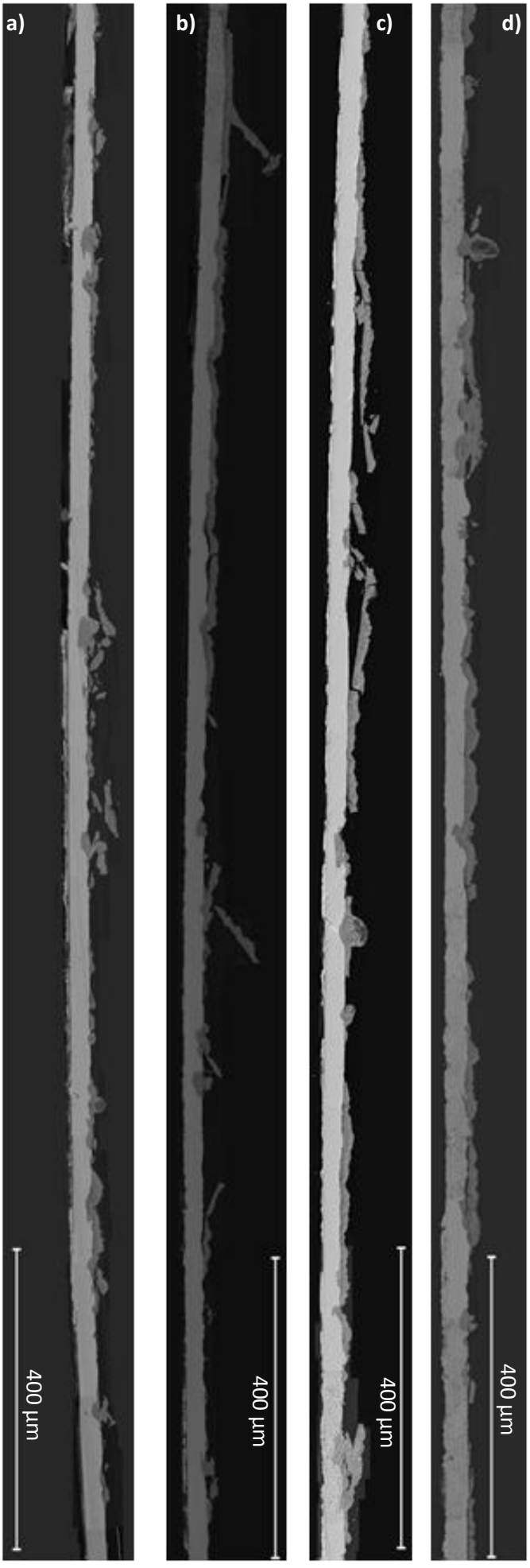


**Figure 7.21**: Combined Scanning electron micrographs of iron foil cross section after application of pre-corrosion methodology. Corroded surfaces are shown on the right. Foils shown were pre-corroded for;

a) 1 repetition

b) 2 repetitions

c) 3 repetitions

d) 4 repetitions

of the pre-corrosion methodology, using a contamination of 100% greyscale.

| Wet/Dry repetitions | Minimum thickness of remnant iron foil (µm) | Typical thickness of remnant iron foil (µm) | Maximum corrosion product thickness (µm) | Typical thickness of uniform corrosion layer (µm) |
|---|---|---|---|---|
| 1 | 8 | 24-25 | 40 | n/a |
| 2 | 7 | 22-23 | 36 | 6-10 |
| 3 | 12 | 22-23 | 35 | 5-13 |
| 4 | 5 | 21-23 | 45 | 10-15 |

**Table 7.10**: Summary table of observed dimensions of scanning electron micrographs of iron foil cross sections, corroded for 1-4 cycles of the wet/dry methodology, pictured in fig 7.21

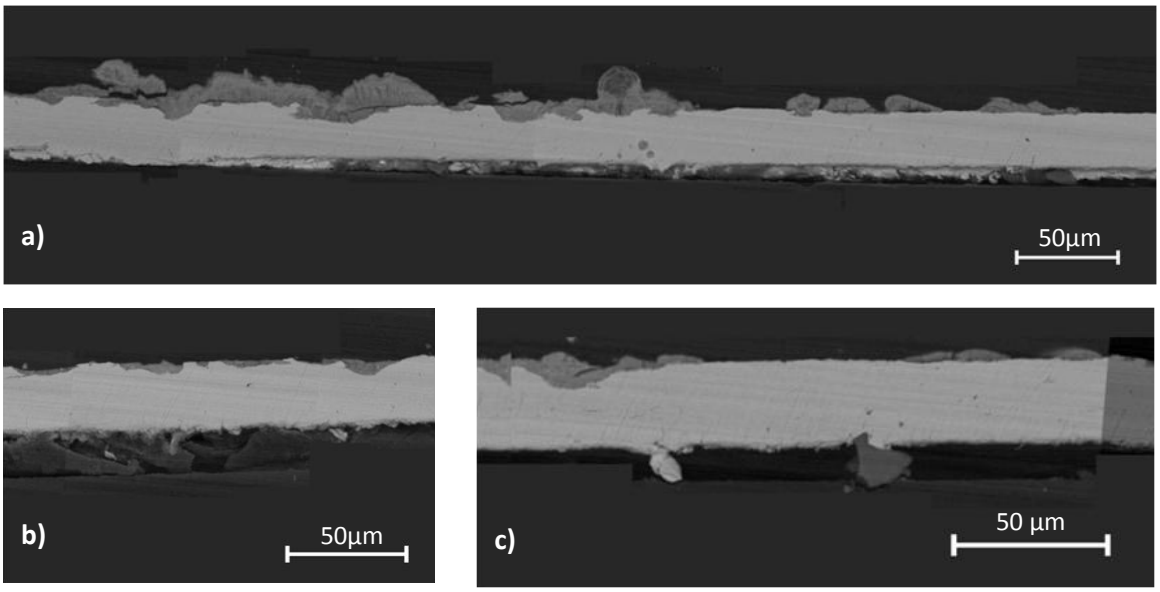


**Figure 7.22**: Scanning electron micrographs of iron foil contaminated with 100% greyscale print of 1M NaCl, subjected to 1 repetition of high and low relative humidity conditions

The deformation of the foil on this sample is clear on the reverse, along with occasional unidentified non-metallic features. These have not been identified as corrosion products. Their lack of associated metal loss and difference in shade (indicating a different atomic weight) from deformed corrosion products on the obverse, make it more likely they are dust or other introduced particulate pollutants. Both these phenomena were also observed on the 2 repetition (though not subsequent) samples.

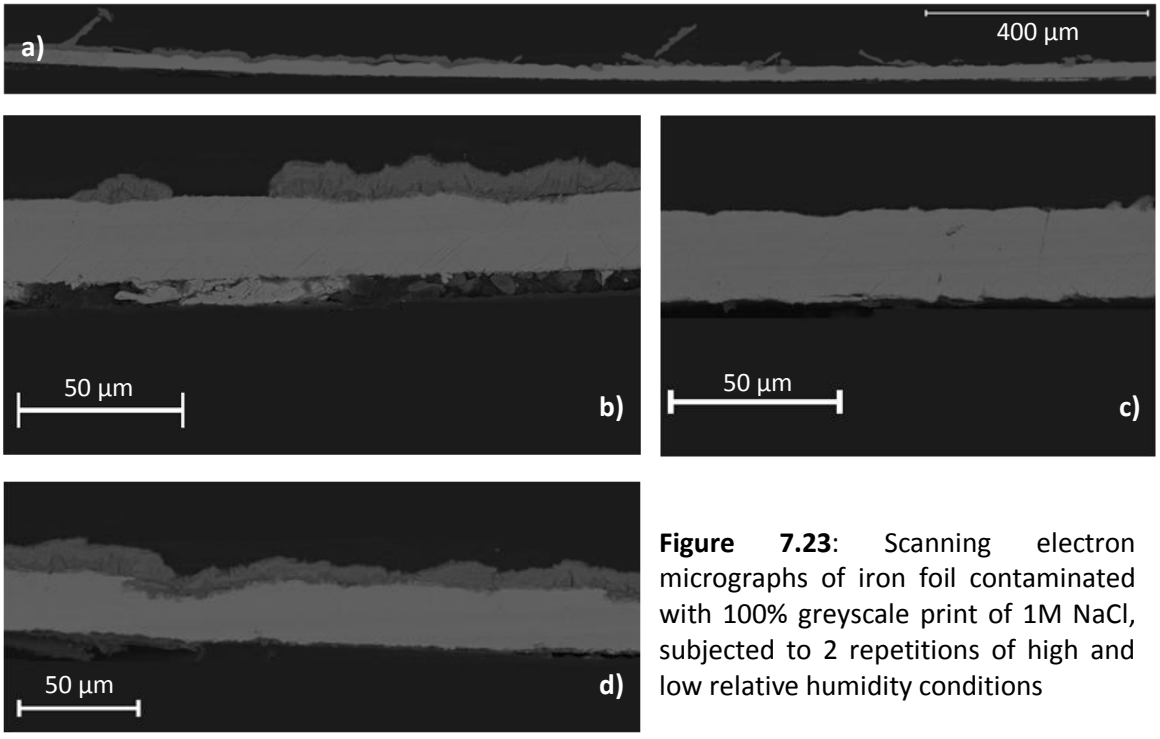


**Figure 7.23**: Scanning electron micrographs of iron foil contaminated with 100% greyscale print of 1M NaCl, subjected to 2 repetitions of high and low relative humidity conditions

After 2 repetitions the corrosion product layer across the contaminated surface is more continuous, increasing in typical thickness to 6-10 μm (figs 7.21b. 7.23a & d). The thickness loss associated with the layer is 2 to 3 μm. Gaps in the layer are present (7.23b & c) but less prevalent. Areas of localised corrosion were identified, similar to above, with minimum extant foil thickness of 7 μm, associated with a corrosion product thickness of 36 μm. These areas were often associated with surrounding gaps in the product layer.

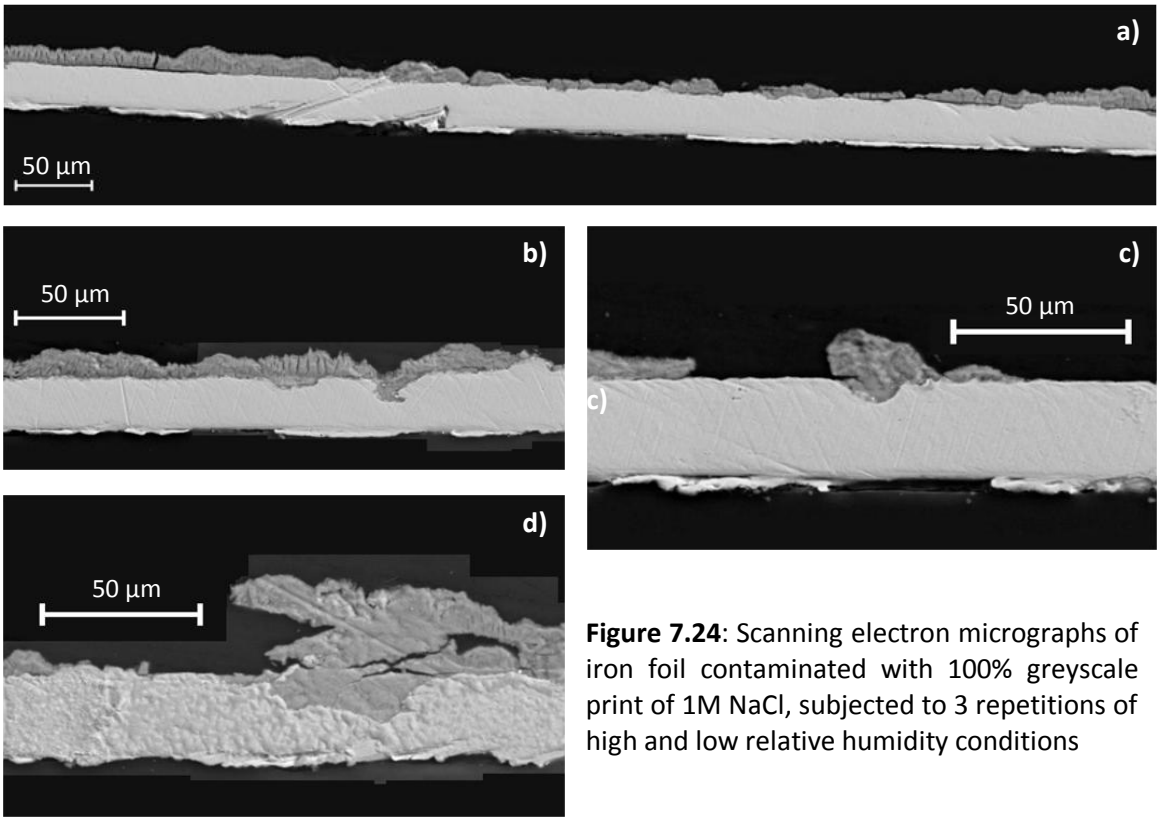


**Figure 7.24**: Scanning electron micrographs of iron foil contaminated with 100% greyscale print of 1M NaCl, subjected to 3 repetitions of high and low relative humidity conditions

For the samples subjected to 3 repetitions (figs 7.21c, 7.24), the corrosion layer forms a fairly continuous layer across the contaminated surface, between 5 and 13 μm thick, with an associated metal thickness loss of 2 to 3 μm. Areas free of visible corrosion products were less frequent, with a maximum length of around 90 μm (fig. 7.24b). Areas of localised corrosion were fewer on these particular samples, where present they formed a maximum corrosion thickness of 35 μm, associated with an extant iron thickness of 12 μm. Slight differences in form are suggested within the corrosion layers (fig 7.24 b & d), discussed below. Small voids can be seen within the layers, more consistent with corrosion phenomena than the detachment of product caused by the grinding methodology (fig. 7.24d).

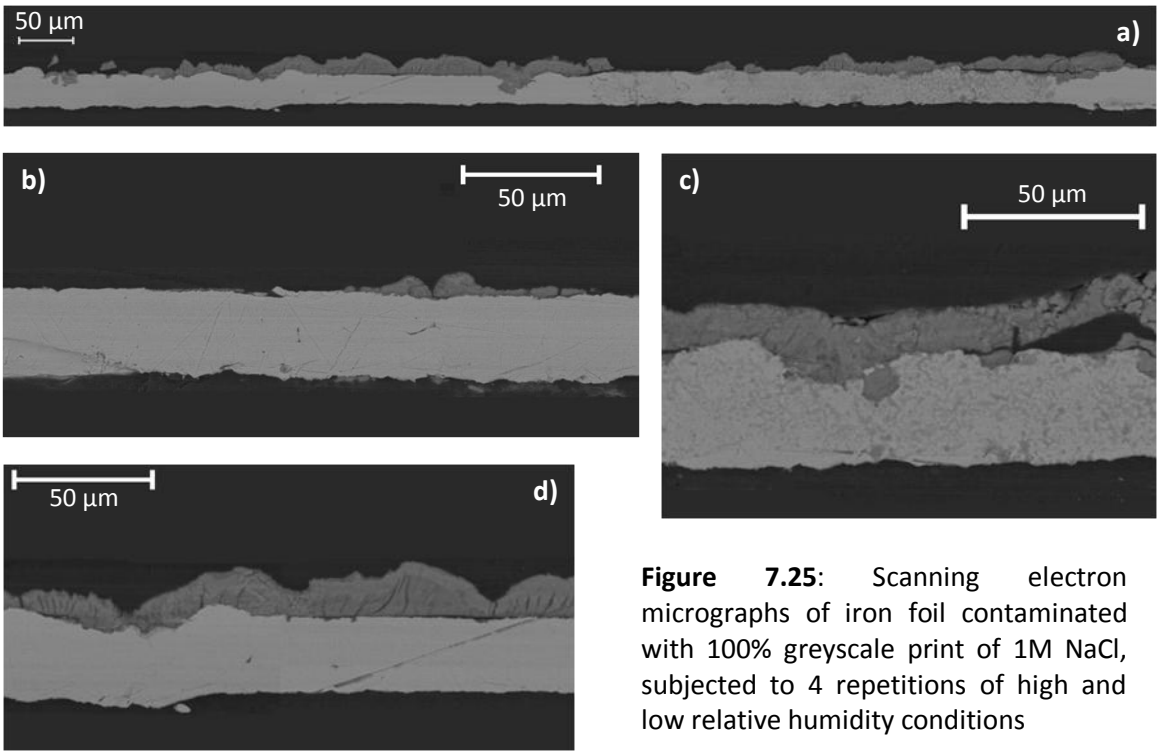


**Figure 7.25**: Scanning electron micrographs of iron foil contaminated with 100% greyscale print of 1M NaCl, subjected to 4 repetitions of high and low relative humidity conditions

After 4 repetitions, the corrosion layer maintains consistent thickness of 10-15 µm and corresponding metal thickness loss of between 2 and 4 µm across nearly the entire surface. Additional areas of greater corrosion, including domed crystalline features similar to those identified on the single repetition sample, were identified with a maximum corrosion product thickness of 45 µm and a minimum metal thickness of 5 µm. Areas free of visible corrosion product measure a maximum of approximately 60 µm.

The level of coverage, even thickness loss and low frequency and depth of localised corrosion evidenced in the SEM micrographs informed our decision to use four repetitions of the two environment corrosion process as our standard pre-corrosion methodology.

### 7.2.3c Comparison of observed thickness loss with resistance measurements

Upon creation, the pre-corroded ERCM were subjected to a 10mA current and their filament resistance measured, as they would be when deployed. These resistances were used to calculate average thickness loss for the corroding filament, using equation 5.7 (repeated below), corroborating the thickness loss observed above (Table 7.11)

$$d_{\Delta} = d_o \left(1 - \left[\frac{R_0}{R_{r0}}\right]\left[\frac{R_r}{R_c}\right]\right) \quad \textbf{[Eq. 5.7]}$$

| Number of sensors | Average calculated thickness loss | Min/ Max calculated average thickness loss | Standard deviation | Kurtosis |
|---|---|---|---|---|
| **20** | 3.56 µm | 2.11 /5.01 µm | 0.81 µm | -0.82 |

**Table 7.11**: Average calculated thickness loss of pre-corroded ERCM immediately after the pre-corrosion methodology, calculated using resistance ratios during application of 10mA current.

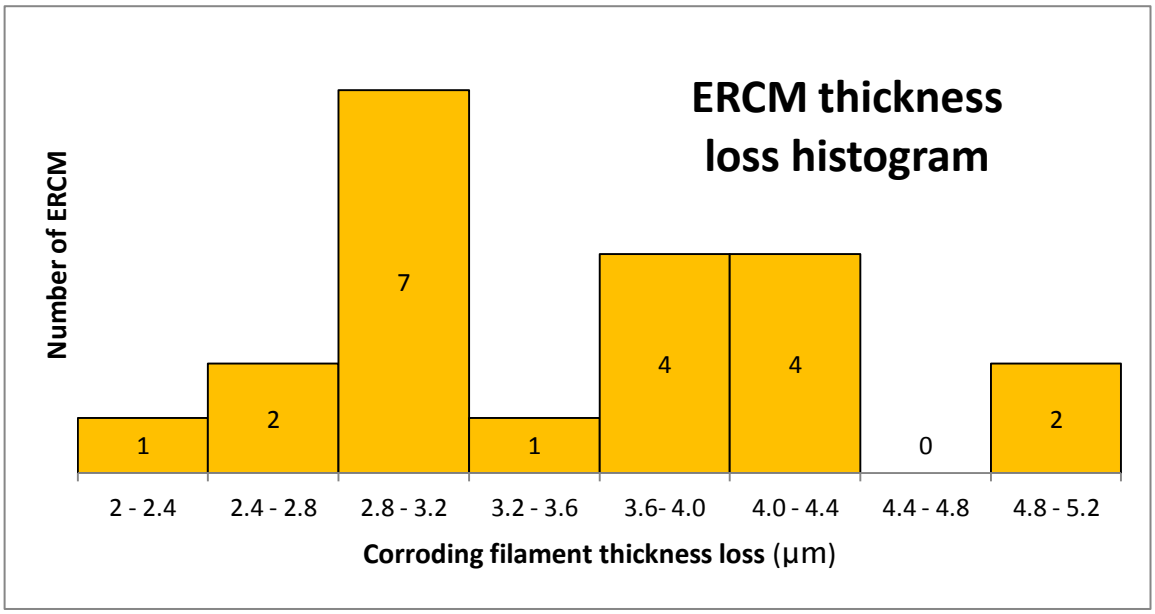


**Figure 7.26:** Histogram illustrating the frequency of average thickness loss for ERCM pre-corroded by the final methodology and the distribution of this data over the range.

The calculated average thickness losses are mainly distributed between 2.8 and 4.4µm, with an average of 3.56 µm. The negative kurtosis, evident in the frequency histogram (figure 7.27), indicates the data are gathered around the mean with a few at the extremes. These agree with the levels of corrosion loss observed by SEM; 2-4 µm average loss, with additional areas of increased localised metal consumption possibly accounting for the additional consumed thickness.

The resistance measurements were used to preferentially select sensors with between 2.8 and 3.2 µm thickness loss for use in environmental monitoring. Where sensors with thickness loss outside these limits were used within the controlled conditions, this was taken into account when resistance results were evaluated, with respect to recorded corrosion rates.

### 7.2.4 Compositional analysis of corrosion layers

Two methods of compositional analysis were applied to the pre-corroded iron foil to examine the identity of corrosion products; X-ray diffraction and Raman spectroscopy. The methodology of both is described in section 6.3.4.

#### 7.2.4a X-Ray diffraction

3 XRD spectra were successfully completed on iron foil corroded identically to the ERCM. One was examined after a single repetition, with two samples examined after the full four repetition methodology; the variation selected to provide evidence of any changes in composition during the method. The summary of the spectra statistics and identified peaks are provided in table 7.12 and the full spectra reported in figure 7.27. All samples show the peak for Bainite, Ferrite and Ledkunite; the crystallography of the underlying iron foil itself (PDF-00-006-0696).

Sample 1, subjected to a single repetition of the pre-corrosion methodology, exhibited peaks indicating the presence of sodium chloride (PDF-04-007-9723) and akaganeite (β-FeOOH, PDF-00-042-1315). Samples 2 and 3 were both subjected to 4 repetitions, the spectra of which both indicate the presence of goethite (α-FeOOH, PDF: 01-081-0463) and lepidocrocite (γ-FeOOH, PDF: 01-074-1877), but without those peaks observed on sample 1.

The disparity of results between one and four repetitions illustrates the dynamic nature of the corrosion process and the importance of using a wet/dry cyclic method for pre-corrosion. This allows deposition/re-deposition processes, creating a more diverse series of corrosion products, more similar to those found on archaeological iron. Three of the most common corrosion products found on archaeological iron were identified on the foil surface, though only two were indicated by the spectra of the four repetition samples.

The loss of any sign of akaganeite in samples 2 and 3 raises questions: It is unlikely that initially deposited corrosion layers would be entirely converted to other phases (through either dissolution repetition or solid state transformation) after so few additional cycles. In addition, the samples were completely dried with no solid chloride containing component: Where had the chloride gone? Further compositional analyses were therefore conducted.

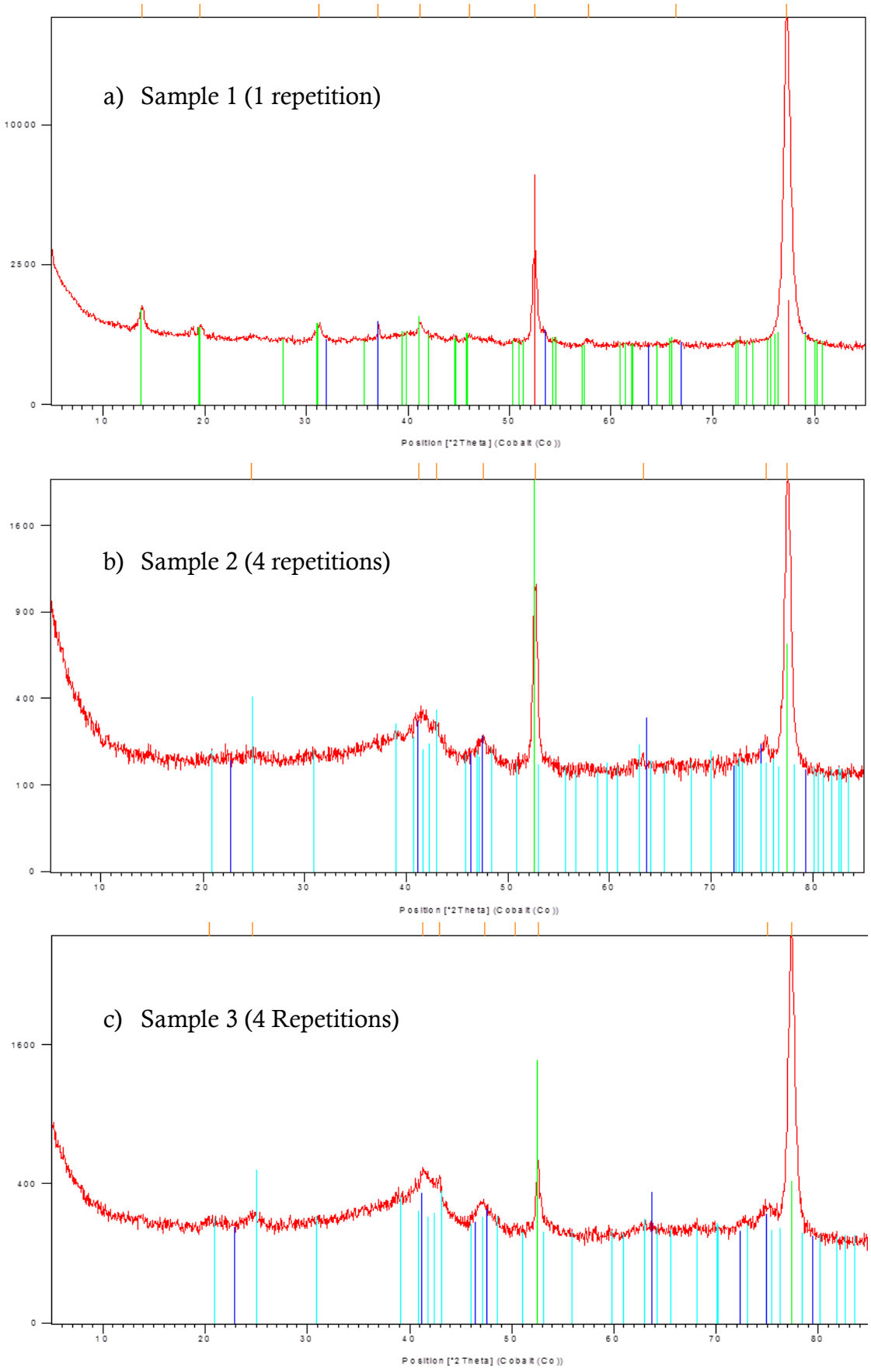


**Figure 7.27**: Spectra obtained using X-ray diffraction methodology as described in section 6.3.4a for iron foil samples after a) 1 repetition, b) 4 repetitions and c) 4 repetitions of the pre-corrosion methodology. For key, see table 7.

| Sample 1: 1 repetition of the alternating pre-corrosion methodology | | | | | |
|---|---|---|---|---|---|
| Ref. Code | Score | Compound Name | Displacement [°2Th.] | Scale Factor | Chemical Formula |
| 00-006-0696 | 43 | **Bainite, Ferrite, Ledkunite** | 0 | 0.235 | Fe |
| 04-007-9723 | 37 | **Sodium Chloride** | 0 | 0.013 | Na Cl |
| 00-042-1315 | 32 | **Akaganeite** | 0 | 0.018 | $FeO(OH).\ Cl_{1.3}$ |
| **Sample 2: 4 repetitions of the alternating pre-corrosion methodology** | | | | | |
| Ref. Code | Score | Compound Name | Displacement [°2Th.] | Scale Factor | Chemical Formula |
| 00-006-0696 | 52 | **Bainite, Ferrite, Ledkunite** | 0.226 | 0.655 | Fe |
| 01-074-1877 | 23 | **Lepidocrocite** | 0.156 | 0.073 | FeO(OH) |
| 04-015-2898 | 9 | **Goethite** | 0.19 | 0.049 | FeO(OH) |
| **Sample 3: 4 repetitions of the alternating pre-corrosion methodology** | | | | | |
| Ref. Code | Score | Compound Name | Displacement [°2Th.] | Scale Factor | Chemical Formula |
| 00-006-0696 | 32 | **Bainite, Ferrite, Ledkunite** | 0.129 | 0.31 | Fe |
| 01-074-1877 | 28 | **Lepidocrocite** | 0.234 | 0.074 | FeO(OH) |
| 04-015-2898 | 7 | **Goethite** | 0.306 | 0.03 | FeO(OH) |

**Table 7.12:** Summary table of calculated peaks from the X-ray diffraction spectra generated from pre-corroded iron foil after 1 or 4 repetitions of the pre-corrosion methodology. Applied colour refers to the highlighted peaks on the relevant spectra in figure 7.27.

### 7.2.4b Raman Spectroscopy

Raman spectroscopy was performed on 3 pre-corroded ERCM samples, created using the final methodology and examined as described in section 6.3.4. Generated spectra were compared to anecdotal reference spectra from the literature, specifically from articles examining the corrosion layers of archaeological iron [12-16]. Example spectra from these sources are given in figure 7.28 and typical observed peaks for some of the most common corrosion prodcuts, also taken from these references, are given in table 7.13.

Initial Raman spectroscopy gave repeated identical spectra, with clear peaks at the points associated with hematite crystals. Given the necessity for highly acidic or high temperature conditions [17-18], the presence of haematite on the samples as prepared was considered suspect. Previous Raman spectroscopic studies of iron corrosion products in the literature had indicated that high intensity laser light would cause transformation of magnetite, and possibly other corrosion products, into maghemite and hematite through a solid state

transformation [16, 19]. To test whether this was the case for our samples, laser intensity was lowered to 10% of initial brightness by application of a rotary filter to the laser source. One spectrum was generated, before boosting to standard intensity and a second and third spectra taken. While the first spectra (at low intensity) gave peaks for various corrosion products, the second and third spectra, after prolonged exposure to higher intensity laser light, gave identical peaks denoting hematite crystals (fig. 7.29). The methodology was therefore tweaked to use the lower laser intensity and to ensure laser light was applied for as little time as possible between spectral imaging. In addition, extra evaluation of result validity was undertaken for spectra exhibiting hematite or maghemite.

| Compound | Formula | Characteristic peaks |
|---|---|---|
| **Wustite** | FeO | 655 |
| **Goethite** | α-FeOOH | 390 |
| **Lepidocrocite** | γ-FeOOH | 250, 1300 |
| **Akaganeite** | β-FeOOH (Cl) | 310, 390, ~1400 |
| **Magnetite** | $Fe_3O_4$ | 670 |
| **Haematite** | $Fe_2O_3$ | 220, 290, ~1320 |
| **Ferroxyhyte** | δ-FeOH | 680, ~1350 |
| **Maghemite** | γ-$Fe_2O_3H$ | 670-720, ~1400 |
| **Iron Chloride** | $FeCl_2$ | 610 |
| **Ferrous Hydroxychloride** | β-$Fe_2(OH)_3Cl$ | 160, 423 |

**Table 7.13:** Characteristic Raman spectroscopy spectra peaks of typical iron corrosion products, adapted from [13]

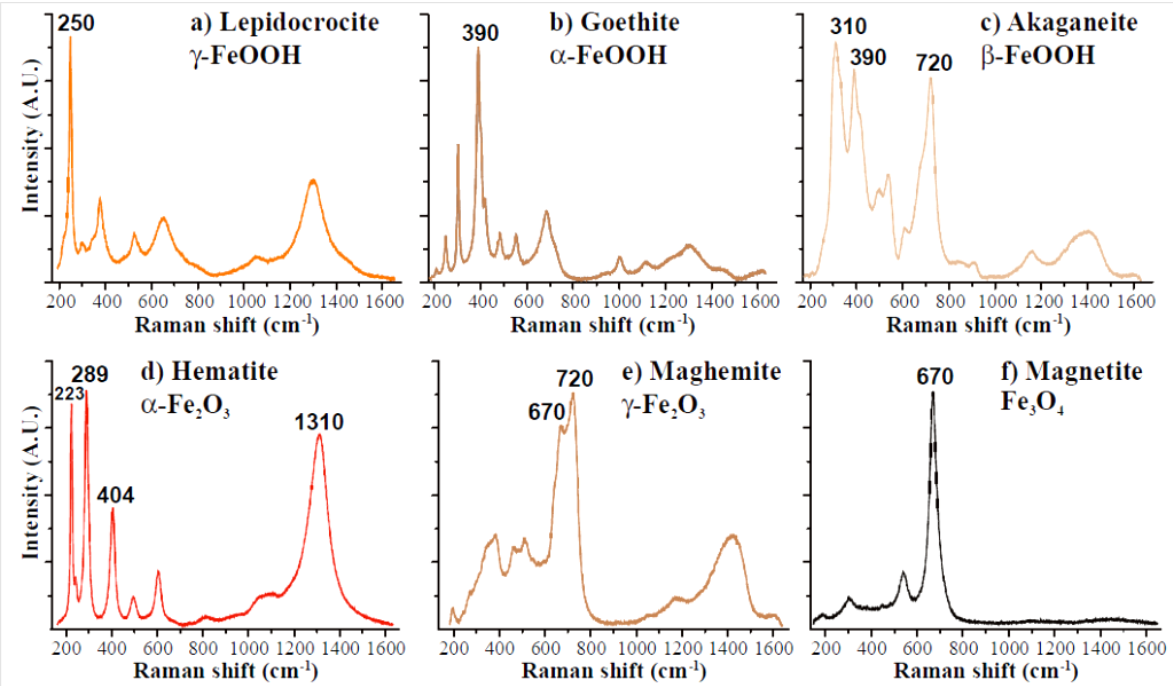


**Figure 7.28**: Example Raman spectra for corrosion products typically found on archaeological iron, taken using λ=532nm, 15/60 minute acquisition time and <100μW laser power, from [12]

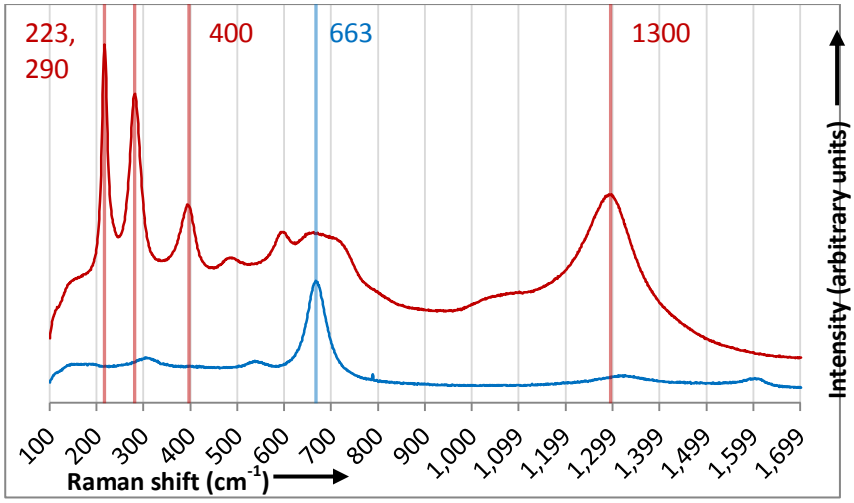


**Figure 7.29**: Spectra generated using Raman spectroscopy from a single location on a pre-corroded ERCM, showing the initial spectra at 10% laser intensity, and the spectra taken after prolonged exposure to more intense laser light.

Vertical lines denote interpreted peaks for magnetite and hematite

For each specimen, multiple sites were examined, attempting to encompass all visibly discernible corrosion products (differentiated by colour and form). Spectra were generated exhibiting peaks indicative of single or multiple corrosion product forms at a single site. All spectra were saved for subsequent analysis, with enough different spectra from each sample to satisfy that the majority of the visible corrosion products were represented. In consideration of the transformational effect described above, spectra containing clear peaks for hematite or maghemite were evaluated for possible over-exposure and the majority discarded, or those specific peaks discounted. Where similar peaks where observed on multiple spectra, only the clearest examples are given. It has been noted that differences in crystal size and form can shift raman peaks from their exact expected values. Therefore, where peaks were not on the exact expected Raman shift, they were only used for identification of a particular product phase where additional peaks were available to aid identification. Example spectra illustrating those corrosion forms found on each sample are given in figures 7.30, 7.31 and 7.32.

For all samples, almost all spectra exhibited clear peaks indicating the presence of goethite, akaganeite or magnetite. Sample 2 and 3 both presented possible evidence of lepidocrocite, with the distinctive peak at a Raman shift of 250 $cm^{-1}$; observed only in spectra displaying characteristic peaks for multiple crystallographies (fig. 7.31d). Sample 3 showed possible Raman shift peaks for ferrous hydroxychloride, at 160 and 423 $cm^{-1}$, noted only once and in conjunction with akaganeite and lepidocrocite peaks (fig. 7.32d).

The results of the compositional analyses together are discussed in section 8.2.1. The results evidence corrosion products which were identified in the literature review as typically found on chloride infested archaeological iron. For the purposes of this study, this allowed us to judge the pre-corrosion methodology sufficient, assuming the corrosion product build up on the ERCM created corrosion rates similar to actual archaeological artefacts in the same environment.

**Figure 7.30:** Spectra obtained from distinct sites on pre-corroded ERCM sample 1 obtained using Raman Spectroscopy.

a) Spectrum interpreted as showing evidence for goethite

b) Spectrum interpreted as showing evidence for akaganeite

c) Spectrum interpreted as showing evidence for magnetite

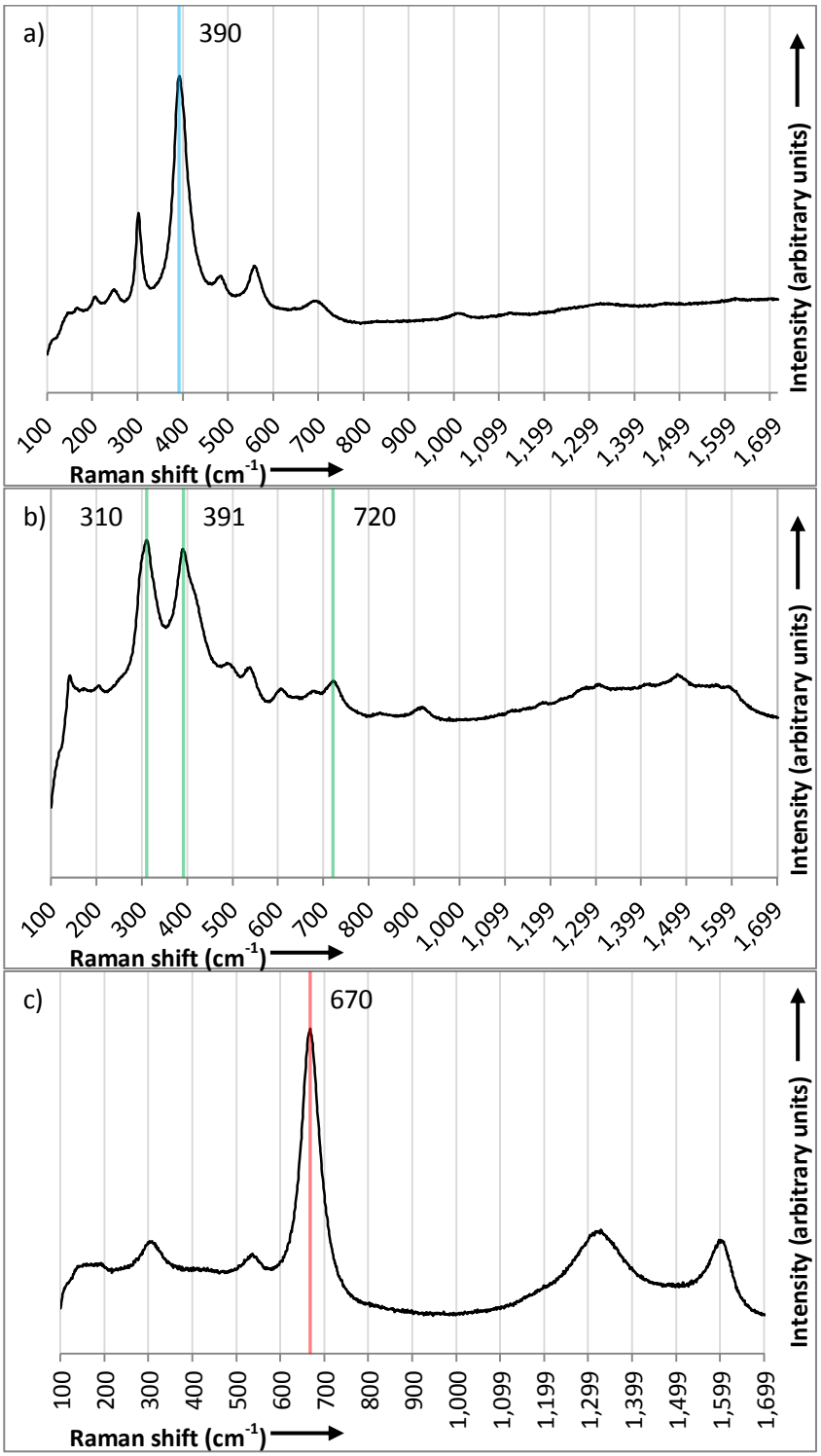


**Goethite associated peaks**

**Akaganeite associated peaks**

**Magnetite associated peaks**

**Figure 7.31**: Spectra obtained from distinct sites on pre-corroded ERCM sample 2 obtained using Raman Spectroscopy.

a) Spectrum interpreted as showing evidence for goethite

b) Spectrum interpreted as showing evidence for akaganeite

c) Spectrum interpreted as showing evidence for magnetite

d) Spectrum interpreted as showing evidence for akaganeite, lepidocrocite and ferrous hydroxychloride

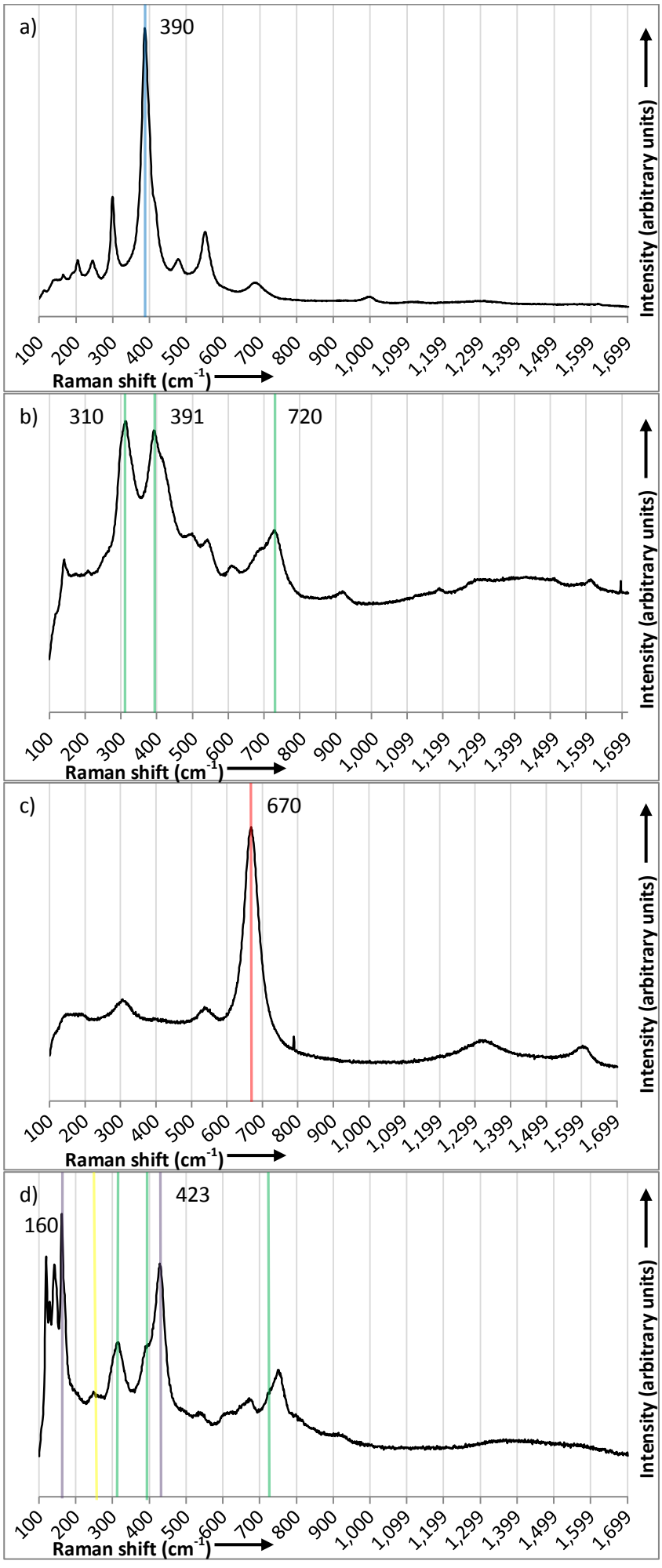


**Goethite associated peaks**

**Akaganeite associated peaks**

**Magnetite associated peaks**

**Lepidocrocite associated peaks**

**Ferrous hydroxychloride associated peaks**

**Figure 7.32**: Spectra obtained from distinct sites on pre-corroded ERCM sample 3 obtained using Raman Spectroscopy.

a) Spectrum interpreted as showing evidence for goethite

b) Spectrum interpreted as showing evidence for akaganeite

c) Spectrum interpreted as showing evidence for magnetite

d) Spectrum interpreted as showing evidence for akaganeite and lepidocrocite

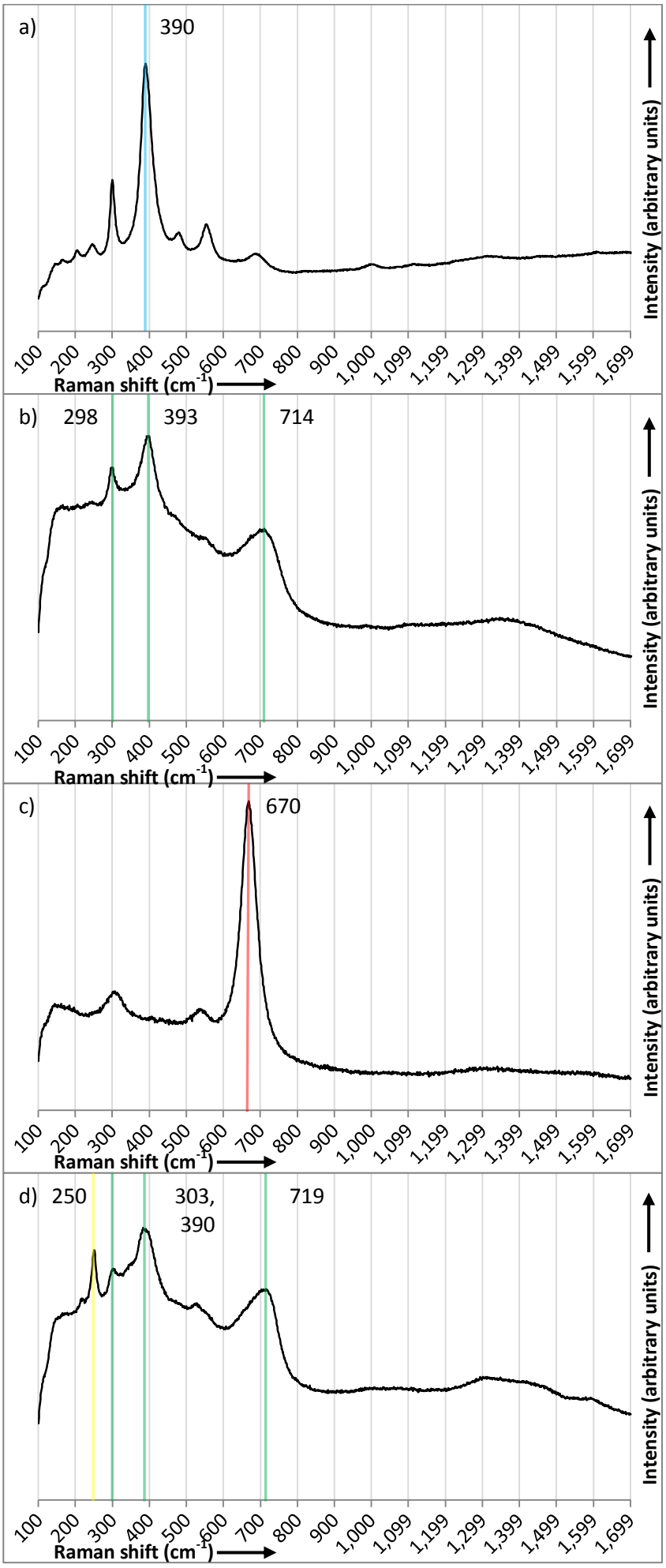

## 7.3 ERCM Thickness loss in atmospheric environments

This section details the results of exposure of pre-corroded ERCM in the controlled atmospheric environments of climate chambers and within heritage style containers.

All ERCM had been subjected to the final pre-corrosion methodology and stored in a desiccated environment prior to use. Calculated initial thickness loss at the time of monitoring commencement ranged from 2.5-5μm, with corrosion products and features assumed to be the same as those observed on the samples studied under microscopy and compositional analyses. Monitoring was performed in consecutive batches. ERCM were replaced where it was judged sufficient corrosion had occurred that it might significantly alter later corrosion methods (after 40%, 50% and 60% stable Relative humidity levels) or where probe failure occurred. The results are displayed in graphs of thickness loss, used as a direct measure of level of corrosion, giving gradients of use as corrosion rates in terms of microns per day. These were converted to microns per year (μm/y) to allow for ease of comparison with previous research in archaeological iron.

### 7.3.1 ERCM result processing, noise and accuracy

Corrosion was monitored via measurement of individual filament voltages and results collated to create tables of measured voltages at five minute intervals over varying time periods. For each reading of each sensor, the ratio of measured voltage of the reference filament over the corroding filament was calculated. This was previously shown (in section 5.1) to be equal to the ratio of the resistances, at constant current (eq. 5.7). These ratios were combined with the initial ratio between the corroding and reference electrode (measured and calculated immediately on probe manufacture, prior to salt deposition or any corrosion methodology) and the original, un-corroded foil thickness (25μm) to give the total metal thickness loss, as shown in equation 5.7 (repeated below).

$$d_{\Delta} = d_o \left(1 - \left[\frac{R_0}{R_{r0}}\right]\left[\frac{R_r}{R_c}\right]\right) \quad \textbf{[Eq. 5.7]}$$

Thickness loss, Δd, was plotted against time, allowing calculation of corrosion rate, identification of changes in corrosion reaction and plotting of cumulative thickness loss.

Initial results show a consistent level of noise. This was confirmed by ongoing testing, equating to a constant error of approximately ±3nm in Δd, evidenced as a 'noise' signal around the overall change in thickness (figures 7.33-7.38). This is most obvious in the slowly corroding atmospheres, where total change in thickness was close to, or below, this level over the course of the monitoring period. The error is attributed to a combination of system

accuracy (the accuracy of the multimeter voltage measurement results in a maximum resolution of 2.5nm), reflecting the limits of precision of the multimeter, and small current fluctuations from the galvanostat.

Results were plotted for each sensor in comparison to others within the same batch. To allow easy comparison, the results were modified to reflect thickness loss from the start of each individual test. This was achieved by subtracting the calculated total thickness loss for the sensor at the start of the test run from each thickness calculation. To account for the inherent system error and prevent the effect of noise; the initial value was calculated from the average of the readings of the first hour of corrosion, not the first measured value. This created thickness loss plots all starting from approximately equal axis points without any loss of corrosion rate (gradient) information.

### 7.3.2 Sensor corrosion in stable state environments.

ERCM were tested in stable environments, held at constant levels of relative humidity and temperature, in atmospheric climate chambers for varying lengths of time to achieve measurable corrosion rates. Four ERCM were deployed in each environment. Occasional failures were experienced, reducing the number of effective sensors to 3 for stable environments at 15% and 40%. These have been attributed to wiring problems and probe failure respectively. Temperature was held at a stable 20°C and relative humidity was kept at either 15%, 20%, 30%, 40%, 50% and 60% for each test. Measured resistances were tabulated and converted to calculated thickness loss measurements. The results for each of the stable environments are plotted below (fig 7.33-7.38). Corrosion rate was calculated by the gradient of a straight trend line for the data, calculated using Microsoft Excel™.

#### 7.3.2a Corrosion data and calculated rates

At 15% RH (figure 7.33) the corrosion sensors were monitored for 40 days. No corrosion was observable over the background noise of the equipment. Two sensors recorded negative corrosion rates over complete monitoring, illustrative of the limits of measurement using this technique. The other recorded a positive corrosion rate of 3.13nm/year, within the margin of error.

At 20% RH (figure 7.34), noticeable corrosion can be observed after two weeks. The final level of corrosion is within the margin of error; a total thickness loss of around 2nm. The gradient is still very low, but all sensors show a linear corrosion rate of between 0.05-0.06μm/year, with the large number of readings and agreement between sensors lending credibility to the calculated results.

At 30% RH (figure 7.35) corrosion is clear even after a single day, with a minimum corrosion thickness loss of 6nm after two weeks. Calculated corrosion rates ranged from 0.16 μm/year to 0.26 μm/year. Corrosion rates remain fairly constant, with a slight decrease towards the end of the two week period.

At 40% RH, (figure 7.36) only three ERCM were operational for the entire run. Total corrosion after two weeks ranged from 23nm to 29nm, giving fairly constant corrosion rates between 0.53μm/year and 0.67μm/year. One ERCM displays a distinctly lower corrosion rate, the lowest RH at which there are differences between ERCM above the noise level.

At 50% RH (figure 7.37), there are noticeable differences between the ERCM corrosion levels. Two sets of two sensors corrode at similar rates; the slower set corroded by around 140nm in total, giving corrosion rates of 3.3 μm/year and 3.4μm/year, while the others corroded around 150nm, exhibiting corrosion rates of 4.16μm/year and 4.35μm/year. Corrosion rates decrease over time for both sets; a trend more pronounced in (and responsible for) the lower corrosion rates. The average corrosion rate falls between the two sets at 3.8μm/year.

At 60% RH (Figure 7.38), data was collected for one week, owing to high corrosion levels. There is large disparity between corrosion rates of different sensors. Two sensors corrode quite closely, reducing in thickness by 125 and 136nm after only 7 days. Another corroded 268nm in the same time period, with the most disparate sensor corroding 417nm. This is illustrated in the corrosion rates, calculated as 5.26μm/year, 8.15μm/year, 15.56μm/year and 21.02μm/year respectively. The rates decrease over time for the three slower corroding sensors, similarly to those at 30% and 50% RH. The fastest corroding, anomalous result was significantly more linear. The average corrosion rate was 12.50μm/year, though the disparity of the plotted data casts doubt on this as a reliable representation of the dataset.

The average corrosion rate, standard deviation of calculated rates and the associated coefficient of variance (standard deviation divided by the mean value) were calculated for each relative humidity (table 7.14) The average calculated corrosion rates are plotted in figure 7.39. It demonstrates the difference in levels of corrosion rate between the separate RH environments. The coefficient of variance provides a useful measure of the variation in corrosion rate data, evidenced in the graphs and highlighted in the preceding paragraphs. The base 10 logarithm was taken of the corrosion rate (table 7.14, figure 7.40). It illustrates the linearity of results thus plotted against relative humidity, showing an increase of approximately half an order of magnitude for each 10% increase in relative humidity over the monitored environments. This calculation was made in order that comparison could be made with archaeological iron, should it exhibit a similar relationship.

**Figure 7.33**: Thickness loss curves for atmospheric corrosion in corrosion chamber at 15% RH and 20°C

| Sensor | Average Corrosion rate |
|---|---|
| | -0.28 nm/year |
| | 3.13 nm/year |
| | -5.68 nm/year |
| **Average** | **-0.94 nm/year** |

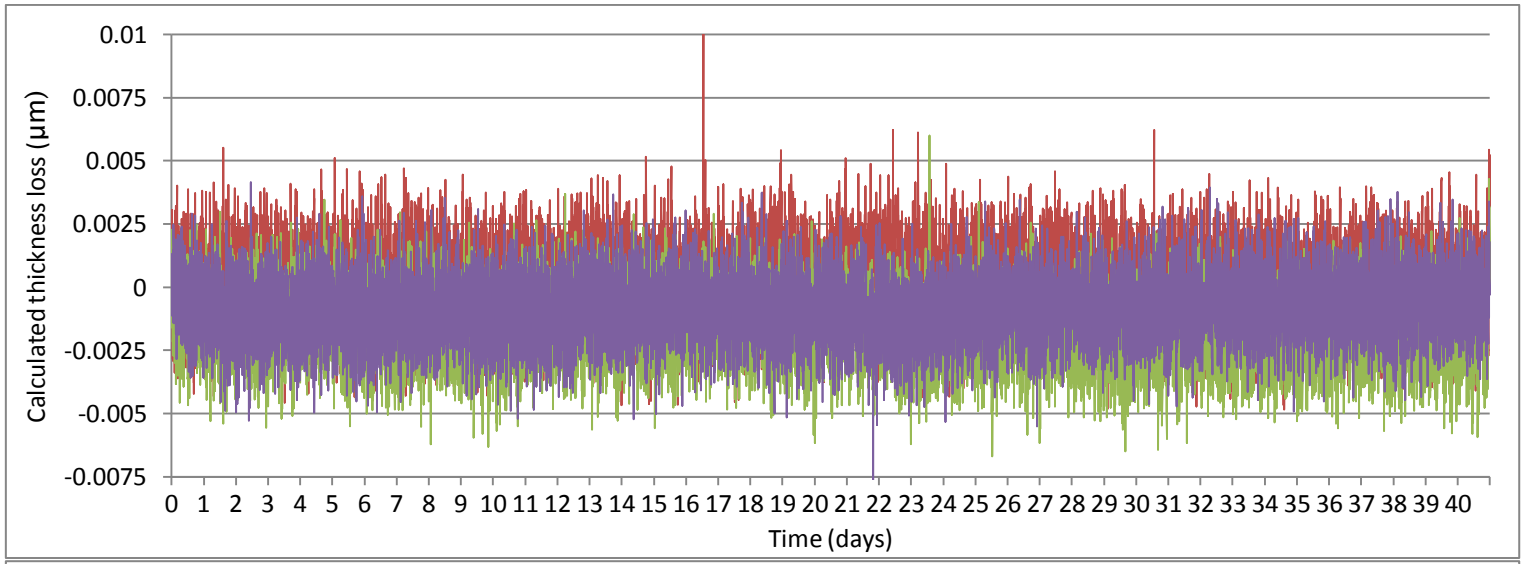


**Figure 7.34**: Thickness loss curves for atmospheric corrosion in corrosion chamber at 20% RH and 20°C

| Sensor | Average Corrosion rate |
|---|---|
| | 0.05 µm/year |
| | 0.05 µm/year |
| | 0.06 µm/year |
| | 0.05 µm/year |
| **Average** | **0.05 µm/year** |

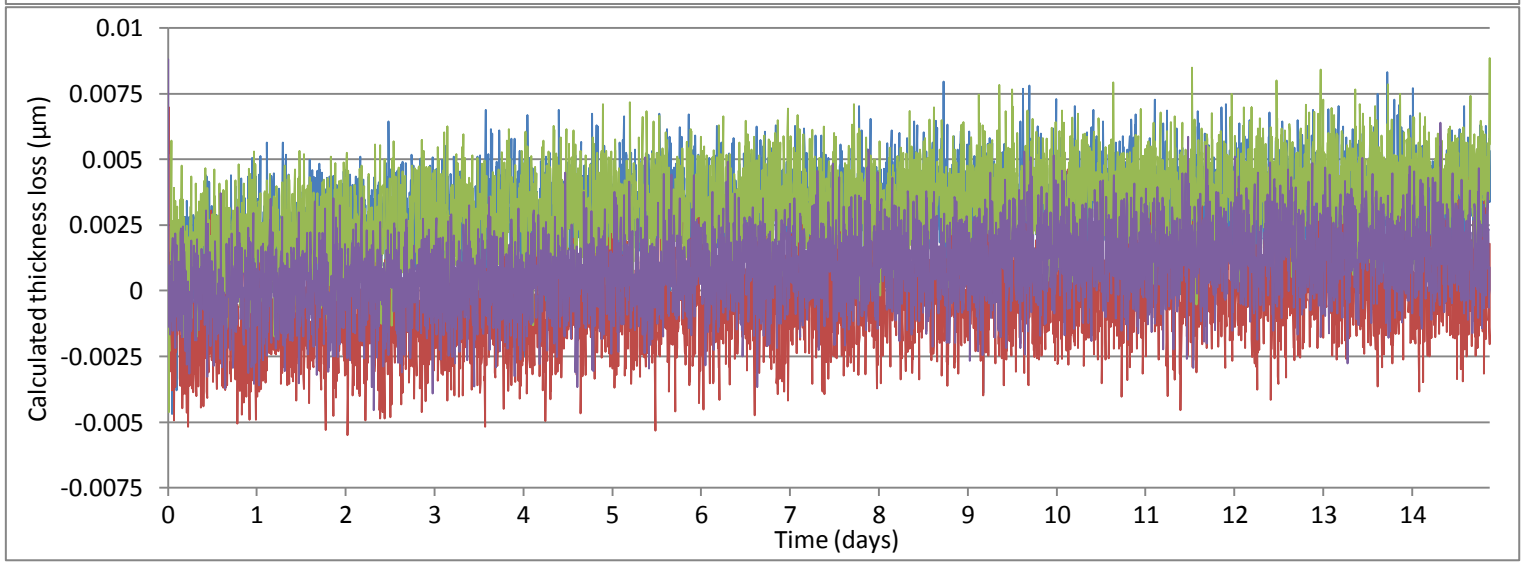

**Figure 7.35**: Thickness loss curves for atmospheric corrosion in corrosion chamber at 30% RH and 20°C

| Sensor | Average Corrosion rate |
|---|---|
| | 0.16 µm/year |
| | 0.23 µm/year |
| | 0.26 µm/year |
| | 0.13 µm/year |
| **Average** | **0.19 µm/year** |

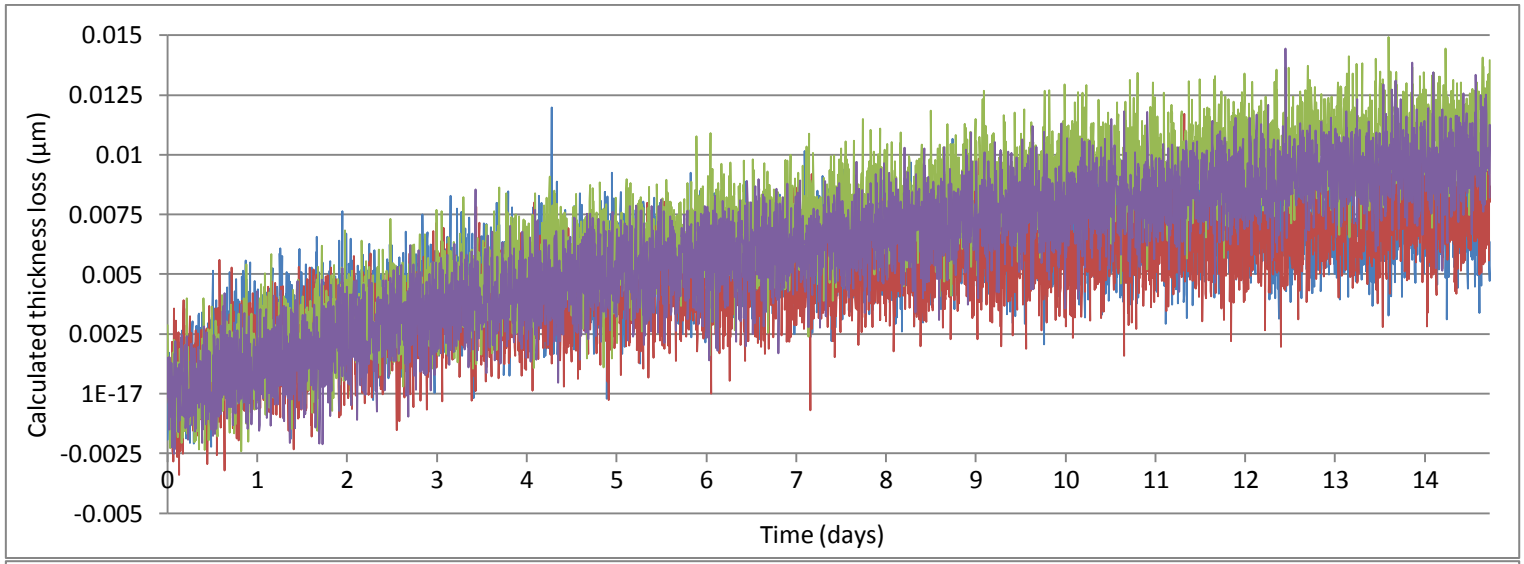


**Figure 7.36**: Thickness loss curves for atmospheric corrosion in corrosion chamber at 40% RH and 20°C

| Sensor | Average Corrosion rate |
|---|---|
| | 0.67 µm/year |
| | 0.64 µm/year |
| | 0.53 µm/year |
| **Average** | **0.70 µm/year** |

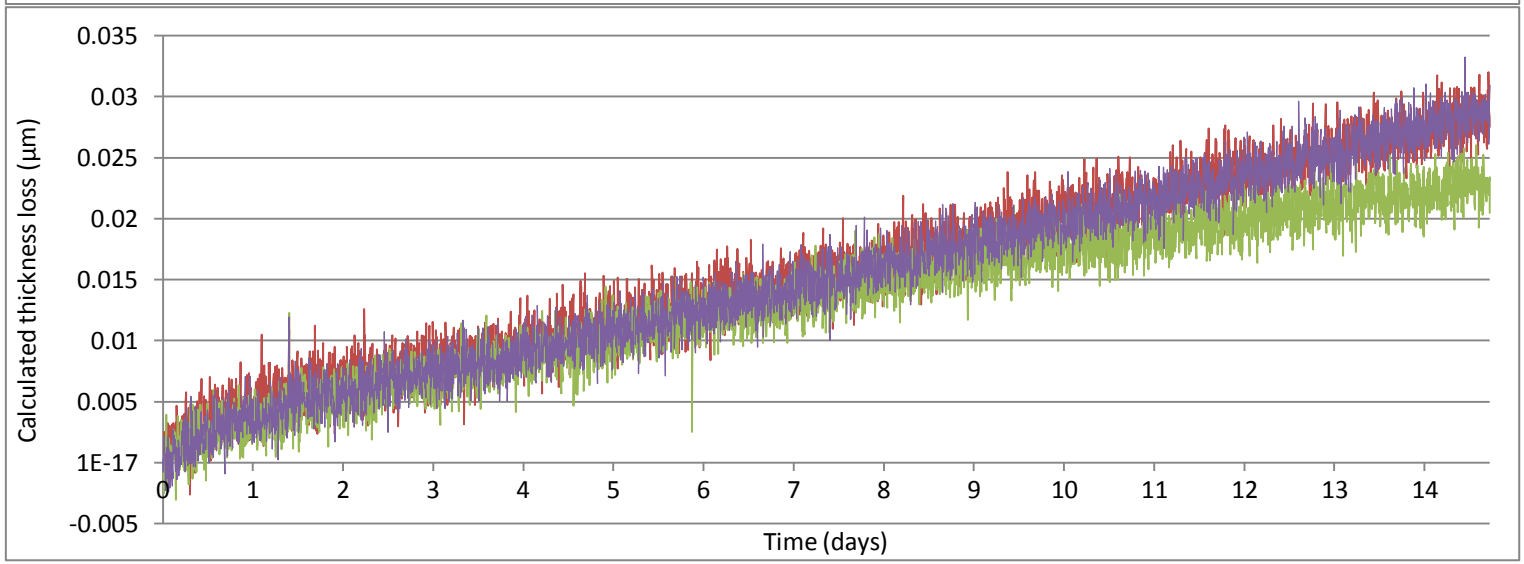

**Figure 7.37**: Thickness loss curves for atmospheric corrosion in corrosion chamber at 50% RH and 20°C

| Sensor | Average Corrosion rate |
|---|---|
| | 4.35 µm/year |
| | 4.16 µm/year |
| | 3.40 µm/year |
| | 3.30 µm/year |
| **Average** | **3.80 µm/year** |

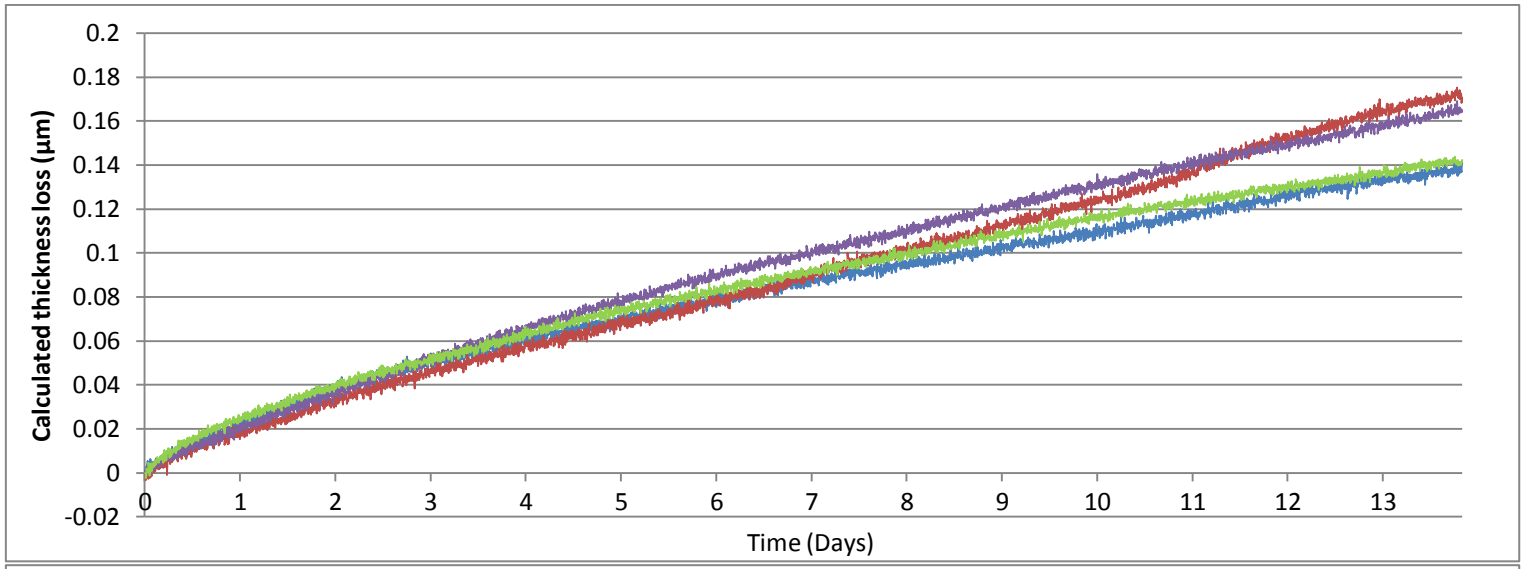


**Figure 7.38**: Thickness loss curves for atmospheric corrosion in corrosion chamber at 60% RH and 20°C

| Sensor | Average Corrosion rate |
|---|---|
| | 5.26 µm/year |
| | 15.56 µm/year |
| | 8.15 µm/year |
| | 21.02 µm/year |
| **Average** | **12.50 µm/year** |

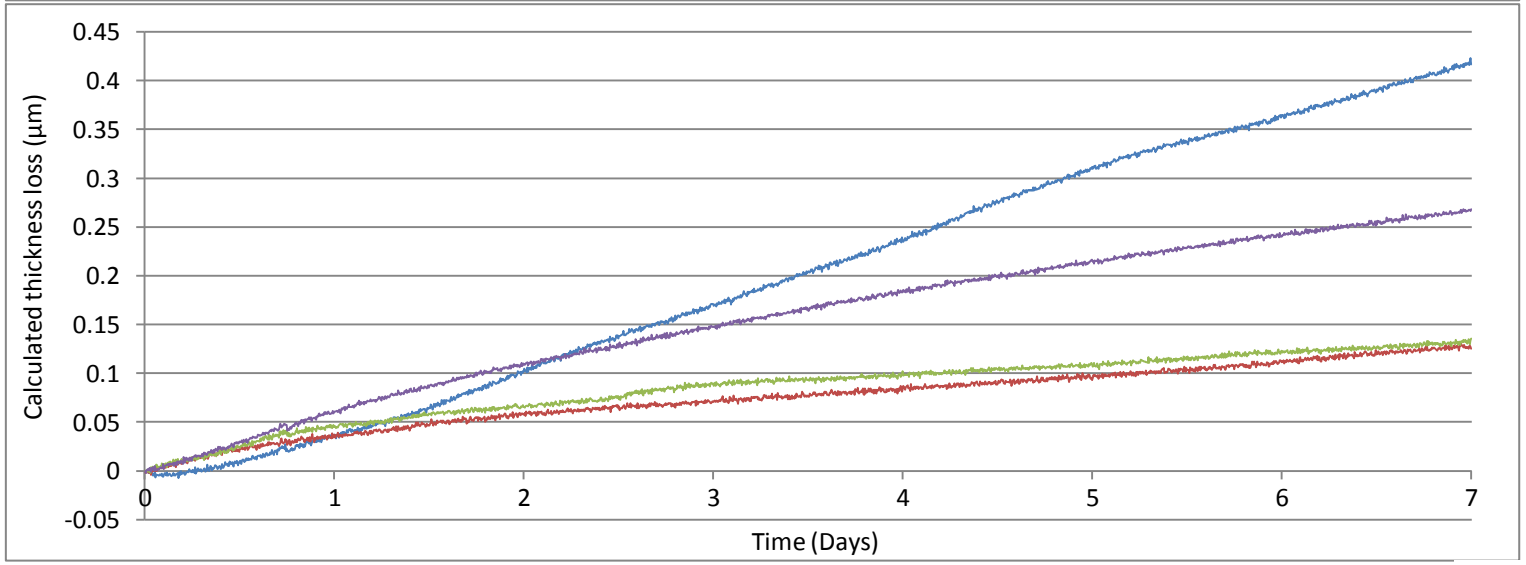

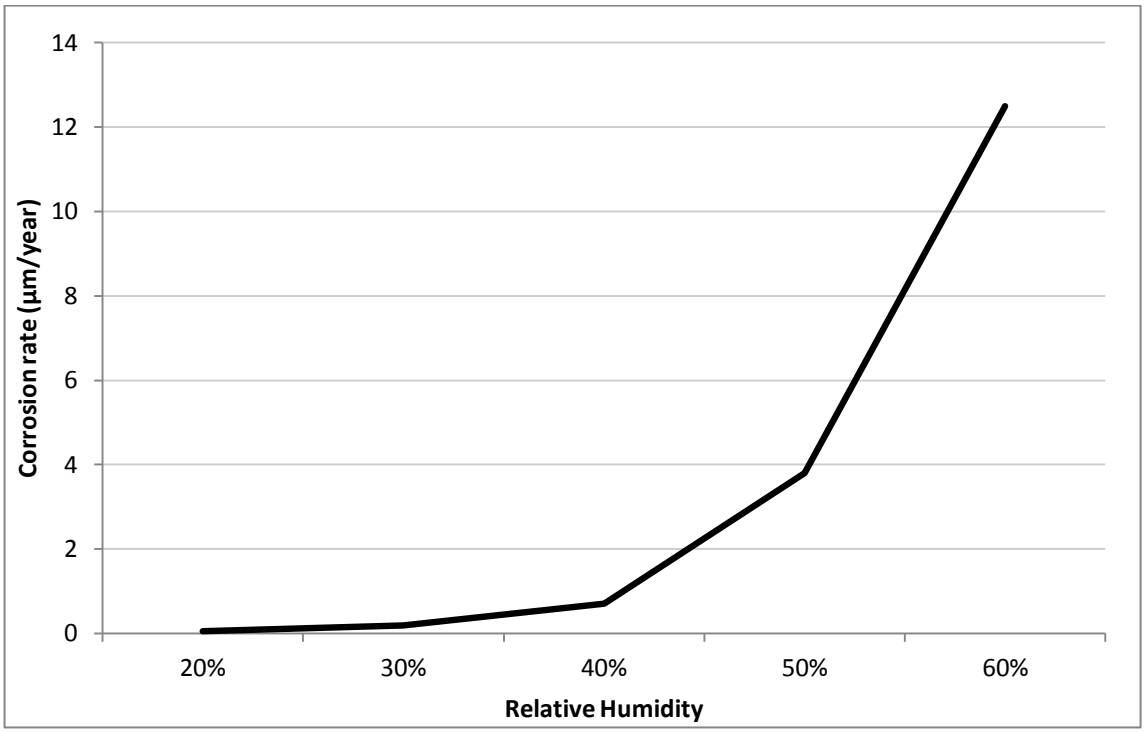


**Figure 7.39:** Graph illustrating the change in average calculated corrosion rate against relative humidity, extrapolated from figures 7.33-38.

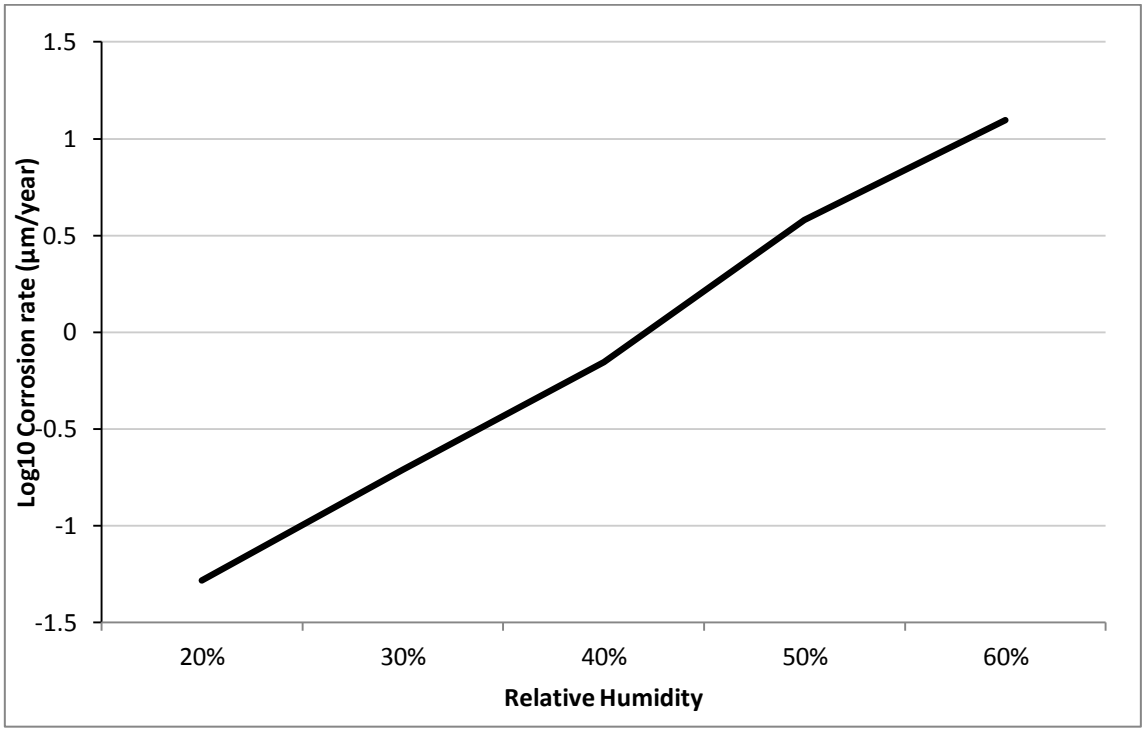


**Figure 7.40:** Graph illustrating the change $Log_{10}$ of the average calculated corrosion rate against relative humidity, extrapolated from figures 7.33-38.

| Relative humidity | Average Corrosion rate (µm/year) | $Log_{10}$ Corrosion rate | Standard deviation (µm/year) | Coefficient of Variance |
|---|---|---|---|---|
| **20%** | 0.05 | -1.28 | 0.01 | 0.10 |
| **30%** | 0.19 | -0.71 | 0.06 | 0.31 |
| **40%** | 0.70 | -0.15 | 0.18 | 0.26 |
| **50%** | 3.80 | 0.58 | 0.53 | 0.14 |
| **60%** | 12.50 | 1.10 | 7.15 | 0.57 |

**Table 7.14:** Summary table of corrosion rate data for sensors exposed in stable temperature and relative humidity environments, extrapolated from figures 7.33-7.38.

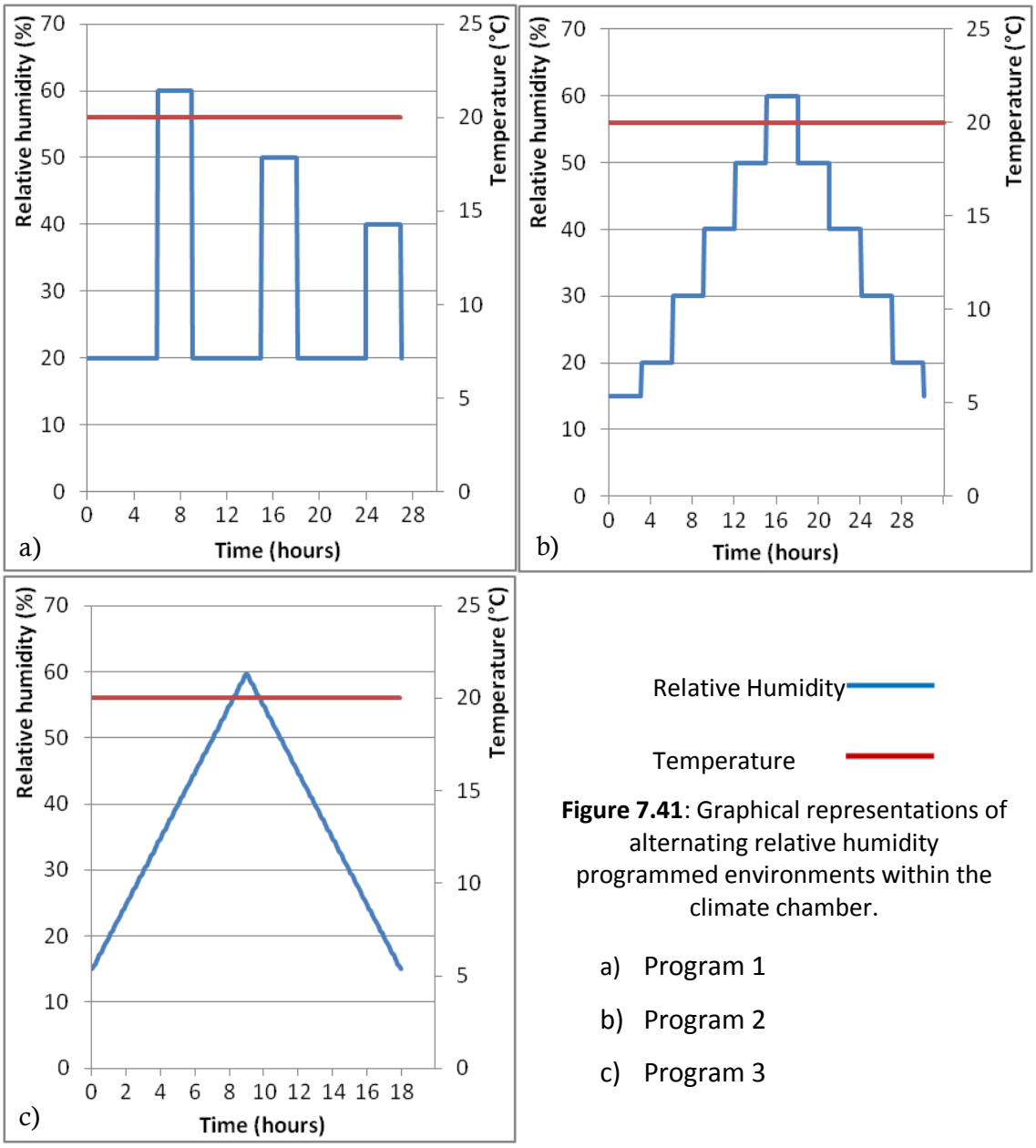


**Figure 7.41**: Graphical representations of alternating relative humidity programmed environments within the climate chamber.

a) Program 1

b) Program 2

c) Program 3

### 7.3.3 Corrosion sensors in changing environmental conditions

ERCM sensors were tested in climate chambers programmed to create varying environments, detailed in section 6.4.2b. Similarly to the stable state tests, four pre-corroded sensors were deployed for each program, monitored for 1 week. Resistance measurements and subsequent calculation of thickness loss were performed identically as for stable environments. Program details are given in section 6.4.2b, reproduced as figure 7.41 for convenience. Programs were examined sequentially (program one was run on repeat for one week, then program two was run on repeat for one week, etc.). The levels of measurement noise from the equipment were observed to be the same as in the stable environment results.

In order to better process the results, different methods were used to examine corrosion rate within each dataset. These are discussed below.

#### 7.3.3a Program 1: Sudden large changes in relative humidity

Program 1 was designed to simulate sudden changes in relative humidity change, emulating movement from a controlled low humidity storage environment to a normal environment. Figure 7.42 illustrates the generated thickness loss curves, compared with the changes in relative humidity. Corrosion rate data was extracted from this plot by calculating the slope of the line over each, and limited by, the time period at each stable humidity (at 60, 50 and 40%). These data are represented graphically in figure 7.43. The same colour is used for each sensor in each plot. The conditions were initially similar to standard room temperature and humidity, then lowered to 20% RH and 20°C; the low resting humidity of program 1. Initial corrosion levels prior to commencement of program 1 were measured but not considered. An increase in corrosion rate was detected almost immediately on relative humidity increase. When RH falls it takes longer for the corrosion rate to return to the lower level.

The results show consistently little detectable corrosion at 20%, with very large increases in corrosion rate in the increased humidity periods. Similarly to the stable state tests, the higher the relative humidity, the higher the corrosion rate (table 7.15)

| Relative humidity | 20% | 40% | 50% | 60% |
|---|---|---|---|---|
| **Average corrosion rate (µm/year)** | -0.90 | 5.90 | 64.57 | 164.35 |
| **Minimum corrosion rate (µm/year)** | -4.36 | -1.25 | 38.72 | 131.80 |
| **Maximum corrosion rate (µm/year)** | 3.85 | 11.67 | 86.38 | 206.99 |
| **$Log_{10}$ Corrosion rate** | - | 0.77 | 1.81 | 2.22 |
| **Standard deviation (µm/year)** | 1.92 | 3.47 | 15.42 | 19.65 |
| **Coefficient of variance** | -2.13 | 0.59 | 0.24 | 0.12 |

**Table 7.115:** Summary statistics for combined corrosion rates during program 1.

**Figure 7.42:** Thickness loss curves for 4 ERCM exposed to repetitions of program 1. Graphical representation of relative humidity change is also plotted against time to illustrate the times of each stage of relative humidity.

| Sensor | Colour |
|---|---|
| 1 | |
| 2 | |
| 3 | |
| 4 | |

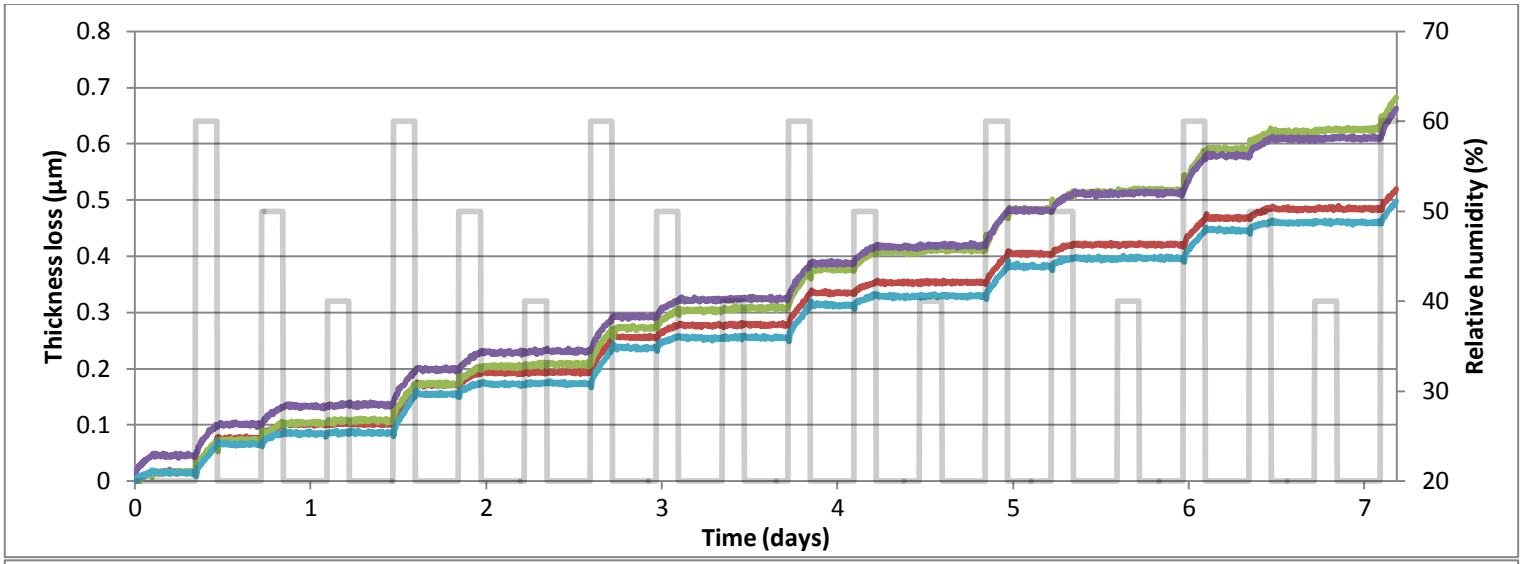


**Figure 7. 43** Graphical representation of corrosion rates for each stage of program one, calculated using the slope of the results for each humidity section in figure 7.44.

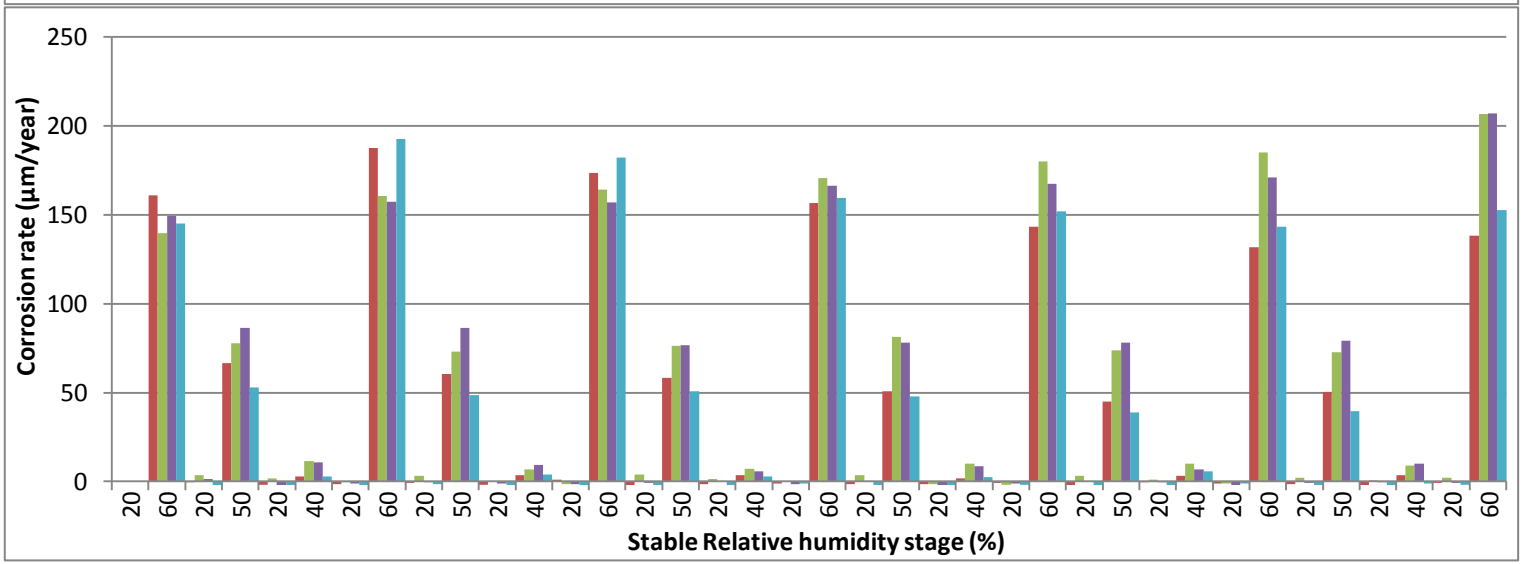

Corrosion rates calculated during program 1 deviate from the corrosion rates acquired for similar relative humidities during steady state tests. Comparison of the average and logarithmic corrosion rates show an increase of approximately one order of magnitude for high relative humidity environments. Calculation of corrosion rates at 20% (and in one case at 40%) frequently gave negative corrosion rates, manifested by negative average calculated thickness loss. This latter effect may be attributed to the methodology used to calculate corrosion rate. The noise signal at 20% is such that any changes in thickness fall within the margins of error, similarly to those readings at 15% in the static tests and discussed below. The calculated slopes are almost flat, with large deviations in the readings creating large effects on the calculated corrosion rate. These errors are exacerbated by short sample time; small errors become significant when multiplied up to yearly corrosion rates. Over the time period in question, the measurements do not exceed equipment noise levels, allowing us to treat the corrosion rates at 20% in these tests as below the limits of detection with the experimental setup. For the 40% negative rate, the same was true, with a few abnormally large errors tilting the calculated corrosion rate further.

Figures 7.45a, b and c illustrate the progressive corrosion phases of the sensors for the 60%, 50% and 40% relative humidity phases respectively (paraphrasing figure 7.43) to highlight patterns in corrosion rate over repeated program repetitions. In both 7.43 and 7.45 it can be observed that sensors two and three corrode similarly; at 60% corrosion rates begin relatively low and increase for each repetition. Higher, more stable corrosion rates were calculated during the 50% phases. Similarly, sensors 1 and 4 corrode faster at 60% initially, but the rates fall away after continued corrosion, decreasing similarly during 50% RH exposure. The similarities are likely for the same reasons as the static tests: Sensors 1 and 4 had significantly more initial thickness loss after pre-corrosion than sensors 2 and 3. The former showed overall decreases in the level of corrosion rate, whereas the latter increase in corrosion rate over time. These differences are most pronounced at 60%, evident at 50% and mostly obscured by the low corrosion rates at 40%. These confirm the models suggested in section 7.3.2b, and discussed there.

Standard deviation levels are plotted in figure 7.45, illustrating the lack of correlation between standard deviation and program repetitions. Standard deviation was higher at higher relative humidity levels, but coefficient of variance was lower. This is likely due to the lower effects of noise at the higher corrosion rates.

To establish greater resolution of corrosion rates and remove noise, results were processed to create a maximal range of measured thickness loss, within which a middle point was taken as representative. Results were assessed against time; first processed so only calculated increases to the maximum level of measured thickness loss were taken into account, then the same working backwards from the last result and calculating the minimum possible value of

thickness loss. Explaining this visually, this has the effect of joining all the peaks and all the troughs, giving two lines between which we know the actual thickness loss must fall (figure 7.44).

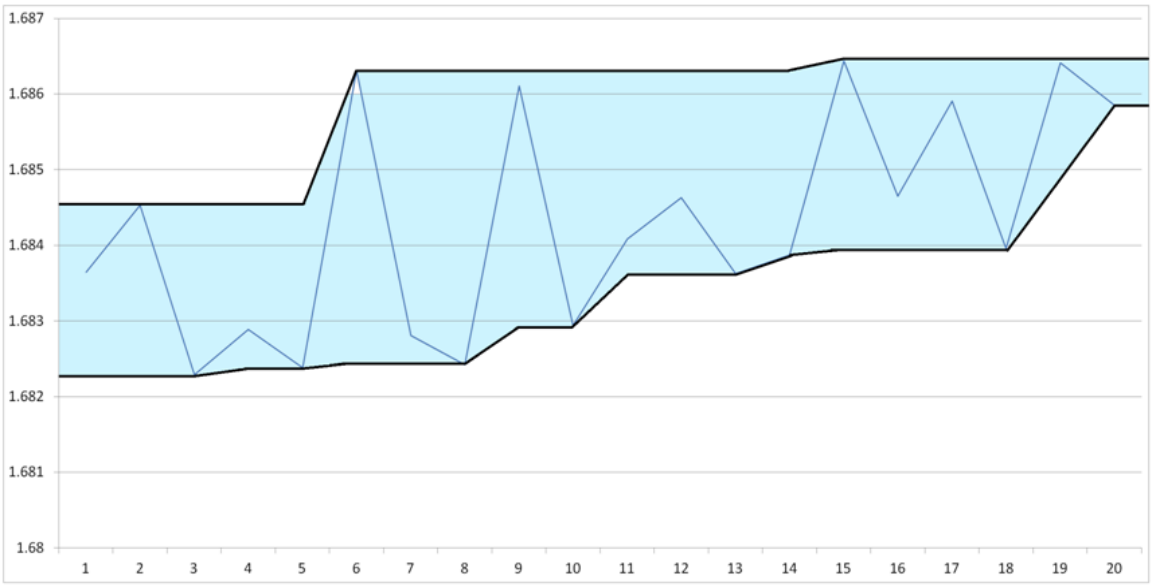


**Figure 7.44**: Graphical example of calculations as applied to thickness loss data. Original data in blue. Maxima and minima calculated lines represented as black lines. Shaded area is the resultant possible range of thickness loss values. The average result was calculated as the midpoint of the maximal and minimal line at any given point in time.

The difference between maximum and minimum thicknesses (the effective noise within the signal) reached a maximum of around 29 nm and an average difference of around 7nm, similar to those observed in the stable corrosion tests. Taking the middle point of the two values gave a comparative value for each measurement, removing the effects of noise, but still taking into account all measured resistances. The statistics for the cleaned data are presented in table 7.26. They do not deviate significantly from the results (reported above) using calculation with the raw data; negative results are removed and overall corrosion rates lowered slightly. Standard deviation and variance between sensors increased slightly.

| Relative humidity | 20% | 40% | 50% | 60% |
|---|---|---|---|---|
| **Average corrosion rate (µm/year)** | 1.46 | 2.61 | 54.90 | 156.66 |
| **Minimum corrosion rate (µm/year)** | 0 | 0 | 19.00 | 95.33 |
| **Maximum corrosion rate (µm/year)** | 8.29 | 9.24 | 83.12 | 204.89 |
| **$Log_{10}$ Corrosion rate** | 0.17 | 0.42 | 1.74 | 2.19 |
| **Standard deviation (µm/year)** | 1.53 | 2.79 | 17.404 | 22.60 |
| **Coefficient of variance** | 1.05 | 1.07 | 0.32 | 0.14 |

**Table 7.16:** Corrosion rates calculated using the full range of possible thickness loss levels from measured results.

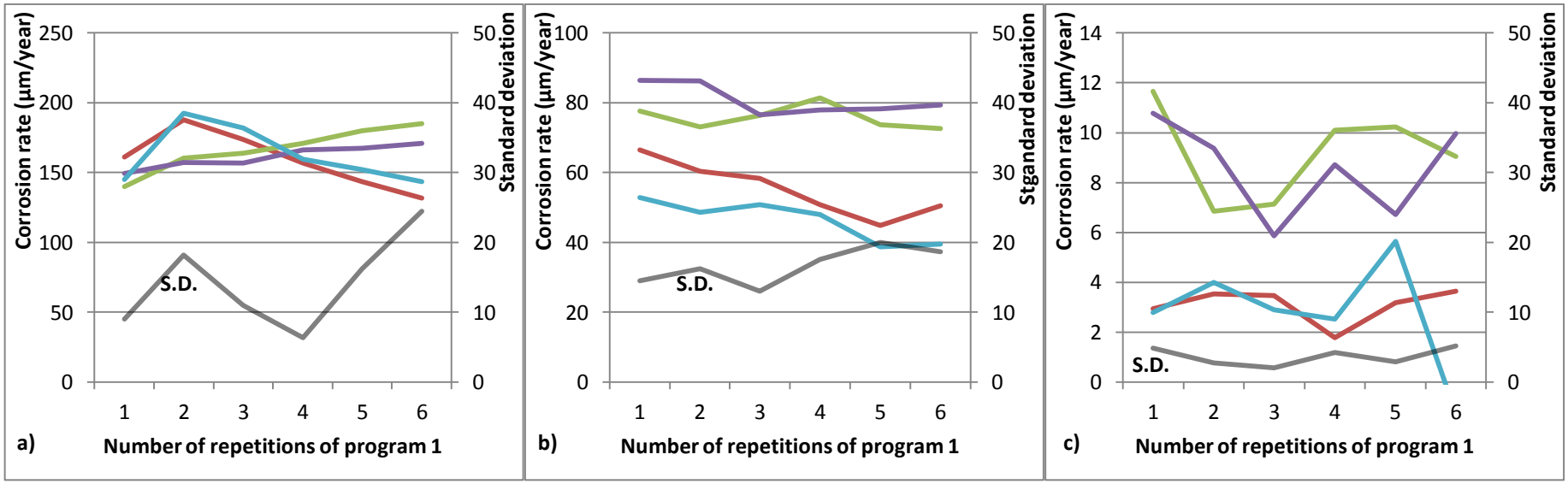


**Figure 7.45:** Graphs of calculated corrosion rates and standard deviation for each phase of higher relative humidity, over repeated repetitions of program 1, at a) 60%, b) 50% and c) 40%

| Sensor | Colour |
|---|---|
| 1 | |
| 2 | |
| 3 | |
| 4 | |

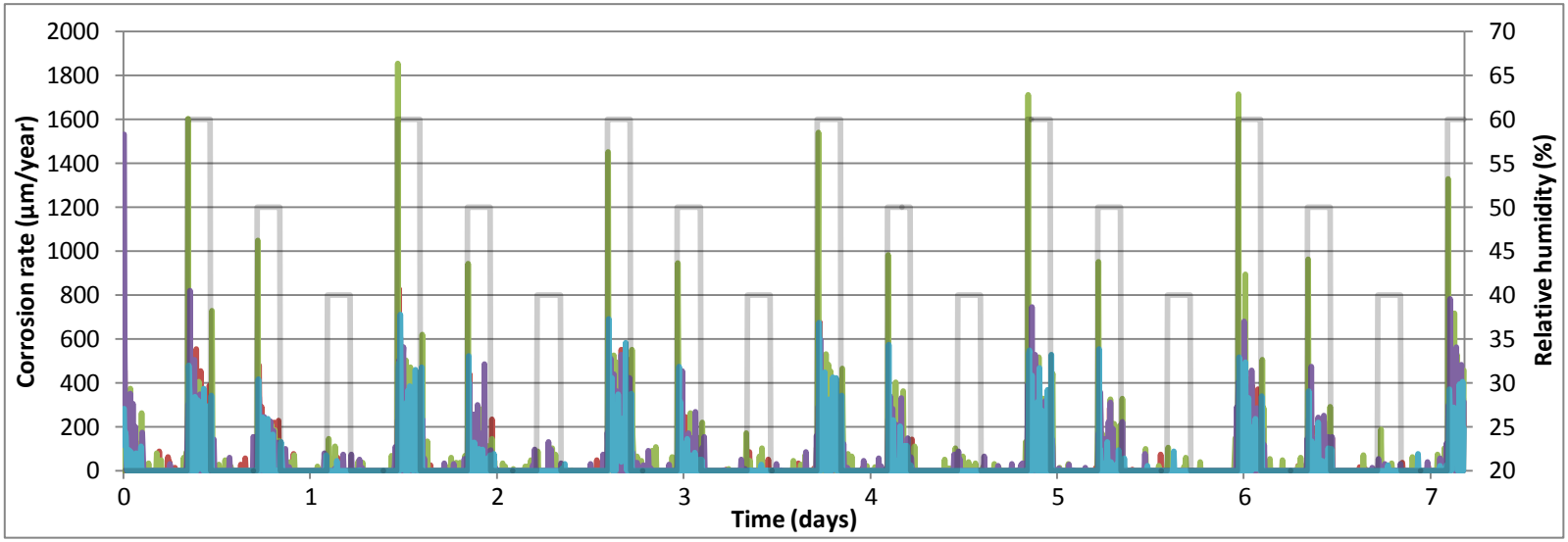


**Figure 7.46**: Graph of corrosion rates calculated for each five minute period, using the average of maximum and minimum corrosion for each point.

The new results allowed calculation of corrosion rates for each 5 minute interval without the skewing associated with negative results, (figure 7.46). They illustrate the change in corrosion rate within each stable phase. While the method leaves gaps (when calculated thickness loss fell between the existing minimal and maximal levels) it serves to highlight differences in corrosion rate within the programmed periods

7.3.3b Program 2: Stepped Increase and decrease in relative humidity

Program 2 increased and decreased relative humidity in stepped, stable periods to test the reactions of the sensors to sudden small increases and decreases in relative humidity and identify differences between the two mechanisms.

All sensors follow the same pattern (figure 7.47); corrosion rates increasing noticeably at the step up to 50% RH and again up to 60%. The rate drops on humidity reduction to 50% and again returning to 40%. Further reduction decrease rates to non-significant levels (figure 7.48). Corrosion rates are significant at 60% and 50% RH, and measurable down to 40% and even 30%. At 20% and 15%, negative rates are recorded in some instances, attributed to the same calculation anomalies as discussed for program 1. Increase in corrosion rate for each level appears similar to those observed in program 1, and at a similar scale as the stable state tests. The figure also suggests that corrosion rates during the decreasing RH section are greater for each stable phase than for the corresponding relative humidity during the increasing section of the program.

Corrosion rates drop for each successive program cycle (figure 7.50), evidence for the creation of protective corrosion products at the metal surface. Sensors 1 and 2 react similarly across both plots, maintaining their corrosion rate at 60%. Sensors 3 and 4 suffer comparatively greater reductions in rate. The latter pair were the most and least corroded at the program commencement. This fits with the mechanisms by which decreasing corrosion rate might occur (discussed in section 7.3.2b), but suggest a more complex interaction. For example, sensor 3 consistently demonstrates relatively higher corrosion rates at the step up to 50% RH, but follows the same pattern as for 60% during the step down to 50%. Sensor 1, while displaying consistently high corrosion rates at high RH, is corroded distinctively more than the other probes during the 'down' phase at 50%. The consistency of these phenomena across program repeats illustrates the complexity of the corrosion process and the multi-faceted relationship between ambient relative humidity and corrosion rate. As in previous tests, the apparent increase in variance over repetitions in figure 7.50 is not borne out by variance statistics, (not reported here), where no changes over repetitions are observed. This may be through the effects of initial corrosion thickness levels, discussed above.

**Figure 7.47:** Graphical representation of thickness loss calculations during program 2, also displaying the changes in relative humidity.

| Sensor | Colour |
|---|---|
| 1 | |
| 2 | |
| 3 | |
| 4 | |

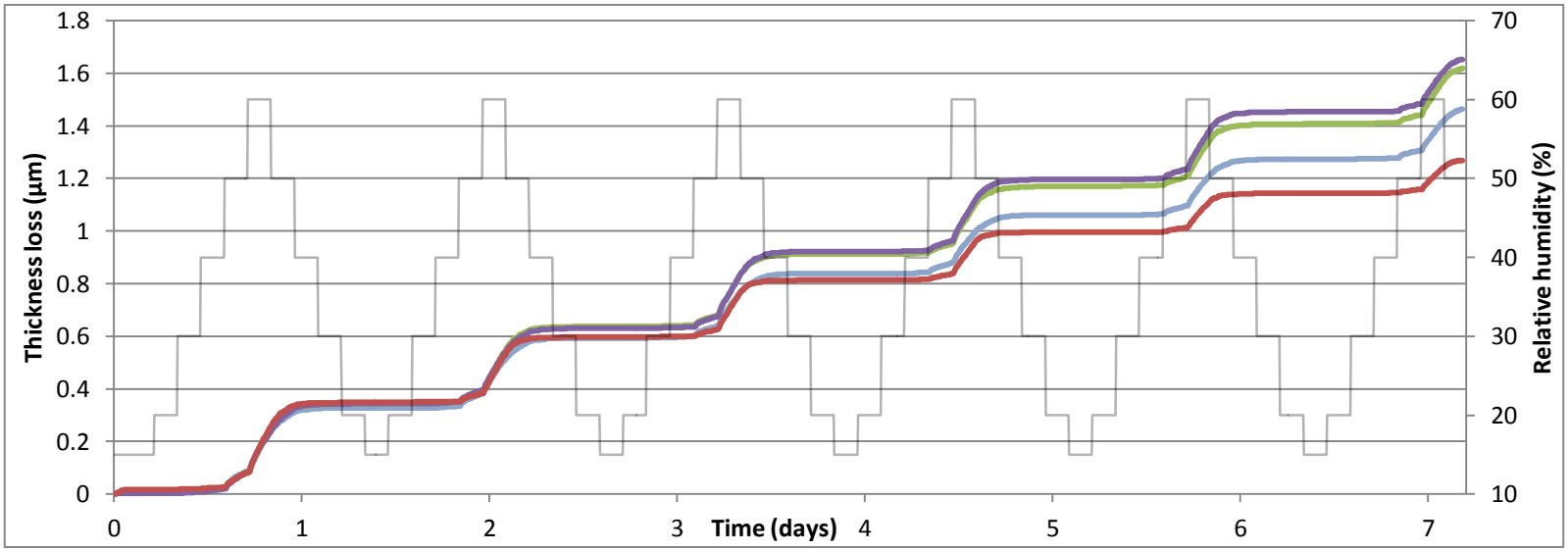


**Figure 7.48:**Graphical representation of corrosion rates for each stage of program one, calculated using the slope of the results for each humidity section in figure 7.49.

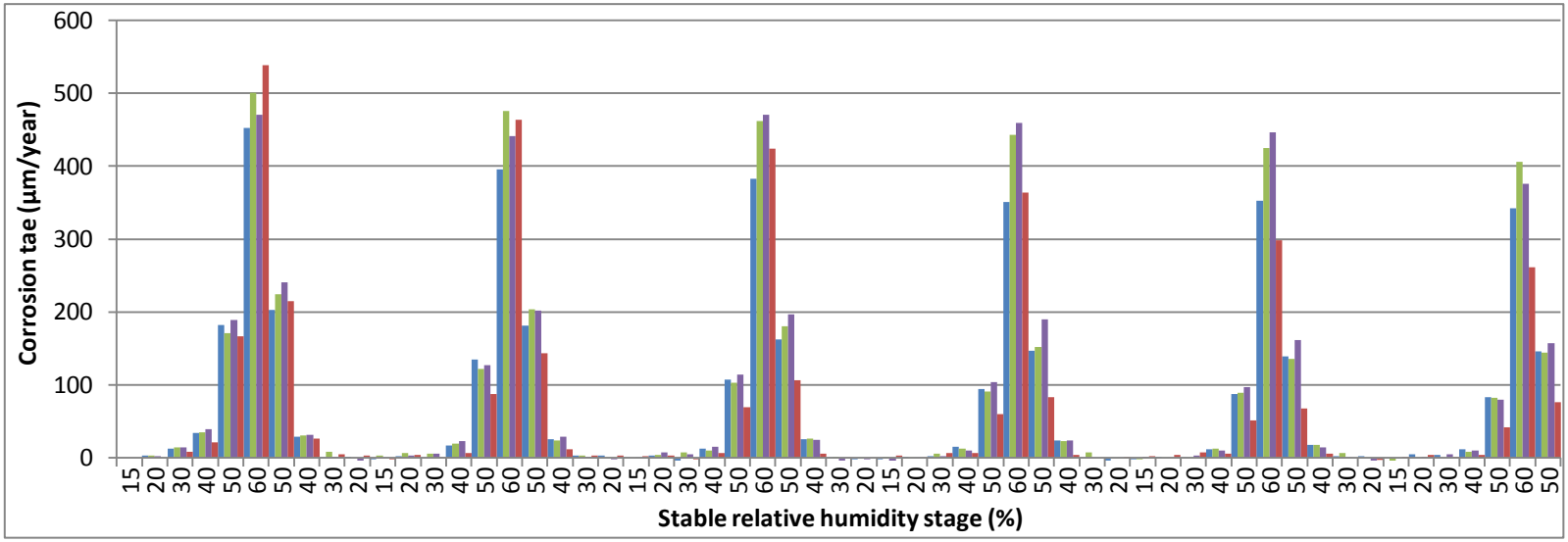

| Relative humidity | 15% | 20% | | | 30% | | | 40% | | | 50% | | | 60% |
|---|---|---|---|---|---|---|---|---|---|---|---|---|---|---|
| ***Phase of Program*** | *Average* | *Up* | *Down* | *Average* | *Up* | *Down* | *Average* | *Up* | *Down* | *Average* | *Up* | *Down* | *Average* | *Average* |
| **Average corrosion rate (µm/year)** | -0.24 | 2.87 | -0.05 | 1.54 | 4.55 | 2.15 | 3.46 | 15.23 | 21.27 | 22.23 | 105.81 | 160.92 | 129.66 | 416.72 |
| **Minimum corrosion rate (µm/year)** | -5.72 | -0.11 | -3.63 | -3.63 | -3.23 | -3.85 | -3.85 | 4.23 | 4.57 | 4.23 | 42.26 | 67.57 | 42.26 | 261.54 |
| **Maximum corrosion rate (µm/year)** | 3.61 | 20.00 | 3.54 | 20.00 | 14.76 | 8.62 | 14.76 | 39.55 | 32.01 | 39.55 | 189.35 | 240.97 | 240.97 | 538.42 |
| **$Log_{10}$ Corrosion rate** | - | 0.46 | - | 0.19 | 0.66 | 0.33 | 0.54 | 1.18 | 1.33 | 1.35 | 2.02 | 2.21 | 2.11 | 2.62 |
| **Standard deviation (µm/year)** | 2.45 | 2.09 | 2.30 | 2.61 | 4.83 | 3.10 | 4.26 | 9.49 | 8.47 | 9.44 | 39.54 | 46.00 | 50.75 | 65.51 |
| **Coefficient of variance** | -10.35 | 0.73 | -50.92 | 1.69 | 1.06 | 1.44 | 1.23 | 0.62 | 0.40 | 0.42 | 0.37 | 0.29 | 0.39 | 0.16 |

**Table 7.17**: Summary statistics for corrosion rates, calculated from the gradient of data within each stable phase in figure 7.49.

| Sensor | Colour |
|---|---|
| 1 | |
| 2 | |
| 3 | |
| 4 | |

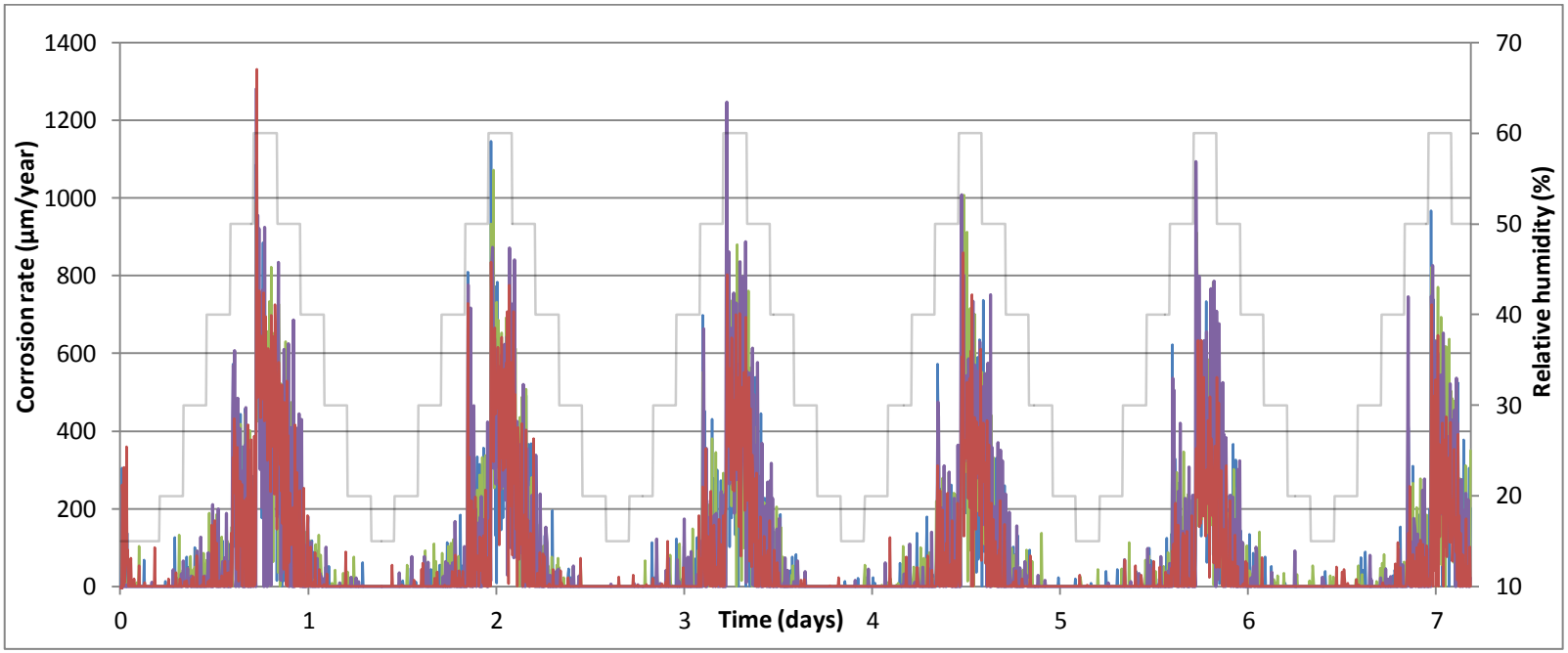


**Figure 7.49**: Graph of corrosion rates calculated for each five minute period in program 2, using the maxima/minima corrosion for each point. Program RH plotted in grey.

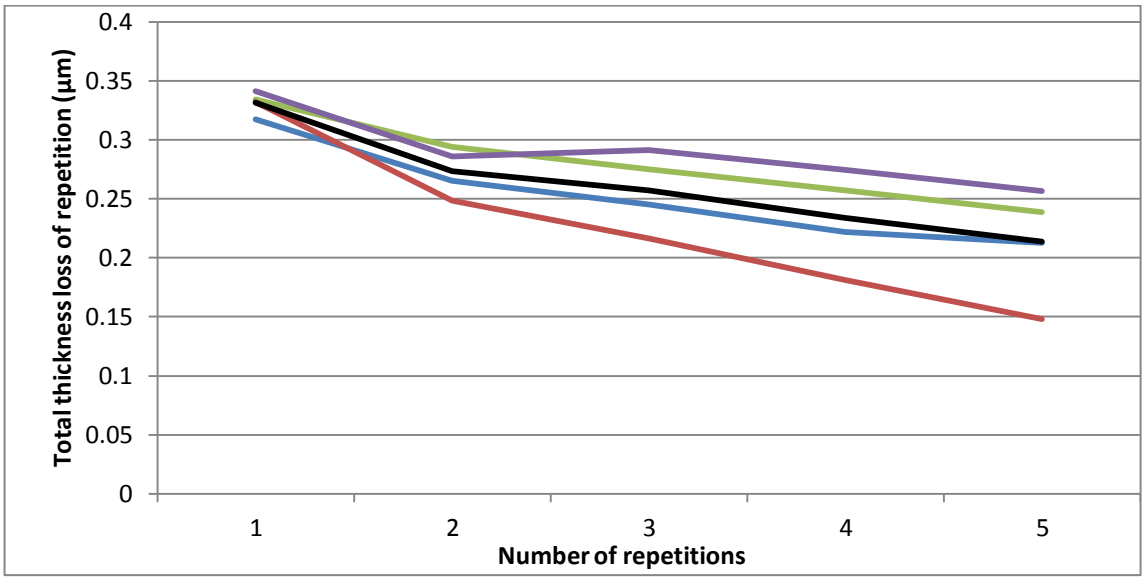


**Figure 7.50:** Change in total corrosion over each repetition. Key is the same as for figures 7.47-49, black line shows average.

To evaluate the differences during the stepped increasing and decreasing phases, both data sets have been considered separately, before combination for comparison with other datasets (table 7.17). This confirms that, during decreases in stepped RH the corrosion rates are significantly higher than during increases in stepped RH at the same relative humidity. This is true at both 40% (a difference of 6.04µm/year or 27% of the average) and 50% (a difference of 55.11µm/year or 42.5% of the average). However, at lower relative humidities, the reverse is true; at both 30% (2.15µm/year decrease) and 20% (~2.5µm/year decrease) rates are lower during decrease. As above, this may be partially attributed to the difference in apparatus performance between increasing and decreasing humidity, but may also be an indication of differences inherent to these step changes.

To explore higher resolution results, the minima/maxima methodology described in section 7.3.3a was applied to remove noise and give corrosion rates for each five minute measurement. Though not reported here, the overall corrosion rates and variances recorded for the data are not significantly different to those of the original data. The results for the whole dataset are recorded in figure 7.49, and for a single repetition in figure 7.51. The humidity increasing steps show a similar pattern as in program 1, evident in figure 7.49 and demonstrated more clearly in figure 7.51. Corrosion rates are highest on initial relative humidity increases at 40, 50 and 60%. These peaks fall almost immediately after the programmed increase in humidity, and are of the same order as those observed in program 1. Corrosion rates progressively fall during the stable phase, with the suggestion that the rate of decrease itself decreases steadily over time. At lower relative humidities, increasing steps are harder to evaluate. At 20% and 30% it would appear that the majority of corrosion occurs late in the stable phase, with increasing corrosion rates in the last hour.

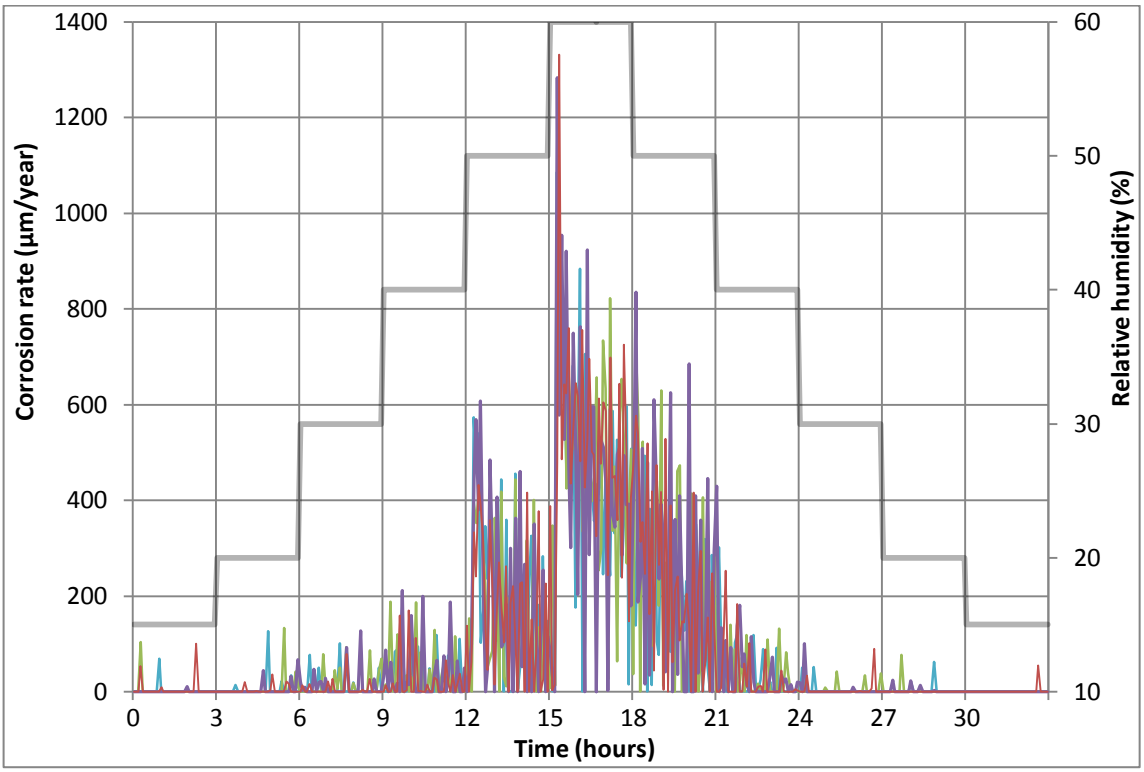


**Figure 7.51:** Plot of corrosion rate data, created using the maxima/minima mid-point methodology, over the course of a single repetition of program 2.

For stepped decreases, the pattern is very different. Instead of a sudden drop in corrosion rate, we observe an immediate and momentary increase in corrosion rate, observed as a peak immediately after the humidity drop. The corrosion rate then returns to a similar level as before and steadily declines, decreasing linearly over the course of the step between 60 and 50% relative humidity, typically dropping by around 200µm/year over the three hours at 50%. Between 50% and 40% the peak and decrease are similar, decreasing to levels around the average of 22µm/year by the end of the cycle. Drops at the lower RH levels were harder to characterise due to the low values, but have been evaluated to follow a similar pattern.

Variance in results decreased at higher humidities, with no significant difference between the 'up' and 'down' phases of the program.

### 7.3.3c Program 3: Progressive rising and falling relative humidity

Program 3 features steady increase from 15% to 60% relative humidity, and back down, to examine gradual increases and decreases in relative humidity affect the ERCM.

**Figure 7.52** Plot of calculated thickness loss against time of sensors subjected to program 3. Relative humidity is plotted in grey.

| Sensor | Colour |
|---|---|
| 1 | |
| 2 | |
| 3 | |
| 4 | |

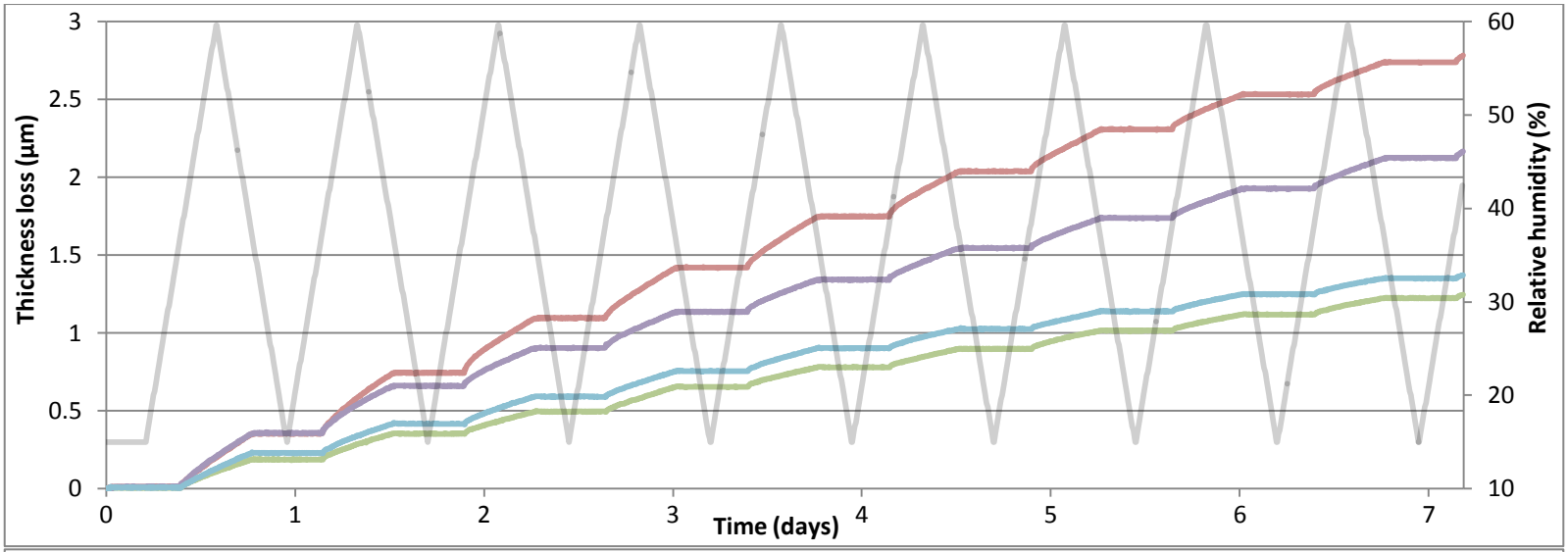


**Figure 7.53** Graph of corrosion rates calculated for each five minute period in program 3, using the maxima/minima corrosion midpoint for each point. Program RH plotted in grey.

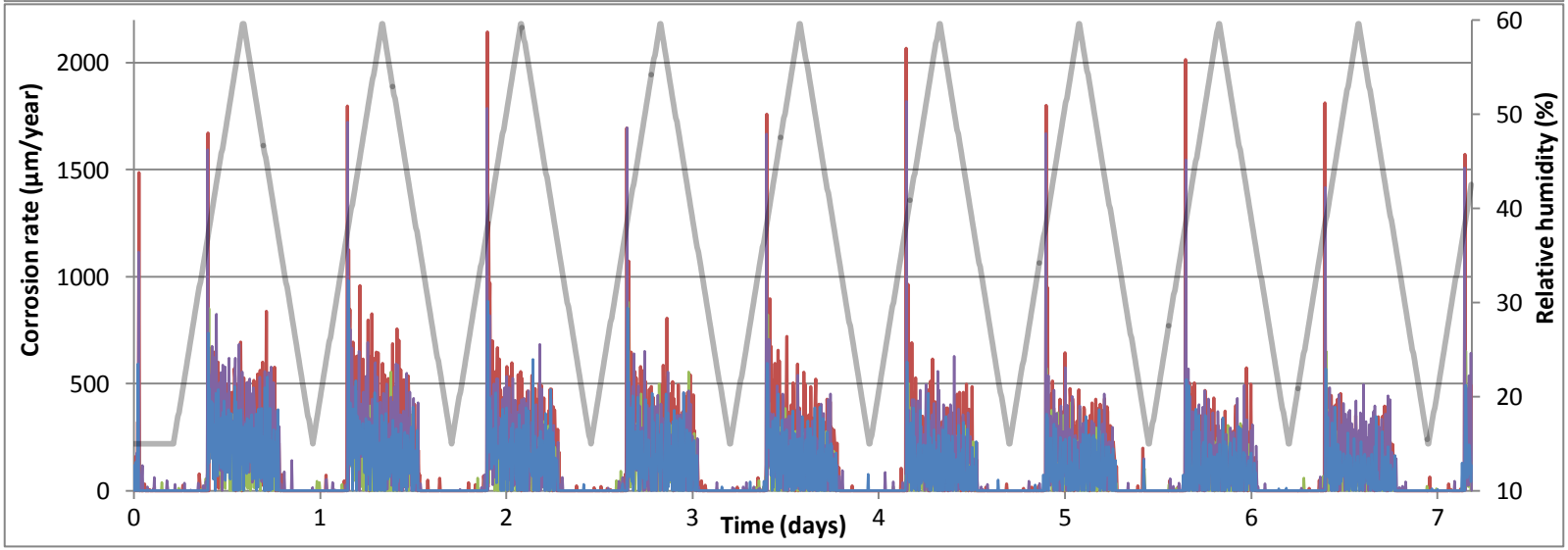

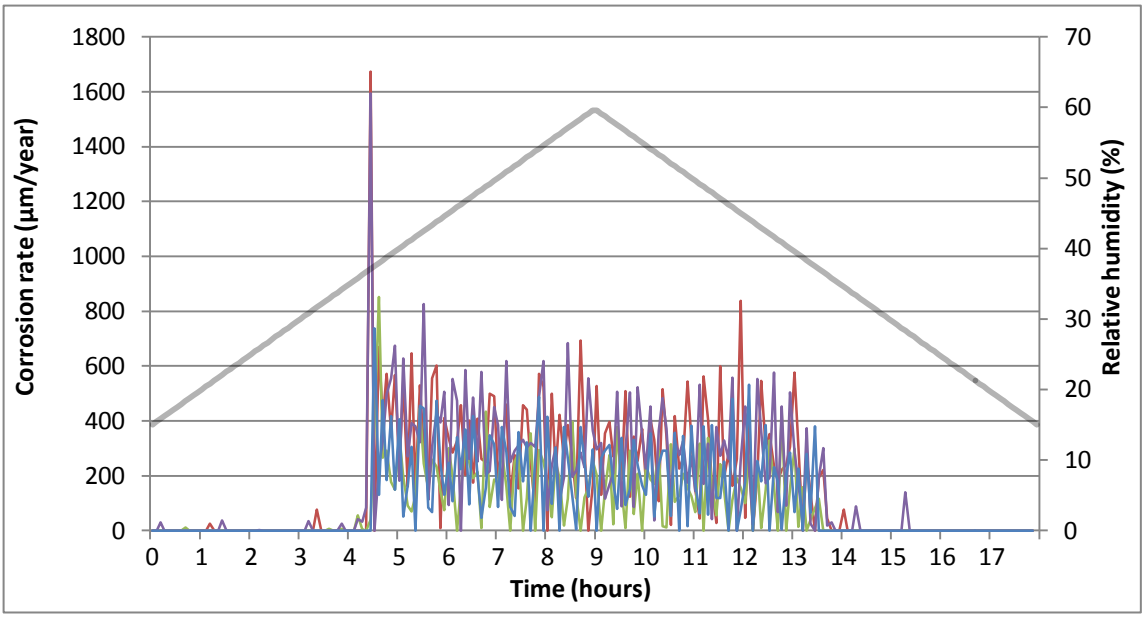


**Figure 7.54**: Plot of individual repetition of program 3, illustrating corrosion rates calculated for each 5 minute measurement, using the maxima/minima mid-points.

Without stable phases it was not possible to plot the corrosion rates in comparison to phases of relative humidity. Instead, corrosion rate within the program has been characterised using the minima/maxima method, to create the five minute interval corrosion rates. These are plotted for the entire monitoring period in figure 7.53, and for an individual repetition in 7.54, allowing more detailed analysis of where corrosion occurs within the cycle.

Corrosion stays at a very low rate, close to the margin of error, on progressive increase of relative humidity (figure 7.52). A very high corrosion rate is recorded as soon as a certain relative humidity is reached. The peak subsides almost immediately and decreases to a level which remains relatively constant as the relative humidity increases to 60% and then subsides. A slight rise in overall corrosion rates, and typically one or two peaks, are observed as decrease continues. There is then a large drop in corrosion rate to non significant levels, occurring at a similar point for each sensor and during each repetition. Increased repetitions are observed to reduce the constant corrosion rates, but not the size of the initial peaks. This happens at the same points for each program repetition and for each sensor. Sensors 3 and 4 react similarly, with low initial corrosion rates in repetition one and ever decreasing corrosion rates for each subsequent. Sensors 1 and 2 maintain higher rates, but also diverge. It is immediately noticeable that the overall loss levels are similar as for program 2, despite lasting for less time over identical maximum and minimum relative humidity levels. Sensors 1 and 2 in particular maintain similar total loss levels as those evidenced in figure 7.50.

The point at which the increase occurred was very slightly different over the course of the repetitions, but always fell between 37% and 38% relative humidity. These differences may be due to the time resolution of the readings. The peaks as relative humidity decreases are

more sporadic, a general increase is observed between 50% and 40% with peaks occurring consistently at around 44%, but also at any point in this range. The decrease in corrosion levels occur at approximately the same humidity that at which the large increase occurs. The decrease is more gradual, with a small decrease observed at around 40%, reaching the lower corrosion rates at between 37% and 35% relative humidity.

The peak corrosion rates occasionally exceed 2000 µm/year, but typically range between 1600 and 1800 µm/year. Their effect on overall corrosion is minimal, as they only last for one of the five minute measurements. Corrosion rates were calculated by using the slope of the thickness loss curve between 38.75% RH (increasing) and 38.75% (decreasing); a length of time over which the vast majority of all corrosion occurred in all sensors over all repetitions. These, and corrosion rates calculated by taking an average of those five minute data from the maxima/minima mid-point method, are plotted in figure 7.5s. They illustrate the similarity of the rates, give comparison to the two methodologies and give an indication of accuracy. The similarities between sensors 3 and 4, and the divergence of 1 and 2 are clear. Corrosion rates vary from 350µm/year to around 100µm/year. These agree with the results plotted in figures 7.53 and 7.54, which have oscillating corrosion rates across centre points of approximately these values.

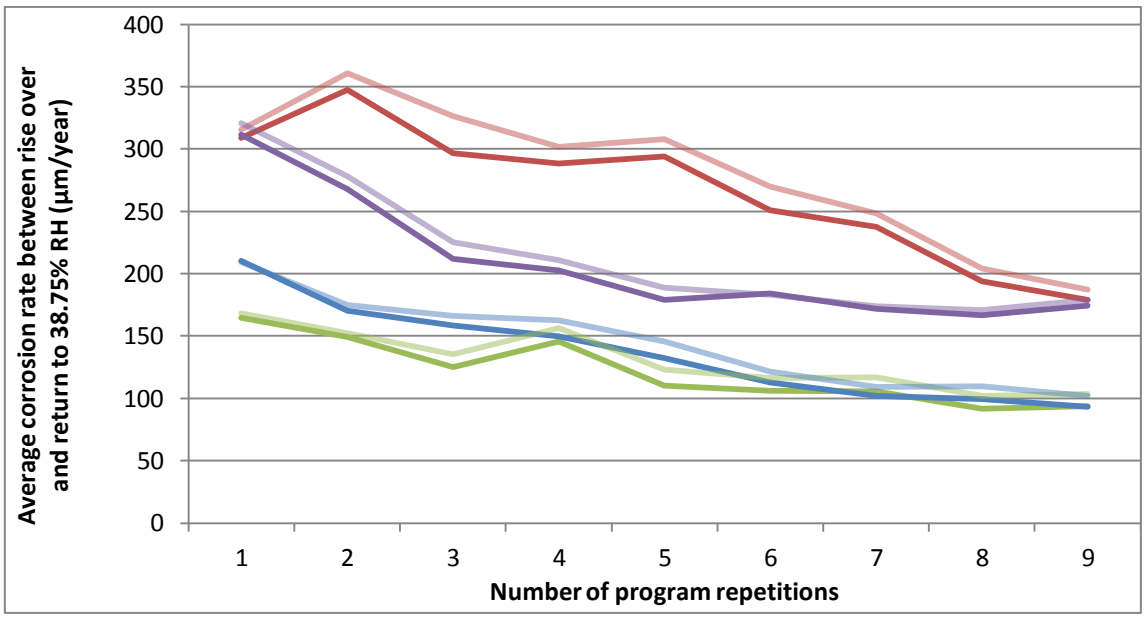


**Figure 7.55:** Corrosion rates for program three during the phase of approximately linear corrosion rate, between 38.75% (rising) and 38.75% (falling). Bold line is calculated from slope of the thickness loss line, faint line from average rates of five minute interval results.

The apparent decrease in thickness loss per repetition is confirmed; lower rates are recorded after each repetition for each sensor. It may be that the stable product created by this form of corrosion is more passivating than previous tests. Despite the apparent disparity, the coefficient of variance of the corrosion rates of the data stays roughly stable after multiple repetitions, indicating sensors continue to react comparatively.

Similarly to previous tests, the corrosion rate takes longer to fall than to increase and initial corrosion increase causes a spike in corrosion rate when a key relative humidity is reached. Disregarding these, corrosion was not as expected. It has originally been assumed that corrosion rate would continue to increase with relative humidity, similarly to the stepped increases of program 2.

### 7.3.4 Non-corroded ERCM in altering environments.

Blank ERCM were created without any pre-corrosion methodology, to provide control readings and illustrate the differences in corrosion rate of the two sets. These ERCM were exposed in the climate chambers concurrently with tests of changing relative humidity levels, monitored by an identical but independent circuit, power supply and multimeter. The probes remained in place throughout all the programs, to allow them the largest variety of humidities. This provided comparison and evidence to demonstrate the necessity of pre-corrosion.

The results (figure 7.46, table 7.16) illustrate the stark difference between blank and pre-corroded sensors. Over forty days of monitoring the maximum thickness loss recorded was 20nm. Taking the data set as a whole, this gave an overall corrosion rate of 0.11 μm/year; the same as stable state tests for the pre-corroded sensors at 20-30%. In contrast, the non-corroded sensors were exposed for twice as long and underwent variation in RH from 15% to 60%, yet corrosion rates are measured as negligible and within the margins of error for the first 17 days. After this point a clear change is noted for two of the probes; Sensors 1 and 2 both increase in corrosion rate significantly, evidenced by corrosion rates over this latter period increasing to 0.1 and 0.2 μm/year respectively. It is not known whether a singular event triggered the change; no obvious spike in corrosion rate or change in the properties of the pre-corroded ERCM can be found in the data. The profile rate is fairly constant for the first 10 days, progressively falling for the remainder of the test run. It may be evidence that a pollutant entered the system, possibly migrated from the pre-corroded ERCM within the same environment. It may also be equipment change; failure of the protective lacquer, for example, which may cause oxidation of the reference electrode.

**Figure 7.56**: Plot off calculated thickness loss over time for non-corroded ERCM in programs 1 to 3. Relative humidity is plotted below, concurrent with the program plots above and scaled identically.

| Sensor | Colour |
|---|---|
| 1 | |
| 2 | |
| 3 | |

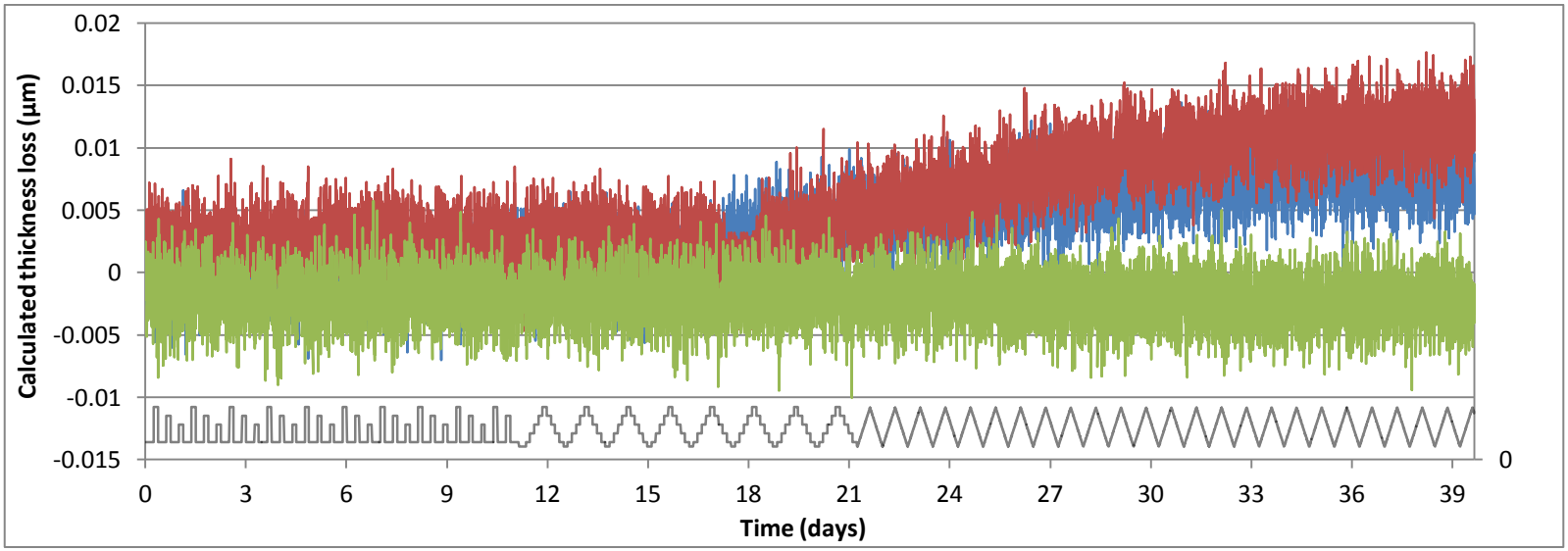


| Sensor | Maximum thickness loss (µm) | Corrosion rate, calculated from slope (µm/year) | Log10 Corrosion rate | Corrosion rate prior to 17 days (µm/year) | Corrosion rate of sensors between 17 and 40 days (µm/year) | Standard deviation of initial corrosion rate (µm/year) | Coefficient of variance of initial corrosion rate |
|---|---|---|---|---|---|---|---|
| **1** | 0.01 | 0.10 | -1.01 | 0.01 | 0.10 | 0.06 | 0.94 |
| **2** | 0.02 | 0.11 | -0.96 | 0.01 | 0.18 | | |
| **3** | 0.01 | -0.01 | - | -0.01 | -0.01 | | |
| **Average** | 0.02 | 0.07 | -1.17 | 0.004 | 0.09 | | |

**Table 7.18:** Corrosion rates and statistics extrapolated from the thickness loss data of non-corroded ERCM in changing environments, plotted in figure 7.56

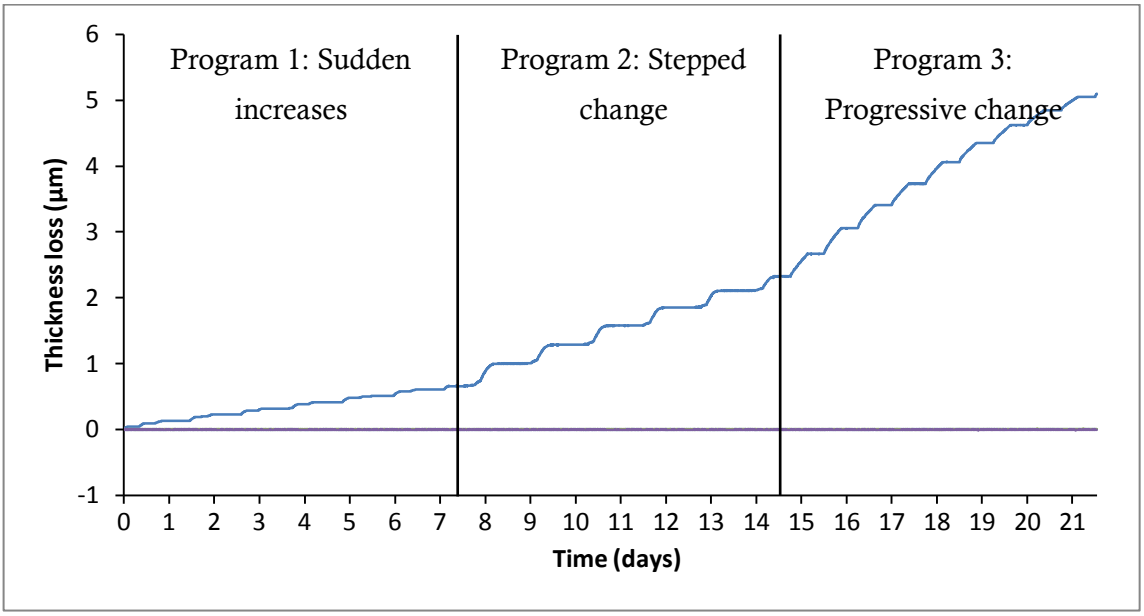


**Figure 7.57:** Plot of pre-corroded ERCM (blue line) and three un-corroded ERCM (purple line) during programmed changing Relative humidity in climate chamber.

Both before and after the shift, the sudden and ramped changes in relative humidity have no noticeable effect on thickness loss (figure 7.56). It may be that small changes in corrosion rate may be present, but are lost within the noise signal. Any increases in corrosion rate are such that they are insignificant compared to the rates for pre-corroded ERCM (compared in figure 7.57). The effect of relative humidity on a pre-corroded ERCM is clear, as is the comparative lack of corrosion of the non-corroded specimens.

Standard deviation and variance were measured of the corrosion rates prior to 17 days, (before whichever event affected two of the probes). The coefficient of variance is higher than for the static tests of pre-corroded ERCM. While this suggests a greater consistency in the pre-corroded ERCM (and therefore a greater degree of predictability), this seems unlikely and may be attributable to the small dataset of the blank tests. The standard deviation remains fairly constant throughout the initial stage, increasing after the 17 day mark. 'Noise' levels are as observed in pre-corroded ERCM, helping to confirm the theory that it is an artefact of the experimental setup and apparatus.

### 7.3.5 Sensors in heritage type environments.

Pre-corroded ERCM were exposed in environments designed to simulate heritage storage, as described in section 6.5. Three variations of the desiccated box were examined, one exposed in an ambient room temperature environment, one in a darkened cupboard and one exposed in the same room conditions, with the lid of the box removed after a set time period.

**Figure 7.58**: Thickness loss curves of pre-corroded and non-corroded ERCM in heritage type desiccated box, exposed on table within standard room conditions.

| Sensor | Colour |
|---|---|
| 1 (Precorroded) | |
| 2 (Precorroded) | |
| 3 (Uncorroded) | |

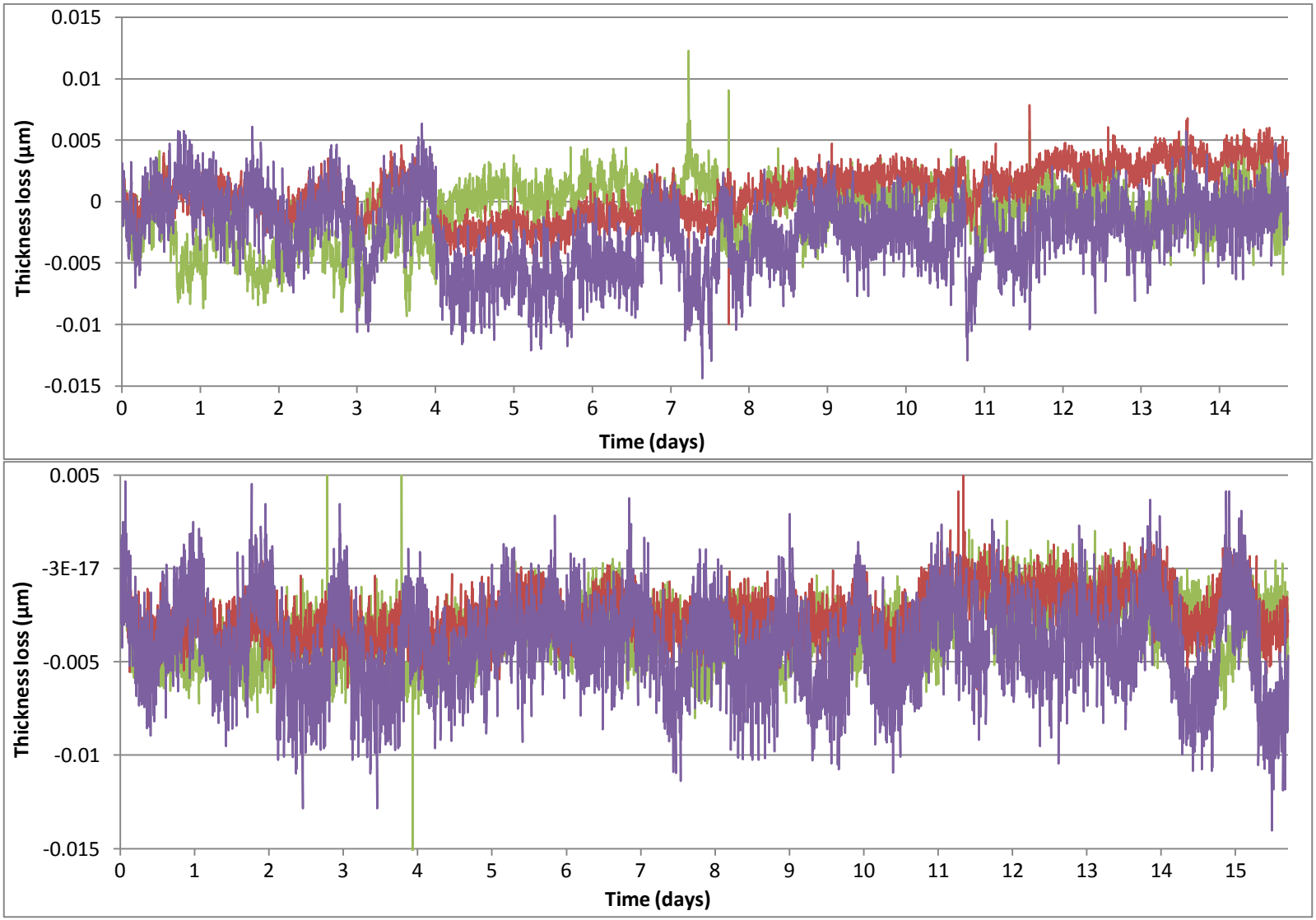


**Figure 7.59**: Thickness loss curves of pre-corroded and non-corroded ERCM in heritage type desiccated box, stored in a sealed and darkened cupboard within standard room conditions.

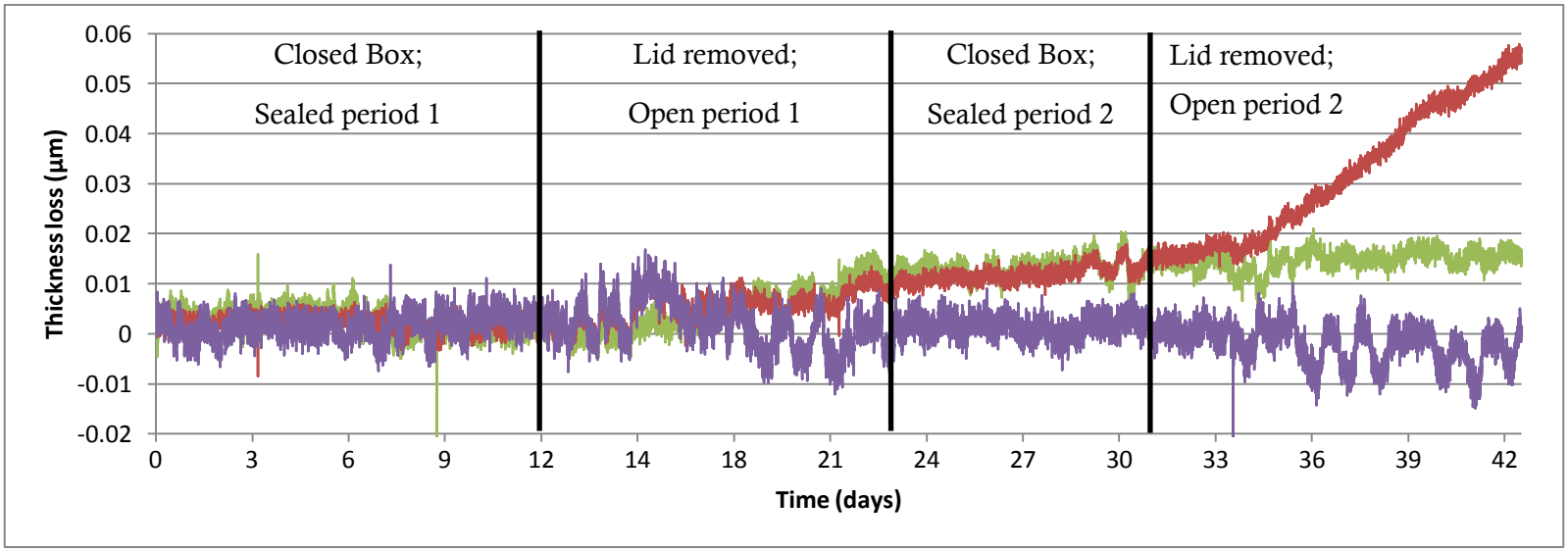


**Figure 7.60** Thickness loss curves of pre-corroded and non-corroded ERCM in heritage type desiccated box, exposed on table within standard room conditions, with lid of box removed and closed for alternating time periods.

| Sensor | Colour |
|---|---|
| 1 (Precorroded) | |
| 2 (Precorroded) | |
| 3 (Uncorroded) | |

| Sensor | Within sealed box | | | | Within sealed box on table, with periods unsealed | | | | | | | | | |
|---|---|---|---|---|---|---|---|---|---|---|---|---|---|---|
| | On table | | In cupboard | | Overall | | Sealed period 1 | | Open period 1 | | Sealed Period 2 | | Open period 2 | |
| | Maximum thickness loss (µm) | Corrosion rate (µm/year) | Maximum thickness loss (µm) | Corrosion rate (µm/year) | Maximum thickness loss (µm) | Corrosion rate (µm/year) | Maximum thickness loss (µm) | Corrosion rate (µm/year) | Maximum thickness loss (µm) | Corrosion rate (µm/year) | Maximum thickness loss (µm) | Corrosion rate (µm/year) | Maximum thickness loss (µm) | Corrosion rate (µm/year) |
| **1** | 0.012 | 0.077 | 0.021 | 0.152 | 0.021 | 0.152 | 0.016 | -0.139 | 0.017 | 0.451 | 0.020 | 0.065 | 0.021 | 0.082 |
| **2** | 0.008 | 0.109 | 0.058 | 0.350 | 0.058 | 0.350 | 0.006 | -0.038 | 0.014 | 0.215 | 0.018 | 0.184 | 0.058 | 1.449 |
| **Uncorroded** | 0.006 | 0.001 | 0.017 | -0.042 | 0.017 | -0.042 | 0.014 | 0.075 | 0.017 | -0.223 | 0.009 | 0.014 | 0.010 | -0.161 |

**Table 7.19:** Summary table of corrosion rates for the 2 Pre-corroded and 1 uncorroded ERCM, calculated from the slopes and maximum vallues in figures 7.58-60, in heritage type desicatted boxes.

7.3.5a Desiccated heritage box exposed in room conditions

Three sensors, 2 pre-corroded and 1 un-corroded, were exposed in the desiccated box and monitored using an identical setup as for the climate chamber tests. Resistance measurements were monitored, identically as previously, for 15 days. Records of internal humidity and temperature were not made, so as to test purely the performance of the sensors in such an environment, without knowledge of contributing factors. Calculated thickness loss from the sensors is plotted in figure 7.58, with corrosion rates calculated from the overall slopes reported in table 7.19.

The observations provide valuable insight into probe performance with variable temperature. Noise levels appear the same, if not slightly reduced, compared to the climate chamber tests. This may be attributable to all the equipment being in the same environment; the same changes in temperature affect all parts of the system. Additional interference is clearly present, with alternating patterns of increases and decreases in resistance ratios. These match to diurnal cycles; higher levels correspond to the periods of most activity within the monitored room, at which temperatures were likely to be highest. Maximum introduced error from this source was evaluated to be around 15nm.

While individual readings would be biased by the temperature dependence, it was judged that over the length of time of exposure and taking into account the regularity of the observed fluctuations, the overall slope would give an accurate indication of change in thickness over time. The un-corroded sensor exhibited negligible levels of corrosion over the monitored time. The two pre-corroded sensors showed overall increases in thickness loss, giving corrosion rates of 0.08μm/year and 0.11μm/year. This would place the conditions as similar to those of the climate chambers held at 30% RH.

7.3.5b Desiccated storage box in a storage cupboard

Subsequent to monitoring in an exposed environment, the desiccated storage box was moved to a confined storage cupboard to examine whether additional shielding from the ambient room environment conferred better stability, and therefore whether this had an effect of corrosion rate or probe response. Monitoring lasted for 16 days, thickness loss is plotted in figure 7.60 and the rates recorded in table 7.19.

Interference, similar and following the same pattern to that observed in the exterior environment, was observed. The magnitude was slightly reduced from the above tests, reaching a maximum of around 10nm of error introduced. This may reflect a greater stability of environment, through lower deviations in temperature.

The corrosion rate for the un-corroded sensor remained negligible, exhibiting a negative corrosion rate. The pre-corroded sensors exhibit increased corrosion rates in comparison to those in the exposed test; 0.15 μm/year and 0.35μm/year respectively. While the measured resistances represent an increase in rate, they are still within the same order of magnitude as the exposed storage box; similar to 30% stable environments.

The difference in noise magnitude and the closeness of the thickness loss to the limits of detection make significant comparisons difficult. From the given results, it cannot be concluded that there was significant differences in thickness loss or corrosion rate between exposure and non-exposure of the storage box.

7.3.5c Desiccated storage box exposed in room environment with lid removed.

The heritage type box was exposed in the laboratory in the same position as for the tests in section 7.5.5a. Monitoring commenced and corrosion observed to ensure thickness loss proceeded in a similar manner and rate as previous. After 12 days, the lid of the box was removed, exposing the ERCM to the room environment. The desiccant was left in place and no other variables changed. After 9 days the lid was re-attached, and an after an additional 10, was removed again. Monitoring was constant throughout this period, to test the effect leakage, malpractice or a drop in desiccant performance can have on sensor performance and therefore corroded iron corrosion rates.

The thickness loss curves are recorded in figure 7.60. The first 12 day cycle showed very similar noise readings to those observed for the identical conditions, discussed in section 7.3.5a. Corrosion rates for both pre-corroded ERCM were logged as negative over the full course of monitoring, but still within the margins of error.

Upon opening of the container, there is no immediate increase in corrosion rate, such as those peaks observed in the altering programs tests. However, after a day or so of monitoring the daily pattern of noise created through temperature variations is noticeably higher than for the closed box tests; up to around 20-25nm of difference between high and low levels. This change is most apparent in the un-corroded sensor, manifested in the highly negative corrosion rate displayed over the entire second period. The two pre-corroded sensors have a smaller increase in noise. In both cases there is an observable increase in corrosion rate, exhibited as 0.45 and 0.22μm/year over the length of the exposure. The majority of this corrosion occurs after five days of the lid being off, possibly indicating the point at which the desiccant began to lose effectiveness. If the rates are taken from the slope of this point onwards instead, they rise to 0.54 μm/year and 0.22μm/year.

Once the lid was reaffixed to the box, noise levels for all sensors immediately fell to similar magnitude as observed over the first period of monitoring. The decrease in corrosion rates

appears to be fairly instantaneous; the corrosion rate for the first 24 hours after the box closure of the two pre-corroded sensors falls to 0.12 μm/year and 0.09 μm/year respectively. These rates remain low over the remaining eight days of closure, though significantly higher than the rates from the first sealed period. This may be continued evidence that the desiccants had become less effective during their exposure to the room atmosphere.

After a total of 31 days from monitoring commencement, the lid was once again removed. Corrosion rates remained stable for the first 24 hours, showed a slight rise during the second day and then diverged. The corrosion rate of sensor two rapidly increased, while that of sensor one rose to levels somewhat below those seen for the first period of the open box, giving overall corrosion rates for the monitored period of 1.45 μm/year and 0.08 μm/year respectively.

The impact of these results on the use of our sensors, corrosion of heritage iron and preventative conservation strategies are discussed below.

# Chapter 8

# Discussion

Isolated results have been discussed in the preceding sections, addressing result validity, variance and initial conclusions. In this chapter, the combined results of this research will be discussed, with respect to the aims of this thesis; the applicability of the inkjet printing methodology to future corrosion tasting, the performance of the ERCM and how they might be used in a conservation strategy for chloride infested heritage iron.

## 8.1 Salt deposition by inkjet printing for corrosion testing

The results of the inkjet printer deposition have shown the final created methodology to be quick, repeatable and sufficiently accurate for our salt loading methodology (sections 7.1 and 7.2). The accuracy of loading was high, with consistent loading density and relatively low error. The deposited crystals were of consistent size and frequency and fitted well to the design as specified within the software.

Our research has indicated sources of error and variables not previously recorded in the referenced literature. Error is increased when varying opacity is attempted, and significant error was introduced from the use of repeat prints. Differences observed in crystal size and distribution at the pattern edges may alter local chloride concentration and cause changes in the way droplets deliquesce or the metal corrodes. These observations influenced the methodology, with prints heavily overlapping the ERCM filaments and the use of repeat prints was avoided.

This study chose to use the simplest form of deposition, a single salt at a single concentration with a single 100% greyscale deposition. Using our improved methodology accuracy and reliability of the deposition was such that the suitability of the method for this study was proved to the satisfaction of the author.

### 8.1.1 Comparison with previous printings and deposition methods.

Our results are directly comparable with the (limited) previous research in inkjet printer salt deposition for corrosion testing. Schindelholz and Kelly [1] used an identical printer and NaCl solution within their research; observing loading densities of $59\pm1\mu g/cm^2$ for 1M NaCl prints at 100% greyscale. A strong linear relationship was established between pattern opacity and deposited chloride density. Observations under scanning electron microscope showed a multimodal distribution of feret diameter frequency, with peaks at 0.5 to $1\mu m$ and a secondary peak spread across 5-$11\mu m$ when examining 40% opacity (figure 5.6a). These peaks were related by the authors to the discrete droplet sizes deposited by the printer. Mi et al. [2] used a different printer and close to saturated $MgCl_2$ solution. A single print of 100% greyscale gave a deposition density of $35\pm5\mu g/cm^2$. Fewer tests were run on reduced opacity/greyscale patterns, but linear correlation similar to that observed by Schindelholz and Kelly is evident.

Our results give a much higher average deposition concentration than both previous studies. It had been hoped that the results would be similar to those achieved by Schindelholz and Kelly, given the similarity of printers and solutions. Possible reasons for the disparity include the increased level of methodology, modifications to the sample input of the printer or differences in software configuration employed in this research. Standard deviations across both studies are identical. While the error in the previous research is considerably lower, this may be attributed largely to this author's preference to use maximum error, not calculated 95% error (reducing our value to $\pm3\mu g/cm$). Comparison with the results of Mi et al. is difficult due to the difference in printer and chemistry of chloride deposited, but we would have expected higher concentration, higher percentage chloride solution to deposit higher chloride concentrations. That the recorded levels are below that of both our own and the other study, allow stipulation that the discrepancy is due to the difference in software settings and hardware, but also indicative of differences in deposition from differing viscosity and mass of solution.

The linear correlation observed for differing opacities, as reported by both studies [1,2], is likewise demonstrated here. The increase in error recorded by this research had not been previously highlighted; perhaps due largely to the small sample sizes in the previous studies. Further investigation is required to sufficiently calibrate the relationship between greyscale (or opacity) and sample error, before the methodology can be employed for precision deposition.

However, it is clear this correlation is strong and would allow, with proper calibration, deposition of precise, predictable and repeatable levels of chloride below the 100% greyscale concentration.

Schindelholz and Kelly report crystal feret diameter frequency to be multimodal for their 40% opacity sample, though only a single result is presented. Comparison is therefore difficult, especially with their small sample size and randomly selected pictures, which fail to take into account the difference in crystal size and distribution at pattern edges. Where comparisons can be made, there is a level of agreement. The limits of detection of our methodology prevent full comparison, as we were unable to observe the primary peak below 1μm. Their secondary peak, however, falls within the ranges observed for our crystal size distributions. In particular, the observed peak is similar to that observed in our own internal, large print pattern. The spread of crystals is much greater and the average size is larger, but this would be as expected for the higher chloride deposition levels and higher concentration represented by 100% black deposition within this research.

The paucity of previous published research using inkjet printers make it difficult to assess how our results compare to those of other research groups. The levels of chloride, crystal size and fidelity of pattern are different, but certainly comparable to both the other studies. This tempts the conclusion that the methodology will produce similar results when applied in a variety of situations, using a variety of printers and methodological steps.

Statistical assessment against alternative salt deposition methodologies are difficult, but qualitative comparison is possible. Against simple droplet deposition of salt solution, the methodology presents significant increases in complexity and cost, but also in control and evenness of distribution. The overall mechanism is similar, but the tiny size of the droplets allows the deposition of smaller crystals, and greater control over distribution. The ability to create any design, down to sub-millimetre resolution, allows far greater flexibility and accuracy than the limited and uncontrolled shape of droplet application. The small size of the crystals, and therefore the small size of the droplets they will initially create on deliquescence and hydration, makes it likely that the spread of additional droplets, shown by Tsuru et al. [3] to inevitably distort and spread manual droplet deposition, will be minimised. Overall spread of the salt crystals from the printed pattern was shown to be no more than 0.2mm around the pattern edge, largely due to printer 'streaking' which can be minimised. Droplet deposition has a tendency to create rings of localised crystals on drying, altering the corrosion dynamics across the footprint of the droplet. Though this effect can be countered by the use of use of ethanol as a solvent, it still creates clusters of crystal nuclei [4-5]. Our methodology creates good consistency of crystal size and frequency across the whole deposition area, illustrated in section 7.1.2d. Where edge states do cause a slight change in crystal density, this may be mitigated by alteration of the pattern size and shape. The small droplet size is also likely to decrease the chances of increased localised corrosion, harmful to our sensors [6].

Droplet deposition may allow for greater accuracy of salt deposition on the surface, dependant on apparatus used and the requirements of the method. Our methodology was repeatedly used to deliver 108 ±9 μg/cm$^2$, though changes in methodology to achieve higher and lower levels (through lower greyscale or repeat prints) were shown to increase this to around ±15 μg/cm$^2$. It is conceivable that a carefully created solution, delivered by micropipette, with very accurate mass and volume measurements, could create greater accuracy than this in terms of weight of salt applied to the surface. However, droplets above 3μl have previously been shown to create clustering of crystals around droplet edges on drying [7], and spread from the initial droplet [3-5]; any deposition using droplets above this size will make it largely impossible to control salt density on the surface in terms of mass per unit area. For our methods, where minimising localised corrosion attack and creating homogenous corrosion products are important, well defined and constant spread of salt will supply better results.

Similarly, placement of individual salt grains on the surface (achieved at sizes down to 50μm when individually placed [8] or down to 10μm when using an aerosol mist [9]) would allow greater control of mass deposited, though with less overall resolution. The problems around the size of the droplets will remain, likely affecting the development of the corrosion products, increasing localised corrosion and distribution of future crystals.

Aerosol deposition is the most similar method to inkjet printing currently in use, depositing extremely small crystal sizes on the metal surface, creating accuracies of down to 1μg/cm$^2$ and homogenous particle distribution [10]. It is conceivable that combined with a mask, this could be used to create very accurate patterns with similar particle size, and possibly even greater accuracy of deposition concentration. The cost and complexity of achieving high accuracy deposition is not known, however. Higher accuracy for low level chloride deposition may be achievable with the inkjet printer using a lower molarity NaCl solution, perhaps approaching similar accuracy as those reported for aerosol deposition. The different salts used by Lobnig et al [10] for their study prevent direct comparison, as crystal formation, electrolyte viscosity and deliquescence will all be different compared to NaCl solutions. It is not known if these results could be repeatable with another salt, though the same could also be said of our results. The studies by Cole et al [7] and Li and Hihara [11] both used NaCl, and while very fine, regular deposition of particles was reported, mass density was not. Continued research into both techniques will allow better comparisons and evaluation of the advantages of both, but for now it is tempting to conclude that the techniques are, broadly speaking, comparable.

Comparison of our methodology to direct exposure of a metal to a polluted, corrosive environment is difficult. While the end result is the same (corroded metal) they differ in the corrosive conditions and mechanisms, frequently creating different corrosion products and phenomena. Pre-corrosion by HCl vapour was used by Kapatou and Lyon [12] to pre-corrode ERCM for examination of heritage iron. The levels of chloride deposited on the surface

(between 0.3 and 1.0mg/cm$^2$) were judged too high, and the methodology too uncontrolled, for this study: The localised corrosion and high corrosion rates the corrosion products and chloride levels produced, compromise the integrity and the lifespan of the ERCM. While low levels of chloride (0.1 mg/cm$^2$) were achieved, the methodology failed to create magnetite on the surface of the corroding iron, a key part of corrosion products as found on heritage iron. Similar methods using a corrosive environment were also evaluated to be too unpredictable in their deposition of chloride and the additional effects which might be introduced. While these methods will still be of primary use when examining high thickness of iron in extreme conditions (such as salt spray chambers to emulate maritime conditions [13] or bulk electrolyte to emulate submerged conditions), the corrosivity of the environment make them inappropriate for use when dealing with devices of this delicacy and with the level of control required for device repeatability.

The deposition or corrosion methodology most appropriate for any given corrosion test or salt loading will depend on the type of corrosion being studied, emulated or encouraged. For the purposes of this study inkjet printing was predicted, and has proved, to be an efficient and effective way of salt loading prior to atmospheric corrosion. The methodology allowed creation of constant thickness corrosion layers, shown to contain all the corrosion products commonly found on heritage iron. For future corrosion tests, suitability of inkjet printing will largely depend on acceptable levels of error, type of corrosion layers required, sample form and complexity of corrosion.

### 8.1.2 Method adaptability

The repeatability of the final methodology produced low error and high consistency (108±9μg/cm²) of salt deposition. The frequency, spread and size of deposited crystals were ideal for our atmospheric corrosion tests, leading to the exact corrosion products and thicknesses we had aimed to create to emulate heritage iron. The methodology is undeniably effective at depositing this set level of NaCl, using this solution concentration. For future applications, changes to the methodology will likely be required; to provide varying levels of varying salts and molarities, different designs, onto different substrates and using different methods of subsequent corrosion or testing.

Within the guidelines of our present methodology, alteration in design and concentration of salt deposition were achieved. Change in design is easy, using the vector driver software provided with the printer. Alteration of the pattern on screen created direct alteration of the pattern deposited. While this lends itself to a wide variety of possible black and white designs, there are some limitations on size and shape. Crystal size and frequency changes at the pattern edges, most pronounced in patterns and designs of small lateral width. This will increase salt

concentration variability and error in intricate or small designs. Small variation in horizontal spread must also be taken into account.

Alteration of the level of greyscale was used to deposit lower levels of chloride, with a linear relationship clearly observed between program greyscale percentage and concentration of deposited chloride. The results illustrate deposited chloride concentration may be finely tuned; there is no reason to believe that the levels could not be controlled to deposit as many concentrations as there are software supported shades of greyscale. While percentage error increases at lower levels, additional methodological steps may improve this. The use of lower molarity NaCl solution would also allow printing of lower concentrations on the surface, not attempted in this study. Future work numerically linking the concentration of the sodium chloride solution to the levels of deposited surface chloride would allow greater calibration. Combined with printing lower intensities, this could allow lower concentrations to be printed with greater accuracy and control.

Increased levels of NaCl were achieved through repeat printings, but showed a high level of variance and deviation from expected values, attributed to removal of salt crystals during additional prints. A similar phenomenon, 'smearing' of the previous salt layer, was recorded by Mi et al. [2], though no subsequent evaluation of chloride levels was conducted to quantify or evaluate the effect to chloride concentration. The level of error prevents endorsement of the use of multiple prints to increase chloride content, unless sufficient alterations may be made to the print process to allow more consistent and predictable chloride levels to be deposited.

An alternative to repeat printings would be to increase the concentration of the electrolyte within the printer sump. This raises its own problems. Initial tests of the printer used 4M NaCl solution, as reported in section 6.2.2. In addition to the introduced errors discussed there, the concentration caused corrosion of the internal working of the printer, causing the eventual malfunction of one printer and a requirement to substantially clean another. While it may be possible to increase the electrolyte concentration from the 1 molar used in our study to an unknown level below 4 molar, there will be a level at which the error and damage caused makes the methodology untenable. Without significant alterations or the acceptance of severe error, the methodology will be inappropriate for deposition of higher levels of sodium chloride concentration.

Assuming maximum deposition of NaCl solution of 110μm/cm$^2$, beneath this level of concentration there are almost limitless variety of designs and concentrations which would be possible using varying molarity solutions and greyscale percentages. Designs could be created combining a variety of greyscale shades, creating regions of higher and lower chloride. Differing concentrations of electrolyte could be inserted into the other coloured ink sumps, unused in our own study. Using shadings of opacity (the colour equivalent of greyscale) would allow the methodology to supply greatest accuracy of deposition by selection of the most

appropriate molarity for each required level. Additional investigation is required to ensure opacity follows the same relationship as greyscale, but it is unlikely the relationship will not be similar, if not identical. Unpredictability and possible error may be envisaged at the boundaries between different concentrations, but it is unlikely the errors will be greater than those seen in the edge conditions in section 7.1.2d. Further testing and research would allow proper evaluation of these factors. Within these constraints, the limits of the vector software and the dimensional accuracy mentioned above, complexity, and therefore adaptability, of design is almost limitless.

Future applications of the methodology will depend on variables which haven't been examined as part of this study. A key part of this will be demonstration that the methodology outlined here is applicable for the deposition of different salts. Using inkjet printing, Schindelholz and Kelly [1] also printed NaCl solution, while Mi et al. [2] deposited $MgCl_2$. $(NH_4)_2SO_4$ has been deposited by aerosol deposition [10], a methodology similar enough to make it likely it would work equally well in an inkjet printer. It is likely that almost any dissolved salt electrolyte would be appropriate for use in this methodology, up to a given concentration. At higher concentrations the error incurred, through deposition of a salts from solution and viscosity, and the damage incurred to the printer from solution causticity, corrosion and salt deposition, will make the methodology unacceptably flawed. This was observed through attempted deposition of NaCl at 4M concentration; it is likely that the critical molarity for other salts will be dependent on the solution properties above.

Mixture of different salts could be achieved either through preparation of the electrolyte, or printing from multiple sumps. Mixture of multiple salts in a single electrolyte is likely to change the solution properties, effecting the maximum printable salt concentration. More flexibility would be created by filling different sumps with different electrolytes, controlled using different opacity and colour settings through the software. The intricacy and shades that this could achieve will be constrained by the software and any changes that affect crystal deposition in the presence of multiple salts. Further investigation is required, utilising titration methods to examine deposited concentrations, microscopy to examine crystallinity and possibly electron dispersive X-ray spectroscopy or Raman microscopy compositional analysis of deposition patterns.

Altering the solvent to allow different deposition patterns of crystal deposition is also theoretically possible, and might serve to prevent internal corrosion of the printer. However the chemistry would have to be carefully chosen. Whilst ethanol might give greater spread and smaller size of crystals, the effects this may have on the plastic of the sump and printer components (dissolution, stiffening, loss of plasticity and crazing) would have to be examined. Prolonged use may cause weakening or even equipment failure. Other solvents may have a similar effect. The simplicity of using water, and the low levels of corrosion observed on initial deposition, infer that for the majority of applications, simple aqueous electrolytes will suffice.

Sample size using the present methodology is limited to a sample which can pass through the print CD mechanism; a sample smaller in width and length than a CD and up to around 4mm in depth. It is conceivable this could be expanded to allow a greater variety of samples. Removal of the lower portion of the printer, calibration of the hardware drivers to remove the sensors and mounting of the whole on a sliding rig would allow greater freedom of deposition. Simple connection of the paper feed to a moving stage beneath would allow printing of samples as thick as could be accommodated and lateral sizes up to the size of an A4 page, without large alteration of the driving software. Further programming could force the printer to deposit over much larger surface areas, limited only by the movement of the sample (or a rig holding the printer itself) and how this could be coupled to the driving software. Changes on this scale would require recalibration of the printer, especially with any change in distance between nozzle and sample. The added complexity and cost is also likely to prevent fruitful investigation.

### 8.1.3 Future applicability of inkjet printer salt deposition

The previous discussion has illustrated the effectiveness of our developed method for depositing NaCl (up to a certain concentration) onto small samples, and the potential for the methodology to be expanded to deposit different salts onto larger samples, in designs of varying concentrations and chemistries.

For future applications, additional factors must be considered. For each test or application, shape and size of pattern must be examined; prediction of chloride levels for repeat prints may not be as directly related as expected. Pattern opacity or greyscale levels allow good prediction of chloride deposition intensity, but increased error requires testing of printed levels to confirm forecasted levels. While the author agrees with previous research that the technique has potential to deposit a precise level of chloride with specified crystal size and distribution [1, 2], it also requires careful calibration for each printer, greyscale or opacity, solution chemistry and methodology. Additional considerations will also be required for different salts. While methodological development is required, the potential is clear for applications in future salt deposition.

For atmospheric corrosion testing requiring salt loading, the methodology is ideal. The deposition type is similar to that expected from atmospheric or bulk solution deposition of pollutants, dependant on electrolyte concentration. Deposition of individual droplets using inkjet methods has been previously demonstrated by Mi et al [2]. The use of multiple depositions of salts in intricate designs could also be used to examine subterranean deposition of pollutants, such as might be found in the intensely localised and varied environments of

soil. Designs could be created to emulate a variety of complex interactions of salts on a surface, with a variety of edge conditions and interactions within a single design.

Future academic applications could include examination of corrosion mechanisms from the point of contamination, during corrosion or in a set environment after a given level of pre-corrosion has been achieved. ERCM from this study would allow specific levels of thickness loss to be achieved during pre-corrosion, allowing methodologies for sample loading to be directly calibrated. Corrosion type could be altered using various salt depositions, in patterns and combinations decided by applied pattern. A strategic approach using knowledge of corrosion mechanisms could match conditions to desired products.

Tested environments will be limited to atmospheric for samples which have simply been contaminated. Submersion would result in dissolution and loss of pollutant from the surface; likewise for subterranean testing. However, after pre-corrosion, where much of the salt will become contained or incorporated within the corrosion products, monitoring could be applied to either environment

Pre-corrosion for tests of this kind would suite corrosion monitoring methods including visual, gravimetric, electrical resistance and respirometric techniques. Electrochemical techniques adapted for atmospheric monitoring (see section 4.3.3d) could also benefit. Samples could be used for academic study, to examine specific corrosion problems, and to act as analogue monitors of existing corroded or contaminated metals.

Outside of corrosion testing, the salt deposition methodology has other potential applications. It is not within the remit of this study to explore them all, but is perhaps worth mentioning a conceived few to emphasise the possibilities without corrosion and conservation. A variety of deposited salts in a pattern atmospherically corroded onto sheet metal or metal interwoven with fabric could create evolving artworks of varying colours. Similarly, the precision of deposition could allow the creation of designs and works to be ‘corrosion etched’ into metals for commercial sale. Deposition of salts onto biological samples would allow precise measurement of reaction to given solutes or create precise colonies of bacteria which thrive on given salts. Deposition onto a surface of a variety of salts which change colour on reaction with specific chemicals would allow the creation of simple and cheap chemical test strips. This flexibility of technique and the range of applications is reflected in the use of piezoelectric printing in other disciplines, from depositing micro-particles to creating circuitry to complex polymers (see section 5.3.2). For salt deposition in corrosion testing, this research has served as an extended feasibility study, illustrating the efficiency, effectiveness and quality of the technique. It has met and surpassed the methodologies asked from the technique and can be fully recommended for further study, applications and research directions.

## 8.2 ERCM Manufacturing Error and Corrosion products

The manufacturing and pre-corrosion methodologies created ERCM with low levels of fabrication error and extensive continuous corrosion layers over the surface of the active electrode. The specific errors and the reliability of the manufacturing were discussed in chapter 7. Fabrication error was observed and calculated to reach a maximum level of 1.4%. Variation in chloride concentration on deposition was $\pm 9\mu g/cm^2$. Pre-corrosion methodologies introduced significantly more variation in the sensors. Corrosion loss over the course of the methodology ranged from 2.11 to 5.01μm. This was combated by selecting those which had lost between 2.8 and 3.2μm in thickness where possible.

The effects of the errors can be seen within the thickness loss curves of chapter 7, with non-identical results generated. The variance between the sensors is discussed in section 7.3.2b. The scale of differences between sensors in the same environment is insignificant compared to the scale of difference between different relative humidity atmospheres. While errors may create a difference observable in our results, and therefore how the sensors will be used, they are not great enough to prevent the methodology from giving clear indications of corrosion rates: The error scale is such that the problem will lie in calculating corrosion rates for monitored iron, not as indication of the corrosivity of an environment. The methodological steps which can therefore be taken will be discussed below in section 8.3.

Optical examination of the corrosion products created by our methodology showed good adhesion and complete coverage of the iron surface. Closer inspection using scanning electron micrographs allowed examination of the structures and thicknesses of corrosion product created, with all samples showing similar phenomena. Most importantly for probe operation, the integrity of the iron core is maintained for every examined sample. While there are points of localised corrosion, excessive pitting corrosion or other phenomena which might create an open circuit are not present. It is unlikely any of the forms observed would affect the working circuit of the ERCM or effect the linearity or fidelity of results.

The progression of corrosion is mapped by samples from different stages of the methodology. Areas of localised corrosion are evident after a single wet/dry cycle, characterised by metal consumption linked with bulbous corrosion products. Subsequent cycles produce a layer of approximately even thickness across the surface, joining up the areas of increased corrosion and increasing in thickness and coverage for each consequent cycle. After three cycles the amount of surface covered exceeds the amount uncovered. At four, the coverage is almost complete. Beneath this product, metal is consumed evenly and proportionally to the amount of corrosion product produced.

The thicker layer of corrosion product appears more analogous with that commonly observed on archaeological iron. Lateral cracks and pores are more pronounced and prevalent,

especially associated with voids (fig. 7.24c) and running vertically from the metal surface (fig. 7.24d). These will provide electrochemical pathways between the exterior of the corrosion products and the metal surface, similar to those discussed in archaeological corrosion layers from buried and chloride infested artefact [13,14], discussed in chapter 3. The layers themselves appear to have two distinct phases, a more diffuse and fragmented under layer close to the metal surface, with a denser and more amorphous upper layer. The slight difference in shade between the two regions indicates a difference in composition. No definite conclusions may be drawn without regionalised compositional analysis, but it suggests a separation of corrosion product phases into distinct lateral layers, as observed in archaeological iron.

Occasional bulbous features filled with crystalline structures do occur on various samples, apparently un-connected with areas of corresponding localised metal consumption (figs 7.21 a,b & c, 7.22a). The increased volume and elongated crystals may indicate the crystal as akaganeite. These may be evidence of individual droplets, formed around the nucleus of a particularly large salt crystal and creating a persistent and concentrated droplet. The final evaporation of the droplet at low humidity (for example prior to preparation for the SEM methodology) would preferentially deposit the bulkier mineral, through high concentration of chloride and low oxygen. If so, the product would closely mimic phenomena observed on archaeological iron. Micro-compositional analysis would be required to confirm this.

Compositional analysis was performed, though without examination of individual parts of the corrosion layers. Instead, XRD examined the bulk of the material, while Raman analysis provided multiple samples of the surface. These two analyses provided differing results, but both illustrate the presence of corrosion products commonly found on heritage iron. After the full four repetition pre-corrosion methodology, both x-ray diffraction and Raman spectroscopy detected goethite and lepidocrocite corrosion products on the foil iron surface. Akaganeite and magnetite were detected with good consistency on full term samples by Raman spectroscopy, though not with x-ray diffraction. Raman spectroscopy also suggested the possible presence of ferrous hydroxychloride. The errors associated with prolonged Raman exposure were discussed above.

The results gained from x-ray diffraction and Raman spectroscopy support each other, while also offering discrepancies. The disparity in results may be indicative of the sampling variance for each methodology. Raman microscopy has a low penetration depth; x-ray diffraction would likely have penetrated the whole sample, evidenced by the extremely strong peaks for the metallic iron on the sample spectra in figure 7.27. While this may reveal underlying corrosion products not present at the surface, the larger peak may also obscure less abundant corrosion products with weak diffraction signals. This may explain the absence of magnetite and akaganeite from x-ray diffraction spectra and identify them as less abundant than lepidocrocite and goethite. The differences may also be due to the small size of crystals

involved. During Raman analysis, many samples failed to show any peaks in each spectrum. While in many cases this was interpreted as an effect of surface roughness, it may also indicate poor crystal formation; it is possible the corrosion products' scale (up to only around 10 μm) allows formation of fully formed crystals. The likely presence of HCl within the corrosion layers when hydrated would exacerbate this, further disrupting crystal growth [15]. The majority of the formation products may be amorphous and therefore not detected using the two methodologies applied.

While analysing the model of corrosion during the pre-corrosion methodology is not the aim of this study, the disparity in the x-ray diffraction results between a single repetition and the full four repetition methodology bears additional analysis and a suggested model. With the amount of chloride on the surface, it is likely that initial wetting of the iron foil leads to electrolyte thickness great enough to bear similarity to bulk aqueous corrosion. On drying, conditions and chloride levels will overwhelmingly favour akaganeite formation, depositing as a solid, fairly continuous layer of corrosion product. Subsequent wettings, created by re-exposure to the high RH environment, form a disrupted electrolyte, with corrosion processes separated and regionalised. More diverse conditions lead to a greater variety of corrosion products and areas of lower chloride content, especially where much is bound up in akaganeite. This may also be evidenced by the presence, through Raman spectroscopic readings, of ferrous hydroxychloride, which forms only in high chloride (above 1.5M or 20% by weight), low oxygen environments. This would imply microenvironments have formed within the corrosion layers, prohibiting oxygen supply to certain areas. That the product was only found once and in combination with lepidocrocite and akaganeite may show the mineral was progressively oxidising to akaganeite; its presence may be short lived after removal from the pre-corrosion chamber. The low levels of oxygen during the pre-corrosion are also evidenced by the levels of magnetite found by Raman spectroscopy; preferentially formed where oxygen supply is low.

The differing concentrations of goethite and lepidocrocite, especially apparent from Raman spectra, may be also due to the higher chloride levels. Goethite can be deposited preferentially to lepidocrocite where high levels of chloride are detected, but without sufficient free chloride or Fe(II) to create akaganeite [16]. Akaganeite re-deposition and solid state transformation typically favours goethite production [17-18]. High levels shown after one repetition combined with falling levels in later XRD spectra providing possible evidence for this action. As discussed above, it may also merely be indicative of methodological bias between the surface and bulk compositions in Raman spectroscopy.

Regardless of the disagreements, or the precise manner of the pre-corrosion system, the techniques show evidence for all four of the hoped for corrosion products on the surface of the precorroded ERCM. For the purposes of this study, the pre-corrosion methodology was

adjudged sufficient to emulate archaeological iron corrosion products, assuming the corrosion rates achieved by ERCM were similar to actual archaeological artefacts in the same environment and high sensor performance was achieved.

## 8.3 Pre-corroded ERCM performance and variability

The corrosion rate data gained from the stable environment tests provide indication of the corrosion rates we can expect in similar external and uncontrolled environments and allow comparison with archaeological iron samples from identical environments. They also provide proof of concept that the sensors as created will work in low corrosion environments.

Probe failures were rare, occurring in two monitoring environments, attributed to wiring issues in both instances. During methodological testing, additional failures were associated with failure of the protective coating. This resulted in methodological change from epoxy resin coating to clear protective lacquer, preventing any repeats. Overall, failure rate was low and traceable; the sensors provide very good reliability when properly deployed.

The similarity of results between sensors in the stable relative humidity corrosion chamber tests allow the best opportunity to evaluate performance As discussed above, it can be assumed that the majority of sensor variance is due to the reaction of the corrosion products to the environment, through initial differences arising during pre-corrosion and those caused by exposure to the environment itself. Those data from the dynamic tests included the additional variable of changing conditions, making variance, as opposed to corrosion rate, difficult to evaluate. Roughly speaking, each set can be seen to increase in variance over time, similarly to the stable conditions. This uncertainty makes it simpler to discuss only the stable state corrosion data here, but the discussion will be no less relevant to the variability of the ERMC in dynamic conditions or when deployed in heritage environments.

It should be noted that the results from the 15% relative humidity tests have been discounted for the discussions of accuracy and variance. No noticeable corrosion occurs at 15% relative humidity, certainly none above the multimeter noise signal.

Within the stable state thickness loss data, the standard deviation of the calculated corrosion rates show large rises with increasing relative humidity; unsurprising, considering the order of magnitude corrosion rate increases. The coefficient of variance provides a better indication of the variety in results at each humidity (table 7.14). The highest variation occurs, observed in figure 7.38, at 60% RH. For the lower relative humidities, there appears to be no clear pattern; the lowest variance occurs at 20%, followed by 50%, 40% and 30%. This only reflects the variation in calculated corrosion rates; not necessarily a true reflection of the variation in sensor performance.

Standard deviation was calculated across sensors of each dataset for each time of monitoring (figure 8.1). Due to result processing employed to minimise noise and allow comparison between sensors, initial values were not necessarily 0. The figure confirms what can be observed in figures 7.33-7.38; as monitoring time progresses, total thickness loss for each sensor deviate as the small differences in corrosion rate create larger and larger gaps. The higher the RH level, the larger the increase in standard deviation over time. This is especially true at higher RH levels; at 60% RH the standard deviation increase is great enough to warrant plotting on a separate scale on figure 8.1. At 50% RH the standard deviation actually decreases somewhat after three days, before climbing as time progresses. 40% shows a more steady increase, with 20% and 30% showing very equal and slight increases over the two week monitoring period. This agrees with corrosion rate data; variety in corrosion rates and thickness loss increase the longer sensors are exposed.

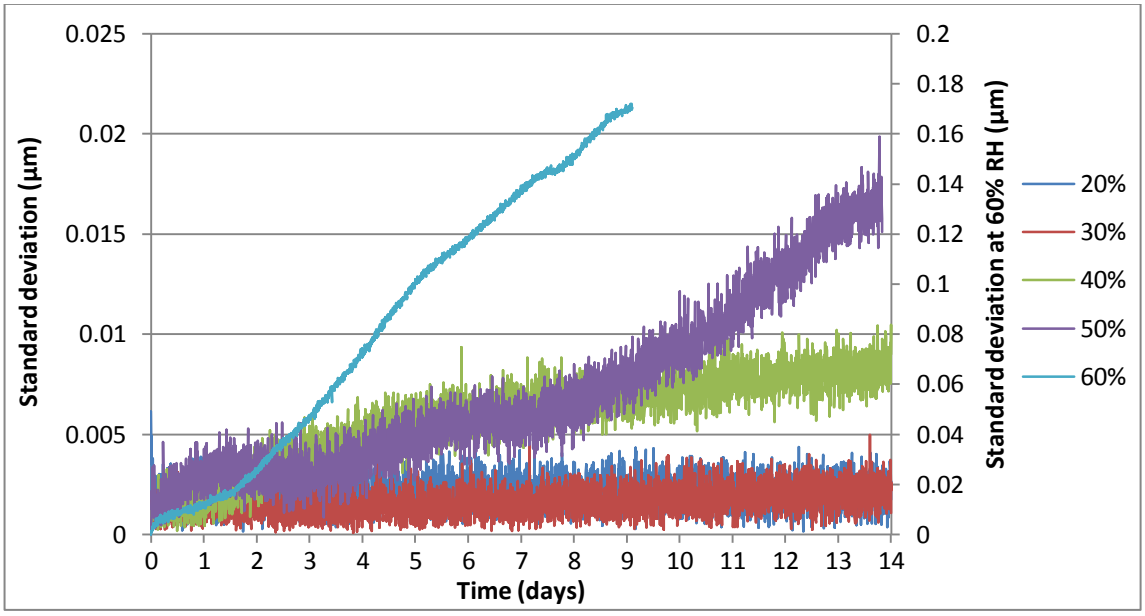


**Figure 8.1:** Graph of changes in Standard deviation over time for monitored ERCM in stable environments

If the increase in the standard deviation of the resistance ratios of each sensor set over time are plotted (figure 8.2) instead of thickness loss, the increases in variation may be analysed. For relative humidity environments stable at 20%, 30% and 40%, the values give similar plots to those observed in figure 7.41. At 50% the standard deviation initially increases steadily, before falling, to give an overall lower level of standard deviation significantly lower than the initial value. At 60%, the increase in standard deviation is initially rapid, but then levels off before dropping significantly and reaching approximately the same level as the initial value after 7 days.

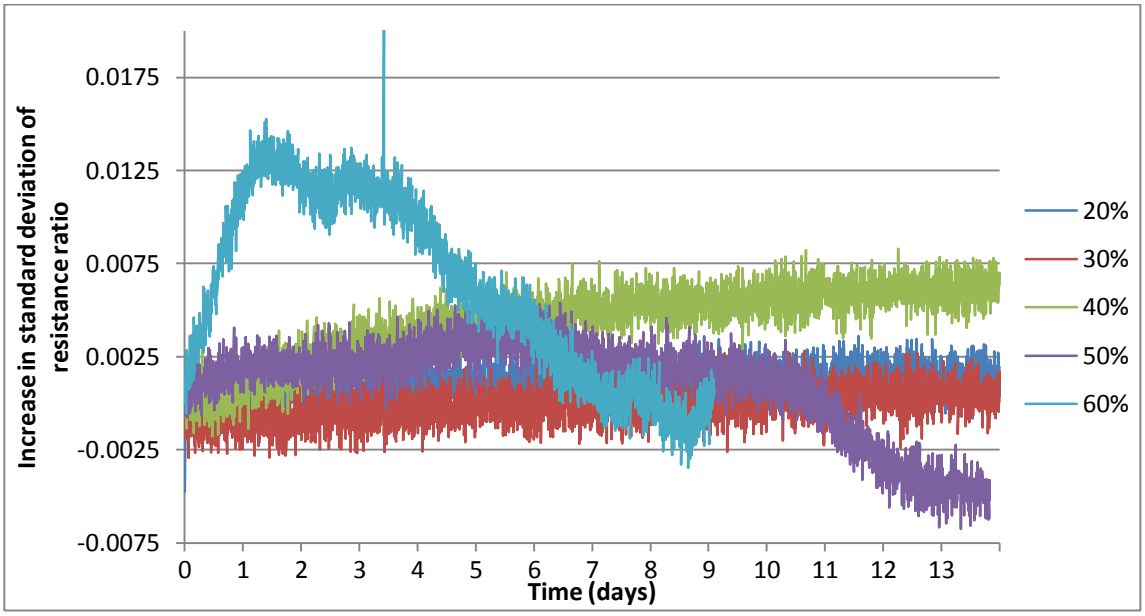


**Figure 8.2:** Graph of changes in the standard deviation of resistance ratios (Rc/Rr) of the time of monitoring.

These results make the question of increasing variance more complex. The two anomalous results (50% and 60%) can be explained by examination of the individual sensors within the datasets. Of the sensors subjected to 50% dataset, the curve with the highest corrosion rate (4.35 μm/year) with a total corrosion of 0.17μm over 14 days had the lowest initial resistance ratio (0.88). This had the effect of drawing the thickness loss closer to, but not surpassing, the mean of all the sensors in the dataset. At 60% RH, the curve with the highest corrosion rate (21.02μm/year) gave a total change in calculated thickness loss of 0.54μm, on the sensor with the second highest starting resistance ratio (0.86). This pattern is continued throughout the results, with the sensors with lower initial levels of corrosion tending to create higher corrosion rates than those which already had significant thickness loss. However, the effect in the other data sets is a lot lower, showing mirrored results in variation of standard deviation and resistance ratio (figures 8.1-2)

These results disagree somewhat with the previous study of pre-corroded ERCM by Kapatou and Lyon [9,20], in which all sensors showed increases of standard deviation with time in environments at 33%, 55% and 83% RH. In addition, it was observed that the most corroded ERCM showed the greatest standard deviation of resistance ratio, attributed to the increased levels of localised corrosion in higher corroded sensors. The results above indicate the reverse; that the least corroded sensors at the start of monitoring were more likely to corrode faster. This may well be due to the pre-corrosion methodology. Kapatou and Lyon used a method of gaseous HCl, from which corrosion levels would be directly proportional to chloride levels (as both would increase fairly linearly with time). However, this study maintains a more constant level of chloride, ±9 μg/cm$^2$. Differences in pre-corrosion levels are controlled by the arrangement and size of salt crystals and the dynamics of the pre-corrosion atmospheric

environment, leading to a range of thickness loss of 2.5µm to 5.0µm after the methodology. Increased levels of thickness loss will be directly linked to increased formation of corrosion layers, but without any increase of chloride. Indeed, it may be that the ERCM which are corroded most by the pre-corrosion methodology will have the least available chloride, as much will have been locked within corrosion layers. Additionally, the corrosion products observed of the probes' surface include more passivating species (magnetite) than in the previous study. The greater thickness and passivity of the corrosion products may therefore serve to increase the protective properties of the layer and reduce subsequent corrosion rates.

This is in contrast to the greater variance shown by examining simply the levels of thickness loss. ERCM will have decreasing corrosion rates as time progresses. At higher relative humidities, greater differences in corrosion rate are observed. This is due partly to the greater corrosion rates themselves, leading to greater gaps in scale, but also small differences in the corrosion layer bearing increased influence at higher humidities. The higher hydration may cause the dissolution of corrosion products or deliquescence of salts, increasing corrosion rates where these aspects of the corrosion layers are exposed or available. It may also be the point at which a more continuous electrolyte layer is formed; corrosion will be driven by direct reaction between the metal surface and a bulk solution, as opposed to localised phenomena in pores and deliquescent droplets. These processes are controlled by corrosion product morphology and permeability, properties more unpredictable than rates controlled by chloride levels and product thickness.

While this variance impacts sensor accuracy and repeatability, it will not hugely effect possible sensor use. The large difference in corrosion rate compared to relative humidity mean small changes in the environment will have large effects on corrosion rate. Higher error will only occur at high corrosion rates, significant only when compared to corrosion rates at lower RH levels. While this presents a problem for exact calibration and measurement of cumulative corrosion at low resolution (see below), it still allows creation of comparative levels of corrosion and the identification of periods and situations of higher than acceptable corrosion.

## 8.4 Pre-corroded ERCM in changing Relative humidity conditions

While the stable environments have provided data for how individual controlled heritage environments will affect our sensors, it is the dynamic environment results which provide the best data for how our ERCM will react in real world situations and when faced with failures in conservation strategies. The preferred storage of archaeological and heritage iron, in low, stable relative humidity environments is often not possible or in some way compromised. These are the situations in which our ERCM will provide the most value, highlighting where corrosion may be greater than expected.

It is therefore interesting that corrosion rates recorded during the dynamic relative humidity tests do not agree with the corrosion rates generated by the stable state environments. For each humidity level, theoretically identical to the stable state environment in atmospheric characteristics, the corrosion rates given by the dynamic tests are higher than during the stable state tests. This can be attributed to the difference between the equilibrium systems, with stable electrolyte thickness and humidity, compared to those systems with changing conditions, with altering electrolyte thickness, concentration and product hydration levels. The differences between how these changes occur, whether the change in humidity is sudden or progressive, and whether the jump is large or small, clearly alter the dynamics of our sensors and therefore the cumulative corrosion rates they will exhibit.

### 8.4.1 Differences between controlled program conditions

Program 1 gave data which followed the anticipated model; more corrosion is caused by higher levels of relative humidity. Corrosion rates are highest during the initial wetting stages, as the relative humidity increased from 20%. In the periods immediately upon humidity decrease, corrosion initially continued, before dropping to the expected lower corrosion rates. The latter reaction was slower than the former. Whether this was due to methodological differences in reducing relative humidity (moving the system further from equilibrium with the exterior environment), rather than increasing, is not certain.

The largest reduction in metal thickness occurs immediately upon increase of the humidity, exhibited in calculated corrosion rates as high as 1854 μm/year upon the start of 60% RH phases. The corrosion rates drop quickly, then progressively slower throughout the period of high humidity. When the humidity is reduced to 20%, there is a smaller spike in corrosion rate, before the rate drops to similar levels as prior to the increase. The same profile is observed during the 50%, and to a lesser extent during the 40%, relative humidity periods. The results are consistent with the wet/dry model of atmospheric corrosion, described in section 3.4.3; higher metal dissolution rates are observed during the wetting and drying phases, when the electrolyte is at its thinnest [19]. While we may have expected to have seen a greater peak in corrosion rate during the drying phase, this may be due to the complexity of the corrosion layers; insoluble corrosion products will quickly impede access to anodic sites by blocking the cracks and pores in the corrosion layers, limiting pathways for oxygen ingress and metal dissolution.

The corrosion rates calculated and displayed in table 7.16 are lower than those from taking the slopes alone, but still show significant disparity compared to stable state corrosion rates. These are somewhat explained by figure 7.46; the corrosion rates progressively fall over the course of the three hour exposures to higher relative humidity and it may be that given sufficient time these would level out close to the rates observed in section 7.3.2. In stable state environments,

the shift in humidity at the start of tests was typically from standard internal humidity (around 50%). This lower magnitude change would create much smaller initial jumps in corrosion rate. The longer monitoring times also dampen the effect of any initially high rates.

Program two shows similar corrosion rate increases, sustained corrosion at lower rates and disparity with the stable state tests. The data illustrate the difference in reaction to pre-corroded iron sensors with varying stepped RH levels, dependant on whether the RH has risen or fallen to its current state. Initial stepped increases caused large increases in corrosion rate, which then fall. During decreases in RH, corrosion rate undergoes a sudden temporary increase, then falls progressively. This contrasts to program 1 where corrosion rate fell very rapidly. Figure 8.3 overlays program 2 with the data of program 1, condensed so that the 60% phase of that program overlaps with the 60% of program 2, 50% to 50% etc. It illustrates the difference in corrosion rates and curve shape. It also highlights the similarities and differences in rate fall off after the initial peak for sudden increases. On RH decrease in program 2, rates take significantly longer to fall, perhaps unsurprisingly considering the smaller drop in RH. It is most pronounced at the fall from 60% to 50%.

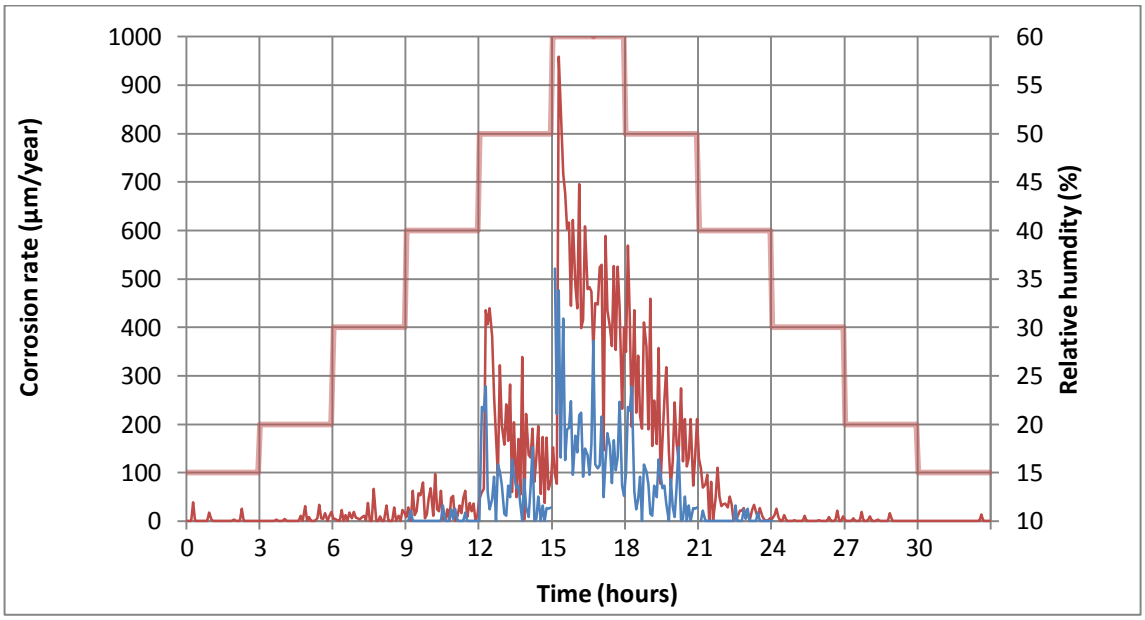


**Figure 8.3:** Overlaid plots of program 2 (red) and program 1 (blue) average results over one repetition. Program 1 results have been moved, repeated and the 20% levels deleted and to illustrate the levels reached at identical RH levels. RH plot therefore applies to both datasets.

At higher RH levels, it takes much longer for corrosion rates to fall than to be increased. This may be attributed to electrolyte taking longer to dry or dissipate than to accumulate, due to deliquescence of salts, hydration of corrosion products and microenvironments within voids in the corrosion layers. Similar mechanisms may also be the reason for corrosion occurring at

20% and 30% during RH decrease: progressive hydration of the corrosion products allows additional pathways to open over time, without the formation of a coherent electrolyte. The low levels of corrosion, coupled with the quirks of the calculations, make it more likely that this is caused by resistance measurements reaching a level in excess of the noise bands as time progresses, the peaks being a function of cumulative corrosion as opposed to any increase in rate.

Higher metal dissolution rates expected in the drying phase [19] and applicable to program 1, may be evident. Higher sustained RH could sustain enough electrolyte such that increased pollutant or ion concentration may have a direct effect on corrosion rates. Increased concentration is also a likely cause for the momentary peaks on decrease, creating significant metal dissolution before depositing out as insoluble corrosion products. The smaller jumps than program 1 make it less likely that the differences are caused by methodological differences between wetting and drying the atmosphere.

Program 3 illustrates the substantial difference between stepped changes and gradual changes in relative humidity. The constant corrosion rate exhibited is much higher than expected at increasing and decreasing RH levels between 40% and 50%. The average rate (from the slope calculations) of 183μm/year during the period of increased corrosion activity, is far in excess of the stable state tests at 60%, comparable to the 60% increase in program 1 and the 50% level of program 2. This may be due to the ever changing thickness of the electrolytic layer, serving to prevent the system reaching equilibrium. As relative humidity increases, the electrolyte thickness increases, exacerbating corrosion and increasing the hydration of corrosion products. During decreases of relative humidity, constant reductions in electrolyte thickness maintain higher concentrations of pollutants and ionic species; the same process as was used to describe the increased corrosion rates after humidity decrease in programs 1 and 2. This keeps corrosion rate high; at equilibrium corrosion rate will be low.

These processes would conceivably maintain the corrosion rate at higher levels than the stable state and earlier programs, but do not explain why the corrosion rate does not increase to the levels observed as for 60% during program 2 (averaging at 416 μm/year). The reasons will largely be attributable to the length of time spent at the highest relative humidity. Figure 8.4 plots programs 2 and 3, along with the average corrosion rate plots for one repetition of each program. Program 3 is only momentarily at 60%, whereas program 2 spends 3 hours at this level. Any sudden rate increase which occurs at close to 60% RH, due to a deliquescent species for example, would be unlikely to register in program 3. Peaks created by the stepped increase in program two are more significant at 60%, with a more gradual decrease than at other relative humidities. Combined these may explain the increased magnitude compared to program 3.

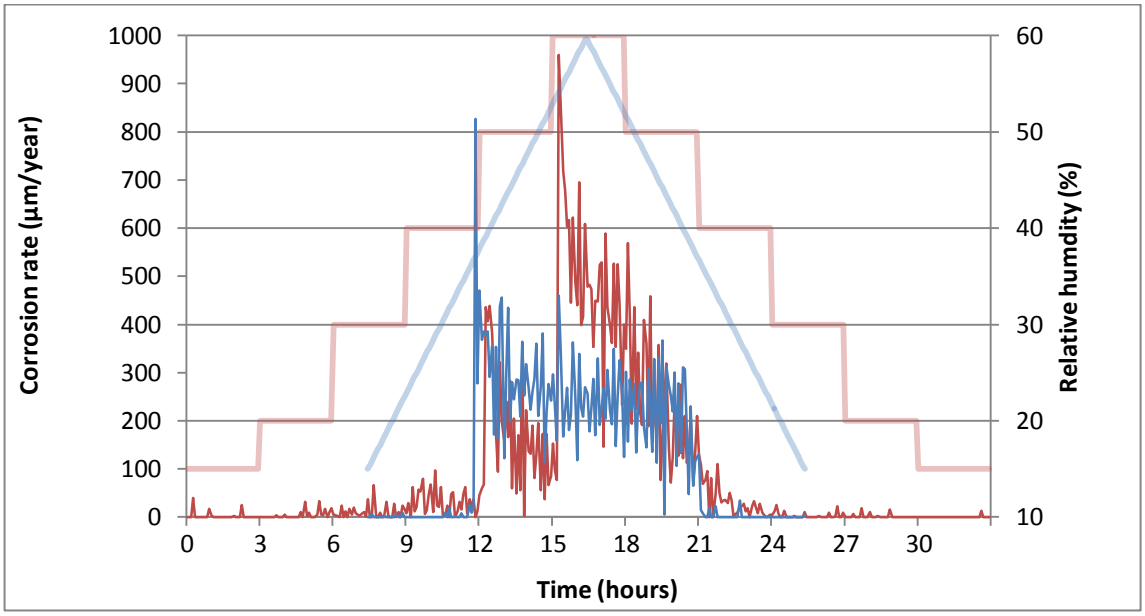


**Figure 8.4:** Overlain plot of programs 2 (red) and three (blue), with associated programmed relative humidities.

The results of the programs provide good indication of expected pre-corroded ERCM reaction to dynamic relative humidity environments at heritage sites. The phenomena observed and the differences between differing stepped and progressive relative humidity change impact how we might expect chlorinated corroded iron artefacts to react in similar environments. The low variance and similarity in sensor response, within each program and repetition, are evidence that the sensors work with a good degree of consistency when subjected to changing environments. The methods used to break down the data to give corrosion rates for each five minute period are a good example of how greater resolution may be reached and noise removed. This creates a trade off in sensitivity, but as a post-monitoring technique is useful for additional data cleaning and analysis.

### 8.4.2 Pre-corroded ERCM in heritage style environments

The reaction of the ERCM to heritage style environments was monitored, providing data on ERCM reaction to the additional variables associated with a sealed, desiccated container; primarily light and temperature with the potential for leaks and changes due to exposure.

The effect of temperature variation was evident for all the box tests. Regular patterns of resistance change were observed, following the day/night pattern of temperature change (higher resistances during the day and lower during the night). The changes in resistance were also felt in the resistance ratios, with the patterns not fully removed by the application of the reference electrode. The additional temperature "signal" introduced a maximum variation of

around 15nm for the exposed tests, 25 nm for the same position when the lid was opened and only 10nm for the box placed in a cupboard. While the error is clearly linked to temperature, its precise nature, why the resistance ratio does not remove it and ,therefore, how it can be mitigated is not known. It may be that the difference in thermal conductivity of the corrosion layers versus the clear protective lacquer creates a time lag between atmospheric temperature change and electrode change, different for each electrode. It may be that it is a light sensitive issue, with the difference in colour and reflection between the two sensors causing temperature rises more pronounced in one than the other. Both explanations would explain the correlation between the exposure of the sensor and the size of the noise signal. However, the magnitude of the signal in the blank, un-corroded sensor is high, indicating that it is not entirely due to the corrosion products present. There may also be more constant factors, such as thermal expansion of the electrodes and corrosion products, exacerbation of small differences in filament dimensions and simple differences in localised atmospheric temperature. It is likely a combination of these factors. Regardless of cause, the additional error is present and will have to be factored into application of the ERCM to heritage environments. This was somewhat mitigated by a decrease in the noise levels from the multimeter, possibly due to operating in the same conditions as the ERCM.

Apart from the noise signal, no large spikes or changes in corrosion rate were observed. This is likely due to the slowness and low magnitude of relative humidity change. It raises the distinct possibility that these phenomena are unlikely to be present, or only present in a reduced capacity, when monitoring in heritage environments. This would allow more simple monitoring and greater ease of methodology and result processing. However, it will also make it harder to pinpoint increases in environment corrosivity.

The magnitude of corrosion rates were similar to those we might have predicted from the controlled environment tests. While closed and exposed, the sensors returned constant corrosion rates of around 0.1μm/year, which increased to around 0.2-0.3μm/year when placed in a sealed and sheltered location. When the box was returned to its location, the rates were initially negative. Upon box opening, rates initially stayed roughly constant, but after about 5 days rose to 0.2-0.5μm/year. These rates fell to similar levels as previously observed when, once again, the box was sealed. Upon reopening, the rates remained stable for the first day, whereupon the two sensors diverge, one exhibiting corrosion rates up to 1.5μm/year and the other remaining at around 0.1μm/year

These corrosion rates correspond to levels observed in stable environment tests. The exposed and closed box induced corrosion rates similar to those recorded in 20% and 30% RH controlled environments, and the box in the cupboard has rates just above the levels seen for 30%. When the box is first opened, corrosion rate increases to around that of the 30% RH environment. At the second time of opening, sensor 2 reaches rates somewhere above the 40% RH environment and up towards the rates of the 50% environment. The desiccants within the

box were previously fired and treated to create a relative humidity of around 20% RH. That the corrosion levels observed would give rates which represent a controlled RH slightly higher than this when compared to our controlled tests may be indication of leaks within the box, temperature fluctuations and other pollutants and corrosion accelerators not present in our climate chamber tests. The differences when opening the box may be indication that it took five days in the first instance for the desiccant to lose effectiveness, up to which point local RH levels were largely maintained. When this failed the corrosion rates increased. The increased rates on box re-closure and the short response time on box re-opening may be further evidence for this. It is good illustration of the inferences that can be made should the ERCM be used in similar environments in the field.

The increased corrosion rates of the box held in a cupboard and the lack of accelerated thickness loss after the second exposure for sensor 1 are more difficult to explain. For the former, it may be that the higher levels of temperature noise were skewing corrosion rates, while the lower noise levels observed in the sheltered box allowed more accurate calculations. Over the time period monitored, the increased error the signal represents make the data difficult to evaluate. Certainly the increase is not greater than the noise level. The much greater variance between sensors on the box opening for a second time is more pronounced and unlikely to be a factor of the inherent error. The difference is significant, much greater than seen during the climate chamber tests between any two sensors in similar environments. While it may be due to significant differences in the corrosion products on the surface of the ERCM, additional external factors may play a part. It may be that foreign bodies, dust or pollutants have been introduced to the surface of the corroding filament of sensor 2. The tests took place exposed in a laboratory environment, making the potential for contamination high. There could have been additional corrosivity in that area of the exposed box, due to a specific microclimate; proximity to a tap, say, or a strong draught. Whatever the cause, it illustrates the additional considerations which must be made when building a methodology for the sensor's use in heritage environments.

## 8.5 ERCM Corrosion rates against relative humidity

The static humidity tests produced thickness loss curves from which corrosion rates were calculated. The overall average linear gradient of these curves, using a line of best fit to remove noise, give corrosion rates in terms of thickness loss against time. The consistency and low variance of the curves for samples exposed in environments between 15% and 50% relative humidity add validity to the observed corrosion rates thus generated. The differences and greater variance between sensors at 60% are discussed above and, while more disparate, still allow for comparison with other data.

A summary of the average corrosion rates for each of the environmental chamber tests is given in table 8.1. In stable conditions, the corrosion rates observed for the sensors range from effectively none at all at 15% RH, up to an average of 12.50µm/year (maximum 21.02µm/year) at 60% RH. Rates increased against environmental humidity in a predictable fashion; by plotting results on a logarithmic (base 10) scale the increase for each 10% increase in humidity was approximately linear, with a line gradient of 0.61. In the changing relative humidity of the climate chamber programmed tests, corrosion rates were much greater than observed in the stable tests, likely as a factor of the altering conditions. For Programs 1 and 2, these rates were recordable, while in program 3, corrosion rate over the entire course of the progressive rising and falling was plotted using five minute interval corrosion rates.

| | Corrosion rates (µm/year) | | | | | |
|---|---|---|---|---|---|---|
| Relative Humidity | Stable | Program 1 | Program 2 | | Program 3 | |
| | | | Rising | Falling | 5 minute rates | |
| 20% | 0.05 | 1.46 | 2.87 | -0.05 | Maximum | 2143 |
| 30% | 0.19 | N/A | 4.55 | 2.15 | Minimum | 0 |
| 40% | 0.7 | 2.61 | 15.23 | 21.27 | Average ~225 | |
| 50% | 3.8 | 54.9 | 105.81 | 160.92 | | |
| 60% | 12.5 | 156.66 | 416.72 | | | |

**Table 8.1**: Summary table of corrosion rates calculated for each type of environmental chamber environment.

The differences in corrosion rate are evident, but the progression between levels of relative humidity is very similar. This can be better illustrated in figure 8.5 and 8.6; graphs of corrosion rate for each of the comparable programs and stable RH levels, and a plot of the $Log_{10}$ corrosion rates respectively. The shapes of the graphs in figure 8.5 illustrate the similarity in changes between relative humidity levels, with similar exponential increases for each of the examined samples.

Figure 8.6 confirms this similarity. The stable and approximately linear logarithmic increase seen in the stable environments is quite closely mirrored by those in program two. Program one has a less similar trend, likely due to the increased effects of the large changes which occur at the start and end of the corrosion period. In addition, no result was available for 30% RH as no reading was taken, skewing the results. These differences are reflected by the square of the Pearson product moment correlation coefficient ($R^2$) for each of the data; the stable results have an $R^2$ of 0.998, Program 2 rising and falling have 0.963 and 0.971 respectively and Program 1 has a much lower 0.846. In terms of their overall trend however, all four datasets give similar values, with gradients of their line of best fit calculated as 0.61, 0.53, 0.77 and 0.57 respectively.

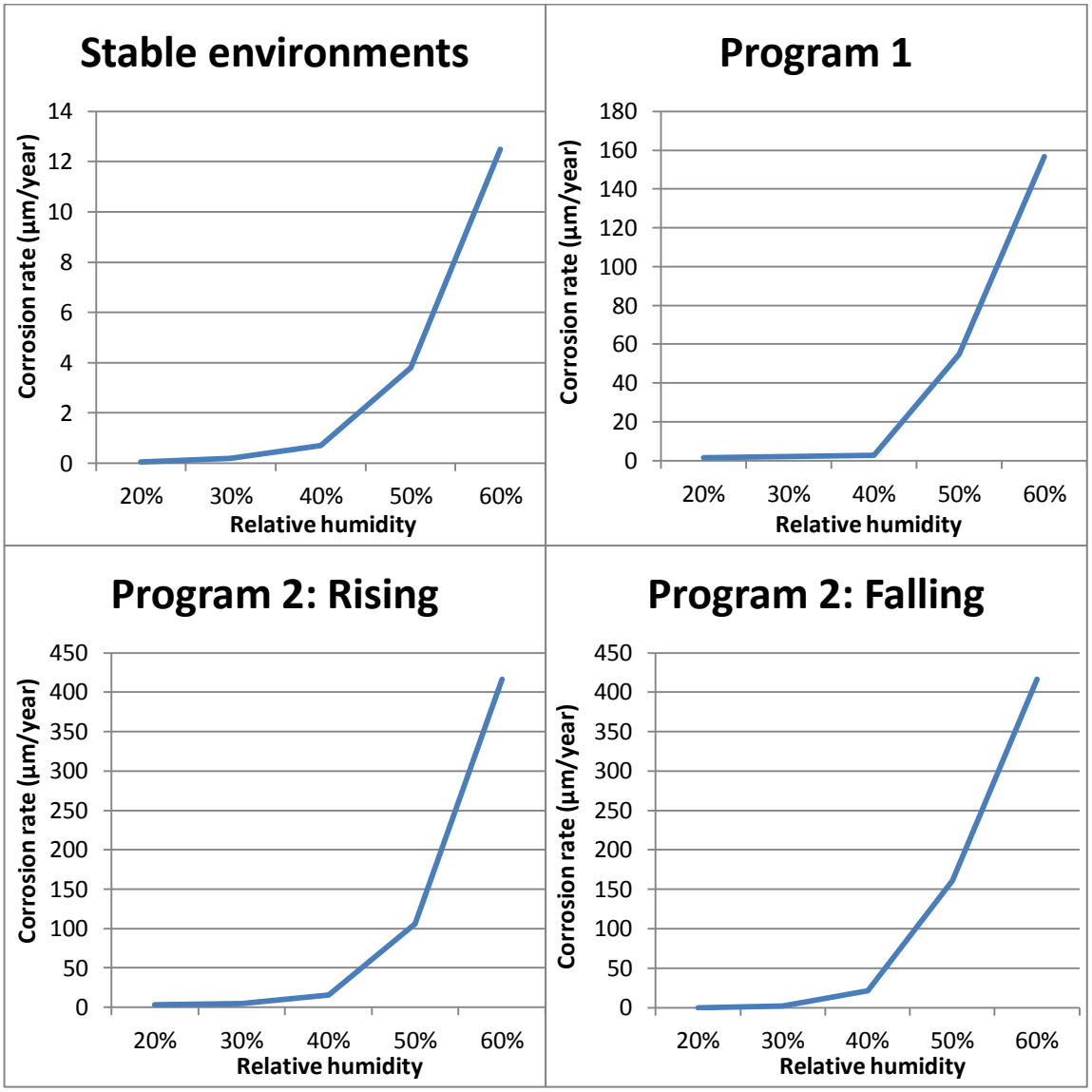


**Figure 8.5:** Graphs of average corrosion rate for atmospheric corrosion in climate chamber during stable and programmed testing.

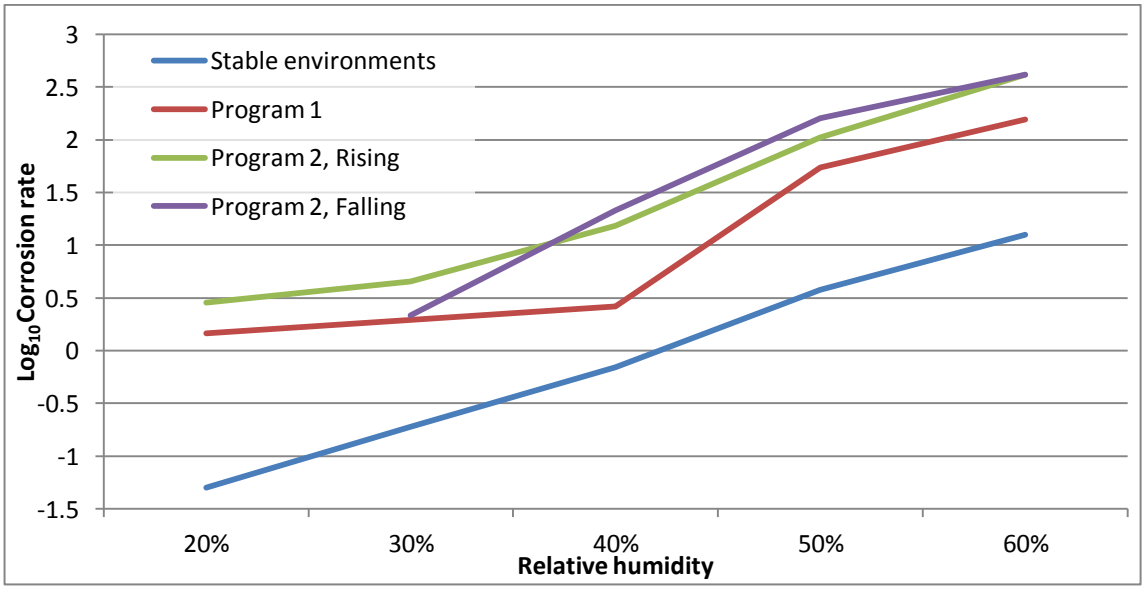


**Figure 8.6: G**raph of $Log_{10}$ of corrosion rates for each different atmospheric corrosion test within the climate chamber.

Apparently identical environments created by the atmospheric corrosion chambers resulted in wildly different corrosion rates, caused by the stability and humidity of the preceding environment. While the rates themselves were very different, the reaction of the sensors was similar, but scaled. In each case, the increase in relative humidity versus corrosion rate followed a roughly linear logarithmic curve. The adherence to this curve was at its lowest when large peaks in corrosion rate were present, caused by very large changes in RH. However, in three out of four cases, the overall progression, when plotted logarithmically, was linear with a gradient of between 0.53 and 0.77.

While these relationships between data are too disparate to draw firm conclusions, it is observed that in all cases where a stable corrosion level was maintained for a few hours, the ERCM create a logarithmic relationship between corrosion rate and relative humidity, regardless of preceding environments or other factors. This is important for comparison with heritage iron and for the use of the sensors in the field, when using generated corrosion data to infer models of past corrosion.

## 8.6 ERCM corrosion rates compared to heritage iron

The corrosion rates observed for our sensors, and their relationship established against changing relative humidity up to 60%, allow comparison to archaeological corrosion rates and characteristics. In turn, these comparisons will allow us to evaluate whether the sensors behave similarly, whether they produce similar corrosion rates and whether they will applicable as a proxy when deployed in similar conditions.

The range and complexity of corrosion processes and the number of factors which have an influence on corrosion rate, covered in chapter 2-5, make it almost impossible to characterise a "standard" corrosion rate for archaeological iron. Nor would it be sensible to; for predictive purposes and for us to use our sensors as proxy measures, we must appreciate that the variety of actual corrosion rates for seemingly similar objects in an environment will be as manifold as the number of artefacts. We may, however, gain an impression of the approximate corrosion rates which we would expect to observe, and how this changes with varying environmental pressures. These rates will inform whether our pre-corroded ERCM will react similarly, how much calibration may be required between results, and ultimately how these sensors might then be used in a heritage environments

Comparison to corrosion rates from the literature is difficult. There are few studies of corrosion rate of actual archaeological artefacts, fewer still of those which evaluate the environments in which they are subsequently corroding. Standard quoted corrosion rates for clean iron in atmospheric conditions are 100µm/year, increasing to 1300µm/year when chloride contamination is present [20]. Ambler and Bain's [21] study of corrosion rates in the

1950s linked atmospheric corrosion rate in the tropics to salinity and chloride content, illustrating a direct link between corrosion rate of iron ingots and distance to the Sea. These corrosion rates peaked at 950 μm/year for samples within 50 metres of the sea, and decrease to only 48μm/year for those 25 miles from the sea. These rates give an indication of clean iron exposed to environments with and without subsequent chloride contamination, corrosion rates of already corroded iron are rarer. De La Fuente et al. [22] studied iron in a range of exterior environments over the course of 13 years. While initial corrosion rates were recorded for relatively clean iron after a number of years the built up corrosion layers created a greater equilibrium with the environment and would have corroded more similarly to heritage iron. These gave corrosion rates of 30-60μm/year for exposed corroded iron (shown to contain akaganeite, goethite and lepidocrocite) in a marine atmosphere. In rural areas the corrosion products were less fully formed and the rates fell below 10μm/year. Carbon steel in atmospheric conditions has also been reported at ranges between 4-65μm/year in similar conditions, with higher rates of 26-104 μm/year for marine conditions [23]. All these data refer to relatively recently corroded iron coupons, but similar rates of 7μm/year are recorded in one of the few studies of atmospherically corroded iron; on 18$^{th}$ century cast iron cannon in a semi arctic environment [24].

The range of environments encapsulated above is unlikely to reflect heritage storage or display conditions. The exposure to exterior climate, weather and pollutants is likely to mean corrosion rates encountered by ERCM so deployed will be far lower and more constant. The rates quoted above for the rural, low pollutant areas are similar to those generated for stable state environments between 50% and 60%, a good estimate for standard atmospheric conditions [25]. Even without this caveat, the higher rates were well within bounds of those which it has been demonstrated the ERCM can monitor using the current setup. The effect such high levels might have on sensor lifetime will be discussed below.

The thickness loss curves can also be altered to compare the corrosion processes which are indicated from the corrosion rates, which themselves may be compared to heritage iron. The atmospheric, long term corrosion of steel follows a predictable kinetic equation;

$$\Delta D = At^B \qquad \textbf{[Eq. 8.1]}$$

Where ΔD is thickness loss at time t, A is the corrosion rate during the firsts unit of time and B is an unknown factor below 1. The equation applies to uniform corrosion and will be skewed by localised corrosion processes. It has previously been applied by Pourbaix [26] to characterise and predict corrosion rates of various steel types in various atmospheric environments, Legault & Preban [27] to predict behaviours of low-alloy steels in atmospheric environments, De la Fuente et al [22], to examine the corrosion rates of steel over long time periods, and Zhang et al. [28] in their study of two stage atmospheric corrosion processes.

The value of A and B are derived from corrosion processes; knowledge of their value can be used to extrapolate the processes occurring on corroding iron. In particular, the value of B indicates the passivating or corrosive tendency of the reactions. Values below 0.5 indicate passivating trends, a compact rust layer which prevents contact with the electrolyte and corrosion rates controlled by the diffusion of ions and electrons. Above this threshold, the value indicates diffusion of aggressive species towards the metal surface and an increase in corrosion rate, indication of direct substrate contact with the electrolyte [28].

This method was used by Kapatou [20], to demonstrate the difference changing levels of chloride and humidity had on her sensors and their assumed corrosion kinetics. In this study, the lack of chloride variance limits use to comparison with other long term data; using the value of B, and therefore the corrosion processes and continued corrosion rates, to evaluate the ERCM data against long term corrosion studies. To calculate B, we can expand both sides of the equation to create;

$$\log \Delta D = \log A + B \log t \qquad \textbf{[Eq. 8.2]}$$

Plotting thickness data against time on logarithmic axes will create a dataset gathered around a line with the gradient B and which crosses the x-axis at Log A. Figures 8.7 and 8.8 plot the stable state environment thickness loss measurements in logarithmic terms against time. The gradient and closeness of fit to the generated line for each set of results is given in table 8.2

The data from the 15 and 20% results were deemed to be too dispersed to allow conclusions to be drawn. Those at 30% are also weak, but are included above for comparison. For 40%, 50% and 60%, the $R^2$ values are sufficient that the lines produced have some validity. For all three data, the B values indicate the processes involved in the atmospheric corrosion involved direct contact between electrolyte and surface, and are activation controlled, strongly suggesting the influence of chloride on the corrosion rate. The higher the relative humidity, the higher the value, and therefore the linearity of corrosion rate and activation energy. This is likely directly linked to the thickness of the electrolyte and the hydration of the corrosion layers.

Despite the growth of corrosion layers on the metal surface, the effect of the chloride is still apparent and increasing. This overlaps with those values observed from the literature. In the De la Fuente study [22], those objects most likely to be in contact with chloride, and themselves observed to develop thick corrosion layers, had the most similar B values to ours in standard atmospheric conditions (40%-60% RH) (figure 8.8, the marine and industrial contexts). Those without pollutants and which developed fewer corrosion layers generally presented, or developed, diffusion controlled characteristics well below our predicted kinetics.

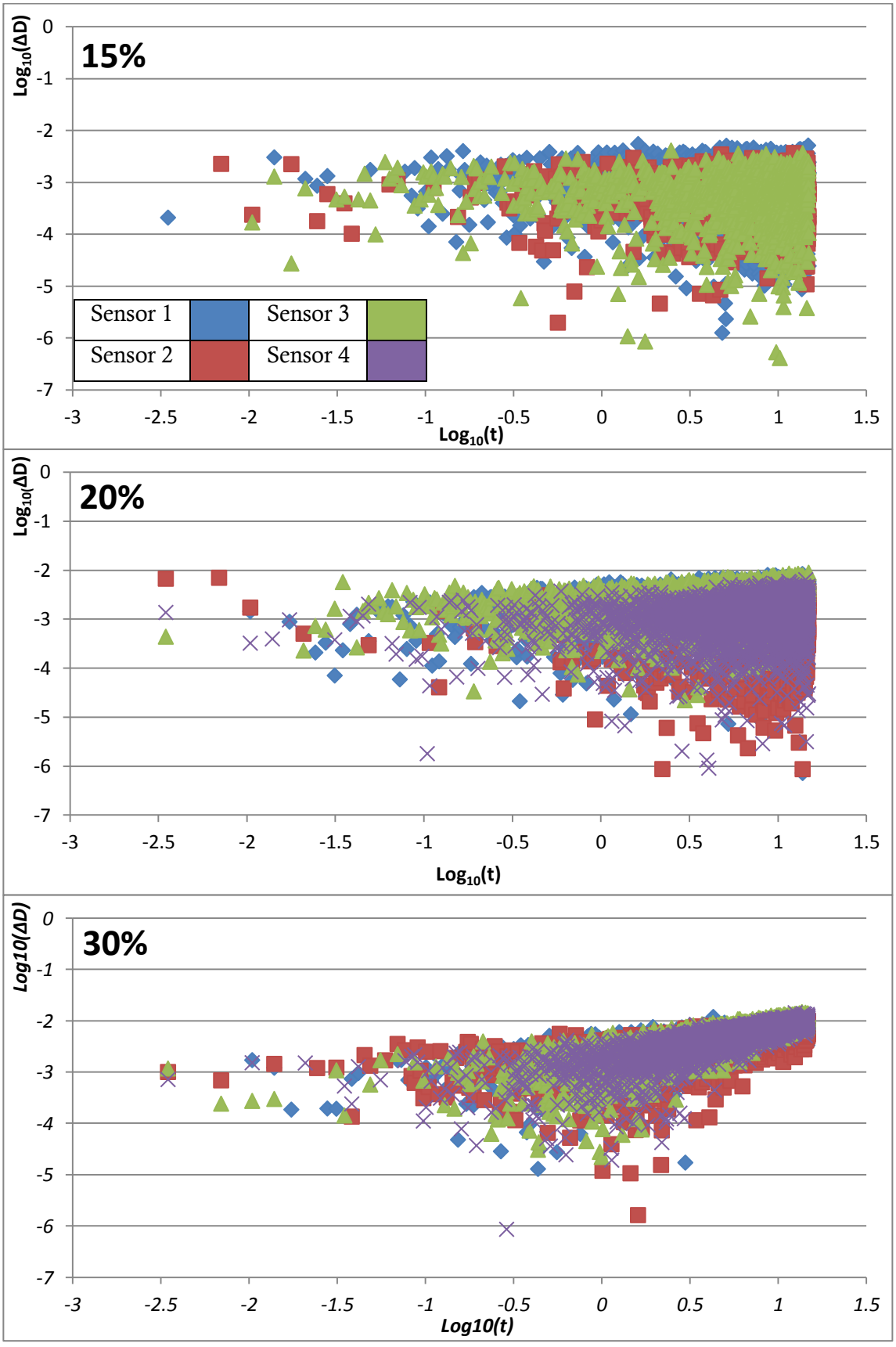


**Figure 8.7:** Bi-logarithmic curves of thickness loss for stable relative humidity levels of 15%, 20% and 30%. Key applies to all charts. Data on the best fit lines used in bi-logarithmic analysis are presented in table 8.2.

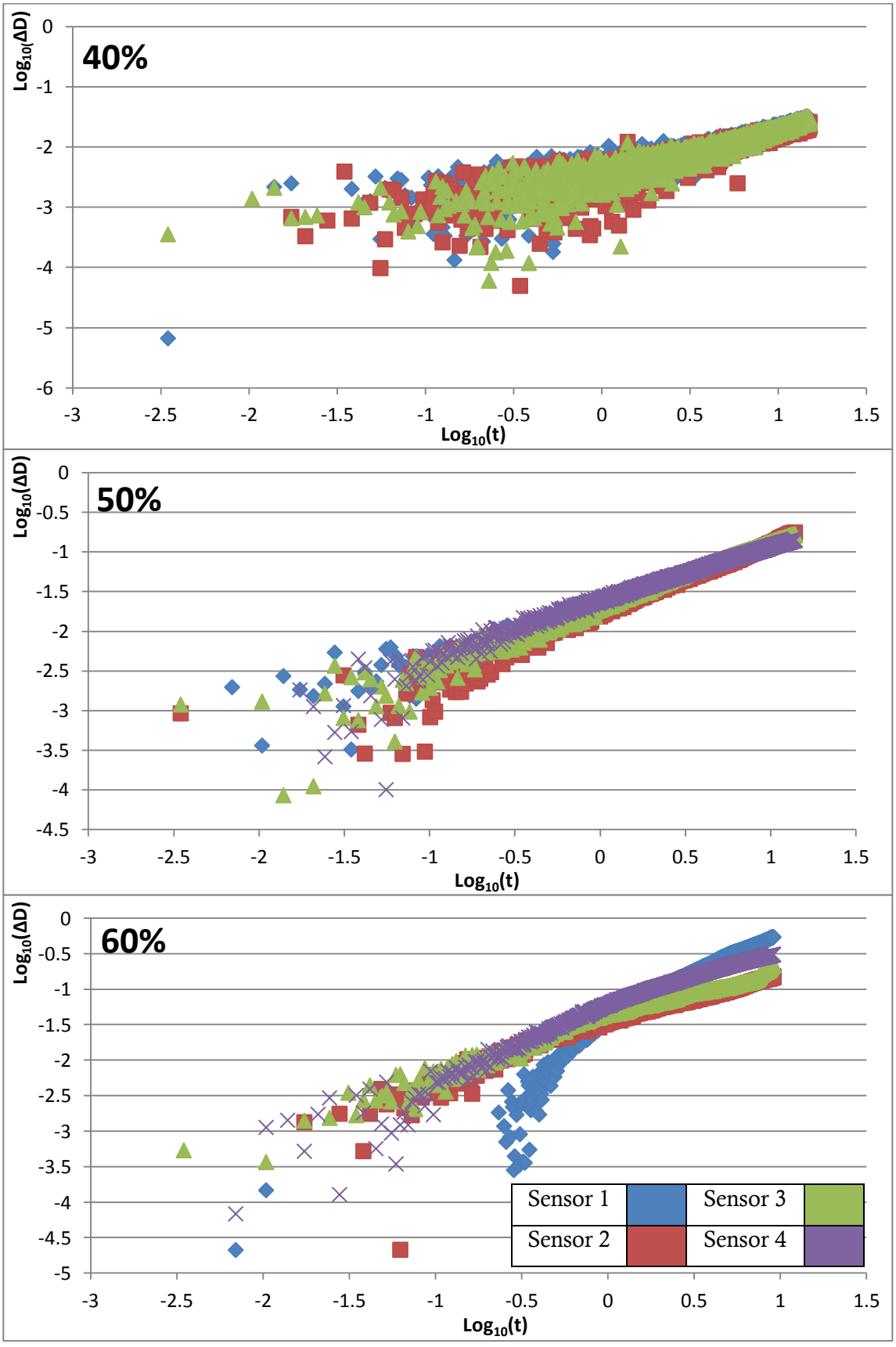


**Figure 8.8**: Bi-logarithmic curves of thickness loss for stable relative humidity levels of 15%, 20% and 30%. Key applies to all charts. Data on the best fit lines used in bi-logarithmic analysis are presented in table 8.2.

| Relative Humidity | Sensor number | $R^2$ Value | Log(ΔD)=B.log(t)+A | | Average B |
|---|---|---|---|---|---|
| | | | A | B | |
| 30% | 1 | 0.533 | -2.6523 | 0.455 | 0.603 |
| | 2 | 0.490 | -2.7707 | 0.530 | |
| | 3 | 0.719 | -2.7643 | 0.710 | |
| | 4 | 0.667 | -2.8241 | 0.716 | |
| 40% | 1 | 0.888 | -2.3693 | 0.664 | 0.703 |
| | 2 | 0.888 | -2.471 | 0.702 | |
| | 3 | 0.902 | -2.458 | 0.744 | |
| 50% | 1 | 0.989 | -1.6523 | 0.701 | 0.762 |
| | 2 | 0.987 | -1.7506 | 0.849 | |
| | 3 | 0.988 | -1.6801 | 0.801 | |
| | 4 | 0.983 | -1.6287 | 0.698 | |
| 60% | 1 | 0.956 | -1.4952 | 1.372 | 0.914 |
| | 2 | 0.959 | -1.4894 | 0.708 | |
| | 3 | 0.971 | -1.4164 | 0.700 | |
| | 4 | 0.967 | -1.2839 | 0.874 | |

**Table 8.2**: Table of statistic for lines of best fit created in the bi-logarithmic graphs in figures 8.7 and 8.8, illustrating the square of the Pearson Product moment correlation coefficient ($R^2$), the slope and the intercept of each dataset.

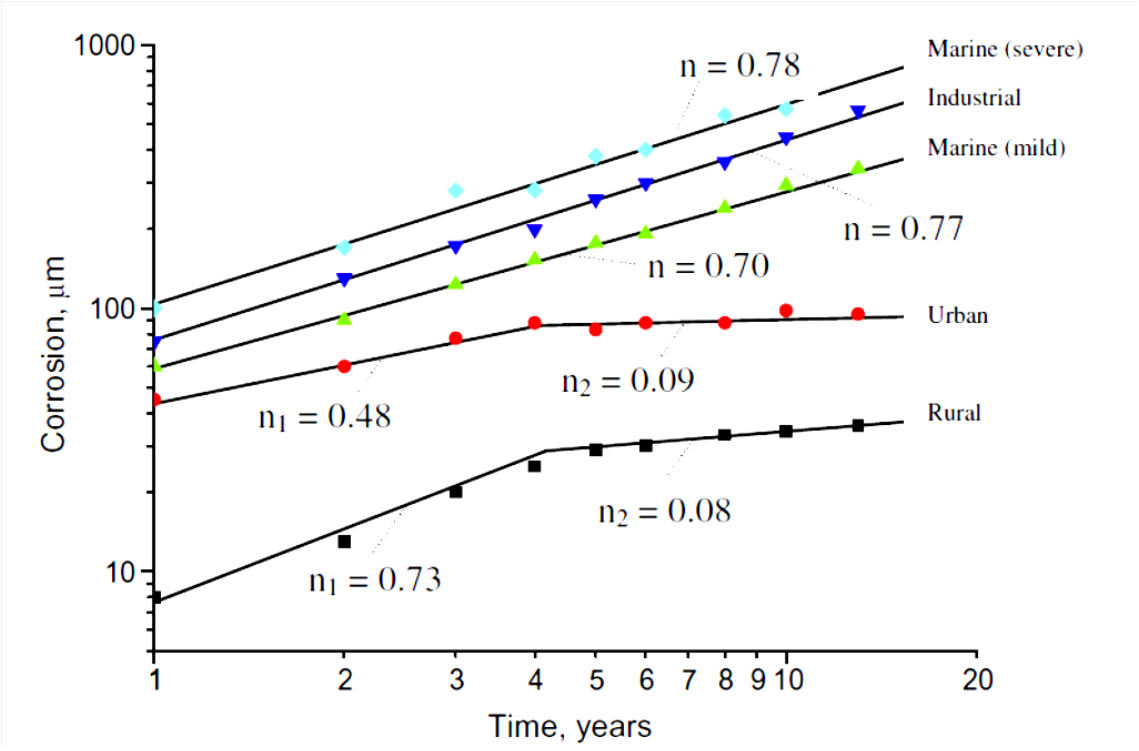


**Figure 8.9:** Figure from De la Fuente et al [22], illustrating bi-logarithmic curves for long term corrosion of mild steel at different sites (taken from [22], page 606)

In the previous study of pre-corroded ERCM, Kapatou and Lyon [12,20] observed B values of 0.88 (at 83% RH with ~0.3mg/cm$^2$ of chloride contamination), and similar values above 0.5 for those sensors exposed in 83% and 55% environments with low overall chloride levels. These are not directly comparable, as the only sensor with similar chloride levels was tested only at 83% RH, well above our observed levels. However, the tendency for higher B values at higher relative humidity, and the rough similarity of the range of B values observed for the lower chloride sensors (between 0.6 and 0.88), confirm that our ERCM are exhibiting similar corrosion processes.

While the linear logarithmic law provides a very good model for predicting atmospheric corrosion rates and mechanisms of steel, true prediction of corrosion reaction will rely on a more complex evaluation of the corrosive environment, material-electrolyte-corrosion product interaction and corrosion pathways. The similarity between the predicted processes of our sensors and those of previous studies make a convincing case that our ERCM will corrode and react similarly to corroded and chloride infested iron. No direct archaeological data was found for such kinetic comparisons, but two scenarios are likely; for archaeological artefacts stored for long periods in stable atmospheric conditions, it is likely compact corrosion layers will have formed, creating B values below 0.5. For chloride infested objects, the additional processes which affect chloride infested iron when moved to a different environments (weeping [29], cracking [11] and chloride nesting [30]) are more likely to allow direct contact between the metal and electrolyte, giving values above 0.5 and up closer to 1.0, similar to our sensors. The aim of the sensors has always been to monitor the more afflicted samples of archaeological iron, chloride infested and therefore prone to the aforementioned post excavation effects. While actual data is needed to corroborate this, it is likely the observed B values for our ERCM indicate similarity to the heritage iron most at risk and for which our sensors will be most applicable.

Direct calibration and comparison of actual rates was provided by data from Cardiff University. Using the methodology described in section 6.4.3, actual chloride infested archaeological iron was monitored in identical conditions to our own stable state tests. The data from these tests have been made available for this study to allow quantitative analysis of the similarity between the ERCM and actual heritage iron. It should be stressed that all methodological work, data capture and analysis was performed at Cardiff University by Prof. David Watkinson and Dr. Melanie Rimmer.

The data collated from the Cardiff tests [31] has been summarised and left without units as they have yet to be published. Artefacts from two sites were examined, one of which had been sorted for an extended period before this analysis. In both cases significant levels of chloride were present within the corrosion layers. The results, summarised in table 8.3, represent corrosion rate in terms of oxygen consumption over time. As such their exact units cannot be

directly attributed to the corrosion rates exhibited by the ERCM, but their relative magnitudes can be used.

| | Corroded Samples in similar environments | | | | | | |
|---|---|---|---|---|---|---|---|
| **Relative humidity** | **Site 1** | | **Site 2** | | **Archaeological average** | **ERCM** | |
| | **Rate** | ***CoV*** | **Rate** | ***CoV*** | **Rate** | **Rate** | ***CoV*** |
| **20%** | 0.004 | *0.660* | 0.013 | *0.467* | 0.008 | 0.052 | *0.105* |
| **30%** | 0.003 | *0.715* | 0.021 | *0.467* | 0.012 | 0.194 | *0.313* |
| **40%** | 0.010 | *0.586* | 0.092 | *0.524* | 0.071 | 0.700 | *0.263* |
| **50%** | 0.015 | *1.667* | 0.145 | *0.467* | 0.080 | 3.803 | *0.140* |
| **60%** | 0.036 | *2.325* | 0.667 | *0.465* | 0.351 | 12.496 | *0.572* |

**Table 8.3:** Corrosion rates and coefficients of variance of archaeological iron monitored using oxygen consumption in identical environments to the pre-corroded ERCM. Units are omitted to protect original data, see text.

The results give numerical value to the relationship between the corrosion rate as calculated and the stable relative humidity environments. Similarly to the comparisons between stable states, we can therefore plot the data in terms of corrosion rate (figure 8.10), and in terms of the logarithmic progression of the corrosion rate (figure 8.11), against each stable humidity environment. It is evident in both cases that the reaction of the archaeological iron is similar to that of the ERCM, though with notable differences.

The most obvious difference between the two curves is the increased corrosion rate at 40% for the archaeological samples compared to our ERCM levels. This difference is more pronounced in site 1 than in site 2. Whether this is an actual reflection of the corrosion or a methodological bias is not known. It should be noted that, for site 1 in particular, significantly fewer samples were available for analysis, allowing small errors and individual erroneous results to have greater effect on average results.

The coefficients of variation for the corrosion rates within each of the relative humidity environments differ from the variance observed within the ERCM results. The greater size of the datasets compared to ERCM may contribute to this difference, and the low numbers of ERCM tested make any comparison very difficult. The two datasets exhibit differences, but both are indicative of an anomaly with the 40% results. Site two exhibits almost constant variance of 0.467 for each of the humidities except 40%, lending additional weight to the possibility these results may present an anomaly. Variance is greater at all humidities for the nails from site 1, increasing with relative humidity except at 40%, where a lower level than might be expected is observed.

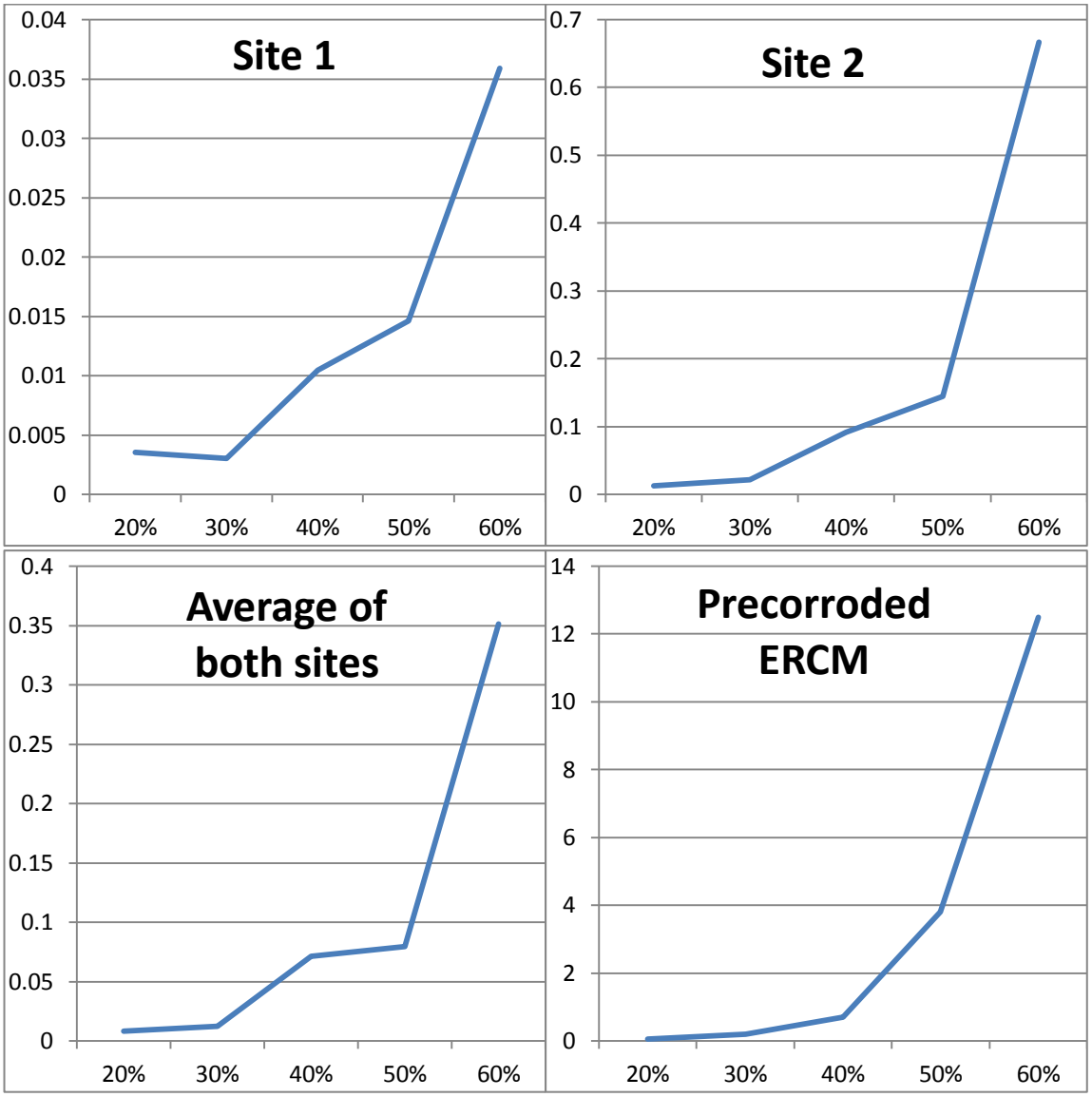


**Figure 8.10:** Graphs of corrosion rate for chloride infested heritage iron from 2 sites (measured by oxygen consumption) and pre-corroded ERCM.

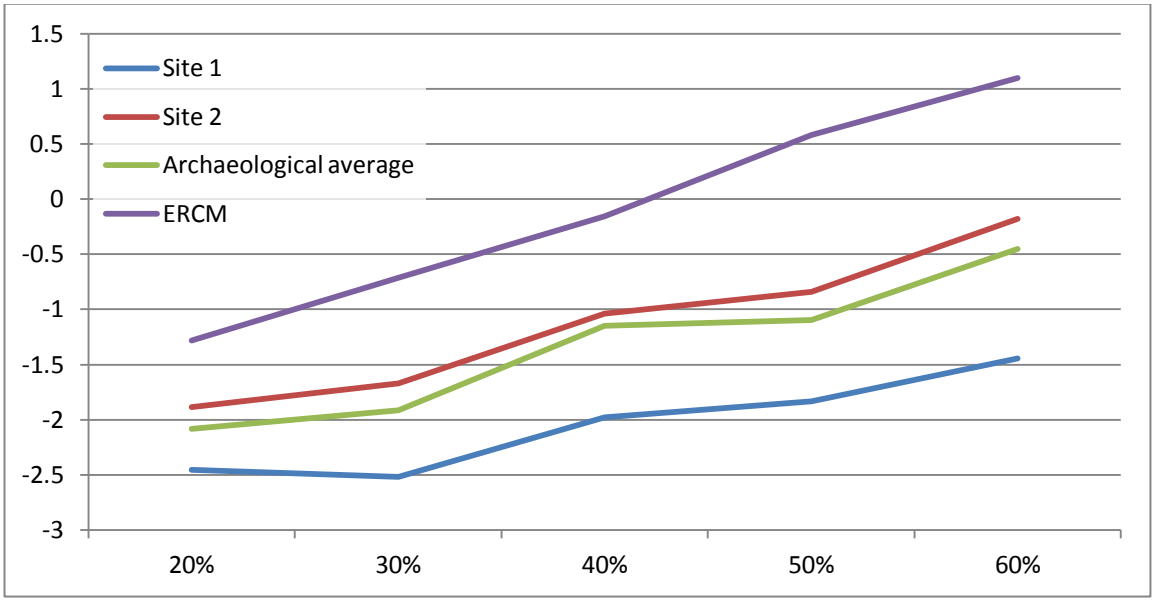


**Figure 8.11:** $Log_{10}$ of corrosion rates of archaeological samples and pre-corroded ERCM in identical environments, plotted in figure 8.5. Position on the x-axis is irrelevant for purposes of rate comparison, evaluation is based on line shape and gradient.

Whether the above make the 40% results correct or not, there are enough differences between the ERCM and archaeological iron data to provoke discussion. The logarithmic lines have distinctly different slopes and Pearson correlation coefficient. The $R^2$ values for site 1, site 2 and the overall average for archaeological iron are 0.91, 0.97 and 0.94 respectively, compared to 1.00 for the ERCM results in identical environments. The closeness to linearity is still significant, but noticeably lower. It should be noted that with the 40% results removed, the correlation increases, though not significantly. The gradient of the lines are 0.27 for program 1 and 0.42 for program 2, compared to the 0.61 of the ERCM.

The differences between the two sets of lines are significant. However, the fact that a linear progression is present allows extrapolation that a relatively simple transformation could be applied the ERCM corrosion rates to adjust them to fit those of the archaeological artefacts. The lower correlation coefficient prevents a direct extrapolation of such an equation using the current data, but the shape of the curves in both figures 8.7 and 8.8 encourage the opinion that an overall formula for transformation will be possible.

The attempt to calibrate the sensors with archaeological iron directly has not been completely successful. It will require significantly more data to create a clear relationship between corrosion rates as monitored and expected archaeological iron within the same environment. However, it has been demonstrated that the reaction of the ERCM to changes in RH are similar to archaeological analogues. Both increase in corrosion rate with increases in relative humidity and, for levels up to 60%, the relationships both manifest as linear logarithmic increases. The decreased closeness to this fit or the archaeological iron will result in any extrapolation leading to a range of possible corrosion rates as opposed to a direct value. This is inevitable even without the differences in observed corrosion reactions. The variety of corrosion rates which might be present in any given archaeological iron assemblage will mean any attempt to directly extrapolate will be flawed, giving results closer to certain artefacts than others. ERCM will be better at judging overall corrosivity, or presenting a range of possible corrosion scenarios, than giving direct measurements of assumed corrosion rate. The gradient of the logarithmic lines are similar but of lower magnitude than the ERCM result; up to 60%, the ERCM are more likely to have an increased reaction to higher relative humidity. This overestimation also contributes to the idea that the sensors will be best suited to highlighting increased corrosivity within an environment, giving exaggerated readings when passive conservation strategies fail.

Future results may allow development of a formula to directly relate ERCM corrosion rates with certain artefact types within an environment; iron artefacts which are known to corrode at an approximate rate at each given relative humidity. In such a model, ERCM results could be transformed mathematically to predict the actual rates of the archaeological iron, based on previous observations of rate and reaction to relative humidity. If such general relationships

were created, the sensors would be of greater use within corrosion strategy than measuring approximate corrosivity of an environment. Such a leap would require a significant corpus of empirical data, however, and would be skewed by any external factors unaccounted for. It is the view of this author that such a model is possible and would form a likely next step for sensors of this type, but it was beyond the ability and resources of this study.

We can conclude that the ERCM react similarly to relative humidity changes as chloride infested heritage iron, can observe a range of rates far in excess of what we could expect from such artefacts and suggest similar corrosion kinetic behaviours. Where there is disagreement, the ERCM tend to exhibit rates higher than that of the iron they are designed to monitor, a quality which enhances them as early warning devices for corrosion damage. While we may not conclude corrosion rates of iron will be identical in a shared environment, it will be reasonable to assume they will be similar. As measures of corrosivity of an environment towards heritage iron and as 'corrosion alarms' they will be of significant use to the iron conservator or corrosion engineer.

## 8.7 Pre-corroded ERCM in Heritage iron conservation

The success of the ERCM in monitoring lab-based environments shows their potential as corrosivity monitors in heritage environments. Chloride infested heritage iron is one of the most ubiquitous and yet unstable commodities held by heritage institutions and contained within our cultural monuments. The ability to detect sudden increases in corrosivity of an environment, map corrosion problems before macro scale damage occurs and create a system of passive conservation maintenance will be vital to prevent further loss of cultural and intellectual value. The data provided will be based on actual corrosion rates, not evaluation of environmental factors. However, it is highly unlikely a similar setup to that used here will be applicable to the majority of heritage situations. In order to realise the applications of the sensors, we must consider their inherent limitations and lifetimes, possible methods of deployment, comparisons and cross over with other monitoring techniques and how they might fit in to current and future heritage strategy.

### 8.7.1 Limits of detection, reaction time and probe lifetime

The pre-corroded ERCM have been shown to detect corrosion rates as low as 0.05µm/year up to a maximum of over 2mm/year within the methodology employed in this study. During deployment in a heritage environment, it is unlikely that they will be deployed similarly to our closely monitored short term tests. Instead, far longer periods of monitoring are envisaged. The tightly budgeted heritage sector is also unlikely to be able to deploy 8.5 digit multimeters and constant monitoring. Their limits of detection in terms of corrosion rate will be different

dependant on the timing between measurements, the inherent error of the system and the accuracy of the experimental setup.

Our sensors used constant monitoring techniques; readings taken every five minutes with a high precision multimeter. In a practical setting, it is more likely probes will be read less regularly or using a different methodology. For constant monitoring techniques, the two methods for calculating corrosion rates (the slope of the line or the slope of a calculated 'clean' dataset based on maximal and minimal values), have been shown to give good results with a strong empirical basis.

Where constant monitoring is not possible or impractical, isolated readings will be used, with thickness change between each reading giving a calculation of cumulative corrosion rate over time. This method will suffer from the full levels of apparatus noise and error. Levels of significance required to detect specific corrosion rates can be calculated. To fall outside the margin of error observed from multimeter noise, isolated readings require an increase in calculated thickness loss of greater than 30nm, to take into account the maximum compounded noise and temperature error observed in our ersatz heritage container. As time progresses, the same thickness loss will represent a lower corrosion rate; lower corrosion rates are detectable over longer periods. Figure 8.12 plots this change over time, demonstrating the sensitivity of the sensors compared to their resolution. If measurements are taken after a week of each other, the minimum observable corrosion rate will be 2.7μm/year or worse. Longer time periods allow far greater accuracy of measurement; to detect the lowest corrosion rate observed in our stable 30% relative humidity environment would require a monitoring pause of five and a half months.

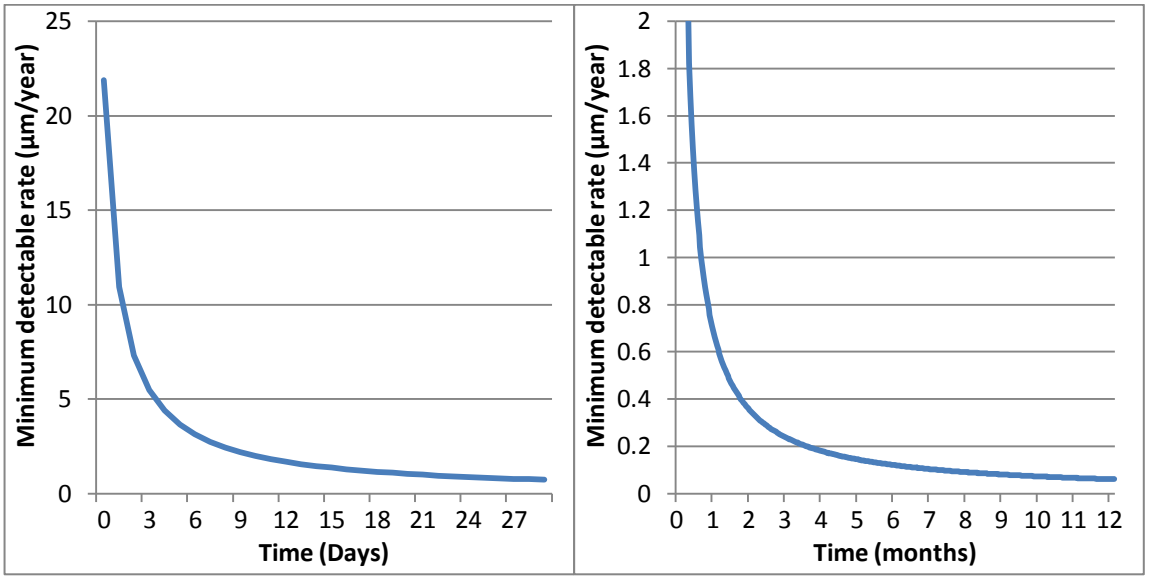


**Figure 8.12:** Plots of minimum detectable corrosion rate, based on thickness loss exceeding double the maximum observed error, against time between individual readings.

This limit assumes a worst case scenario implementing the least amount of time and manpower. This accuracy can be dramatically improved through methodological means. ERCM monitored for an hour to generate a large number of readings at each data capture point would generate a range of possible thickness loss data, from which an average or the most suitable result taken. Removal of the sensor to a controlled temperature environment would also allow much of the noise to be removed from readings, though this is likely to compromise the continued corrosion kinetics and introduce additional corrosion rate changes and phenomena. Smaller methodological alterations may be more beneficial, such as ensuring readings are taken at the same time of day and external factors are similar for each reading.

Accuracy might also be compromised in the field by lower quality equipment, for the sake of budget and usability. Much of the apparatus could be swapped without compromising too much accuracy; powering the circuit by a more simple battery powered galvanostatic circuit, logging the data by manual reading of the multimeter and using simple clip on attachments to connect the wires. However, a lower resolution and accuracy multimeter will have a direct effect on accuracy. Our study utilised an 8.5 digit multimeter, allowing measurement down to $10^{-10}$ V, equating to minimum resolution of 2.5nm. Each increase in magnitude of the minimum detectable voltage will create a corresponding increase in the minimum thickness loss detectable. It is difficult to estimate the levels of apparatus available to conservators, but a minimum accuracy will be required to allow effective use. A tenfold decrease in accuracy would be acceptable, but an accuracy level as high as 100μV would create a minimum resolution of 0.25μm in thickness loss. Such an inaccuracy would make detection of corrosion rates in any relative humidity below 50% difficult except in very long term monitoring tests.

Methodological setup will also affect sensor reaction time. The methodology used for this study was shown to give almost instant measurements of corrosion rate change; in the moving relative humidity tests, large increases in thickness loss were recorded in the first five minutes of environment change. For lower accuracy multimeters or much smaller or gradual changes in relative humidity, the length of time to detect change will be the same as taken for the thickness to change by the value of error, creating a progression similar to figure 8.12. During continuous tests, the change may be easier to see, but will require enough data to provide a convincing change in line gradient. The results from the heritage style box tests illustrate that the sensors reacted to the removal off the lid of a box in ambient conditions after around a day and half, with clear results after three days. When using isolated readings, the reaction time will be less important, as the cumulative corrosion measurements will not distinguish between events, but give an average corrosion rate for the period between observations.

When considering deployment, methodological and budgetary strategy, probe lifetime is important; indicating how often they must be renewed, the cost this will incur and when data will be lost. This will depend entirely on the nature of the environment in which they are exposed. ERCM cease to operate correctly after 50% of their thickness is consumed,

producing exponentially increased resistance after this; higher corrosion rates will decrease probe lifetime. If we assume ~4μm of thickness is consumed by the pre-corrosion methodology, we can provide estimates of probe lifetime dependant on relative humidity. The calculated lifetime from our previous data are summarised in table 8.4. At low humidity and in stable environments, the probe lifetime is likely to be measured in years. For the dynamic humidity tests, an illustration is provided of the number of repetitions of that particular program which would result in probe failure. These present much lower probe lifetimes, in the order of weeks or months. It is unlikely such environments will be present in a heritage environment, but it illustrates the amount of probe lifetime which will be lost for a single similar event. Assuming the deployment of these probes will be similar to those currently used to store heritage iron, we can predict that an atmosphere will either be closely controlled, with a low relative humidity, or kept at ambient conditions in a controlled mixed material environment or within standard storage. For the former, our results make probe failure within the first few years unlikely. In the latter, more regular probe monitoring will be needed to prevent the loss of data associated with probe failure. Of course, probe failure itself can be viewed as a result, perhaps the most effective way to illustrate a high corrosion rate and therefore a conservation problem.

| **Stable state** | | | |
|---|---|---|---|
| **Relative humidity** | | | **Probe lifetime (years)** |
| **15%** | | | Indefinite |
| **20%** | | | 170.0 |
| **30%** | | | 44.7 |
| **40%** | | | 12.1 |
| **50%** | | | 2.2 |
| **60%** | | | 0.7 |
| **Dynamic relative humidity environments** | | | |
| **Program number** | **Thickness loss per repetition (μm)** | **Repetitions before probe failure** | **Lifetime (days)** |
| **1** | 0.09 | 94 | 118.1 |
| **2** | 0.26 | 33 | 24.5 |
| **3** | 0.23 | 37 | 43.1 |
| **Sensor in heritage environments** | | | |
| **Heritage Box state** | | | **Minimum probe lifetime (years)** |
| **On the side, closed lid** | | | 46.2 |
| **In cupboard, closed lid** | | | 24.3 |
| **On the side, open lid** | | | 5.9 |

**Table 8.4**: Table of estimated sensor lifetime for pre-corroded ERCM within our test environments.

### 8.7.2 Suggested probe application to iron conservation

From the limitations above we can consider how the probes might be deployed in a heritage context or to answer conservation questions. Methodology will depend on the storage or display environment, whether the probes are addressing a specific corrosion question or providing passive generic monitoring, and the budgetary and manpower constraints of an institution.

The methodology of continuous monitoring within this study was shown to be effective for recording similar corrosion rates to archaeological iron with excellent accuracy, reaction time and repeatability. To monitor internal architectural iron or large conservation projects (where very long term monitoring could occur and substantial resources are available) large scale wiring networks could be envisaged and constant logging networked through a centralised computer system. It would allow testing of proposed archaeological storage environments, creating three dimensional maps of corrosivity within a room or large storage container. This could be deployed in a storage or display environment where artefact degradation has been identified as a problem, aiding identification of environmental factors. Such a method would be impractical for the majority of stored iron, through expense, access for wiring, placement of sensors, and distance over which the circuitry would have to operate.

The methodology would also be applicable for investigating specific heritage iron corrosion questions. Previous research by Kapatou and Lyon [12] examined the effect of desalination treatments (alkaline sulphite impregnation and electrolytic reduction) on the corrosion rates of the sensors to provide information on how it may affect archaeological artefacts. Similar evaluation of other active conservation techniques is easily envisaged; low temperature plasma treatments [32] or the application of coatings for example. Their use in the development of new conservation techniques would allow direct comparison of corrosion data before, after and during treatment to help improve, streamline or highlight problems with the methodology.

For passive conservation techniques, constant monitoring of the pre-corroded ERCM in additional atmospheric environments will not only improve our knowledge of sensor performance, but could provide information on the corrosion kinetics and rate resulting from variances in relative humidity, temperature, pollutants, light intensity and changes in environment stability, directly applicable to heritage iron. Specific suspected variables could be tested to investigate the increased corrosion of individual heritage iron examples, allowing environmental factors to be ruled out or highlighted as the cause of additional or strange corrosion behaviour.

The bulk and wiring of our system are not appropriate for the majority of heritage environments. Small cases, iron on display and where wires are not feasible to deploy could not be monitored by this method. Continuous monitoring in these cases would only be

achievable through additional equipment and miniaturisation. The MUSECORR designed sensors [33-5] have developed an autonomous monitoring station, allowing the whole system to be deployed as a small box. This allows deployment in limited space storage containers and within display cases, unobtrusively collecting data which can be accessed and processed wirelessly. Assuming a high accuracy voltmeter within the design, this system would be ideal for curated displays. The high cost of the system however, compared to the use of coupons [36] or colorimetricly monitoring relative humidity, is likely to rule it out for the majority of heritage institutions.

The alternative to continuous monitoring, as mentioned in the preceding sections, is to take individual measurements over longer, regular time periods. In this case the ERCM would be deployed similarly to coupons [36], connected to the circuitry only when data was collected. Our ERCM were designed with all connecting pads clearly spaced at one end to allow quick insertion into a circuit with a suitable connecting port. A prototype connector was made in the course of the investigation for this study, and was shown to allow quick, if somewhat unreliable, insertion of ERCM to be monitored using the same equipment as for our tests. During exposure, additional protection for the connecting pads may be required to allow good connection, through a temporary oil coating or close fitting cover. The individual data of thickness loss would lack data on individual corrosion events, but provide cumulative corrosion rates over the time between monitoring events.

ERCM could either be monitored *in situ* or taken (or sent) away for processing. *In situ* observation would require only a small movement out of the monitored environment, reducing the amount of error introduced by exposure, but suffers from the inconvenience, time and manpower cost of moving the multimeter to each site. Such a system would likely mean short monitoring times. Assuming a large number of measurements could be taken in a short time period, measurement error could be minimised, but would be at the mercy of temperature noise, introducing a level of error based on the time of day or year. Removing the ERCM to another location could be achieved by transferring the sensor to a highly desiccated environment and transported, or even sent long distances. This would allow the ERCM to be placed in a controlled temperature environment at a very low RH to prevent additional corrosion, with monitoring over a longer time period to provide a precise calculation of measured thickness loss. However, the changes this would create in the ERCM would alter the potential for future results, removing the cumulative similarities to heritage iron created by shared exposure with the same environment. Such a method would therefore be more useful for 'one shot' applications. I*n situ*, or very short range removal with methodological steps (an ambient low relative humidity and pollutant environment and a stable, similar temperature) to reduce error, would be preferable. Monitoring could take place as often as manpower and cost would allow, also taking into account conservation strategy, observed corrosion rates, perceived threat levels and value of the heritage iron itself.

This model could drastically reduce costs, with a single monitoring system required to survey as many individual ERCM boards as needed. It is estimated that the boards themselves cost around £9 each (For a chemically milled set of four: Iron foil £10, Substrate £5, Photo-plotting film and photoresist laminate £10, Developer, etchant and resist stripper £5 and tooling charge £5). While this assumes access to a photochemical milling setup, these are common across universities, with which the majority of heritage bodies are partnered or associated. In situations where even a single high accuracy multimeter would be beyond an institutions budget (not unlikely in the heritage sector) other solutions would be available. Simple sharing between organisations or rental of the equipment for short term use could cut costs. For public museums, a centralised regional pool is envisaged, loaned out for each period of monitoring. Heritage consultancies could offer a cheaper option than in house, along with appropriate expertise. For every level of institution, the sensors could offer a degree of corrosion monitoring capability, tailored to individual situations and budgets.

The results of these suggested methodologies would provide corrosion rates of the ERCM based on either curves, as this study, or individual measurements converted to rates through recording the time period between observations. As discussed above, the rates themselves will give a good impression of heritage iron corrosion contained within the same environment. Extrapolation of approximate rates for each artefact is possible through knowledge of the materials and corrosion products compared to the ERCM data and previous research results. Corrosion rates from actual archaeological iron, by respirometry or other method, compared directly to the ERCM results, will allow greater approximation of these rates. At the present time, however, the data will be of more use for general corrosivity measurements. High thickness loss measurements will indicate possibility of corrosion control failure and action will be required. Non-zero corrosion rates in heavily desiccated environments would give approximate estimates of heritage iron lifetimes within the same environment. While this data is less useful than precise corrosion rates of the iron itself, they will allow empirical feedback to conservation strategy, demonstrating where passive conservation is failing or succeeding. It will highlight problems as soon as they occur (within the time resolution of the methodology). Where severe issues are identified they will allow direct action, through a change in storage, active conservation methods, or application of a continuous ERCM monitoring methodology to acquire additional information to better identify the individual corrosion accelerators.

The suggested uses of the sensors discussed above could form the basis for an empirically based conservation strategy for heritage iron at institutional, regional and national levels. The projected relatively low cost makes the methodology available to answer academic questions and play a part in providing feedback to conservators and curators. Used in conjunction with existing techniques, and to evaluate, improve and create additional methods, iron pre-corroded electrical resistance monitors have the potential to be a powerful tool for forming and executing cultural heritage conservation strategy.

### 8.7.3 Comparison to other corrosion monitoring techniques

The different methodologies discussed above make the application of the pre-corroded ERCM comparable to a wide range of corrosion monitoring techniques. These can be applied as complementary sensors to the ERCM, or provide valuable experiment specific data to allow increased calibration compared to heritage iron and elucidate corrosion processes. They also provide an opportunity for discussion of our ERCM performance.

Other ERCM studies have been applied frequently in industry to monitor atmospheric [37], subterranean [38], structural [39] and aqueous [40] corrosion rates. In the majority, monitoring has proceeded, initially, with a clean surface. As shown by the results in section 7.3.4, pre-corroded ERCM corrode entirely differently to clean sensors in the environments we have chosen to monitor. The sensors developed by MUSECORR [33-35], have demonstrated excellent accuracy and corrosion rates for more noble metals [35] and demonstrating similarity to clean metal corrosion rates [41]. The latter study illustrates well how ERCM can be applied in long term monitoring to influence conservation strategy. The significant effect of chlorides on iron corrosion rates and reactions make such sensors far less applicable to heritage iron, where extant corrosion layers and incorporated chlorides are ubiquitous.

Previous comparable studies will therefore be constrained to those with corrosion products introduced to the corroding electrode prior to monitoring. McKenzia and Vassie's [42] application of previously corroded ERCM provide comparable results, but with much lower accuracy and resolution. They do illustrate environments and applications for our own sensors. The studies by Cai and Lyon [5] and Kapatou and Lyon [12] both provided similar accuracy levels and corrosion rate ranges. That there is difference in corrosion rates and kinetics is testament to the complexity of the corrosion processes and the necessity to achieve consistent chloride levels, initial thickness loss and corrosion product make-up and structure. Our own research has built on these studies, increasing reliability of manufacture, reducing fabrication and chloride level error, increasing the similarity of corrosion products to archaeological iron and applying the ERCM to lower relative humidities, measuring lower corrosion rates. Additional calibration and comparison to heritage iron has helped increase validity of both our ERCM and those used in the above studies.

Many corrosion methods measure corrosion directly. These methods are most likely to complement and work in tandem with pre-corroded ERCM, even providing data with which the ERCM may be calibrated. Respirometry has great potential for further use as a complementary technique for sensor calibration and artefact monitoring. Due to the methodological constraints, it will be limited to academic examinations and to address specific corrosion questions rather than active monitoring of collections. Previous studies have shown results very similar to those created by pre-corroded ERCM, specifically comparing the

evaluations of chloride removal techniques from heritage iron of Rimmer et al. [43] (for respirometry) and Kapatou and Lyon [12] (for pre-corroded ERCM). Studies by Thickett et al. [44] and Matthiesen and Wonsyld [45] have both demonstrated the similarity between respirometry oxygen consumption rates and mass-change corrosion rates for various metals, including chloride infested heritage iron. Direct calibration, further than that attempted in this study, of both techniques could be achieved through a combination of pre-corroded ERCM and respirometry; measuring the oxygen consumption of pre-corroded ERCM in different environments, while simultaneously monitoring the resistances. Respirometry values could be directly relatable to metal loss, potentially allowing a greater confidence in predicting iron corrosion rates based on oxygen consumption results. Applied in conjunction with heritage iron in identical environments, oxygen loss could be directly related to amount of corrosion. Additional examinations and knowledge of the corrosion products themselves could provide models for the corrosion mechanisms and pathways to oxygen consumption. Using X-ray tomography, or simply artefact size or mass as a proxy for metallic surface area, could allow further comparison of the corrosion rates in terms of metal loss per unit area. Combined, these factors could allow complete calibration of both ERCM and respirometry for future studies.

Digital image comparisons can provide excellent information for corrosion product growth and physical damage, allowing the mapping of crack propagation, field strain and spread of corrosion products [46]. Such data obtained in the same environment as the ERCM would allow linking of thickness loss rates to actual artefact damage and loss of heritage value. X-radiographic techniques using the same software [47], could also be applied, but it is highly unlikely such a technique could be applied *in situ*. Coupled with the high cost, it is difficult to imagine it would be used as a monitoring strategy.

Electrochemical methods provide an instant, not cumulative, measure of corrosion loss. While this can be converted to thickness loss over time, it does not allow for measuring changing conditions. Electrochemical studies are generally confined to inspecting heritage metal in terms of answering specific corrosion [48] or conservation [49] questions, but applications to monitor actual heritage items has been acheived. In atmospheric conditions, o-ring [50] or foam bound [51] electrochemical cells have been used, even on metals with extant corrosion layers [52-3]. The problems of alteration of the corrosion system itself can be dealt with by use of a gel based electrode [54]. The technique is of limited use for corrosion monitoring however, instead providing specific, and plentiful, corrosion data. For application to general collections, the expense of the technique, necessity for high levels of corrosion training and large size of sample needed make it impractical. As a combination, pre-corroded ERCM can provide information on corrosion rate data to illuminate problems in conservation which can be investigated more fully by electrochemical techniques. Electrochemical measurements of the sensors themselves could help to give comparisons to archaeological iron similarly tested, especially in evaluation of the similarity of corrosion layer reactions.

For *in situ* monitoring of heritage iron, alternative methodologies will be almost exclusively proxy measurements and directly comparable to ERCM measurements and methods. When deployed for individual monitoring events, the ERCM would act very similarly to coupons, previously used in both interior and exterior corrosion monitoring. Both can be pre-corroded and both will provide individual measurements of cumulative corrosion. The comparison also illustrates the additional data which can be extracted from our sensors. Similarly to coupons, on monitoring end corrosion products may be examined by microscopy and compositional analysis techniques. While coupons will undoubtedly be lower cost, in time, skills and money [55], the precision of the ERCM, their ease of reuse and the accuracy of the measurement will be higher. In addition, the value of metal loss provides a more direct, and less prone to modelling error, measure of corrosion rate than mass gain. Mass loss may provide comparable accuracy, but it prevents the coupons reuse and requires greater expense and techniques.

Electrochemical proxies, using pre-corroded electrodes of similar metal to that which is to be monitored, could be used as a better comparison for actual monitoring. Zhang and Lyon [56] have applied multi-electrode systems to monitor atmospheric corrosion electrochemically, and the sensors designed by Fu et al. [57] can operate in low relative humidity environments. They have even been used as online corrosion loggers, similarly to the methodology suggested for the pre-corroded ERCM [58]. Lack of corrosion products on the electrode surface qill not allow comparison with chloride infested heritage iron, and pre-corrosion will not be possible for current designs. Future improvements in design could remedy this and make such devices complementary to our sensors.

Quartz crystal microbalances are used in heritage institutions, providing very similar proxy results to the ERCM and with similar resolution of monitoring periods. QCM have previously been outperformed by clean ERCM in varyingly corrosive or polluted environments in terms of both accuracy and reliability [59]. However, at highest quoted accuracy (down to $10^{-8}$ $gcm^{-1}$ [60]) and considering the higher error introduced by the pre-corrosion methodology and the effect of dynamic temperature conditions, comparable accuracy is likely. They may be deployed similarly to autonomous ERCM systems, but suffer from the same drawbacks as all gravimetric techniques; it is difficult to directly link corrosion rate with mass gain without proper knowledge of corrosion processes. The cost for both systems is comparable for continuous monitoring, though ERCM allow the additional flexibility of redeployment as a sporadic monitoring device and the option to multiplex many sensors into a single monitoring centre. Pre-corrosion is theoretically possible for QCM, but is untested, would introduce large amounts of error and, considering the low thickness of metal used, will be unlikely to provide corrosion products similar to heritage iron. For monitoring heritage iron, this author's conclusion is that the ERCM from this study will provide more representative and revealing results. QCM will be better suited for examination of bare metal, with or without introduced pollutant, to map the early stages of corrosion to high accuracy.

Certain monitoring techniques used on archaeological items do not translate well for chloride infested iron and are unlikely to cross over with the use of the ERCM. Thermal imaging of heritage iron has the potential to be used as a continuous monitoring system, but is likely to work poorly when thick corrosion layers are present; it is unlikely to be as successful for chloride infested iron as for bronze statues [61]. Ultrasonic methods are not used in atmospheric contexts and require removal of corrosion layers [62], unlikely to be of use in land based heritage environments or monitoring ongoing corrosion. Acoustic emissions have been shown to provide additional data on individual corrosion events, but are untested on ironwork and are unlikely to provide useful data on corrosion rates.

Methodologies suggested for application of pre-corroded ERCM complement, and are complemented by, the alternative monitoring techniques, while providing a valuable, empirically based proxy measuring tool. For examination of specific corrosion problems, identifying corrosion mechanisms and modelling corrosion processes, electrochemical methods will provide the optimum strategy. For measurement of actual corrosion rates of archaeological iron in a confined space, respirometry and visual techniques may be applied. For very cheap, low resolution and accuracy results, gravimetric and optical observation of pre-corroded coupons may be used. For general corrosivity of an environment on clean or very slightly corroded metal, quartz crystal microbalances can provide excellent corrosion rates. However, for proxy monitoring of heritage iron with significant corrosion layers and chloride content, the methodology used in this program, and those suggested above, are likely to provide the most accurate, similar and effective corrosion rates.

## 8.8 Suggested future research directions

This work has shown ERCM sensors can be made to high precision, pre-corroded and present corrosion rates similar to heritage iron in environments similar to heritage storage and display. The techniques developed and the information gained suggest a number of obvious routes for future research.

The pre-corrosion methodology deserves additional attention. As discussed in section 8.1, various salt concentrations and salt types may be printable onto a surface, in an endless variety of patterns. Additional work to achieve multi-salt depositions should be initiated and is likely to involve a number of methodological alterations. This could be extended by varying the method of controlled corrosion to create a variety of corrosion products. Metal need not be constrained to iron; while the milling methodology may have to be altered, varying thicknesses and metals could be implemented. Sustained research could allow specific methodologies for the formation of specific corrosion products on a metal surface. This could be eventually applied to a system by which corrosion products could be created ‘on demand’ for corrosion testing, with given levels and controlled regionality of pollutants.

ERCM corrosion rates could be further calibrated to archaeological iron, both during manufacture and for adaptation of the results to archaeological iron corrosion rates. The additional methodologies which could be created for multiple salts and corrosion products make it possible that sensors could equally be created 'on demand' specifically for each environment and heritage iron type. Specific metal could be combined with planned and designed corrosion products to create a sensor with highly similar metallurgy, corrosion layers and chemistry to a given and specific artefact, heritage iron structure or collection, vastly improving the chances of creating similar corrosion rates.

ERCM in the same state as those used in this study have been shown to be fit for purpose for monitoring of generic chloride infested heritage iron and additional research would benefit their calibration to actual heritage iron corrosion rates. Continued comparison with respirometry, visual and other corrosion monitoring techniques on artefacts in identical environments will allow better algorithms for conversion of the thickness loss rates. While incremental, this could elevate the ERCM form corrosivity monitors to more direct corrosion rate sensors, allowing application of empirical, numerical corrosion rates for corrosion strategy. Additional testing at differing corrosion levels, specifically concentrating on deliquescence humidities of likely present salts, will also help define expected kinetics within environments. This could also include application to alternative environments or situation. Underwater monitoring would be difficult, but possible with low enough applied current. Examination of corrosion rates while the ERCM are in contact with other materials, such as additional metals or organics (both of which could be expected to alter corrosion rates) could be used to simulate composite artefacts or buried contexts. Incorporation of the ERCM into ersatz heritage building materials could emulate corroded building materials.

Specific examples of applications to measure, evaluate and monitor conservation strategy have been discussed above. Implementation of ERCM in heritage environments will allow evaluation and validation of this study. It is likely that deployment in heritage environments will illustrate additional methodological challenges and complexities; doing so in a research context, examining corrosion phenomena or passive conservation methods, will allow appreciation of these to feed in to any commercial applications. The concurrent development of a standalone monitor, likely an engineering challenge rather than scientific, would likewise improve the usability of the sensors. Direct collaboration and sharing of knowledge with the MUSECORR project, or an industrial partner with current technology in this area, could easily provide significant steps to achieving device autonomy and flexibility of use.

The potential applications of the ERCM are manifold and the ranges of possible research direction reflect this. Ultimately it is hoped that the number of possible applications, especially for the inkjet printer methodology, will exceed this authors experience and skills, leading to novel techniques in a range of disciplines.

# Chapter 9

# Conclusions

Corrosion monitoring of chloride infested heritage iron has previously been difficult to achieve due to the fundamentally different corrosion rate, processes and phenomena caused by extant corrosion layers and pollutants. Direct measurement is near impossible without altering the artefact or corrosion factors, while proxy methods struggle to create similar rates and react differently to environmental humidity change. This difficulty made writing conservation strategy demanding, with methodology based around control of environmental factors to limit apparent corrosivity. This methodology does not allow for easy detection of strategy failure and relies on anecdotal, not empirical evidence.

This study aimed to recreate pre-corroded electrical resistance monitors, previously created and tested to examine atmospheric corrosion of corroded iron and test conservation techniques. It was hoped that fabrication error could be reduced, accuracy increased, and the sensors tested in environments similar to chloride rich heritage iron. Execution of these aims has lead to the following methodological advancements and conclusions.

Photochemical milling, using approximately the same methodology as for circuit board manufacture, created precision sinuous patterns of iron. Combined with a mounting methodology this allowed creation of blank electrical corrosion monitors with a maximum fabrication error of 10μm at lateral edges, equating to a 2% error overall. Design and methodology created equivalent sensors across each created batch

Inkjet printers have been shown to be accurate, consistent and reliable deposition apparatus for sodium chloride. The methodology was shown to be tuneable using either different levels of greyscale or repeat printings, depositing between 85μg/cm$^2$ and 110μg/cm$^2$ using single prints of varying intensity and up to 390μg/cm$^2$ using repeat prints. Highest accuracy was achieved using 100% intensity prints, depositing 108±9μg/cm$^2$. The methodology results in

salt crystals spread evenly across the contaminated surface, suitable for subsequent use in corrosion studies. The methodology was shown to be adaptable, could print onto a variety of samples and allowed effective contamination and controlled corrosion. It is easily envisaged that the methodology could be adapted for different combinations, intensities and patterns of salts, varied samples sizes and use in any methodology which calls for even deposition of salts onto a surface. For this study, the method was used to effectively contaminate our ERCM with a specific amount of chloride.

Controlled atmospheric corrosion of inkjet printed salts was created corrosion products of an even layer with good adhesion, similar to chloride contaminated heritage iron; magnetite, goethite, lepidocrocite and akaganeite. No severe localised corrosion was detected, with good maintenance of core integrity. The methodology is sufficient and effective for pre-corroding ERCM to bear similar material and chemical characteristics to the corrosion product–metal interface of heritage iron.

ERCM created in this way give corrosion rates in controlled, heritage type environments. Sensor accuracy allowed detection of corrosion rates down to 0.05μm/year. For large jumps in relative humidity, changes in corrosion rate were logged almost instantly. The rates monitored and the reactions to relative humidity changes were similar to anecdotal and respirometry generated rates of heritage iron. This similarity, the limits of detection and the success of the methodology make it very likely the ERCM would be extremely proficient at rating the corrosivity of an environment for other chloride infested iron.

The results of the ERCM tests give additional information for heritage iron conservation. The highest corrosion rates occurred with sudden large increases in humidity. No corrosion was logged at 15% RH, but at 20% RH (the level often achieved using passive conservation methods to prevent corrosion) metal loss was recorded. These factors may influence future conservation strategy of how to store, expose and plan future lifetimes of heritage iron. The logarithmic scale of corrosion rate against relative humidity, suggest that relatively little conservation strategy would need to be applied to give a significant reduction in metal loss. Corrosion will still occur at very low humidities; the rates observed in this study will help to inform whether the large resources required to lower corrosion rates to below these levels will be worth the resources, or whether smaller decreases with low levels of corrosion will be acceptable within budgetary limits. Comparisons of this kind illustrate the effect our ERCM may have on conservation strategy.

The difference between pre-corroded ERCM and blank ERCM were considerable and demonstrate the necessity of pre-corrosion or other treatments for proxy monitoring of chloride infested iron. Comparison of the results with other corrosion monitoring techniques highlight the quality and flexibility of the system. Suggested methodologies can cater for a range of budgetary, skill and capability levels while providing high or low resolution, high

accuracy corrosion rate results. While direct calibration of the sensors was not possible, they were shown to give higher corrosion rates than actual heritage iron. This makes them ideal as an early warning system for passive conservation method failure.

Future work and further research will improve the efficacy of the sensors, offer the opportunity for direct calibration and continue to provide information of corrosion rates, mechanisms and kinetics of chloride infested iron. Ultimately the improved sensors represent a powerful tool for continued conservation and study of chloride infested heritage iron.

# Bibliography

## Chapter 1 Introduction


1. ANHOLT, S., *The Anholt-GfK Roper Nation Brands Index*, New York, GfK Roper, 2009

2. ENGLISH HERITAGE, *Heritage counts 2014,* Portsmouth, English Heritage/Park communications, Accessed Online at http://hc.english-heritage.org.uk/content/pub/2014/heritage-counts-national-2014.pdf. Last accessed 21/07/2014

3. WATKINSON, D., 'Degree of Mineralization: Its Significance for the Stability and Treatment of Excavated Ironwork', *Studies in Conservation*, **28**(2), 1983, pp. 85-90

4. TURGOOSE, S., 'Post-Excavation Changes in Iron Antiquities', *Studies in Conservation*, **27**(3), 1982: pp. 97-101

5. SCOTT, D. A. AND G. EGGERT., *Iron and Steel in Art*. London, Archetype. 2009

6. XAVIER-ROWE A., FRY C. AND STANLEY B., 2011. Collections at risk, In: *Preprints of 16th Triennial Meeting of ICOM-CC*, ICOM-CC

7. NORTH, N. A. AND C. PEARSON 'Washing methods for chloride removal from marine iron artifacts.', *Studies in Conservation*, **23**(4) 1978, pp. 174-86.

8. KNIGHT, B. , 'The stabilisation of archaeological iron; past, present and future' in *Metal 95: Proceedings of the International Conference on Metals Conservation, Semur en Auxois, 25-28 Sept. 1995,* edited by I. D. MacLeod, S. L. Pennec and L. Robbiola. London, James & James, 1997, pp. 36-40.

9. BRADLEY, S., 'Preventative Conservation Research and Practice at the British Museum', *Journal of the American Institute for Conservation*, **44**(3), 2005: pp. 159-73

10. ASHLEY-SMITH, J., *Risk assessment for object conservation*. Oxford, Butterworth-Heinemann, 1999

11. KAPATOU, E. & S. B. LYON, 'An Electrical Resistance Monitor Study of the Post-Excavation Corrosion of Archaeological Iron' in *Art2008: 9th International Conference on Non-Destructive Testing of Art, Jerusalem, Israel, 25-30 May 2008, 2008: pp.25-30*

12. SCHINDELHOLZ, E. & R. G. KELLY, 'Application of Inkjet Printing for Depositing Salt Prior to Atmospheric Corrosion Testing', *Electrochemical and Solid State Letters*, **13**(10), 2010: pp. C29-C31

## Chapter 2: Iron Corrosion: Mechanisms and Products


1. JONES, D., *Principles and Prevention of Corrosion*, Second edition, Prentice Hall, New Jersey, 1996.

2. SHRIER, L. L., *Corrosion, 2nd edition, volumes 1 & 2*, London, Newnes-Butterworths, 1976

3. TRETHAWAY, K.R. & J. CHAMBERLAIN, *Corrosion for Science and Engineering 2nd edition*, London, Longman Group, 1995

4. STANSBURY, E. & R. BUCHANAN, *Fundamentals of Electrochemical Corrosion*, ASM International, USA, 2000

5. BARDAL, E., *Corrosion and Protection*, Springer, London, 2004

6. FONTANA, M. & N. GREENE, *Corrosion Engineering*, McGraw Hill, New Jersey, 1986.

7. SZKLARSKA, Z., *Pitting Corrosion of Metals*, NACE, USA, 1986.

8. AVNER, S. *Introduction to Physical Metallurgy*, Second edition, Mcgraw-Hill, USA, 1988

9. ASKELAND, D. & P. WEBSTER, *The Science and Engineering of Materials,* Second Edition, Chapman and Hall, London, 1990

10. TURGOOSE, S., 'Structure composition and Deterioration of Unearthed Iron Objects' in *Current Problems in the Conservation of Metal Artifacts: 13th International Symposium on the Conservation and Restoration of Cultural Property*, Tokyo, Tokyo National Research Institute of Cultural Properties, 1989 : pp35-53

11. STRATMANN, M., 'The Atmospheric Corrosion of Iron- A Discussion of the Physio-chemical Fundamentals of this omnipresent Corrosion Process Invited review', *Berichte der Bunsenges. Fuer Physikalische Chemie*, **94**(6), 1990: pp. 626-39

12. NORTH, N. A. and I. D. MACLEOD, 'Corrosion of metals' in *Conservation of Marine Archaeological Objects*. Edited by C. Pearson. London, Butterworths, 1987: pp. 68-98.

13. SCOTT, D. A. and G. EGGERT., *Iron and Steel in Art*. London, Archetype. 2009

14. ROBERGE, P. R., *Handbook of Corrosion Engineering*, New York, Mcgraw-Hill, 2000

15. NEFF, D., P. DILLMANN, L. BELLOT-GURLET, G. BERANGER, 'Corrosion of iron archaeological artefacts in soil: characterisation of the corrosion system', *Corrosion Science*, **47**(2), 2005: pp. 515-35

16. DILLMAN, PH., F. MAZAUDIER & S. HŒRLÉ, 'Advances in understanding atmospheric corrosion of iron. I. Rust characterisation of ancient ferrous artefact exposed to indoor atmospheric corrosion', *Corrosion Science*, **46**(6), 2004: pp. 1401-29

17. CORNELL, R. M. & U. SCHWERTMANN, *The Iron Oxides, Structure, Properties, Reactions, Occurrences and Uses* 2nd Edition; VCH Verlagsgesellschaft. Weinheim, Germany, 2003

18. CORNELL, R. M. AND R. GIOVANOLI, 'Transformation of Akaganeite into Goethite and Hematite in Alkaline Media' *Clays and Clay Minerals,* **38**(5), 1990: pp. 469-76.

19. FRINI, A. AND M. EL MAAOUI, 'Kinetics of the formation of goethite in the presence of sulfates and chlorides of monovalent cations', *Journal of Colloid and Interface Science* **190**(2), 1997: pp. 269-77

20. STRATMANN, M. & K. HOFFMANN, 'In Situ Mossbauer Spectroscopic Study of Reactions within Rust Layers', *Corrosion Science*, **29**(11), 1989: pp. 1329-52

21. WATKINSON, D. & M. R. T. LEWIS, 'Desiccated Storage of chloride-contaminated iron: A study of the effects of loss of environment control', in *Heritage Microbiology and Science: Microbes, Monuments and Maritime Materials*, Edited by Jones, M. E. & S. Woodcock, Special Publication 315, Royal Society of Chemistry, Cambridge,2008: pp. 279-89

22. TURGOOSE, S., 'The Nature of Surviving Iron Objects' in *Conservation of Iron. Maritime Monographs & Reports No. 53*, edited by Clarke, R. W. & and S. M. Blackshaw, National Maritime museum: Greenwich, 1982: pp.1-7

23. NEFF, D., P. DILLMANN, M. DESCOSTES & G. BERANGER, 'Corrosion of iron archaeological artefacts in soil: Estimation of the average corrosion rates involving analytical techniques and thermodynamic calculations', *Corrosion Science*, **48**(10) 2006: pp.2947-70

24. MONNIER, J., L. BELLOT-GURLET, L. LEGRAND, P. DILLMANN, S. RÉGUER, D. NEFF AND I. GUILLOT, 'The long term indoor atmospheric corrosion of iron: rust layer characterisation' in: C. DEGRIGNY, R. VAN LANGH, B. ANKERSMIT & I. JOOSTEN, eds. *Metal 07, Proceedings of the Interim Meeting of the ICOM-CC Metal WG vol.* 3Amsterdam: Rijksmuseum, 2007: pp. 32–7.

25. GILBERG, M. R. & N. J. SEELEY, 'The Identity of Compounds Containing Ions in Marine Iron Corrosion Products: A Critical Review', *Studies in Conservation,***26**(2),1981: pp. 50-6

26. KAPATOU, E., *Development of an Electrical Resistance Monitor on the Corrosivity Assessment of Museum Environments for Iron*, Manchester, University of Manchester, 2010

27. WANG, Z., C. C. XU, X. CAO AND B. XU, 'The morphology, phase composition and effect of corrosion product on simulated archaeological iron', *Chinese Journal of Chemical Engineering*, **15**(3), 2007: pp. 433-8.

28. SELWYN, L. S., P. J. SIROIS & V. ARGYROPOULOS, 'The Corrosion of Excavated Archaeological Iron with Details on Weeping and Akaganéite', *Studies in Conservation*, **44**(4) 1999, pp. 217-32

29. RÉMAZEILLES, C. AND P. REFAIT, 'On the formation of beta-FeOOH (akaganeite) in chloride-containing environments', *Corrosion Science,* **49**(2), 2007: pp. 844-57.

30. WATKINSON, D. AND M. R. T. LEWIS, 'The Role of beta-FeOOH in the Corrosion of Archaeological Iron' in *Materials Issues in Art and Archaeology VII*. Edited by P. B. Vandiver, J. L. Mass and A. Murray. Warrendale, PA, Materials Research Society of America Symposium, 2005: pp. 103-14.

31. BLAND, P. A., S. P. KELLEY, F. J. BERRY, J. M. CADOGAN AND C. T. PILLINGER, 'Artificial weathering of the ordinary chondrite Allegan: Implications for the presence of Cl- as a structural component in akaganeite', *American Mineralogist*, **82**(11-12), 1997: pp. 1187-97.

32. DEGRIGNY C., L. DURIVAULT, B. CHEVALIER & B. DARRIET, *Réalisation et caractérisation d'éprouvettes base fer simulant l'altération des objets archéologiques. PCR 'Fer chlorures'*, Institut de Chimie de la Matière Condensée de Bordeaux, Arc'Antique Laboratoire de Restauration et de Recherche sur les objets d'art de Nantes, Septembre 1999. 1999.

33. ELLIS, J., R. GIOVANOLI AND W. STUMM, 'Anion exchange properties of b-FeOOH', *Chimia*, **30**, 1976: pp. 194-7.

34. STAHL, K., K. NIELSEN, J. Z. JIANG, B. LEBECH, J. C. HANSON, P. NORBY AND J. VAN LANSCHOT, 'On the akaganeite crystal structure, phase transformations and possible role in post-excavational corrosion of iron artifacts.', *Corrosion Science*, **45**(11), 2003: pp. 2563-75.

35. CAI, J., J. LIU, Z. GAO, A. NAVROTSKY AND S. L. SUIB, 'Synthesis and anion exchange of tunnel structure akaganeite', *Chemistry of Materials*, **13**(12), 2001: pp. 4595-602.

36. KANEKO, K. AND K. INOUYE, 'Adsorption of water on FeOOH as studied by electrical conductivity measurements.' *Bulletin of the Chemical Society of Japan* **52**(2), 1979: pp. 315-20.

37. KAESCHE, H., *Corrosion of Metals: Physiochemical Principles and Current Problems*, New York, Springer-Verlag, 2003

38. THICKETT, D., *Post Excavation Changes and Preventative Conservation of Archaeological Iron*, Birkbeck College, London, 2012

39. ISHIKAWA, T., Y. KONDO, A. YASUKAWA AND K. KANDORI, 'Formation of magnetite in the presence of ferric oxyhydroxides', *Corrosion Science*, **40**(7), 1998: pp. 1239-51.

40. PATERSON E., R. SWAFFIELD R. & D. R. CLARK, 'Thermal decomposition of synthetic akaganeite', *Thermochim. Acta*, **54**, 1982: 201-211.

41. HŒRLÉ, S., F MAZAUDIER, PH. DILLMANN & G. SANTARINI, 'Advances in understanding atmospheric corrosion of iron. II. Mechanistic modelling of wet-dry cycles', *Corrosion Science*, **46**(4), 2004, pp. 1431-65

42. SANTARINI, G., 'Corrosion behaviour of low alloy steels: From Ancient Past to far future' in *Corrosion of metallic heritage artefacts; Investigation, Conservation and prediction for long term behaviour, European Federation of Corrosion Publications Number 48*, edited by DILLMANN, P., G. BERANGER, P. PICARDO & H. MATTHIESEN, Woodhead; Cambridge, 2007, pp. 18-30

43. CUDENNEC, Y. AND A. LECERF , 'Topotactic transformations of goethite and lepidocrocite into hematite and maghemite', *Solid State Sciences*, **7**(5), 200: pp. 520-9.

44. GARCIA, K. E., 'On the Rust Products Formed on Weathering and Carbon Steels Exposed to Chloride in Dry–Wet Cyclical Processes', *Hyperfine Interactions,* **161**(1-4), 2005: pp. 127-37.

45. TORRENT, J., R. GUZMAN & M. A. PARRA,' Influence of Relative Humidity on the Crystallisation of Fe(III) Oxides from Ferrihydrite'. *Clay and Clay minerals*, **30**(5), 1982: pp. 37-40

46. STAHL, K., K. NIELSEN, J. C. HANSON, P. NORBY, J. Z. JIANG AND J. VAN LANSCHOT, 'The akaganeite-hematite reaction on the possibilities for chloride removal from iron artifacts' in *25 Years School of Conservation Preprints of Jubilee Symposium 18-20 May 1998* edited by K. Borchersen. Copenhagen, Det Kongelige Danske Kunstakademi, Konservatorskolen, 1998: pp. 157-60.

47. SATO, N., K. KUDO & R. NISHIMURA, 'Depth analysis of Passive Films on Iron in Neutral Borate Solution' Journal of the Electrochemical Society, 128(10), 1976: pp. 1419-23

48. OH, S. J., D. C. COOK & H. E. TOWNSEND, 'Atmospheric corrosion of different steels in marine, rural and industrial environments', *Corrosion Science*, **41**(9), 1999: pp. 1687-702

49. STANJEK, H. 'The formation of maghemite and hematite from lepidocrocite and goethite in a Cambisol from Corsica, France, *Zeitschrift für Pflanzenernährung und Bodenkunde*, **150**(5), 1987: pp. 314-8.

50. RÉGUER, S., P. DILLMANN, F. MIRAMBET AND L. BELLOT-GURLET, 'Local and structural characterisation of chlorinated phases formed on ferrous archaeological artefacts by mu XRD and mu XANES', *Nuclear Instruments & Methods in Physics Research Section B-Beam Interactions with Materials and Atoms* **240**(1-2), 2005: pp.500-4.

51. FOLEY, R. T., 'Role of the chloride Ion in Corrosion', *Corrosion*, **26**(2) 1970: pp. 58-70

52. REGUER, S., P. DILLMANN, F. MIRAMBET, J. SUSINI & P. LAGARDE, 'Investigation of Cl Corrosion products of iron archaeological artefacts using micro-focused synchrotron X-ray absorption spectroscopy' *Applied Physics A; Materials Science and Processing*, **83**(2), 2006: pp 189-93

53. RÉGUER, S., P. DILLMANN AND F. MIRAMBET, 'Buried iron archaeological artefacts: Corrosion mechanisms related to the presence of Cl-containing phases', *Corrosion Science*, **49**(6), 2007: pp. 2726-44.

54. RÉMAZEILLES, C., D. NEFF, F. KERGOURLAY, E. FOY, E. CONFORTO, E. GUILMINOT, S. REGUER, PH. REFAIT & PH. DILLMANN, 'Mechanisms of long-term anaerobic corrosion of iron archaeological artefacts in seawater', *Corrosion Science*, **51**(12), 2009: pp. 2932-41

55. NEMER, M., Y. XIONG, A. ISMAIL & J-H. JANG, 'Solubility of Fe2(OH)3Cl (pure-iron end-member of hibbingite) in NaCl and Na2SO4 brines', *Chemical Geology*, **280**, 2011: pp 26-32

56. NORTH, N. A. AND C. PEARSON 'Alkaline sulfite reduction treatment of marine iron' *in ICOM Committee for Conservation, 4th Triennial Meeting Venice, 75/13/3.* Paris, International Council of Museums, 1975, pp. 1-14.

57. GILBERG, M. R. AND N. J. SEELEY, 'The Alkaline Sodium Sulphite Reduction Process for Archaeological Iron: A Closer Look." *Studies in Conservation,* **27**(4), 1982, pp. 180-4.

58. REFAIT, P., S. H. DRISSI, J. PYTKIEWICZ AND J.-M. R. GÉNIN, 'The anionic species competition in iron aqueous corrosion: role of various green rust compounds', *Corrosion Science*, **39**(9), 1997: pp. 1699-710.

59. MATTHIESEN, H., L. R. HIBBERT & D. J. GREGORY, 'Siderite as a Corrosion Product on Archaeological Iron from a Waterlogged Environment', *Studies in Conservation*, **48**(3), 2003: pp. 183-94

60. MATTHIESEN, H., D. GREGORY & B. SØRENSON, 'Long-term corrosion of iron at the waterlogged site of Nydam in Denmark: studies of environment, archaeological artefacts and modern analogues' in *Corrosion of metallic heritage artefacts; Investigation, Conservation and prediction for long term behaviour, European Federation of Corrosion Publications Number 48*, edited by Dillmann, P., G. Beranger, P. Picardo & H. Matthiesen, Woodhead; Cambridge, 2007: pp. 272-92

61. GU, J. D., T. E. FORD & R. MITCHELL, 'Microbiological Corrosion of Metals', in in *Uhlig's Corrosion handbook, 2nd Edition* edited by Revie, R. W., John Wiley and Sons, New York, pp. 915-28

62. FELL, V. AND WARD M., 1998. Iron sulphides corrosion products on artifacts from waterlogged deposits. In *Metal 98;Proceedings of the International Conference on Metals Conservation* Draguignan-Figanieres, France 27-29 May 1998, London, James and James, 111-115.

63. FELL, V. & M. WARD, 'Monitoring of archaeological and experimentaliron at Fiskerton, England' in *Metal 04: Proceedings of the International Conference on Metals Conservation, Canberra, Australia, October 2004*, edited by. J. Ashton and D. Hallam. Canberra, National Museum of Australia, 2004, pp. 17-2

64. BOURDOISEAU, J.-A., M. JEANNIN, R. SABOT, C. REMAZEILLES & PH. REFAIT, 'Characterisation of Mackinawite by Raman Spectroscopy: Effects of crystallisation, drying and oxidation' *Corrosion Science*, **50**(11), 2008: pp. 3247-55

65. MA. H,. X. CHENG, G. LI, S. CHEN, Z. QUAN, S. ZHAO & L, NIU, 'The influence of hydrogen sulphide on corrosion of iron under different conditions', *Corrosion science,* **42**(10), 2000: pp. 1669-83

66. MCGOWAN, G. & J. PRANGNELL 'The Significance of Vivianite in Archaeological Settings." *Geoarchaeology* **21**(1), 2006: pp. 93-111.

## Chapter 3 Archaeological Iron: Metallurgy and Corrosion


1. NAVROTSKY, A., L. MAZEINA AND J. MAJZLAN, 'Size-Driven Structural and Thermodynamic Complexity in Iron Oxides', *Science* **319**(5870), 2008: pp. 1635-8.

2. RAPP, G. & C. L. HILL, *Geoarchaeology; The Earth-Science Approach to Archaeological Interpretation, 2nd Edition*, Yale, Yale University Press, 2006

3. MIDANT-REYNES, B., *The Prehistory of Egypt: From the First Egyptians to the First Pharaohs*, Blackwell, Oxford, 2000

4. JOHNSON, D., J. TYLDESLEY, T. LOWE, P. J. WITHERS & M. M. GRADY, 'Analysis of a prehistoric Egyptian iron bead with implications for the use and perception of meteorite iron in ancient Egypt', *Meteoritics and Planetary Science*, **48**(6), 2013: pp. 997-1006

5. RICHARDSON, S. R., 'Iron, Prehistoric and Ancient', *American Journal of Archaeology*, **38**(4), 1934, pp. 555-83

6. PHOTOS, E., 'The Question of Meteoritic versus smelted Nickel-Rich Iron: Archaeological Evidence and Experimental Results', *World Archaeology*, **20**(3), 1989, pp. 403-21

7. KING, E. A., *Space Geology*, New York, Wiley, 1976

8. PIASKOWSKI, J., 'A Study of the Origin of the Ancient High-nickel Iron Generally Regarded as Meteoritic' in *Early Pyrotechnology. The Evolution of the First Fire-using Industries*, edited by T. A. Wertime and S. F Wertime, Washington DC, Smithsonian Institution Press, 1982: pp. 237-43

9. BUCHWALD, V. F., 'On the Use of Iron by the Eskimos of Greenland', *Materials Characterization*, **29**(2), 1992, pp. 139-76

10. COGHLAN, H.H., *Notes on prehistoric and early iron in the Old World 2nd Edition*, Oxford, Pitt Rivers Museum, 1977

11. VAN DER MERWE, N. J. & D. H. AVERY, 'Pathways to Steel', *American Scientist*, **70**(2), 1982: pp. 146-55

12. YALÇIN, Ü, 'Early Iron Metallurgy in Anatolia', *Anatolian Studies*, **49**(4), 1999: pp. 177-87

13. COGHLAN, H. H., 'Prehistoric Iron Prior to the Dispersion of the Hittite Empire', *Man*, **41**, 1941: pp. 74-80

14. BUCHWALD, V. F., *Iron and Steel in Ancient Times*, Copenhagen, Det Kongelige Danske Videnskabernes Selskab, 2005

15. SHERBY, O. D. & J. WADSWORTH, 'Ancient Blacksmiths, the Iron Age, Damascus steels, and modern metallurgy', *Journal of Materials Processing Technology*, **117**(3), 2001: pp. 347-353

16. GóMEZ DE SALAZAR, J. M. AND A. SORIA, 'Characterising ancient iron pieces from la olmeda', *JOM Journal of The Minerals, Metals and Materials Society*, **52**(12), 2000: pp. 15-7

17. MUHLY, J. D., R. MADDIN & T. STECH, 'The Metal Artifacts' in *Kinneret: Ergebnisse der Ausgrabungen auf dem Tell el-'Orēme am See Gennesaret 1982-1985,*edited by F. Volkmar Wiesbaden, 1990: pp. 159-75

18. STECH-WHEELER, T., J. D. MUHLY, K. R. MAXWELL-HYSLOP, & R. MADDIN, 'Iron at Taanach and Early Iron Metallurgy in the Eastern Mediterranean', *American Journal of Archaeology*, **85**(3), 1981: pp. 245-68

19. VERHOEVEN, J. D., 'Damascus Steel, Part 1: Indian Wootz Steel', *Metallography*, **20**(2), 1987: pp. 145-51

20. BALASUBRAMANIAM, R. & A. V. RAMESH KUMAR, 'Corrosion resistance of the Dhar iron pillar', *Corrosion Science*, **45**(11), 2008, pp. 2451-65

21. WAGNER, D. B*., Iron and Steel in Ancient China*, Lieden, Brill, 1993.

22. SCHUBERT, H. R., *History of the British Iron and Steel Industry from c.450BC to 1775*, London, Routledge & Kegan Paul, 1957

23. BARRACLOUGH, K. C., *Steelmaking Before Bessemer, Vol 1: Blister Steel, the Birth of an Industry*, London, The Metals Society, 1984

24. RIDEN, P. 'The final phase of charcoal iron-smelting in Britain, 1660-1800', *Historical Metallurgy*, 28(1), 1994: pp. 14-26

25. CLEARY, H. J. & N. D. GREENE, 'Corrosion Properties of Iron and Steel', Corrosion Science, 7(), 1967: pp. 821-31

26. AL-QURAN, F. M. F & H. I. AL-ITAWI, 'Effects of Heat Treatment on Corrosion Resistance and Microhardness of Alloy Steel', *European Journal of Scientific Research*, **39**(2), 2010: pp. 251-6

27. MELCHER, R. E., 'Effect on marine immersion corrosion of carbon content of low alloy steels' , *Corrosion Science*, **45**(11), 2003: pp. 2609-25

28. CRONYN, J.M., *The Elements of Archaeological Conservation*, London, Routledge, 1990

29. DILLMANN, P. & R. BALASUBRAMANIAM, 'Characterisation of Ancient Indian Iron and Entrapped Slag Inclusions using Electron, Photon and Nuclear Microprobes' *Bulletin of Materials Science*, **24**(3), 2001: pp. 317-22

30. DEVOS, W., M. SENN-LUDER, C. MOOR & C. SALTER, 'Laser ablation inductively coupled mass spectrometry (LA-ICP-MS) for spatially resolved

trace analysis of early-medieval archaeological iron finds' , *Fresenius' Journal of Analytical Chemistry*, **336(**8), 2000: pp. 873-80

31. DILLMAN, P., R. BALASUBRAMANIAM & G. BERANGER, 'Characterisation of Protective Rust on Ancient Indian Iron Microprobe Analysis', *Corrosion Science*, **44**(10), 2002: pp. 2231-42

32. MISAWA, T., K. KYONO, W. SUËTAKA & S. SHIMODAIRA, 'The Mechanism of Atmospheric Rusting and the Effect of Cu and P on the Rust Formation of Low Alloy Steels', Corrosion Science, **11**(1), 1971: pp. 35-48

33. TRETHAWAY, K.R. & J. CHAMBERLAIN*, Corrosion for Science and Engineering 2nd edition*, London, Longman Group, 1995

34. FYFE, D., 'The Atmosphere' in *Corrosion 3rd Edition,* edited by Schrier, L. L., R. A. Jarman & G. T. Burstein, Butterworth-Heinemann, Oxford, 1994

35. RUNK, R. B. & H. J. KIM, 'The Oxidation of Iron-Carbon Alloys at Low Temperatures', *Oxidation of Metals*, **2**(3), 1970: pp. 285-306

36. LEYGRAF, C. & T. E. GRAEDEL, *Atmospheric Corrosion*, New York, Wiley, 2000

37. KARP, C., 'Calculating Atmospheric Humidity', *Studies in Conservation*, **28**(1), 1983: pp. 24-8

38. AHMAD, Z., *Principles of Corrosion Engineering and Corrosion Control,* Butterworth-Heinemann , Oxford, 2006

39. TULLMIN, M. & P. R. ROBERGE 'Atmospheric Corrosion' in *Uhlig's Corrosion handbook, 2nd Edition* edited by Revie, R. W., John Wiley and Sons, New York, 2000: pp. 305-21

40. EVANS, R., U. MARINI BETTOLO MARCONI & P. TARAZONA, 'Fluids in narrow pores: Adsorption, capillary condensation, and critical points', *Journal of Chemical Physics*, **84**(4), 1986: pp. 2376-99

41. PHIPPS, P. B. P. & D. W. RICE, 'The Role of Water in Atmospheric Corrosion' in *Corrosion Chemistry; ACS Symposium series 89* edited by Gould, R. F., American Chemical Society, Washington: pp. 235-61

42. CAI, J. –P. & S. B. LYON, 'A mechanistic study of initial atmospheric corrosion kinetics using electrical resistance sensors', *Corrosion Science*, **47**(12), 2005: pp. 2956-73

43. FARMER, J., D. MCCRIGHT, G. GDOWSKI, F. WANG, T. SUMMERS, P. BEDROSSIAN, J. HORN, T. LIAN, J. ESTILL, A. LINGENFETLER & W. HALSEY, *General and Localized Corrosion of Outer Barrier of High-Level Waste Container in Yucca Mountain, May 2000 Preprint UCRL-JC-138890*, Lawrence Livermore National Library, Technical Information Department Digital Library , Accessed online at: https://e-reports-ext.llnl.gov/pdf/238141.pdf on 20/01/2012

44. WATKINSON, D. & M. R. T. LEWIS, 'Desiccated Storage of chloride-contaminated iron: A study of the effects of loss of environment control', in *Heritage Microbiology and Science: Microbes, Monuments and Maritime Materials*, Edited by Jones, M. E. & S. Woodcock, Special Publication 315, Royal Society of Chemistry, Cambridge,2008: pp. 279-89

45. HŒRLÉ, S., F MAZAUDIER, PH. DILLMANN & G. SANTARINI, 'Advances in understanding atmospheric corrosion of iron. II. Mechanistic modelling of wet-dry cycles', *Corrosion Science*, **46**(4), 2004, pp. 1431-65

46. EVANS, U. R. & A. J. TAYLOR, 'Mechanisms of Atmospheric Rusting', *Corrosion Science*, **12**(3), 1972, pp. 227-46

47. STRATMANN, M., 'The Atmospheric Corrosion of Iron- A Discussion of the Physio-chemical Fundamentals of this omnipresent Corrosion Process Invited review', *Berichte der Bunsenges. Fuer Physikalische Chemie*, **94**(6), 1990: pp. 626-39

48. MISAWA, T., K. KYONO, W. SUËTAKA & S. SHIMODAIRA, 'The Mechanism of Atmospheric Rusting and the Effect of Cu and P on the Rust Formation of Low Alloy Steels', Corrosion Science, **11**(1), 1971: pp. 35-48

49. SUZUKI, I., N. MASUKO & Y. HISAMATSU, 'Electrochemical properties of Iron Rust', *Corrosion Science*, **19**(8) 1979: pp. 521-35

50. COX, A. & S. B. LYON, 'An electrochemical study of the atmospheric corrosion of iron- II. Cathodic and anodic processes on uncorroded and pre-corroded iron', *Corrosion Science*, **36**(7), 1994: pp.1177-92

51. ANTONY, H., L. LEGRAND, L. MARÉCHAL, S. PERRIN, PH. DILLMANN & A. CHAUSSÉ, 'Study of lepidocrocite γ-FeOOH Electrochemical Reduction in Neutral and Slightly Alkaline Solutions at 25°C', *Electrochemica Acta*, **51**(4), 2005, pp. 745-53

52. MARÉCHAL, L., S. PERRIN, P. DILLMANN & G. SANTARINI, 'Study of the atmospheric corrosion of iron by ageing historical artefacts and contemporary low-alloy steel in a climatic chamber: comparison with mechanistic modelling' in *Corrosion of metallic heritage artefacts; Investigation, Conservation and prediction for long term behaviour, European Federation of Corrosion Publications Number 48*, edited by Dillmann, P., G. Beranger, P. Picardo & H. Matthiesen, Woodhead; Cambridge, 2007: pp. 131-51

53. DUNN, D. S., G. A. CRAGNOLINO, M. S. BOGART & C. S. BROSSIA, 'Corrosion or Iron Under Alternating Wet and Dry Conditions', *Corrosion*, **56**(5), 2000: pp. 470-81

54. NEFF, D., P. DILLMANN, M. DESCOSTES & G. BERANGER, 'Corrosion of iron archaeological artefacts in soil: Estimation of the average corrosion rates involving analytical techniques and thermodynamic calculations', *Corrosion Science*, **48**(10) 2006: pp.2947-70

55. MONNIER, J., L. BELLOT-GURLET, L. LEGRAND, P. DILLMANN, S. RÉGUER, D. NEFF AND I. GUILLOT, 'The long term indoor atmospheric corrosion of iron: rust layer characterisation' in *Metal 07: Interim Meeting of the ICOM-CC Metal Working Group, Volume 2: Innovative Investigation of Metal Artefacts, 17-21 September 2007, Amsterdam, edited by*. C. Degrigny, R. van Langh, I. Joosten and B. Ankersmit. Amsterdam, Rijksmuseum, 2007: pp. 47-54.

56. SONG, F. M., D. W. KIRK, J. W. GRAYDON AND D. E. CORMACK, 'Effect of ferrous ion oxidation on corrosion of active iron under an aerated solution layer', Corrosion **58**(2), 2002: pp. 145-55.

57. DÜNNWALD, J. AND A. OTTO, 'An investigation of phase transitions in rust layers using Raman Spectroscopy', *Corrosion Science*, **29**(9), 1989: pp. 1167-76.

58. GARCIA, K. E., 'On the Rust Products Formed on Weathering and Carbon Steels Exposed to Chloride in Dry–Wet Cyclical Processes', *Hyperfine Interactions,* **161**(1-4), 2005: pp. 127-37.

59. ANTONY, H., S. PERRIN, P. DILLMANN, L. LEGRAND & A. CHAUSSÉ, 'Electrochemical study of indoor atmospheric corrosion layers formed on ancient iron artefacts', *Electrochemica Acta*, **52**(27), 2007: pp. 7754-9

60. YAMASHITA, M., H. MIYUKI, Y. MATSUDA, H. NAGANO & T. MISAWA, 'The Long Term Growth of Protective Rust Layer Formed on Weathering Steel By Atmospheric Corrosion During a Quarter of A Century', *Corrosion Science*, **36**(2), 1994: pp. 283-99

61. NISHITKATE, A., Y. YAMASHITA, H. KATAYAMA, T. TSURU, A. USAMI, K. TANABE & H. MABUCHI, 'An Electrochemical Impedance Study on Corrosion of Steels in a cyclic Wet-Dry Condtion', *Corrosion Science*, **37**(12), 1995: pp. 2059-69

62. HARA, S., T. KAMIMURA, H. MIYUKI, M. YAMASHITA, 'Taxonomy for protective ability of rust layer using its composition formed on weathering steel bridge', *Corrosion Science*, **49**(3), 2007: pp. 1131-42

63. KAPATOU, E. & S. B. LYON, 'An Electrical Resistance Monitor Study of the Post-Excavation Corrosion of Archaeological Iron' in *Art2008: 9th International Conference on Non-Destructive Testing of Art, Jerusalem, Israel, 25-30 May 2008, 2008: pp.25-30*

64. DE LA FUENTE, D., I. DÍAZ, J. SIMANCAS, B. CHICO & M. MORCILLO, 'Long-term atmospheric corrosion of mild steel', *Corrosion Science*, **53**(2), 2011, pp. 604-17

65. GRAEDEL, T. E. & R. P. FRANKENTHAL, 'Corrosion mechanisms for Iron and Low Alloy steels exposed to the atmosphere', *Journal of the Electrochemical Society*, **137**(8), 1990, pp. 2385-94

66. MA, Y., Y. LING, F. WANG, 'Corrosion of low carbon steel in atmospheric environments of different chloride content', *Corrosion Science*, **51**(5), 2009: pp. 997-1006

67. DE LA FUENTE, D., I. DÍAZ, J. SIMANCAS, B. CHICO & M. MORCILLO, 'Long-term atmospheric corrosion of mild steel', *Corrosion Science*, **53**(2), 2011, pp. 604-17

68. BIASINI, V. & E. CRISTOFERI, 'A Study of the Corrosion Products on Sixteenth- and Seventeenth-Century Armour from the Ravenna National Museum', *Studies in Conservation*, **40**(4), 1995: pp. 250-6

69. KEISER, J. T., C. W. BROWN AND R. H. HEIDERSBACH, 'The Oxidation of Fe3O4 on Iron and Steel Surfaces.' *Corrosion*, **38**(7), 1982: pp. 357-60.

70. S. OESCH, 'The effect of SO2, NO2, NO and O3 on the corrosion of unalloyed carbon steel and weathering steel- The results of laboratory exposures', *Corrosion Science*, **38**(8), 1996: pp. 1357-68

71. SKERRY, B. S., J. B. JOHNSON & G. C. WOOD, 'Corrosion in smoke, hydrocarbon and SO2 polluted atmospheres- I. General behaviour of iron', *Corrosion Science*, **28**(7), 1988: pp. 657-95

72. APTED, M., R. ARTHUR, F. KING, D, LANGMUIR & J. KESSLER, 'The unlikelyhood of localised corrosion of nuclear waste packages arising from deliquescent brine forrmation', *Journal of the Minerals*, **57**(1), 2005; pp. 43-8

73. FELIU, S., M. MORCILLO & S. FELIU, JR, 'The prediction of atmospheric corrosion from meteorological and pollution parameters- I. Annual corrosion', *Corrosion Science*, **34**(3), 1993: pp. 403-14

74. OGUZIE, E. E., I. B. AGOCHUKWU AND A. I. ONUCHUKWU, 'Monitoring the corrosion susceptibility of mild steel in varied soil textures by corrosion product count technique', *Materials Chemistry and Physics,* **84**(1), pp. 1-6.

75. SELWYN, L. S., P. J. SIROIS & V. ARGYROPOULOS, 'The Corrosion of Excavated Archaeological Iron with Details on Weeping and Akaganéite', *Studies in Conservation*, **44**(4) 1999, pp. 217-32

76. REFAIT, PH. & J. M. R. GÉNIN, 'The Oxidation of Ferrous Hydroxide in Chloride-containing Aqueous Media and Pourbaix Diagrams of Green Rust one', *Corrosion Science*, **34**(5), 1993, pp. 797-819

77. SELWYN, L., 'Overview of archaeological iron: the corrosion problem, key factors affecting treatment, and gaps in current knowledge', in *Metal 2004: proceedings of the International Conference on Metals Conservation, Canberra, Australia 4-8 October 2004*, Edited by Ashton, J. & D. Hallam, National museum of Australia, Canberra, 2004, pp. 294-306

78. TURGOOSE, S., 'The Nature of Surviving Iron Objects' in *Conservation of Iron. Maritime Monographs & Reports No. 53*, edited by Clarke, R. W. & and S. M. Blackshaw, National Maritime museum: Greenwich, 1982: pp.1-7

79. FOLEY, R. T., 'Role of the chloride Ion in Corrosion', *Corrosion*, **26**(2) 1970: pp. 58-70
80. RÉGUER, S., P. DILLMANN, F. MIRAMBET AND L. BELLOT-GURLET, 'Local and structural characterisation of chlorinated phases formed on ferrous archaeological artefacts by mu XRD and mu XANES', *Nuclear Instruments & Methods in Physics Research Section B-Beam Interactions with Materials and Atoms* **240**(1-2), 2005: pp.500-4.

81. MACLEOD, I. D., 'Shipwrecks and Applied Electrochemistry', *Journal of Electroanalytical Chemistry*, **118**, 1981: pp.291-303

82. OUYANG, W. Z. AND C. C. XU , 'Studies on localized corrosion and desalination treatment of simulated cast iron artifacts', *Studies in Conservation*, **50**(2), 2005, pp. 101-8.

83. NEFF, D., P. DILLMANN, L. BELLOT-GURLET, G. BERANGER, 'Corrosion of iron archaeological artefacts in soil: characterisation of the corrosion system', *Corrosion Science*, 47(2), 2005: pp. 515-35

84. TURGOOSE, S., 'Post-Excavation Changes in Iron Antiquities', *Studies in Conservation*, 27(3), 1982: pp. 97-101

85. OUYANG, W. Z. AND C. C. XU, 'Studies on localized corrosion and desalination treatment of simulated cast iron artifacts', *Studies in Conservation*, 50(2), 2005, pp. 101-8.

86. CHITTY, W. J., P. DILLMANN, V. L'HOSTIS AND C. LOMBARD, 'Long-term corrosion resistance of metallic reinforcements in concrete - a study of corrosion mechanisms based on archaeological artefacts', *Corrosion Science*, 47(6), 2005, pp. 1555-81.

87. SCULLY, J. C., *The Fundamentals of Corrosion*, Oxford, Pergamom, 1990

88. VEGA, E., P. BERGER & P. DILLMANN, 'A study of the transport phenomena in the corrosion products of ferrous archaeological artefacts using $^{18}O$ tracing and nuclear microprobe analysis', *Nuclear Instruments and Methods in Physics Research*, 240(1-2) 2005, pp. 554-8

89. RÉGUER, S., P. DILLMANN AND F. MIRAMBET, 'Buried iron archaeological artefacts: Corrosion mechanisms related to the presence of Cl-containing phases', *Corrosion Science*, 49(6), 2007: pp. 2726-44.

90. SAHEB, M., D. NEFF, PH. DILLMANN, H. MATTHIESSEN & E. FOY, 'Long Term Corrosion Behaviour of Low-carbon Steel in Anoxic Soils: Characterization of Archaeological Artefacts', *Journal of Nuclear Materials*, 379(1-3), 2008, pp. 118-123

91. GU, J. D., T. E. FORD & R. MITCHELL, 'Microbiological Corrosion of Metals', in in *Uhlig's Corrosion handbook, 2nd Edition* edited by Revie, R. W., John Wiley and Sons, New York, pp. 915-28

92. WOODTLI, J. & R. KIESELBACH, 'Damage due to hydrogen embrittlement and stress corrosion cracking', *Engineering failure analysis*, 7(), 2000:pp. 427-50

93. NORTH, N. A. AND I. D. MACLEOD, 'Corrosion of metals' in *Conservation of Marine Archaeological Objects*. Edited by C. Pearson. London, Butterworths, 1987: pp. 68-98.

94. NORTH, N. A., 'Corrosion products on marine iron', *Studies in Conservation*, 27(2), 1982: pp. 75-83.

95. TURGOOSE, S., 'The Corrosion of Archaeological Iron during Burial and Treatment', *Studies in Conservation*, 30(1), 1985, pp. 13-18

96. OUYANG, W. Z., C. C. XU, L. J. YUE AND F. WANG, 'A study of localised corrosion within occluded cells on a simulated cast iron artefact in chloride solution', *Anti-Corrosion Methods and Materials*, 51(4), 2004, pp. 259-65.

97. CARPENTER, J. AND I. D. MACLEOD, 'Conservation of Corroded Iron Cannon and the Influence of Degradation on Treatment Times' in *International Council for Museums Committee for Conservation 10th Triennial Meeting, Washington DC*, Edited by. J. Bridgland. Paris, James and James, 1993, pp. 759-66.

98. JONES, D. A., *Principles and Prevention of Corrosion*. Upper Saddle River, Prentice Hall, 1996

99. REFAIT, P., J. B. MEMET, C. BON, R. SABOT AND J. M. R. GÉNIN, 'Formation of the Fe(II)-Fe(III) hydroxysulphate green rust during marine corrosion of steel', *Corrosion Science*, 45(4), 2003, pp. 833-45.

100. DEGRIGNY, C. & L. SPITERI, 'Electrochemical Monitoring of Marine Iron Artefacts during their Storage/Stabilization in Alkaline Solutions' in *Metal 04: Proceedings of the International Conference on Metals Conservation, Canberra, Australia, October 2004*, edited by. J. Ashton and D. Hallam. Canberra, National Museum of Australia, 2004, pp. 315-31.

101. GÉNIN, J. M. R., A. A. OLOWE, N. D. BENBOUZID-ROLLET, D. PRIEUR, M. CONFENTE AND B. RESIAK, 'The simultaneous presence of green rust 2 and sulfate reducing bacteria in the corrosion of steel sheet piles in a harbour area', *Hyperfine Interactions*, 69(1-4), 1992, pp. 875-8.

102. MATTHIESEN, H., L. R. HIBBERT & D. J. GREGORY, 'Siderite as a Corrosion Product on Archaeological Iron from a Waterlogged Environment', *Studies in Conservation*, 48(3), 2003: pp. 183-94

103. MEMET, J. B., 'The Corrosion of metallic heritage artefacts in seawater: descriptive analysis' in *Corrosion of metallic heritage artefacts; Investigation, Conservation and prediction for long term behaviour, European Federation of Corrosion Publications Number 48*, edited by Dillmann, P., G. Beranger, P. Picardo & H. Matthiesen, Woodhead; Cambridge, 2007: pp. 152-169

104. RIOS., G., *Effect of Chlorides on the Electrochemical Behaviour or Thermally Sprayed Aluminium Protective Coatings*, Manchester, University of Manchester, 2012

105. WATKINSON, D., 'Degree of Mineralization: Its Significance for the Stability and Treatment of Excavated Ironwork', *Studies in Conservation*, **28**(2), 1983, pp. 85-90

106. MATTHIESEN, H., D. Gregory & B. Sørenson, 'Long-term corrosion of iron at the waterlogged site of Nydam in Denmark: studies of environment, archaeological artefacts and modern analogues' in *Corrosion of metallic heritage artefacts; Investigation, Conservation and prediction for long term behaviour, European Federation of Corrosion Publications Number 48*, edited by Dillmann, P., G. Beranger, P. Picardo & H. Matthiesen, Woodhead; Cambridge, 2007: pp. 272-92

107. DREWS, M. J., P. DE VIVIES, G. NESTOR, N. GONZALEZ AND P. MARDIKIAN,' A study of the analysis and removal of chloride in samples from the Hunley' in *Metal 04: Proceedings of the International Conference on Metals Conservation, Canberra, Australia, October 2004*, edited by. J. Ashton and D. Hallam. Canberra, National Museum of Australia, 2004, pp. 247-260

108. WANG, Z., C. C. XU, X. CAO AND B. XU, 'The morphology, phase composition and effect of corrosion product on simulated archaeological iron', *Chinese Journal of Chemical Engineering*, **15**(3), 2007: pp. 433-8.

109. SCOTT, D. A. AND G. EGGERT., *Iron and Steel in Art*. London, Archetype. 2009

110. WATKINSON, D. & M. T. LEWIS, 'Desiccated Storage of Chloride-Contaminated Archaeological Iron Objects', *Studies in Conservation*, **50**(4), 2005, pp. 241-52

111. TURGOOSE, S., 'Structure composition and Deterioration of Unearthed Iron Objects' in *Current Problems in the Conservation of Metal Artifacts: 13th International Symposium on the Conservation and Restoration of Cultural Property*, Tokyo , 1993: pp35-53

112. ASKEY, A., S.B. LYON, G. E. THOMPSON, J. B. JOHNSON, G. C. WOOD, M. COOKE & P. SAGE, 'The atmospheric corrosion of iron and zinc by atmospheric hydrogen chloride' *Corrosion Science*, **34**(2), 1993, pp. 233-47

113. DILLMAN, PH., F. MAZAUDIER & S. HŒRLÉ, 'Advances in understanding atmospheric corrosion of iron. I. Rust characterisation of ancient ferrous artefact exposed to indoor atmospheric corrosion', *Corrosion Science*, **46**(6), 2004: pp. 1401-29

114. GILBERG, M. R. & N. J. SEELEY, 'The Identity of Compounds Containing Ions in Marine Iron Corrosion Products: A Critical Review', *Studies in Conservation,***26**(2),1981: pp. 50-6

## Chapter 4: Treatment and storage of archaeological iron


1. NORTH, N. A. AND C. PEARSON 'Washing methods for chloride removal from marine iron artifacts.', *Studies in Conservation*, **23**(4) 1978, pp. 174-86.

2. ROSENBERG, G. A., *Antiquites en Fer et en Bronze, leur Transformation...et leur Conservation.* Copenhagen, Gyldendalske Boghandels Sortiment, 1917

3. TYLECOTE, R. F. AND J. W. B. BLACK, 'The Effect of Hydrogen Reduction on the Properties of Ferrous Materials', *Studies in Conservation*, **25**(2), 1980, pp. 87-96.

4. ODDY, W. A., 'A New Method for the Conservation of Iron: Ionophoresis in a Non-Aqueous Electrolyte' in *Recent Advances in the Conservation and Analysis of Artifacts,* edited by J. Black. London, Summer Schools Press, 1987, pp. 155-8.

5. KNIGHT, B. , 'The stabilisation of archaeological iron; past, present and future' in *Metal 95: Proceedings of the International Conference on Metals Conservation, Semur en Auxois, 25-28 Sept. 1995,* edited by I. D. MacLeod, S. L. Pennec and L. Robbiola. London, James & James, 1997, pp. 36-40.

6. ARGYROPOULOS, V., L. S. SELWYN AND J. A. LOGAN, 'Developing a conservation treatment using ethylenediamine as a corrosion inhibitor for wrought iron objects found at terrestrial archaeological sites' in *Metal 95: Proceedings of the International Conference on Metals Conservation, Semur en Auxois, 25-28 Sept. 1995* edited by I. D. MacLeod, S. L. Pennec and L. Robbiola. London, James & James, 1997, pp. 153-8.

7. SELWYN, L. S. & V. ARGYROPOULOS, 'Removal of Chloride and Iron Ions from Archaeological Wrought Iron with Sodium Hydroxide and Ethylenediamine Solutions', *Studies in Conservation*, **50**(2), 2005, pp. 81-100

8. NORTH, N. A. AND C. PEARSON 'Alkaline sulfite reduction treatment of marine iron' *in ICOM Committee for Conservation, 4th Triennial Meeting Venice, 75/13/3.* Paris, International Council of Museums, 1975, pp. 1-14.

9. NORTH, N. A. AND C. PEARSON, 'Methods for treating marine iron' in *ICOM Committee for Conservation 5th Triennial Meeting, Zagreb, 78/23/3*. Paris, International Council of Museums, 1978, pp. 1-10

10. AOKI, S., 'Conservation of excavated iron objects in Japan' in *Recent Advances in the Conservation and Analysis of Artifacts*, edited by J. Black. London, Summer Schools Press, 1987, pp. 93-8.

11. SELWYN, L. S. AND J. A. LOGAN, ' Stability of Treated Iron: A Comparison of Treatment Methods', in *International Council for Museums Committee for Conservation 10th Triennial Meeting, Washington DC*, edited by J. Bridgland. Paris, James and James, 1993, pp. 803-7

12. KEENE, S. (1994). 'Real-time survival rates for treatments of archaeological iron' in *Ancient & Historic Metals: Conservation and Scientific Research* edited by D. A. Scott, J. Podany and B. Considine. Marina del Rey, Getty Conservation Institute, 1994: pp. 249-64.

13. LOEPER-ATTIA, M.-A. AND W. WEKER, 'Dechloruration d'Objets Archeologiques en Fer par la Methode du Sulfite Alcalin a l'IRRAP' in *Metal 95: Proceedings of the International Conference on Metals Conservation, Semur en Auxois, 25-28 Sept 1995* edited by. I. D. MacLeod, S. L. Pennec & L. Robbiola. London, James & James, 1997, pp. 162-6.

14. GILBERG, M., 'The Storage of Archaeological Iron in Deoxygenated Aqueous Solutions' *Journal of the International Institute for Conservation- Canadian Group*, 12,1987 pp. 20-7

15. GILBERG, M. R. AND N. J. SEELEY, 'The Alkaline Sodium Sulphite Reduction Process for Archaeological Iron: A Closer Look." *Studies in Conservation,* **27**(4), 1982, pp. 180-4.

16. SCHMIDT-OTT, K. AND N. OSWALD, 'Alkaline Sulfite Desalination: Tips and Tricks.' In *VDR conference handbook Archaeological Metal Finds - From Excavation to Exhibition*. October 11-13th 2006, Mannheim, Germany, **17**, 2006

17. SELWYN, L. S., W. R. MCKINNON & V ARGYROPOULOS, 'Models for Chloride Ion Diffusion in Archaeological Iron', *Studies in Conservation*, **46**(2), 2001, pp. 109-20

18. SKERRY, B. S., 'How Corrosion Inhibitors work', in *Corrosion Inhibitors in Conservation, Occasional Papers number 4 1985: the proceedings of a conference held by United Kingdom Institute for Conservation 1984 at the Museum of London* edited by S. Keene, London, United Kingdom Institute for Conservation, 1985, pp. 5-12

19. HJELM-HANSEN, N., J. VAN LANSCHOT, C. D. SZALKAY & S. TURGOOSE, 'Electrochemical assessment and monitoring of stabilisation of heavily corroded archaeological iron artefacts', *Corrosion Science*, **35**(1-4), pp. 767-74

20. DEGRIGNY, C. & L. SPITERI, 'Electrochemical Monitoring of Marine Iron Artefacts during their Storage/Stabilization in Alkaline Solutions' in *Metal 04: Proceedings of the International Conference on Metals Conservation, Canberra, Australia, October 2004*, edited by. J. Ashton and D. Hallam. Canberra, National Museum of Australia, 2004, pp. 315-31.

21. PEARSON, C., *Conservation of Marine Archaeological Objects*, London, Butterworth 1987

22. NISHITKATE, A., Y. YAMASHITA, H. KATAYAMA, T. TSURU, A. USAMI, K. TANABE & H. MABUCHI, 'An Electrochemical Impedance Study on Corrosion of Steels in a cyclic Wet-Dry Condtion', *Corrosion Science*, **37**(12), 1995: pp. 2059-69

23. DALARD, F., Y. GOURBEYRE & C. DEGRIGNY, 'Chloride Removal from Archaeological Cast Iron by Pulsating Current', *Studies in Conservation*, **47**(2), 2002, pp. 117-21

24. GILBERG, M., 'The Storage of Archaeological Iron in Deoxygenated Aqueous Solutions' *Journal of the International Institute for Conservation- Canadian Group*, 12,1987 pp. 20-7

25. BEAUDOIN, A., M.-C. CLERICE, J. FRANCOISE, J.-P. LABBE, M.-A. LOEPER-ATTIA AND L. ROBBIOLA 'Corrosion d'Objets Archeologiques en Fer apres Dechloruration par la Methode au Sulfite Alcalin; Caracterisation Physico-Chimique et Retraitement Electrochimique' *in Metal 95: Proceedings of the International Conference on Metals Conservation, Semur en Auxois, 25-28 Sept 1995,* edited by. I. D. MacLeod, S. L. Pennec and L. Robbiola. London, James & James, 1997, pp. 170-7.

26. TURGOOSE, S., 'Corrosion Inhibitors for Conservation' in *Corrosion Inhibitors in Conservation, Occasional Papers number 4 1985: the proceedings of a conference held by United Kingdom Institute for Conservation 1984 at the Museum of London* edited by S. Keene, London, United Kingdom Institute for Conservation, 1985, pp. 13-7

27. EGGERT, G. AND B. SCHMUTZLER, 'Lässt sich die Konservierung von Eisenfunden 'auf Standard' bringen?' in *kulturGUTerhalten: Standards in der Restaurierungswissenschaft und Denkmalpflege,* edited by. P. von Zabern. Berlin, Staatliche Museen zu Berlin, 2009: pp. 91-5.

28. SCHMIDT-OTT, K. AND V. BOISSONAS, '"Low-pressure hydrogen plasma: An assessment of its application on archaeological iron', *Studies in Conservation*, **47**(2), 2002, pp.81-7.

29. SCHMIDT-OTT, K., 'Plasma-Reduction: Its Potential for Use in the Conservation of Metals' in *Metal 04: Proceedings of the International Conference on Metals Conservation, Canberra, Australia, 4-8 October 200.* edited by J. Ashton and D. Hallam. Canberra, National Museum of Australia, 2004, pp. 235-46.

30. OSWALD, N., 'In Search of the Lost Surface. 10 Years of Active Hydrogen Research: An attempt to Convert Destructive Criticism into Improvements of the Plasma Method' in *Metal 95: Proceedings of the International Conference on Metals Conservation, Semur en Auxois, 25-28 Sept 1995* edited by I. D. MacLeod, S. L. Pennec and L. Robbiola. London, James & James, 1997, pp. 133-7.

31. SCHARFF, W. AND I. HUESMANN, 'Conservation of archaeological metal artifacts: Thermal treatment methods for iron objects and temporary consolidation of fragile corrosion products with volatile binders' in *Metal 98 proceedings of the international conference on metals conservation, Draguignan-Figani res, France, 27-29 May 1998* edited by. W. Mourey and L. Robbiola. London, James & James, 1998, pp. 155-61.

32. DREWS, M. J., P. DE VIVIES, G. NESTOR, N. GONZALEZ AND P. MARDIKIAN,' A study of the analysis and removal of chloride in samples from the Hunley' in *Metal 04: Proceedings of the International Conference on Metals*

*Conservation, Canberra, Australia, October 2004*, edited by. J. Ashton and D. Hallam. Canberra, National Museum of Australia, 2004, pp. 247-260

33. GREEN, W. K., S. B. LYON & J. D. SCANTLEBURY, 'Electrochemical changes in Chloride-contaminated Reinforced Concrete Following Cathodic Polarisation', *Corrosion Science*, **35**(5-8), 1993, pp. 1627-31

34. WESTERN, A. C., 'The Conservation of Excavated Iron Objects', *Studies in Conservation*, **17**(2), 1972, pp. 83-7

35. SMITH, H. A., 'Conserving Iron Objects from Shipwrecks: A New Approach' *MRS Online Proceedings Library*, **185**, 1990, pp.761-91

36. CARLIN, W., D. KEITH & J. RODRIQUEZ, 'Less is more: Measures of Chloride Removal Rate from Wrought Iron Artifacts during Electrolysis', *Studies in Conservation*, **46**(1), 2001, pp.68-76

37. THOMPSON, G., *The Museum Environment, 2nd Edition*, London, Butterworth, 1986

38. WATKINSON, D. AND M. R. T. LEWIS, 'The Role of beta-FeOOH in the Corrosion of Archaeological Iron' in *Materials Issues in Art and Archaeology VII*. Edited by P. B. Vandiver, J. L. Mass and A. Murray. Warrendale, PA, Materials Research Society of America Symposium, 2005: pp. 103-14.

39. THICKETT, D., 'Analysis of iron corrosion products with Fourier transform infra-red and Raman spectroscopies', in *Proceedings of the Sixth Infra-Red and Raman Users Group Conference (IRUG6), Florence, Italy, March 29th - April 1st 2004* edited by M. Picollo. Padua, Il Prato, 2005, pp. 86-93.

40. ASHLEY-SMITH, J., *Risk assessment for object conservation*. Oxford, Butterworth-Heinemann, 1999

41. WATKINSON, D. & M. LEWIS, 'SS *Great Britain* iron hull: modelling corrosion to define storage relative humidity', in *Metal 2004: proceedings of the International Conference on Metals Conservation, Canberra, Australia 4-8 October 2004*, Edited by Ashton, J. & D. Hallam, National museum of Australia, Canberra, 2004: pp. 88-102

42. WATKINSON, D AND TANNER, M.' ss Great Britain: conservation and access – synergy and cost', in *Conservation and Access, IIC London Congress 15-19 September 2008*, Edited by Saunders, D., Townsend, J. and S. Woodcock, IIC, London, 2008, pp. 109-14.

43. PADFIELD, T., 'The Control of Relative Humidity and Air Pollution in Showcases and Picture Frames', *Studies in Conservation*, **11**(1), 1966, pp.8-30

44. SHINER, J., 'Trends in Microclimate Control of museum display cases' in *Museum Microclimates: Contributions to the conference in Copenhagen 19-2 November 2007* edited by Padfield, T. & K. Borschersen, Copenhagen, The National Museum of Denmark, 2007, pp. 267-76

45. SCHMUTZLER, B. AND N. EBINGER-RIST, 'The conservation of iron objects in archaeological preservation - Application and further development of alkaline sulphite method for conservation of large quantities of iron finds', *Materials and Corrosion,* **59**(3), 2008, pp.248-53

46. MATHIAS, C., K. RAMSDALE AND D. NIXON, 'Saving archaeological iron using the Revolutionary Preservation System' in *Metal 04: Proceedings of the International Conference on Metals Conservation, Canberra, Australia, 4-8 October 2004* edited by J. Ashton and D. Hallam. Canberra, National Museum of Australia, 2004, pp. 28-42.

47. MACLEOD, K. J., *Relative Humidity: Its Importance, Measurement and Control in Museums, Technical bulletin 1*, Ottowa, Canadian Conservation Institute and the National Museums of Canada, 1975

48. BRADLEY, S., 'Preventative Conservation Research and Practice at the British Museum', *Journal of the American Institute for Conservation*, **44**(3), 2005: pp. 159-73

49. BAER, N. S. & P. N. BANKS, 'Conservation Notes, Microenvironments', *The International Journal of Museum Management and Curatorship*, **6**(3), 1987: pp. 301-5

50. BAER, N. S. & P. N. Banks, 'Indoor Air Pollution: Effects on Cultural and Historic Materials', *The International Journal of Museum Management an Curatorship*, **4**(1), 1985: pp. 9-20

51. PAVLOGEORGATOS, G., 'Environmental parameters in museums', *Building and Environment*, **38**(12), 2003, pp. 1457-62

52. PADFIELD, T., P. K. LARSEN, L. A. JENSEN & M. RHYL-SVENDSEN, 'The Potential and Limits for Passive Air Conditioning of Museums, Stores and Archives' in *Museum Microclimates: Contributions to the conference in Copenhagen 19-2 November 2007* edited by Padfield, T. & K. Borschersen, Copenhagen, The National Museum of Denmark, 2007, pp. 191-98

53. YANG, L., 'Introduction' in *Techniques for Corrosion Monitoring* edited by L. Yang, Cambridge, Woodhead Publishing, 2008

54. HOAR, T. P., *Report of the committee on Corrosion and Protection*, London, Department of Trade and industry, 1971

55. XAVIER-ROWE, A. & C. FRY, *State of English Heritage Collections report*, unpublished internal report, English Heritage London, 2010

56. KEENE, S. 'Real time survival rates for treatments of archaeological iron' in *Ancient and Historic Metals: Conservation and Scientific Research*, edited by Scott, A. D., J. Podany And B. Considine, Los Angeles, The Getty Conservation institute, 1994: pp. 249-64

57. DA FONSECA, J. Q., P. M. MUMMERY & P. J. WHITHERS, 'Full field strain mapping by optical correlation of micrographs during deformation', *Journal of Microscopy*, **218**(1), 2005: pp. 9-21
58. ISAACS, H.S., Y. M. LOOI & J. H. W DE WIT, 'Behaviour of Laser welded steel in chloride solution using difference imaging', *Corrosion Science*, 49(1), 2007; pp. 53-62

59. ROUX, S., J. RÉTHORÉ & F HILD, 'Digital image correlation and fracture: an advanced technique for estimating stress intensity factors of 2D and 3D cracks', *Journal of Physics D: Applied Physics*, 42(21), 2009: pp. 1-37

60. COOK, A. J. DUFF, N. STEVENS, S. LYON, A SHERRY & T. J. MARROW, 'Preliminary Evaluation of Digital Image Correlation for In-situ Observation of Low Temperature Atmospheric-Induced Chloride Stress Corrosion Cracking in Austenitic Stainless Steels', *ECS Transactions*, **25**(37), 2010: pp. 119-32

61. RAHIMI, S., D. L. ENGELBERG, J. A. DUFF & T. J. MARROW, 'In Situ observation of intergranular crack nucleation in a grain boundary controlled austenitic stainless steel', *Journal of Microscopy*, **233**(3), 2009: pp. 423-31

62. JIN, F. & F. P. CHIANG, 'ESPI and Digital Speckle Correlation Applied to Inspection of Crevice Corrosion on Aging Aircraft', *Research in Nondestructive Evaluation*, **10**(2), 1998: pp 63-73

63. HUANG, R-S, C-J LIN & H. S. ISAACS, 'A Difference-Imaging Technique Used to Study Streaking Corrosion of Aluminum Alloys AA7075 and AA8006 in Chloride Solution', *Electrochemical and Solid-State Letters*, **9**(2), 2006: pp B11-B14

64. ANGELINI, E., S. GRASSINI, D. MOMBELLO & A. NERI, 'An imaging approach for contactless monitoring of the conservation state of metallic works of art', *Applied Physics A: Materials, Science and Processing*, **100**(3), 2010: pp. 919-25

65. GROS. X. E., J. BOUSIGUE & K. TAKAHASHI, 'NDT data fusion at pixel level', *NDT&E International*, **32**(5), 1999: pp 283-92

66. CHOI, K. Y. & S. S. KIM, 'Morphological analysis and classification of types of surface corrosion damage by digital image processing', *Corrosion Science*, **47**(1), 2005:pp 1-15

67. SALGADO, J. A .M., J. U. CHAVARIN & D. M. CRUZ, 'Observation of Copper Corrosion Oxide Products Reduction in Metallic Samples by Means of Digital Image Correlation', *International Journal of Electrochemical Science*, **7**(2), 2012: pp. 1107-17

68. FELL. V., Q. MOULD & R. WHITE, *Guidelines on the X-radiography of archaeological metal work*, Swindon, English heritage publishing, 2006

69. ZHAO, X., G. S. FRANKEL, B. ZOOFAN & S. I.ROKHLIN, 'In Situ X-Ray Radiographic Study of Intergranular Corrosion in Aluminum Alloys', *Corrosion*, **59**(11), 2003: pp: 1012-8

70. LIU, X. G. S. FRANKEL, B. ZOOFAN & S. I. ROKHLIN, 'In-Situ observation of intergranular stress corrosion cracking in AA2024-T3 under constant load conditions', Corrosion Science

71. EDELATI, K., N. RASTKHAH, A. KERMANI, M. SEIEDI & A. MOVEFEGHI, 'The use of radiography for thickness measurement and corrosion monitoring in pipes', *International Journal of Pressure Vessels and Piping*, **83**(10), 2006: pp. 736-41

72. MATTHIESEN, H., E. SALOMONSEN & B. SØRENSEN, 'The use of radiography and GIS to assess the deterioration of archaeological iron objects from a water logged environment', *Journal of Archaeological Science*, **31**(10), 2004: pp. 1451-61

73. GERWIN, W. & R. BAUMHAUER, 'Effect of soil parameters on the corrosion of archaeological metal finds', *Geoderma*, **96**(1-2), 2000:pp. 63-80

74. YAHAGHI, E., A. MOVAFEGHI, S. AHMADI, S. ANSARI, M. TAHERI & N. RASTKHAH, 'Cultural Heritage Object Identification by Radiography Nondestructive Method and Digital Image Processing', *Applied Mechanics and Materials*, **83**, 2011:pp 35-40

75. SCUDIERI, F., F. MERCURI & R. VOLTERRI, 'Non-invasive analysis of artistic heritage and archaeological findings by time resolved IR Thermography', *Journal of Thermal analysis and Calorimetry*, **66**(1), 2001: pp 307-14

76. SHEN. G. & T. LI, 'Infrared thermography for high-temperature pressure pipe', *Insight-Non-destructive Testing and Condition Monitoring*, **49**(3), 2007: pp. 151-3

77. KOBOYASHI, K. & N. BANTHIA, 'Corrosion detection in reinforced concrete using induction heating and infrared thermography', *Journal of Civil Structural Health Monitoring*, **1**(1-2), 2011: pp. 25-35

78. GOUFENG, J., Z. WEI, S. JUN, Y. ZHENGWEI, H. YU, H. ZHIYONG & T. GAN, 'Numerical Analysis of influencing factors and capability for thermal wave NDT in Liquid Propellant Tank Corrosion Damage Detection', *Measurement Science Review*, **13**(4), 2013: pp 214-22

79. SAKAGAMI, T. & S. KUBO, 'Applications of pulse heating thermography and lock-in thermography to quantitative non-destructive evaluations', *Infrared Physics and Technology*, **43**(3-5), 2002: pp. 211-8

80. CHIANG, K. & T. MINTZ, 'Gravimetric techniques' in *Techniques for corrosion monitoring*, edited by L. Yang, Cambridge, Woodhead Publishing Ltd, 2008: pp. 247-64

81. BACCI, M., C. CUCCI, A. A. MENCAGLIA & A. G. MIGNANI, 'Innovative Sensors for Environmental Monitoring in Museums', *Sensors*, **8**(3), 2008: pp. 1985-2005

82. INTERNATIONAL ORGANIZATION FOR STANDARDIZATION, ISO 118844-2 *Corrosion of Metal and alloys. Classification of low corrosivity of indoor atmospheres- Part 1: Determination of corrosion attack in indoor atmospheres*, International Organization for standardization, Geneva, 2005

83. INTERNATIONAL ORGANIZATION FOR STANDARDIZATION, ISO 118844-1; *Corrosion of Metal and alloys. Classification of low corrosivity of indoor atmospheres- Part 2: Determination and estimation of indoor corrosivity*, International Organization for standardization, Geneva, 2005

84. RYHL-SVENDSEN, M., 'Corrosivity measurements of indoor museum environments using lead coupons as dosimeters', *Journal of Cultural Heritage*, **9**(3), 2008: pp. 285-93

85. JOHANSSON, E. & C. LEYGRAF, 'Corrosion measurements of silver and copper in indoor atmospheres using different evaluation techniques', *British Corrosion Journal*, **34**(1), 1999: pp. 27-33

86. MOHAMED, W. A., N. M RATEB & A. A. SHAKOUR, 'Performance of copper corrosion inhibitors in a museum environment- A comparative study using FTIR spectroscopy', in *Metal 04: Proceedings of the International Conference on Metals Conservation, Canberra, Australia, October 2004*, edited by. J. Ashton and D. Hallam. Canberra, National Museum of Australia, 2004: pp. 369-378

87. COSTAIN, C. G., 'Evaluation of Storage Solutions for Archaeological Iron', *Journal of the Canadian Association for Conservation*, **25**, 2000: pp 11-20

88. BAEK, Y. & G. S. FRANKEL, 'Elecctrochemical Quartz Crystal Microbalance Study of Corrosion of Phases in AA2024', *Journal of the Electrochemical Society*, **150**(1), 2003: pp. B1-B9

89. CURKOVIC, H. O., E. STUPNISEK-LISAC & H. TAKENOUTI, 'Electrochemical quartz crystal microbalance and electrochemical impedance spectroscopy study of copper corrosion inhibition by imidazoles', *Corrosion Science*, **51**(10), 2009: pp. 2342-8

90. WEISSENRIEDER, J. & C. LEYGRAF, 'In Situ Studies of Filiform Corrosion of Iron', *Journal of the Electrochemical Society*, **151**(3), 2004: pp. B165-B171

91. FORSBERG, J., L.-C. DUDA, A. OLSSON, T SCHMITT, J. ANDERSON, J. NORDGREN, J HEDBERG, C. LEYGRAF, T. AASTRUP, D. WALLINDER & J.-H. GUO, 'System for in Situ studies of atmospheric corrosion of metal films using Soft x-ray spectroscopy and quartz crystal microbalance', *Review of Scientific Instruments*, **78**(8), 2007: pp. 083110.1-083110.7

92. ENGLAND, W. G., M. W. OSBORNE & Z. XIUYU, 'Applications of a Real-Time Electronic Contact Corrosion Monitor" in *Proceedings of Advances in Instrumentation and Control, Vol. 46, Part 1*, Anaheim, Instrument Society of America, 1991: pp. 929-55

93. SCHUBERT, R., B. MEAGHER & C. C. CHANG, 'Monitoring of In Situ Corrosion Rates in a Telephone Switching Office in Burbank, California', *Journal of the Electrochemical society*, **142**(9), 1995: pp. 3157-64

94. FORLSUND, M. & C. LEYGRAF, 'A Quartz Crystal Microbalance Developed for Outdoor In Situ Atmospheric Corrosivity Monitoring', *Journal of the Electrochemical Society*, **143**(3), 1996: pp. 839-44

95. ODLYHA, M., C. THEODORAKOPOLUS, D. THICKETT, M. RHYL-SVENDSEN, J. M. SLATER & R. CAMPANA, 'Dosimeters for indoor microclimate monitoring for cultural heritage', in *Museum Microclimates. Contributions to the Copenhagen conference, 19 - 23 November 2007, The National Museum of Denmark, Copenhagen.*, edited by T. Padfield & K. Borchersen. Copenhagen, The National Museum of Denmark, 2007: pp 73-80

96. SJÖGREN, L. & N. LE BOZEC, 'On-line Corrosion Monitoring of indoor atmospheres' in *Corrosion of metallic heritage artefacts; Investigation, Conservation and prediction for long term behaviour, European Federation of Corrosion Publications Number 48*, edited by Dillmann, P., G. Beranger, P. Picardo & H. Matthiesen, Woodhead; Cambridge, 2007: pp. 293-307

97. ZAKIPOUR, S. & C. LEYGRAF, 'Quartz crystal microbalance applied to studies of atmospheric corrosion of metals', *British Corrosion Journal*, 1992, **27**(4): pp. 295-8

98. SHRIER, L. L., *Corrosion, 2nd edition, volumes 1 & 2*, London, Newnes-Butterworths, 1976

99. PAPAVINASAM, S, 'Electrochemical polarization techniques for corrosion monitoring' in *Techniques for corrosion monitoring*, edited by L. Yang, Cambridge, Woodhead Publishing Ltd, 2008: pp. 49-85

100. STRATMANN, M., H. STRECKEL, K. T. KIM & S. CROCKETT, 'On the atmospheric corrosion of metals which are covered with thin electrolyte layers – III. The measurement of polarisation curves on metal surfaces which are covered by thin electrolyte layers', *Corrosion Science*, **30**(6/7), 1990: pp: 715-34

101. ZHANG, S. H. & S. B. LYON, 'The electrochemistry of iron, zinc and copper in thin layer electrolytes', *Corrosion science*, **35**(8), 1993: pp. 713-8

102. ZHANG, S. H. & S. B. LYON, 'Anodic processes on iron covered by thin, dilute electrolyte layers (II)- A.C. impedance measurements', *Corrosion Science*, **36**(8), 1994: pp. 1309-21

103. NISHIKATA, A., Y. ICHIHARA, Y. HAYASHI & T. TSURU, 'Influence of Electrolyte Layer Thickness and pH on the Initial Stage of the Atmospheric Corrosion of Iron', *Journal of the Electrochemical Society*, **144**(4), 1997: pp 1244-52

104. SHI, Y. Y., Z. ZHANG, J. SU & J. Q. ZHANG, 'EIS study on 2024-T3 aluminum alloy corrosion in simulated acid rain under cyclic wet-dry conditions', *Materials and Corrosion*, 56(10), 2005: pp 701-6

105. LI, C., Y. MA, & F. WANG, 'EIS monitoring study of atmospheric corrosion under variable relative humidity', *Corrosion Science*, **52**(11), 2010: pp 3677-86

106. FU, X., J. DONG, E. HAN & W. KE, 'A New Experimental method for in situ Corrosion Monitoring under Alternate Wet-Dry Conditions', *Sensors*, **9**(12), 2009: pp. 10400-10

107. THEE, C., L. HAO, J. DONG, X. MU, W. WEI, X. LI & W. KE, 'Atmospheric corrosion monitoring of a weathering steel under an electrolyte film in cyclic wet-dry condition', *Corrosion science*, **78**, 2014: pp. 130-7

108. STERN, M., 'A method for Determining Corrosion Rates From Linear Polarization Data', *Corrosion*, **14**(9), 1958: pp. 440t-444t

109. ASTM STANDARD G3-13, 'Standard Practice for Conventions Applicable to Electrochemical Measurements in Corrosion Testing', *Annual book of GSTM Standards* **3**(2), West Conshohoken, PA, ASTM International, 2013: DOI: 10.1520/G0003

110. ASTM STANDARD G5-13E2, 'Standard Reference Test Method for Making Potentiodynamic Anodic Polarization Measurements', *Annual book of GSTM Standards* **3**(2), West Conshohoken, PA, ASTM International, 2013: DOI: 10.1520/G0005

111. ASTM STANDARD G59-97(2009), 'Standard Reference Test Method for Conducting Potentiodynamic Polarization Resistance Measurements', *Annual book of GSTM Standards* **3**(2), West Conshohoken, PA, ASTM International, 2013: DOI: 10.1520/G0059-97R09

112. HLADKY, K., L. M. CALLOW & J. L. DAWSON, 'Corrosion Rates from Impedance Measurements: An Introduction', *British Corrosion Journal*, **15**(1), 1980: pp. 20-5

113. HAMDY, A. S., E. EL-SHENAWY & T. EL-BITAR, 'Electrochemical Impedance Spectroscopy Study of the Corrosion Behaviour of Some Niobium Bearing Stainless Steels in 3.5% NaCl', *International Journal of Electrochemical Science*, **1**(4), 2006: pp. 171-80

114. DAROWICKI, K., 'Corrosion rate measurements be non-linear electrochemical impedance spectroscopy', *Corrosion Science*, **37**(6), 1995: pp. 913-25

115. ANDRADE, C. & C. ALONSO, 'Corrosion rate monitoring in the laboratory and on-site', *Construction and Building Materials*, **10**(5), 1996: pp. 315-28

116. ROBERGE, P .R. & V. S. SASTRI, 'On-line Corrosion Monitoring with Electrochemical Impedance Spectroscopy', *Corrosion*, **50**(10), 1994: pp. 744-51

117. KLASSEN, R. D. & P. R. ROBERGE, 'Zero resistance ammetry and galvanic sensors' in *Techniques for Corrosion Monitoring* edited by L. Yang, Cambridge, Woodhead Publishing, 2008, pp. 111-26

118. COTTIS, R. A., 'Electrochemical noise for corrosion monitoring' in *Techniques for Corrosion Monitoring* edited by L. Yang, Cambridge, Woodhead Publishing, 2008, pp. 86-110

119. COTTIS, R. A., 'Interpretation of Electrochemical noise data', *Corrosion*, **57**(3), 2001: pp. 265-85

120. COTTIS, R. A., M. A. A. AL-AWADHI, H. AL-MAZEEDI & S. TURGOOSE, 'Measures for the detection of localized corrosion with electrochemical noise', *Electrochemical Acta*, **24-5**, 2001: pp. 3665-74

121. EDGEMON, G. L., M. J. DANIELSON & G. E. C. BELL, 'Detection of stress corrosion cracking and general corroision of mild steel in simulated defense nuclear waster solutions using electrochemical noise analysis', *Journal of Nuclear Materials*, **245**(2), 1997: pp. 201-9

122. PONS, E., C. LEMAITRE & D. DAVID, 'Electrochemical study of steel artefacts from World War I: Contribution of A.C. impedance spectroscopy and chronoamperometry to describe the behaviour of the corrosion layers', in *Corrosion of metallic heritage artefacts; Investigation, Conservation and prediction for long term behaviour, European Federation of Corrosion Publications Number 48*, edited by Dillmann, P., G. Beranger, P. Picardo & H. Matthiesen, Woodhead; Cambridge, 2007: pp. 77-91

123. CHAVES, I. A. & R. E. MELCHERS, 'Long term localised corrosion of marine steel piling welds', Corrosion Engineering, Science and Technology, 48(6), 2013: pp 469-74

124. ADRIAENS, A., M. DOWSETT, K. LEYSSENS & B. VAN GASSE, 'Insights into electrolytic stabilization with weak polarization as treatment for archaeological copper objects', *Analytical and Bioanalytical Chemistry*, **387**(3), 2007: pp. 861-8

125. ADRIAENS, A. & M. G. DOWSETT, 'Observing Corrosion, passivation and cleaning as they happen – in situ spectroelectrochemistry for the conservation of metals', in *COST Action G8: Non-destructive testing and analysis of museum objects*, edited by A. Denker, A. Adriaens, M. Dowsett & A. Giumlia-Mair,

Brussels, European Cooperation in the field of scientific and technical research, 2006: pp 31-46

126. ROCCA, E. & F. MIRAMBET, 'Corrosion inhibitors for metallic artefacts: temporary protection', in *Corrosion of metallic heritage artefacts; Investigation, Conservation and prediction for long term behaviour, European Federation of Corrosion Publications Number 48*, edited by Dillmann, P., G. Beranger, P. Picardo & H. Matthiesen, Woodhead; Cambridge, 2007: pp. 308-34

127. DEGRIGNY, C., 'Use of electrochemical techniques for the conservation of metal artefacts: a review', *Journal of Solid State Electrochemistry*, **14**(3), 2010: pp. 353-61

128. HJELM-HANSEN, N., J. VAN LANSCHOT, C. D. SZALKAY & S. TURGOOSE, 'Electrochemical assessment and monitoring of stabilisation of heavily corroded archaeological iron artefacts', *Corrosion science*, **35**(1-4), 1993: pp. 767-74

129. DEGRIGNY, C. & L. SPITERI, 'Electrochemical monitoring of marine iron artefacts during their storage/stabilisation in alkaline solutions', in *Metal 04: Proceedings of the International Conference on Metals Conservation, Canberra, Australia, October 2004*, edited by. J. Ashton and D. Hallam. Canberra, National Museum of Australia, 2004: pp. 315-31

130. HERNANDEZ-ESCAMPA, .M, J. GONZALEZ & J. URUCHURTU-CHAVARIN, 'Electrochemical assessment of the restoration and conservation of a heavily corroded archaeological artifact', *Journal of Applied Electrochemistry*, **40**(2), 2010: pp. 345-56

131. DOMONÉCH-CARBÓ, A., M. LASTRAS, F. RODRIGUEZ, E. CANO, J. PIQUERO-CILLA & L. OSETE-CORTINA, 'Monitoring stabilizing procedures of archaeological iron using electrochemical impedance spectroscopy', *Journal of Solid State Electrochemistry*, **18**(2), 2014: pp. 399-409

132. MACLEOD, I. D. & H. STEYNE, 'Managing a Monitor – the Case of HMVS Cerberus in Port Phillip Bay: Integration of Corrosion Measurements with Site Management Strategies', *Conservation and management or archaeological sites*, **13**(4), 2011: pp. 334-61

133. MACLEOD, I. D., 'The Mechanism and Kinetics of In Situ Conservation of Iron Cannon on Shipwreck Sites', *The International Journal of Nautical Archaeology*, **42**(2), 2013: pp. 382-91

134. GREGORY, D., 'In situ corrosion studies on the submarine Resurgam: A preliminary assessment of her state of preservation', *Conservation and Management of Archaeological Sites*, **4**(2), 2000: pp. 93-100

135. HELDTBERG, M., I. D. MACLEOD & V. L. RICHARDS, 'Corrosion and cathodic protection of iron in seawater: a case study of the James Matthews (1841)', in *Metal 04: Proceedings of the International Conference on Metals*

*Conservation, Canberra, Australia, October 2004*, edited by. J. Ashton and D. Hallam. Canberra, National Museum of Australia, 2004: pp. 75-87

136. CARULLO, A., F. FERRARIS, M. PARVIS, A. VALLAN, E. ANGELINI & P. SPINELLI, 'Low-Cost Electrochemical Impedance Spectroscopy System of Corrosion Monitoring of Metallic Antiquities and Works of Art', *IEEE Transactions on Instrumentation and measurement*, **49**(2), 2000: pp. 371-6

137. ANGELINI, E., S. GRASSINI, S. CORBELLINI, G. M. INGO, T. DE CARO, P. PLESCIA, C. RICCUCCI, A. BIANCO & S. AGOSTINI, ' Potentialities of XRF and EIS portable instruments for the characterisation of ancient artefacts', *Applied Physics A: Materials Science and Processing*, **83**(4), 2006: pp 643-9

138. MUDALI, U. K. & B. RAJ, 'Insitu corrosion investigations on Delhi iron pillar', *Transactions of The Indian Institute of Metals*, **62**(1), 2009: pp. 25-33

139. GRASSINI, S., E. ANGELINI, M. PARVIS, M. BOUCHAR, P. DILLMANN & D. NEFF, 'An in situ corrosion study of Middle Ages wrought iron bar chains in the Amiens Cathedral', *Applied Physics A: Materials, Science and Processing,* **113**(4), 2013: pp. 971-9

140. CORBELLINI, S., M. PARVIS & S. GRASSINI, 'Noninvasive Solution for Electrochemical Impedance Spectroscopy on Metallic Works of Art', *IEEE Transactions on Instrumentation and Measurement*, **63**(5), 2012: pp. 1193-200

141. ASTM STANDARD C876-09, 'Standard Test Method for Corrosion Potentials of Uncoated Reinforcing Steel in Concrete' *Annual book of GSTM Standards* **3**(2), West Conshohocken, PA, ASTM International, 2009: DOI: 10.1520/C0876-09

142. DUFFÓ, G. S., M. REINOSO, C. P. RAMOS & S. B. FARINA, 'Characterisation of steel rebars embedded in a 70-year old concrete structure', *Cement and Concrete Research*, **42**(1), 2012: pp. 111-7

143. MARIE-VICTOIRE, E., V. BOUTEILLER, J-L. GARCIAZ, J-F. CHERRIER, J. DAUTHUILLE, F. MARZIN & J. SCHNEIDER, 'On-site instantaneous corrosion rate measurements on a historical building', *European Journal of Environmental and Civil Engineering*, **16**(3-4), 2012: pp. 505-23

144. LIGHT, G., 'Nondestructive evaluation technologies for monitoring corrosion' in *Techniques for corrosion monitoring*, edited by L. Yang, Cambridge, Woodhead Publishing Ltd, 2008: pp. 293-312

145. MACLEOD, I. D., D. COOK & E. SCHINDELHOLZ, Corrosion and Conservation of the American civil war ironclad USS Monitor (1862), in *ICOM-CC Preprints, 15th Triennial meeting, New Delhi, 22-2, September 2008*, edited by E. Hermens & J. Townsend, London, Archetype Press Ltd, 2009: pp 279-85

146. BROSSIA, C. S., M. YUNOVICH, D. HILL, K. M. LAWSON, R. DENZINE, J. T. SCHMIDT, E. KLECHKA, E. SCHINDELHOLZ, E. NORDGREN, K. DROP, R. BABOIAN, H. HACK, J. D. FLESSAS & D. C.

COOK, 'Corrosion condition assessment, mitigation, and preservation of USS Montior artifacts', in *CORROSION 2007, Corrosion conference and expo, Nashville, Tennesse, 11-15 March 2007, Paper 07239,* Houston, NACE international, 2007: pp 1-15

147. SMITH, T., T. ROACH, I. D. MACLOED, R. NEIL, P. GRAHAM, M. RIKARD-BELL & R. TURNER, *Report of Operation ANZAC; Maritime Archaeological assessment of HMAS AE2,* Black Rock, Australia, AEC Commemorative Foundation, 2008

148. RUSSELL, M. A., D. L. CONLIN, L .E. MURPHY, D. L. JOHNSON, B. WILSON & J. D. CARR, 'A Minimum-Impact Method of measuring Corrosion rate of Steel-Hulled Shipwrecks in Seawater', *The International Journal of Nautical Archaeology*, **35**(2), 2006: pp. 310-8

149. BASSIM, M. N. & D. L. PIRON, 'Acoustic Emission Monitoring of Large structures Under Corrosive Environment', *British Journal of Nondestructive Testing*, **24**(5), 1982: pp. 259-62

150. SEAH, K. H. W., K. B. LIM, C. H. CHEW & S. H. TEOH, 'The Correlation of acoustic emission with rate of corrosion', *Corrosion Science*, **34**(10), 1993: pp. 1707-13

151. ACCARDO, G., C. CANEVA & S. MASSA, 'Stress monitoring by temperature mapping and acoustic emission analysis: A case study of Marcus Aurelius', *Studies in Conservation*, **28**(2), 1983: pp. 67.74

152. CANEVA, C., A. PAMPALLONA & S. VISKOVIC, 'Acoustic emission to assess the structural condition of Bronze statues, case of the "Nike" of Brescia', in *26th European Conference on Acoustic Emission Testing, Berlin September 15-7 2004*, Berlin, European Working Group on Acoustic Emission, 2004: pp. 567-74

153. MATTHIESEN, H. & K. WONSYLD, 'In situ measurement of oxygen consumption to estimate corrosion rates', *Corrosion Engineering, Science and Technology*, **45**(5), 2010: pp. 350-6

154. RIMMER, M., D. WATKINSON & Q. WANG, 'The impact of chloride desalination on the corrosion rate of archaeological iron', *Studies in Conservation*, **58**(4), 2013: pp. 326-37

155. THICKETT, D., S. LAMBARTH & P. WYETH, 'Determining the stability and durability of archaeological materials', in *9th International Conference on Non-Destructive Testing of Art, Jerusalem, Isreal, 25-30 May 2008*, [Accessed 3 December 2012]: Available at http://www.ndt.net/article/art2008/papers/024Thickett.pdf

156. EBERLE, D. C., 'Radioactive Tracer methods' in *Techniques for corrosion monitoring*, edited by L. Yang, Cambridge, Woodhead Publishing Ltd, 2008: pp. 265-76

157. LAGUZZI, G., L. LUVIDI & G. BRUNORO, 'Atmospheric corrosion of B6 bronze evaluated by the thin layer activation technique', *Corrosion Science*, **43**(4), 2001: pp. 747-53

158. CHITTY, W-J, P. BERGER, P. DILLMANN & V. L'HOSTIS, 'Long-term corrosion of rebars embedded in aerial and hydraulic binders- Mechanisms and crucial physica-chemical parameters', *Corrosion Science*, **50**(8), 2008: pp. 2117-23

159. SOPHIAN, A., G. Y. TIAN & S. ZAIRI, 'Pulsed magnetic flux leakage techniques for crack detection and characterisation', Sensors and Actuators A: Physical, 125(2), 2006: pp. 186-91

160. DEAN, F., 'Hydrogen flux measurements in petrochemical applications' in *Techniques for corrosion monitoring*, edited by L. Yang, Cambridge, Woodhead Publishing Ltd, 2008: pp. 313-21

## Chapter 5: Electrical Resistance Corrosion Monitors


1. ASTM STANDARD G96-90, 'Standard Guide for On-line Monitoring of Corrosion in Plant Equipment (Electrical and Electrochemical methods)' , *Annual book of GSTM Standards* **3**(2), West Conshohoken, PA, ASTM International, 2013: DOI: 10.1520/G0096

2. BROSSIA, C. S., 'Electrical resistance techniques', in *Techniques for Corrosion Monitoring* edited by L. Yang, Cambridge, Woodhead Publishing, 2008: pp.277-92

3. WINEGARTNER, E. C., 'Laboratory and Plant Applications of Recording Electrical Resistance Corrosion Meters', *Corrosion*, **16**(6), 1960: pp. 265t-270t

4. CHAWLA, S. K., T. ANGUISH & J. H. PAYER, 'Microsensors for Corrosion control', *Corrosion*, **45**(7), 1989: pp: 595-601

5. STROPKI, J. T., G. H. KOCH, & M. T. BYRNE, 'Monitoring Corrosion with an Automated electrical resistance corrosion probe monitoring system', in *Proceedings of the 1989 Tri-service Conference on Corrosion*, edited by V. S. Agarwala, New Jersey, Department of Defense, 1989: pp. 544-61

6. WHITED, T., 'Mitigation of Soil-Side Corrosion on Double-Contained Above ground Storage Tank Floors', *Materials Performance*, **50**(6), 2011: pp. 7-11

7. FITZGERALD, J. H., P. R. NICHOLS & R. NEIBLING, 'Measuring the effectiveness of cathodic protection on the exterior bottoms of new aboveground asphalt storage tanks using corrosion monitoring probes', in Corrosion 99; paper 519; Houston , NACE International, 1999

8. FARRELL, D., B. ROBBINS, P. SIKKA & M. SEAMAN, 'On-line monitoring and control of furnace wall corrosion in PF-fired boilers', *Power Plant: Operation Maintenance and Materials Issues*, **3**(2), 2004: pp. 1-10

9. CAI, J. –P. & S. B. LYON, 'A mechanistic study of initial atmospheric corrosion kinetics using electrical resistance sensors', *Corrosion Science*, **47**(12), 2005: pp. 2956-73

10. KAPATOU, E. & S. B. LYON, 'An Electrical Resistance Monitor Study of the Post-Excavation Corrosion of Archaeological Iron' in *Art2008: 9th International Conference on Non-Destructive Testing of Art, Jerusalem, Israel, 25-30 May 2008, 2008: pp.25-30*

11. MØLLER, P., 'Evaluation of Atmospheric Corrosion on Electroplated Zinc and Zinc-Nickel Coatings by Electrical Resistance (ER) Monitoring', *NASF Surface technology white papers*, **78**(5), 2014: pp. 1-10

12. PROSEK, T., N. LE BOZEC & D. THIERRY, 'Application of automated corrosion sensors for monitoring the rate of corrosion during accelerated corrosion tests', *Materials and Corrosion*, **63**(9999), 2012: pp. 1-9

13. KHAN, N. A., 'Using Coupons and ER Soil Corrosion Probes in Applying Pipeline CP Criteria', *Materials Performance*, **46**(4), 2007: pp. 26-30

14. JANKOWSKI, J., W. SOKÓLSKI & A. HOFFMAN, 'Application of the electrical resistance technique to monitoring of cathodic protection effectiveness', *Ochrona przed Korozja*, **8**, 2012: pp. 347-50

15. DONIGUIAN, T. M. & R. C. ROBINSON, 'Corrosion measuring techniques confirm effectiveness of pulse cathodic protection for buried steel pipeline', in *Corrosion/1999 NACE conference papers, Paper 215*, Houston, NACE International, 1999: pp. 1-6

16. NIELSEN, L.V., B. BAUMGARTEN & P. COHN, 'On-site measurement of AC induced corrosion: Effect of AC and DC parameters', in *CeoCor Conference June 2004 Dresden sector A*, Brussels, Ceocorr, 2004: pp.1-15

17. BELL, G. E. C., C. G. MOORE & S. WILLIAMS, 'Development and application of ductile iron pipe electrical resistance probes for monitoring underground external pipeline corrosion', in *NACE International Corrosion 2007 Conference and expo, Paper 07335*, Houston, NACE International, 2007: pp. 1-14

18. BLUMER, D. J., R. L. BARNES & A. PERKINS, 'Field experience with a new high resolution programmable downhole corrosion monitoring tool' in *Corrosion 98; 22-27 March 1998, San Diego California*, Houston, NACE international; pp 193-207

19. LI, S. Y., Y-G. KIM, S. JUNG, H-S. SONG & S-M LEE, 'Application of steel thin film electrical resistance sensor for in situ corrosion monitoring', *Sensors and Actuators B: Chemical*, **120**(2), 2007: pp. 368-77

20. LI, S. Y., S. JUNG, K. PARK, S-M. LEE & Y-G. KIM, 'Kinetic study on corrosion of steel in soil environments using electrical resistance sensor', *Materials, Chemistry and Physics*, **103**(1), 2007: pp. 9-13

21. LEGAT, A., 'Monitoring of steel corrosion in concrete by electrode arrays and electrical resistance probes', *Electrochemica Acta*, **52**(27), 2007: pp. 7590-8

22. ZHENG, Z.P. & Y. SONG, 'Physical based techniques for monitoring corrosion in RC', *Applied Mechanics and Materials*, **501-4**(4), 2014: pp. 881-4

23. TAVEIRA, L. V., A. A. SAGÜÉS, J. LOPEZ-SABANDO & B. JOSEPH, 'Detection of corrosion of post-tensioned strands on grouted assemblies', in *Corrosion 2008, 16-20 March, New Orleans, Louisiana, Paper 08398*, Houston, NACE International, 2008: pp.1-19

24. ŽIVICA, V., 'Utilisation of electrical resistance method for the evaluation of the state of steel reinforcement in concrete and the rate of its corrosion', *Construction and Building Materials*, **14**(6-7), 2000, pp. 351-8

25. YANG, I., X. SUN, & F. STEWARD, 'An on-line electrical resistance corrosion monitor for studying flow assisted corrosion of carbon steel under high-temperature and high-pressure conditions', in *Corrosion/1999 NACE conference papers, Paper 459*, Houston, NACE International, 1999: pp. 1-6

26. JEVREMOVIĆ, I, V. MIŠKOVIĆ-STANKOVIĆ, M. ACHOUR, M. SINGER & S. NEŠIĆ, 'Evaluation of a Novel Top-of-the-Line (TLC) Mitigation Method in a Large Scale Flow Loop', *Corrosion 2013, 17-21 March, Orlando, Florida*, Houston, NACE International, 2013

27. BIERI, T. H., D. HORSUP, M. READING & R. C. WOOLLAM, 'Corrosion inhibitor screening using rapid response corrosion monitoring', in *Corrosion 2006, March 12-16, 2006, SanDiego, California*, Paper 06692, Houston, NACE International, 2006

28. WEIMER, P. J., M. J. VAN KAVELAAR, C. B. MICHEL & T. K. NG, 'Effect of Phosphate on the Corrosion of Carbon Steel and on the Composition of Corrosion Products in Two-Stage Continuous Cultures of Desulfovibrio desulfuricans', *Applied and Environmental Microbiology*, **54**(2), 1988; pp. 386-96

29. HARDY, J. A., J. L. BOWN, 'The corrosion of mild steel by biogenic sulphide films exposed to air', *Corrosion*, **42**(), 1984: pp. 650-4

30. ISA STANDARD S.71.04-1985, 'Environmental conditions for process measurements and control system: airborne contaminants', Instrument Society of America, North Carolina, 1985

31. JOHANSSON, E. & C. LEYGRAF, 'Corrosion measurements of silver and copper in indoor atmospheres using different evaluation techniques', *British Corrosion Journal*, **34**(1), 1998: pp. 27-33

32. PROSEK, T., M. KOURIL, L. R. HILBERT, Y. DEGRES, V. BLAZEK, D. THIERRY & M. Ø. HANSEN, 'Real time corrosion monitoring in atmosphere using automated battery driven corrosion loggers', *Corrosion Engineering, Science and Technology*, **43**(2), 2008: pp. 129-33

33. PROSEK, T., D. THIERRY, M. KOURIL & Y. DEGRES, 'Automated corrosion loggers for corrosion monitoring in the atmosphere', in *Proceedings of CORROSION, NACE, Paper No. 08296, New Orleans, USA, March 16-20, 2008*, Houston, NACE International, 2008 pp. 1-6

34. SJÖGREN, L. & N. LE BOZEC, 'On-line Corrosion Monitoring of indoor atmospheres' in Corrosion of metallic heritage artefacts; Investigation, Conservation and prediction for long term behaviour, European Federation of Corrosion Publications Number 48, edited by Dillmann, P., G. Beranger, P. Picardo & H. Matthiesen, Woodhead; Cambridge, 2007: pp. 293-307

35. PROSEK, T., M. KOURIL, F. DUBOIS, B. SCHEFFEL, M. DUBUS, Y. DEGRES, V. HUBERT, M. TAUBE & D. THIERRY, 'Corrosion monitoring in model indoor atmospheres polluted with organic acids using automated real time corrosion sensors', in *Proceedings of the European Workshop on Cultural Heritage Preservation, EWCHP 2011, Berlin, Germany, September 26-28,* Fraunhofer IRB Verlag, 2011.

36. KOURIL, M., T. PROSEK, B. SCHEFFEL & F. DUBOIS, 'High sensitivity electrical resistance sensors for indoor corrosion monitoring', *Corrosion Engineering, Science and Technology*, **48**(4), 2013: pp. 282-7

37. DUBUS, M. & T. PROSEK, 'Standardized assessment of cultural heritage environments by electrical resistance measurements', *e-preservation science*, **9**, 2012: pp. 67-71

38. KOURIL, M., T. PROSEK, B. SCHEFFEL & Y. DEGRES, 'Corrosion monitoring in archives by the electrical resistance tecchnique', *Journal of Cultural Heritage*, In Press

39. PROSEK, T., M. KOURIL, M. DUBUS, M. TAUBE, V. HUBERT, B. SCHEFFEL, Y. DEGRES, M. JOUANNIC & D. THIERRY, 'Real-time monitoring of indoor air corrosivity in cultural heritage institutions with metallis electrical resistance sensors', *Studies in Conservation*, **58**(2), 2013: pp. 117-28

40. MATTHIESEN, H., D. GREGORY & B. SØRENSON, 'Long-term corrosion of iron at the waterlogged site of Nydam in Denmark: studies of environment, archaeological artefacts and modern analogues' in *Corrosion of metallic heritage artefacts; Investigation, Conservation and prediction for long term behaviour, European Federation of Corrosion Publications Number 48*, edited by Dillmann, P., G. Beranger, P. Picardo & H. Matthiesen, Woodhead; Cambridge, 2007: pp. 272-92

41. MCKENZIE, M. & P. R. VASSIE, 'Use of weight loss coupons and electrical resistance probes in atmospheric corrosion tests', *British Corrosion Journal*, **20**(3), 1985: pp. 117-24

42. KAPATOU, E., *Development of an Electrical Resistance Monitor on the Corrosivity Assessment of Museum Environments for Iron*, Manchester, University of Manchester, 2010

43. TSURU, T., K. I. TAMIVA & A. NISHIKATA, 'Formation and growth of micro-droplets during the initial stage of atmospheric corrosion', *Electrochemica Acta*, **49**(17-18), 2004: pp. 2709-15

44. TSUTSUMI, Y., A. NISHIKATA & T. TSURU, 'Pitting corrosion mechanism of Type 304 stainless steel under a droplet of chloride solutions', *Corrosion Science*, **49**(3), 2007: pp. 1394-1407

45. DUBUISSON, E., P. LAVIE, F. DALARD, J. P. CLAIRE & S. SZUNERITS, 'Study of the atmospheric corrosion of galvanised steel in a micrometric electrolytic droplet', *Electrochemistry Communications*, **8**(6), 2006: pp. 911-5

46. DUBUISSON, E., P. LAVIE, F. DALARD, J. P. CLAIRE & S. SZUNERITS, 'Corrosion of galvanised steel under an electrolytic drop', *Corrosion Science*, **49**(), 2007: pp. 910-9

47. ZHANG, J., J. WANG & Y. WANG, 'Micro-Droplets Formation During the Deeliquescence of Salt Particles in Atmosphere', *Corrosion*, **61**(12), 2005: pp. 1167-72

48. CHEN, Z. Y., S. ZAKIPOUR, D. PERSSON & C. LEYGRAF, 'Effect of sodium chloride particles on the atmospheric corrosion of pure copper', *Corrosion*, **60**(5), 2004: pp. 479-91

49. LOBNIG, R., J. D. SINCLAIR, M. UNGER & M. STRATMANN, 'Mechanism of Atmospheric Corrosion of Copper in the Presence of Ammonium sulphate Particles', *Journal of Electrochemical Society*, **150**(6), 2003: pp. A835-49

50. COLE, I. S., D. LAU & D.A. PATERSON, 'Holistic model for atmospheric corrosion – part 6 – From wet aerosol to salt deposit', *Corrosion Engineering, Science and Technology*, **39**(3), 2004: pp. 209-18

51. LI, S. X. & L. H. HIHARA, 'Atmospheric corrosion initiation on steel from predeposited NaCl salt particles in high humidity atmospheres', *Corrosion Engineering, Science and Technology*, **45**(1), 2010: pp. 49-56

52. CHUNG, J. W., S.W. KO, N.R. BIERI, C.P. GRIGOROPOULOS & D. POULIKAKOS, 'Conductor microstructures by laser curing of printed gold nanoparticle ink', *Applied Physics Letters*, **84**, 2004: pp. 801–803.

53. LEE, H. H., K. S. CHOU & K.C. HUANG, 'Inkjet printing of nanosized silver colloids', *Nanotechnology*, **16**, 2005: pp. 2436–2441.

54. HASTUTY, S., A. NISHIKATA & T. TSURU, 'Pitting corrosion of Type 430 stainless steel under chloride solution droplet', *Corrosion Science*, **52**, 2010: pp. 2035–2043.

55. CROUCHER, M.D. & M.L. HAIR, 'Design criteria and future-directions in inkjet ink technology', *Industrial & Engineering Chemistry Research*, **28**, 1989: pp. 1712–1718.

56. SCHINDELHOLZ, E. & R. G. KELLY, 'Application of Inkjet Printing for Depositing Salt Prior to Atmospheric Corrosion Testing', *Electrochemical and Solid State Letters*, **13**(10), 2010: pp. C29-C31

57. MI, N., M. GHAHARI, T. RAYMENT & A. J. DAVENPORT, 'Use of inkjet printing to deposit magnesium chloride salt patterns for investigation of atmospheric corrosion of 304 stainless steel', *Corrosion Science*, **53**, 2011: pp.3114-3121

## Chapter 6: Experimental Materials and Methodology


1. CAI, J. –P. & S. B. LYON, 'A mechanistic study of initial atmospheric corrosion kinetics using electrical resistance sensors', *Corrosion Science*, **47**(12), 2005: pp. 2956-73

2. KAPATOU, E. & S. B. LYON, 'An Electrical Resistance Monitor Study of the Post-Excavation Corrosion of Archaeological Iron' in *Art2008: 9th International Conference on Non-Destructive Testing of Art, Jerusalem, Israel, 25-30 May 2008, 2008: pp.25-30*

3. KAPATOU, E., *Development of an Electrical Resistance Monitor on the Corrosivity Assessment of Museum Environments for Iron*, Manchester, University of Manchester, 2010

4. PROSEK, T., M. KOURIL, L. R. HILBERT, Y. DEGRES, V. BLAZEK, D. THIERRY & M. Ø. HANSEN, 'Real time corrosion monitoring in atmosphere using automated battery driven corrosion loggers', *Corrosion Engineering, Science and Technology*, **43**(2), 2008: pp. 129-33

5. PROSEK, T., D. THIERRY, M. KOURIL & Y. DEGRES, 'Automated corrosion loggers for corrosion monitoring in the atmosphere', in *Proceedings of CORROSION, NACE, Paper No. 08296, New Orleans, USA, March 16-20, 2008*, Houston, NACE International, 2008 pp. 1-6

6. DR ZHU LIU and Postdoctoral Research assistant WEI GUO, School of Materials, University of Manchester, Personal correspondence, 14/09/2011

7. WASA, K. & S. HAYAKAWA, *Handbook of Sputter deposition technology: principles, technology and applications*, New Jersey, Noyes Publications, 1992

8. SINGH, J. & D. E. WOLFE, 'Review Nano and macro-structured component fabrication by electron beam-physical vapour deposition (EB-PVD)', *Journal of Materials Science*, **40**(1), 2005: pp. 1-26

9. SCHILLER, S., CHR. METZNER & O. ZYWITZKI, 'New coatings on metal sheets produced using EB PVD technologies'*, Surface and Coatings technology*, **125**(1-3), 2000: pp. 240-5

10. KRUTH, J. P., L. FROYEN, J. VAN VAERENBERGH, P. MERCELIS, M. ROMBOUTS & B. LAUWERS, 'Selective laser melting of iron-based powder', *Journal of Materials Processing Technology*, **149**(1-3), 2004: pp. 616-22

11. IVERSON, A., J. POWELL, J. KAMALU & C. MAGNUSSON, 'The oxidation dynamics of laser cutting of mild steel and the generation of striations on the cut edge', *Journal of Materials Processing Technology,* **40**(3-4), 1994, pp. 359-74

12. NAGESWARA RAO, P. & D. KUNZRU, 'Fabrication of microchannels on stainless steel by wet chemical etching', *Journal of Micromechanics and Microengineering*, **17**(12), 2007: pp. N99-N106

13. ALLEN, D. M. & H. J. A. ALMOND, 'Characterisation of aqueous ferric chloride etchants used in photochemical machining', *Journal of Materials Processing Technology*, **149**(1-3), 2004: pp. 238-45

14. ALLEN, D. M. & L. T. LER, 'Increasing utilisation efficiency of ferric chloride etchant in industrial photochemical machining', *Journal of Environmental Monitoring*, **1**, 1999: pp. 103-8

15. TSURU, T., K. I. TAMIVA & A. NISHIKATA, 'Formation and growth of micro-droplets during the initial stage of atmospheric corrosion', *Electrochemica Acta*, **49**(17-18), 2004: pp. 2709-15

16. TSUTSUMI, Y., A. NISHIKATA & T. TSURU, 'Pitting corrosion mechanism of Type 304 stainless steel under a droplet of chloride solutions', *Corrosion Science*, **49**(3), 2007: pp. 1394-1407

17. DUBUISSON, E., P. LAVIE, F. DALARD, J. P. CLAIRE & S. SZUNERITS, 'Study of the atmospheric corrosion of galvanised steel in a micrometric electrolytic droplet', *Electrochemistry Communications*, **8**(6), 2006: pp. 911-5

18. DUBUISSON, E., P. LAVIE, F. DALARD, J. P. CLAIRE & S. SZUNERITS, 'Corrosion of galvanised steel under an electrolytic drop', *Corrosion Science*, **49**(), 2007: pp. 910-9

19. CHEN, Z. Y., S. ZAKIPOUR, D. PERSSON & C. LEYGRAF, 'Effect of sodium chloride particles on the atmospheric corrosion of pure copper', *Corrosion*, **60**(5), 2004: pp. 479-91

20. ZHANG, J., J. WANG & Y. WANG, 'Micro-Droplets Formation During the Deliquescence of Salt Particles in Atmosphere', *Corrosion*, **61**(12), 2005: pp. 1167-72

21. LOBNIG, R., J. D. SINCLAIR, M. UNGER & M. STRATMANN, 'Mechanism of Atmospheric Corrosion of Copper in the Presence of Ammonium sulphate Particles', *Journal of Electrochemical Society*, **150**(6), 2003: pp. A835-49

22. COLE, I. S., D. LAU & D.A. PATERSON, 'Holistic model for atmospheric corrosion – part 6 – From wet aerosol to salt deposit', *Corrosion Engineering, Science and Technology*, **39**(3), 2004: pp. 209-18

23. LI, S. X. & L. H. HIHARA, 'Atmospheric corrosion initiation on steel from predeposited NaCl salt particles in high humidity atmospheres', *Corrosion Engineering, Science and Technology*, **45**(1), 2010: pp. 49-56

24. SCHINDELHOLZ, E. & R. G. KELLY, 'Application of Inkjet Printing for Depositing Salt Prior to Atmospheric Corrosion Testing', *Electrochemical and Solid State Letters*, **13**(10), 2010: pp. C29-C31

25. MI, N., M. GHAHARI, T. RAYMENT & A. J. DAVENPORT, 'Use of inkjet printing to deposit magnesium chloride salt patterns for investigation of atmospheric corrosion of 304 stainless steel', *Corrosion Science*, **53**, 2011: pp.3114-3121

26. MØLLER, P., 'Evaluation of Atmospheric Corrosion on Electroplated Zinc and Zinc-Nickel Coatings by Electrical Resistance (ER) Monitoring', *NASF Surface technology white papers*, **78**(5), 2014: pp. 1-10

27. SHERWOOD SCIENTIFIC LIMITED, *Model 926 Chloride Analyser Operator's Manual*, Cambridge, Sherwood Scientific Ltd, 2011

28. GREENSPAN, L., 'Humidity fixed points of binary saturated aqueous solutions', *Journal of research of the National Bureau of Standards*, **81A**(1), 1977: pp. 89-96

29. ASTM STANDARD E104-2 , 'Standard Practice for Maintaining Constant Relative Humidity by Means of Aqueous Solutions' , *Annual book of GSTM Standards* **3**(2), West Conshohoken, PA, ASTM International, 2013: DOI: 10.1520/E0104-2R12

30. NEFF, D., L. BELLOT-GURLET, P. DILLMANN, S. REGUER & L. LEGRAND, 'Raman imaging of ancient rust scales on archaeological iron artefacts for long-term atmospheric corrosion mechanisms study', *Journal of Raman spectroscopy*, **37**(10), 2006: pp. 1228-37

31. BOUCHARD, M. & D. C. SMITH, 'Catalogue of 45 reference Raman spectra of minerals concerning research in art history or archaeology, especially on corroded metals and coloured glass', *Spectrochimica Acta Part A*, **59**(10), 2003: pp 2247-66

## Chapter 7: Experimental Results


1. NAGESWARA RAO, P. & D. KUNZRU, 'Fabrication of microchannels on stainless steel by wet chemical etching', *Journal of Micromechanics and Microengineering*, **17**(12), 2007: pp. N99-N106

2. AVNER, S. *Introduction to Physical Metallurgy*, Second edition, Mcgraw-Hill, USA, 1988

3. SCHINDELHOLZ, E. & R. G. KELLY, 'Application of Inkjet Printing for Depositing Salt Prior to Atmospheric Corrosion Testing', *Electrochemical and Solid State Letters*, **13**(10), 2010: pp. C29-C31

4. MI, N., M. GHAHARI, T. RAYMENT & A. J. DAVENPORT, 'Use of inkjet printing to deposit magnesium chloride salt patterns for investigation of atmospheric corrosion of 304 stainless steel', *Corrosion Science*, **53**, 2011: pp.3114-3121

5. DEEGAN, R. D., 'Pattern formation in drying drops', Physics Review E, **61**(1), 2000: pp. 475-85

6. COLE, I. S., D. LAU & D.A. PATERSON, 'Holistic model for atmospheric corrosion – part 6 – From wet aerosol to salt deposit', *Corrosion Engineering, /Science and Technology*, **39**(3), 2004: pp. 209-18

7. COLE, I. S., D. LAU & D.A. PATERSON, 'Holistic model for atmospheric corrosion – part 6 – From wet aerosol to salt deposit', *Corrosion Engineering, Science and Technology*, **39**(3), 2004: pp. 209-18

8. LI, S. X. & L. H. HIHARA, 'Atmospheric corrosion initiation on steel from predeposited NaCl salt particles in high humidity atmospheres', *Corrosion Engineering, Science and Technology*, **45**(1), 2010: pp. 49-56

9. KAPATOU, E. & S. B. LYON, 'An Electrical Resistance Monitor Study of the Post-Excavation Corrosion of Archaeological Iron' in *Art2008: 9th International Conference on Non-Destructive Testing of Art, Jerusalem, Israel, 25-30 May 2008, 2008: pp.25-30*

10. SCOTT, D. A. AND G. EGGERT., *Iron and Steel in Art*. London, Archetype. 2009

11. RÉGUER, S., P. DILLMANN AND F. MIRAMBET, 'Buried iron archaeological artefacts: Corrosion mechanisms related to the presence of Cl-containing phases', *Corrosion Science*, 49(6), 2007: pp. 2726-44.

12. BELLOT-GURLET, L., D. NEFF, S. REGUER, J. MONNIER, M. SAHEB & P. DILLMANN, 'Raman Studies of Corrosion Layers Formed on Archaeological Irons in various media', *Journal of Nano Research*, **8**, 2009: pp. 147-56

13. COLUMBAN, P., 'Potentials and Drawbacks of Raman (Micro)Spectrometry for the understanding of Iron and Steel Corrosion', in *New Trends and Developments in Automotive System Engineering*, M. CHIABERGE (ed). 2011, Intech

14. NEFF, D., L. BELLOT-GURLET, P. DILLMANN, S REGUER & L. LEGRAND, 'Raman imaging of ancient rust scales on archaeological iron artefacts for long term atmospheric corrosion mechanisms study', *Journal of Raman Spectroscopy*, **37**(1), 2006: pp. 1228-37

15. BOUCHARD, M. & D. C. SMITH, 'Catalogue of 45 reference Raman spectra of minerals concerning research in art history or archaeology, especially on corroded metals and coloured glass', *Spectrochemica Acta Part A*, **59**, 2003: pp. 2247-66

16. RULL-PEREZ, F. (ed), *Selected Topics in Raman Spectroscopic Applications: Geology, Biomaterials, Art.*2007, Universidad de Valladolid, Valladolid

17. CUDENNEC, Y. AND A. LECERF , 'Topotactic transformations of goethite and lepidocrocite into hematite and maghemite', *Solid State Sciences*, **7**(5), 200: pp. 520-9.

18. GARCIA, K. E., 'On the Rust Products Formed on Weathering and Carbon Steels Exposed to Chloride in Dry–Wet Cyclical Processes', *Hyperfine Interactions,* **161**(1-4), 2005: pp. 127-37.

19. NEFF, D., S. REGUER, L. BELLOT-GURLET, P. DILLMANN & R. BERTHOLON, 'Structural characterisation of corrosion products of archaeological iron. An integrated analytical approach to establish corrosion forms', Journal *of Raman Spectroscopy*, **35**, 2004: pp. 739-45

20. KAPATOU, E., *Development of an Electrical Resistance Monitor on the Corrosivity Assessment of Museum Environments for Iron*, Manchester, University of Manchester, 2010

## Chapter 8: Discussion


1. SCHINDELHOLZ, E. & R. G. KELLY, 'Application of Inkjet Printing for Depositing Salt Prior to Atmospheric Corrosion Testing', *Electrochemical and Solid State Letters*, **13**(10), 2010: pp. C29-C31

2. MI, N., M. GHAHARI, T. RAYMENT & A. J. DAVENPORT, 'Use of inkjet printing to deposit magnesium chloride salt patterns for investigation of atmospheric corrosion of 304 stainless steel', *Corrosion Science*, **53**, 2011: pp.3114-3121

3. TSURU, T., K. I. TAMIVA & A. NISHIKATA, 'Formation and growth of micro-droplets during the initial stage of atmospheric corrosion', *Electrochemica Acta*, **49**(17-18), 2004: pp. 2709-15

4. CHEN, Z. Y., S. ZAKIPOUR, D. PERSSON & C. LEYGRAF, 'Effect of sodium chloride particles on the atmospheric corrosion of pure copper', *Corrosion*, **60**(5), 2004: pp. 479-91

5. CAI, J. –P. & S. B. LYON, 'A mechanistic study of initial atmospheric corrosion kinetics using electrical resistance sensors', *Corrosion Science*, **47**(12), 2005: pp. 2956-73

6. TSUTSUMI, Y., A. NISHIKATA & T. TSURU, 'Pitting corrosion mechanism of Type 304 stainless steel under a droplet of chloride solutions', *Corrosion Science*, **49**(3), 2007: pp. 1394-1407

7. COLE, I. S., D. LAU & D.A. PATERSON, 'Holistic model for atmospheric corrosion – part 6 – From wet aerosol to salt deposit', *Corrosion Engineering, Science and Technology*, **39**(3), 2004: pp. 209-18

8. ZHANG, J., J. WANG & Y. WANG, 'Micro-Droplets Formation During the Deeliquescence of Salt Particles in Atmosphere', *Corrosion*, **61**(12), 2005: pp. 1167-72

9. LI, S. X. & L. H. HIHARA, 'Atmospheric corrosion initiation on steel from predeposited NaCl salt particles in high humidity atmospheres', *Corrosion Engineering, Science and Technology*, **45**(1), 2010: pp. 49-56

10. LOBNIG, R., J. D. SINCLAIR, M. UNGER & M. STRATMANN, 'Mechanism of Atmospheric Corrosion of Copper in the Presence of Ammonium sulphate Particles', *Journal of Electrochemical Society*, **150**(6), 2003: pp. A835-49

11. SCOTT, D. A. AND G. EGGERT., *Iron and Steel in Art*. London, Archetype. 2009

12. KAPATOU, E. & S. B. LYON, 'An Electrical Resistance Monitor Study of the Post-Excavation Corrosion of Archaeological Iron' in *Art2008: 9th International Conference on Non-Destructive Testing of Art, Jerusalem, Israel, 25-30 May 2008, 2008: pp.25-30*

13. MØLLER, P., 'Evaluation of Atmospheric Corrosion on Electroplated Zinc and Zinc-Nickel Coatings by Electrical Resistance (ER) Monitoring', *NASF Surface technology white papers*, **78**(5), 2014: pp. 1-10

14. RÉGUER, S., P. DILLMANN AND F. MIRAMBET, 'Buried iron archaeological artefacts: Corrosion mechanisms related to the presence of Cl-containing phases', *Corrosion Science*, 49(6), 2007: pp. 2726-44.

15. GUILMINOT, E., D. NEFF, C. REMAZEILLES, S. REGUER, F. KERGOURLAY, C. PELE, P. DILLMANN, P. REFAIT, F. NICOT, F. MIELCAREK, N. HUET & J. REBIERE, 'Influence of crucial parameters on the dechlorination treatments of ferrous objects from seawater', *Studies in Conservation*, **57**(4), 2012:pp. 227- 36

16. REMAZEILLES, C. & P. REFAIT, 'On the formation of β-FeOOH (akaganeite) in chloride-containing environments', *Corrosion Science*, **49**, 2007: pp. 844-57

17. KAESCHE, H., *Corrosion of Metals: Physiochemical Principles and Current Problems*, New York, Springer-Verlag, 2003

18. THICKETT, D., *Post Excavation Changes and Preventative Conservation of Archaeological Iron*, Birkbeck College, London, 2012

19. COX, A. & S. B. LYON, 'An electrochemical study of the atmospheric corrosion of iron- II. Cathodic and anodic processes on uncorroded and pre-corroded iron', *Corrosion Science*, **36**(7), 1994: pp.1177-92

20. KAPATOU, E., *Development of an Electrical Resistance Monitor on the Corrosivity Assessment of Museum Environments for Iron*, Manchester, University of Manchester, 2010

21. AMBLER, H. R., & A. A. J. BAIN, 'Corrosion of metals in the tropics', *Journal of Chemical technology and Biotechnology*, 5(9), 1955; pp. 437-67

22. DE LA FUENTE, D., I. DÍAZ, J. SIMANCAS, B. CHICO & M. MORCILLO, 'Long-term atmospheric corrosion of mild steel', *Corrosion Science*, **53**(2), 2011, pp. 604-17

23. MATTSSON, E., 'The atmospheric corrosion properties of some common structural metals- a comparative study', *Materials performance*, **21**(7), 1982; pp. 9-19

24. CROOME, H. L., 'Corrosion rate of cannon at the Prince of Wales' fort' in *Metal 2004: proceedings of the International Conference on Metals Conservation, Canberra, Australia 4-8 October 2004*, Edited by Ashton, J. & D. Hallam, National museum of Australia, Canberra, 2004; pp. 195-206

25. MACLEOD, K. J., *Relative Humidity: Its Importance, Measurement and Control in Museums, Technical bulletin 1*, Ottowa, Canadian Conservation Institute and the National Museums of Canada, 1975

26. POURBAIX, M., 'The linear bilogarithmic law for atmospheric corrosion' in AILOR, W. H. (ed) *Atmospheric corrosion*, London, Wiley, 1982; pp. 107-21

27. LEGAULT, R. A. & A. G. PREBAN, 'Kinetics of the Atmopsheric Corrosion of Low-Alloy Steels in an Industrial Environment', *Corrosion*, **31**(4), 1975; pp 117-22

28. ZHANG, Q. C., J. S. WU, J. J. WANG, W. L. ZHENG, J.G. CHEN & A. B. LI, 'Corrosion behaviour of weathering steel in a marine atmosphere', *Materials, Chemistry and Physics*, **77**(2), 2003; pp. 603-608

29. DILLMAN, PH., F. MAZAUDIER & S. HŒRLÉ, 'Advances in understanding atmospheric corrosion of iron. I. Rust characterisation of ancient ferrous artefact exposed to indoor atmospheric corrosion', *Corrosion Science*, **46**(6), 2004: pp. 1401-29

30. TURGOOSE, S., 'Post-Excavation Changes in Iron Antiquities', *Studies in Conservation*, 27(3), 1982: pp. 97-101

31. WATKINSON, D. & RIMMER, *As yet untitled article*, forthcoming (Data received as a personal communication, 19th November 2014)

32. SCHMIDT-OTT, K. AND V. BOISSONAS, '"Low-pressure hydrogen plasma: An assessment of its application on archaeological iron', *Studies in Conservation*, **47**(2), 2002, pp.81-7.

33. PROSEK, T., M. KOURIL, L. R. HILBERT, Y. DEGRES, V. BLAZEK, D. THIERRY & M. Ø. HANSEN, 'Real time corrosion monitoring in atmosphere using automated battery driven corrosion loggers', *Corrosion Engineering, Science and Technology*, **43**(2), 2008: pp. 129-33

34. PROSEK, T., D. THIERRY, M. KOURIL & Y. DEGRES, 'Automated corrosion loggers for corrosion monitoring in the atmosphere', in *Proceedings of CORROSION, NACE, Paper No. 08296, New Orleans, USA, March 16-20, 2008*, Houston, NACE International, 2008 pp. 1-6

35. SJÖGREN, L. & N. LE BOZEC, 'On-line Corrosion Monitoring of indoor atmospheres' in Corrosion of metallic heritage artefacts; Investigation, Conservation and prediction for long term behaviour, European Federation of Corrosion Publications Number 48, edited by Dillmann, P., G. Beranger, P. Picardo & H. Matthiesen, Woodhead; Cambridge, 2007: pp. 293-307

36. INTERNATIONAL ORGANIZATION FOR STANDARDIZATION, ISO 118844-2 *Corrosion of Metal and alloys. Classification of low corrosivity of indoor atmospheres- Part 1: Determination of corrosion attack in indoor atmospheres*, International Organization for standardization, Geneva, 2005

37. MØLLER, P., 'Evaluation of Atmospheric Corrosion on Electroplated Zinc and Zinc-Nickel Coatings by Electrical Resistance (ER) Monitoring', *NASF Surface technology white papers*, **78**(5), 2014: pp. 1-10

38. KHAN, N. A., 'Using Coupons and ER Soil Corrosion Probes in Applying Pipeline CP Criteria', *Materials Performance*, **46**(4), 2007: pp. 26-30

39. ŽIVICA, V., 'Utilisation of electrical resistance method for the evaluation of the state of steel reinforcement in concrete and the rate of its corrosion', *Construction and Building Materials*, **14**(6-7), 2000, pp. 351-8

40. YANG, I., X. SUN, & F. STEWARD, 'An on-line electrical resistance corrosion monitor for studying flow assisted corrosion of carbon steel under high-temperature and high-pressure conditions', in *Corrosion/1999 NACE conference papers, Paper 459*, Houston, NACE International, 1999: pp. 1-6

41. DUBUS, M. & T. PROSEK, 'Standardized assessment of cultural heritage environments by electrical resistance measurements', *e-preservation science*, **9**, 2012: pp. 67-71

42. MCKENZIE, M. & P. R. VASSIE, 'Use of weight loss coupons and electrical resistance probes in atmospheric corrosion tests', *British Corrosion Journal*, **20**(3), 1985: pp. 117-24

43. RIMMER, M., D. WATKINSON & Q. WANG, 'The impact of chloride desalination on the corrosion rate of archaeological iron', *Studies in Conservation*, **58**(4), 2013: pp. 326-37

44. THICKETT, D., S. LAMBARTH & P. WYETH, 'Determining the stability and durability of archaeological materials', in *9h International Conference on Non-Destructive Testing of Art, Jerusalem, Isreal, 25-30 May 2008*, [Accessed 3 December 2012]: Available at http://www.ndt.net/article/art2008/papers/024Thickett.pdf

45. MATTHIESEN, H. & K. WONSYLD, 'In situ measurement of oxygen consumption to estimate corrosion rates', *Corrosion Engineering, Science and Technology*, **45**(5), 2010: pp. 350-6

46. ROUX, S., J. RÉTHORÉ & F HILD, 'Digital image correlation and fracture: an advanced technique for estimating stress intensity factors of 2D and 3D cracks', *Journal of Physics D: Applied Physics*, 42(21), 2009: pp. 1-37

47. EDELATI, K., N. RASTKHAH, A. KERMANI, M. SEIEDI & A. MOVEFEGHI, 'The use of radiography for thickness measurement and corrosion monitoring in pipes', *International Journal of Pressure Vessels and Piping*, **83**(10), 2006: pp. 736-41

48. PONS, E., C. LEMAITRE & D. DAVID, 'Electrochemical study of steel artefacts from World War I: Contribution of A.C. impedance spectroscopy and chronoamperometry to describe the behaviour of the corrosion layers', in *Corrosion of metallic heritage artefacts; Investigation, Conservation and prediction for long term behaviour, European Federation of Corrosion Publications Number 48*, edited by Dillmann, P., G. Beranger, P. Picardo & H. Matthiesen, Woodhead; Cambridge, 2007: pp. 77-91

49. DEGRIGNY, C., 'Use of electrochemical techniques for the conservation of metal artefacts: a review', *Journal of Solid State Electrochemistry*, **14**(3), 2010: pp. 353-61

50. CARULLO, A., F. FERRARIS, M. PARVIS, A. VALLAN, E. ANGELINI & P. SPINELLI, 'Low-Cost Electrochemical Impedance Spectroscopy System of Corrosion Monitoring of Metallic Antiquities and Works of Art', *IEEE Transactions on Instrumentation and measurement*, **49**(2), 2000: pp. 371-6

51. GRASSINI, S., E. ANGELINI, M. PARVIS, M. BOUCHAR, P. DILLMANN & D. NEFF, 'An in situ corrosion study of Middle Ages wrought iron bar chains in the Amiens Cathedral', *Applied Physics A: Materials, Science and Processing,* **113**(4), 2013: pp. 971-9

52. ANGELINI, E., S. GRASSINI, S. CORBELLINI, G. M. INGO, T. DE CARO, P. PLESCIA, C. RICCUCCI, A. BIANCO & S. AGOSTINI, ' Potentialities of XRF and EIS portable instruments for the characterisation of ancient artefacts', *Applied Physics A: Materials Science and Processing*, **83**(4), 2006: pp 643-9

53. MUDALI, U. K. & B. RAJ, 'Insitu corrosion investigations on Delhi iron pillar', *Transactions of The Indian Institute of Metals*, **62**(1), 2009: pp. 25-33

54. CORBELLINI, S., M. PARVIS & S. GRASSINI, 'Noninvasive Solution for Electrochemical Impedance Spectroscopy on Metallic Works of Art', *IEEE Transactions on Instrumentation and Measurement*, **63**(5), 2012: pp. 1193-200

55. BACCI, M., C. CUCCI, A. A. MENCAGLIA & A. G. MIGNANI, 'Innovative Sensors for Environmental Monitoring in Museums', *Sensors*, **8**(3), 2008: pp. 1985-2005

56. ZHANG, S. H. & S. B. LYON, 'The electrochemistry of iron, zinc and copper in thin layer electrolytes', *Corrosion science*, **35**(8), 1993: pp. 713-8

57. FU, X., J. DONG, E. HAN & W. KE, 'A New Experimental method for in situ Corrosion Monitoring under Alternate Wet-Dry Conditions', *Sensors*, **9**(12), 2009: pp. 10400-10

58. THEE, C., L. HAO, J. DONG, X. MU, W. WEI, X. LI & W. KE, 'Atmospheric corrosion monitoring of a weathering steel under an electrolyte film in cyclic wet-dry condition', *Corrosion science*, **78**, 2014: pp. 130-7

59. KOURIL, M., T. PROSEK, B. SCHEFFEL & F. DUBOIS, 'High sensitivity electrical resistance sensors for indoor corrosion monitoring', *Corrosion Engineering, Science and Technology*, **48**(4), 2013: pp. 282-7

60. ZAKIPOUR, S. & C. LEYGRAF, 'Quartz crystal microbalance applied to studies of atmospheric corrosion of metals', *British Corrosion Journal*, 1992, **27**(4): pp. 295-8

61. ACCARDO, G., C. CANEVA & S. MASSA, 'Stress monitoring by temperature mapping and acoustic emission analysis: A case study of Marcus Aurelius', *Studies in Conservation*, **28**(2), 1983: pp. 67.74

62. MACLEOD, I. D., D. COOK & E. SCHINDELHOLZ, Corrosion and Conservation of the American civil war ironclad USS Monitor (1862), in *ICOM-CC Preprints, 15th Triennial meeting, New Delhi, 22-2, September 2008*, edited by E. Hermens & J. Townsend, London, Archetype Press Ltd, 2009: pp 279-85

## Chapter 9: Conclusions

-